TRANSACTIONS
OF THE ASME
Series E

Journal of APPLIED MECHANICS

December 1961

DYNAMICS • VIBRATIONS • ELASTICITY • LUBRICATION AND WEAR
RHEOLOGY • FRACTURES • STRUCTURES • HYDRAULICS • AERODYNAMICS
INTERNAL FLOW • MECHANICAL PROPERTIES OF METALS • THERMODYNAMICS
TURBULENCE • HEAT TRANSFER • COMPUTING DEVICES AND METHODS
BOUNDARY LAYERS • AEROELASTICITY • EXPERIMENTAL STRESS ANALYSIS

Published Quarterly by
THE AMERICAN SOCIETY OF MECHANICAL ENGINEERS

TRANSACTIONS
OF THE ASME
Series E

EDITORIAL DEPARTMENT

Editor, J. J. JAKLITSCH, JR.
Consulting Editor, LEO BLOCKETT
Art Editor, HENRY BALFOUR
Production, NILDA K. WILBUR

APPLIED MECHANICS DIVISION

Chairman, A. M. WAHL
Secretary, E. REISSNER
Technical Editor, H. C. BRUCKER
Technical Editor, J. KESTIN

OFFICERS OF THE ASME

President, W. H. BYRNE
Secretary, O. B. SCHIER, II
Treasurer, E. J. KATES
Assistant Treasurer, H. J. BAUER

PUBLICATIONS COMMITTEE

Chairman, HEWLEY H. BLACKBURN
MARTIN GOLAND
VITO L. SALERNO
F. J. HEINZE
R. E. DERBY

Junior Representatives
J. W. FOLLANSBEE
STEWART H. ROSS

REGIONAL ADVISORY BOARD

Region I, H. H. ROGERS, JR.
Region II, ROBERT E. ABBOTT
Region III, A. F. BOCHENEK
Region IV, FRANCIS C. SMITH
Region V, WM. J. TITZEL
Region VI, C. K. EARLE
Region VII, RALPH L. SCORAH
Region VIII, G. CORRY McDONALD
Region IX, M. S. UNRENHAUER
Region X, CARL J. ECKHARDT

Published quarterly by The American Society of Mechanical Engineers. Publication office at 20th and Northampton Streets, Easton, Pa. The editorial Department is at ASME headquarters, United Engineering Center, 345 East 47th Street, New York 17, N. Y. Cable address, "Mechanover," New York. Price $3.00 a copy, $10.00 annually; to members, $1.50 a copy, $6.00 annually. Add 50 cents for postage to all countries outside the United States and Canada. Changes of address must be received at Society headquarters seven weeks before they are to be effective on the mailing list. Please send old as well as new address. . . . By-Laws: The Society shall not be responsible for statements or opinions advanced in papers or . . . printed in its publications (B13, Par. 4). . . . Second-Class mail privileges authorized at Easton, Penna. . . . This publication is authorized to be mailed at the special rates of postage prescribed by Section 132.122. . . . © Copyrighted, 1961, by The American Society of Mechanical Engineers. Reprints from this publication may be made on condition that full credit be given the Transactions of the ASME, Series E—Journal of Applied Mechanics, and the author, and that date of publication be stated.

TRANSACTIONS OF THE ASME
is indexed by the Engineering Index, Inc.

Journal of APPLIED MECHANICS

VOLUME 28 • SERIES E • NUMBER 4

December 1961

CONTENTS

TECHNICAL PAPERS

481 **Linearized Transonic Flow About Slender Bodies at Zero Angle of Attack** (61—APMW-12)
P. F. Maeder and H. U. Thommen

491 **Surface Oscillations of a Rotating Liquid**
J. W. Miles and B. A. Troesch

497 **Theoretical Pressure Distribution in Journal Bearings** (61—APM-20)
Kichiye Habata

507 **An Approximate Analytical Solution for the Stepped Bearing** (61—APMW-11)
C. F. Kettleborough

511 **Torque and Cavitation Characteristics of Butterfly Valves** (60—WA-105)
Turgut Sarpkaya

519 **Permanent Periodic Surface Deformations Due to a Traveling Jet** (61—APMW-6)
G. R. Abrahamson

529 **Elastic-Plastic Design of Rectangular Pressure Tubing** (61—APMW-8)
R. D. Gauthier and E. E. Weibel

535 **Gas-Lubricated Cylindrical Journal Bearings of the Finite Length—Static Loading** (61—APM-17)
B. Sternlicht

544 **Theory of Stress Concentration for Shear-Strained Prismatical Bodies With Arbitrary Nonlinear Stress-Strain Law**
H. Neuber

551 **On a Restricted Class of Coupled Hill's Equations and Some Applications** (61—WA-7)
C. S. Hsu

557 **A Numerical Solution of the Nonlinear Equations for Axisymmetric Bending of Shallow Spherical Shells**
G. A. Thurston

563 **Transient Response of a Dynamic System Under Random Excitation** (61—APMW-20
T. K. Caughey and H. J. Stumpf

567 **On the Stability of Rotation of a Rotor With Rotationally Unsymmetric Inertia and Stiffness Properties**
S. H. Crandall and P. J. Brosens

571 **Torsional Vibrations of Shells of Revolution** (61—WA-6)
H. Garnet, M. A. Goldberg, and V. L. Salerno

574 **Dynamics of Nonholonomic Systems** (61—APMW-9)
T. R. Kane

579 **The Effect of Rotatory Inertia and of Shear Deformation on the Frequency and Normal Mode Equations of Uniform Beams With Simple End Conditions** (61—APM-25)
T. C. Huang

585 **Analysis for Calculating Lateral Vibration Characteristics of Rotating Systems With Any Number of Flexible Supports. Part 1—The Method of Analysis** (61—APMW-16A)
E. C. Koenig

591 **Analysis for Calculating Lateral Vibration Characteristics of Rotating Systems With Any Number of Flexible Supports. Part 2—Application of the Method of Analysis** (61—APMW-16B)
T. G. Guenther and D. C. Lovejoy

(Continued on inside back cover)

P. F. MAEDER
Professor,
Division of Engineering,
Brown University,
Providence, R. I.
Mem. ASME

H. U. THOMMEN[2]
Design Specialist,
Convair Division,
General Dynamics Corporation,
San Diego, Calif.

Linearized Transonic Flow About Slender Bodies at Zero Angle of Attack[1]

The simple linearized transonic flow theory as originally proposed by Oswatitsch and Keune [1][3] and by the present authors [2] is improved by considering and partially correcting its error. In this manner a theory which is easy to apply and which should be valid for a great number of smooth bodies is obtained. This improved theory predicts shock waves in the lower transonic regions. It is applied to a number of significant body and airfoil shapes and its predictions are compared with experiments and results of other theoretical investigations.

1 Introduction

The basic equations governing transonic potential flow over slender bodies are well established. Owing to their nonlinearity, however, analytical treatment is possible only in a few special cases. Several authors have therefore sought approximate solutions. Oswatitsch and Keune [1] considered the sonic flow over the front part of a half-body of revolution. They linearized the potential equation by assuming a linear variation of the longitudinal perturbation velocity $u = \varphi_x$, i.e., they assumed u_x constant in the nonlinear term of the differential equation. The resulting pressure distribution on the body agreed surprisingly well with experimental observations. The present authors [2–4] generalized this simple approach to the entire transonic Mach-number range and applied the theory to full bodies of revolution as well as two-dimensional airfoils. The results agreed favorably with experiments for the cases investigated, but as Spreiter pointed out in [5], the method failed in other cases. Spreiter proceeded by applying the same basic approximation locally (see reference [6] for résumé). This method gave very favorable agreement with experimental data, although it involves procedures that seem at present not justifiable from the mathematical or physical point of view. The application of the theory also involves considerable numerical computations.

The authors have tried to improve the original simple linearized theory by considering the error [7] and [8]. An attempt was made to minimize the error locally by varying two parameters introduced into the differential equation. These attempts, however, gave still unsatisfactory results and required considerable numerical calculations.

In this paper an alternative approach will be described. Its basic ideas were obtained from physical reasoning. In the next section, therefore, some physical properties of the flow field will be discussed. The simple results obtained in the following sections were also derived in a different manner by Hosokawa [9].[4]

2 Some Properties of the Transonic Flow Field

In order to describe the transonic flow field we assume a slender airfoil moving in the direction of the negative x-axis in air at rest, Fig. 1. Every point of the airfoil surface emits signals in

[1] This work was sponsored by the United States Air Force through the Office of Scientific Research of the Air Research and Development Command under Contract AF 49(638)-444.

[2] Formerly Assistant Professor of Engineering, Brown University.

[3] Numbers in brackets designate References at end of paper.

Presented at the West Coast Conference of the Applied Mechanics Division, Seattle, Wash., August 28–30, 1961, of THE AMERICAN SOCIETY OF MECHANICAL ENGINEERS.

Discussion of this paper should be addressed to the Editorial Department, ASME, United Engineering Center, 345 East 47th Street, New York 17, N. Y., and will be accepted until January 10, 1962. Discussion received after the closing date will be returned. Manuscript received by ASME Applied Mechanics Division, October 14, 1960. Paper No. 61—APMW-12.

[4] Hosokawa's paper was received during the preparation of this paper. It was felt, however, that there was sufficient difference in reasoning to present it.

Nomenclature

A = cross-sectional area
C_D = drag coefficient
C_p = pressure coefficient
G = kernel function
I_n = modified Bessel function of order n, 1st kind
K_n = modified Bessel function of order n, 3rd kind
$\mathbf{M}$ = Mach number
P = surface point
S = dimensionless cross-sectional area
h = lateral distance from airfoil
a = sonic velocity
$\mathbf{c}$ = velocity
g = generating function
$\mathbf{i}, \mathbf{j}, \mathbf{k}$ = unit vectors
r = body radius, radial co-ordinate
u, v, w = velocity components
x, y, z = Cartesian co-ordinates
$\beta = (1 - \mathbf{M}_\infty^2)^{1/2}$
$\Gamma = (\kappa + 1)\mathbf{M}_\infty^2$
ϵ = small quantity
ξ, η, ζ = auxiliary Cartesian co-ordinates
Θ = dimensionless stream density
θ = perturbation, dimensionless stream density
κ = ratio of specific heats
ρ = density
φ = perturbation potential
τ = time, thickness ratio
δ = unit impulse function

Subscripts

1, 2, 3 = components in x, y, z-directions, respectively
x, y, z = derivatives with respect to co-ordinates, respectively
ξ, η, ζ = derivatives with respect to co-ordinates, respectively
∞ = free-stream conditions

Superscripts

* = critical values ($M = M^* = 1$)
$'$ = derivative

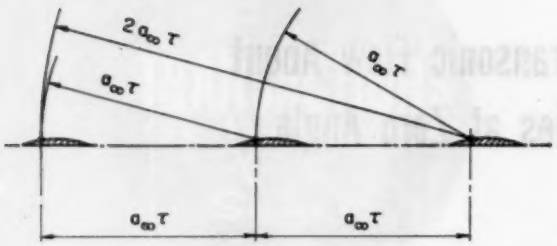

Fig. 1 Transonic flow field

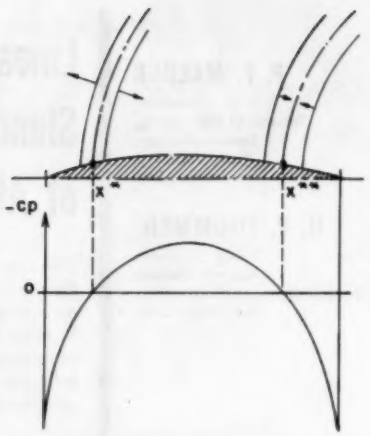

Fig. 2 Transonic flow field

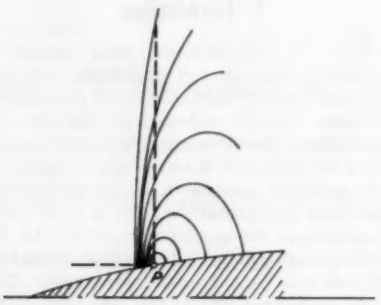

Fig. 3 Sonic flow field

the form of acoustic disturbances which propagate with the velocity of sound through the air. If we assume that the propagation velocity is the same, a_∞, at every point in the air, a situation as indicated in Fig. 1 will ensue. If the airfoil velocity $u_\infty < a_\infty$, the signals will travel freely in all directions. If the airfoil velocity is increased to the propagation velocity a_∞, the signals move freely only in the downstream direction but travel with the airfoil in the upstream direction. Thus the pressure disturbances accumulate on the airfoil surface and, in the absence of dissipative effects, the pressures on the airfoil become infinite.

The assumption of constant speed of propagation, which gives good results at subsonic speeds (linearized subsonic theory) has to be dropped at transonic speeds. At purely supersonic speeds, the same assumption again leads to good approximations (linearized supersonic theory).

Consider now the airfoil originally at rest and accelerated rapidly to the propagation velocity a_∞ in the undisturbed air. Assuming in the first instance uniform propagation velocity in the air, a pressure distribution as indicated in Fig. 2 will be built up on the airfoil. Subsequently, emitted signals will, however, propagate at slightly different speeds. In the high-pressure region near the leading edge, the propagation velocity $a > a_\infty$, in the low-pressure region in the middle of the airfoil $a < a_\infty$. Thus the disturbances travel relative to the airfoil surface, except at one point, the sonic point. Since the signals move away from the forward sonic point in both directions, a continuous pressure distribution results. Near the rear sonic point, conditions are different. Here disturbances arrive from two directions as indicated in Fig. 2. They accumulate at a particular position and finally form a shock wave of finite strength. This shock wave is situated at the trailing edge if $u_\infty = a_\infty$; for lower airfoil speeds it is formed at a point ahead of the trailing edge.

If $u_\infty = a_\infty$, disturbances originating at the nose section travel ahead of the airfoil and no bow shock is formed. If the airfoil speed is increased slightly, disturbances originating at the nose section will accumulate at a position ahead of the airfoil where the propagation velocity of the signals has dropped to the speed of the airfoil. Thus a bow wave is formed, the position of which cannot yet be predicted theoretically.

Consider now the airfoil moving at sonic velocity. Fig. 3 shows the propagation of signals originating at a certain surface point P located at the nose section ahead of the sonic point. In the upstream direction, the signals move only slowly relative to the airfoil surface. Thus the flow field in front of P is governed by disturbances whose radii of curvature are large; i.e., by nearly plane waves. If is also seen that the variation of the influence of P is much larger in the x-direction than in the direction normal to the airfoil axis. In the absence of viscous dissipation, the influence of P is noticeable at very large lateral distances. If one places a flat plate parallel to the airfoil axis at some distance h of the airfoil, these signals are reflected toward the airfoil surface. Even at a large lateral distance h, a large number of signals is reflected, accounting for the well-known experimental difficulties encountered at transonic speeds.

3 Basic Transonic Equations

In this section the basic equations of transonic flow are summarized, introducing at the same time the notation used in the subsequent sections.

Let φ be the perturbation potential, such that the dimensionless velocity vector is given by

$$\frac{\mathbf{c}}{u_\infty} = \mathbf{i} + \nabla\varphi = \mathbf{i}(1 + u) + \mathbf{j}v + \mathbf{k}w$$

where $\mathbf{i}$, $\mathbf{j}$, and $\mathbf{k}$ are the unit vectors in the x, y, and z-directions, respectively. We further introduce the dimensionless stream density vector $\boldsymbol{\Theta}$ by

$$\boldsymbol{\Theta} = \frac{\rho\mathbf{c}}{\rho_\infty u_\infty} = \mathbf{i} + \boldsymbol{\theta} = \mathbf{i}(1 + \theta_1) + \mathbf{j}\theta_2 + \mathbf{k}\theta_3$$

where $\boldsymbol{\theta}$ will be called the perturbation stream density. Since $\boldsymbol{\Theta}$ and $\mathbf{c}$ are parallel we must have

$$\boldsymbol{\Theta} \times \frac{\mathbf{c}}{u_\infty} = 0$$

which reduces to

$$\theta_2 = \varphi_y \qquad \theta_3 = \varphi_z \tag{1}$$

provided quadratic perturbation terms are neglected.

The continuity equation for steady flow is:

$$\nabla \cdot \boldsymbol{\Theta} = \nabla \cdot \boldsymbol{\theta} = 0 \tag{2}$$

Introducing equation (1) and denoting the differential operator in the cross plane by

$$\nabla_0 = \mathbf{j}\frac{\partial}{\partial y} + \mathbf{k}\frac{\partial}{\partial z}$$

equation (2) reduces to

$$\theta_{1x} \equiv \theta_x = -\nabla_0^2\varphi \tag{3}$$

The subscript 1 will be omitted in the following for convenience. Thus θ means the x-component of the perturbation stream density. For small perturbations, the magnitude of $\boldsymbol{\Theta}$ is very nearly

$$\boldsymbol{\Theta} \doteq 1 + \theta$$

Assuming isentropic, isoenergetic flow, the stream density $\boldsymbol{\Theta}$ can be expressed as a function of the velocity $\mathbf{c}$. If $\boldsymbol{\Theta}$ is expanded into a Taylor series around $\varphi_x = 0$, the following expression is found for θ:

$$\theta = (1 - \mathbf{M}_\infty^2)\varphi_x - \frac{\kappa + 1}{2}\mathbf{M}_\infty^2\varphi_x^2 + \ldots$$

$$= \beta^2\varphi_x - \frac{\Gamma}{2}\varphi_x^2 + \ldots \tag{4}$$

where κ is the ratio of specific heats and β and Γ are defined by equation (4). $\mathbf{M}_\infty$ is the free-stream Mach number.

If $\mathbf{M}_\infty$ is sufficiently removed from unity, only the first term in equation (4) need be carried along, leading to the conventional linearized subsonic or supersonic theory with $\beta^2 \gtrless 0$, respectively. If $\mathbf{M}_\infty$ is close to unity, the quadratic term in equation (4) cannot be neglected since $\beta^2 \ll 1$.

According to equation (4) the stream density reaches a maximum at the sonic point where $\varphi_x = \varphi_x^*$. The critical perturbation velocity as found from equation (4) is

$$\varphi_x^* = \frac{\beta^2}{\Gamma} \tag{5}$$

and the maximum stream density becomes

$$\theta^* = \frac{\beta^4}{2\Gamma} \tag{6}$$

If equation (4) is introduced into equation (3) the nonlinear differential equation for the velocity potential is given by

$$\beta^2\varphi_{xx} + \varphi_{yy} + \varphi_{zz} = \Gamma\varphi_x\varphi_{xx} \tag{7}$$

4 Approximate Solutions

Consider the flow field in the neighborhood of the sonic line where $\varphi_x = \varphi_x^*$. Equation (7) reduces to

$$\varphi_{yy} = 0 \tag{8}$$

for the two-dimensional case and to

$$\varphi_{yy} + \varphi_{zz} = \varphi_{rr} + \frac{1}{r}\varphi_r = 0 \tag{9}$$

for the axisymmetric case ($r^2 = y^2 + z^2$).

Solutions to equations (8) and (9) are

$$\varphi(x, y) = yf(x) + g(x) \tag{10}$$

$$\varphi(x, r) = \ln r f(x) + g(x) \tag{11}$$

where $f(x)$ and $g(x)$ are arbitrary functions. The slope of the streamlines is given approximately by φ_y and φ_r, respectively. From the discussion in the preceding section, we conclude that the sonic line $x = x^*$ is nearly perpendicular to the free-stream direction in the neighborhood of the body; i.e., $x^* = \text{const}$.

The slope of the steamlines in the two-dimensional case, $\varphi_y^* = f(x^*)$, is therefore nearly constant, i.e., the streamlines close to the body are parallel along the sonic line.

In the axisymmetric case, on the other hand, the slope $\varphi_r^* = r^{-1}f(x^*)$ varies inversely proportional to the radius r.

In both cases, the slope of the streamlines at the body is given by the body geometry. This allows us to calculate the function (x) at the sonic point, giving

$$f(x^*) = \left(\frac{dy_0}{dx}\right)_{x=x^*}$$

$$= \left[\, r_0\left(\frac{dr_0}{dx}\right)\right]_{x=x^*} \tag{12}$$

where $y_0(x)$ and $r_0(x)$ denote the body surfaces.

It is informative to consider the degenerated differential equations (8) and (9) to hold in the whole flow field. They are arrived at by neglecting the quadratic term in the expansion of the stream density, equation (4), and assuming $\mathbf{M}_\infty = 1$.

According to the foregoing discussion, the streamlines in the two-dimensional case are then parallel along lines $x = \text{const}$, while their slope decreases as r in the axisymmetric case. The function $f(x)$ is then given everywhere by equation (12). The sonic line is given by $\varphi_x = 0$. By inspection of equations (10) and (11) it is seen that the sonic line must be curved and approach the position $x_\infty^* = x_1$ where $f'(x_1) = 0$; i.e., where

$$\frac{d^2y_0}{dx^2} = 0 \quad \text{and} \quad \frac{d^2r_0^2}{dx^2} = 0$$

It is immediately noted, however, that at large distances from the body φ_x becomes large except at the sonic line. Thus while equations (8) and (9) may give good approximate results in the immediate neighborhood of the body, the results far from the body are physically impossible, with the exception of a body with vanishing thickness, for which $f(x) = 0$. Thus this simple linearized approach can be used only for the zero-thickness body, notably for wings without thickness (see e.g., reference [10]).

As mentioned earlier, the stream density is a maximum at the sonic line. The perturbation velocity has to differ appreciably

from the sonic value in order to produce a noticeable change in stream density. Conversely, a small change in distance between streamlines causes large changes in velocity.

From equations (4) and (6) the deviation from the maximum stream density is found as

$$\Delta\theta = \theta^* - \theta = \frac{\Gamma}{2}(\varphi_x{}^* - \varphi_x)^2 \tag{13}$$

We now proceed to find an approximate solution for $\Delta\theta$ using the linearized theory of references [2–4]. The body will be replaced by a separate flow field in which $\nabla \cdot \rho \mathbf{c} \neq 0$; i.e., by sources and sinks. Thus equation (7) is replaced by

$$\beta^2\varphi_{xx} - \Gamma\varphi_x\varphi_{xx} + \varphi_{yy} + \varphi_{zz} = g(x, y, z) \tag{14}$$

with the generating function $g(x, y, z) \equiv 0$ outside the body. Let us consider the linear equation

$$\beta^2\varphi_{1xx} - K\varphi_{1x} + \varphi_{1yy} + \varphi_{1zz} = g(x, y, z) \tag{15}$$

Equation (15) can easily be solved by standard methods, giving

$$\varphi_1(x, y, z) = \iiint_{-\infty}^{\infty} g(\xi, \eta, \zeta)G(x - \xi, y - \eta, z - \zeta)d\xi\, d\eta\, d\zeta \tag{16}$$

where the Kernel function G (see Appendix) is a solution to the equation

$$\beta^2 G_{xx} - KG_x + G_{yy} + G_{zz} = \delta(x - \xi)\delta(y - \eta)\delta(z - \zeta) \tag{17}$$

subject to the boundary condition that G and its derivatives vanish at infinity.

In equation (17) the function δ denotes the unit impulse function which is infinite at the origin but zero elsewhere, such that

$$\int_{-\infty}^{\infty} F(\xi)\delta(x - \xi)d\xi = F(x)$$

The function G is therefore singular at $x = \xi$, $y = \eta$, $z = \zeta$. For $K = 0$ it becomes the potential of a source in linearized subsonic or supersonic flow for $\beta^2 \gtrless 0$, respectively. For $K \neq 0$, analogous solutions exist although distorted in the sense that the potential is dampened rapidly in the upstream direction but less downstream. We will refer to these singularities as transonic sources. Their potential lines resemble the sketch in Fig. 3 (see reference [3]) and, therefore, they seem to be particularly suited for the description of the transonic flow field.

If we introduce an equal term, $-K\varphi_x$, on both sides of equation (14) we obtain a modified differential equation:

$$\beta^2\varphi_{xx} - K\varphi_x + \varphi_{yy} + \varphi_{zz} = g(x, y, z) + (\Gamma\varphi_{xx} - K)\varphi_x \tag{18}$$

The solution to equation (18) can be found by standard methods, for instance with the aid of Fourier transforms [8], giving

$$\varphi(x, y, z) = \iiint_{-\infty}^{\infty} \{g(\xi, \eta, \zeta) + (\Gamma\varphi_{\xi\xi} - K)\varphi_\xi\}G(x - \xi, y - \eta, z - \zeta)d\xi\, d\eta\, d\zeta = \varphi_1(x, y, z) + \iiint_{-\infty}^{\infty} (\Gamma\varphi_{\xi\xi} - K)\varphi_\xi G d\tau \tag{19}$$

For brevity, the argument of the Kernel function will be omitted as indicated in the last equation and the notation $d\tau = d\xi\, d\eta\, d\zeta$ will be used.

Equation (19) is a nonlinear integral equation, representing the superposition of the approximate solution φ_1 and a distribution of transonic sources in the whole flow field. The generating function $g(x, y, z)$ will be chosen such that φ_1 satisfies the linearized boundary condition at the body surface; i.e.,

$$\varphi_{1y} = \frac{dy_0}{dx} \text{ (two-dimensional)}$$

$$r\varphi_{1r} = r_0\frac{dr_0}{dx} \text{ (axisymmetric)} \tag{20}$$

for bodies at zero angle of attack. For a nonzero angle of attack, an antisymmetric Kernel function can be used. This can be obtained as a solution to equation (17) if on the right-hand side $\delta(x - \zeta)$ is replaced by its derivative $\delta'(x - \zeta)$. Again the generating function g will be chosen such that the linearized boundary conditions are satisfied (see reference [8] for details).

In reference [8] an attempt was made to choose a value K locally, such that the contribution of the integral in equation (19) was presumably small compared to φ_1. The results which require a considerable amount of numerical computation were unsatisfactory. In reference [7], an alternative approach was suggested. There the flow between the blades of a straight cascade was assumed to be essentially one-dimensional. With this assumption equation (19) could be integrated in closed form for a special case, giving very favorable agreement with experimental results. In view of the discussion in Section 2, this is not surprising.

Here a similar approach will be suggested. From equation (19) we obtain after integrating by parts:

$$\varphi = \varphi_1 + \iiint_{-\infty}^{\infty} \left(\frac{\Gamma}{2}\varphi_\xi{}^2 - K\varphi\right) G_x d\tau \tag{21}$$

and for the perturbation velocity φx

$$\varphi_x = \varphi_{1x} + \iiint_{-\infty}^{\infty} \left(\frac{\Gamma}{2}\varphi_\xi{}^2 - K\varphi\right) G_{xx}\, d\tau \tag{22}$$

Now, multiplying equation (22) by β^2 and equation (21) by $-K$ and adding the two, the resulting equation can be simplified using equation (17) to obtain

$$\theta = \beta^2\varphi_{1x} - K\varphi_1 - \iiint_{-\infty}^{\infty} \left(\frac{\Gamma}{2}\varphi_\xi{}^2 - K\varphi\right)(G_{yy} + G_{zz})\, d\tau \tag{23}$$

$$= \beta^2\varphi_{1x} - K\varphi_1 - \iiint_{-\infty}^{\infty} \left\{\nabla_0{}^2\left(\frac{\Gamma}{2}\varphi_\xi{}^2 - K\varphi\right)\right\} G\, d\tau$$

where $\nabla_0{}^2$ in the last integral is the two-dimensional Laplace-operator with respect to η and ζ. Denoting the integral by I we find for the deviation of θ from its maximum θ^*

$$\Delta\theta = \frac{\Gamma}{2}\left\{2\varphi_x{}^*(\varphi_{1x} - \varphi_{1x}{}^*) - (\varphi_{1x} - \varphi_{1x}{}^*)^2\right\} - \int_{x^*}^{x} (\Gamma\varphi_{1\xi\xi} - K)\varphi_{1\xi}\, d\xi - (I^* - I) \tag{24}$$

where the potential $\varphi_1{}^*$ has been adjusted, such that $\Delta\theta = 0$ at the sonic point $x = x^*$. Differentiating with respect to x gives

$$\theta_x = \Gamma\varphi_x{}^*\varphi_{1xx} - K\varphi_{1x} - I_x \tag{25}$$

The function I_x can be expressed using equations (21) and (23) as

$$I_x = \nabla_0{}^2 \iiint_{-\infty}^{\infty} \left(\frac{\Gamma}{2}\varphi_\xi{}^2 - K\varphi\right) G_x d\tau = \nabla_0{}^2(\varphi - \varphi_1) \tag{26}$$

At the sonic line, where equation (14) degenerates to $\nabla_0^2\varphi = 0$, we find I_x^* from equation (15):

$$I_x^* = \beta^2\varphi_{1xx}^* - K\varphi_{1x}^* \tag{27}$$

It follows from equations (27) and (25) that θ_x vanishes at the sonic line independent of the value of K.

We now make the simplifying assumption that the sonic point x^* on the body is predicted with sufficient accuracy by the approximate solution φ_1. This assumption is well substantiated by experimental evidence. We then put

$$\varphi_{1x}^* = \varphi_x^* = \frac{\beta^2}{\Gamma} \tag{28}$$

and equations (24) and (27) simplify to

$$\Delta\theta = \Delta\theta_1 - \int_{x^*}^{x} (\Gamma\varphi_{1\xi\xi} - K)\varphi_{1\xi}d\xi - \Delta I \tag{29}$$

$$I_x^* = \frac{\beta^2}{\Gamma}\,(\Gamma\varphi_{1xx}^* - K) \tag{30}$$

where

$$\Delta\theta_1 = \frac{\Gamma}{2}\,(\varphi_x^* - \varphi_{1x})^2$$

analogous to $\Delta\theta$, and $\Delta I = I^* - I$.

The function I is now expanded into a Taylor series around $x = x^*$, and the parameter K is chosen such that I_x^* vanishes; i.e., from equation (30)

$$K = \Gamma\varphi_{1xx}^* \tag{31}$$

Retaining only the first nonzero term of the Taylor series of I, equation (29) reduces (with $x - x^* = \Delta x$) to

$$\Delta\theta = \Delta\theta_1 - \Gamma\int_{x^*}^{x} (\varphi_{1\xi\xi} - \varphi_{1xx}^*)\varphi_{1\xi}d\xi + \frac{1}{2}\,\Delta x^2 I_{xx}^* \tag{32}$$

After carrying out the indicated integration, this can also be written in the form:

$$\Delta\theta = \Gamma\varphi_x^*(\varphi_x^* - \varphi_{1x}) + \Gamma\varphi_{1xx}^*(\varphi_1 - \varphi_1^*) + \frac{1}{2}\,\Delta x^2 I_{xx}^* \tag{33}$$

where the first term on the right vanishes for the free-stream Mach number $M_\infty = 1$.

Differentiating equations (14) and (15) we obtain

$$I_{xx}^* = \beta^2\varphi_{1xxx}^* + \Gamma(\varphi_{xx}^{*2} - \varphi_{1xx}^{*2}) \tag{34}$$

where use has been made of equation (28). If φ_{xx} is predicted by φ_{1xx} at the sonic point with sufficient accuracy, then the second term in equation (34) can be neglected. In the case of $M_\infty = 1$ then, the last term in equation (33) vanishes.

For all cases, for which we may assume $\varphi_{1xx}^* \doteq \varphi_{xx}^*$, equation (33) is a simple quadratic equation for the perturbation velocity φ_x. The validity of this approximation will be discussed in the following text.

Consider again equation (25). Introducing equation (26) yields

$$\theta_x = \beta^2\varphi_{1xx} - K\varphi_{1x} - \nabla_0^2(\varphi - \varphi_1) \tag{35}$$

It will be noted that equation (35) can also be obtained by equating equations (14) and (15).

If β^2 and K approach zero simultaneously, equation (35) reduces to the linearized equation $\nabla_0^2\varphi = 0$ which is applicable only to bodies of zero thickness. Hence for $M_\infty = 1$ the parameter K has to remain finite in all other cases.

In a recent paper, Hosokawa [9] derived the same equation (35). He demonstrates that the last term in the equation is negligible compared to the other terms near the body, provided φ_1 satisfies the linearized boundary condition, equation (20).

From the physical point of view, neglecting the last term, equation (35) represents a one-dimensional approximation of the flow field near the body; i.e., it is assumed that $\varphi - \varphi_1$ is a function of x only. This seems to be a reasonable assumption according to the discussion in Section 2.

However, equation (26) shows that this assumption can only be made if K has the proper order of magnitude as given by equation (31).

Equations (33) and (34) further indicate that the correction term may be appreciable, if the slope of the velocity-distribution curve at the sonic point is not predicted by φ_{1xx}^* with sufficient accuracy. It also follows that the value of K is then poorly chosen. This point will be demonstrated by some examples for the free-stream Mach number one. In Fig. 4 the reduced pres-

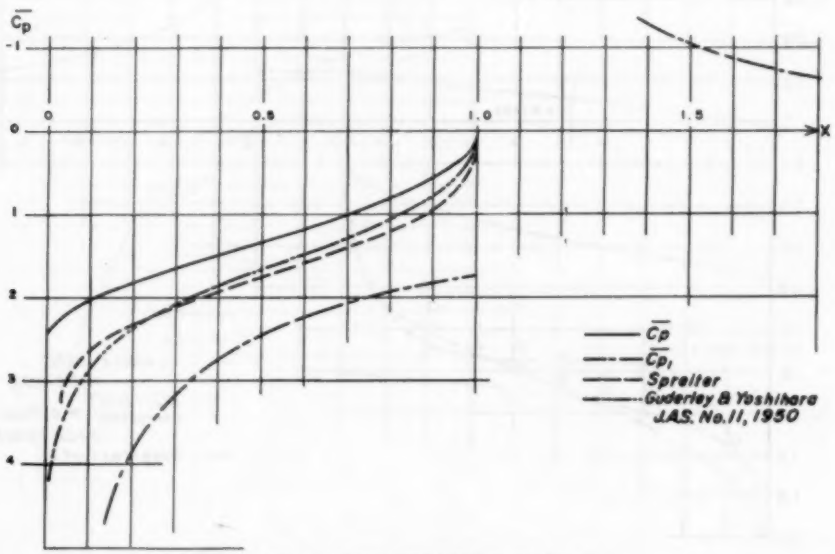

Fig. 4 Pressure distribution on wedge

sure distribution on a wedge profile is shown. It is defined as

$$\bar{C}_p = \left(\frac{\Gamma}{\tau^2}\right)^{1/3} C_p = -2\left(\frac{\Gamma}{\tau^2}\right)^{1/3} \varphi_x \tag{36}$$

The dash-dot line gives $\bar{C}_{p1}$, calculated from φ_{1x}. Since φ_{1x} is discontinuous at the shoulder (which coincides with the sonic point), $\varphi_{1xx}{}^*$ was taken as the slope of the φ_{1x}-curve at

$$x = \lim_{\epsilon \to 0} (1 - \epsilon)$$

where $x = 1$ is the position of the shoulder.

From this approximation, $\bar{C}_p$ was calculated using φ_x given by equation (33) neglecting $I_{xx}{}^*$. The result is shown by a solid line. Also plotted is the pressure distribution obtained by Guderley and Yoshihara [11] which can be considered an exact solution, except in the immediate neighborhood of the leading edge. It is evident that the present theory compares poorly with the exact result, except qualitatively. In this example, φ_{xx} at the sonic point is infinite, while φ_{1xx} has a small value and one would expect the theory to fail. A similar situation is found in the case of a cone cylinder, shown in Fig. 5. Here the pressure distribution was calculated on the surface of the body; i.e., the pressure is given by

$$C_p = -2\varphi_x(x, r_0) - \varphi_r{}^2 = -2\varphi_x(x, r_0) - \frac{\delta^2}{4}\frac{S'^2(x)}{S(x)} \tag{37}$$

where

$$S(x) = \frac{\pi r_0{}^2}{\pi \delta^2} = \frac{A(x)}{A_{max}}$$

where the boundary condition, equation (20), has been used to determine the quadratic term $\varphi_r{}^2$. Again, the prediction $\varphi_{1xx}{}^*$ at the shoulder differs in the same manner as for the wedge and the approximation fails.

A less drastic example is shown in Fig. 6. The shape of the airfoil considered is given by

$$y_0(x) = \frac{\tau\, n^{n/n-1}}{2n-1}\left[(1-x) - (1-x)^n\right] \quad 0 \le x \le 1 \tag{38}$$

The calculation was carried out for $n = 6$ and compared with measurements of reference [12] which were carried out for $n = 6.05$. These profiles have their maximum thickness at $x = 0.3$. Under these conditions, φ_{1x} is a poor approximation to φ_x as shown in the figure.

The pressure distribution calculated by neglecting $I_{xx}{}^*$ in equation (33) gives poor agreement with the measurements. From the experimental pressure distribution the value of $I_{xx}{}^*$ was estimated according to equation (34) and the corrected distribution was also plotted. It is seen that the correction is appreciable, although probably overestimated near the trailing edge.

The measurements of reference [12] were performed on half airfoils embedded in the test section wall. Some criticism of this technique was given in reference [13]. The thick boundary layer tends to make the airfoil appear more slender and therefore the experimental pressures are presumably too high.

Also shown in Figs. 4 and 6 are the pressure distributions calculated by Spreiter [5]. Spreiter's method can be summarized as follows:

For $M_\infty = 1$ the potential φ_1 and its x-derivative reduce to the simple forms

$$\varphi_1 = -\frac{1}{(\pi K)^{1/2}}\int_{-\infty}^{x} \frac{y_0'(\xi)d\xi}{(x-\xi)^{1/2}}$$

$$\varphi_{1x} = -\frac{1}{(\pi K)^{1/2}}\int_{-\infty}^{x} \frac{y_0''(\xi)d\xi}{(x-\xi)^{1/2}} \tag{39}$$

Spreiter then assumes that $\varphi_x = \varphi_{1x}$, if the parameter is chosen locally as $K = \Gamma\varphi_{xx}$. This leads to the nonlinear differential equation

$$\varphi_x = \frac{K^{1/2}\varphi_{1x}}{(\Gamma\varphi_{xx})^{1/2}} \tag{40}$$

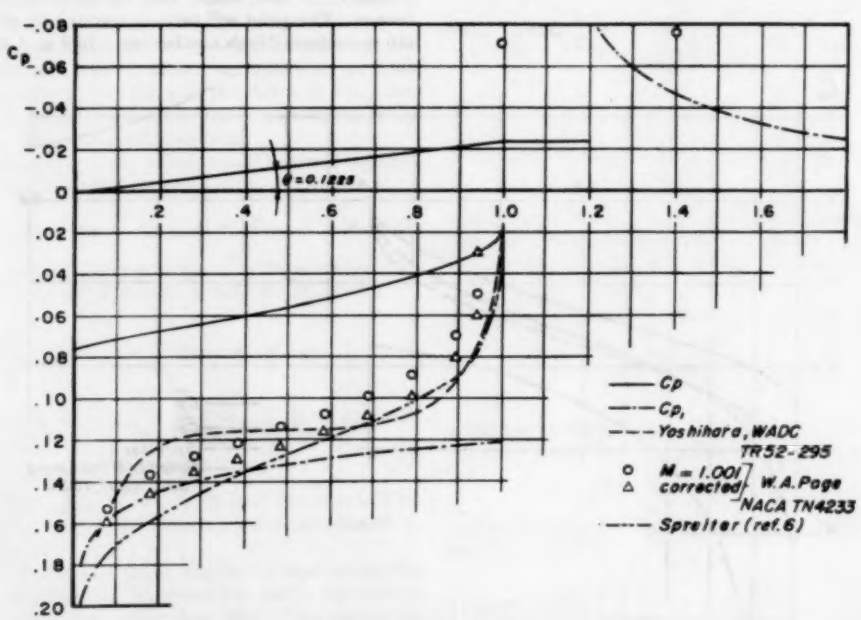

Fig. 5 Pressure distribution on cone cylinder

Equation (40) can be solved easily, if the assumption is made, that the sonic point x^* is predicted with sufficient accuracy by $\varphi_{1x}^* = 0$. The solution is

$$\varphi_x = \left\{\frac{3}{\Gamma}\int_{x^*}^{x} K\varphi_{1\xi}^2 d\xi\right\}^{1/3} \tag{41}$$

For free-stream Mach numbers slightly different from unity, the procedure is analogous. Retaining the same Kernel function as for $M_\infty = 1$, Spreiter derives the relation

$$\varphi_x = \varphi_x^* + \varphi_{1x(M_\infty = 1)}$$

Upon introduction of $K = \Gamma\varphi_{xx}$ as before and solving the resulting differential equation, one obtains

$$\varphi_x = \varphi_x^* + \left\{\frac{3}{\Gamma}\int_{x^*}^{x} K\varphi_{1\xi}^2\, d\xi\right\}^{1/3} \tag{41a}$$

Introducing the thickness ratio τ by

$$y_0(x) = \tau\mathcal{Y}_0(x), \quad \text{where} \quad 0 \leq \mathcal{Y}_0 \leq 1 \tag{42}$$

it becomes evident that φ_{1x} is proportional to τ. Equation (41) then clearly implies the transonic similarity law; i.e., the distribution of the reduced pressure coefficient $\bar{C}_p(x)$ [equation (36)] is the same for a family of airfoils having the same distribution $\mathcal{Y}_0(x)$ but different thickness ratios.

Denoting the transonic parameter or the von Karman number by

$$\xi_\infty = \frac{M_\infty^2 - 1}{[(\kappa+1)M_\infty^2\tau]^{2/3}} = -\frac{\beta^2}{[\Gamma\tau]^{2/3}} \tag{43}$$

equation (41a) yields for the reduced pressure coefficient for free stream Mach numbers slightly different from unity

$$\bar{C}_p = 2\xi_\infty + \bar{C}_{p_{M_\infty = 1}} \tag{44}$$

This result, which indicates that the quantity $\bar{C}_p - 2\xi_\infty$ is invariant to small deviations of M_∞ from unity, is known as the Mach-number freeze. Its experimental verification seems at present rather questionable because of the uncertainty of the measurements. Exact calculations on a wedge profile show that the phenomenon exists over a small range of Mach numbers. However, the flow over a wedge profile should be considered a special case since the sonic point is fixed by the body geometry. For smooth bodies it seems doubtful that such a freeze really exists over an appreciable range of M_∞.

For the sonic free stream the present theory yields particularly simple results, since the Kernel function reduces to the simple forms given in the Appendix. Using the notation

$$M(x) = \frac{1}{\pi^{1/3}}\int_{-\infty}^{x} \frac{\mathcal{Y}_0'(\xi)d\xi}{(x-\xi)^{1/3}}$$

equation (33) (omitting I_{xx}^*) gives the reduced pressure coefficient

$$\bar{C}_{p_{M_\infty = 1}} = \mp 2[M'(x^*)]^{1/3}\{2[M(x) - M(x^*)]\}^{1/3} \tag{45}$$

where the negative or positive sign has to be taken for $\varphi_{1x} \gtrless 0$, respectively. Equation (45) shows that the transonic similarity law is fulfilled by this theory. However, the Mach-number freeze is not predicted by the theory as can be verified by inspection of the Kernel function for $M_\infty \neq 1$.

It is particularly interesting, that equation (33) predicts a shock wave due to the two real roots of the quadratic. This shock wave is located at a position x^{**} where φ_1 predicts the rear sonic point. This point coincides with the trailing edge for $M_\infty = 1$ but lies ahead of it for $M_\infty < 1$. Qualitatively, this behavior is observed in the experiments, but the shock position is influenced by the interaction between shock wave and boundary layer. The shift in shock-wave position seems to contradict the assumption of Mach-number freeze.

The pressure distribution on a parabolic airfoil is shown in Fig. 7 for $M_\infty = 1$. It is compared with measurements of reference [14] and with Spreiter's results [5]. Both theories are in good agreement with the experiment. Spreiter's theory, however, gives infinite pressures at the leading edge while the present theory predicts a finite pressure.

In Fig. 8 the pressure distribution on a 10 per cent thick parabolic airfoil for $M_\infty = 1.05$ is shown. Again the theory predicts a finite pressure at the leading edge. Except near the trailing edge, the agreement with the experiment [14] is excellent. The deviation from the theory near the trailing edge is attributed to boundary-layer shock-wave interaction.

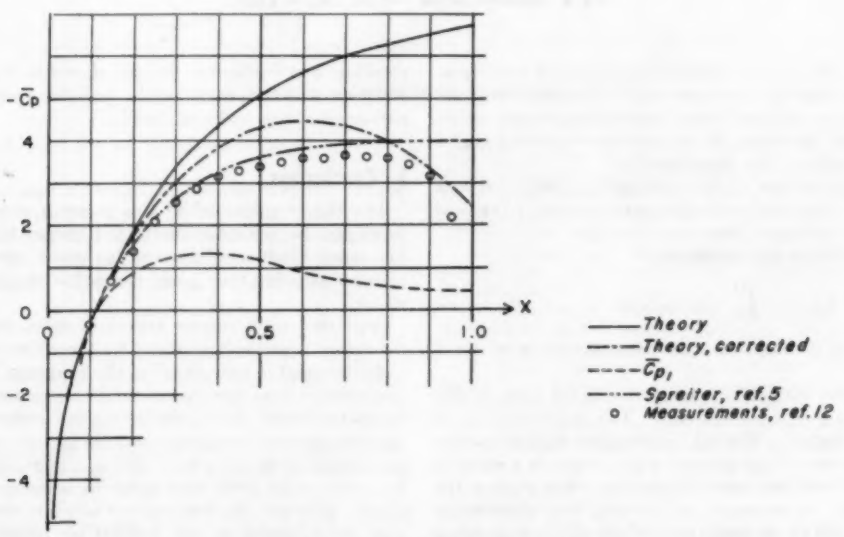

Fig. 6 Airfoil with maximum thickness at $X = 0.3$

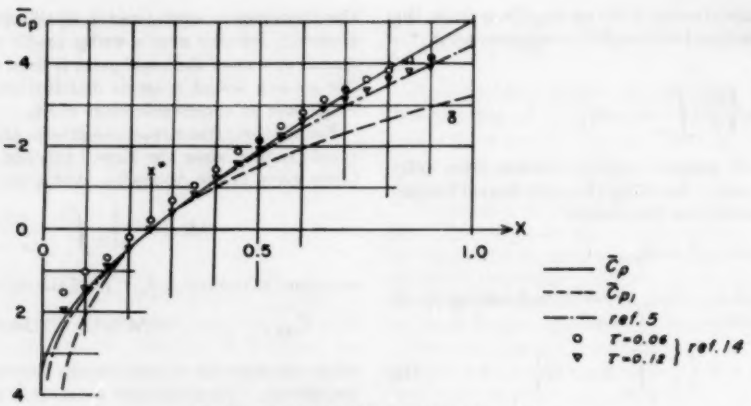

Fig. 7 Parabolic airfoil, $\tau = 0.1$ $M_\infty = 1$

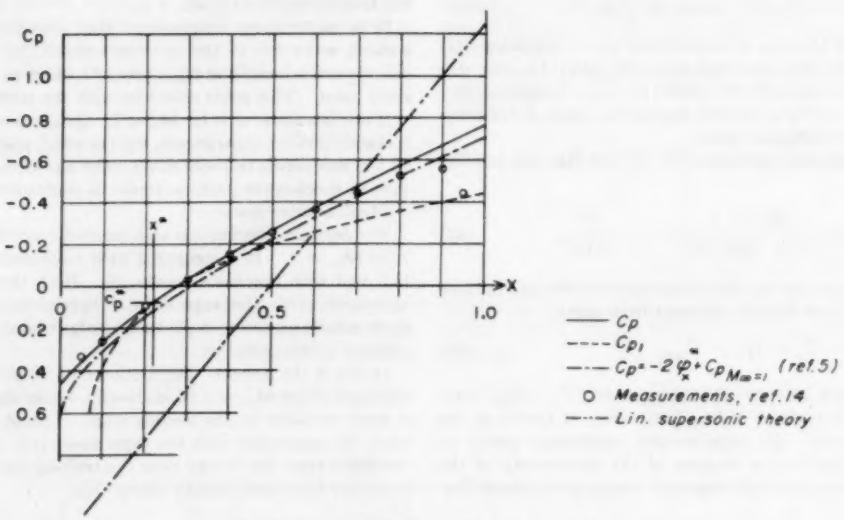

Fig. 8 Parabolic airfoil, $\tau = 0.1$ $M_\infty = 1.05$

Also plotted in Fig. 8 is the distribution calculated from equation (44) which is slightly less satisfactory. For comparison, the pressure distribution calculated from linearized supersonic theory has been included. Of course, this theory is not expected to give any reasonable results at this Mach number.

The pressure distribution on the same airfoil for $M_\infty = 0.95$ is shown in Fig. 9. It is compared with measurements of [14] and with the pressure calculated from equation (44).

Finally in Fig. 10 the drag coefficient

$$C_D = 2\int_0^1 C_p(x) y_0'(x) dx \qquad (46)$$

of the same airfoil is compared with measurements of reference [14].

These latter were obtained by integration of the pressure distribution according to equation (46). The theoretical points are considerably higher. This can be attributed to the fact that near the trailing edge a high-pressure region exists as a result of the shock-wave boundary-layer interaction; this reduces the drag considerably. In reference [14] the drag that would result in the absence of this phenomenon was estimated by extrapolating the pressure curve in the neighborhood of the trailing edge. The resulting drag coefficients are also shown in Fig. 10. They are still lower than the present results, probably because the foregoing phenomenon was underestimated.

5 Conclusions

The theory presented in this paper is characterized by its simplicity, in particular for the free-stream Mach number one. For other Mach numbers, the numerical calculations are still rather tedious but their programming for computers is extremely simple.

Since the results can be written in closed form at each step, the theory is particularly suited for theoretical applications.

As discussed in some detail in the foregoing, the theory yields acceptable results only under certain restrictions: (*a*) The body has to be smooth, i.e., no discontinuities in the slope of the area distributions are admissible, because in this case φ_{1x} is a poor approximation to φ_x; (*b*) φ_{1x} and φ_{1xx} must approximate φ_x and φ_{xx} at the sonic point with sufficient accuracy. This condition implies of course the first one, but is much stronger. It seems that the condition is well fulfilled for bodies whose point of maximum thickness is not too close to the leading edge. This

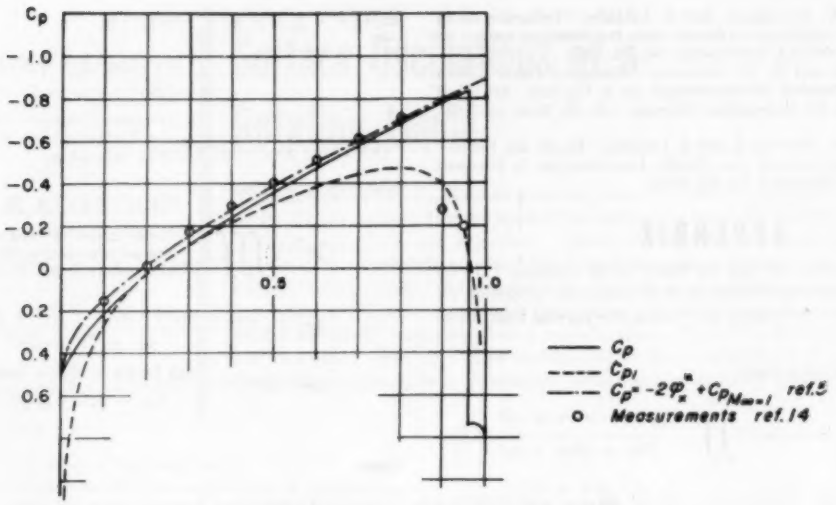

Fig. 9 Parabolic airfoil, $\tau = 0.1$ $M_\infty = 0.95$

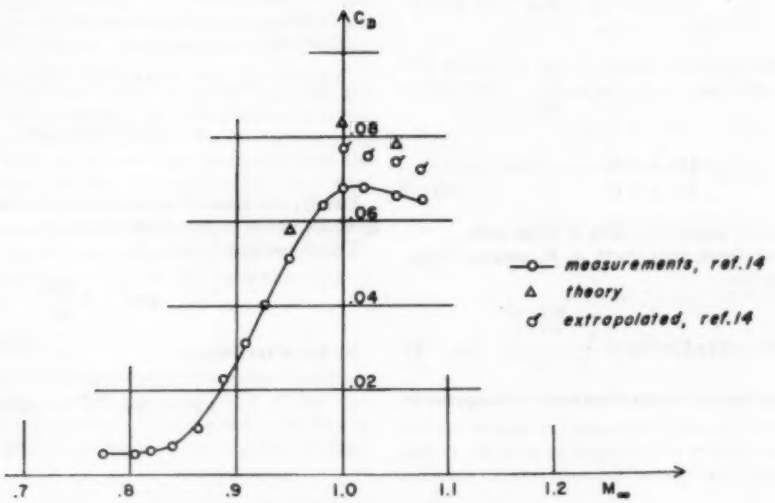

Fig. 10 Drag coefficient for parabolic airfoil, $\tau = 0.1$

may result from the fact that φ_{1x} has the usual singularity at the nose.

In this paper no results for bodies of revolutions are presented. An example has, however, been given by Hosokawa in reference [9] for $M_\infty = 1$. The agreement with the experiments is excellent. It is particularly interesting that the theory predicts a shock wave ahead of the rear end. This shock wave has actually been observed.

References

1 K. Oswatitsch and F. Keune, "The Flow Around Bodies of Revolution at Mach Number One," *Proceedings of the Conference on High-Speed Aeronautics*, Polytechnic Institute of Brooklyn, January, 1955.

2 P. F. Maeder and H. U. Thommen, "Some Results of Linearized Transonic Flow About Slender Airfoils and Bodies of Revolution," *Journal of the Aeronautical Sciences*, vol. 23, 1956, pp. 187–188.

3 P. F. Maeder and H. U. Thommen, "Linearized Transonic Flow About Slender Bodies of Revolution at Zero Incidence," Brown University, Division of Engineering, Technical Report WT-25, July, 1957.

4 P. F. Maeder and A. D. Wood, "Linearized Transonic Flow Past Isolated Non-Lifting Airfoils," Brown University, Division of Engineering, Technical Report WT-24, June, 1957.

5 J. R. Spreiter and A. Y. Alksne, "Thin Airfoil Theory Based on Approximate Solution of the Transonic Flow Equation," NACA TN 3970, May, 1957.

6 J. R. Spreiter, "Aerodynamics of Wings and Bodies at Transonic Speeds," *Journal of the Aero/Space Sciences*, vol. 26, 1959, pp. 465–486 and 517.

7 A. D. Wood, "Transonic Flows Through a Straight Cascade of Slender Airfoils," Brown University, Division of Engineering, Technical Report WT-28, August, 1958.

8 H. U. Thommen, "On Transonic Flow About Slender Three-Dimensional Bodies," Brown University, Division of Engineering, Technical Report WT-27, September, 1958.

9 I. Hosokawa, "A Refinement of the Linearized Transonic Flow," *Journal of the Physical Society of Japan*, vol. 15, 1960, p. 149.

10 K. G. Guderley, "Theorie Schallnaher Stroemungen," Springer Verlag, Berlin, Germany, 1957.

11 K. G. Guderley and H. Yoshihara, "The Flow Over a Wedge Profile at Mach Number 1," *Journal of the Aeronautical Sciences*, vol. 17, 1950, pp. 723–735.

12 R. Michel, F. Marchand, and J. LeGallo, "Influence de la position du maitre-couple sur les écoulements transsonique autour de profils à pointes," ONERA, Publication No. 72, 1954.

13 J. B. Carrol and G. F. Anderson, "Boundary-Layer Effect on Local Mach Number Measurements on a Circular Arc Half Profile," *Journal of the Aeronautical Sciences*, vol. 23, 1956, pp. 604–605.

14 R. Michel, F. Marchand, and J. LeGallo, "Étude des Ecoulements Transsonique autour des Profils Lenticulaires, à Incident Nulle," ONERA, Publication No. 65, 1953.

APPENDIX

The Kernel function G can be found from equation (17) by taking triple Fourier transforms on both sides (see reference [8] for details). After rearranging and taking the inverse transforms one obtains:

(a) Two-dimensional case:

$$G(x-\xi, y-\eta) = -(2\pi)^{-2}\iint_{-\infty}^{\infty} \frac{e^{i[p_1(x-\xi)+p_2(y-\eta)]}}{\beta^2 p_1 + iKp_1 + p_2^2}\,dp_1dp_2$$

$$= -(2\pi\beta)^{-1}e^{\alpha(x-\xi)}K_0\{\alpha[(x-\xi)^2+\beta^2(y-\eta)^2]^{1/2}\} \quad \beta^2 > 0$$

$$= -(2m)^{-1}e^{\alpha(x-\xi)}I_0\{\alpha[(x-\xi)^2 - m^2(y-\eta)^2]^{1/2}\} \cdot 1[x-\xi-m|y-\eta|] \quad \beta^2 < 0$$

where

$$m^2 = -\beta^2 = M_\infty^2 - 1, \quad \alpha = \frac{K}{2\beta^2}$$

and

$$1(s) = \begin{cases} 0 & s < 0 \\ 1 & s > 0 \end{cases}$$

K_0 and I_0 are the modified Bessel functions of order zero.

If β^2 approaches zero, such that $2\alpha\beta^2 = K$ remains finite, then G has the limiting form:

$$\lim_{\beta^2\to 0} G(x-\xi, y-\eta) = -[(4\pi K)^{-1/2}]^{-1}\,\frac{e^{-\frac{K(y-\eta)^2}{4(x-\xi)}}}{(x-\xi)^{1/2}} \cdot 1(x-\xi)$$

If $\alpha \to 0$, G takes the form of linearized subsonic and supersonic theory, i.e.,

$$\lim_{\alpha\to 0} G(x-\xi, y-\eta) = (4\pi\beta)^{-1}\ln \{(x-\xi)^2 + \beta^2(y-\eta)^2\} \quad \beta^2 > 0$$

$$= -(2m)^{-1}\,1[(x-\xi) - m|y-\eta|] \quad \beta^2 < 0$$

(b) Three-dimensional case:

$$G(x-\xi, y-\eta, z-\zeta) = -(2\pi)^{-3}\iiint_{-\infty}^{\infty} \frac{e^{i[p_1(x-\xi)+p_2(y-\eta)+p_3(z-\zeta)]}}{\beta^2 p_1^2 + iKp_1 + p_2^2 + p_3^2}\,dp_1dp_2dp_3$$

$$= -(4\pi)^{-1}\,e^{\alpha(x-\xi)}\,\frac{\exp\{-\alpha[(x-\xi)^2+\beta^2r^2]^{1/2}\}}{[(x-\xi)^2+\beta^2r^2]^{1/2}} \quad \beta^2 > 0$$

$$= -(2\pi)^{-1}e^{\alpha(x-\xi)}\,\frac{\cosh\{\alpha[(x-\xi)^2 - m^2r^2]^{1/2}\}}{[(x-\xi)^2 - m^2r^2]^{1/2}} \quad 1[x-\xi-mr]\ \beta^2 < 0$$

where $r^2 = (y-\eta)^2 + (z-\zeta)^2$

Again, the following limiting cases are obtained·

$$\lim_{\beta^2\to 0} G(x-\xi, r) = -(4\pi)^{-1}\,\frac{e^{-\frac{Kr^2}{4(x-\xi)}}}{x-\xi}\,1(x-\xi)$$

$$\lim_{\alpha\to 0} G(x-\xi, r) = -(4\pi)^{-1}[(x-\xi)^2+\beta^2r^2]^{-1/2} \quad \beta^2 > 0$$

$$= -(2\pi)^{-1}[(x-\xi)^2 - m^2r^2]^{-1/2}\,1[x-\xi-rm] \quad \beta^2 < 0$$

Finally, the generating functions g [see equation (14)] will be given for bodies at zero angle of attack.

Two-dimensional case:

$$g(x) = 2\,\frac{dy_0}{dx}$$

Bodies of revolution:

$$g(x) = 2\pi r_0\,\frac{dr_0}{dx} = \pi\delta^2 S'(x)$$

J. W. MILES[1]
Professor of Engineering and Geophysics, University of California, Los Angeles, Calif.

B. A. TROESCH[2]
Member of the Senior Staff, Space Technology Laboratories, Inc., Los Angeles, Calif.

Surface Oscillations of a Rotating Liquid

The free oscillations of a fluid in a rotating, axially symmetric container are investigated under the assumption that the equilibrium motion of the fluid be a rigid-body rotation. Gravitational forces are neglected. The resulting boundary-value problem leads to an elliptic or hyperbolic partial differential equation, depending on the frequency/angular velocity ratio. The problem is solved for a cylindrical container and discussed exhaustively. Due to the Coriolis force, there exist modes with the radial velocity component vanishing inside the fluid ("nodal cylinders"), besides the usual nodes in axial and azimuthal direction. The oscillations in the neighborhood of critical container dimensions are analyzed. Numerical results are presented in graphs.

We consider here the free oscillations of an annular cylinder of an inviscid liquid contained in a rotating (about its axis) cylindrical tank of radius a and height h and having an inner, free surface of (equilibrium) radius b. We shall assume that the gravitational acceleration (if any) is negligible compared with the centripetal acceleration and that the equilibrium configuration of the liquid is a rigid-body rotation.

The problem described here arises in connection with the motion of fuel in a spinning rocket. Related problems are presented by a liquid-filled top [7],[3] a liquid-filled cylinder rotating about a horizontal axis in a relatively weak (compared with the centrifugal force) gravitational field [5], and a liquid-filled cylinder rotating about a vertical axis with a parabolic (but approximately plane) free surface [4]. The present investigation is more restricted than any of these antecedents, but we shall obtain rather more complete results for the natural modes of centrifugal oscillation.

The Eigenvalue Problem

Let (r, θ, z) be a set of cylindrical polar co-ordinates rotating with the angular velocity ω about the z-axis, (u, v, w) the corresponding components of relative velocity, p the perturbation pressure, and ρ the density of the liquid. The equations of small motion then are [6]

$$u_t - 2\omega v = -\psi_r, \quad v_t + 2\omega u = -r^{-1}\psi_\theta, \quad w_t = -\psi_z \quad (1a, b, c)$$

where

$$\psi = \rho^{-1}p - \frac{1}{2}\omega^2 r^2 + \text{const} \qquad (2)$$

is an acceleration potential that satisfies

$$\nabla^2\psi_{tt} + 4\omega^2\psi_{zz} = 0. \qquad (3)$$

We seek solutions for (u, v, w, p) that satisfy the boundary conditions (of vanishing normal velocity)

$$u = 0 \text{ at } r = a, \qquad w = 0 \text{ at } z = 0, h \qquad (4a, b)$$

at the tank walls and that correspond to an oscillatory displacement of the free surface, say

$$r = b + \eta(\theta, z, t). \qquad (5)$$

The kinematic and dynamic boundary conditions at this free surface are

$$u = \eta_t \quad \text{and} \quad p = 0. \qquad (6a, b)$$

We may assume an oscillatory solution to (1)–(3) and (4b) in the form

$$u = [f'(r) + \mu m r^{-1} f(r)]e^{i(\sigma t + m\theta)} \cos(n\pi z/h), \qquad (7a)$$

$$v = i[\mu f'(r) + m r^{-1} f(r)]e^{i(\sigma t + m\theta)} \cos(n\pi z/h), \qquad (7b)$$

$$w = (\mu^2 - 1)(n\pi/h) f(r) e^{i(\sigma t + m\theta)} \sin(n\pi z/h), \qquad (7c)$$

$$\frac{p}{\rho} = \frac{1}{2}\omega^2(r^2 - b^2) + i\sigma(\mu^2 - 1) f(r) e^{i(\sigma t + m\theta)} \cos(n\pi z/h), \qquad (7d)$$

where σ denotes the angular frequency (*in the rotating co-ordinate system;* the angular frequency for a fixed observer is $\sigma - m\omega$), m and n are integers, $f(r)$ must satisfy the (modified) Bessel equation

$$f''(r) + \frac{1}{r} f'(r) - \left(k^2 + \frac{m^2}{r^2}\right) f(r) = 0, \qquad (8)$$

and

$$\mu = 2\omega/\sigma, \quad k^2 = (1 - \mu^2)(n\pi/h)^2. \qquad (9a, b)$$

It then remains to satisfy the boundary conditions (4a) and (6a, b). Substituting (7a) in (4a) yields

$$af'(a) + m\mu f(a) = 0. \qquad (10a)$$

Letting $r = b + \eta$ in (7d), assuming $|\eta| \ll b$, and invoking (6b), we obtain the free-surface condition

$$0 = \omega^2 b\eta - i\sigma(1 - \mu^2) f(b) e^{i(\sigma t + m\theta)} \cos(n\pi z/h). \qquad (11)$$

Differentiating (11) with respect to t, eliminating η_t through (6a) and (7a), and multiplying the result by $4/\sigma^2$ yields

$$\mu^2 b f'(b) + \{4(1 - \mu^2) + m\mu^2\} f(b) = 0. \qquad (10b)$$

The investigation of the free oscillations is now reduced to the following eigenvalue problem: find those values of the parameter

[1] Also Consultant, Space Technology Laboratories, Inc., Los Angeles, Calif.

[2] Now with Aerospace Corporation, Los Angeles, Calif.

[3] Numbers in brackets indicate References at end of paper.

Presented at the Tenth International Congress of Applied Mechanics, Stresa, Italy, August 31–September 7, 1960.

Discussion of this paper should be addressed to the Editorial Department, ASME, United Engineering Center, 345 East 47th Street, New York 17, N. Y., and will be accepted until January 10, 1962. Discussion received after the closing date will be returned. Manuscript received by ASME Applied Mechanics Division, November 15, 1960.

μ for which the differential equation (8) has nonzero solutions that satisfy the boundary conditions (10a, b). The frequency for any given mode then is determined by $\sigma = 2\omega/\mu$, while the nodal pattern of the mode is described by the integers m (the number of θ-nodes), n (the number of z-nodes), and the zeros of the function f (the radial nodes).

Two-Dimensional Oscillations

The simplest of all special cases is two-dimensional motion, for which $n = 0$. A solution to (8) then is given by

$$f(r) = Ar^m + Br^{-m}. \tag{12}$$

Substituting (12) in (10a, b) and equating the determinant of the results to zero, we obtain the eigenvalue equation

$$m\mu^2 - 4\mu - 4\gamma = 0, \quad \gamma = \frac{(a/b)^{2m} + 1}{(a/b)^{2m} - 1}, \tag{13}$$

whence

$$\mu = \frac{2}{m}\,[1 \pm (1 + m\gamma)^{1/2}] \tag{14}$$

and

$$\sigma = \frac{\omega}{\gamma}\,[-1 \pm (1 + m\gamma)^{1/2}]. \tag{15}$$

We note that $m\gamma > 0$ independently of the sign of m, so that the frequencies given by (15) are real. The frequencies for a fixed observer are

$$\sigma_{abs} = \sigma - m\omega = -\frac{\omega}{\gamma}\,[(1 + m\gamma) \mp (1 + m\gamma)^{1/2}]. \tag{16}$$

Three-Dimensional Oscillations

The more general, three-dimensional, solution can be expressed in terms of Bessel functions (cf. [7]), namely

$$f(r) = AI_m(kr) + BK_m(kr) \quad \text{for} \quad \mu^2 < 1 \tag{17a}$$

or

$$f(r) = AJ_m(lr) + BY_m(lr) \text{ for } \mu^2 > 1, \tag{17b}$$

where

$$k = [1 - \mu^2]^{1/2}\,\frac{n\pi}{h}, \quad l = [\mu^2 - 1]^{1/2}\,\frac{n\pi}{h}. \tag{18a, b}$$

A nontrivial solution exists only if the determinant obtained from the boundary conditions (10a, b) vanishes:

$$\begin{vmatrix} kaI_m'(ka) + m\mu I_m(ka) & kaK_m'(ka) + m\mu K_m(ka) \\ \mu^2 kbI_m'(kb) + [4(1 - \mu^2) + m\mu^2]I_m(kb) & \mu^2 kbK_m'(kb) + [4(1 - \mu^2) + m\mu^2]K_m(kb) \end{vmatrix} = 0 \tag{19}$$

for $\mu^2 < 1$, and the corresponding equation involving J_m and Y_m for $\mu^2 > 1$. For the most important case, $m = 1$, the determinants are rewritten as

$$\begin{vmatrix} kaI_0(ka) + (\mu - 1)I_1(ka) & -kaK_0(ka) + (\mu - 1)K_1(ka) \\ \mu^2 kbI_0(kb) + [4 - 5\mu^2 + \mu^2]I_1(kb) & -\mu^2 kbK_0(kb) + [4 - 5\mu^2 + \mu^2]K_1(kb) \end{vmatrix} = 0 \tag{20a}$$

for $\mu^2 < 1$,

and

$$\begin{vmatrix} laJ_0(la) + (\mu - 1)\,J_1(la) & laY_0(la) + (\mu - 1)\,Y_1(la) \\ \mu^2 lbJ_0(lb) + (4 - 5\mu^2 + \mu^2)J_1(lb) & \mu^2 lbY_0(lb) + (4 - 5\mu^2 + \mu^2)\,Y_1(lb) \end{vmatrix} = 0 \tag{20b}$$

for $\mu^2 > 1$.

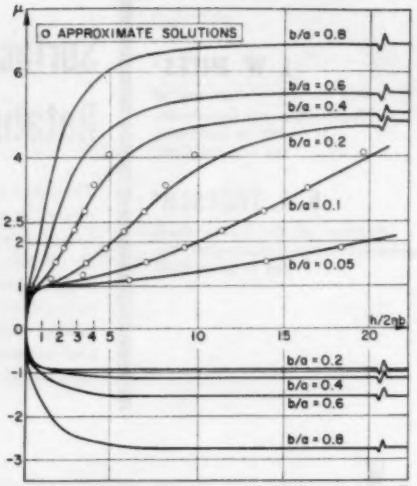

Fig. 1 Eigenvalue μ for modes without nodal cylinders. The approximate solutions are based on equation (51).

These equations form the basis for the further discussion of the problem. For the numerical computation of μ the values for a, b, and k (or l) are assumed, and the Bessel functions computed, so that the determinants (20a, b) reduce to fourth-degree polynomials in μ. Having k and μ, the value of $h/2n$ then is determined [cf. (9b)]. If the eigenvalues were to be found for a given situation, i.e., with a, b, and h prescribed, this method could be combined with an iteration procedure.

If the solution $f(r)$ does not vanish for $b \leq r \leq a$, there exists another representation that is quite convenient for numerical computations. It can also be used to obtain bounds for the eigenvalue μ (see Appendix 1). We introduce

$$y = k^2r^2, \quad F(y) = rf'(r)/f(r) \tag{21a, b}$$

and transform (8) to the Riccati equation

$$2yF'(y) + F^2(y) = m^2 + y \tag{22}$$

and (10a, b) to

$$F[\alpha^2(1 - \mu^2)] + m\mu = 0, \tag{23a}$$

$$\mu^2 F[\beta^2(1 - \mu^2)] + 4(1 - \mu^2) + m\mu^2 = 0, \tag{23b}$$

where

$$\alpha = n\pi a/h \text{ and } \beta = n\pi b/h.$$

For the computation of the frequencies presented in Fig. 1, we proceed as follows.

Given preassigned values of m, α, β, and an assumed (i.e., guessed) value of μ, say μ_a, we integrate the ordinary first-order differential equation (22) numerically from

$$y_0 = \beta^2(1 - \mu_a^2), \quad F(y_0) = -[4(1 - \mu_a^2) + m\mu_a^2]/\mu_a^2 \tag{24a, b}$$

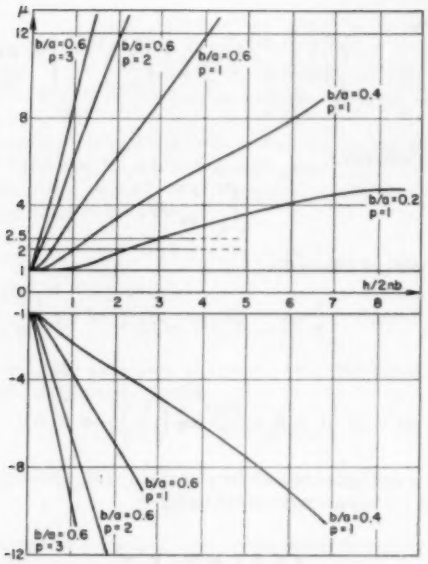

Fig. 2 Eigenvalue μ for modes with p nodal cylinders

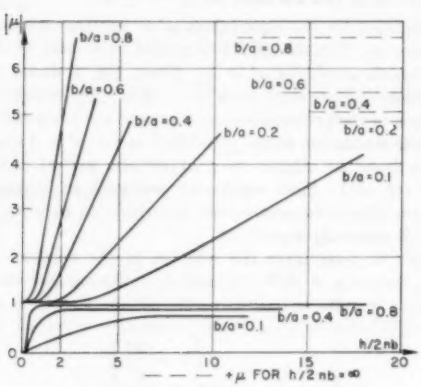

Fig. 3 Upper and lower bounds of $|\mu|$

to

$$\gamma_1 = \alpha^2(1 - \mu_n^2), \tag{25}$$

determine

$$\gamma_n = -m^{-1}F(\gamma_1), \tag{26}$$

and proceed by iteration until γ_n agrees with μ_n to the required accuracy. The selection of the initial guess, μ_0, is based on the results of the two-dimensional motion [see (14)] and on the bounds

$$A - [A^2 - B]^{1/2} < \mu^2 < A + [A^2 - B]^{1/2}, \tag{27}$$

where

$$B = \frac{8}{\alpha^2 - \beta^2}, \quad A = \frac{1}{2}(1 + B) + \frac{Bm^2}{8}\log\left(\frac{\alpha}{\beta}\right). \tag{28}$$

The result (27) is derived in Appendix 1 and displayed in Fig. 3.

Discussion of the Results

A given tank is characterized by its inner radius b, outer radius a, and depth h or, more conveniently, by the dimensionless ratios b/a and $h/2b$; a given mode is characterized by the integers m (number of θ-nodes), n (number of z-nodes), and p (number of r-nodes). The motions between any two z-nodes are, however, essentially identical and depend only on the effective depth ratio $h/2nb$, rather than on $h/2b$ and n independently. We therefore may describe our results in terms of the four dimensionless parameters b/a, $h/2nb$, m, and p. We may prescribe b/a and $h/2nb$ arbitrarily (except that $0 < b/a < 1$) and choose any integral value for m, say $m = 0, \pm 1, \pm 2, \ldots$ (the restriction to integral values of m is a consequence of the requirement that the motion be periodic in θ); there then exist two infinite sets of eigenvalues μ and corresponding frequencies σ for each triplet of b/a, $h/2nb$, and m—namely, two eigenvalues for each $p = 0, 1, 2, \ldots$. The reader might find it interesting to compare this state of affairs with that for a nonrotating cylindrical tank under the influence of gravity.

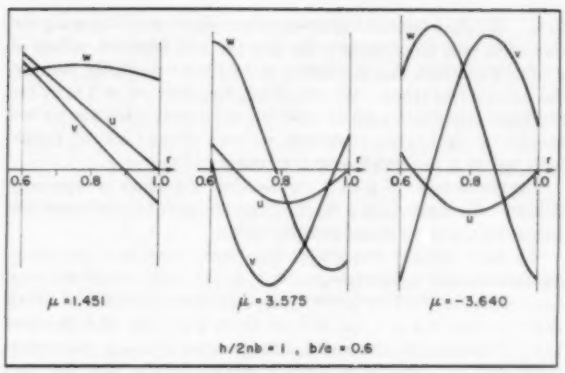

Fig. 4 Velocity components for modes with and without nodal cylinders

The fact that radial nodes (at which the radial velocity vanishes) are possible for free surface oscillations on a rotating liquid and that the two frequencies for a given nodal pattern differ in magnitude as well as sign are both consequences of the Coriolis force. Neither of these phenomena would be possible under the influence of centrifugal force alone. If we were to ignore the Coriolis accelerations $2\omega v$ and $2\omega u$ in the equations of motion $(1a, b)$ we would have to replace $(9b)$ by

$$k^2 = (n\pi/h)^2 \tag{9b}'$$

and the boundary conditions $(10a, b)$ by

$$f'(a) = 0 \tag{10a}'$$

and

$$\mu^2 bf'(b) + f(b) = 0. \tag{10b}'$$

The solutions of (8) then would involve only the nonoscillatory Bessel functions I_m and K_m, radial nodes would be impossible, and the two eigenvalues for given b/a, $h/2nb$, and m would differ only in sign.

The distributions of velocity for typical modes without and with radial nodes with $h/2nb = 1$, $b/a = 0.6$, and $m = 1$ are illustrated in Fig. 4. We emphasize that the existence of a radial node implies that a fixed cylinder could be inserted at such a node without altering the velocity distribution (but this cylinder would have to transmit pressure unchanged if the motion outside of it were to be unchanged). Cylindrical nodes also may exist for v or w (e.g., $v = 0$ at $r = 0.9a$ for $\mu = 1.451$ in Fig. 4), but these are not radial nodes in the present sense.

Let us now consider the behavior of the eigenvalue μ as a function of the geometric and modal parameters, bearing in mind that the corresponding natural frequency σ is inversely proportional

to μ. We shall restrict our discussion to $m = \pm 1$ (changing the sign of m only interchanges the positive and negative values of μ), but we remark that increasing m does not necessarily increase the natural frequency. We also emphasize that $|m| = 1$ is by far the most important case in practice, since only such modes are excited by rigid-body, transverse motions of the tank, all modes with $|m| \neq 1$ being orthogonal to the mode $|m| = 1$.

The dependence of μ on n, the number of z-nodes is especially simple: the eigenvalue μ decreases monotonically, and hence the frequency increases monotonically with n.

We have already remarked that there exist two oppositely signed values of μ for each $p = 0, 1, 2, \ldots$. If $p = 0$ we may have either $|\mu| < 1$ or $|\mu| > 1$, depending on the value of $h/2nb$ and b/a; but if $p \geq 1$, $|\mu| > 1$ (or $|\sigma| < 2\,|\omega|$) for all $h/2nb$ and b/a. Furthermore, the natural frequencies decrease monotonically with p. This is intimately related to the fact that the natural frequencies increase monotonically with the outer radius a. (We recall the analogous fact that the natural frequencies for gravity waves in a fixed tank increase monotonically with the depth of the tank.) Thus, if we have found a solution with, let us say, one nodal cylinder (see Fig. 4), then this same solution also describes the motion in a tank with smaller outer radius a, corresponding to the position of the nodal cylinder. The motion (in a given cylinder, with fixed m and n) between the free surface $r = b$ and the first radial node for any mode for which $p > 0$ then is identical, except for scale, with the motion for $p = 0$.

By comparing our numerical results with previous work we note that there exists full agreement with the eigenfrequencies given by Stewartson [7] for the range $2.0 < \mu < 2.5$ (cf. Figs. 1 and 2), whereas the curves given by Phillips [5] for the case $\mu = 2$ are rather inaccurate (up to 15 per cent deviation). Incidentally, the more accurate numerical values tend to improve the agreement between computed and observed frequencies as reported by Phillips.

Acknowledgments

The authors wish to thank Dr. M. Knopp for suggesting the method used in Appendix 1, and Mr. W. Bentley and Mr. L. Stoller for aid in carrying out the computations.

APPENDIX 1

Bounds for the Eigenvalues

Bounds for the eigenvalues μ can be conveniently obtained from (22) and the boundary conditions (23a, b).

By integrating (22)

$$F' = \frac{1}{2} + \frac{m^2}{2y} - \frac{F^2}{2y}$$

between the values

$$y_0 = \beta^2(1 - \mu^2) \quad \text{and} \quad y_1 = \alpha^2(1 - \mu^2) \qquad (29a, b)$$

we obtain

$$F(y_1) - F(y_0) = \int_{y_0}^{y_1} \left(\frac{1}{2} + \frac{m^2}{2y} - \frac{F^2}{2y} \right) dy. \qquad (30)$$

We note that

$$y_1 - y_0 = (\alpha^2 - \beta^2)(1 - \mu^2) \qquad (31)$$

and from (23a, b)

$$F(y_1) - F(y_0) = \frac{4}{\mu^2}(1 - \mu^2). \qquad (32)$$

Therefore,

$$\frac{4}{\mu^2}(1 - \mu^2) = \frac{1}{2}(y_1 - y_0) + \frac{m^2}{2} \log \left(\frac{y_1}{y_0} \right) - \int_{y_0}^{y_1} \frac{F^2}{2y}\, dy. \qquad (33)$$

Since the inequality

$$0 < \int_{y_0}^{y_1} \frac{F^2}{2y}\, dy \qquad (34)$$

always holds, it follows that

$$\frac{4}{\mu^2}(1 - \mu^2) < \frac{1}{2}(\alpha^2 - \beta^2)(1 - \mu^2) + m^2 \log \left(\frac{\alpha}{\beta} \right) \qquad (35)$$

or

$$\mu^4 - \mu^2 \left\{ 1 + B + \frac{Bm^2}{4} \log \left(\frac{\alpha}{\beta} \right) \right\} + B < 0. \qquad (36)$$

The lower and upper bounds for μ^2 given by (27) then are readily obtained. They are represented in Fig. 3.

APPENDIX 2

The Behavior of the Solution for $\mu = \pm 1$.

The solutions for the eigenvalues $\mu = \pm 1$ are of interest for several reasons. First of all, it is apparent from (20a, b) that this solution breaks down for $\mu^2 = 1$. Then, Fig. 2 shows that infinitely many curves start from $\mu = \pm 1$; furthermore, in the formulation of the problem for containers of arbitrary shape (i.e., without the separation of the variables r and z) $\mu^2 = 1$ marks the transition from an elliptic to a hyperbolic partial differential equation (cf. [2]). Since eigenvalue problems are usually associated with elliptic equations, this transition to another type of equation is especially significant.

In order to investigate the solution in the neighborhood of $\mu = \pm 1$, we put $\mu = \pm(1 - \epsilon)$ and, by retaining only the lowest order terms in (20a or b), we readily obtain at $\mu = -1$

$$\left(\frac{n\pi a}{h} \right)^2 = \frac{2\left(9 - \frac{a^2}{b^2} \right)}{\left(\frac{a}{b} \right)^2 - \left(\frac{b}{a} \right)^2}, \qquad (37)$$

and in the neighborhood of $\mu = -1$

$$\frac{n\pi a}{h} = \frac{x_i}{\sqrt{-2\epsilon}}, \qquad (38)$$

where x_i are the roots of

$$J_2(x_i)Y_2\left(x_i \frac{b}{a} \right) = J_2\left(x_i \frac{b}{a} \right) Y_2(x_i). \qquad (39)$$

For $\mu = +1$ the container dimensions are

$$\left(\frac{n\pi a}{h} \right)^2 = \frac{1 + 7\left(\frac{a^2}{b^2} \right)}{\log \left(\frac{a^2}{b^2} \right)}, \qquad (40)$$

and near $\mu = +1$

$$\frac{n\pi a}{h} = \frac{x_j}{\sqrt{-2\epsilon}} \qquad (41)$$

where x_j are the roots of

$$J_0(x_j)Y_0\left(x_j\frac{b}{a}\right) = J_0\left(x_j\frac{b}{a}\right)Y_0(x_j). \tag{42}$$

The results of (37) and (40) agree with the numerical computations (see Fig. 1).

The container dimensions which lead to an eigenvalue of $\mu = \pm 1$ can also be obtained directly from (22) and (23a, b). We again put $\mu = \pm(1 - \epsilon)$, then introduce η as a new independent variable according to

$$y = \alpha^2(1 - \mu^2)\eta = 2\epsilon\alpha^2\eta \tag{43}$$

and, in view of (22) and (23a),

$$F(y) = \mp m + \epsilon g(\eta). \tag{44}$$

For $m = 1$, the only case of interest here, the function $g(\eta)$ satisfies the differential equation

$$\eta g'(\eta) \mp g(\eta) = \alpha^2\eta, \tag{45a}$$

and

$$g(1) = 1 \tag{45b}$$

as one boundary condition, whereas the other boundary condition furnishes the desired result.

Treating the case $\mu = +1 - \epsilon$ first, the solution of (45a, b) is obtained as

$$g(\eta) = \alpha^2\eta \log \eta + \eta,$$

and the lowest-order terms of (23b), i.e., the boundary condition at

$$\eta = \frac{\beta^2}{\alpha^2},$$

lead then to the relation (40).

Similarly, for $\mu = -1 + \epsilon$,

$$g(\eta) = \frac{1}{\eta} + \frac{1}{2}\alpha^2\eta, \tag{46}$$

and (37) is readily obtained by inserting $g(\eta)$ into (23b) at $\eta = \beta^2/\alpha^2$.

APPENDIX 3

Discussion of Some Limiting Cases

It is worth mentioning some special cases for which the eigenvalue problem is appreciably simplified. These cases represent approximations to the results shown in certain regions of Figs. 1 and 2. Fig. 5 indicates in what regions the approximations give good results.

(a) For tanks where $k(a - b) \gg 1$ and $|\mu| < 1$, the sloshing is confined to the neighborhood of the free surface, as in the deep-water approximation for gravity waves. Starting from (20a) we find, using the asymptotic expansion of I_1 and K_1 [1],

$$\begin{vmatrix} (ak + \mu)e^{2kb} & -ak + \mu \\ \mu^2kbI_0(kb) + [4 - 5\mu^2 + \mu^3]I_1(kb) & -\mu^2kbK_0(kb) + [4 - 5\mu^2 + \mu^3]K_1(kb) \end{vmatrix} = 0, \tag{47}$$

and hence

$$-\mu^2kbK_0(kb) + [4 - 5\mu^2 + \mu^3]K_1(kb) = 0. \tag{48}$$

Numerical results are easily computed and show that for small $(h/2nb)$, where all curves coincide near the origin in Fig. 1, the representation is very good.

For small $h/2nb$, we can replace K_1 and K_0 in (47) by their asymptotic expansion and the approximation becomes

$$\mu = \pm 2\sqrt{\frac{h}{n\pi b}}. \tag{49}$$

This result is valuable because the numerical method described in the section, "Three-Dimensional Oscillations," is not very efficient for these values of $h/2nb$.

(b) At the other extreme, if $h/2nb$ is very large, i.e., $n \to 0$, then μ tends to the values for the two-dimensional problem given by (14).[4] Fig. 1 shows that for negative μ these approximations are actually quite accurate down to $(h/2nb) \approx 5$.

(c) Assuming $\mu^2 > 1$, and both b/a and lb small, i.e., $(h/2nb)$ large, leads to a good approximation in a certain region of positive μ's. It follows from (20b) that

$$\{laJ_0(la) + (\mu - 1)J_1(la)\}(4 - 5\mu^2 + \mu^3) \tag{50}$$

is the leading term. The solution

$$\mu = 2(\sqrt{2} + 1)$$

of the second factor represents the asymptotic value of μ for $(h/2nb) \to \infty$, $(b/a) \to 0$, in agreement with (14).

The solutions of

$$laJ_0(la) + (\mu - 1)J_1(la) = 0 \tag{51}$$

are marked in Fig. 1 and are observed to give surprisingly good approximations for small b/a, and in the intermediate region of $(h/2nb)$ up to $b/a = 0.4$. Since these solutions depend solely on a, the radius of the tank, but not on b, the positive μ hardly changes as the amount of fluid in the container decreases, within the parametric range of this approximation.

A last remark refers to the curves represented in Fig. 2 for modes with nodal cylinders. From the numerical procedure described in the section, "Three-Dimensional Oscillations," it follows that

$$\mu = +1, \quad \text{if } J_0(la)Y_0(lb) - J_0(lb)Y_0(la) = 0, \tag{52a}$$

$$\mu = -1, \quad \text{if } J_2(la)Y_2(lb) - J_2(lb)Y_2(la) = 0, \tag{52b}$$

$$\mu = \pm\infty, \quad \text{if } J_1(la)Y_1(lb) - J_1(lb)Y_1(la) = 0. \tag{52c}$$

For large arguments, i.e., for large p, the solution of these three equations is identical, namely

$$l = \frac{p\pi}{(a - b)}, \tag{53a}$$

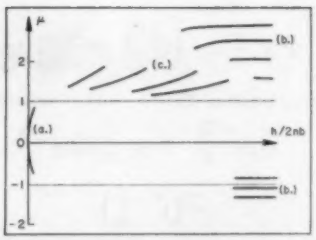

Fig. 5 Regions where limiting cases represent good approximations; (a), (b), (c) refer to the corresponding paragraphs of Appendix 3

[4] For motions with nodal cylinders, μ tends to infinity for large $(h/2nb)$.

or

$$\sqrt{\mu^2 - 1} = \left(\frac{h}{2na}\right) \frac{2p}{1 - (b/a)}^{5} \tag{53b}$$

[5] In Stewartson's notation [7] this would be written as

$$\left[\frac{4 - (1 - \tau)^2}{(1 - \tau)^2}\right]^{1/2} = \frac{c}{(2j + 1)a} \frac{p_k}{(1 - b/a)},$$

where

$$\tau = \left(1 \pm \frac{2}{\mu}\right).$$

A large part of Stewartson's tables [7] can then, with good accuracy, i.e., within a fraction of one per cent, be obtained by computing just the constant p_k for $\tau = 0.1$ and deriving the results for the other τ values from the formula above. According to our remarks, p_k is near an even integer.

References

1 H. B. Dwight, "Tables of Integrals and Other Mathematical Data," The Macmillan Company, New York, N. Y., 1947, p. 178.

2 H. Görtler, "On Forced Oscillations in Rotating Fluids," Proceedings of the Fifth Midwestern Conference on Fluid Mechanics, Ann Arbor, Mich., 1957, pp. 1–10.

3 H. Lamb, "Hydrodynamics," Cambridge University Press, 1932.

4 J. W. Miles, "Free Surface Oscillations in a Rotating Liquid," *The Physics of Fluids*, vol. 2, 1959, pp. 297–305.

5 O. M. Phillips, "Centrifugal Waves," *Journal of Fluid Mechanics*, vol. 7, 1960, pp. 340–352.

6 H. Poincaré, "Sur l'équilibre d'une masse fluide animée d'un mouvement de rotation," *Acta Math.*, vol. 7, 1885, p. 259 (cited in [3], p. 717).

7 K. Stewartson, "On the Stability of a Spinning Top Containing Liquid," *Journal of Fluid Mechanics*, vol. 5, 1959, pp. 577–592.

Theoretical Pressure Distribution in Journal Bearings

KICHIYE HABATA
Research Engineer,
Satō Agricultural Machine Manufacturing Company,
Shimane Prefecture, Japan

By assuming oil viscosity constant, Reynolds' equation for journal bearings has been solved in a manner similar to Hill's method. Two approximate solutions using E. O. Waters' method and Ritz's method have been added. Numerical computations have been carried out for a centrally supported 120-deg bearing with a unity slenderness ratio. Isobarriers have been determined from the pressure distributions. In order to show a justification for assuming the viscosity constant, the Reynolds equation was solved for the infinitely long bearing with variable viscosity, and the solution compared with that of Sommerfeld.

As far as the author is aware, an analytical solution of Reynolds' equation for journal bearings having a finite width was first given in 1932 by Kyujiro Kino [1].[1] Later, in 1938, it was also solved analytically by E. O. Waters [2], and it was again attacked by Kino in 1940 [3]. In all those cases the problem was solved by means of Hill's method.

In 1943 it was again solved by Vogelpohl [4] who used the Ritz method.

In this paper a solution similar to Hill's method will be given, but an attempt has been made to avoid the infinite determinant inherent in Hill's method. Ritz's method and Waters' approximate method will also be included for purposes of comparison.

Fig. 1 gives a geometric representation of a partial journal bearing with running clearance.

1 Solutions of Reynolds' Equation for Finite Bearings

If viscosity μ is assumed constant, then the Reynolds equation for the finite-length bearing will be given by

$$\frac{\partial}{\partial x}\left(h^3\frac{\partial p}{\partial x}\right)+\frac{\partial}{\partial z}\left(h^3\frac{\partial p}{\partial z}\right)=6\mu U\frac{dh}{dx} \tag{1}$$

or by putting $x = a\theta$ and $h = cg$,

$$\frac{\partial}{\partial\theta}\left(g^3\frac{\partial p}{\partial\theta}\right)+a^2g^3\frac{\partial^2 p}{\partial z^2}=\frac{6\mu Ua}{c^2}\frac{dg}{d\theta} \tag{2}$$

[1] Numbers in brackets designate References at end of paper.

Presented at the Summer Conference of the Applied Mechanics Division, Chicago, Ill., June 14–16, 1961, of The American Society of Mechanical Engineers.

Discussion of this paper should be addressed to the Editorial Department, ASME, United Engineering Center, 345 East 47th Street, New York 17, N. Y., and will be accepted until January 10, 1962. Discussion received after the closing date will be returned. Manuscript received by ASME Applied Mechanics Division, December 22, 1960. Paper No. 61—APM-20.

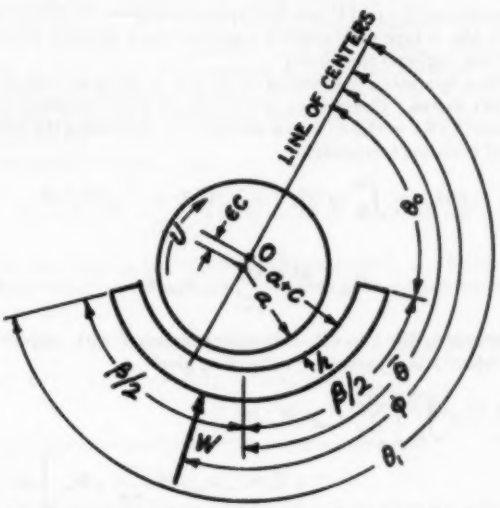

Fig. 1 Geometric representation of partial journal bearing

Now let

$$p=\Theta(\theta)\cdot Z(z)$$

Then (2) becomes

$$(g^3\Theta')'Z+a^2g^3\Theta Z''=\frac{6\mu Ua}{c^2}g'$$

Following the process of separation of variables and taking the axial configuration as shown in Fig. 2, we get

$$p=\sum_{1,\,3,\,\ldots}^{\infty}\Theta_m\cos m\pi\frac{z}{b} \tag{3}$$

Nomenclature

- a = radius of journal
- b = axial width
- c = radial clearance
- $g = h/c = 1+\epsilon\cos\theta$
- $h = c(1+\epsilon\cos\theta)$ = film thickness
- l = linear, length of bearing arc $= \beta a$
- p = pressure within oil film
- T = temperature
- u = relative velocity of bearing surface
- w = mean load per unit bearing width
- $x = a\theta$ = periphery along bearing
- z = distance in axial direction of journal
- β = angular extent of bearing
- ϵ = eccentricity factor
- θ = angle from line of centers to any position in film
- θ_0 = angle from line of centers to inlet edge of bearing
- θ_1 = angle from line of centers to outlet edge of bearing
- ϕ = angle from line of centers to mean load w
- μ = coefficient of viscosity
- μ_m = exponent
- ln = natural logarithm
- log = common logarithm

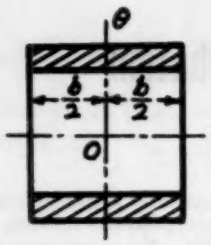

Fig. 2

where Θ_m is the solution of

$$(g^2\Theta_m')' - \lambda_m^2 g^2 \Theta_m = \gamma_m g' \tag{4}$$

where

$$\lambda_m = m\pi a/b, \quad \gamma_m = (-1)^{\frac{m-1}{2}} \frac{24\mu Ua}{m\pi c^3}, \quad m = 1, 3, 5, \ldots$$

Expressions (3) and (4) are the expressions given by Kino, and (4) is also a type of Mathieu's equation whose solution has not yet been explored completely.

Three approximate solutions of (4) will be given as follows:

Ritz's Method. The solution of (4) with the given boundary conditions $\Theta_m(\theta_0) = \Theta_m(\theta_1) = 0$ is obtained by minimizing the calculus of variation formulation

$$I(\Theta_m) = \int_{\theta_0}^{\theta_1} [g^2(\Theta_m'^2 + \lambda_m^2\Theta_m^2) + 2\gamma_m g'\Theta_m]d\theta \tag{5}$$

Let

$$\Theta_m = \frac{\mu Ua}{c^3} \sum_{n=i}^{N} a_{mn}\Psi_{mn}(\theta) \tag{6}$$

Substituting (6) into (5), and differentiating I with respect to $a_{m\nu}$ where ν is a particular value of n, gives

$$\frac{\partial I}{\partial a_{m\nu}} = 2\int_{\theta_0}^{\theta_1} \left[\sum_{n=i}^{N} a_{mn} g^2(\Psi_{m\nu}'\Psi_{mn}' + \lambda_m^2\Psi_{m\nu}\Psi_{mn}) + \frac{24}{m\pi} g'\Psi_{m\nu}\right] d\theta \tag{7}$$

According to Ritz $a_{m\nu}$ is determined so that (7) vanishes; i.e.,

$$\int_{\theta_0}^{\theta_1} \left[\sum_{n=i}^{N} a_{mn} g^2(\Psi_{m\nu}'\Psi_{mn}' + \lambda_m^2\Psi_{m\nu}\Psi_{mn}) + \frac{24}{m\pi} g'\Psi_{m\nu}\right] d\theta = 0 \tag{8}$$

Now let

$$\Psi_{mn}(\theta) = \sin\frac{n\pi}{\beta}(\theta - \theta_0)$$

the expression proposed by Professor Vogelpohl. Then (8) becomes

$$\int_{\theta_0}^{\theta_1} \left\{\Sigma a_{mn}\left[(m^2 + n^2)g^2 \sin\frac{n\pi}{\beta}(\theta - \theta_0) + ng^2 \sin\theta\cos\frac{n\pi}{\beta}(\theta - \theta_0)\right] + (-1)^{\frac{m}{2}} \frac{32\epsilon}{3m\pi} \sin\theta\right\} \sin\frac{n\pi}{\beta}(\theta - \theta_0)d\theta = 0 \tag{9}$$

For the 120-deg bearing, in particular,

$$\pi/\beta = 3/2 \tag{10}$$

Then (9) gives

$$\Sigma A_{m\nu n}a_{mn} = (-1)^{\frac{m-1}{2}} \frac{1}{m} Q(\epsilon, \nu) \tag{11}$$

where

$$A_{m\nu n} = A_{mn\nu} = (\nu n + m^2)P(\epsilon, \nu - n) + (\nu n - m^2)P(\epsilon, \nu + n)$$

$$P(\epsilon, 0) = (\tfrac{3}{8} + \epsilon^2)\pi + 3\sqrt{3}\,\epsilon(1 + \epsilon^2/4)\cos\phi + \tfrac{3}{4}\sqrt{3}\,\epsilon^2\cos 2\phi$$

$$P(\epsilon, \pm 2) = -\tfrac{3}{32}\sqrt{3}\,\epsilon(4 + \epsilon^2)\cos\phi - \tfrac{3}{8}\sqrt{3}\,\epsilon^2\cos 2\phi - \frac{\pi}{12}\epsilon^3\cos 3\phi$$

$$P(\epsilon, \pm i) = \begin{cases} \dfrac{3\epsilon(4 + \epsilon^2)}{9i^2 - 4}\sin\phi - \dfrac{12\epsilon^2}{9i^2 - 16}\sin 2\phi - \dfrac{2\epsilon^3}{3i^2 - 12}\sin 3\phi & (i = 1, 3, 5, \ldots) \\ -\dfrac{3\sqrt{3}\,\epsilon}{9i^2 - 4}(4 + \epsilon^2)\cos\phi - \dfrac{12\sqrt{3}\,\epsilon^2}{9i^2 - 16}\cos 2\phi & (i = 4, 6, 8, \ldots) \end{cases}$$

$$Q(\epsilon, \nu) = \begin{cases} \dfrac{128\epsilon}{\pi}\sin\phi\,\dfrac{\nu}{9\nu^2 - 4} & (\nu \text{ odd}) \\ -\dfrac{128\sqrt{3}\,\epsilon}{\pi}\cos\phi\,\dfrac{\nu}{9\nu^2 - 4} & (\nu \text{ even}) \end{cases}$$

Assigning values 1, 2, 3 . . . for ν and n in succession, (11) gives

$$\left.\begin{aligned} A_{m11}a_{m1} + A_{m12}a_{m2} + A_{m13}a_{m3} + \ldots &= (-1)^{\frac{m-1}{2}} Q(\epsilon, 1) \\ A_{m21}a_{m1} + A_{m22}a_{m2} + A_{m23}a_{m3} + \ldots &= (-1)^{\frac{m-1}{2}} Q(\epsilon, 2) \\ A_{m31}a_{m1} + A_{m32}a_{m2} + A_{m33}a_{m3} + \ldots &= (-1)^{\frac{m-1}{2}} Q(\epsilon, 3) \\ \ldots\ldots\ldots\

A More Accurate Method. No simple solution which is valid for the larger values of ϵ is known. Perhaps Hill's method deserves the first mention. This method was applied to the journal bearing by Kino [1, 3]. His solution for

$$(g^2\Theta_m')' - \lambda_m^2 g^2 \Theta_m = 0$$

may be summarized as follows: Let

$$\Theta_m = g^{-1/2}\Phi_m \tag{15}$$

Then the foregoing differential equation becomes

$$\phi_m'' + \left(\frac{3}{4} - \lambda_m^2 - \frac{3}{g} + \frac{3}{4}\frac{1-\epsilon^2}{g^2}\right)\phi_m = 0 \tag{16}$$

Substituting identical relations

$$\frac{1}{g} = \frac{1}{(1-\epsilon^2)^{1/2}} + \frac{2}{(1-\epsilon^2)^{1/2}} \sum_1^\infty \left[-\frac{1-(1-\epsilon^2)^{1/2}}{\epsilon}\right]^n \cos n\theta$$

$$\frac{1}{g^2} = (1-\epsilon^2)^{-1/2} + 2(1-\epsilon^2)^{-1/2} \sum_1^\infty [1 + n(1-\epsilon^2)^{1/2}] \left[-\frac{1-(1-\epsilon^2)^{1/2}}{\epsilon}\right]^n \cos n\theta \tag{17}$$

$$\cos n\theta = \tfrac{1}{2}(e^{jn\theta} + e^{-jn\theta})$$

into (16) and letting $\theta = 2\psi$, we get

$$\frac{d^2\Phi_m}{d\psi^2} - \left[a_{m0} + \sum_1^\infty a_n(e^{j2n\psi} + e^{-j2n\psi})\right]\Phi_m = 0 \tag{18}$$

where

$$a_{m0} = 4\lambda_m^2 + 9\left[\frac{1}{(1-\epsilon^2)^{1/2}} - 1\right],$$

$$a_n = \frac{3}{(1-\epsilon^2)^{1/2}}[3 - n(1-\epsilon^2)^{1/2}]\left[-\frac{1-(1-\epsilon^2)^{1/2}}{\epsilon}\right]^n$$

Let

$$\Phi_m = e^{\mu_m\psi} \sum_{-\infty}^{\infty} b_{mn} e^{j2n\psi} \tag{19}$$

Then (18) becomes

$$\sum_{-\infty}^{\infty} (\mu_m + j2n)^2 b_{mn} e^{j2n\psi} - \left[a_{m0} + \sum_{s=1}^{\infty} a_s(e^{j2s\psi} + e^{-j2s\psi})\right]\sum_{-\infty}^{\infty} b_{mn} e^{j2n\psi} = 0 \tag{20}$$

$$\therefore [(\mu_m + j2n)^2 - a_{m0}]b_{mn} - \sum_{s=1}^{\infty} a_s(b_{m,n-s} + b_{m,n+s}) = 0 \tag{21}$$

Relation (21) gives the infinite determinant

$$\Delta(j\mu_m) = \begin{vmatrix} \cdots & \cdots & \cdots & \cdots \\ \cdots \dfrac{(j\mu_m+2)^2 + a_{m0}}{2^2 + a_{m0}} & \dfrac{a_1}{2^2 + a_{m0}} & \dfrac{a_2}{2^2 + a_{m0}} & \cdots \\ \cdots \dfrac{a_1}{0^2 + a_{m0}} & \dfrac{(j\mu_m)^2 + a_{m0}}{0^2 + a_{m0}} & \dfrac{a_1}{0^2 + a_{m0}} & \cdots \\ \cdots \dfrac{a_2}{2^2 + a_{m0}} & \dfrac{a_1}{2^2 + a_{m0}} & \dfrac{(j\mu_m-2)^2 + a_{m0}}{2^2 + a_{m0}} & \cdots \\ \cdots & \cdots & \cdots & \cdots \end{vmatrix} = 0 \tag{22}$$

and this determinant is known to reduce to the following compact form:

$$\Delta(j\mu_m) = \Delta(0) - \left[\frac{\sinh\frac{\pi}{2}\mu_m}{\sinh\frac{\pi}{2}(a_{m0})^{1/2}}\right]^2 \tag{23}$$

Hence μ_m is determined from the relation

$$\sinh\frac{\pi}{2}\mu_m = \pm[\Delta(0)]^{1/2}\sinh\frac{\pi}{2}(a_{m0})^{1/2} \tag{24}$$

Detailed accounts are given by Whittaker [5] as well as in Kino's papers [1, 3].

The first difficulty is experienced in evaluating $\Delta(0)$. For $\epsilon = 0.9$ in the 120-deg bearing, for example, taking 1^2, 2^2, and 3^2 elements, respectively, gives 1, 0.5769, and 0.40968. Many more elements would have to be taken into account to obtain the stationary value of $\Delta(0)$. For larger values of m, of course, we may assume $\Delta(0) = 1$ without serious error. Another difficulty will be experienced in evaluating $b_{m,n}$ in terms of b_{m0}, especially when $m = 1$. Thus Hill's method, so far as the bearings under consideration here are concerned, is found to be rather impractical, and some other means must be devised. One method will be as follows:

Homogeneous Solution. Assume

$$\Theta_m = A_{m0}(\theta) + \sum_{n=1}^{\infty} [A_{mn}(\theta)\cos n\theta + B_{mn}(\theta)\sin n\theta] \tag{25}$$

where A_{mn} and B_{mn} are nonperiodic functions of θ; i.e., functions independent of $\cos n\theta$ and $\sin n\theta$. Omitting subscript m for simplicity, then

$$\Theta' = A_0' + \Sigma[(A_n' + nB_n)\cos n\theta + (-nA_n + B_n')\sin n\theta]$$

$$\Theta'' = A_0'' + \Sigma[(A_n'' - n^2A_n + 2nB_n')\cos n\theta + (-2nA_n' + B_n'' - n^2B_n)\sin n\theta]$$

Substituting these relations in the original equation

$$(g^2\Theta_m')' - \lambda_m^2 g^2\Theta_m = 0,$$

and equating the coefficients for $\cos n\theta$ and $\sin n\theta$ to zero gives

$$\begin{aligned}
&2(A_0'' - \lambda^2 A_0) + \epsilon[A_1'' - (\lambda^2 - 2)A_1] - \epsilon B_1' = 0 \\
&2\epsilon(A_0'' - \lambda^2 A_0) + 2[A_1'' - (\lambda^2 + 1)A_1] + 4B_1' + \epsilon[A_2'' - (\lambda^2 - 2)A_2] + \epsilon B_2' = 0 \\
&-6\epsilon A_0'' - 4A_1' + 2[B_1'' - (\lambda^2 + 1)B_1] - \epsilon A_2' + \epsilon[B_2'' - (\lambda^2 - 2)B_2] = 0 \\
&\epsilon[A_1'' - (\lambda^2 + 4)A_1] + 5\epsilon B_1' + 2[A_2'' - (\lambda^2 + 4)A_2] + 8B_2' + \epsilon(A_3'' - \lambda^2 A_3) + 3\epsilon B_3' = 0 \\
&-5\epsilon A_1' + \epsilon[B_1'' - (\lambda^2 + 4)B_1] - 8A_2' + 2[B_2'' - (\lambda^2 + 4)B_2] - 3\epsilon A_3' + \epsilon(B_3'' - \lambda^2 B_3) = 0 \\
&\cdots\cdots\cdots

$$A_{mn} = a_{mn}e^{\mu_m\theta}, \quad B_{mn} = b_{mn}e^{\mu_m\theta} \tag{27}$$

Then (26) becomes, still omitting the subscript m,

$$2(x^2)a_0 + \epsilon(x^2 + 2)a_1 - \epsilon\mu b_1 = 0$$

$$2\epsilon(x^2)a_0 + 2(x^2 - 1)a_1 + 4\mu b_1 + \epsilon(x^2 + 2)a_2 + \epsilon\mu b_2 = 0$$

$$-6\epsilon\mu a_0 - 4\mu a_1 + 2(x^2 - 1)b_1 - \epsilon\mu a_2 + \epsilon(x^2 + 2)b_2 = 0$$

$$\epsilon(x^2 - 4)a_1 + 5\epsilon\mu b_1 + 2(x^2 - 4)a_2 + 8\mu b_2 + \epsilon(x^2)a_3 + 3\epsilon\mu b_3 = 0$$

$$-5\epsilon\mu a_1 + \epsilon(x^2 - 4)b_1 - 8\mu a_2 + 2(x^2 - 4)b_2 - 3\epsilon\mu a_3 + \epsilon(x^2)b_3 = 0 \tag{28}$$

$$\epsilon(x^2 - 10)a_2 + 7\epsilon\mu b_2 + 2(x^2 - 9)a_3 + 12\mu b_3 + \epsilon(x^2 - 4)a_4 + 5\epsilon\mu b_4 = 0$$

$$-7\epsilon\mu a_2 + \epsilon(x^2 - 10)b_2 - 12\mu a_3 + 2(x^2 - 9)b_3 - 5\epsilon\mu a_4 + \epsilon(x^2 - 4)b_4 = 0$$

.....

where $x_m^2 = \mu_m^2 - \lambda_m^2$. The reduction of the infinite determinant of (28) into terms of known functions of μ_m or x_m, i.e., the expression corresponding to (23), is unknown. We are forced to consider only the first few coefficients because of complications encountered in developing the determinant. To obtain the same degree of accuracy, however, fewer terms are required than those in Hill's method. The slower convergence of the latter results from having substituted the first two relations in (17).

Let us take the first two b_{mn} into consideration ignoring the rest. Then (28) becomes, still omitting the subscript m,

$$2(0)a_0 + \epsilon(2)a_1 - \epsilon\mu b_1 = 0$$

$$2\epsilon(0)a_0 + 2(-1)a_1 + 4\mu b_1 + \epsilon(2)a_2 + \epsilon\mu b_2 = 0$$

$$6\epsilon\mu a_0 + 4\mu a_1 - 2(-1)b_1 + \epsilon\mu a_2 - \epsilon(2)b_2 = 0$$

$$\epsilon(-4)a_1 + 5\epsilon\mu b_1 + 2(-4)a_2 + 8\mu b_2 + \epsilon(0)a_3 = 0$$

$$5\epsilon\mu a_1 - \epsilon(-4)b_1 + 8\mu a_2 - 2(-4)b_2 + 3\epsilon\mu a_3 = 0$$

$$\epsilon(-10)a_2 + 7\epsilon\mu b_2 + 2(-9)a_3 + \epsilon(-4)a_4 = 0$$

$$7\epsilon\mu a_2 - \epsilon(-10)b_2 + 12\mu a_3 + 5\epsilon\mu a_4 = 0$$

$$\epsilon(-18)a_3 + 2(-16)a_4 + \epsilon(-10)a_5 = 0$$

$$\epsilon(-28)a_4 + 2(-25)a_5 + \epsilon(-18)a_6 = 0$$

.....

$$\epsilon[-(n-1)(n+2)]a_{n-1} + 2(-n^2)a_n + \epsilon[-(n+1)(n-2)]a_{n+1} = 0 \tag{29}$$

.....

where

$$(0) = x_m^2, (2) = x_m^2 + 2, \ldots, (k) = x_m^2 + k = \mu_m^2 - \lambda_m^2 + k, \ldots$$

Since the diagonal product of the determinant D of the coefficients of the first seven rows of (29) can be factored out, x_m and hence μ_m may be found from the determinantal equation $D = 0$. Having determined x_m and μ_m, the coefficients b_{m1}, b_{m2}, $a_{m1} \ldots a_{m4}$ can be determined in terms of a_{m0} by solving simultaneously any six of the first seven equations of (29).

A few more coefficients a_{mn} may be obtained from the eighth and other remaining equations. Thus

$$a_5 = -[\epsilon(-18)a_3 + 2(-16)a_4]/\epsilon(-10)$$

.....

$$a_{n+1} = -[\epsilon\{-(n-1)(n+2)\}a_{n-1} + 2(-n^2)a_n]/\epsilon\{-(n+1)(n-2)\} \tag{30}$$

.....

However, they cannot be extended indefinitely, because sooner or later they begin to diverge. This phenomenon, of course, is due to the fact that the b_{mn} beyond b_{m2} were ignored.

It has been found that the values of b_{mn} decrease as ϵ increases. Thus for larger values of ϵ, b_{m2} may be omitted. This means that the form of the pressure (in this case) justifies omission of b_{m3} and those of the higher orders of n. Hence (29) becomes

$$2(0)a_0 + \epsilon(2)a_1 - \epsilon\mu b_1 = 0$$

$$2\epsilon(0)a_0 + 2(-1)a_1 + 4\mu b_1 + \epsilon(2)a_2 = 0$$

$$6\epsilon\mu a_0 + 4\mu a_1 - 2(-1)b_1 + \epsilon\mu a_2 = 0$$

$$\epsilon(-4)a_1 + 5\epsilon\mu b_1 + 2(-4)a_2 + \epsilon(0)a_3 = 0$$

$$5\epsilon\mu a_1 - \epsilon(-4)b_1 + 8\mu a_2 + 3\epsilon\mu a_3 = 0$$

$$\epsilon(-10)a_2 + 2(-9)a_3 + \epsilon(-4)a_4 = 0$$

$$\epsilon(-18)a_3 + 2(-16)a_4 + \epsilon(-10)a_5 = 0$$

..... (31)

The values of x_m and μ_m can be determined from the determinantal equations formed from the first five equations of (31), and then the coefficients b_{m1}, $a_{m1} \ldots a_{m3}$ can be found in terms of a_{m0} by solving simultaneously any four of the said first five equations. A few more may be found subject to the restriction already mentioned.

When $\epsilon = 1$ the foregoing determinantal equation gives

$$-504x^4 - 504x^2 - 1080\lambda^2 = 0, \quad \text{or} \quad 7x^4 + 7x^2 + 15\lambda^2 = 0$$

which has no real root, showing that the solution of equation (13) ceases to contain exponential terms. So the determinantal equation which is roughly approximate has turned out to give a correct conclusion. In fact, Θ_m in this limiting case is given in terms of hypergeometric functions.

For values of ϵ very close to 1 or those of m larger than 1, b_{mn} may be omitted altogether. We then have

$$x^2 = \left(\frac{25}{4} + \frac{6\epsilon^2}{1 - \epsilon^2}\right)^{1/2} - \frac{5}{2}, \quad \mu_m = \pm(\lambda_m^2 + x^2)^{1/2},$$
$$a_1 = -\frac{2x^2}{\epsilon(x^2 + 2)}a_0, \quad a_2 = \left[\frac{8x^2}{\epsilon^2(x^2 + 2)} - 6\right]a_0. \tag{32}$$

The subscript m has been dropped from x_m and a_{mn} because they are independent of m in this case. The other a_n may be found from (30) subject to the restriction already mentioned. In this case then, the solution of

$$(g^2\Theta_m')' - \lambda_m^2 g^2\Theta_m = 0$$

becomes

$$\Theta_m = (A_m e^{\mu_m\theta} + B_m e^{-\mu_m\theta})\Phi(\theta) \tag{33}$$

where

$$\Phi(\theta) = 1 + \Sigma a_n \cos n\theta$$

Particular Solution. Let

$$J_m = g^{-2}\sum_1^\infty c_{mn} \sin n\theta \tag{34}$$

Substituting J_m and its derivatives in (4) gives

$$[2(\lambda_m^2+1)c_{m1}+\epsilon(\lambda_m^2+4)c_{m2}-2\epsilon\gamma_m]\sin\theta$$
$$+\sum_2^\infty [\epsilon\{\lambda_m^2+n(n-3)\}c_{m,n-1}+2(\lambda_m^2+n^2)c_{mn}$$
$$+\epsilon\{\lambda_m^2+n(n+3)\}c_{m,n+1}]\sin n\theta=0 \quad (35)$$

Equating the coefficients of each term to zero yields an infinite number of equations for determining c_{mn}. The foregoing particular integral becomes simply

$$\frac{\epsilon\gamma_m}{\lambda_m^2+1}g^{-2}\sin\theta$$

when $\lambda_m^2=2$ or $m\pi a/b=\sqrt{2}$. When $m=1$, in particular, $\pi a/b=\sqrt{2}$, and for a bearing having a unity slenderness ratio, $\beta=\pi/\sqrt{2}=127.3$ deg. Thus the convergence of J_m slows down as λ_m^2 deviates from 2. This is also true when ϵ is large. Likewise, J_m reduces to the same simple form when ϵ is very small.

For the reason stated previously we have to seek another form of particular integral when ϵ is large and λ_m^2 not close to 2. To this let

$$J_m=g^{-2}\Xi_m,\quad \Xi_m=\sum_1^\infty c_{mn}\sin n\theta \quad (36)$$

Then (4) gives

$$g\Xi_m''-3g'\Xi_m'-[\lambda_m^2g-3+3(1-\epsilon^2)g^{-1}]\Xi_m=\gamma_m gg' \quad (37)$$

Proceeding in the same way as before, and omitting the subscript m, we get the simultaneous equations

$$\begin{aligned}
&[(4+2\epsilon^2)(\lambda^2+1)-12\epsilon^2]c_1+\epsilon(4\lambda^2+22)c_2\\
&\qquad+\epsilon^2(\lambda^2+18)c_3=(4+\epsilon^2)\epsilon\gamma\\
&\epsilon(4\lambda^2-8)c_1+[(4+2\epsilon^2)(\lambda^2+4)-12\epsilon^2]c_2\\
&\qquad+\epsilon(4\lambda^2+48)c_3+\epsilon^2(\lambda^2+28)c_4=4\epsilon^2\gamma\\
&\epsilon^2(\lambda^2-2)c_1+\epsilon(4\lambda^2-2)c_2\\
&\qquad+[(4+2\epsilon^2)(\lambda^2+9)-12\epsilon^2]c_3\\
&\qquad+\epsilon(4\lambda^2+82)c_4+\epsilon^2(\lambda^2+40)c_5=\epsilon^2\gamma\\
&\epsilon^2(\lambda^2-2)c_2+\epsilon(4\lambda^2+12)c_3+\\
&\qquad+[(4+2\epsilon^2)(\lambda^2+16)-12\epsilon^2]c_4\\
&\qquad+\epsilon(4\lambda^2+124)c_5+\epsilon^2(\lambda^2+54)c_6=0\\
&\cdots\cdots\cdots\cdots\cdots\cdots\cdots\cdots\cdots\cdots\cdots\cdots
\end{aligned} \quad (38)$$

from which c_{mn} can be determined. The procedure, however, becomes much more laborious than is the case with (34).

Complete Solution. The complete solution of equation (4) or

$$(g^3\Theta_m')'-\lambda_m^2g^3\Theta_m=\gamma_m g'$$

is given, in general, by

$$\frac{c^2}{\mu Ua}\Theta_m=J_m(\theta)+A_me^{\mu_m\theta}\Phi_m(\theta)+B_me^{-\mu_m\theta}\Phi_m(-\theta) \quad (39)$$

where

$$\Phi_m(\pm\theta)=1+a_{m1}\cos\theta+a_{m2}\cos 2\theta+\ldots.\pm(b_{m1}\sin\theta+b_{m2}\sin 2\theta+\ldots.),$$

and J_m is given either by (34) or by (36).

From the boundary conditions

$$\Theta_m(\theta_0)=\Theta_m(\theta_1)=0 \quad (40)$$

we have

$$\begin{aligned}
A_me^{\mu_m\theta_0}\Phi_m(\theta_0)+B_me^{-\mu_m\theta_0}\Phi_m(-\theta_0)&=-J_m(\theta_0)\\
A_me^{\mu_m\theta_1}\Phi_m(\theta_1)+B_me^{-\mu_m\theta_1}\Phi_m(-\theta_1)&=-J_m(\theta_1)
\end{aligned} \quad (41)$$

Hence we get

$$\begin{aligned}
A_m&=\frac{1}{\Delta_m}\left[-\frac{J_m(\theta_1)}{e^{\mu_m\theta_1}\Phi_m(\theta_1)}+\frac{e^{\mu_m\theta_0}}{e^{2\mu_m\theta_1}}\frac{\Phi_m(-\theta_1)}{\Phi_m(\theta_1)}\frac{J_m(\theta_0)}{\Phi_m(-\theta_0)}\right]\\
B_m&=\frac{1}{\Delta_m}\left[-\frac{e^{\mu_m\theta_0}J_m(\theta_0)}{\Phi_m(-\theta_0)}+\frac{e^{2\mu_m\theta_0}}{e^{\mu_m\theta_1}}\frac{\Phi_m(\theta_0)}{\Phi_m(-\theta_0)}\frac{J_m(\theta_1)}{\Phi_m(\theta_1)}\right]
\end{aligned} \quad (42)$$

where

$$\Delta_m=1-\frac{e^{2\mu_m\theta_0}}{e^{2\mu_m\theta_1}}\frac{\Phi_m(\theta_0)}{\Phi_m(-\theta_0)}\frac{\Phi_m(-\theta_1)}{\Phi_m(\theta_1)}$$

For larger values of m the following approximations are found to be sufficiently accurate:

$$\begin{aligned}
A_2&=-\frac{J_2(\theta_1)}{e^{\mu_2\theta_1}\Phi_2(\theta_1)}+\frac{e^{\mu_2\theta_0}}{e^{2\mu_2\theta_1}}\frac{\Phi_2(-\theta_1)}{\Phi_2(\theta_1)}\frac{J_2(\theta_0)}{\Phi_2(-\theta_0)}\\
B_2&=-\frac{e^{\mu_2\theta_0}J_2(\theta_0)}{\Phi_2(-\theta_0)}+\frac{e^{2\mu_2\theta_0}}{e^{\mu_2\theta_1}}\frac{\Phi_2(\theta_0)}{\Phi_2(-\theta_0)}\frac{J_2(\theta_1)}{\Phi_2(\theta_1)}
\end{aligned} \quad (43)$$

$$A_m=-\frac{J_m(\theta_1)}{e^{\mu_m\theta_1}\Phi_m(\theta_1)}\qquad B_m=-\frac{e^{\mu_m\theta_0}J_m(\theta_0)}{\Phi_m(-\theta_0)}\quad m\geq 5$$

2 Numerical Examples

Pressure Distribution. The numerical examples to follow are limited to a centrally supported 120-deg partial bearing with slenderness ratio equal to 1. First let us establish the angle θ_0 when $\epsilon=0$. When ϵ is very small, the solution of (4) is found to be

$$\frac{c^2}{\mu Ua}\Theta_m=(-1)^{\frac{m-1}{2}}\frac{30.56}{m(9m^2+4)}\left(-g'+A_me^{\frac{3m}{2}\theta}+B_me^{-\frac{3m}{2}\theta}\right) \quad (44)$$

Referring to the axis $\theta=\phi$ in Fig. 3, equation (44) becomes

$$\frac{c^2}{\mu Ua}\Theta_m(\theta')=(-1)^{\frac{m-1}{2}}\frac{30.56}{m(9m^2+4)}\left[\epsilon\sin(\theta'+\phi)+A_me^{\frac{3m}{2}(\theta'+\phi)}+B_me^{-\frac{3m}{2}(\theta'+\phi)}\right]$$

$$\frac{c^2}{\mu Ua}\Theta_m(-\theta')=(-1)^{\frac{m-1}{2}}\frac{30.56}{m(9m^2+4)}\left[\epsilon\sin(-\theta'+\phi)+A_me^{\frac{3m}{2}(-\theta'+\phi)}+B_me^{-\frac{3m}{2}(-\theta'+\phi)}\right]$$

Since Θ_m becomes symmetric about the new axis as ϵ approaches zero,

$$\Theta_m(\theta')=\Theta_m(-\theta')\quad\text{as}\quad\epsilon\to 0$$

Hence

$$\begin{aligned}
&\sin(\theta'+\phi)=\sin(-\theta'+\phi)\\
&2\left(A_me^{\frac{3m}{2}\phi}-B_me^{-\frac{3m}{2}\phi}\right)\sinh\frac{3m}{2}\theta'=0
\end{aligned} \quad (45)$$

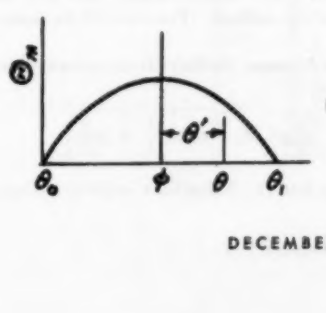

Fig. 3

The first relation gives

$$\phi = 90°, \theta_0 = 30°, \theta_1 = 150° \tag{46}$$

the angles sought when $\epsilon = 0$.

Pressure distributions were computed for $\epsilon = 0.1$, 0.2, 0.4, 0.6, 0.8, 0.9, 0.95, and 0.99. Most of the computations were done before formulations (29) to (33) were developed. Computations for $\epsilon = 0.2$ to 0.8 were carried out years ago by means of the Ritz method given in Section 1. They were also recomputed with the addition of $\epsilon = 0.1$ by the method given in the "Simple Solution" of Section 1. For the foregoing reason, the computations for $\epsilon = 0.8$, 0.9, and 0.95 were obtained, instead of the method discussed under "Homogeneous Solution" in Section 1, by the following formulas.

$$\begin{aligned}(32 - 32\epsilon^2 + 4\epsilon^4)x_m^{10} - (352 - 184\epsilon^2 - 40\epsilon^4)x_m^8 \\ + [(32 - 50\epsilon^2 + 19\epsilon^4)4\lambda_m^2 + 352 + 1328\epsilon^2 - 532\epsilon^4]x_m^6 \\ - [(416 - 500\epsilon^2 + 121\epsilon^4)4\lambda_m^2 - 1888 + 2344\epsilon^2 + 1864\epsilon^4]x_m^4 \\ + [(1552 - 234\epsilon^2 - 468\epsilon^4)4\lambda_m^2 + 1152 - 3456\epsilon^2 - 1296\epsilon^4]x_m^2 \\ - (1296\epsilon^2 + 324\epsilon^4)4\lambda_m^2 = 0\end{aligned}$$

$$a_{m1} = 2x_m^2 a_{m0}\frac{\Delta_{m1}}{\Delta_m}, \quad b_{m1} = -2x_m^2 a_{m0}\frac{\Delta_{m2}}{\Delta_m},$$

$$a_{m2} = 2x_m^2 a_{m0}\frac{\Delta_{m3}}{\Delta_m}, \quad a_{m3} = -2x_m^2 a_{m0}\frac{\Delta_{m4}}{\Delta_m}$$

where

$$\begin{aligned}\Delta_{m1} &= \mu_m[(16 + 4\epsilon^2)(-4)(-9) \\ &\quad - (4\epsilon^2 + \epsilon^4)(0)(-10) - 10\epsilon^2(2)(-9)] \\ \Delta_{m2} &= 8(-1)(-4)(-9) - 6\epsilon^2(2)(-4)(-9) \\ &\quad - 2\epsilon^2(0)(-1)(-10) + \epsilon^4(0)(2)(-10) \\ \Delta_{m3} &= \epsilon\mu_m[20(-1)(-9) - 10\epsilon^2(2)(-9) \\ &\quad - (8 + 2\epsilon^2)(-4)(-9)] \\ \Delta_{m4} &= \epsilon^2\mu_m(-10)[10(-1) - 5\epsilon^2(2) - (4 + \epsilon^2)(-4)] \\ \Delta_m &= -\epsilon(2)\Delta_{m1} - \epsilon\mu_m\Delta_{m2}\end{aligned} \tag{47}$$

For $m = 3$ and larger,

$$\begin{aligned}(16 - 12\epsilon^2)x_m^8 - (32 + 48\epsilon^2 - 24\epsilon^4)x_m^6 \\ + [(16 - 12\epsilon^2 + 6\epsilon^4)4\lambda_m^2 + (-112 + 156\epsilon^2 + 96\epsilon^4)]x_m^4 \\ - [(64 - 21\epsilon^2 - 24\epsilon^4)4\lambda_m^2 - (-64 + 192\epsilon^2 + 72\epsilon^4)]x_m^2 \\ + (72\epsilon^2 + 18\epsilon^4)4\lambda_m^2 = 0\end{aligned}$$

$$a_{m1} = -\frac{\mu_m x_m^2[8(-4) - 3\epsilon^2(6)]a_{m0}}{3\epsilon\mu_m(1)[2(-4) - \epsilon^2(2)]},$$

$$b_{m1} = \frac{(0)(-4)[4(-1) - 3\epsilon^2(2)]a_{m0}}{3\epsilon\mu_m(-1)[2(-4) - \epsilon^2(2)]}, \quad a_{m2} = -\frac{2(1-\epsilon^2)(0)a_{m0}}{2(-4) - \epsilon^2(2)}. \tag{48}$$

Formula (47) was obtained by considering the first four and the sixth equations in (29). Inadvertently, the fifth instead of the sixth equation was omitted. For $\epsilon = 0.99$ formulas (32) and (33) were used.

Constant-Pressure Contours. Isobarriers or constant-pressure contours are given by

$$\sum_{1,3,\ldots} \Theta_m \cos m\pi\frac{x}{b} = p_{const} \tag{49}$$

and shown in Figs. 5 to 11. Those for $\epsilon = 0.2$ to 0.8 are based on Ritz's method, and those for 0.9 to 0.99 on the more analytical method discussed previously.

Mean Load per Bearing Width. The total load W or bw, referring to Fig. 4, is given by

$$\begin{aligned}bw &= \int_{\theta_0}^{\theta_1}\int_{-b/2}^{b/2} p_{||}\,d\theta dz \\ &= \int_{\theta_0}^{\theta_1}\int_{-b/2}^{b/2} \Sigma\Theta_m \cos(\theta - \phi)\cos m\pi\frac{z}{b}\,d\theta dz \\ &= (-1)^{\frac{m-1}{2}}\frac{2b}{m\pi}\int_{\theta_0}^{\theta_1}\Sigma\Theta_m\cos(\theta-\phi)d\theta \\ \therefore w &= (-1)^{\frac{m-1}{2}}\frac{2}{m\pi}\int_{\theta_0}^{\theta_1}\Sigma\Theta_m\cos(\theta-\phi)d\theta\end{aligned} \tag{50}$$

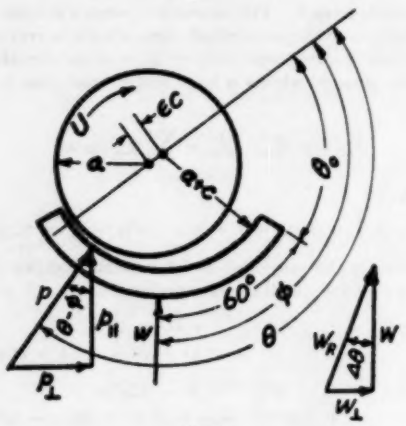

Fig. 4

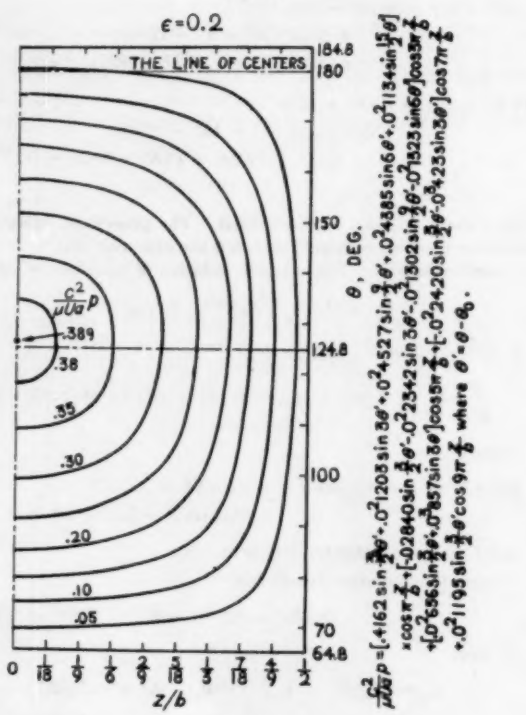

Fig. 5

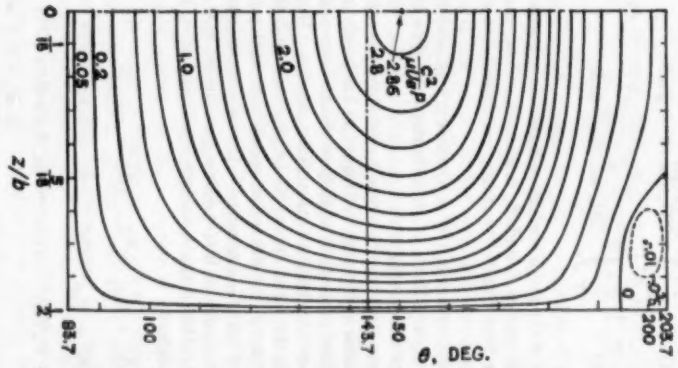

Fig. 7

$\frac{c^2}{\mu U a}p=(2.6864\sin\frac{3}{2}\theta'-.1581\sin3\theta'-.3689\sin\frac{9}{2}\theta'+.2044\sin6\theta'-.0870\sin\frac{15}{2}\theta'+.0343\sin9\theta'-.01185\sin\frac{21}{2}\theta')\cos\pi\frac{z}{b}+(-.2212\sin\frac{3}{2}\theta'-.01202\sin3\theta'+.05510\sin\frac{9}{2}\theta'-.04088\sin6\theta'+.01879\sin\frac{15}{2}\theta'-.0^2837\sin9\theta')\cos3\pi\frac{z}{b}+(.05107\sin\frac{3}{2}\theta'+.0^2802\sin3\theta'-.01772\times\sin\frac{9}{2}\theta'+.01117\sin6\theta')\cos5\pi\frac{z}{b}+(-.01924\sin\frac{3}{2}\theta'-.0^3458\sin3\theta')\cos7\pi\frac{z}{b}+.0^29354\sin\frac{3}{2}\theta'\cos9\pi\frac{z}{b}-.0^25165\sin\frac{3}{2}\theta'\cos11\pi\frac{z}{b}$ where $\theta'=\theta-\theta_0$.

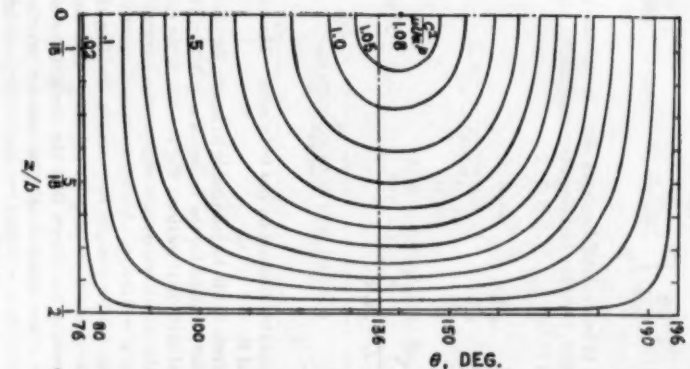

Fig. 6

$\frac{c^2}{\mu U a}p=(1.1083\sin\frac{3}{2}\theta'-.02461\sin3\theta'-.04719\sin\frac{9}{2}\theta'+.02823\sin6\theta'-.01074\sin\frac{15}{2}\theta'+.0^2598\times\sin9\theta')\cos\pi\frac{z}{b}+(-.08038\sin\frac{3}{2}\theta'-.0^2732\sin3\theta'+.0^2556\sin\frac{9}{2}\theta'-.0^2639\sin6\theta'+.0^3648\sin\frac{15}{2}\theta')\cos3\pi\frac{z}{b}+(.01871\sin\frac{3}{2}\theta'+.0^22480\sin3\theta'-.0^21543\sin\frac{9}{2}\theta'+.0^22306\times\sin6\theta')\cos5\pi\frac{z}{b}+(-.0^26953\sin\frac{3}{2}\theta'-.0^3953\sin3\theta')\cos7\pi\frac{z}{b}+.0^23501\sin\frac{3}{2}\theta'\times\cos9\pi\frac{z}{b}-.0^21928\sin\frac{3}{2}\theta'\cos11\pi\frac{z}{b}$ where $\theta'=\theta-\theta_0$.

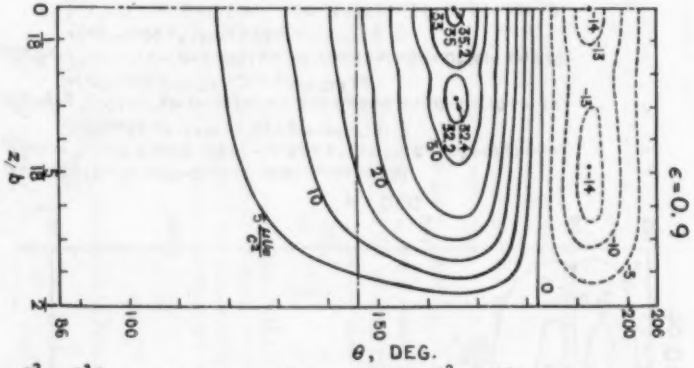

Fig. 9

$\frac{c^2}{\mu U a}p=\frac{c^2}{\mu U a}(\Theta_1\cos\pi z/b+\Theta_3\cos3\pi z/b+\Theta_5\cos5\pi z/b)$, $\frac{c^2}{\mu U a}\Theta_1=g^{-2}(2.1525\sin\theta-.04267\sin2\theta+.0^24448\sin3\theta-.0^37500\sin4\theta+.0^48664\sin5\theta-.02064\sin6\theta)+.0^222664\,e^{\lambda_1\theta}\phi_1(\theta)-87.480\,e^{-\lambda_1\theta}\phi_1(-\theta)$, $\frac{c^2}{\mu U a}\Theta_3=g^{-2}(-.13913\sin\theta+.06091\sin2\theta-.02456\sin3\theta+.0^29489\times\sin4\theta-.0^23499\sin5\theta+.0^21071\sin6\theta)-.0^74402\,e^{\lambda_3\theta}\phi_3(\theta)+201.5\,e^{-\lambda_3\theta}\phi_3(-\theta)$, $\frac{c^2}{\mu U a}\Theta_5=g^{-2}(.03238\sin\theta-.01765\sin2\theta+.0^2916\sin3\theta-.0^24514\sin4\theta+.0^22053\sin5\theta-.0^37435\times\sin6\theta)+.0^{12}4478\,e^{\lambda_5\theta}\phi_5(\theta)-316.1\,e^{-\lambda_5\theta}\phi_5(-\theta)$ where $\lambda_1=2.3660$, $\lambda_3=4.8507$, $\lambda_5=7.7128$; $\phi_1(\pm\theta)=1-1.4042\cos\theta\mp.02948\sin\theta+.1759\cos2\theta-.0932\cos3\theta$, $\phi_3(\pm\theta)=1-1.4055\cos\theta\mp.02738\sin\theta+.2180\cos2\theta$, $\phi_5(\pm\theta)=1-1.4007\cos\theta\mp.01832\sin\theta+.2134\cos2\theta$.

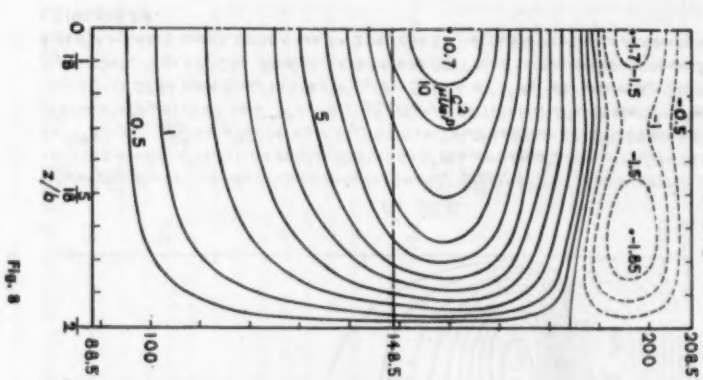

Fig. 8

$\frac{c^2}{\mu U a}p=(7.851\sin\frac{3}{2}\theta'-.933\sin3\theta'-2.580\sin\frac{9}{2}\theta'+1.899\sin6\theta'-.726\sin\frac{15}{2}\theta'+.1241\sin9\theta'-.0^23176\sin\frac{21}{2}\theta')\cos\pi\frac{z}{b}+(-.8040\sin\frac{3}{2}\theta'-.02459\sin3\theta'+.4950\sin\frac{9}{2}\theta'-.3925\times\sin6\theta'+.1596\sin\frac{15}{2}\theta'-.03447\sin9\theta')\cos3\pi\frac{z}{b}+(.4293\sin\frac{3}{2}\theta'-.01651\sin3\theta'-.3680\times\sin\frac{9}{2}\theta'+.3016\sin6\theta'-.09615\sin\frac{15}{2}\theta'+.0^2858\sin9\theta')\cos5\pi\frac{z}{b}+(-.8655\sin\frac{3}{2}\theta'+.03465\sin3\theta'-.0^2666\sin\frac{9}{2}\theta'-.0^2814\sin6\theta'+.0^2730\sin\frac{15}{2}\theta')\cos7\pi\frac{z}{b}+(.03308\times\sin\frac{3}{2}\theta'+.01113\sin3\theta'-.03457\sin\frac{9}{2}\theta'+.01959\sin6\theta')\cos9\pi\frac{z}{b}+(-.01773\sin\frac{3}{2}\theta'-.0^2829\sin3\theta'+.02231\sin\frac{9}{2}\theta'-.01255\sin6\theta')\cos11\pi\frac{z}{b}$ where $\theta'=\theta-\theta_0$.

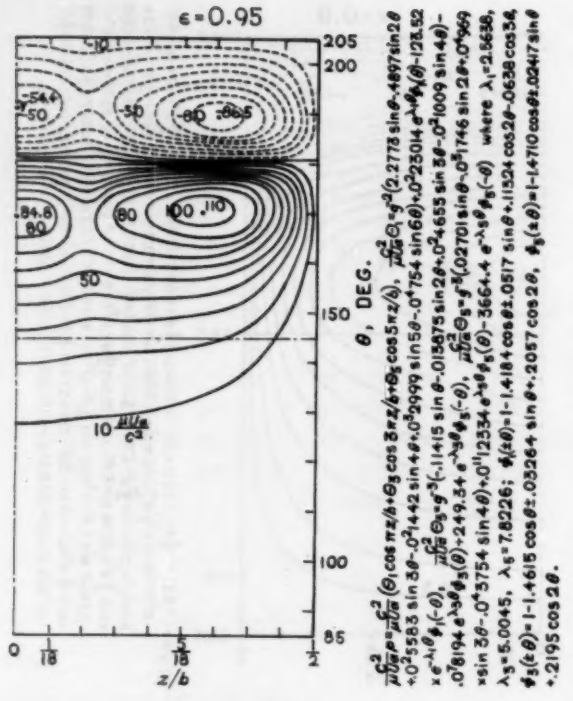

Fig. 10

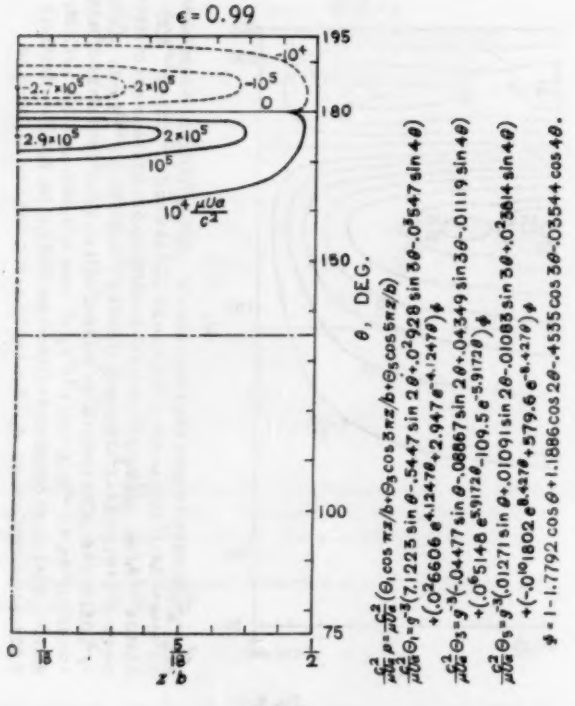

Fig. 11

and likewise

$$w_\perp = (-1)^{\frac{m-1}{2}} \frac{2}{m\pi} \int_{\theta_0}^{\theta_1} \Sigma\Theta_m \sin(\theta - \phi) d\theta \qquad (51)$$

Both w and $w_\perp$ have to be evaluated numerically. In the case of Ritz's method, however, they can be integrated analytically, and the results are found to be

$$\frac{c^2}{\mu Ua} w = \frac{12}{\pi} \sum_{1,3,\ldots}^{M}{}_m \sum_{1,3,\ldots}^{N}{}_n (-1)^{\frac{m-1}{2}} \frac{n}{m(9n^2 - 4)} a_{mn}$$

$$\frac{c^2}{\mu Ua} w_\perp = \frac{12\sqrt{3}}{\pi} \sum_{1,3,\ldots}^{M}{}_m \sum_{2,4,\ldots}^{N'}{}_n (-1)^{\frac{m-1}{2}} \frac{n}{m(9n^2 - 4)} a_{mn} \qquad (52)$$

For the centrally supported bearing $w_\perp$ has to be zero. Thus $w_\perp$ determines θ_0, ϕ, and θ_1.

In the examples given, it will be reasonable to ignore the effect of the negative-pressure regions for the values of $\epsilon \geq 0.8$ for the reason to be discussed in the next section. For $\epsilon = 0.8$, in the case of Ritz's method, the negative-pressure region was integrated both by replacing the $p = 0$ line, the border between the positive and negative regions, with a straight line, and by dividing the negative region into eighteen rectangular sections. The comparison of the two results has shown that the straight-line assumption of the $p = 0$ line is sufficiently accurate for practical purposes. For $\epsilon \geq 0.9$, the $p = 0$ lines became so nearly straight that they were all assumed to be so.

In those cases, then, the mean load and the vertical component become, designating them by w' and $w_\perp'$, respectively,

$$w' = (-1)^{\frac{m-1}{2}} \frac{2}{m\pi} \int_{\theta_0}^{\theta_2} \Sigma\Theta_m \cos(\theta - \phi) d\theta$$

$$w_\perp' = (-1)^{\frac{m-1}{2}} \frac{2}{m\pi} \int_{\theta_0}^{\theta_2} \Sigma\Theta_m \sin(\theta - \phi) d\theta \qquad (53)$$

where θ_2 is the angle of the mean borderline between the positive and negative-pressure regions. Angle θ_2, in general, will be somewhat greater than π (the Gümbel boundary condition), but will approach π as the limit as $\epsilon \to 1$.

In Table 1 are given values of $(c^2/\mu Ua)w$ and $(c^2/\mu Ua)w'$ together with θ_0 and $w_\perp/w$. Ratio $w_\perp/w$ indicates how close the bearing is to being centrally supported.

Discussion. Owing to the author's lack of knowledge concerning the physical phenomena in the negative region, he has tacitly assumed that the negative pressure actually prevails, and computations for $\epsilon \geq 0.8$ were carried out with this assumption. However, in reality, this does not appear to be the case, and the generally accepted concept for the region seems to be that p remains zero instead of becoming negative. If this were the case, then, the continuity of the oil film requires that $\partial p/\partial\theta = 0$ in addition to $p = 0$. Hence the boundary conditions give, by assuming θ_2 to be constant,

$$A_m e^{\mu_m \theta_0} \Phi_m(\theta_0) + B_m e^{-\mu_m \theta_0} \Phi_m(-\theta_0) = -J_m(\theta_0)$$

$$A_m e^{\mu_m \theta_2} \Phi_m(\theta_2) + B_m e^{-\mu_m \theta_2} \Phi_m(-\theta_2) = -J_m(\theta_2)$$

$$A_m e^{\mu_m \theta_2} [\mu_m \Phi_m(\theta_2) + \Phi_m'(\theta_2)] - B_m e^{-\mu_m \theta_2} [\mu_m \Phi_m(-\theta_2) + \Phi_m(-\theta_2)] = 0$$

Eliminating the undetermined coefficients A_m and B_m gives

Table 1

ϵ		θ_0, deg	$\frac{c^2}{\mu U a} w$	$\frac{c^2}{\mu U a} w_\perp$	$w_\perp/w$	$\frac{c^2}{\mu U a} w'$
0.1		(14)47.5	0.1143	0.0^4518	0.0^3331	...
0.2	R	64.8	0.3274	-0.0^3966	-0.0^3289	...
		(14)60.0	0.3365	0.0^3619	0.0^3184	...
0.4	R	76	0.863	0.0^3356	0.0^3413	...
		(14)74	0.8833	0.0^3228	0.0^3258	...
0.6	R	83.7	2.027	0.0207	0.0102	...
		(14)82	2.473	0.0^3877	0.0^3355	...
0.8	R	88.5	5.635	-0.0^37	-0.0^31	5.814
		(47, 48)87	6.810	0.0144	0.0^321	6.995
0.9		86	11.99	0.0100	0.0^383	13.87
0.95		85	25.51	−0.896	−0.0351	34.88
0.99		75	6908	411.8	0.0596	15950

R = Ritz's method; $0.0^2 = 0.00$, $0.0^3 = 0.000$, and so on.

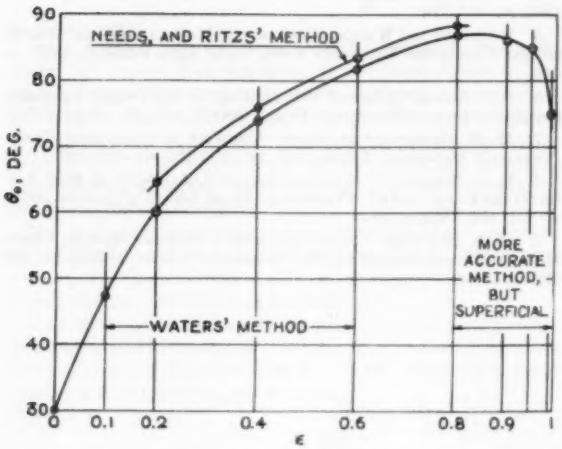

Fig. 12 θ_0 versus ϵ-curves

It may be due to an inconsistency between the assumed trigonometric function and equation (4). The value of θ_0 obtained by Waters' simple solution, however, would be the more correct because it is quite likely that it would give accurate results for the smaller values of ϵ. The Waters simple solution, on the other hand, fails to give a reliable value of θ_0 when $\epsilon = 0.8$; so it will be safe to use it for values of ϵ up to 0.6.

At present no experimental evidence for the three pressure maxima indicated for $\epsilon = 0.9$ and 0.95 is available. The author hopes that this will be examined by some enthusiastic experimenters. At the same time, the fact that two outer maxima can exceed the middle value should be also verified.

3 Conclusion—Effect of Variable Viscosity

The constant-pressure contours are self-explanatory. However, it should be stressed that the terminating line of the positive-pressure region for $\epsilon = 0.8$ lies beyond 180 deg and is not straight, but approaches 180 deg and a straight line, and coincides with the $\theta = \pi$ line when ϵ reaches 0.99, and the Gümbel boundary conditions prevail.

$$\frac{e^{-\mu_m(\theta_2-\theta_0)}\Phi_m(\theta_0)[\mu_m\Phi_m(-\theta_2) + \Phi_m'(-\theta_2)] + e^{\mu_m(\theta_2-\theta_0)}\Phi_m(-\theta_0)[\mu_m\Phi_m(\theta_2) + \Phi_m'(\theta_2)]}{\Phi_m(\theta_2)[\mu_m\Phi_m(-\theta_2) + \Phi_m'(-\theta_2)] + \Phi_m(-\theta_2)[\mu_m\Phi_m(\theta_2) + \Phi_m'(\theta_2)]} = \frac{J_m(\theta_0)}{J_m(\theta_2)}$$

from which a mean θ_2 may be determined by assuming an appropriate value for θ_0. A_m and B_m may then be determined either from (41) or (42) by replacing θ_1 by θ_2. The problem of determining θ_2 may, perhaps, be simplified by putting $\theta_2 = \pi + \delta$ where δ is small. If the assumption $\theta_2 = \text{const}$ were not permissible, the problem would become very difficult to solve.

As Fig. 11 shows, θ_2 becomes precisely equal to π when ϵ reaches 0.99, and the boundary conditions reduce to the Gümbel form.

In the light of the foregoing discussion, the results for $\epsilon \geq 0.8$ become superficial, and the values of θ_0 will be somewhat different from those which would have been obtained by using the foregoing boundary conditions. Eventually, for $\epsilon \geq 0.8$, the bearing ceases to be centrally supported. However, the general conclusions drawn therefrom may still hold.

When ϵ is very large or approaches 1, the maximum pressure or pressures (there are three pressure maxima when $\epsilon = 0.9$ and 0.95) can readily exceed the ultimate strength of the bearing materials, resulting in the formation of pitting.

The values of θ_0 given in Table 1 are reproduced in Fig. 12 for easy visualization. In Fig. 12 are given curves showing the relation between ϵ and the initial angle θ_0. As far as the respective formulas are concerned, θ_0 will be correct to 0.1 deg for $\epsilon = 0.1$ and 0.2, and to 1.0 deg for the higher values of ϵ. Ritz's method, which checks with the values of θ_0 given by S. J. Needs [6], gives somewhat larger values than Waters' simple solution and the more analytical one. The reason for the discrepancy is not clear.

Generally, viscosity μ is a function of p and temperature T. No solution for finite bearings with variable μ can be obtained at present.

For a moderate range of p the viscosity μ can be given, quite accurately, by the expression

$$\mu = \mu_1 e^{Bp} \quad \text{where} \quad \mu_1 = \mu_0 e^{-AT} \tag{54}$$

With this expression of μ, the Reynolds equation for variable viscosity can be solved for the infinitely long bearing. The solution is given by

$$p = -\frac{2.303}{B}\log\left(1 - \frac{\mu_1}{\bar{\mu}}Bp\right) \tag{55}$$

where p is the well-known Sommerfeld solution for the infinitely long bearing with constant viscosity.

As a specific example let us take castor oil at $T = 39$ C. Then, according to Hersey and Shore [7], we have

$$B = 2.303 \times 4.39 \times 10^{-8} \times 14.22 = 1.437 \times 10^{-7}\ \text{cm}^2/\text{kg} \tag{56}$$

To make the problem precise let us define $\bar{\mu}$ by the arithmetical mean; i.e., by

$$\bar{\mu} = \frac{\mu_1 \int_0^{\bar{p}} e^{Bp}\,dp}{\int_0^{\bar{p}} dp} = \frac{\mu_1(e^{B\bar{p}} - 1)}{B\bar{p}} \tag{57}$$

Table 2

p, kg/cm^2.....	0	50	100	150	200	300	400	500
$\bar{p}$, kg/cm^2.....	0	50.0	99.8	149.5	198.3	294.0	385.4	470
$(p - \bar{p})/p \times 100\%$.	0	−0.0	−0.2	−0.3	−0.9	−2.0	−3.8	−6.4

Substituting (56) and (57) into (55), we get

$$p = -1602 \log \left[1 - \frac{(0.001437\bar{p})^2}{e^{0.001437\bar{p}} - 1} \right] \tag{58}$$

The pressure has been computed for a few values of $\bar{p}$ and given in Table 2. From the table it can be observed that, within the range of the pressure, the errors introduced by assuming the viscosity to be constant are surprisingly small. The fact that the discrepancies between p and $\bar{p}$ are very small was confirmed by the experimental work of Stanton [8] for $\bar{p}$ up to about 210 kg/cm^2. According to his work the errors appear to be even less than those listed in Table 2. Although the foregoing analysis is for the infinitely long bearing, the conclusion drawn therefrom may also hold approximately for actual bearings; that is, to state it more clearly, the discrepancies between the solution of Reynolds' equation for the infinitely long bearing with the variable μ, and that of (2) may be of the same order as that between p and $\bar{p}$ given in Table 2.

According to the extensive data collected by H. A. Howarth [9] the range that has been considered covers every item including the steel-mill rollneck bearing. Hence the mathematical analyses given in this paper should apply precisely to every possible type of journal bearing.

References

1 K. Kino, "New Theory on the Bearings," *Transactions of the Japan Society of Mechanical Engineers*, vol. 35, 1932, p. 552.

2 E. O. Waters, "Theoretical Pressure Distribution in Journal Bearings," TRANS. ASME, vol. 60, 1938, p. A-134 (abstract). Also the complete edition of the same.

3 K. Kino, "A Mathematical Investigation on the Distribution of the Oil Pressure in the Journal Bearings," *Transactions of the Japan Society of Mechanical Engineers*, vol. 6, part 3, 1940, p. 14.

4 G. Vogelpohl, "On the Integration of the Reynolds Equation for the Journal Bearings of Finite Width," *Ingenieur-Archiv*, vol. 14, 1943, pp. 192–212.

5 Whittaker and Watson, "A Course of Modern Analysis," fourth edition, Cambridge University Press, Cambridge, England, 1927, p. 417.

6 S. J. Needs, "Effect of Side Leakage in 120 Degree Centrally Supported Journal Bearings," TRANS. ASME, vol. 56, 1934, p. 721.

7 M. D. Hersey and H. Shore "Viscosity of Lubricants Under Pressure," *Mechanical Engineering*, vol. 50,1928, pp. 221–232.

8 R. E. Stanton, "Cylindrical Journal Lubrication at High Values of the Eccentricity," *Proceedings, Royal Society of London*, series A, vol. 102, 1922, p. 241.

9 H. A. Howarth, "Current Practice in Pressure, Speeds, Clearances, and Lubrication of Oil-Film Bearings," TRANS. ASME, vol 56, 1934, p. 891.

An Approximate Analytical Solution for the Stepped Bearing

C. F. KETTLEBOROUGH[1]
Professor,
School of Mechanical Engineering,
University of New South Wales,
Sydney, Australia

Previously, solutions of the problem of the Rayleigh-type bearing with a step which is not straight have involved the use of the electrolytic tank or the use of relaxation methods, both of which are somewhat inconvenient as compared with the approximate analytical method described in this paper. The solution of the derived differential equation is in the form of a convergent infinite series, but for rapid computation it is shown that an economized series (the τ method for the solution of linear differential equations) yields results of high accuracy.

RAYLEIGH'S classical paper on hydrodynamic lubrication [1][2] proved that neglecting side leakage, optimum load capacity was obtained when there was a stepped convergence to the oil film. Later Archibald [2] considered the stepped bearing with side leakage and further work was carried out by Kettleborough [3, 4]. A more general case of the stepped bearing is Wilcock's hydrodynamic pocket bearing [5] in which the bearing area has a central depression.

The bearing under consideration is shown in Fig. 1, in which the side lands taper to zero width at the entrance. The general case with a pocket is examined, noting that this reduces to a simple stepped bearing when the pocket disappears.

Examination of the lines of equal pressure in Fig. 6 of reference [3] shows little evidence of side leakage The continuity equation for the elemental area shown in Fig. 2, and assuming a linear pressure gradient across the side lands is

$$F_1 = F_2 + 2F_3$$

where

$$F_1 = g\left[\frac{Uh_2}{2} - \frac{h_2^3}{12\mu}\frac{dp}{dx}\right]$$

$$F_2 = F_1 + \frac{dF_1}{dx}dx$$

$$F_3 = \left(\frac{h_1^3}{12\mu}\frac{p}{c}\right)dx$$

$$\therefore g\left[\frac{Uh_2}{2} - \frac{h_2^3}{12\mu}\cdot\frac{dp}{dx}\right] = g\left[\left(\frac{Uh_2}{2} - \frac{h_2^3}{12\mu}\cdot\frac{dp}{dx}\right) + \frac{d}{dx}\left(\frac{Uh_2}{2} - \frac{h_2^3}{12\mu}\cdot\frac{dp}{dx}\right)dx\right] + 2\left[\frac{h_1^3}{12\mu}\cdot\frac{p}{c}\right]dx \quad (1)$$

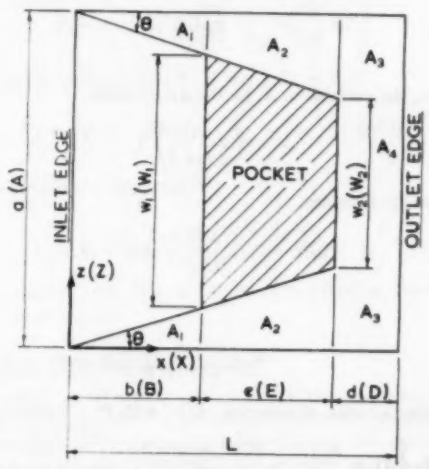

Fig. 1 Plan of bearing described; symbols used as indicated. Letters in brackets are nondimensional in terms of *L*.

[1] Formerly of University of Auckland, New Zealand.

[2] Numbers in brackets designate References at end of paper.

Presented at the West Coast Conference of the Applied Mechanics Division, Seattle, Wash., August 28–30, 1961, of THE AMERICAN SOCIETY OF MECHANICAL ENGINEERS.

Discussion of this paper should be addressed to the Editorial Department, ASME, United Engineering Center, 345 East 47th Street, New York 17, N. Y., and will be accepted until January 10, 1962. Discussion received after the closing date will be returned. Manuscript received by ASME Applied Mechanics Division, June 17, 1960. Paper No. 61—APMW-11.

Nomenclature

a, A, b, B, c, C, d, D, e, E, g, G, w_1, W_1, w_2, W_2 are as defined in Figs. 1 and 2.

Capital letters refer to nondimensional lengths in terms of length in direction of motion, L.

A_1, A_2, A_3, A_4 are areas as in Fig. 1.

F_1, F_2, F_3 are flows per unit length as in Fig. 2.

Symbols

- a_n = coefficients of polynomial (infinite)
- b_n = coefficients of polynomial (economized)
- f = coefficients of friction
- h_1 = film thickness, outlet land region 1
- h_2 = film thickness, inlet land region 2
- k = film ratio = h_2/h_1
- m = constant in equation (18)
- n = index
- p = pressure
- x, z = co-ordinates
- A_0 = constant of integration
- F = friction force
- K = constant, equation (5)
- L = length of pad in direction of motion
- P = nondimensional pressure
- P_p = nondimensional pocket pressure
- U = velocity of moving member
- W = pocket width
- W_L = total load
- X, Z = nondimensional co-ordinates in terms of L
- X_1 = new variable defined in equation (3)
- α = coefficient in economized polynomial
- β = coefficient in economized polynomial
- θ = defined in Fig. 1
- μ = viscosity

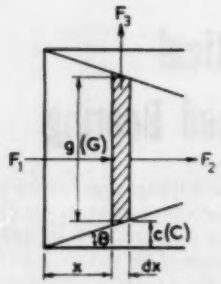

Fig. 2 Elemental area

Simplifying

$$\frac{\partial^2 p}{\partial x^2} - \frac{2}{cgk^3}\, p = 0 \tag{2}$$

Substituting

$$c = x \tan \theta$$

$$g = (a - 2x \tan \theta)$$

making equation (2) nondimensional in terms of L by the substitutions

$$a = AL;\ x = XL;\ c = CL;\ g = GL$$

$$p = \frac{6\mu UL}{h_1^2} P$$

changing the variable to X_1 by the substitution

$$X = \left(\frac{A}{2 \tan \theta}\right) X_1 \tag{3}$$

equation (2) becomes,

$$X_1(1 - X_1)\frac{\partial^2 P}{\partial X_1^2} - KP = 0 \tag{4}$$

where

$$K = \frac{1}{k^3 \tan^3 \theta} \tag{5}$$

The series solution of equation (4) is, with $P = 0$ when $X = 0$,

$$P = A_0\left\{X_1 + \frac{KX_1^3}{2!} + \frac{K(K+2)X_1^3}{3!2!} + \frac{K(K+2)(K+6)X_1^4}{4!3!} + \frac{K(K+1.2)(K+2.3)(K+3.4)\ldots.[K+(n-1)(n-2)]X_1^n}{n!(n-1)!}\right. \tag{6}$$

$$P = A_0\left[X_1 + \sum_{n=2}^{\infty} \frac{K(K+1.2)(K+2.3)\ldots\ldots(K+(n-1)(n-2))}{n!(n-1)!} \cdot X_1^n\right]$$

This series is convergent when $X_1 < 1$. This equation gives the pressure over the inlet land and the pressure in the pocket when

$$X_1 = B\left(\frac{2 \tan \theta}{A}\right)$$

Load Capacity

Load capacity is found by integration of the pressure over the bearing surface

$$W = \int\int p dz dx$$

It is assumed that the hydrodynamic oil pressure is constant in the pocket and that linear pressure gradients exist between the outlet edges and the pocket and inlet land.

Load Supported by Inlet Land

$$= \int_0^b p(a - 2x \tan \theta) dx$$

$$= \frac{6\mu UL^3}{h_1^2}\int_0^B P(A - 2X \tan \theta) dX$$

$$= \frac{6\mu UL^3}{h_1^2}\left\{A\int_0^B P dX - 2 \tan \theta \int_0^B PX dX\right\} \tag{7}$$

$$\int P dX = \left(\frac{A}{2 \tan \theta}\right) A_0\left[\frac{X_1^2}{2} + \sum_{n=2}^{\infty} \frac{K(K+1.2)(K+2.3)\ldots.[K+(n-2)(n-3)]}{n!(n-2)!} X_1^n\right]$$

$$\int PX dX = \left(\frac{A}{2 \tan \theta}\right)^2 A_0\left[\frac{X_1^3}{3} + \sum_{n=2}^{\infty} \frac{K(K+1.2)(K+2.3)\ldots.[K+(n-3)(n-4)]}{n(n-2)!(n-3)!} X_1^n\right]$$

Load Supported by Pocket. The pocket pressure (P_p) is found by putting the value of X_1 corresponding to $X = B$ in equation (6) and summing. The load supported by the pocket is then

$$\frac{6\mu UL^3}{h_1^2} P_p\{A - 2B \tan \theta - E \tan \theta\} E \tag{8}$$

Load Supported by Region 1. The component of the load supported by the other areas indicated in Fig. 1 is as follows:

Both areas A_1

$$\frac{6\mu UL^3}{h_1^2} \tan \theta \int_0^B PX dX \tag{9}$$

Both areas A_2

$$\frac{6\mu UL^3}{h_1^2} P_p E \tan \theta\left(B + \frac{E}{2}\right) \tag{10}$$

Both areas A_3

$$\frac{6\mu UL^3}{h_1^2}\{P_p D(B + E) \tan \theta\}/2 \tag{11}$$

Area A_4

$$\frac{6\mu UL^3}{h_1^2} P_p D\{A - 2(B + E) \tan \theta\}/2 \tag{12}$$

The total load capacity is the sum of the components given in equations (7) through (12). The constant A_0 appearing in equation (6) is yet to be found, and is determined from the continuity considerations.

Oil Continuity for Pocket. The flow components are given in Fig. 3, and a balance of the flow into and out of the pocket is

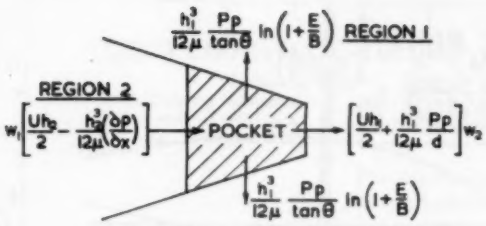

Fig. 3 Continuity equations for pocket

$$w_1\left\{\frac{Uh_2}{2}-\frac{h_2^3}{12\mu}\left(\frac{dp}{dx}\right)_{(x=b)}\right\}=w_2\left\{\frac{Uh_1}{2}+\frac{h_1^3}{12\mu}\frac{p_p}{d}\right\}+2\frac{h_1^3}{12\mu}\frac{p_p}{\tan\theta}\log_e\left(\frac{B+E}{B}\right) \quad (13)$$

$$W_1k^3\frac{2\tan\theta}{A}\left(\frac{dP}{dX_1}\right)_{(x=b)}+P_p\left\{\frac{2}{\tan\theta}\log_e\left(\frac{B+E}{B}\right)+\frac{W_2}{D}\right\}=(W_1k_1-W_2) \quad (14)$$

From equation (6)

$$\frac{dP}{dX_1}=A_0\left[1+\sum_{n=1}^{\infty}\frac{K(K+2)(K+6)\ldots(K+n(n-1))}{n!n!}X_1^n\right] \quad (15)$$

This series is convergent provided $X_1 < 1$. For a given pad geometry and film ratio the constant A_0 is uniquely determined.

Solution of Equation (4) Using Economized Polynomial

The solution of equation (4) has been found in the form

$$P=\sum_{n=0}^{\infty}a_nX_1^n \quad (16)$$

The formal working can be greatly simplified using the method described by Luke [6] assuming the solution takes the form of an economized solution.

$$P=\sum_{n=0}^{n}b_nX_1^n \quad (17)$$

If equation (17) is placed in (4) and like powers of X_1 are equated to zero, the coefficients b_n are indeterminant. Lanzos' technique is to append to the right-hand side of (4) a polynomial of order n:

$$X_1(1-X_1)\frac{d^2P}{dX_1^2}-KP=mb_n(X_1) \quad (18)$$

where m is a constant. By a suitable choice of polynomial within the range of X_1 a solution in the form of (17) is evolved.

Worked Example. The slider shown as in Fig. 1 was considered with $\tan\theta = 1/3$, $B = 0.6$, $E = 0.3$, $D = 0.1$, $A = L = 1$, and $k = 2.08$.

The constant K in equation (4) is unity. The length of the inlet region in the direction of motion is 0.6 thus

$$0 \leqslant X_1 \leqslant 0.4$$

Summing equation (6) to seven terms when $X_1 = 0.4$

$$P_p = A_0 \times 0.501056$$

From equation (15)

$$\left(\frac{dP}{dX_1}\right)_{X_1=0.4} = A_0 \times 1.574048 = P_p \times 3.143257$$

From the continuity equation for the pocket, equation (14),

$$P_p = 0.047781$$

Therefore A_0 and $(dP/dX_1)_{X_1=0.4}$ can be found.

The load capacity using equations (7) through (12) is found to be

$$W_L = 0.1432\left(\frac{\mu UL^3}{h_1^2}\right) \quad (19)$$

Using the economized polynomial method it was decided to determine a suitable series with $n = 3$

$$X_1(1-X_1)\cdot\frac{d^2P}{dX_1^2}-P=mX_1(X_1-0.1)(X_1-0.3) \quad (20)$$

The polynomial on the right-hand side of (20) satisfies the boundary condition $P = 0$, $X_1 = 0$ and also has zero values when $X_1 = 0.1$ and 0.3.

Assuming

$$P = A_0(X_1 + \alpha X_1^2 + \beta X_1^3)$$

where A_0 is an arbitrary constant as in equation (6) and equating coefficients

$$P = A_0\left(X_1 + \frac{320}{703}X_1^2 + \frac{300}{703}X_1^3\right)$$

This equation gives the following when $X_1 = 0.4$:

$$P_p = A_0 \times 0.50014; \quad \frac{dP}{dX_1} = A_0 \times 1.56899$$

The load capacity is found to be

$$W_L = 0.1429\left(\frac{\mu UL^3}{h_1^2}\right)$$

These values are very close to those previously given by the infinite series solution.

Comparison With Previous Results

As a check on the accuracy of the approximations of the theoretical approach it is desirable to compare with results presented in reference [4]. Consider Fig. 9(d) of this reference in which $A = L = 1$; $B = 0.7$; $E = 0$; $D = 0.3$; and $\tan\theta = 3/7$ and $k = 1.76$. With these values the constant $K = 1$.

The range of X is $0 \leqslant X \leqslant 0.7$ and therefore the range of X_1 is $0 \leqslant X_1 \leqslant 0.6$; equation (4) with a suitable polynomial on the right-hand side is

$$X_1(1-X_1)\frac{d^2P}{dX_1^2}-P=mX_1(X_1-0.2)(X_1-0.4) \quad (21)$$

The right-hand side equals zero when $X_1 = 0$, 0.2 and 0.4. The solution of equation (21) is

$$P = A_0\left(X_1 + \frac{180}{528}X_1^2 + \frac{300}{528}X_1^3\right) \quad (22)$$

Further computation gives the load capacity

$$W_L = 0.110\left(\frac{\mu UL^3}{h_1^2}\right)$$

For this case Fig. 10 of reference [4] gives

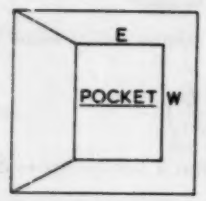

Fig. 4 Bearing shape modified

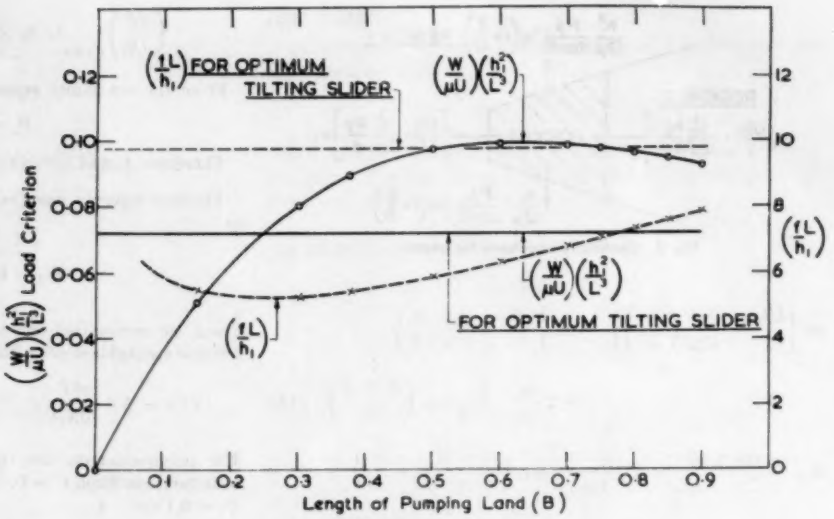

Fig. 5 Performance characteristics

$$W_L = 0.114\left(\frac{\mu UL^3}{h_1^2}\right)$$

a difference slightly less than 4 per cent.

Friction

Once the pressure distribution is known, the other operating factors can be determined. By the usual method

$$\left(\frac{F}{\mu U}\right)\left(\frac{h_1}{L^2}\right) = \iint_{\text{region 1}} dXdZ + \frac{1}{k}\iint_{\text{region 2}} dXdZ + 3(k-1)\int P_p dZ \quad (23)$$

The friction-coefficient criterion is

$$\left(\frac{fL}{h_1}\right) = \left(\frac{F}{\mu U}\right)\left(\frac{h_1}{L^2}\right)\Big/\left(\frac{W_L}{\mu U}\right)\left(\frac{h_1^2}{L^3}\right) \quad (24)$$

For the pad considered in the preceding section the values of

$$\left(\frac{F}{\mu U}\right)\left(\frac{h_1}{L^2}\right)$$

were 0.836 using the economized series method and 0.848 using the electrolytic tank [4].

Effect of Pocket Size

In order to investigate this factor the pad shown in Fig. 4 was investigated with $\tan\theta = 1/3$ and $k = 2.08$. As a variation the pocket was made rectangular in shape. As a result equation (8) becomes

$$\frac{6\mu UL^3}{h_1^2} P_p EW,$$

Equation (10) becomes

$$\frac{6\mu UL^3}{h_1^2} P_p 2EB\tan\theta$$

and equation (14) becomes

$$k^3\frac{2\tan\theta}{A}\left(\frac{dP}{dX_1}\right)_{x=0} + \frac{P_p}{W}\left\{\frac{2}{\tan\theta}\frac{E}{B} + \frac{W}{D}\right\} = (k-1)$$

The polynomial solution given with equations (21) and (22) was used. The individual lengths of the pumping land and pocket were varied but the sum of these always equaled $0.9L$; i.e., the outlet edge of the pocket was fixed. When $X = 0.9$ the pocket is eliminated.

Computed results are graphed in Fig. 5. The graphs show that compared with the tilting-pad bearing this bearing supports a greater load with a reduced friction coefficient. Maximum load capacity is achieved when the pocket length is $0.3L$; minimum friction coefficient is obtained for a pocket length of $0.6L$. However, such nontilting bearings have their limitations as discussed in reference [7].

Conclusions

The analytical solution of the stepped thrust bearing presented in the paper yields accurate results. Although the "τ-method" is usually associated with Chebyshev polynomials, the use of polynomials of a suitable order produces satisfactory economized series. For the particular worked example, the pocket-type bearing is superior to the simpler stepped bearing.

References

1 Lord Rayleigh, "Notes on the Theory of Lubrication," *Philosophical Magazine*, vol. 35, 1918, p. 1.

2 F. R. Archibald, "A Simple Hydrodynamic Thrust Bearing," TRANS. ASME, vol. 72, 1950, p. 393.

3 C. F. Kettleborough, "The Stepped Thrust Bearing—A Solution by Relaxation Methods," JOURNAL OF APPLIED MECHANICS, vol. 21, TRANS. ASME, vol. 76, 1954, p. 19.

4 C. F. Kettleborough, "An Electrolytic Tank Investigation Into Stepped Thrust Bearings," *Proceedings of The Institution of Mechanical Engineers*, vol. 169, 1955, p. 679.

5 D. F. Wilcock, "The Hydrodynamic Pocket Bearing," TRANS. ASME, vol. 77, 1955, p. 311.

6 Y. L. Luke, "Remarks on the τ-Method for the Solution of Linear Differential Equations With Rational Coefficients," *Transactions of Society of Industrial Applied Mathematics*, vol. 3, 1955, p. 179.

7 C. F. Kettleborough, "Further Experiments on Stepped Thrust Bearings; the Effect of Step Height," *Proceedings of The Institution of Mechanical Engineers*, International Lubrication Conference, London, England, October, 1957.

TURGUT SARPKAYA
Professor,
Department of Engineering Mechanics,
University of Nebraska,
Lincoln, Neb.

Torque and Cavitation Characteristics of Butterfly Valves

The present study deals with torque and cavitation characteristics of idealized two-dimensional and axially symmetrical butterfly valves. Theoretical results obtained for the two-dimensional case are compared with the ones obtained experimentally and by a relaxation technique. Based on the results of the two-dimensional case, an approximate solution is presented for the more general and practical case of three-dimensional butterfly valves. The results are in good agreement with the actual flow tests.

Valves are assemblies of one or more basic flow-restricting elements, and nearly all of these basic elements belong to one of the three main classes; namely, sliding, seating, and flow-dividing elements. Butterfly valves which belong to both the second and third classes are installed in pipes or penstocks and are normally used for either closure valves or for flow-rate control or governing. The major geometric variables affecting flow performance are the piping arrangement, shape of blade, and the angle of closure.

Butterfly valves have been studied by many researchers. Among those notable are the studies of Armanet [1],[1] Bleuler [2], Cohn [3], Dickey and Coplen [4], Gaden [5, 6], Keller [7], Keller and Salzmann [8], Kerr [9], McPherson et al. [10], Netsch and Schulz [11, 12], and the closely associated study of Ball [13] on the cavitation characteristics of gate and globe valves. It should be noted that all of these studies were basically experimental and semiempirical in nature. In a previous paper [14] the author presented an analysis for the theoretical determination of contraction coefficients for two-dimensional butterfly valves. Discharge coefficients for free discharge flow based on the contraction coefficients determined analytically have been found in excellent agreement with the test results reported by others [14].

It is the purpose of this paper to expand this analysis to the determination of hydrodynamic torque and to the prediction of cavitation behind the valve plate.

[1] Numbers in brackets designate References at end of paper.

Contributed by the Applied Mechanics Division and presented at the Winter Annual Meeting, New York, N. Y., November 27–December 2, 1960, of The American Society of Mechanical Engineers.

Discussion of this paper should be addressed to the Editorial Department, ASME, United Engineering Center, 345 East 47th Street, New York 17, N. Y., and will be accepted until January 10, 1962. Discussion received after the closing date will be returned. Manuscript received by ASME Applied Mechanics Division, April 26, 1960. Revised draft received September 8, 1961. Paper No. 60—WA-105.

Basic Analysis-Discharge Coefficients

Information available on contraction and flow coefficients of butterfly valves is rather limited and obtained primarily from experiments conducted on two and three-dimensional models and prototypes. It has been shown [14] that the contraction and discharge coefficients for two-dimensional butterfly valves may be determined analytically by the theory of free streamlines devised by Helmholtz and Kirchhoff. The formation of two jets by a finite, two-dimensional stream impinging obliquely upon a fixed plane lamina placed between two infinite parallel planes, Fig. 1, is well suited to free-streamline analysis because of the dominance of inertia and pressure in the establishment of the flow pattern. Since the flow accelerates rapidly, shear is not a primary factor and the differences between comparable ideal and real flows are small. The importance of gravitational effects for the coefficient of contraction is already known to be secondary. However, the significance of the various restrictions can be shown only by comparing the calculated results with those obtained from experiments of real flows.

If the coefficient of contraction at points B and H are C_{c1} and C_{c2}, respectively, as shown in Fig. 1, then the following relationships exist:

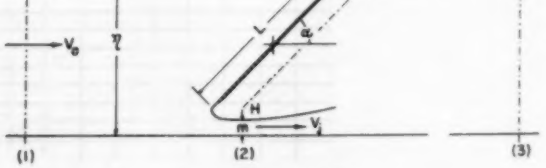

Fig. 1 Butterfly valve

Nomenclature

A = cross-sectional area of conduit
C_{c1} = contraction coefficient
C_{c2} = contraction coefficient
C_Q = discharge coefficient for free discharge flow
C_{Qs} = discharge coefficient for continuous pipe flow
C_{T2} = torque coefficient for two-dimensional valve
C_{T3} = torque coefficient for axially symmetrical valve
D = diameter of conduit
F_n = normal force on valve plate
g = gravitational acceleration
h_0 = head at upstream side
h_c = head in cavity behind valve plate
h_3 = head at downstream side
ΔH = valve loss
K = cavitation index
L = length of valve plate

(Continued on next page)

$$(a)\quad n = C_{c1}\frac{\eta}{2}\left(1-\frac{\sin\alpha}{\sin\beta}\right)\quad (c)\quad \beta = \sin^{-1}\frac{\eta}{L},$$

$$(d)\quad \frac{n}{m} = \frac{C_{c1}}{C_{c2}} \tag{1}$$

$$(b)\quad m = C_{c2}\frac{\eta}{2}\left(1-\frac{\sin\alpha}{\sin\beta}\right),\quad (e)\quad \frac{V_0}{V_j} = \frac{C_{c1}+C_{c2}}{2}\left(1-\frac{\sin\alpha}{\sin\beta}\right)$$

The velocities of both jets are equal to V_j and the velocity far upstream from the valve plate is V_0.

The results or the functional relationships obtained from the free-streamline analysis are reproduced in Fig. 2. The rate of flow is expressed in terms of the discharge coefficient C_Q since it is the most accustomed and widely used coefficient and more readily determined experimentally. Hence [10]

$$Q = C_Q D^2(g\cdot\Delta H)^{1/2} \tag{2}$$

in which ΔH is the net difference in total head between the sections 1 and 3, in feet of the fluid flowing; i.e., the valve loss. In the case of free discharge into the atmosphere the valve loss is determined from

$$\frac{V_0^2}{2g} + h_0 - \frac{V_j^2}{2g} = \Delta H \tag{3}$$

In the case of flow in a continuous pipe of constant diameter we have

$$h_0 - h_3 = \Delta H \tag{4}$$

and finally for the flow from a valve discharging directly into a large body of fluid, we have

$$\frac{V_0^2}{2g} + h_0 - h_3 = \Delta H \tag{5}$$

where h_3 is the depth of still water above the valve centerline.

Although the results of such calculations are immediately applicable only to two-dimensional flow of incompressible fluids, the scope of application is less restrictive than it would appear. The bulk characteristics of certain free-streamline flows such as the ratio of comparable areas have been found to be essentially the same for two-dimensional and axisymmetric patterns [15, 16, 17]. This observation led the author to make a similar comparison for the discharge and torque coefficients of two and three-dimensional butterfly valves.

In the case of free discharge into the atmosphere we finally arrive at

$$C_Q = \frac{\pi}{4\sqrt{2}}(C_{c1}+C_{c2})\left[1-\frac{\sin\alpha}{\sin\beta}\right] \tag{6}$$

The agreement of experimental data with the curve calculated by equation (6) was found to be good for all practical purposes [14].

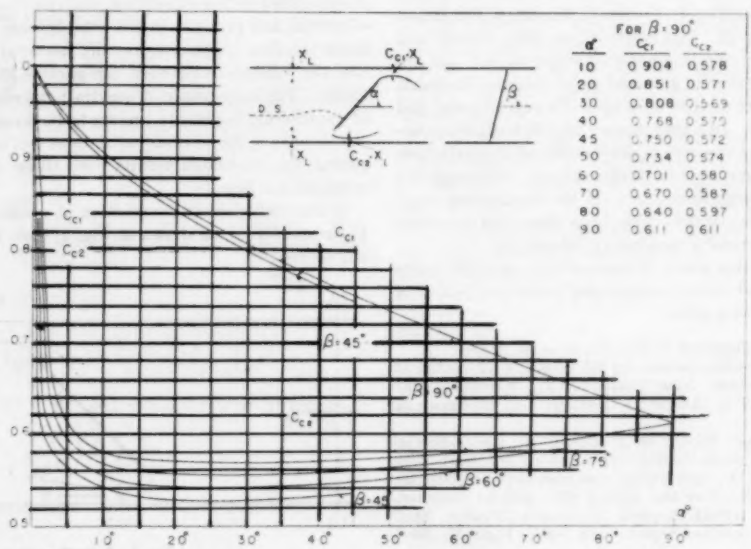

Fig. 2 Contraction coefficients

Nomenclature

m = thickness of jet, Fig. 1
n = thickness of jet, Fig. 1
p = pressure intensity
Q = discharge
T = torque
V_0 = velocity at upstream
V_3 = velocity at downstream
V_j = velocity of jet
x = co-ordinate along axis of conduit
X_{1c} = distance from axis of valve plate to center of pressure
X_{2c} = distance from axis of valve plate to center of pressure
α = angle of opening
π = angle of complete closure
δ = width of valve plate
η = height of conduit
η_c = distance from axis of valve to center of pressure
ρ = density of fluid

In the case of flow in a continuous pipe of constant diameter the discharge coefficient may be evaluated by taking into consideration the over-all change in total head in the conduit. This change in total head is primarily due to an abrupt enlargement of the jets and may readily be evaluated from

$$\Delta H = \frac{(V_j - V_2)^2}{2g} \tag{7}$$

Hence the discharge coefficient for an axisymmetric continuous flow is

$$C_{Qs} = \frac{\frac{\pi}{4\sqrt{2}}(C_{c1} + C_{c2})\left[1 - \frac{\sin\alpha}{\sin\beta}\right]}{1 - \frac{1}{2}(C_{c1} + C_{c2})\left[1 - \frac{\sin\alpha}{\sin\beta}\right]} \tag{8}$$

which indicates that for a given α and β, C_{Qs} for continuous flow is greater than C_Q for free-discharge flow. The difference between the two becomes substantially larger as the value of α becomes smaller. The comparison between the results obtained from equation (8) and the experimental results reported by others [4, 10, 11, 12] are once again in good correspondence as seen in Figs. 3 and 4. This substantiates the author's belief that the calculation of the irrotational flow pattern for the two-dimensional butterfly valve is directly applicable to a comparable three-dimensional case, provided that the ratios of comparable areas are equal.

Cavitation

A phenomenon of considerable practical importance associated with butterfly valves is cavitation. Cavitation and resulting vibrations had already been observed several decades ago [18]. On the basis of the results obtained from the free-streamline theory, cavitation may be analyzed as follows:

Neglecting the head loss due to friction, the equation of Ber-

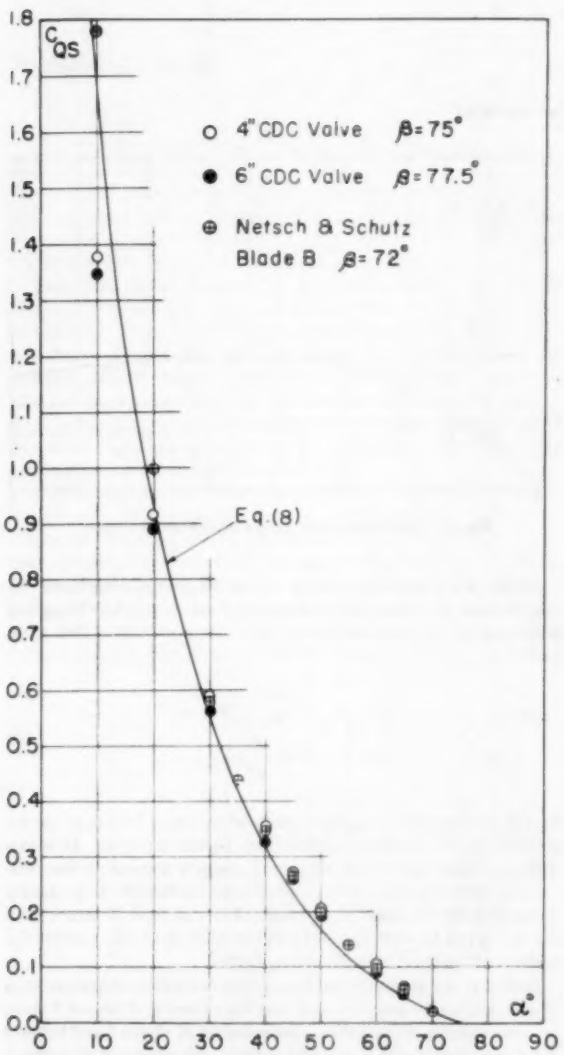

Fig. 3 Discharge coefficients for continuous pipe flow

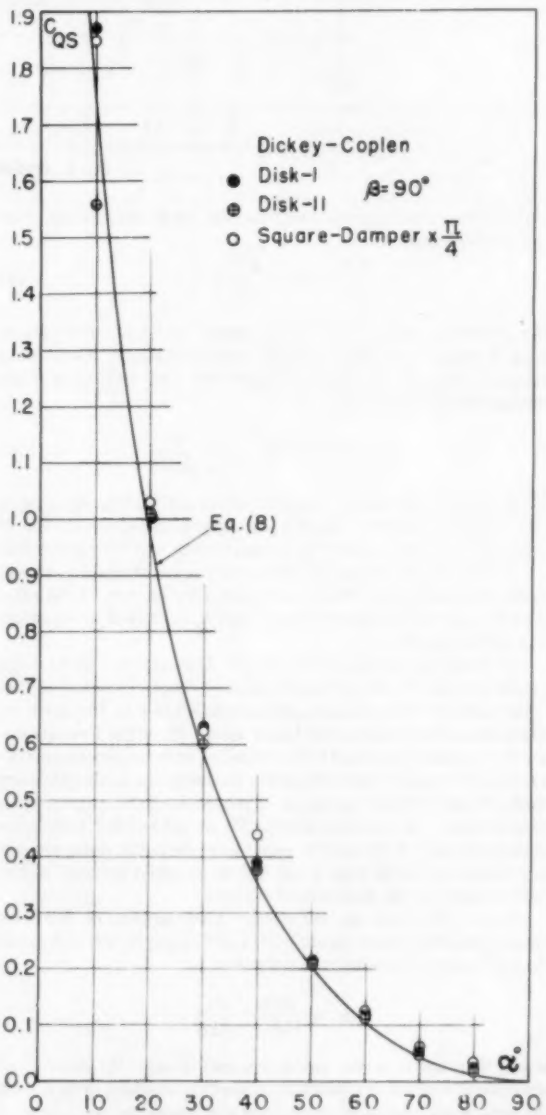

Fig. 4 Discharge coefficients for continuous pipe flow

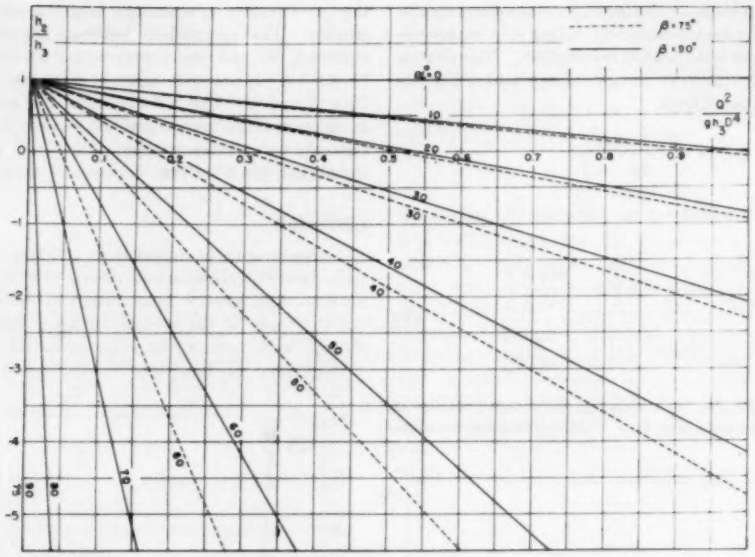

Fig. 5 Prediction of cavitation

noulli between the upstream section and cavity behind the plate may be written as

$$\frac{V_0^2}{2g} + h_0 = \frac{V_j^2}{2g} + h_v \tag{9}$$

The prediction of h_v, hence the prediction of liquid vaporization state, is the primary object of this cavitation study. Combining equation (9) with equations (2) and (4), and writing in a dimensionless form leads to

$$\frac{h_v}{h_3} = 1 - \frac{4\sqrt{2}}{\pi}\frac{1}{C_{QS}}\frac{Q^2}{gh_3D^4} \tag{10}$$

which shows that h_v/h_3 is a linear function of Q^2/gD^4h_3, for a given pair of α and β-values. In Fig. 5, a graphical representation of equation (10) is given for $\beta = 75$ and 90 deg, and for various values of the angle of opening α. From this figure, therefore, one can determine readily h_v, if Q, D, h_3, α, and β are known. Evidently, h_0 and h_v are related directly to h_3, and h_c is limited to vaporization of the liquid.

The foregoing analysis is for steady flows and is based on the results obtained from the free-streamline theory as noted earlier. Consequently, the cavitation analysis is subject to the same restrictions as the analysis it is based upon. Since the free-streamline theory assumes a dead body of fluid of uniform pressure everywhere in the wake of the valve plate, the foregoing analysis is more likely to indicate the beginning of severe cavitation rather than its inception. As a matter of record it should be cited that, prior to the reduction of pressure to vapor pressure in the wake, various degrees of cavitation may occur due to localized pressure reductions caused by the presence of vortices.

Bleuler [2] made an exhaustive investigation of butterfly valves operating under conditions involving cavitation and found that, if the cavitation index K defined as

$$K = \frac{2g(h_3 - h_v)}{V_0^2 + 2g\Delta H}$$

is less than unity, severe cavitation can occur. He determined the critical zone for cavitation by observing a sudden drop in both the torque and discharge coefficients and found the upper limit of K, which corresponds to the inception of cavitation, to be 2.5.

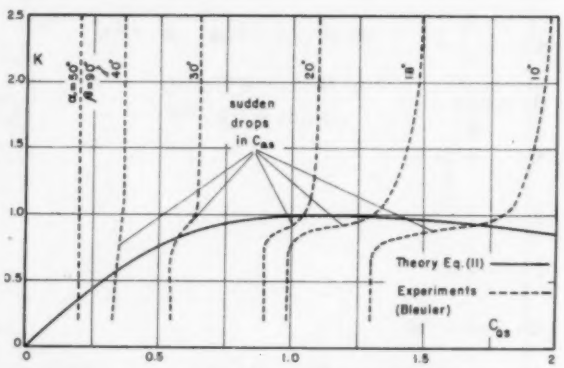

Fig. 6 Cavitation index versus discharge coefficient

Bleuler's experimental results can be compared with those obtained from the analysis given here by combining the foregoing definition of K with equations (2), (4), and (10) which then yields

$$K = \frac{\frac{4\sqrt{2}}{\pi}C_{QS}}{1 + \frac{8}{\pi^2}C_{QS}^2} \tag{11}$$

In Fig. 6 a graphical representation of equation (11) is given together with the results obtained from Bleuler's paper. It is evident from this figure that the theory predicts accurately the critical zone of cavitation where the discharge coefficients drop rapidly depending on the angle of opening. For values of K larger than the one given by equation (11) and smaller than 2.5, various degrees of intensity of cavitation may occur.

Ball [13] in a thorough analysis of the cavitation characteristics of gate and globe valves found that for values of K above 2 there was no evidence of cavitation; for values of K above 1 and below 2 the cavitation was of very mild nature; for values of K below 1 the intensity of cavitation increased as the value of K decreased;

and for values of K above about 0.4 the damage caused by cavitation was confined to the downstream end of the valve.

The difference between the upper limits of K values as determined by Bleuler and Ball might be due to the fact that the valves are of different shape and that Bleuler's experiments were conducted by recirculating laboratory water back to sump. As a result of this recirculation the water might have become aerated, thereby increasing the possibility of cavitation. Practical experience of Henry Pratt Company [19] indicates that cavitation may be a matter of serious consideration for values of K equal to or less than unity. We may, therefore, conclude that the theory predicts fairly reasonably the values of K for which the pressure practically everywhere in the wake reduces to vapor pressure, the consequence of which is severe cavitation.

Several methods have been devised to alleviate the problem of cavitation, the most common being the introduction of atmospheric air into the vapor cavity. A new method developed by Henry Pratt Company introduces atmospheric air through the butterfly valve shaft. The air is allowed to escape into the vapor cavity through a number of holes in the downstream face of the valve plate.

Hydrodynamic Torque

The operating member of a butterfly valve is subjected to a number of different forces while it is in operation. There is, of course, the force supplied by the valve-operating device, but, in addition, other forces may either aid or oppose the operating force. These forces have various origins and various characteristics, and it is necessary to know their magnitudes and natures in order to design for successful operation of the valve. It is not always possible to calculate every force acting on the valve accurately.

The axial forces that act on a valve in motion include the inertial force and the frictional forces which are not accurately calculable. In any valve, under normal conditions, there will be a pressure difference between upstream and downstream faces, and this pressure difference which is nonuniformly distributed exerts a force and a torque on the operating member of the valve. The distribution of pressure acting along the downstream face of the valve plate is approximately a rectangle with a height equal to the pressure in the downstream section.

A direct theoretical determination of hydrodynamic torque is confronted with insurmountable mathematical difficulties. There are, however, several topological models of flow past an inclined lamina for which the torque may be determined using classical hydrodynamic methods. These models and the butterfly valve differ from each other considerably because the latter is placed in a confined medium. It will be seen that, despite this gross difference, the results obtained from a particular topological model come surprisingly close to actual torque calculations These models, therefore, will be mentioned here briefly:

1 For the Cisotti [20] model, which is shown in Fig. 7, it is evident that the fluid pressures on the lamina are equivalent to a couple tending to set it broadside on to the flow. The moment of this couple when the general direction of the stream makes an angle α with the lamina is given by

$$\frac{T}{\rho V_0^2 \eta^2 \delta} = \frac{\pi}{8} \sin 2\alpha \tag{12}$$

The torque calculated from this model is the largest one among all other topological models considered, and quite unrealistic for obvious reasons.

2 The second and more realistic model is the Kirchhoff [21]-Rayleigh [22] model shown in Fig. 8. According to this model the total excess pressure on the upstream face of the lamina is given by

$$\frac{F_n}{\rho \eta \delta V_j^2} = \frac{\pi \sin \alpha}{4 + \pi \sin \alpha} \tag{13}$$

Here the velocity of the free streamline is equal to the velocity of approaching undisturbed flow. In reality, the velocity of the free streamline depends on the wake under pressure behind the plate. Experiments [23, 24] have shown that the free-streamline velocity is approximately 1.4 V_0. Theoretical solution of the flow with

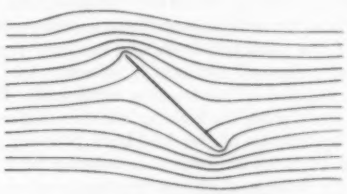

Fig. 7 Cisotti model

Fig. 8 Kirchhoff-Rayleigh model

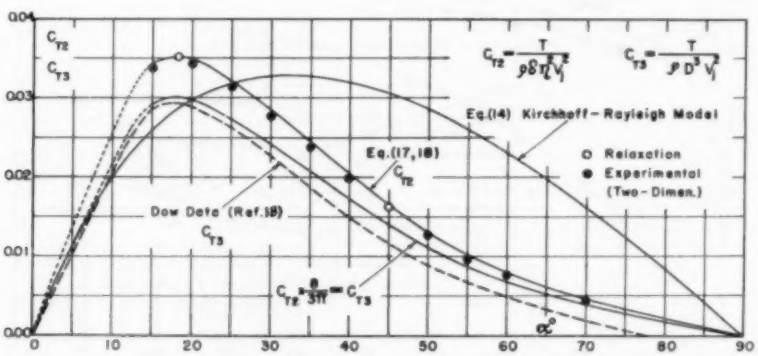

Fig. 9 Torque coefficients for two-dimensional and axially symmetrical butterfly valves

wake past an oblique plate is given by Mimura [25] using Roshko's [26] notched hodograph method. The butterfly valve requires a similar solution for a better understanding of torque and particularly of cavitation.

For the Kirchhoff-Rayleigh model, the moments about the center of the lamina give the following torque expression:

$$\frac{T}{\rho V_j^2 \eta^3 \delta} = \frac{3\pi}{8} \frac{\sin 2\alpha}{(4 + \pi \sin \alpha)^2} \tag{14}$$

The results obtained from equation (14) are shown in Fig. 9, together with the other torque-coefficient diagrams for the purposes of comparison. The torque coefficient is maximum for $\alpha = 32°20'$. It should be noted that in all the models, as well as in an actual butterfly valve, the approach flow is assumed to be uniform. In reality the flow is nonuniform and there is an increase in the moment coefficient as the flow becomes symmetrically more nonuniform.

For the two-dimensional butterfly valve, determination of the torque coefficient proceeds as follows: Upon writing the equation of momentum between sections 1 and 2 in Fig. 1, and combining it with equations (1) and (3), we obtain the total normal force acting on the valve plate:

$$\frac{F_n}{\rho V_j^2 \eta \delta} = \frac{1}{2 \sin \alpha} \left[1 - \frac{V_0}{V_j}\right]^2 \tag{15}$$

The results obtained from equations (13) and (15) are shown in Fig. 10, together with the two values obtained from the application of the relaxation technique and from experiments. Since the application of the relaxation technique has been presented elsewhere [27], no additional comment is necessary here except that theoretically determined contraction coefficients, Fig. 2, have been used in establishing the limiting free streamlines.

From the equilibrium of the fluid body between AC and BD shown in Fig. 10 in the direction perpendicular to the main flow, we find that the difference between the total pressure forces acting on AB and CD reduces to:

$$\int_{AB} p\, dz - \int_{CD} p\, dz = \frac{F_n \cos \alpha}{\rho \eta \delta V_j^2} = \frac{\cos \alpha}{2 \sin \alpha} \left[1 - \frac{V_0}{V_j}\right]^2 \tag{16}$$

Now, the torque acting on the valve may be computed in two different ways:

1 By taking the moment of all forces with respect to the valve axis,

$$\frac{T}{\rho \delta \eta^3 V_j^2} = \frac{\int_{AB} pz\, dx - \int_{CD} pz\, dx}{\rho \delta \eta^3 V_j^2} + \tfrac{1}{4}(1 - \sin \alpha)(C_{a1} - C_{a2}) \left(1 - \frac{V_0}{V_j}\right) \tag{17}$$

2 By taking the moment of normal force acting on the valve plate with respect to valve axis,

$$\frac{T}{\rho \delta \eta^3 V_j^2} = \frac{1}{2 \sin \alpha} \left[1 - \frac{V_0}{V_j}\right]^2 \eta_c \tag{18}$$

Defining

$$\frac{\int_{AB} pz\, dx}{\int_{AB} p\, dx} = X_{1c}, \quad \text{and} \quad \frac{\int_{CD} pz\, dx}{\int_{CD} p\, dx} = X_{2c}$$

it is obvious that in order to be able to compute the torque from either equation (17) or (18), it is necessary to determine X_{1c}, X_{2c}, or η_c. A direct integral calculation of these values which are merely the distances from the valve axis to appropriate pressure centers is practically impossible though mathematically feasible. Instead, the pressure at suitable intervals along AB and CD and the valve plate is computed from the results previously obtained for two-dimensional butterfly valves [14]. It was then possible to determine by the method of composite areas not only the pressure centers but also the normal force acting on the valve plate and the total normal forces acting on AB and CD.

The foregoing method is neither too approximate nor subject to errors. On the one hand, equation (16) provided an excellent check on the difference of total normal force acting on AB and CD, since it was possible to compute the right side of the equation exactly and directly; and on the other hand, the torque computed independently from equation (17) provided a check on the torque computed from equation (18), and vice versa.

The hydrodynamic torque coefficient computed by the method outlined is shown in Fig. 9 together with the two values obtained from the application of the relaxation technique and from experiments. In addition, another curve representing the torque coefficient for axially symmetrical valves is shown in the same figure. This curve was obtained by multiplying the two-dimensional torque coefficients obtained from equations (17) and (18) by $8/3\pi$. The constant $8/3\pi$ was obtained easily by applying the previously mentioned idea of equal area ratios and identical pressure centers for infinitesimal two-dimensional strips perpendicular

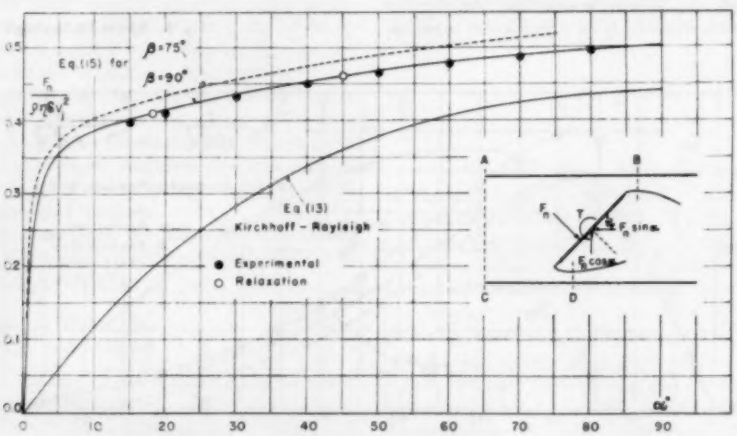

Fig. 10 Normal force on valve plate

to the valve axis. Furthermore, it should be noted that the velocity on the free streamline was chosen in accordance with the equations 1(*e*) and (3).

Representative pressure distributions and streamlines resulting from the relaxation technique are shown in Figs. 11 and 12.

Experimental Investigation

Experiments were conducted on a two-dimensional transparent model, the cross section of which was 8 in. by 1 in., and the length was 50 in. The valve plate was constructed of brass plate 8 in. long, $^1/_8$ in. thick, and 1 in. deep. The upstream face of the blade was polished and the upper and lower edges were sharpened at 45-deg angles. The axis of rotation of the blade was made to coincide with the upstream face as shown in Fig. 13. Piezometer holes were made along the long axis of symmetry of the valve plate on 1-in. intervals. The first and the last piezometer holes were at $^1/_2$ in. distance from the sharp edges. Cylindrical brass pieces $^1/_2$ in. long and $^1/_8$ in. diam. were welded at the location of piezometer holes behind the plate and a $^1/_{16}$-in. drill was made through each cylindrical extension piece and plate. This insured a 10-diam-long straight entrance into the piezometer tube. Holes were carefully drilled and edges sharpened so as to eliminate any burrs that might have developed during the drilling process. To eliminate any leakage that might have existed between the plate and the Plexiglas walls, two very small channels were carved out along an 8-in. length of 8-in. by $^1/_8$-in. faces of the valve, and two round rubber pieces were partly embedded in them. When the Plexiglas walls were tightened (the upper plate was always removable), the rubber pieces flattened between the

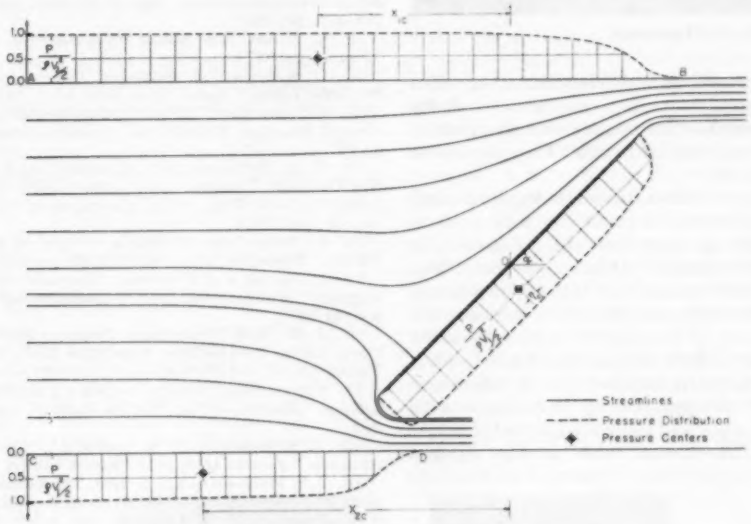

Fig. 11 Flow pattern and pressure distributions for $\alpha = 45$ deg

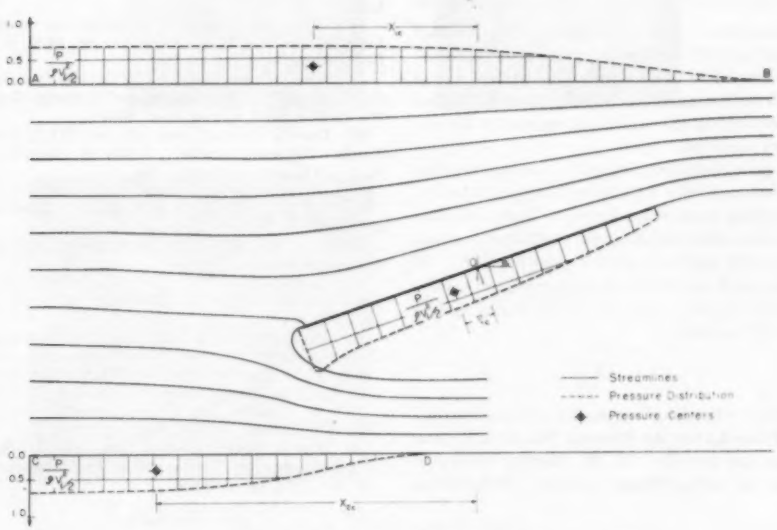

Fig. 12 Flow pattern and pressure distributions for tan $\alpha = 1/3$

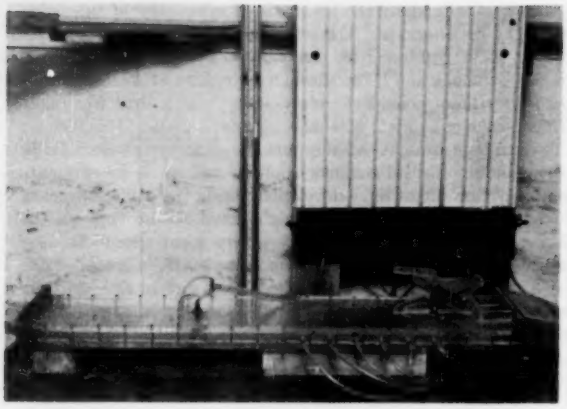

Fig. 13 Equipment

valve plate and the Plexiglas walls and prevented leakage completely. During experiments the angle α was varied simply by loosening the upper plastic plate and rotating the valve plate to the desired setting with an external handle Then the plastic plate was once again tightened.

Discharges were measured with a calibrated 60-deg sharp-edged triangular weir. Pressures were measured by means of 10 piezometer tubes. In addition, a pitot tube at the upstream side of the model measured the static and dynamic pressures. Pressures along the side walls were measured with the help of piezometer openings prepared carefully and attached to a manometer board. In order to measure all the pressures at once, too many manometers were necessary. To reduce their number to ten, first the pressures along the plate were measured and the others were sealed leakage tight, and vice versa. During the experiments the thicknesses of jets at the upper and lower sides of the blade were measured (m and n). Experimental values were in excellent agreement with the theoretical results obtained from equations 1 (a) and (b).

Conclusions

The detailed laboratory and theoretical investigations of butterfly valves described herein warranted the following conclusions:

1 The bulk characteristics of flows through two-dimensional and axially symmetrical butterfly valves are essentially the same.

2 The conditions essential to the occurrence of severe cavitation can be predicted from comparative two-dimensional studies as a function of the geometry of the valve system and of the upstream and downstream conditions.

3 The torque to be provided for varies widely for various conditions but is nevertheless perfectly definite and subject to calculations when the controlling factors are known. For a free-discharge valve the maximum value of the torque coefficient is about 0.03, and occurs at about 20 deg from the full-open position. As a result of the theoretical and experimental data presented herein, the moments to be expected for a butterfly valve in any setting and under any head can be calculated.

Acknowledgments

The author is indebted to the Engineering Experiment Station of the University of Nebraska for the Summer Research Fellowship. Especial thanks are due Mr. W. W. Norton (engineer, Henry Pratt Company) for calling Bleuler's work to the attention of this author. The previous work done by Prof. M. B. McPherson and his associates has been invaluable in the preparation of this paper.

References

1 L. Armanet, "Vannes-papillon des turbines" (Genissiat hydropower development), *La Houille Blanche*, 1950, pp. 199–219.

2 H. Bleuler, "Flow phenomena in hydraulic butterfly valves subjected to cavitation," *Escher Wyss News*, 1938, pp. 31–35. (A copy of this paper can be borrowed from T. Sarpkaya.)

3 Sylva D. Cohn, "Performance Analysis of Butterfly Valves," *Instruments*, vol. 24, 1951, pp. 880–884.

4 T. S. Dickey and H. L. Coplen, "A Study of Damper Characteristics," TRANS. ASME, vol. 64, 1942, pp. 137–154.

5 D. Gaden, "A Contribution to the Study of Butterfly Valves," *Water Power*, Part 1, pp. 456–474, Dec. 1951; and Part 2, pp. 16–22, January, 1952.

6 D. Gaden, "Contribution à l'étude des vannes-papillons," *Schweizerische Bauzeitung*, May 21, 28, and June 4, 1938, pp. 262–268, 275–277, 291–295.

7 C. Keller, "The Escher Wyss Butterfly Valves," *Escher Wyss News*, no. 2, 1937.

8 C. Keller and F. Salzmann, "Aerodynamic Model Tests on Butterfly Valves," *Escher Wyss News*, no. 1, 1936.

9 S. Logan Kerr, "Effect of Valve Operation on Water Hammer," *Journal American Water Works Association*, vol. 52, no. 1, 1960, pp. 65–75.

10 M. B. McPherson, H. S. Strausser, and J. C. Williams, "Butterfly Valve Flow Characteristics," *Proc. ASCE*, J. Hydraulics Div., 83: Paper No. 1167 (Feb., 1957); discussions in vol. 93 (Aug., 1957) and vol. 84 (Feb., 1958).

11 F. Netsch and F. Schulz, "Tests on Streamlined Butterfly Valves," *Engineers Digest*, vol. 11, 1950, pp. 280–282.

12 F. Netsch and F. Schulz, "Versuche an profilierten Drosselklappen," *Maschinenbau und Warmewirtschaft*, vol. 4, no. 9, 1949, pp. 141–147.

13 J. W. Ball, "Cavitation Characteristics of Gate Valves and Globe Valves Used as Flow Regulators Under Heads Up to 125 Ft," TRANS. ASME, vol. 79, 1957, pp. 1275–1281.

14 T. Sarpkaya, "Oblique Impact of a Bounded Stream on a Plane Lamina," *Journal of The Franklin Institute*, vol. 267, 1959, pp. 229–242.

15 M. S. Plesset and P. A. Shaffer, Jr., "Cavity Drag in Three Dimensions," *Journal of Applied Physics*, vol. 19, 1948, pp. 934–939.

16 J. S. McNown and E. Y. Hsu, "Application of Conformal Mapping to Divided Flow," *Proceedings of the Midwestern Conference on Fluid Dynamics*, J. W. Edwards, Ann Arbor, Mich., 1951, pp. 143–155.

17 H. Rouse and A. H. Abul-Fetouh, "Characteristics of Irrotational Flow Through Axially Symmetric Orifices," JOURNAL OF APPLIED MECHANICS, vol. 17, TRANS. ASME, vol. 72, 1950, pp. 421–426.

18 "Penstock Valves," a committee report, National Electric Light Association Proceedings, vol. 86, 1929; p. 669, contains *Mr. E. Dow's data also.*

19 Henry Pratt Company, "Engineering Data-General Information, Cavitation Characteristics of Butterfly Valves Flowing Water," No. 100R-4-D13, revised May, 1959.

20 Cisotti, *Ann. di. mat.* (3), vol. XIX, 1912, p. 83 (see also H. Lamb, "Hydrodynamics," Dover Publications, Inc., New York, N. Y., 1945, sixth edition, p. 86).

21 G. R. Kirchhoff, "Zur Theorie Freier Flussigkeitastrahlen," *Crelle*, vol. 19, 1869 (see also H. Lamb, "Hydrodynamics," sixth edition, 1945, p. 103).

22 Lord Rayleigh, "On the Resistance of Fluids," *Philosophical Magazine*, December, 1876.

23 A. Fage and F. C. Johansen, "On the Flow of Air Behind an Inclined Flat Plate and Infinite Span," R. & M. no. 1104, British ARC, 1927.

24 A. Roshko, "On the Drag and Shedding Frequency of Two-Dimensional Bluff Bodies," NACA TN 3169, July, 1954.

25 Y. Mimura, "The Flow With Wake Past an Oblique Plate," *Journal of the Physics Society*, Japan, vol. 13, 1958, pp. 1048–1055.

26 A. Roshko, "A New Hodograph for Streamline Theory," NACA TN 3168, 1954.

27 J. S. McNown, En-Yun Hsu, and Chia-Shun Yih, "Application of the Relaxation Technique in Fluid Mechanics," *Trans. ASCE*, vol. 120, 1955, pp. 650–686.

G. R. ABRAHAMSON
Research Engineer,
Stanford Research Institute,
Menlo Park, Calif.
Formerly, Research Assistant,
Stanford University.

Permanent Periodic Surface Deformations Due to a Traveling Jet[1]

A steel bullet in the form of a right circular cylinder which strikes a 10-mil-thick plane lead target at 45 deg incidence and at 2700 fps acquires on its front surface a series of corrugations, or waves, approximately 10 mils in amplitude and 40 mils in wave length. This phenomenon is investigated from a hydrodynamic point of view and it is found that similar waves develop at much lower velocities with materials which are viscous liquids under ordinary conditions. A mechanism of wave formation based on a hydrodynamic instability is presented.

When a flat-nosed steel bullet is shot obliquely at a thin metal target, wavelike surface deformations, as shown in Fig. 1, may be produced.[2] This phenomenon was first reported by Allen, Mapes, and Wilson [1].[3] Similar waves have been produced with other metals.

Two features of the waves in Fig. 1 should be noted. The main horizontal deformation, indicated by the orientation of the grain structure in the vicinity of the waves, is to the left; that is, in the direction which the lead sheet traversed the surface of the bullet. The peaks of the waves, however, turn in the opposite direction.

The effect of varying the angle of incidence is shown in Fig. 2. At an angle of incidence of 5 deg no waves are produced. Instead, the front surface of the bullet is essentially undeformed and a large part of the side of the bullet away from the point of first contact with the target is broken off. At an angle of incidence of 15 deg very small waves appear. At larger angles of incidence amplitude and wave length increase. These data suggest the existence of a critical angle of incidence above which waves occur and below which they do not. This was observed by Allen, Mapes, and Wilson.

Fig. 3 illustrates generally similar waves which may be produced when a thin metal sheet is projected obliquely against a thick metal slab.[4] Many examples of this effect are found on the

[1] Supported in part by U. S. Army Ordnance.

[2] William A. Allen and Earle B. Mayfield of the Naval Ordnance Test Station at China Lake, Calif., supplied all bullet specimens and data used in this paper.

[3] Numbers in brackets designate References at end of paper.

Presented at the West Coast Conference of the Applied Mechanics Division, Seattle, Wash., August 28–30, 1961, of The American Society of Mechanical Engineers.

Discussion of this paper should be addressed to the Editorial Department, ASME, United Engineering Center, 345 East 47th Street, New York 17, N. Y., and will be accepted until January 10, 1962. Discussion received after the closing date will be returned. Manuscript received by ASME Applied Mechanics Division, September 26, 1960. Paper No. 61—APMW-6.

[4] Experiments of this type were carried out by S. Katz at Stanford Research Institute.

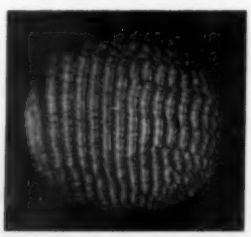

(a) END VIEW

(b) CROSS SECTION

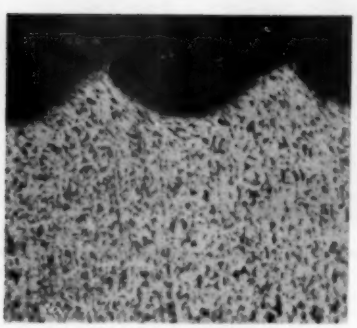

(c) PHOTOMICROGRAPH SHOWING GRAIN STRUCTURE

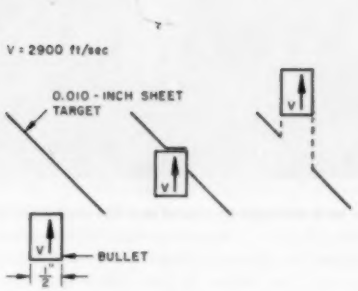

Fig. 1 Waves produced by oblique impact of a steel bullet on a thin lead target

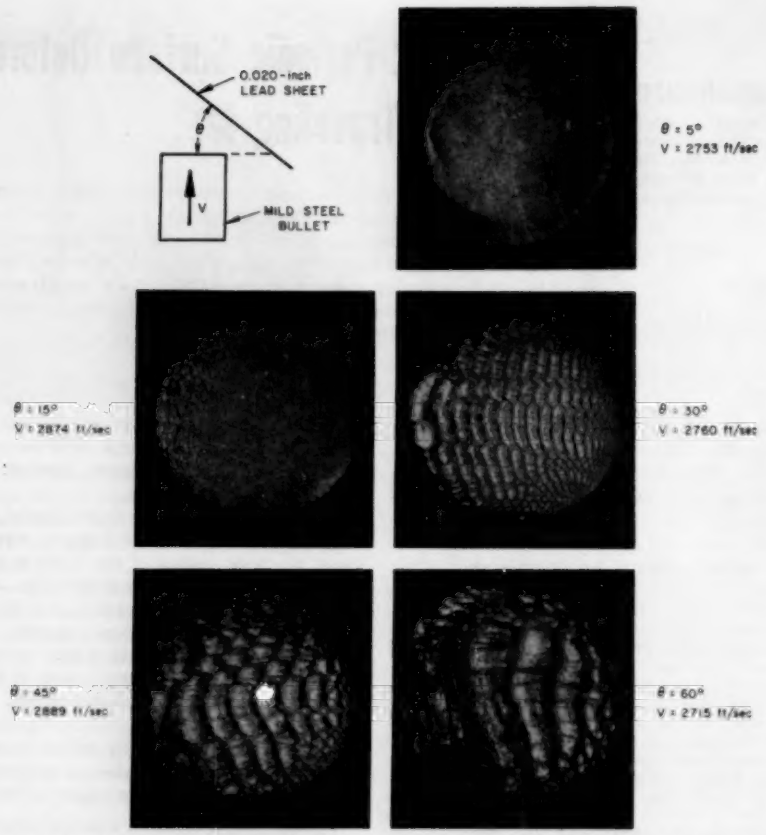

Fig. 2 End views of mild-steel bullets, illustrating effect of angle of incidence on wave length

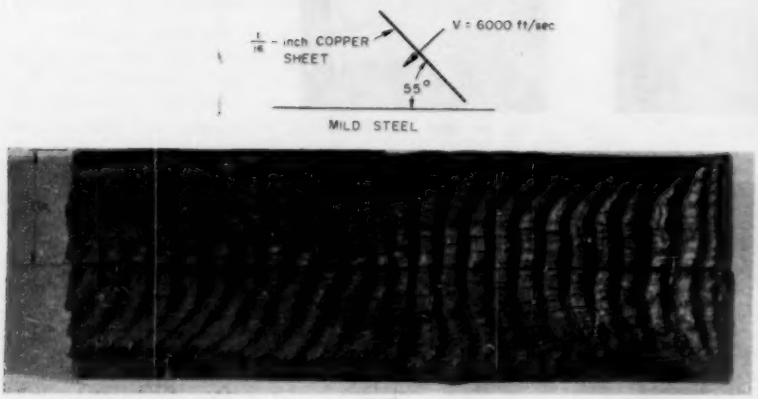

Fig. 3(a) Waves formed on a steel slab by impact of a thin copper sheet driven by high explosive

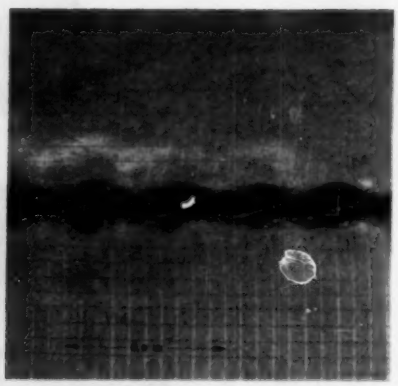

Fig. 3(b) Closeup showing grid embossed on upper piece from force of impact

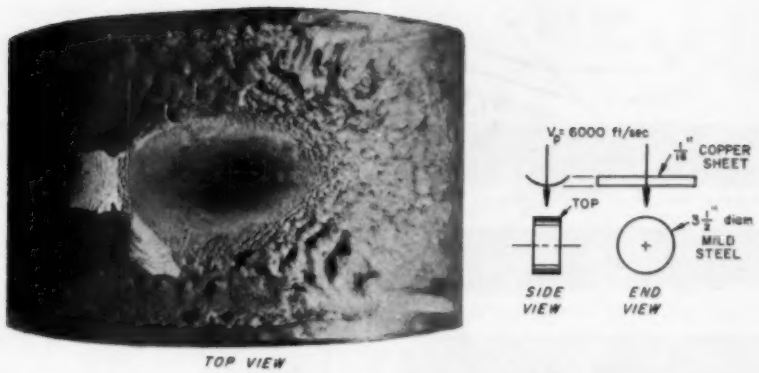

Fig. 4 Experiment showing effect of angle of incidence on wave length. Photograph shows deformed slab; point of first contact is in center; scratches in center were made in pulling copper sheet off to expose surface on left half of steel slab

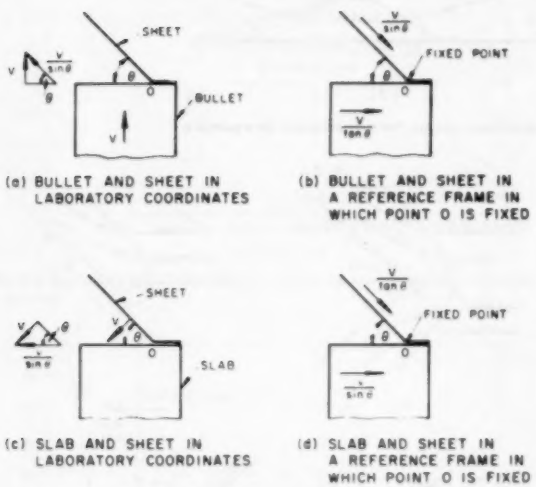
SHEET
BULLET
FIXED POINT
SLAB
(a) BULLET AND SHEET IN LABORATORY COORDINATES
(b) BULLET AND SHEET IN A REFERENCE FRAME IN WHICH POINT O IS FIXED
(c) SLAB AND SHEET IN LABORATORY COORDINATES
(d) SLAB AND SHEET IN A REFERENCE FRAME IN WHICH POINT O IS FIXED

Fig. 5 Transformation to moving co-ordinates

facings of shelters used in high-velocity impact experiments. The slab in Fig. 3 originally consisted of two 1-in-square, cold-rolled, mild-steel bars which were held together by tack welds on the ends. The contacting surfaces of the bars were lapped and a square grid was scribed on the lapped surface of the bottom piece in Fig. 3(*b*); the grid was embossed on the opposite surface by the force of the impact. The horizontal deformation of the slab, indicated by the deformed grid, is in the direction which the sheet swept across the surface of the slab, as was observed with the bullet. The peaks turn in the same direction, which is oposite to the direction of the peaks on the bullet. Waves of the latter type have been produced with other materials. A noteworthy example is the combination of an aluminum sheet projected against a lucite slab. Although lucite is normally a brittle material, waves similar to those in Fig. 3 were produced on the slab.[5]

The effect of varying angle of incidence is shown in Fig. 4. A cold-rolled, mild-steel bar of 3$^1/_2$ in. diam was used as a slab to obtain a continuously varying angle of incidence. At the time of impact the copper sheet was in the form of a cylindrical shell. The absence of waves in the central region suggests a critical angle below which waves do not occur. This is similar to the behavior observed in the bullet experiment.

[5] This experiment was performed by J. O. Erkman at Stanford Research Institute.

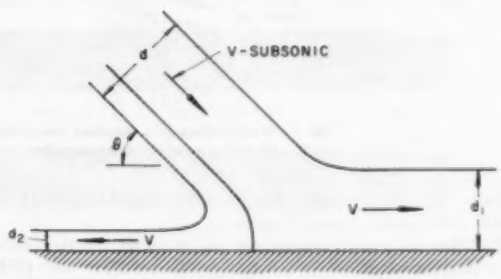

Fig. 6 Subsonic jet impinging on a rigid base

Analysis of the Metal-Impact Experiments

The relatively large permanent deformations of the surfaces of the bullets and the slabs in the experiments described in the foregoing indicate that the stresses in the region of impact were far in excess of the yield stresses of the metals. If the metals are treated as fluids, the contact pressure will be approximately $^1/_2\rho V^2$, where ρ is the density of the bullet and V is the velocity of impact. For the case of a bullet striking a lead target at 3000 fps, the pressure, neglecting the compressibilities of the metals, will be about 5×10^5 psi. This is much greater than the metals can sustain without yielding. Thus the stress field in the region of impact will be composed of a high hydrostatic pressure and relatively small shear stresses, similar to the stress field usually found in fluids of low viscosity. One is led, therefore, to consider the wave-formation phenomenon as a problem in hydrodynamics. This approach has been used successfully by others [2, 3, 4] to explain the behavior of metals in various high-velocity impact experiments. In the present paper it leads to a plausible explanation of the wave-formation phenomenon.

The experiments are analyzed most conveniently in a frame of reference moving with the instantaneous point of impact. As illustrated in Fig. 5, when observed in this manner the two types of experiments have the appearance of a jet directed against a moving base. The difference is in the relative magnitudes of the jet and base velocities.

An important aspect of the experiments becomes apparent from the consideration of the flow of a two-dimensional, compressible, fluid jet incident upon a smooth rigid wall. Three flow patterns are possible corresponding to (1) subsonic jet velocities, (2) supersonic jet velocities at angles of incidence less than a certain critical value, and (3) supersonic jet velocities at angles of incidence greater than the critical value.

The flow pattern for subsonic jet velocities is illustrated in Fig. 6. The most significant feature is the division of the jet into two

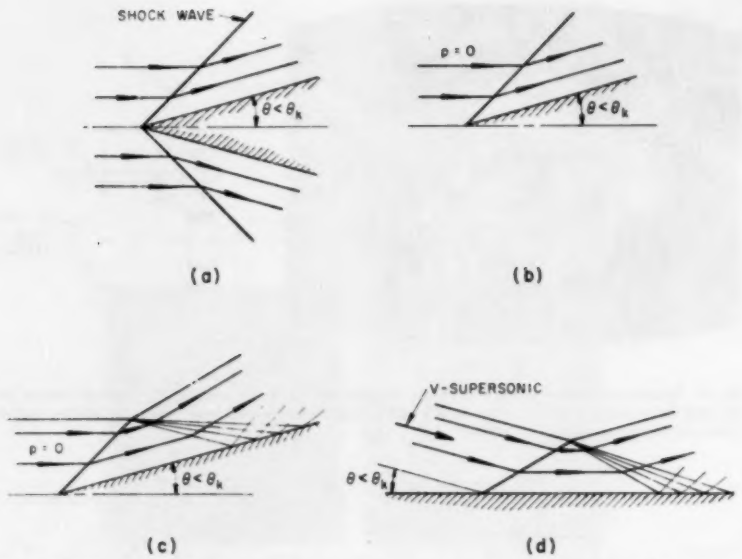

Fig. 7 Modification of a classical wedge flow to obtain flow pattern for a supersonic jet against a rigid wall at angles of incidence less than critical

streams, the relative sizes of which may be determined from simple momentum considerations.

The flow pattern for supersonic jet velocities can be obtained from classical solutions to the wedge flow problem [5]. In Fig. 7(*a*) the flow of a supersonic jet past a wedge is illustrated for wedge angles 2θ less than a certain critical value. Taking the pressure to be zero ahead of the shock, the lower half of the flow may be removed, as shown in Fig. 7(*b*). The upper part of the stream in Fig. 7(*b*) may be removed to obtain a jet if the necessary changes are made to satisfy the zero pressure boundary condition along the new upper surface. As indicated in Fig. 7(*c*) this is accomplished through a centered rarefaction wave originating at the intersection of the shock wave and the free surface. Finally, the flow pattern is rotated clockwise and the rigid wall is extended to the left to obtain a jet incident on a rigid base, as shown in Fig. 7(*d*).

The flow of a supersonic jet over a wedge for wedge angles 2θ larger than the critical value is illustrated in Fig. 8(*a*). Taking the pressure to be zero upstream of the shock wave, the bottom half of the flow may be removed as before, provided a suitable pressure distribution is supplied along OA, as indicated in Fig. 8(*b*). Rotating the flow clockwise through an angle θ and extending the rigid wall to the left, the configuration of Fig. 8(*c*) is obtained. As shown in Fig. 8(*d*), removal of the pressure distribution along OA allows part of the incident jet to flow to the left, reducing the pressure behind the shock wave. The lower pressure results in a reduction in the velocity of propagation of the shock wave relative to the flow, and hence the shock moves downstream toward point A. However, the shock wave cannot reach point A, for this would not be compatible with the fact that the flow cannot be turned through an angle greater than the critical angle by an attached oblique shock wave. Therefore the shock wave must eventually find a position somewhere upstream of point A. The upper part of the flow of Fig. 8(*d*) may be removed if appropriate changes in the flow pattern are provided. With the assumption that the flow after the shock is supersonic, the adjustment to the free surface is accomplished through a centered rarefaction wave originating at the intersection of the shock wave and the free surface as shown in Fig. 8(*e*). The division of the jet into two streams is similar to the flow pattern of the subsonic jet. This

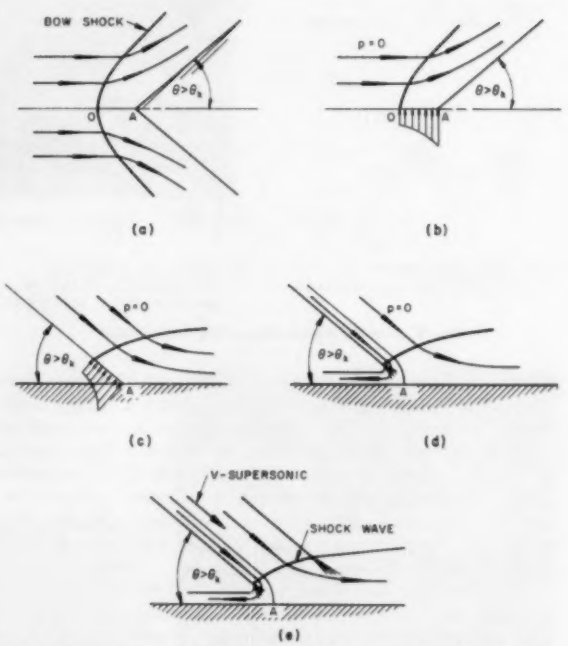

Fig. 8 Modification of a classical wedge flow to obtain flow pattern for a supersonic jet against a rigid wall at angles of incidence greater than critical

similarity is very significant in the interpretation of the experimental data.

In Fig. 9 the available data on the occurrence of waves in the bullet experiments are shown on graphs of angle of incidence versus jet velocity.[6] Three regions are indicated corresponding to (1) subsonic jet velocities, (2) supersonic jet velocities with $\theta > \theta_c$, and (3) supersonic jet velocities with $\theta < \theta_c$.

[6] Critical angles in Fig. 9 are based on references [6, 7].

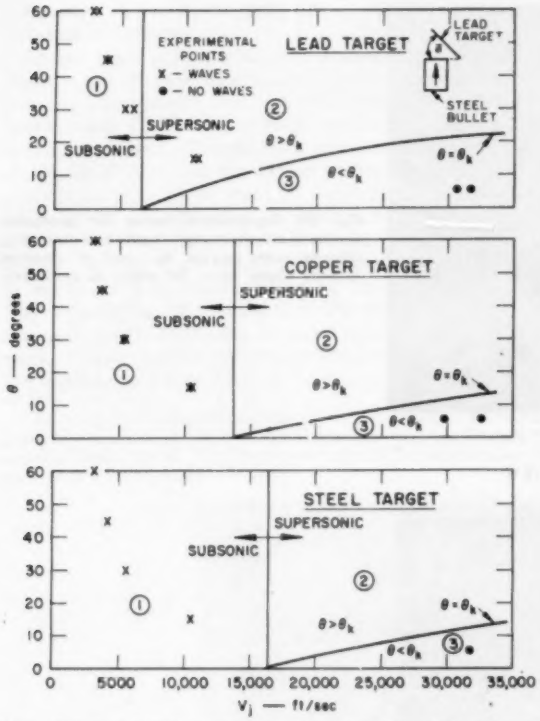

Fig. 9 Data from bullet experiments indicating conditions for occurrence of waves

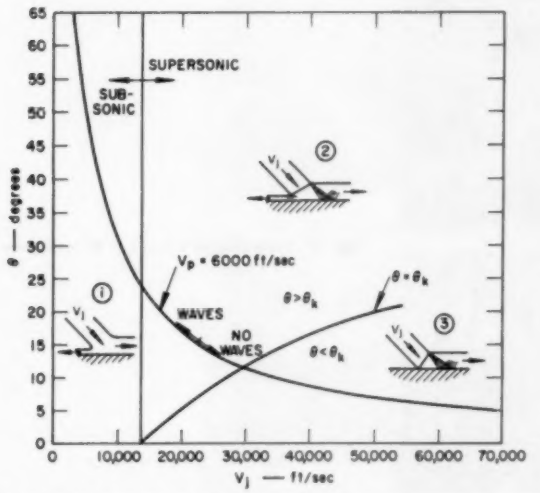

Fig. 10 Data from Fig. 4 indicating conditions for occurrence of waves

The data, although limited, indicate that waves form in regions (1) and (2) but not in region (3). A plot similar to that of Fig. 9 for the second type of experiment is shown in Fig. 10. These data also show that waves occur in regions (1) and (2) but not in region (3). (The fact that the no-wave boundary extends into region (2) can be attributed to the compressibility of the base.) The loci of critical angles separating regions (2) and (3) in Figs. 9 and 10 were calculated for a jet incident upon a rigid base. This idealization seems reasonable for the cases in which waves did not form, since the surfaces of the specimens were not noticeably

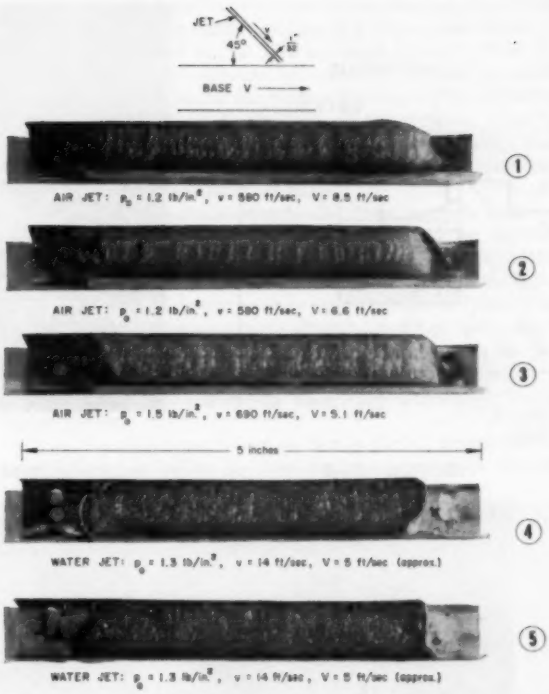
JET
45°
BASE V
AIR JET: v = 580 ft/sec, V = 8.5 ft/sec
AIR JET: v = 580 ft/sec, V = 6.6 ft/sec
AIR JET: v = 690 ft/sec, V = 9.1 ft/sec
5 inches
WATER JET: v = 14 ft/sec, V = 5 ft/sec (approx.)
WATER JET: v = 14 ft/sec, V = 5 ft/sec (approx.)

Fig. 11 Periodic surface deformations in grease. Waves were produced by passing grease under a jet of air or water as indicated. Surfaces of samples 1, 2, and 3 were originally convex upward in cross section; samples 4 and 5 were flat. Undisturbed surface is shown along edges of sample 2 and along lower edges of samples 4 and 5. Waves were about 24 hr old when photograph was taken. Stagnation pressure of jet is denoted by p_0.

deformed (see Fig. 2). Therefore it is plausible to assume that in region (3) the jet is diverted as a single stream upon impact, but in regions (1) and (2) it divides into two streams. This observation leads to the speculation that the division of the jet may be essential for the formation of waves. If such is the case it would appear that the wave-formation process is essentially a subsonic phenomenon and hence should be reproducible at lower velocities with materials which are liquids under ordinary conditions.

Experiments With Jets Impinging on Grease and Silicone Putty

To investigate the possibility of waves forming at low velocities, experiments were undertaken in which various soft materials, such as grease, were passed under a jet of air or water. After many trials it was found that periodic waves could be readily produced in heavy automotive grease. Some examples are shown in Fig. 11.

Waves were produced at still lower velocities using silicone putty instead of grease. The experimental arrangement is shown in Fig. 12. A slab of silicone putty with a convex upper surface is contained in a transparent plastic tray. The latter moves to the right at a steady velocity under a rectangular jet of water. The jet impinges upon the surface of the silicone putty and divides into two streams, as indicated in the figure. Direct measurement shows that the greater part of the jet is diverted to the right, although the relative depth of the streams might lead one to believe otherwise. The excessive depth of the left stream is due to surface-tension effects, as indicated in the sketch. The spots on

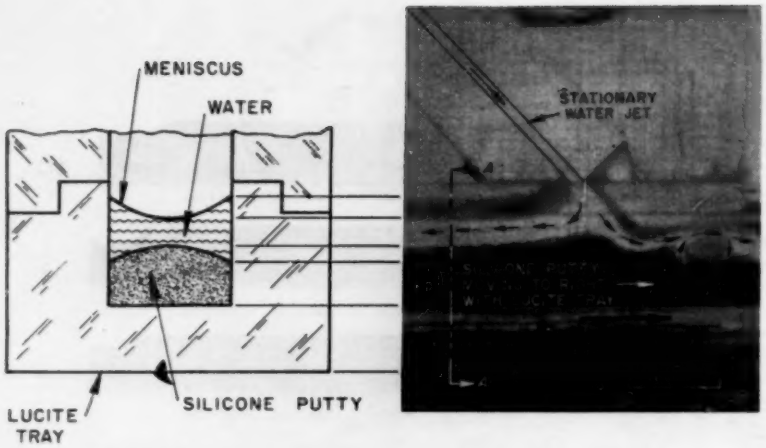

Fig. 12 Experimental setup for producing waves in silicone putty. Lucite tray containing silicone putty moves to right at constant velocity under water jet which is stationary.

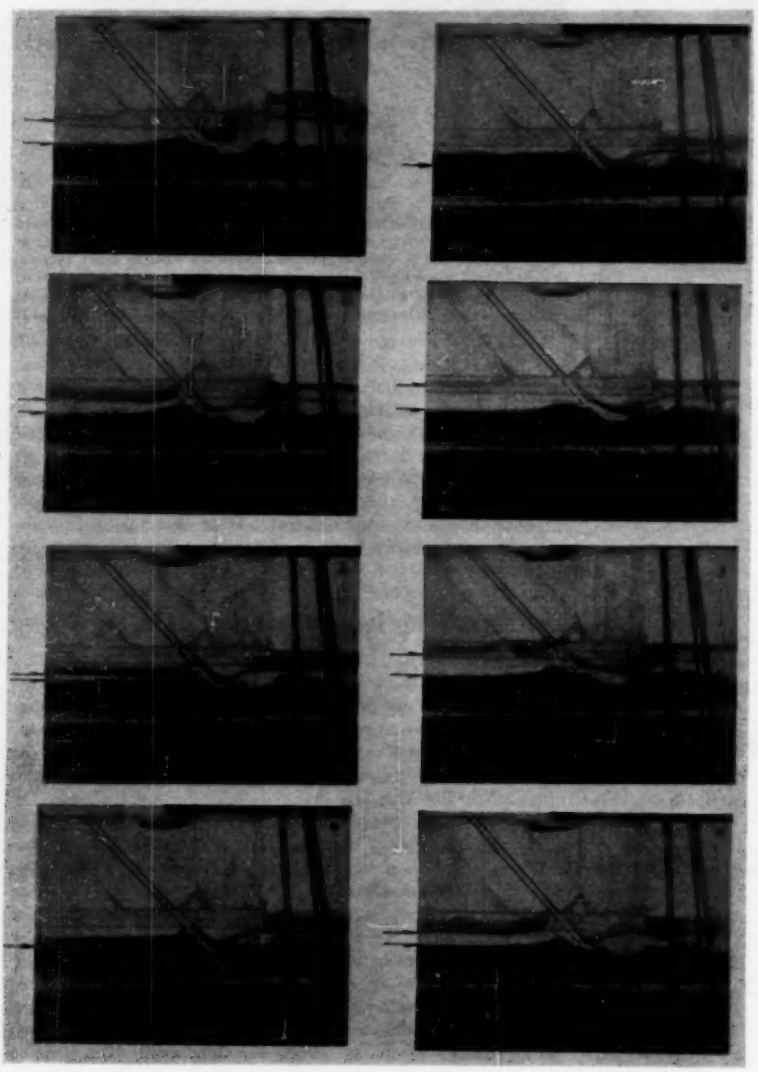

Fig. 13 Formation of a wave in silicone putty

the surface of the silicone putty are air bubbles which become attached momentarily.

Several stages in the formation of a wave in silicone putty are shown in Fig. 13. The velocity of the jet was 6 fps, corresponding to a stagnation pressure of 0.3 psi. The temperature of the water stream was 31 C. The base velocity was 22 mils per min and the time required for the formation of a wave was about 12 min. Development of the wave in Fig. 13 may be considered in two phases: (1) A build-up phase, in which the hump gradually increases in size,[7] and (2) a release phase, in which part of the hump passes under the jet, forming a wave. The build-up phase is shown in frames 1 through 4; the release phase is shown in frames 5 and 6. Frames 7 and 8 show the beginning of the next build-up phase. The arrows in Fig. 13, showing the depth of the left stream, indicate that the division of the jet varies during the evolution of a wave. The depth of the left stream decreases in frames 2, 3, and 4, and increases in frames 5 and 6; in frames 7 and 8 it decreases again. This effect may be attributed to the changing shape of the hump. As the hump builds up, it tends to form a vane for the jet and diverts more of the jet into the main stream. When the wave begins to pass under the jet (frame 5), the flow to the left increases, as indicated by the rough appearance of the surface of the left stream. (Note the short time between frames 4 and 5.) In frame 6 the flow to the left has increased substantially from that in frame 5, and in frames 7 and 8 it decreases again, corresponding to the next build-up phase.

The variation in the division of the jet in the cycle shown in Fig. 13 is illustrated in greater detail in Fig. 14 for the time interval from 200 to 315 sec. In frames 2 and 3 of Fig. 14 the flow in the left stream decreases, and in frames 3 and 4 the entire jet appears to be diverted into the right stream. In frame 5 the surface of the left stream is rough and the tip of the hump is visible through the jet again, indicating an increase in the flow in the left stream. In frames 6 to 8 the flow in the left stream increases further. As seen in Fig. 13, a wave subsequently passes under the jet.

From Fig. 14 it appears that the flow in the left stream reaches a minimum just before the wave begins to pass under the jet.

[7] An analytical treatment of this phase, for a viscous material, is given in a companion paper, "The Hump Deformation Preceding a moving Load," by G. R. Abrahamson and J. N. Goodier, see this issue of the JOURNAL, pp. 608–610.

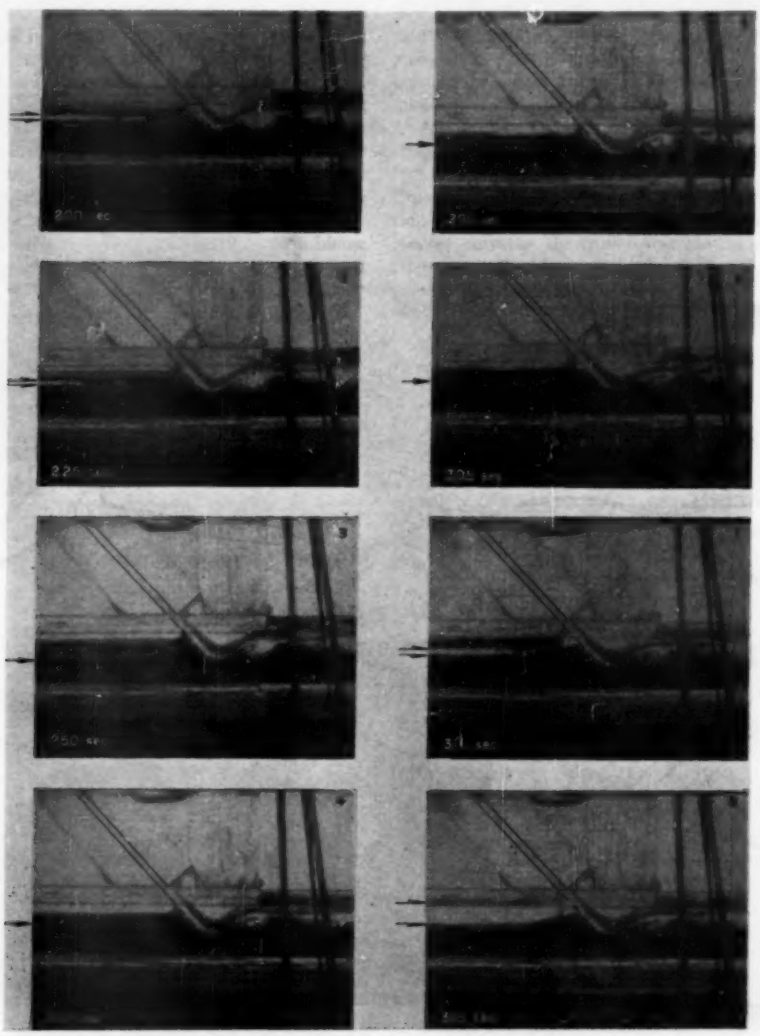

Fig. 14 Variation in division of jet from 200 to 315 sec

This observation is the basis for the wave-formation mechanism presented in the following section.

A Mechanism of Periodic Wave Formation

In the discussion of the development of periodic waves in silicone putty it was observed that the two phases in the formation of a wave are (1) the build-up phase and (2) the release phase. The build-up of a hump may be most easily visualized if the penetrating action of the jet and the motion of the base are imagined to occur in successive stages. Fig. 15 shows a two-dimensional jet impinging upon an initially flat base. The jet tends to penetrate the base, forming a depression. (The base is assumed to be incompressible, and hence the depression of the surface directly under the jet is accompanied by elevation of the surface elsewhere. Experiments show that this elevation occurs near the load as indicated in Fig. 15.)

As illustrated in Fig. 16, the motion of the base tends to move the upstream side of the depression under the jet. Hence, the jet must continually penetrate new material to maintain the depression. The change in shape of the surface under the jet causes more of the jet to be diverted into the right stream. As the jet penetrates farther into the base, it must penetrate an ever-increasing amount of new material to maintain the depression and eventually a "permanent" regime may be established in which the penetration of the jet is just able to nullify the effect of the motion of the base. The hypothetical permanent regime is illustrated in Fig. 17.

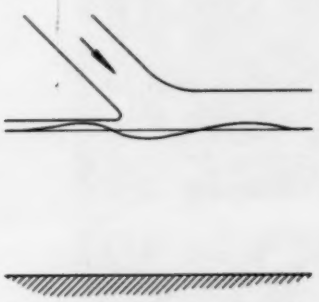

Fig. 15 Deformation to penetration of jet

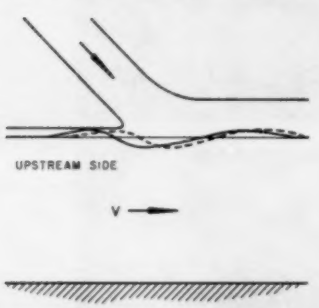

Fig. 16 Change due to horizontal movement of base

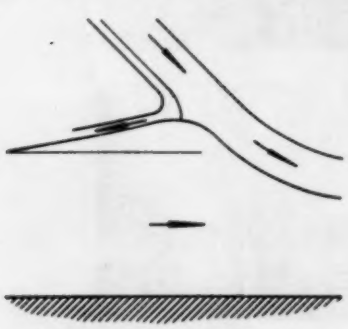

Fig. 17 "Permanent" regime

In Fig. 18 the effect of a momentary decrease in jet velocity is illustrated. The decrease in jet velocity results in a momentary decrease in the penetration of the jet, allowing the hump to shift downstream slightly. As shown in Fig. 18, this would cause a change in the division of the jet due to the change in the slope of the surface under the jet, and the right stream would become smaller and the left stream larger. The net result is a further decrease in the effectiveness of the jet in preventing the hump from moving downstream. Thus the permanent regime could not be re-established until after the release of a wave, even if the jet velocity were to increase to its original value. Fluctuations in the density or thickness of the jet, or in the properties of the base, would be equally as effective in initiating the release of a wave.

To initiate the release of a wave, the penetration of the jet must be reduced to less than that necessary to maintain the hump. In the early stages of the build-up phase, the penetration of the jet is in excess of that needed to maintain the hump. As build-up proceeds, the excess penetration decreases, and if a permanent regime were attained the penetration would just be sufficient to maintain the hump. The point in the build-up phase at which fluctuations become effective in initiating the release of a wave depends upon the size of the fluctuations. The smaller the fluctuations, the more nearly a permanent regime would be approached. Inasmuch as there must always be some random fluctuations in the flow, the build-up of a hump by a divided jet would always be expected to result in periodic surface deformations. In this sense the permanent regime which has been envisaged is unstable.

The wave-formation process suggested in the foregoing requires

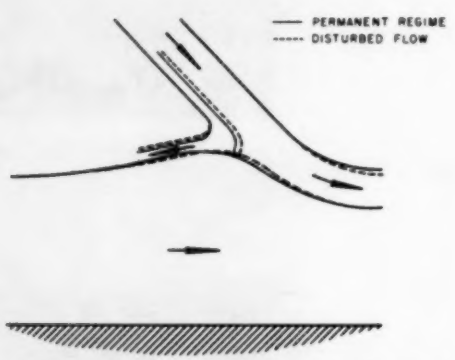

Fig. 18 Change in division of jet due to a slight downstream movement of hump

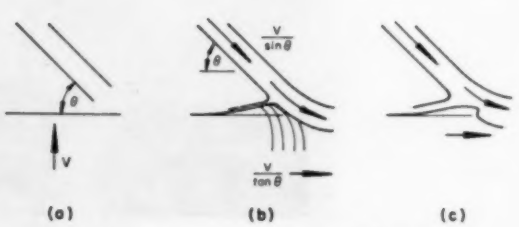

Fig. 19 Formation of a wave on a bullet

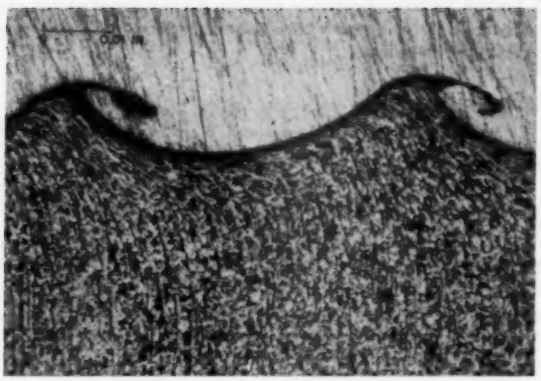

(a) MILD STEEL BULLET
0.022-inch-THICK COPPER TARGET
$\theta = 30°$, VELOCITY = 2707 ft/sec

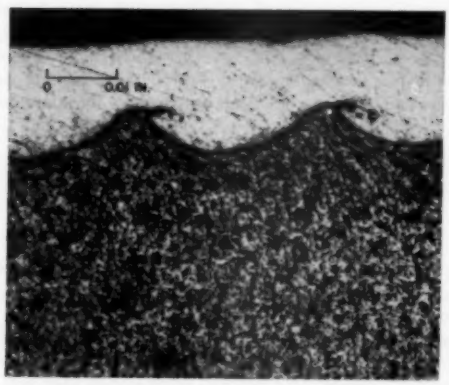

(b) MILD STEEL BULLET
0.010-inch-THICK COPPER TARGET
$\theta = 30°$, VELOCITY = 2778 ft/sec

Fig. 20 Bullets and copper targets which remained in contact after impact

that the jet: (*a*) be fluid, (*b*) be able to penetrate the base, and (*c*) divide into two streams upon impact. The properties of the base are significant only as they affect the build-up of the hump. The three requirements on the jet are satisfied in the metal impact experiments as well as the silicone-putty experiments. Therefore it seems reasonable to suppose that they are two extremes of a very general phenomenon. The fact that waves do not form in the metal impact experiments when the jet is diverted as a single stream supports this conclusion.

Waves may be produced on a base even though they are not permanent. Hence one can imagine situations in which transient waves might be produced by impinging gas streams, leading to noise and vibrations.

Remarks on the Metal-Impact Experiments

It was pointed out earlier, in the description of the waves formed in metals, that the peaks of the waves on the bullets turn in one direction and the peaks of the waves on the slabs turn in the opposite direction. This difference is readily explained by the process of wave formation described in the foregoing.

The formation of a wave in the bullet experiment is illustrated in Fig. 19. The build-up of the hump produces plastic deformation to the left, as indicated by the curved lines. When the hump passes under the jet during the release phase, the surface of the hump experiences a drag to the right, since the jet velocity is greater than the base velocity, and a crest develops as indicated. In Fig. 20 two bullet specimens are shown which illustrate the drag-produced crests.

A similar illustration of the wave-forming process for the second type of experiment is shown in Fig. 21. The horizontal deformation of the base is similar to that observed in the bullet experiments; however, the crest formed as the hump passes under the jet turns to the left since the base velocity is greater than the jet velocity. The effect is shown in Fig. 22.

The waves previously discussed occur in so-called "explosive

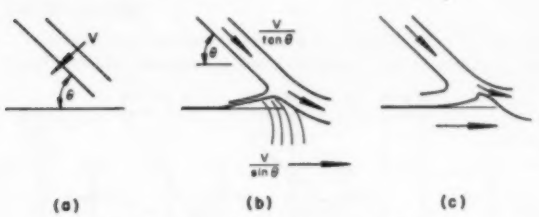

Fig. 21 Formation of a wave on a slab

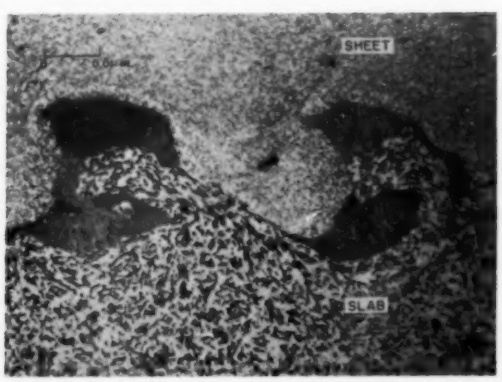

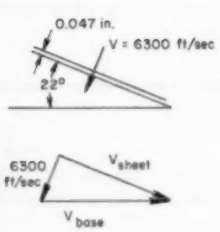

Fig. 22 Mild steel sheet and slab which remained together after impact; outline of waves is shown in the sheet; material between sheet and slab is polishing debris

welding" of metal plates. To produce a good bond by this mechanism it is necessary to use low angles of incidence to achieve nearly equal jet and base velocities and thus prevent separation and erosion. At such low angles of incidence the impact velocity required to produce waves becomes greater.

In the present paper the mechanism of wave formation was considered. Further study of waves produced by traveling jets should include the development of a mathematical model for the observed hydrodynamic instability and the formulation of quantitative relationships for amplitude and wave length as functions of target thickness, velocity, angle of incidence, and material properties.

Acknowledgments

The author wishes to thank Dr. Samuel Katz for suggesting the problem and for his interest and co-operation, and Messrs. W. A. Allen and Earle B. Mayfield for their co-operation in providing bullet specimens for analysis. Thanks are also due to John O. Erkman for many interesting and valuable discussions throughout the course of the investigation; through these discussions it first became clear that periodic surface deformations in metals occur at subsonic as well as supersonic jet velocities. The author is grateful to Prof. J. N. Goodier of Stanford University for many helpful and stimulating discussions. Professor Goodier suggested the idea of imagining the penetration of the jet and motion of the base to occur in successive steps, and the concept of a permanent regime. Finally, appreciation is expressed to Thos. C. Poulter for the opportunity to carry out this investigation and to George E. Duvall for reviewing the manuscript and suggesting several improvements.

References

1 W. A. Allen, J. M. Mapes, and W. G. Wilson, "An Effect Produced by Oblique Impact of a Cylinder on a Thin Target," *Journal of Applied Physics*, vol. 25, 1954, pp. 675–676.

2 E. M. Pugh, R. J. Eichelberger, and N. Rostoker, "Theory of Jet Formation by Charges With Lined Conical Cavities," *Journal of Applied Physics*, vol. 23, 1952, pp. 532–536.

3 R. J. Eichelberger and E. M. Pugh, "Experimental Verification of the Theory of Jet Formation by Charges With Lined Conical Cavities," *Journal of Applied Physics*, vol. 23, 1952, pp. 537–542.

4 J. M. Walsh, R. G. Shreffler, and F. J. Willig, "Limiting Conditions for Jet Formation in High Velocity Collisions," *Journal of Applied Physics*, vol. 24, 1953, pp. 349–359.

5 R. Sauer, "Theoretical Gas Dynamics," J. W. Edwards Company, Inc., Ann Arbor, Mich., 1947.

6 J. O. Erkman, Poulter Laboratories Internal Report No. 030-56, Stanford Research Institute, Menlo Park, Calif.

7 G. E. Duvall and B. J. Zwolinski, "Entropic Equations of State and Their Application to Shock Wave Phenomena in Solids," *Journal of the Acoustical Society of America*, vol. 27, 1955, pp. 1054–1058.

R. D. GAUTHIER
The Dow Chemical Company,
Denver, Colo.
Mem. ASME

E. E. WEIBEL
(Deceased)
Professor,
Department of Mechanical Engineering,
University of Colorado,
Boulder, Colo.
Mem. ASME

Elastic-Plastic Design of Rectangular Pressure Tubing

Elastic-plastic design permits the most effective use of the strength of the rectangular tube section. The condition of failure for a tube of perfectly elastic-plastic material is analyzed, and a formula is derived from which the limit load can be computed directly. A procedure is developed for determining by the area-moment method the wall deflection at any load from a bending-moment diagram modified to account for reduced rigidity. The total deflections thus found are plotted against the various loads. This theoretical load-deflection curve then becomes the basis for design.

Although rectangular tubing is not regarded as pressure conduit in the conventional sense, specific applications for a member of this cross section require that it withstand internal fluid pressure during some portion of its functional life. The analysis provides a theoretical load-deflection curve extended through the plastic range to ultimate failure. The capacity of a given tube can be based upon this load-deflection curve.

The analysis used in this paper assumes a perfectly elastic-plastic material. The stress condition at any point in the tube wall is then

$$\sigma = \frac{E\epsilon}{1 - \nu^2} \qquad (0 \leq \epsilon \leq \epsilon_y)$$

$$\sigma = \sigma_y \qquad (\epsilon \geq \epsilon_y)$$

Neglecting loading in the direction of the tube axis, the problem reduces to one of plane strain. The tubing is of such dimensions that the shearing stresses are small enough to be considered negligible in comparison to the bending and tensile stresses. Radial stresses are also neglected. The stresses in the tube wall are then due only to combined bending and tension. Although the analysis takes into account the interaction between tension and bending moment, the bending-moment diagram does not include the effect of tensile forces. The idealized stress distributions through the wall for various degrees of loading are shown in Fig. 1. The linear pattern in Fig. 1(*a*) is typical throughout the elastic range. Yield stress at an extreme fiber denotes incipient plastic flow. Increased load causes inward progression of plasticity as shown in (*b*) and (*c*). The condition represented by (*d*) delimits the process and establishes the theoretical limit design situation for combined bending and tension. At this stage deformation continues without increase of the load.

The load-deflection curve for a rectangular tube is derived by area-moments. The elastic portion of the curve is a straight line passing from the origin to the elastic limit, p_{el}, which is determined by ordinary stress analysis. Deflections in the plastic range are computed from modified bending-moment diagrams incorporating the effects of reduced rigidity in the tube wall due to plastic flow. The limit load, p_{li}, may be found directly by use of a formula derived herein.

Elastic Loading

The tube cross section is treated as a rectangular frame with round corners. Because of the symmetry, it is necessary to deal

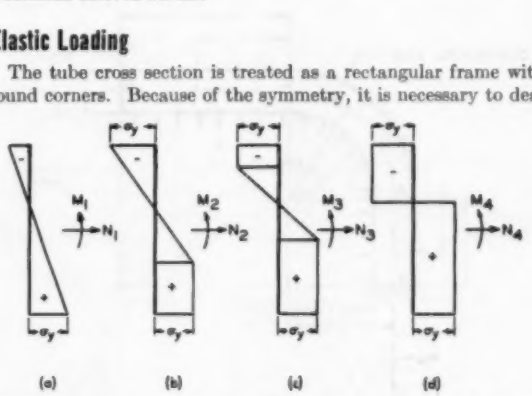

Fig. 1 Stress distribution for combined bending and tension in plastic range

Presented at the West Coast Conference of the Applied Mechanics Division, Seattle, Wash., August 28–30, 1961, of The American Society of Mechanical Engineers.

Discussion of this paper should be addressed to the Editorial Department, ASME, United Engineering Center, 345 East 47th Street, New York 17, N. Y., and will be accepted until January 10, 1962. Discussion received after the closing date will be returned. Manuscript received by ASME Applied Mechanics Division, June 15, 1960; revised draft, Jan. 26, 1961. Paper No. 61—APMW-8.

Nomenclature

e = distance between neutral and centroidal axes of wall section, in.
h, m, n, r = dimensions of tube section quadrant, in.
p, p_{el}, p_{li} = internal pressure, elastic load, limit load, psi
s = distance along centroidal axis, in.
A = area per unit width of wall section parallel to tube axis, in.²/in.
E = modulus of elasticity, psi
M = moment of force per unit width acting on wall section, lb-in/in.
N = tensile force per unit width acting on wall section, lb/in.
R = radius of centroidal axis of corner, in.
α = angular deflection of transverse section about neutral axis
β = reduced rigidity coefficient
δ = linear deflection of mid-point of wall, in.
ϵ, ϵ_y = unit strain, yield strain
ν = Poisson's ratio
σ, σ_y = unit stress, yield stress, psi

with but one quadrant, $\overline{ABOCD}$, as depicted in Fig. 2. The positions of arbitrary points on the centroid of the wall are denoted by x, y, and ϕ. Point O is the intersection with the centroid of a straight line extending from the axis of the tube through the center of radius of the corner, and is located by

$$\phi_O = \tan^{-1} \frac{m}{n} \tag{1}$$

Typical bending-moment curves for rectangular and square sections are shown in Fig. 3. The M/p-curve is parabolic except between points B and C, where it is sinusoidal. The equations for bending moment are

$$\left.\begin{aligned} M_{CD} &= \frac{p}{2}(m - x)^2 + M_D \\ M_{CB} &= pmR \sin\phi - pnR(1 - \cos\phi) + \frac{pm^2}{2} + M_D \\ M_{BA} &= \frac{p}{2}(m^2 + y^2) - pny + pR(m - n) + M_D \end{aligned}\right\} \tag{2}$$

where

$$M_D = -\frac{p\left[\frac{m^3}{6} + \frac{m^2 n}{2} - \frac{n^3}{3} + nR(m - n)\right]}{m + n + \frac{\pi h^2}{24e}} - \frac{p\left[R(m + n) + \frac{\pi}{2}\left(\frac{m^2}{2} - nR\right)\right]}{\frac{12e}{h^2}(m + n) + \frac{\pi}{2}} \tag{3}$$

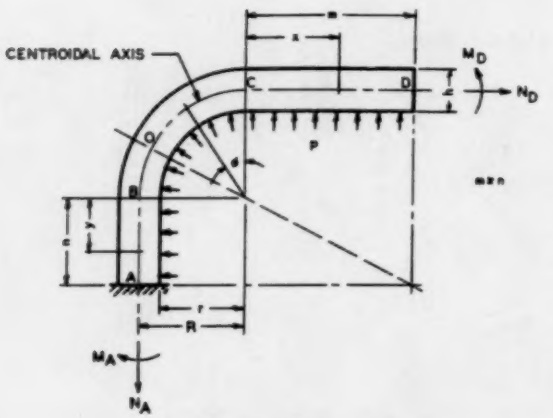

Fig. 2 Tube section loading diagram

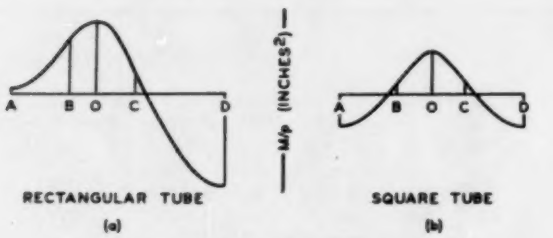

Fig. 3 Typical M/p diagram

The distance between centroidal and neutral axes in the corner is given by[1]

$$e = \frac{h^2}{12R}\left[1 + \frac{1}{15}\left(\frac{h}{R}\right)^2\right] \tag{4}$$

The points of zero bending moment are

$$\left.\begin{aligned} x_0 &= m - \left(-2\frac{M_D}{p}\right)^{1/2} \\ y_0 &= n - \left[n^2 - 2R(m - n) - m^2 - 2\frac{M_D}{p}\right]^{1/2} \end{aligned}\right\} \tag{5}$$

Points A, O, and D on the bending-moment curve are *extrema*.

The tensile force in the wall is given by the following equations:

$$\left.\begin{aligned} N_{CD} &= p(n + r) \\ N_{CB} &= p\left[(m^2 + n^2)^{1/2}\cos\left(\tan^{-1}\frac{m}{n} - \phi\right) + r\right] \\ N_{BA} &= p(m + r) \end{aligned}\right\} \tag{6}$$

Bending stresses are determined by use of the flexure formulas for straight and curved bars. Superposing these upon the stresses caused by tension in the tube wall, the following equations for maximum combined stress at the critical points are obtained:

$$\left.\begin{aligned} \left(\frac{\sigma_{max}}{p}\right)_A &= \frac{m + r}{h} + \frac{6}{h^2}\left|\frac{M_A}{p}\right| \\ \left(\frac{\sigma_{max}}{p}\right)_O &= \frac{h/2 - e}{her}\frac{M_O}{p} + \frac{1}{h}\left[(m^2 + n^2)^{1/2} + r\right] \\ \left(\frac{\sigma_{max}}{p}\right)_D &= \frac{n + r}{h} + \frac{6}{h^2}\left|\frac{M_D}{p}\right| \end{aligned}\right\} \tag{7}$$

The highest of these σ/p-values controls and is used to determine the elastic design load, p_{el}.

Plastic Loading

In the elastic range the bending moment, or resisting moment, varies in direct proportion to the load; i.e., the value of M/p remains constant. As plastic flow begins at some position in the tube section and progresses toward the neutral axis of the wall, the resisting moment no longer varies linearly with the load; M/p diminishes. When all fibers at this position have been stressed to the yield point, a so-called *plastic hinge* is formed at which the resisting moment remains constant with further deformation.

The bending-moment diagram in Fig. 4 is limited to the region $\overline{OCD}$ because failure will occur on this longer side of the tube section. The form of the M/p-curve is established by conditions

[1] S. Timoshenko, "Strength of Materials," D. Van Nostrand Company, New York, N. Y., second edition, part 2, 1941, p. 70.

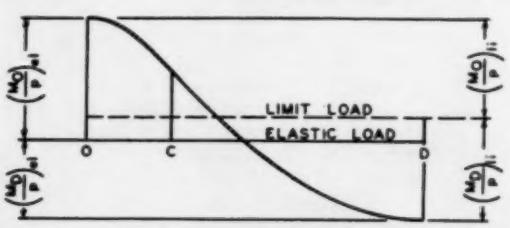

Fig. 4 Effect of inelastic action upon M/p diagram of rectangular tube

of equilibrium and remains unchanged during inelastic action. The solid reference line defines the curve for the elastic range. As the internal pressure increases to the limit load, the reference line shifts parallelwise to a new position shown by the broken line. When plastic flow commences at point O, the M/p-value diminishes. But since statics demands that the sum of the M/p-values at points O and D remains constant, the value at D must increase. In other words, weakening of the material at one point results in shifting a portion of the burden elsewhere. Ultimately, plastic hinges are formed at both points O and D, simultaneously, and the system becomes unstable. This occurs at the limit load, and the position of the reference line for the M/p-curve can be calculated.

The derivation of the limit-load formula is given in the Appendix. This formula is

$$p_{lt} = \sigma_y \left[-\frac{Z}{Q} + \left(\frac{Z^2}{Q^2} + \frac{h^2}{Q} \right)^{1/2} \right] \tag{8}$$

Z and Q are dimensional properties of the tube section and are

$$\left.\begin{aligned} Z &= R[(m^2 + n^2)^{1/2} - n] + \frac{m^2}{2} \\ Q &= \tfrac{1}{2}\{[(m^2 + n^2)^{1/2} + r]^2 + (n + r)^2\} \end{aligned}\right\} \tag{9}$$

Deflection of a Loaded Tube

Elastic Loading. Fig. 5 shows the cross-sectional quadrant of the tube before and during loading. Deflection of the longer side can produce an inward deflection of the shorter side by effecting a rotation of the entire corner. The originally circular corner $\overline{BOC}$ is assumed to deform into a circle of different radius even though the bending-moment distribution is not constant. From the geometry of the figure the principal deflections, those along the section axes, may be evaluated readily. Assuming small deflections,

$$\frac{\delta_x}{2} = R + \Delta R - [R + (R + \Delta R)\alpha_C] + \Delta_B$$

$$\frac{\delta_y}{2} = R + \Delta R - [R - (R + \Delta R)\alpha_B] + \Delta_C$$

Expanding and dropping higher degrees of small quantities,

$$\left.\begin{aligned} \delta_x &= 2(\Delta R - R\alpha_C + \Delta_B) \\ \delta_y &= 2(\Delta R + R\alpha_B + \Delta_C) \end{aligned}\right\} \tag{10}$$

The individual terms in equations (10) can be evaluated from the bending-moment diagram by area-moments. It will be noted that flexural rigidity for thin plates is used in the following equations for deflections:[2]

$$\left.\begin{aligned} \alpha_B &= \frac{12(1 - \nu^2)}{Eh^3}\,\text{Area}_{BA} \\ \alpha_C &= -\frac{12(1 - \nu^2)}{Eh^3}\,\text{Area}_{CD} \\ \Delta_B &= -\frac{12(1 - \nu^2)}{Eh^3}\,\bar{y}\,\text{Area}_{BA} \\ \Delta_C &= -\frac{12(1 - \nu^2)}{Eh^3}\,\bar{x}\,\text{Area}_{CD} \\ \Delta\phi &= \frac{1 - \nu^2}{REAe}\,\text{Area}_{BC} \\ \Delta R &= \frac{2(1 - \nu^2)}{\pi EAe}\,\text{Area}_{BC} \end{aligned}\right\} \tag{11}$$

The change of the corner angle during loading is the difference between the angular deflections of points C and B,

$$\Delta\phi = \alpha_C - \alpha_B \tag{12}$$

The following expressions are useful for determining the areas and area-moments of a particular bending-moment diagram:

$$\left.\begin{aligned} \text{Area}_{BA} &= nM_B + \frac{2n}{3}(M_A - M_B) \\ \text{Area}_{BC} &= pR^2\left(m + n - \frac{\pi n}{2}\right) + \frac{\pi R}{2}M_C \\ \text{Area}_{CD} &= mM_C + \frac{2m}{3}(M_D - M_C) \\ \bar{y}\,\text{Area}_{BA} &= \frac{n^2}{2}M_B + \frac{5n^2}{12}(M_A - M_B) \\ \bar{x}\,\text{Area}_{CD} &= \frac{m^2}{2}M_C + \frac{5m^2}{12}(M_D - M_C) \end{aligned}\right\} \tag{13}$$

Plastic Loading. To extend the area-moment method of computing deflections into the plastic range, it is necessary to divide the ordinates of the bending-moment diagram by reduced rigidity coefficients. In Fig. 6, β is plotted against $M/h^2\sigma_y$ for different

[2] Timoshenko, ibid., p. 120.

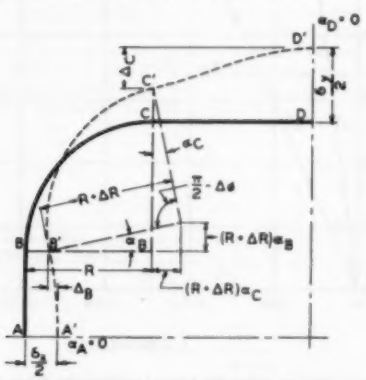

Fig. 5 Deflection in tube-section quadrant

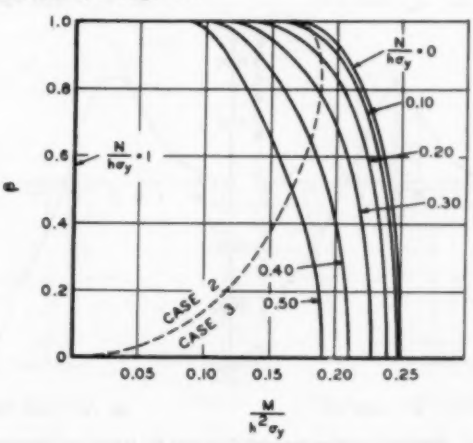

Fig. 6 β versus $M/h^2\sigma_y$

values of $N/h\sigma_y$. There are three separate and distinct cases of combined bending and tension in the tube wall. The first is that of elasticity throughout the wall thickness at a given point. The second case is that in which plasticity exists any distance inward from the extreme fiber on one side of the neutral axis (the tension side), but elasticity exists throughout the other side. The third case is that in which plasticity occurs any distance inward from the extreme fibers on both sides of the neutral axis.

In the first case β_1 has a constant value of 1, and obtains within the limits

$$0 \leq \frac{M}{h^2\sigma_y} \leq \frac{1}{6}\left(1 - \frac{N}{h\sigma_y}\right)$$

The equation for Case 3, derived in the Appendix, is

$$\beta_3 = 6\,\frac{M}{h^2\sigma_y}\left\{3\left[1 - 4\,\frac{M}{h^2\sigma_y} - \left(\frac{N}{h\sigma_y}\right)^2\right]\right\}^{1/2} \qquad (14)$$

and its limits are

$$\frac{M}{h^2\sigma_y} = \frac{1}{6}\left[1 + \frac{N}{h\sigma_y} - 2\left(\frac{N}{h\sigma_y}\right)^2\right]$$

$$\frac{M}{h^2\sigma_y} = \frac{1}{4}\left[1 - \left(\frac{N}{h\sigma_y}\right)^2\right] \quad (\beta = 0)$$

The derivation of β for Case 2 is included in the Appendix. This results in the expression

$$\beta_2 = 54\,\frac{M}{h^2\sigma_y}\,\frac{\left(\dfrac{M}{h^2\sigma_y} + \dfrac{1}{2}\,\dfrac{N}{h\sigma_y} - \dfrac{1}{2}\right)^2}{\left(1 - \dfrac{N}{h\sigma_y}\right)^3} \qquad (15)$$

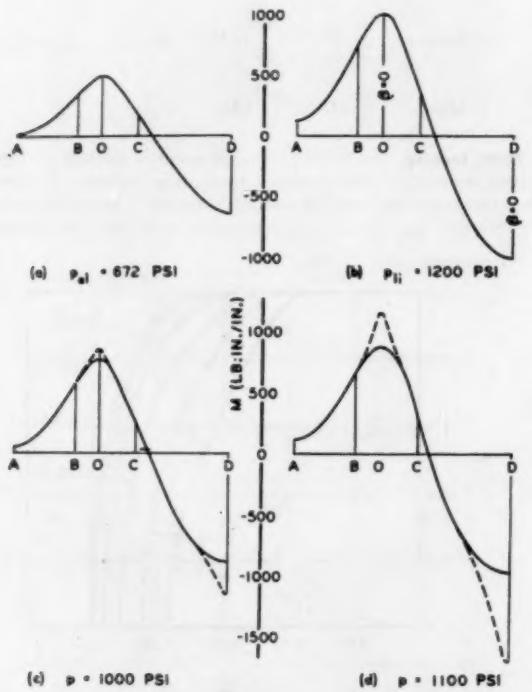

Fig. 7 Modified bending-moment diagrams for typical rectangular tube; $m = 1\frac{1}{2}$ in., $n = 1$ in., $r = \frac{1}{2}$ in., $h = \frac{3}{8}$ in., $\sigma_y = 30{,}000$ psi

Although the β-curves in Fig. 6 are represented by three different formulas, it can be shown readily that no slope discontinuities exist.

The procedure by which a plastic deflection is found is as follows: For any particular value of p, the form of the bending-moment curve is established by equations (2). The reference line is then arbitrarily positioned between the limits shown in Fig. 4, thus giving ordinate values to the curve. Now having the necessary $M/h^2\sigma_y$ and $N/h\sigma_y$-values, β for various points may be found from Fig. 6. Dividing the ordinates of the bending-moment curve by these values of β, points on a modified curve are fixed. The areas under the modified curve can be measured by use of a planimeter, and equations (11) provide the angular deflections, α_B, α_C, and $\Delta\phi$. Equation (12) is then applied as a test. With sufficient iterations the correct modified bending-moment diagram is obtained and the true plastic deflection can be computed therefrom in the manner used for elastic deflections. If this method is applied for the limit load, β for points O and D will be found to equal zero and the modified curve will be undefined.

Modified bending-moment diagrams for a typical rectangular tube subjected to various loads are shown in Fig. 7. The elastic load is represented by Fig. 7(a) and the limit load by (b), while (c) and (d) represent intermediate loads. The broken curves delineate the plastic regions of the tube section.

Load-Deflection Curve. The principal wall deflections computed from the bending-moment diagrams in Fig. 7 are plotted in Fig. 8. The elastic portion of the load-deflection curve is straight. The δ_y-curve is asymptotic to p_{li}, where theoretical failure occurs. The δ_x-curve, representing the shorter side which does not fail, is discontinuous at the limit load.

Conclusions

The limit design recognizes that failure of a ductile tube does not occur with incipient yielding. The limit load for a given tube is the pressure at which the strength of the tube, both elastic and plastic, has been realized and the system becomes unstable. This load is given directly by equation (8). The load-deflection curve is a graphic representation of the behavior of the tube as it undergoes the full range of pressurizing. In many applications the deflection under load is pertinent to the design criteria.

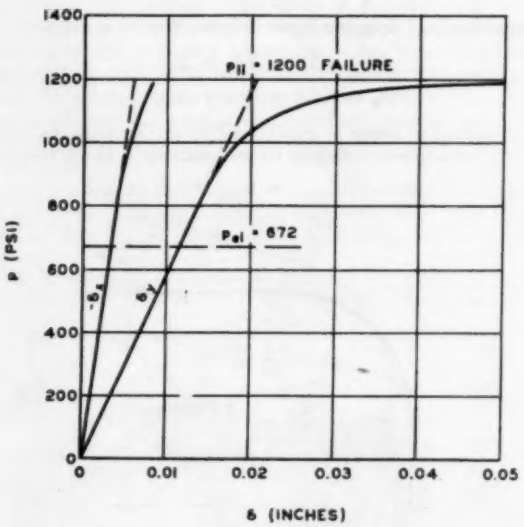

Fig. 8 Load-deflection curve for typical rectangular tube; $m = 1\frac{1}{2}$ in., $n = 1$ in., $r = \frac{1}{2}$ in., $h = \frac{3}{8}$ in., $\sigma_y = 30{,}000$ psi

APPENDIX

Derivation of the Limit-Load Formula. Fig. 9 shows the limit-load stress distribution at point O with the resultant force, $(N_O)_{li}$, and resisting moment, $(M_O)_{li}$.[3] Summing forces,

$$(N_O)_{li} = \sigma_y(h_i - h_o),$$

h_i and h_o being positive. But

$$h_i + h_o = h$$

Therefore,

$$\left.\begin{aligned} h_i &= \frac{1}{2}\left[h + \frac{(N_O)_{li}}{\sigma_y}\right] \\ h_o &= \frac{1}{2}\left[h - \frac{(N_O)_{li}}{\sigma_y}\right] \end{aligned}\right\} \tag{16}$$

Taking moments about the centroidal axis,

$$(M_O)_{li} = \sigma_y h_i\left(\frac{h_i}{2} - e\right) + \sigma_y h_o\left(\frac{h_o}{2} + e\right),$$

and since

$$e = \tfrac{1}{2}(h_i - h_o),$$

$$(M_O)_{li} = \sigma_y h_i h_o$$

Substituting equations (16),

$$(M_O)_{li} = \frac{\sigma_y}{4}\left[h^2 - \frac{(N_O)_{li}^2}{\sigma_y^2}\right]$$

By means of a similar development,

$$(M_D)_{li} = -\frac{\sigma_y}{4}\left[h^2 - \frac{(N_D)_{li}^2}{\sigma_y^2}\right]$$

Combining these two equations,

$$(M_O - M_D)_{li} = \frac{\sigma_y}{4}\left[2h^2 - \frac{(N_O^2 + N_D^2)_{li}}{\sigma_y^2}\right] \tag{17}$$

In equation (2), M_O corresponds to ϕ_O, so that

$$M_O = pmR \sin\tan^{-1}\frac{m}{n} - pnR\left(1 - \cos\tan^{-1}\frac{m}{n}\right) + \frac{pm^2}{2} + M_D$$

$$M_O - M_D = \frac{pm^2R}{(m^2+n^2)^{1/2}} - pnR + \frac{pn^2R}{(m^2+n^2)^{1/2}} + \frac{pm^2}{2}$$

From equation (9)

$$(M_O - M_D)_{li} = p_{li}\left\{R[(m^2+n^2)^{1/2} - n] + \frac{m^2}{2}\right\} = Zp_{li}$$

Using equations (6) and (9),

$$(N_O^2 + N_D^2)_{li} = p_{li}^2\{[(m^2+n^2)^{1/2} + r]^2 + (n+r)^2\} = 2Qp_{li}^2$$

Equation (17) now yields

$$Zp_{li} = \frac{\sigma_y h^2}{2} - \frac{Q}{2\sigma_y}p_{li}^2,$$

$$p_{li} = \sigma_y\left[-\frac{Z}{Q} + \left(\frac{Z^2}{Q^2} + \frac{h^2}{Q}\right)^{1/2}\right] \tag{8}$$

Derivation of Reduced Rigidity Coefficient. Case 3 is illustrated in Fig. 10. The distance from the neutral axis to the elastic boundary is v, and is positive in both directions. It is assumed that a plane section before loading remains a plane section during both elastic and plastic loading.

By summing the forces on the section in Fig. 10(b), we evaluate

$$e = \frac{N}{2\sigma_y} \tag{18}$$

Summing the moments about the neutral axis gives

$$v^2 = 3\left(\frac{h^2}{4} + e^2 - \frac{M}{\sigma_y} - \frac{Ne}{\sigma_y}\right)$$

Substituting equation (18),

$$\frac{v}{h} = \frac{1}{2}\left\{3\left[1 - 4\frac{M}{h^2\sigma_y} - \left(\frac{N}{h\sigma_y}\right)^2\right]\right\}^{1/2} \tag{19}$$

Introducing the reduced rigidity coefficient into the differential equation of the deflection curve for plates,[4]

$$d\alpha = \frac{12(1-\nu^2)M}{\beta E h^3}\,ds \tag{20}$$

Fig. 10(d) provides the following relation:

$$d\alpha = \frac{\frac{\sigma_y}{E}(1-\nu^2)}{v}\,ds \tag{21}$$

[3] Similar moment expressions for combined bending and tension are developed in two papers by E. T. Onat and W. Prager, "The Influence of Axial Forces on the Collapse Load of Frames," *Proceedings of the First Midwestern Conference on Solid Mechanics*, Urbana, 1953, pp. 40–42, 1954; "Limit Analysis of Arches," *Journal of Mechanics and Physics of Solids*, vol. 1, 1953, pp. 77–89.

[4] Timoshenko, op. cit.

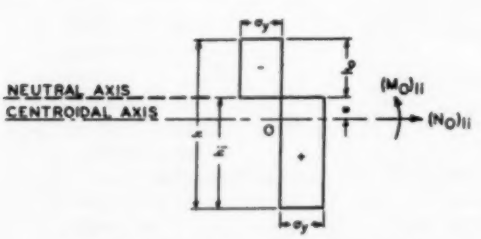

Fig. 9 Limit-load stress distribution at point O

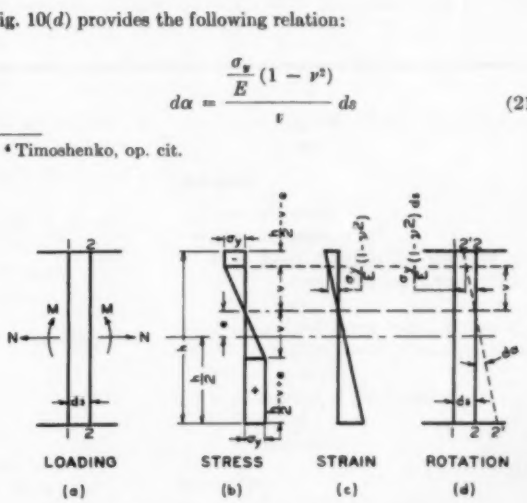

Fig. 10 Combined bending and tension in tube wall

Combining equations (20) and (21),

$$\beta = 12 \frac{M}{h^2\sigma_y} \frac{v}{h}, \tag{22}$$

and from equation (19)

$$\beta_3 = 6 \frac{M}{h^2\sigma_y} \left\{3 \left[1 - 4 \frac{M}{h^2\sigma_y} - \left(\frac{N}{h\sigma_y}\right)^2\right]\right\}^{1/2} \tag{14}$$

The upper limit of Case 3 exists when

$$v = \frac{h}{2} - e = \frac{h}{2} - \frac{N}{2\sigma_y},$$

and equation (22) becomes

$$\beta = 6 \frac{M}{h^2\sigma_y} \left(1 - \frac{N}{h\sigma_y}\right)$$

From equation (14) the upper limit for Case 3 is obtained,

$$\frac{M}{h^2\sigma_y} = \frac{1}{6} \left[1 + \frac{N}{h\sigma_y} - 2 \left(\frac{N}{h\sigma_y}\right)^2\right]$$

The lower limit occurs when β is zero, and

$$\frac{M}{h^2\sigma_y} = \frac{1}{4} \left[1 - \left(\frac{N}{h\sigma_y}\right)^2\right]$$

The Case 2 formula is developed in a similar manner. Fig. 10(*b*) is considered modified so that σ_y is not reached on the upper side of the neutral axis. Summing the forces on the section,

$$e = v + \frac{h}{2} \pm \left[2v\left(h - \frac{N}{\sigma_y}\right)\right]^{1/2} \tag{23}$$

Summation of moments provides the following cubic equation:

$$v^3 + 3 \left[\frac{2M}{\sigma_y} + \frac{2N}{\sigma_y} e - \left(\frac{h}{2} + e\right)^2\right] v - 2 \left(\frac{h}{2} - e\right)^3 = 0 \tag{24}$$

By means of equations (23) and (24), v is defined explicitly and its substitution in equation (22) provides the expression for β_2:

$$\beta_2 = 54 \frac{M}{h^2\sigma_y} \frac{\left(\frac{M}{h^2\sigma_y} + \frac{1}{2} \frac{N}{h\sigma_y} - \frac{1}{2}\right)^2}{\left(1 - \frac{N}{h\sigma_y}\right)^3} \tag{15}$$

Gas-Lubricated Cylindrical Journal Bearings of the Finite Length[1]

Static Loading

B. STERNLICHT
General Electric Company,
Schenectady, N. Y.
Assoc. Mem. ASME

This paper presents numerical solutions of the Reynolds equation for finite length, gas-lubricated cylindrical journal bearings under static loading (this corresponds to a load of constant magnitude and direction with respect to the bearing). It is shown that the incompressible results are but only limiting cases to the more general compressible solutions. The results of the two solutions are dovetailed together through the use of two dimensionless parameters: the inverse of the Sommerfeld number and the compressibility number. Comparisons of the iterative solutions and the first-order perturbation and the "linearized ph" methods are made. The advantages and disadvantages of these methods of analysis are discussed.

THE Reynolds equation for self-acting gas-lubricated bearings is a nonlinear partial differential equation. This equation can be approximated by finite differences and can be solved by an iterative process [1][2] using high-speed computers. This paper presents results using this method of analysis and compares it with other methods and experiments. One of the disadvantages of this procedure is that each case requires a considerable amount of computer time. Since solutions to a large number of cases are necessary to cover the full range of variables, this method of analysis represents considerable expense. On the other hand, one important advantage of this method is that once an iterative program is developed it is applicable to other journal bearing geometries; e.g., partial bearings, grooved bearings, and so on. Another advantage is that this method of analysis has more correlation with accurately conducted experiments than do other analytical solutions available at this time. High accuracy is especially important in dynamic and stability analysis where accurate determination of radial and tangential-force derivatives with respect to displacement and velocity is required.

The analytical solution which employs the perturbation technique [2] has several major limitations: (*a*) The results yield force directly proportional to the eccentricity and attitude angle independent of eccentricity. This makes the results accurate only for small eccentricity ratios $\epsilon < 0.3$. (*b*) As a consequence of the first condition, the bearing stiffness is independent of eccentricity, whereas the actual bearing stiffness increases with increase in eccentricity ratio.

The "linearized *ph*" method of analysis [3] represents an improvement over the first-order perturbation. This method of analysis yields stiffness and attitude angles which are dependent on eccentricity ratio, as they should be. Again, however, this

[1] This work was sponsored by the Office of Naval Research, Contract No. NONR 2844(00), Task No. NR 097-348. Reproduction of this report in whole, or in part, is permitted for any purpose of the United States Government.

[2] Numbers in brackets designate References at end of paper.

Presented at the Summer Conference of the Applied Mechanics Division, Chicago, Ill., June 14–16, 1961, of THE AMERICAN SOCIETY OF MECHANICAL ENGINEERS.

Discussion of this paper should be addressed to the Editorial Department, ASME, United Engineering Center, 345 East 47th Street, New York 17, N. Y., and will be accepted until January 10, 1962. Discussion received after the closing date will be returned. Manuscript received by ASME Applied Mechanics Division, October 6, 1960. Paper No. 61—APM-17.

Nomenclature

A = coefficient, equation (11)
a = coefficient, equation (10)
C = diametral clearance, in.
D = journal-bearing diameter, in.
e = eccentricity, in.
f = dimensionless force, $\dfrac{12\pi W}{\Lambda p_a L D}$
g = accelerating factor
h = film thickness, in.
K = constant
L = axial length of bearing, in.
m = number of mesh subdivisions in θ or x-direction
n = number of mesh subdivisions in z-direction
p = pressure, psi
W = force
u, v, w = components of fluid velocity in x, y, z-direction, respectively
x, y, z = rectangular co-ordinates of a point
γ = ratio of specific heat of gas lubricant
Δ = incremental distance
ϵ = eccentricity ratio
Λ = compressibility number, $\dfrac{6\mu\omega}{p_a}\left(\dfrac{D}{C}\right)^2$
θ = angle, radians
μ = viscosity, lb-sec/in.^{2}
ρ = mass density, lb-sec^2/in.^{4}
ϕ = attitude angle, radians
ω = angular velocity radians per sec

Subscripts

a = ambient
avg = average
i = index defining the value of z in journal bearing running from 1 to n
j = index defining value of x or θ in journal bearing running from 1 to m
k = number of iterations
r = radial
t = tangential

Superscript

$'$, prime is dimensional

method does not correlate very closely with the iterative method. The divergence in force and phase angle is especially pronounced at high eccentricity ratios $\epsilon > 0.5$.

The analytical method for infinite length bearing outlined in [4] and corrected for finite length by use of end-flow factor, calculated by perturbation method, yields the closest correlation to the iterative analysis.

The foregoing discussion is not intended to detract from the value of analytical methods, which in general can provide good physical insight into the problem, but points out the value of the iterative method which is presented here. This report extends the range of variables studied in [1]. It covers practical range of operating eccentricity ratios 0–0.8 and $L/D = 0.5, 1, 1.5, 2$, for compressibility number $\Lambda = 0 \rightarrow \infty$. Extrapolation to higher eccentricity ratios, or L/D, can be done quite accurately by cross-plotting the presented results. The results are given in graphical form so that they can be readily used in design. Comparison of pressure distribution, force, and attitude angle with other methods of analysis and experiments are also presented.

Theoretical Analysis

The following approximations are made in the Navier-Stokes equation:

1 Isothermal conditions are assumed.

2 Inertia terms are neglected with respect to pressure-gradient terms.

3 Vertical fluid velocity v is neglected with respect to horizontal fluid velocities.

4 The predominant viscous shear stresses are $\partial^2 u/\partial y^2$ and $\partial^2 w/\partial y^2$. All other viscous shear stresses are negligible by comparison.

5 Pressure is independent of y-co-ordinate.

6 Density is independent of the y-co-ordinate.

7 The fluid is Newtonian.

Neglecting the effect of curvature, it is possible to analyze the circular bearing using the configuration shown in Fig. 1.

The film thickness h' in the bearing with certain eccentricity e' is calculated approximately from the following equation (see Fig. 2):

$$h' = \frac{C'}{2} + e' \cos\theta \tag{1}$$

Substituting the parameter $h = h'/C'$, equation (1) is made dimensionless,

$$\therefore h = \tfrac{1}{2} + \tfrac{1}{2}\epsilon \cos\theta \tag{2}$$

From the Navier-Stokes equation and the continuity equation for compressible fluid flow we get

$$\frac{\partial}{\partial x'}\left[\rho' \frac{h'^3}{\mu'} \frac{\partial p'}{\partial x'}\right] + \frac{\partial}{\partial z'}\left[\frac{\rho' h'^3}{\mu'} \frac{\partial p'}{\partial z'}\right] = 3D'\omega' \frac{\partial}{\partial x'}(\rho' h') \tag{3}$$

To write equation (3) in dimensionless form, the following dimensionless parameters are used:

$$\left.\begin{aligned} x &= \frac{x'}{D'} \quad D'\,\partial x = \partial x' \\ z &= \frac{z'}{L'} \quad L'\partial z = \partial z' \\ h &= \frac{h'}{C'} \\ \rho &= \frac{\rho'}{\rho_a'} \\ \mu &= \frac{\mu'}{\mu'_{avg}} \\ p &= \frac{12\pi}{\Lambda}\frac{p'}{p_a'}, \quad \frac{\Lambda p_a'}{12\pi}\partial p = \partial p' \end{aligned}\right\} \tag{4}$$

Substituting (4) in equation (3) we get

$$\frac{\partial}{\partial x}\left[\frac{\rho h^3}{\mu}\frac{\partial p}{\partial x}\right] + \left(\frac{D}{L}\right)^2 \frac{\partial}{\partial z}\left[\frac{\rho h^3}{\mu}\frac{\partial p}{\partial z}\right] = 6\pi \frac{\partial}{\partial x}(\rho h) \tag{5}$$

For the incompressible case, the density remains constant. Therefore ρ is canceled in each term of equation (5).

Writing equation (5) in difference form, we get

$$\frac{\partial}{\partial x}\left[\frac{\rho h^3}{\mu}\frac{\partial p}{\partial x}\right] = \frac{\left(\frac{h^3\rho}{\mu}\right)_{i,j+\frac{1}{2}}\left(\frac{p_{i,j+1} - p_{i,j}}{\Delta x}\right) - \left(\frac{h^3\rho}{\mu}\right)_{i,j-\frac{1}{2}}\left(\frac{p_{i,j} - p_{i,j-1}}{\Delta x}\right)}{\Delta x}$$

$$\frac{\partial}{\partial z}\left[\frac{\rho h^3}{\mu}\frac{\partial p}{\partial z}\right] = \frac{\left(\frac{h^3\rho}{\mu}\right)_{i+\frac{1}{2},j}\left(\frac{p_{i+1,j} - p_{i,j}}{\Delta z}\right) - \left(\frac{h^3\rho}{\mu}\right)_{i-\frac{1}{2},j}\left(\frac{p_{i,j} - p_{i-1,j}}{\Delta z}\right)}{\Delta z}$$

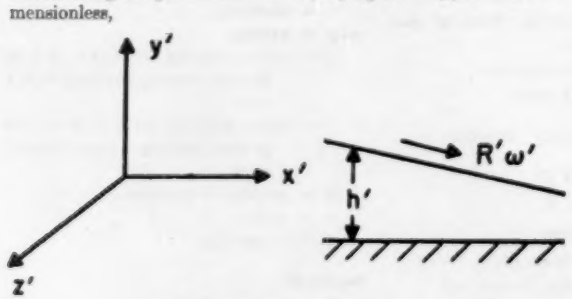

Fig. 1 Co-ordinate system

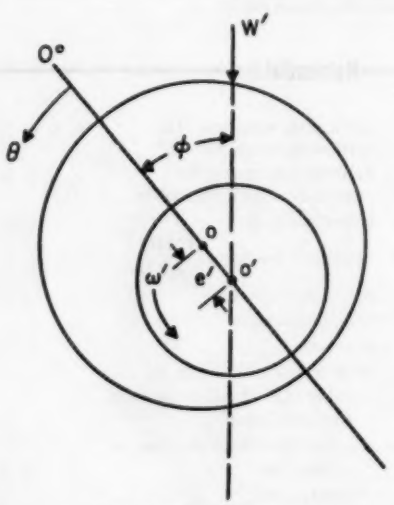

Fig. 2 Journal bearing

$$\frac{\partial}{\partial x}(\rho h) = \frac{(\rho h)_{i,j+\frac{1}{2}} - (\rho h)_{i,j-\frac{1}{2}}}{\Delta x} \tag{6}$$

Recombining the terms, equation (5) as a difference equation is

$$\frac{\left(\frac{h^3\rho}{\mu}\right)_{i,j+\frac{1}{2}}\left(\frac{p_{i,j+1}-p_{i,j}}{\Delta x}\right) - \left(\frac{h^3\rho}{\mu}\right)_{i,j-\frac{1}{2}}\left(\frac{p_{i,j}-p_{i,j-1}}{\Delta x}\right)}{\Delta x}$$

$$+\left(\frac{D'}{L'}\right)^2 \frac{\left(\frac{h^3\rho}{\mu}\right)_{i+\frac{1}{2},j}\left(\frac{p_{i+1,j}-p_{i,j}}{\Delta z}\right) - \left(\frac{h^3\rho}{\mu}\right)_{i-\frac{1}{2},j}\left(\frac{p_{i,j}-p_{i-1,j}}{\Delta z}\right)}{\Delta z}$$

$$= 6\pi \frac{[(\rho h)_{i,j+\frac{1}{2}} - (\rho h)_{i,j-\frac{1}{2}}]}{\Delta x} \tag{7}$$

The pressure at the center of any grid is

$$p_{i,j} = \frac{6\pi \frac{[(\rho h)_{i,j-\frac{1}{2}} - (\rho h)_{i,j+\frac{1}{2}}]}{\Delta x} + \left(\frac{h^3\rho}{\mu}\right)_{i,j+\frac{1}{2}} \frac{p_{i,j+1}}{\Delta z^2} + \left(\frac{h^3\rho}{\mu}\right)_{i,j-\frac{1}{2}} \frac{p_{i,j-1}}{\Delta z^2}}{\left(\frac{h^3\rho}{\mu}\right)_{i,j+\frac{1}{2}} \frac{1}{\Delta z^2} + \left(\frac{h^3\rho}{\mu}\right)_{i,j-\frac{1}{2}} \frac{1}{\Delta z^2} + \left(\frac{D'}{L'}\right)^2 \left[\left(\frac{h^3\rho}{\mu}\right)_{i+\frac{1}{2},j} \frac{1}{\Delta z^2} + \left(\frac{h^3\rho}{\mu}\right)_{i-\frac{1}{2},j} \frac{1}{\Delta z^2}\right]}$$

$$+ \frac{\left(\frac{D'}{L'}\right)^2 \left[\left(\frac{h^3\rho}{\mu}\right)_{i+\frac{1}{2},j} \frac{p_{i+1,j}}{\Delta z^2} + \left(\frac{h^3\rho}{\mu}\right)_{i-\frac{1}{2},j} \frac{p_{i-1,j}}{\Delta z^2}\right]}{\left(\frac{h^3\rho}{\mu}\right)_{i,j+\frac{1}{2}} \frac{1}{\Delta z^2} + \left(\frac{h^3\rho}{\mu}\right)_{i,j-\frac{1}{2}} \frac{1}{\Delta z^2} + \left(\frac{D'}{L'}\right)^2 \left[\left(\frac{h^3\rho}{\mu}\right)_{i+\frac{1}{2},j} \frac{1}{\Delta z^2} + \left(\frac{h^3\rho}{\mu}\right)_{i-\frac{1}{2},j} \frac{1}{\Delta z^2}\right]} \tag{8}$$

The pressure is related to density by equation (9)

$$\rho' = \rho_a' \left(\frac{p'}{p_a'}\right)^{1/\gamma} \tag{9}$$

This, written in dimensionless form, becomes

$$\rho = \left[p \frac{\Lambda}{12\pi}\right]^{1/\gamma}$$

Using the foregoing relationship, the density in equation (8) can be replaced by pressure. For isothermal case $\gamma = 1$ which further simplifies equation (8).

For the journal bearing under investigation there is no film-thickness variation in the axial, or z-direction, hence

$$h_{i+\frac{1}{2},j} = h_{i-\frac{1}{2},j}$$

Also, it is assumed that the viscosity is constant throughout the field. Hence:

$$\mu_{i+\frac{1}{2},j} = \mu_{i-\frac{1}{2},j} = \mu_{i,j+\frac{1}{2}} = \mu_{i,j-\frac{1}{2}} = 1$$

Thus equation (8) can be written in the following form:

$$p_{i,j} = a_0 + a_1 p_{i+1,j} + a_2 p_{i,j+1} + a_3 p_{i-1,j} + a_4 p_{i,j-1} \tag{10}$$

where

$$a_0 = \frac{6\pi[(\rho h)_{i,j-\frac{1}{2}} - (\rho h)_{i,j+\frac{1}{2}}]}{A\Delta x}$$

$$a_1 = \left(\frac{D'}{L'}\right)^2 \frac{(h^3\rho)_{i+\frac{1}{2}}}{A\Delta z^2}$$

$$a_3 = \left(\frac{D'}{L'}\right)^2 \frac{(h^3\rho)_{i-\frac{1}{2},j}}{A\Delta z^2}$$

$$a_2 = \frac{(h^3\rho)_{i,j+\frac{1}{2}}}{A\Delta z^2} \tag{11}$$

$$a_4 = \frac{(h^3\rho)_{i,j-\frac{1}{2}}}{A\Delta z^2} \tag{11 (cont.)}$$

$$A = \left(\frac{D'}{L'}\right)^2 \frac{(h^3\rho)_{i+\frac{1}{2},j} + (h^3\rho)_{i-\frac{1}{2},j}}{\Delta z^2} + \frac{1}{\Delta x^2}[(h^3\rho)_{i,j+\frac{1}{2}} + (h^3\rho)_{i,j-\frac{1}{2}}]$$

The following boundary conditions are set:

$$p = 1 \quad \text{at} \quad \pm z/2$$

The pressure and pressure gradients are periodic, therefore

$$p|_0 = p|_{2\pi}$$

$$\left.\frac{\partial p}{\partial x}\right|_0 = \left.\frac{\partial p}{\partial x}\right|_{2\pi}$$

Solution of equation (10) is performed in the following manner:

1 L'/D', ϵ, Λ, m, and n are set. (For majority of cases solved $m = 12$ and $n = 6$.)

2 The value of the film thickness at every point is determined from equation (2).

3 $p_{i,j}$ is assumed equal to zero throughout the field.

4 Having h and $p_{i,j}$, the first approximation to the pressure field is determined from equation (10).

5 This pressure field is improved several times by iteration.

6 The iterated pressure field is now used to calculate the density distribution from equation (9).

7 Another pressure field can now be calculated from equation (10) by using h as calculated in step 2, ρ calculated in step 6, and the last iterated pressure $p_{i,j}$ from step 5.

8 This cycle of pressure and density iteration is continued until $p_{i,j}$ reaches the tolerance factor specified for the run.

$$\text{Residual factor} = \frac{\sum_{j=1}^{m}\sum_{i=1}^{n} |(p_{i,j})_k - (p_{i,j})_{k-1}|}{\sum_{j=1}^{m}\sum_{i=1}^{n} |(p_{i,j})_k|} < 0.1 \text{ per cent} \tag{12}$$

(This tolerance was found to give sufficient accuracy.)

9 The final pressure field is then used to compute the radial and tangential components of force.

The force at a point is equal to the pressure at that point times the area. The total force on the bearing is the integral of pressure times area summed over the whole bearing.

$$f_r = \frac{12\pi W_r'}{\Lambda p_a' L' D'} = -\sum_{j=1}^{m}\sum_{i=1}^{n} (p_{i,j})_k \cos\theta \Delta x \Delta z$$

$$f_t = \frac{12\pi W_t'}{\Lambda p_a' L' D'} = \sum_{j=1}^{m}\sum_{i=1}^{n} (p_{i,j})_k \sin\theta \Delta x \Delta z \tag{13}$$

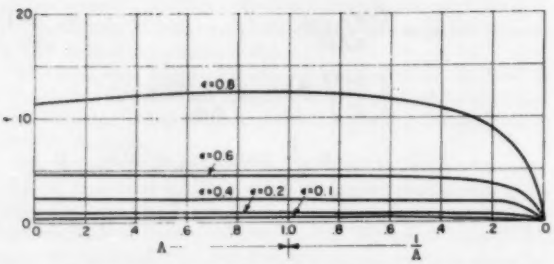

Fig. 3 Dimensionless force versus compressibility number for L/D = 0.5

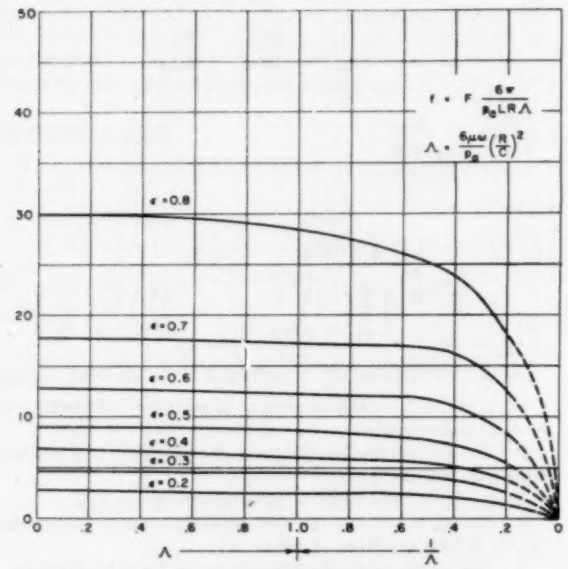

Fig. 4 Dimensionless force versus compressibility number for L/D = 1

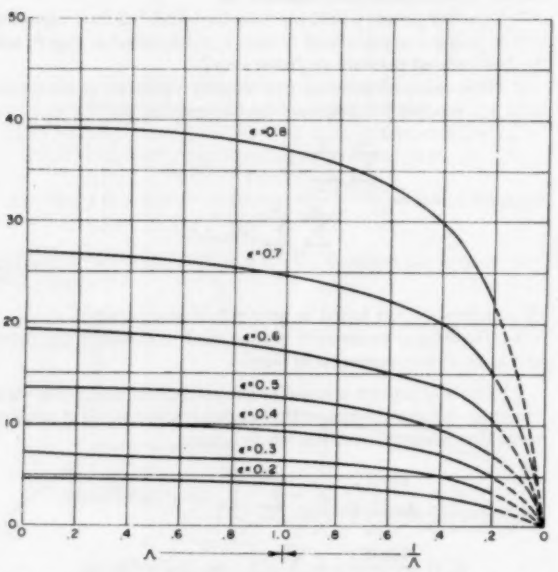

Fig. 5 Dimensionless force versus compressibility number for L/D = 1.5

From the pressure profile it is also possible to calculate the frictional force and flow.

In order to accelerate the process of iterations, an accelerating factor g is employed. This factor may vary from row to row or from iteration to iteration. The value chosen at any time is based on experience. The following equation is used for the adjustment of pressure between successive iterations:

$$p_{i,j} = g[(p_{i,j})_k - (p_{i,j})_{k-1}] + (p_{i,j})_{k-1} \qquad (14)$$

Results

Figs. 3–6 show a plot of dimensionless force $f = (f_r^2 + f_t^2)^{1/2}$ versus compressibility number Λ for various eccentricity ratios. The four figures are for L/D = 0.5, 1, 1.5, and 2, respectively.

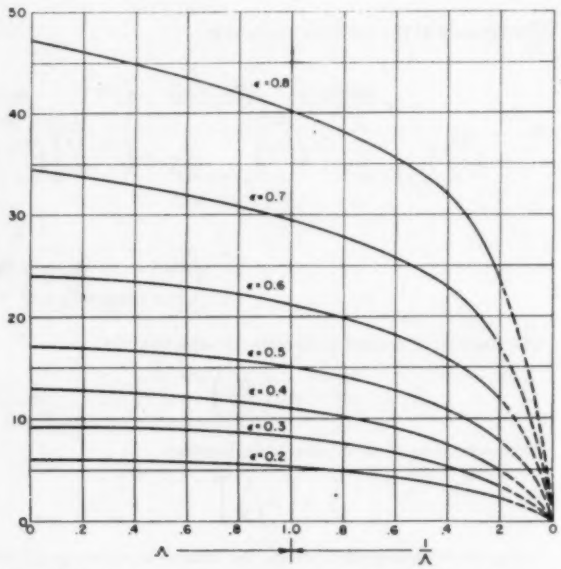

Fig. 6 Dimensionless force versus compressibility number for L/D = 2

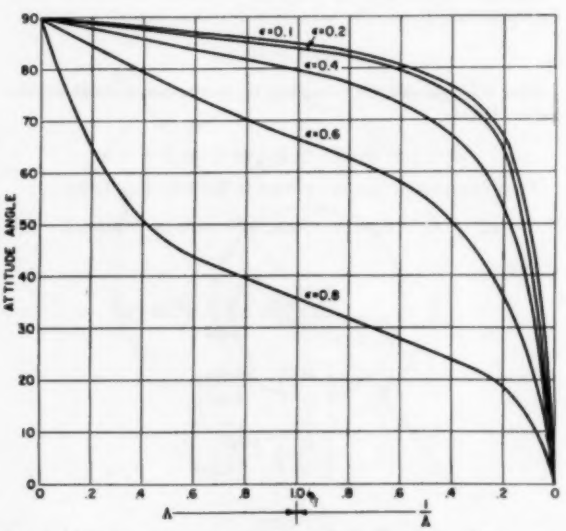

Fig. 7 Attitude angle versus compressibility number for L/D = 0.5

This scale for the abscissa was chosen because it conveniently covers the complete range of Λ from $0 \rightarrow \infty$. One of the reasons for choosing the dimensionless force f for the ordinate is that it gives a very convenient plot; furthermore, f is the reciprocal of the Sommerfeld number which enables an easy comparison of the results with incompressible results. Note that, for a specific eccentricity ratio, the value of f is virtually constant at low compressibility number $\Lambda < 1.0$. The range of Λ over which f is virtually constant decreases with an increase in eccentricity and L/D ratios. This leads to the conclusion that for low Λ, $W \approx K\Lambda$.

Figs. 7–10 give the attitude angle, ϕ versus compressibility number Λ for various eccentricity ratios. The four figures are for $L/D = 0.5$, 1, 1.5, and 2, respectively. Using these figures with corresponding figures for dimensionless force, it is possible to resolve the force to radial and tangential components:

$$f_r = f \cos \phi$$
$$f_t = f \sin \phi \tag{15}$$

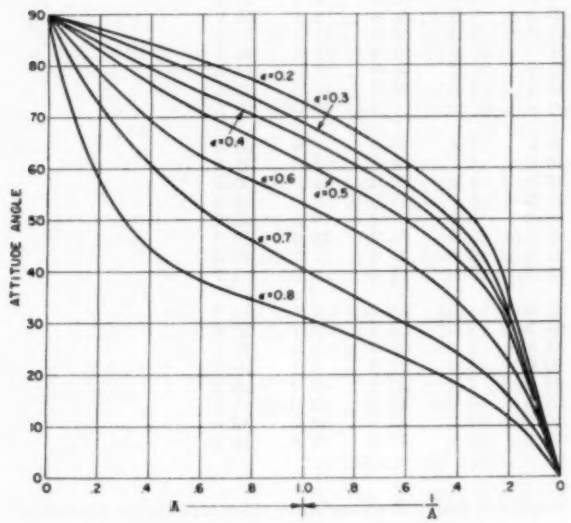

Fig. 8 Attitude angle versus compressibility number for $L/D = 1$

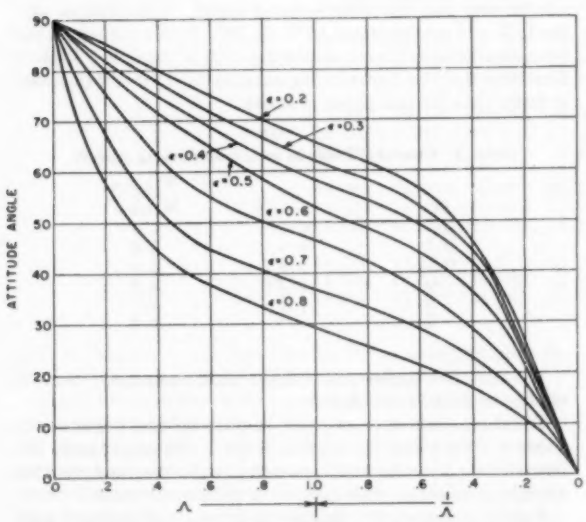

Fig. 9 Attitude angle versus compressibility number for $L/D = 1.5$

Table 1 gives numerical values of dimensionless force and attitude angle. (The results for $L/D = 0.5$ are from reference [6].) These values were used to plot Figs. 3–10. Fig. 11 gives the dimensionless frictional force versus compressibility number for different values of L/D and eccentricity ratio. Note that the incompressible results give the highest frictional loss. Employing the results presented in Figs. 3–11, one is able to design the appropriate bearing from the standpoint of steady load-carrying capacity.

Fig. 12 is a cross plot of Figs. 3–6; it gives dimensionless force and attitude angle versus L/D ratio for several values of ec-

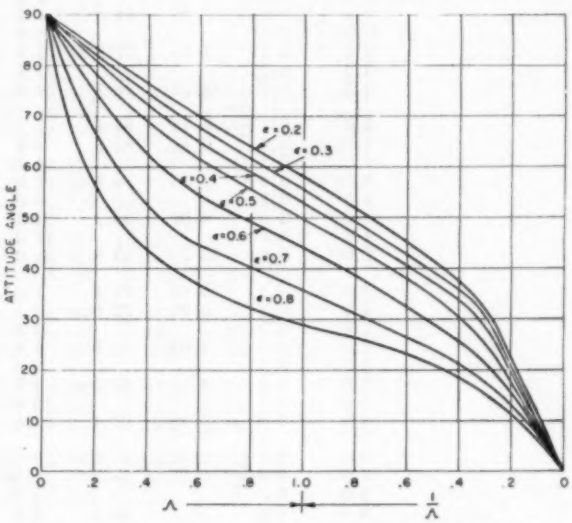

Fig. 10 Attitude angle versus compressibility number for $L/D = 2$

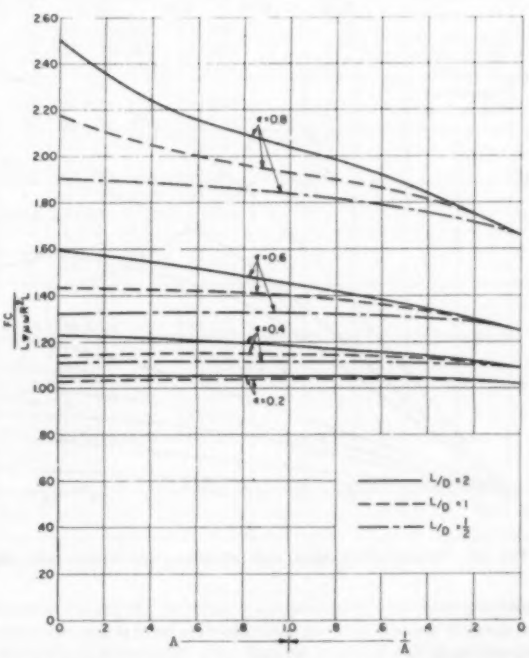

Fig. 11 Dimensionless frictional force versus compressibility number

Table 1 Dimensionless static load and attitude angle

		L/D = 0.5		L/D = 1.0		L/D = 1.5		L/D = 2.0	
Λ	ε	f	φ	f	φ	f	φ	f	φ
0	0.1	0.45	90	1.4	90	2.4	90	3.1	90
0	0.2	0.94	90	2.9	90	4.8	90	6.3	90
0	0.3		90	4.7	90	7.1	90	9.3	90
0	0.4	2.21	90	6.5	90	10.0	90	13.3	90
0	0.5		90	9.0	90	13.7	90	16.8	90
0	0.6	4.57	90	12.4	90	19.2	90	23.5	90
0	0.7		90	17.7	90	26.8	90	34.0	90
0	0.8	11.49	90	29.8	90	39.0	90	46.8	90
0.5	0.1	0.45	87.8	1.3	82.0	2.3	79.9	3.0	73.4
0.5	0.2	0.94	87.0	2.8	81.3	4.6	79.0	6.0	72.0
0.5	0.3			4.5	80.5	7.1	74.8	9.0	71.0
0.5	0.4	2.25	84.8	6.4	77.0	10.0	72.0	12.6	68.0
0.5	0.5			8.8	73.5	13.5	68.3	16.8	64.4
0.5	0.6	4.55	77.1	12.0	65.4	28.8	58.0	21.3	58.0
0.5	0.7			17.7	56.1	26.2	48.0	32.4	48.0
0.5	0.8	12.30	46.7	29.0	40.7	38.6	40.5	43.0	40.2
1.0	0.1	0.45	84.9	1.4	74.0	2.2	70.8	2.7	59.0
1.0	0.2	0.94	84.0	2.3	72.5	4.3	66.0	5.4	57.8
1.0	0.3			4.5	69.0	6.5	62.0	8.1	56.0
1.0	0.4	2.20	79.6	6.0	66.0	9.3	58.5	11.3	52.5
1.0	0.5			8.5	61.1	12.6	52.8	15.2	49.2
1.0	0.6	4.50	66.3	11.6	52.0	17.2	46.0	21.0	44.0
1.0	0.7			17.2	40.5	24.8	36.8	29.4	35.5
1.0	0.8	12.5	35.8	28.0	30.3	37.1	29.3	40.0	29.5
3.0	0.1	0.44	74.4	1.0	49.5	1.4	40.0	1.6	33.0
3.0	0.2	0.90	72.5	2.2	48.0	2.7	38.0	3.0	31.5
3.0	0.3			3.6	46.0	4.6	37.0	4.9	30.5
3.0	0.4	2.05	63.6	4.8	41.5	6.7	35.0	7.0	28.6
3.0	0.5			6.8	38.4	9.1	31.8	10.5	26.0
3.0	0.6	4.10	45.5	9.9	30.3	13.0	25.2	13.5	23.0
3.0	0.7			15.0	22.0	19.0	20.0	21.7	19.0
3.0	0.8	10.48	22.4	22.8	16.7	27.0	15.6	29.0	15.7
5.0	0.1	0.40	67.0	0.87	37.0	1.03	30.0	1.1	22.0
5.0	0.2	0.87	64.2	1.50	34.5	2.0	25.0	2.1	20.8
5.0	0.3			2.7	31.8	3.2	23.5	3.4	19.3
5.0	0.4	2.0	53.1	3.9	30.0	5.0	23.0	5.1	19.0
5.0	0.5			5.5	28.4	7.1	21.4	7.9	18.0
5.0	0.6	3.7	36.1	8.0	22.0	10.6	18.0	12.0	15.8
5.0	0.7			12.5	16.0	15.0	14.5	16.9	13.0
5.0	0.8	9.0	19.0	17.7	12.5	21.9	11.0	22.6	10.9

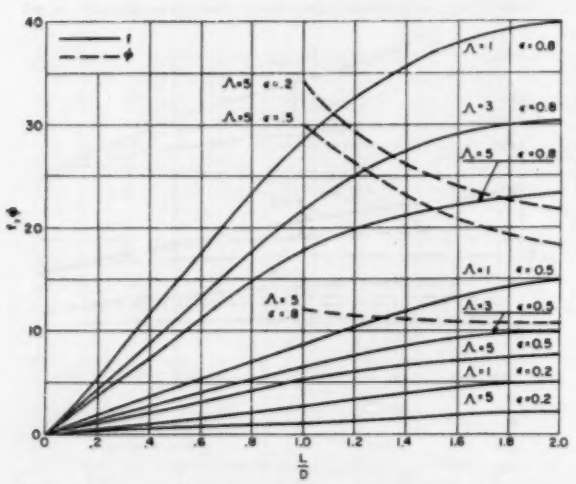

Fig. 12 Dimensionless force and attitude angle versus L/D ratio

centricity ratio and compressibility numbers. From the shape of the curve it appears that the dimensionless force is approximately constant at $L/D > 2$ ($f \approx K$ at $L/D > 2$). This would explain why the experimental results reported in [5], Fig. 11, for several L/D ratios greater than 2 fit on one curve which is plotted on dimensionless force, p/p_a versus Λ-co-ordinate system. This same figure also shows that for $L/D < 2$ the load-carrying capacity increases at a faster rate than the linear power of length. This explains why the $L/D = 1$ results presented in [5], Fig. 11, did not fall on the same dimensionless curve as did the $L/D > 2$ result. Table 2 illustrates that the load-carrying capacity for $L/D < 2$ increases at faster than the first power of length.

Table 2 Effect of L/D ratio on static load-carrying capacity

Λ	ε	$\frac{W\|_{L/D=2}}{W\|_{L/D=1}}$
0.5	0.2	4.3
0.5	0.5	3.9
0.5	0.8	3.0
5	0.2	2.9
5	0.5	2.8
5	0.8	2.5

The next few figures and Table 3 show comparison between various methods of calculation.

The comparison of pressure distribution for case 5 is shown in Table 4. Note that the attitude angle is still considerably different in the iterative and linearized ph-solutions, and that the divergence increases with increase in eccentricity ratio.

Fig. 13 compares the dimensionless force and attitude angle versus eccentricity ratio for the three methods of analysis, for

Table 3 Comparison of results employing various methods of analysis: $L/D = 1$

			W			ϕ		
Case	Λ	ϵ	1st order perturbation	$\frac{W}{p_a LD}$ Linearized $p\bar{h}$	Iteration	1st order pert.	$p\bar{h}$	Iteration
1	0.5	0.3	0.0552	0.057	0.060	82	81.6	80.5
2	0.5	0.5	0.0920	0.099	0.117	82	80.8	73.5
3	0.5	0.7	0.1288	0.151	0.234	82	78.8	56.1
4	0.5	0.8	0.1472	0.187	0.392	82	76.8	41.4
5	1.0	0.5	0.1770	0.191	0.224	74	71.7	61.1

Table 4 Comparison of pressure distribution for Case 5

$L/D = 1$ (z ⟶) $\Lambda = 1$ $\epsilon = 0.5$ $p_a = 14.7$ $\pm L/2$

θ	0	1/6	1/3	1/2	2/3	5/6	1	
0°	13.987	14.010	14.078	14.188	14.335	14.509	14.700	1st order pert.
	14.225	14.240	14.285	14.359	14.456	14.573	14.700	linearized $p\bar{h}$
	14.709	14.708	14.706	14.704	14.703	14.702	14.700	iteration
30°	15.272	15.263	15.231	15.173	15.076	14.925	14.700	
	14.099	14.093	15.071	15.030	14.962	14.857	14.700	
	14.753	14.750	14.747	14.740	14.730	14.720	14.700	
60°	16.404	16.365	16.243	16.031	15.717	15.281	14.700	
	16.063	16.032	15.934	15.765	15.513	15.165	14.700	
	15.900	15.880	15.770	15.610	15.375	15.100	14.700	
90°	17.080	17.020	16.840	16.532	16.085	15.481	14.700	
	17.080	17.020	16.840	16.532	16.085	15.481	14.700	
	16.910	16.800	16.620	16.490	15.960	15.450	14.700	
120°	17.118	17.055	16.865	16.543	16.082	15.472	14.700	
	17.923	17.840	17.586	17.157	16.542	15.729	14.700	
	18.630	18.465	18.250	17.830	17.135	16.195	14.700	
150°	16.508	16.458	16.309	16.059	15.709	15.256	14.700	
	17.888	17.800	17.537	17.098	16.479	15.680	14.700	
	19.800	19.600	19.300	18.740	17.870	16.650	14.700	
180°	15.413	15.390	15.322	15.212	15.065	14.891	14.700	
	16.126	16.080	15.944	15.724	15.430	15.081	14.700	
	19.100	18.830	18.500	17.930	17.375	16.220	14.700	
210°	14.128	14.137	14.169	14.227	14.324	14.475	14.700	
	13.691	13.708	13.763	13.866	14.037	13.302	14.700	
	13.650	13.750	13.900	13.975	14.070	14.150	14.700	
240°	12.996	13.035	13.157	13.369	13.683	14.119	14.700	
	12.428	12.481	12.643	12.926	13.345	13.925	14.700	
	12.180	12.285	12.390	12.600	13.000	13.700	14.700	
270°	12.320	12.380	12.560	12.868	13.315	13.919	14.700	
	12.320	12.380	12.560	12.868	13.315	13.919	14.700	
	12.125	12.270	12.475	12.800	13.200	13.900	14.700	
300°	12.282	12.345	12.535	12.857	13.318	13.928	14.700	
	12.766	12.816	12.968	13.226	13.595	14.083	14.700	
	13.250	13.300	13.425	13.605	13.865	14.235	14.700	
330°	12.892	12.942	13.091	13.341	13.691	14.144	14.700	
	13.439	13.473	13.577	13.751	13.996	14.312	14.700	
	14.000	14.020	14.100	14.190	14.300	14.465	14.700	
360°	13.987	14.010	14.078	14.188	14.335	14.509	14.700	
	14.225	14.240	14.285	14.359	14.456	14.573	14.700	
	14.709	14.708	14.706	14.704	14.703	14.702	14.700	

$L/D = 1$ and $\Lambda = 1$. Note that for low eccentricity ratios the three methods give results which agree quite closely.

In order to show how the compressibility number influences the various methods of analysis, a comparison was made for $L/D = 1$ and eccentricity ratio $\epsilon = 0.8$ in Fig. 14. This figure shows comparison of dimensionless force and attitude angle versus compressibility number for the various methods of analysis. The infinite-length bearing, analyzed by Elrod-Burgdorfer [4] with end-flow factor correction by perturbation method, is also included for comparison. Note that this method of analysis compares most closely with the iterative-computer solution and that the comparisons improve with increase in Λ. This is because other analytical solutions give for an asymptotic solution

$$\lim_{\omega \to \infty} p\bar{h} = p_a C$$

while Elrod and Burgdorfer [4] have shown that correct asymptotic solution is

$$\text{Lim } ph = p_a C (1 + \tfrac{3}{2}\epsilon^2)^{1/2}$$
$$\omega \to \infty$$

Thus as $\omega \to \infty$ or $\Lambda \to \infty$ this method of analysis approaches the correct finite-difference solution.

Fig. 15 shows comparison between theory and experiment. Note that the experimental results agree most closely with the iterative solution; this justifies the expense of employing numerical methods for analysis of the Reynolds equation. It is worth while to point out that the authors in [5] used analytical solutions for infinitely long journal bearings in their comparison with experiments where finite-length journal bearings were used. For this reason their experimental results of load-carrying capacity fall below theoretical results. The reverse condition exists when analytical solutions for finite-length bearings are compared with experiment. The finite-length perturbation solutions give load-carrying capacity which is below the experimental values. This is especially true at $\epsilon > 0.3$.

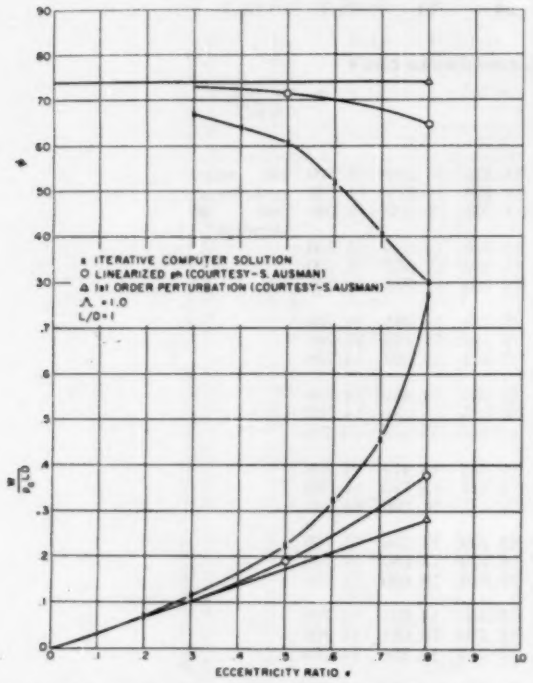

Fig. 13 Comparative results of dimensionless force versus eccentricity ratio for $L/D = 1$, $\Lambda = 1$

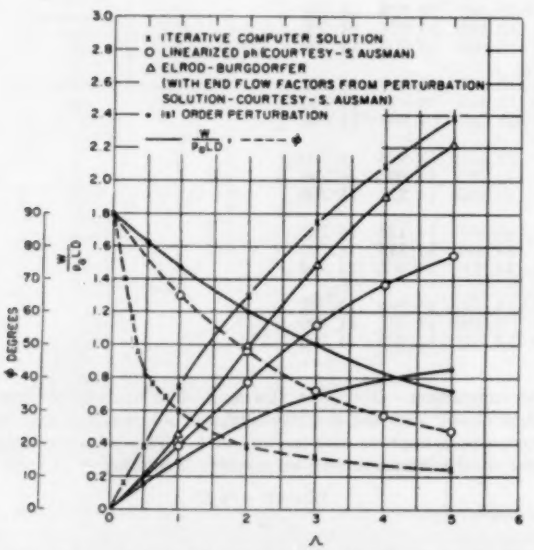

Fig. 14 Comparative results of dimensionless force and attitude angle versus compressibility number for $L/D = 1$, $\epsilon = 0.8$

Conclusions

1 It is shown that the incompressible solutions are but limiting cases to the more general compressible solutions. By proper choice of dimensionless parameters they are herein dovetailed together.

2 The solution employing iterative procedure of the finite-difference Reynolds equation offers an accurate method for the analysis of finite-length journal bearings.

3 Once the program is developed, it is applicable over the complete range of bearing parameters and can be used for other than plain cylindrical journal bearings; e.g., partial bearings, axial groove, and so on.

4 The results obtained by iterative procedure correlate best with experiment.

5 At this time the Elrod-Burgdorfer method of analysis for infinitely long journal bearings [4] with end-flow correction factors obtained first-order perturbation correlates best with the iterative procedure.

6 At low eccentricity ratios, $\epsilon > 0.3$, the load-carrying capacity obtained by first-order perturbation agrees very well with iterative procedure. The attitude angle does not correlate very closely.

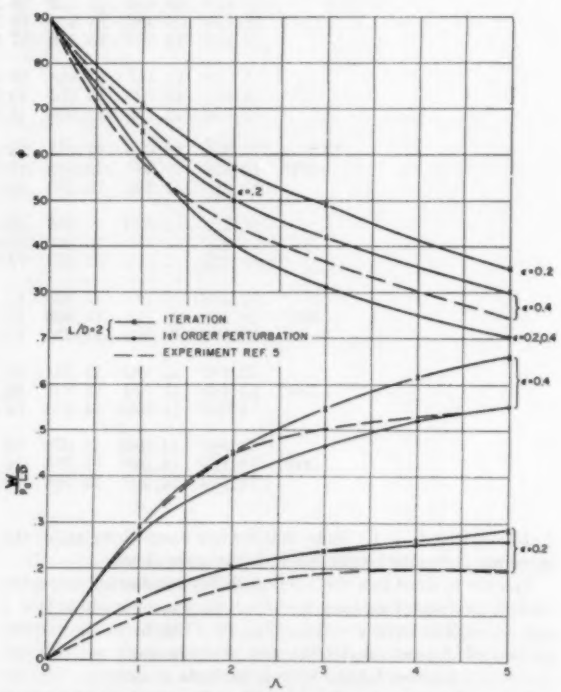

Fig. 15 Comparison between theory and experiment of dimensionless force and attitude angle versus compressibility number

7 The linearized ph-method of analysis presents an improvement over the first-order perturbation and it has closer correlation with the iterative method. Up to $\epsilon > 0.5$ the load-carrying capacity obtained by this method agrees very well with the iterative procedure. The attitude angle does not correlate closely, but it is closer than the first-order perturbation.

Recommendations

1 Conduct a similar analyses for other bearing geometries; e.g., grooved bearings, partial bearings, pivoted shoe, and so on. This analysis will be especially important for stability investigations since plain cylindrical journal bearings tend to have low stability threshold.

2 Conduct a similar analysis for journal bearings which have high-pressure sources.

3 Conduct accurate experiments in order to get better comparison between theory and practice.

Acknowledgment

This study was supported under the ONR Contract Number NONR-2844(00). The author is especially indebted to Dr. J. S. Ausman of Autonetics, Downey, Calif., for his co-operation in supplying a number of cases for comparison. In addition, I would like to thank Mrs. A. Pagliara for assisting in these calculations.

References

1 B. Sternlicht and R. C. Elwell, "Theoretical and Experimental Analysis of Hydrodynamic Gas-Lubricated Journal Bearings," TRANS. ASME, vol. 80, 1958, pp. 865–878.

2 J. S. Ausman, "Finite Gas Lubricated Journal Bearing," The Institution of Mechanical Engineers, *Proceedings of the Conference on Lubrication and Wear*, 1957, pp. 39–45.

3 J. S. Ausman, "An Improved Analytical Solution for Self-Acting Gas-Lubricated Journal Bearings of Finite Length," *Journal of Basic Engineering*—TRANS. ASME, vol. 83, Series D, June, 1961, p. 188.

4 H. G. Elrod and A. Burgdorfer, "Refinement of the Theory of Gas Lubricated Journal Bearings of Infinite Length," *Proceedings of the First International Symposium on Gas Lubricated Bearings*, Washington, D. C., October, 1959.

5 S. Whitley and C. Betts, "A Study of Gas-Lubricated Hydrodynamic Full Journal Bearings," *British Journal of Applied Physics*, vol. 10, 1959, pp. 455–463.

6 A. A. Raimondi, "A Numerical Solution for the Gas Lubricated Full Journal Bearing of Finite Length," ASLE Paper No. 60—LC-14.

Theory of Stress Concentration for Shear-Strained Prismatical Bodies With Arbitrary Nonlinear Stress-Strain Law

H. NEUBER

Professor of Engineering Mechanics, and Director of the Laboratory for Strength of Materials, Technical University, Munich, Germany

Knowledge of stress concentration is very important for engineers in many practical cases. But the stress-concentration factors for Hooke's law often cannot be used because most technical materials have stress-strain laws deviating from Hooke's law. In the second edition of his book "Kerbspannungslehre" the author gave a calculation method for a special nonlinear deformation law. In the present paper a general theory for arbitrary stress-strain laws is established which leads to a calculation method for the real values of the concentrated stresses in the material.

In the second edition of his book "Kerbspannungslehre" (Springer, Berlin, 1958), in the following referred to as KSL-2, the author investigated the behavior of stress and strain concentrations in the case of deviations from Hooke's law for the range of greater deformations. In that work the problem of shear distribution in prismatical bodies served as a suitable mechanical model to encounter the mathematical difficulties. Extensive calculations based on a special nonlinear deformation law resulted in a relation between the "ideal" maximum stress τ_H for Hooke's law and the real maximum stress τ as well as the nominal stress τ_N for all notch shapes.

In the meantime, a further exploration of the mathematical circumstances seemed to be desirable in order to attain a general calculation method applicable to arbitrary nonlinear deformation laws. Some hints were found in the fact that in the limit case of strong stress concentration at small nominal stresses, i.e., very great Hookian stress-concentration factors (SCF), there exists an identical relationship for flat as well as deep notches.

In this paper the Hookian stress of the sharply curved notch is denoted as "leading-function" $N(\tau)$. A hypothesis is established by which the connection between real stress and nominal stress as well as Hookian (elastic) SCF can be represented by a simple relation using the leading function. The relationship found in this way is applicable without contradiction to arbitrary nonlinear deformation laws.

Herewith the problem is reduced to the determination of the leading function corresponding to a given (e.g., measured) deformation law. By means of geometrical conditions for orthogonal nets, general relations for $N(\tau)$ are established in this paper. For any deformation law $F(\tau)$ the leading function is reducible to the integration of a linear second-order differential equation the coefficients of which are connected with $F(\tau)$.

For the special nonlinear deformation law as used in KSL-2 the leading function is derived with exact consideration of the notch-angle influence. In the case of arbitrary deformation law the leading function of 0-deg notch is proved to be the geometrical mean value of stress and deformation. As the notch-angle influence indeed is insignificant, this relation can be used approximately for any deformation law and any notch angle.

Further, it is shown that *the geometrical mean value of the stress and strain-concentration factors at any stress-strain law is equal to the Hookian stress-concentration factor.*

This theory, which for the present is derived for two-dimensional shear only, could be generalized with good approximation to arbitrary two or three-dimensional states of stress by means of one of the well-known theories of failure.

The Basic Equations

The complicated behavior of stress and strain concentration under any nonlinear deformation law can be studied by means of the shear flow in prismatic bodies. Fig. 1 shows a symmetrically notched prismatic body which serves as a mechanical model.

The following notation is used:

τ = shear stress
$\gamma(\tau)$ = shear deformation
G = shear modulus in Hookian range
$F = G\gamma$ = deformation function

The general deformation law is

$$F = F(\tau) \tag{1}$$

with the restricting condition

$$\lim_{\tau \to 0} F(\tau) = \tau \tag{1a}$$

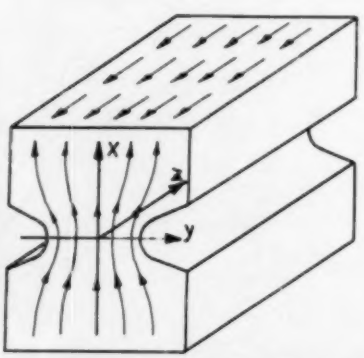

Fig. 1 Example for model of prismatic notch effect

Presented at the Tenth International Congress of Applied Mechanics, Stresa, Italy, August 31–September 7, 1960.

Discussion of this paper should be addressed to the Editorial Department, ASME, United Engineering Center, 345 East 47th Street, New York 17, N. Y., and will be accepted until January 10, 1962. Discussion received after the closing date will be returned. Manuscript received by ASME Applied Mechanics Division, September 26, 1960; revised draft, Feb. 22, 1961.

i.e., the material satisfies Hooke's law in the case of small loading.

The first step in the region of nonlinear deformation laws was realized in KSL-2 with regard to the special deformation law

$$F(\tau) = \frac{\tau}{[1 - (\tau/\tau^*)^2]^{1/2}} \tag{1b}$$

where τ^* represents a mathematical limit-stress value which can be chosen for good correspondence with experimental results in the interesting range, Fig. 2.

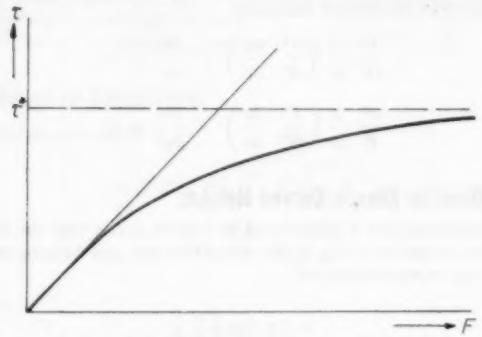

Fig. 2 Special deformation law as used in KSL-2

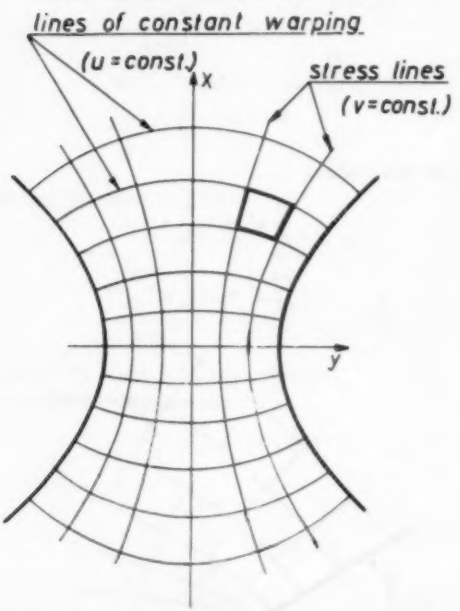

Fig. 3 Example of curvilinear co-ordinate system of stress lines and lines of constant warping

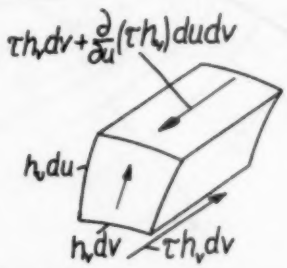

Fig. 4 Forces on curvilinear element

The solution for the stress function can be represented in this case by a superposition of two conformal mappings. The results are applicable for materials with similar characteristic stress-strain curves (for instance, some steels) but not for all metals.

As isotropy is presumed, the main directions of shear stress and shear deformation coincide along the stress lines. The latter may be denoted by v = const (v stress function). Let u be the only displacement, which goes in the direction of the axis of the prism (warping of the cross section) so that the gradient of u yields the shear deformation and the curves u = const are orthogonal to the stress lines. $ds_u = h_u du$ and $ds_v = h_v dv$ are the line elements, Fig. 3.

From Fig. 4 there follows the condition of equilibrium

$$\tau h_v = C \tag{2}$$

The shear deformation is equal to the gradient of the warping function

$$\gamma = \frac{d\delta}{ds_u} = \frac{1}{h_u} \tag{3}$$

Corresponding to equation (1)

$$F = G\gamma = \frac{G}{h_u} \tag{4}$$

For simplification the warping function is normalized by

$$G = C \tag{5}$$

and with equation (1) it follows that

$$F = \frac{C}{h_u} \qquad \tau = \frac{C}{h_v} \tag{6}$$

Geometrical Conditions

Considering the components of the line elements, Fig. 5, one obtains

$$\cos\varphi = \frac{1}{h_u}\frac{\partial x}{\partial u} = \frac{1}{h_v}\frac{\partial y}{\partial v}$$
$$\sin\varphi = \frac{1}{h_u}\frac{\partial y}{\partial u} = -\frac{1}{h_v}\frac{\partial x}{\partial v} \tag{7}$$

Hence

$$\frac{\partial x}{\partial u} = h_u \cos\varphi \tag{8}$$

$$\frac{\partial y}{\partial u} = h_u \sin\varphi \tag{9}$$

$$\frac{\partial x}{\partial v} = -h_v \sin\varphi \tag{10}$$

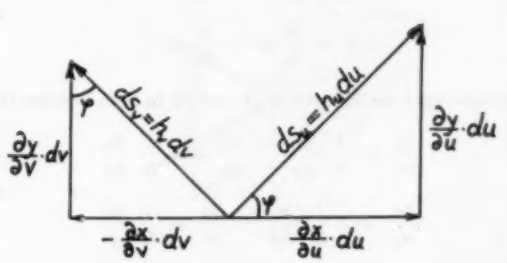

Fig. 5 Geometrical connection between components of line elements

$$\frac{\partial y}{\partial v} = h_v \cos\varphi \tag{11}$$

Differentiation of (8) and (9) with respect to v and (10) and (11) with respect to u, and subtraction, yields

$$\begin{aligned}\cos\varphi\left(\frac{\partial h_u}{\partial v} + h_v\frac{\partial\varphi}{\partial u}\right) + \sin\varphi\left(\frac{\partial h_v}{\partial u} - h_u\frac{\partial\varphi}{\partial v}\right) = 0\\ \sin\varphi\left(\frac{\partial h_u}{\partial v} + h_v\frac{\partial\varphi}{\partial u}\right) - \cos\varphi\left(\frac{\partial h_v}{\partial u} - h_u\frac{\partial\varphi}{\partial v}\right) = 0\end{aligned} \tag{12}$$

Therefrom follow the Lamé equations

$$\frac{1}{h_u}\frac{\partial h_v}{\partial u} = \frac{\partial\varphi}{\partial v} \qquad \frac{1}{h_v}\frac{\partial h_u}{\partial v} = -\frac{\partial\varphi}{\partial u} \tag{13}$$

From (6) and (2)

$$h_u = \frac{C}{F(\tau)} \qquad h_v = \frac{C}{\tau} \tag{14}$$

and with (13) one obtains

$$\frac{F}{\tau^2}\frac{\partial\tau}{\partial u} = -\frac{\partial\varphi}{\partial v} \qquad \frac{\tau F'}{F^2}\frac{\partial\tau}{\partial v} = \frac{\partial\varphi}{\partial u} \tag{15}$$

Only for materials with the special deformation law (1*b*) will these two coupled differential equations become linear. In this case it is practical to introduce a parameter h by the relation:

$$\tau = C\frac{h}{h^2 + k} \quad \text{with} \quad k = \left(\frac{C}{2\tau^*}\right)^2 \tag{15a}$$

Then follows from (1*b*)

$$F = C\frac{h}{h^2 - k} \tag{15b}$$

and one gets the Cauchy-Riemann equations for $\ln h$ and φ

$$\frac{\partial}{\partial u}(\ln h) = \frac{\partial\varphi}{\partial v} \qquad \frac{\partial}{\partial v}(\ln h) = -\frac{\partial\varphi}{\partial u} \tag{15c}$$

This solution can be represented by means of two conformal mappings as treated in KSL-2.

In the general case equations (15) can be linearized by the Tschapligin-Molenbroek transformation (known in gas dynamics). Considering the total differentials

$$\left.\begin{aligned}d\tau &= \frac{\partial\tau}{\partial u}du + \frac{\partial\tau}{\partial v}dv\\ d\varphi &= \frac{\partial\varphi}{\partial u}du + \frac{\partial\varphi}{\partial v}dv\end{aligned}\right\} \tag{16}$$

$$\left.\begin{aligned}du &= \frac{\partial u}{\partial\tau}d\tau + \frac{\partial u}{\partial\varphi}d\varphi\\ dv &= \frac{\partial v}{\partial\tau}d\tau + \frac{\partial v}{d\varphi}d\varphi\end{aligned}\right\} \tag{17}$$

it follows from the identity of $d\tau$ and $d\varphi$ in both systems that

$$\begin{aligned}\frac{\partial\tau}{\partial u} &= \frac{1}{D}\frac{\partial v}{\partial\varphi} \qquad \frac{\partial\tau}{\partial v} = -\frac{1}{D}\frac{\partial u}{\partial\varphi}\\ \frac{\partial\varphi}{\partial u} &= -\frac{1}{D}\frac{\partial v}{\partial\tau} \qquad \frac{\partial\varphi}{\partial v} = \frac{1}{D}\frac{\partial u}{\partial\tau}\end{aligned} \tag{18}$$

with

$$D = \frac{\partial u}{\partial\tau}\frac{\partial v}{\partial\varphi} - \frac{\partial v}{\partial\tau}\frac{\partial u}{\partial\varphi}$$

Substituting in (15) one obtains the two linear differential equations

$$\frac{F}{\tau^2}\frac{\partial v}{\partial\varphi} = -\frac{\partial u}{\partial\tau} \qquad \frac{\tau F'}{F^2}\frac{\partial u}{\partial\varphi} = \frac{\partial v}{\partial\tau} \tag{19}$$

For u and v alone there follow by differentiation the two linear second-order differential equations

$$\begin{aligned}\frac{F^2}{\tau F'}\frac{\partial}{\partial\tau}\left(\frac{\tau^2}{F}\frac{\partial u}{\partial\tau}\right) + \frac{\partial^2 u}{\partial\varphi^2} = 0\\ \frac{\tau^2}{F}\frac{\partial}{\partial\tau}\left(\frac{F^2}{\tau F'}\frac{\partial v}{\partial\tau}\right) + \frac{\partial^2 v}{\partial\varphi^2} = 0\end{aligned} \tag{20}$$

Solutions for Sharply Curved Notches

Considering the neighborhood of a sharp notch with the flank angle ω as shown in Fig. 6, the stress function and warping function can be represented by

$$\begin{aligned}v &= f(\tau)\cos\left(\frac{\varphi}{2n}\right)\\ u &= -g(\tau)\sin\left(\frac{\varphi}{2n}\right)\end{aligned} \tag{21}$$

with

$$2n = 1 - \frac{\omega}{\pi} \tag{22}$$

From (19) there follows

$$\begin{aligned}\frac{\tau^2}{F}g' &= -\frac{1}{2n}f\\ \frac{F^2}{\tau F'}f' &= -\frac{1}{2n}g\end{aligned} \tag{23}$$

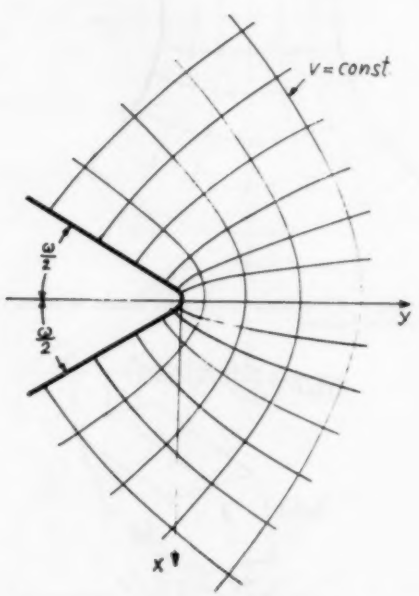

Fig. 6 Example of stress lines in neighborhood of a notch

or from (20)

$$\frac{F^2}{\tau F'}\left(\frac{\tau^2}{F}g'\right)' - \frac{1}{4n^2}g = 0$$
$$\frac{\tau^2}{F}\left(\frac{F^2}{\tau F'}f'\right)' - \frac{1}{4n^2}f = 0 \tag{24}$$

For any deformation law found experimentally, these linear differential equations can be integrated by means of known numerical or graphical methods.

However, solutions in closed form can be derived also.

Solutions in Closed Form

(a) For Hooke's Law ($F = \tau$)

$$u = -A\tau^{-\frac{1}{2n}}\sin\left(\frac{\varphi}{2n}\right)$$
$$v = A\tau^{-\frac{1}{2n}}\cos\left(\frac{\varphi}{2n}\right) \tag{25}$$

From

$$\frac{\partial x}{\partial \tau} = \frac{\partial x}{\partial u}\frac{\partial u}{\partial \tau} + \frac{\partial x}{\partial v}\frac{\partial v}{\partial \tau},$$
$$\frac{\partial x}{\partial \varphi} = \frac{\partial x}{\partial u}\frac{\partial u}{\partial \varphi} + \frac{\partial x}{\partial v}\frac{\partial v}{\partial \varphi},$$
$$\frac{\partial y}{\partial \tau} = \ldots, \quad \frac{\partial y}{\partial \varphi} = \ldots$$

we find, with regard to (8) ÷ (11):

$$x = -\frac{AC}{2n+1}\tau^{-\frac{2n+1}{2n}}\sin\left(\frac{2n+1}{2n}\varphi\right)$$
$$y = \frac{AC}{2n+1}\tau^{-\frac{2n+1}{2n}}\cos\left(\frac{2n+1}{2n}\varphi\right) \tag{26}$$

Fig. 7 shows the case $n = 1/3$ as an example.

(b) For the Special Deformation Law:

$$F = \tau/(1 - \tau^2/\tau^{*2})^{1/2}$$

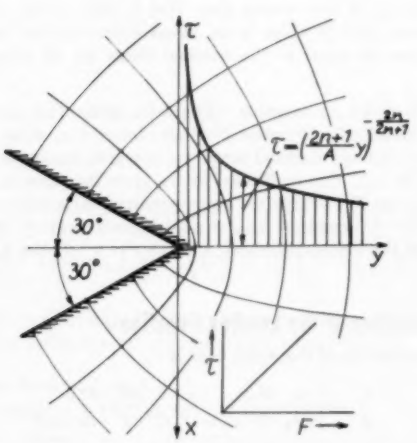

Fig. 7 Stress lines and stress distribution at a 60-deg notch for Hooke's law

$$u = -A\left[h^{\frac{1}{2n}} + \left(\frac{k}{h}\right)^{\frac{1}{2n}}\right]\sin\left(\frac{\varphi}{2n}\right)$$
$$v = A\left[h^{\frac{1}{2n}} - \left(\frac{k}{h}\right)^{\frac{1}{2n}}\right]\cos\left(\frac{\varphi}{2n}\right) \tag{27}$$

with

$$h = \frac{1}{2\tau}\left\{1 + [1 - (\tau/\tau^*)^2]^{1/2}\right\} \quad k = \left(\frac{1}{2\tau^*}\right)^2 \tag{28}$$

Further, in the same way as before, we have

$$x = -\frac{A}{2n+1}\left[h^{\frac{2n+1}{2n}} - \left(\frac{k}{h}\right)^{\frac{2n+1}{2n}}\right]\sin\left(\frac{2n+1}{2n}\varphi\right) + \frac{AK}{1-2n}\left[h^{\frac{1-2n}{2n}} - \left(\frac{k}{h}\right)^{\frac{1+2n}{2n}}\right]\sin\left(\frac{1-2n}{2n}\varphi\right)$$
$$y = \frac{A}{2n+1}\left[h^{\frac{2n+1}{2n}} - \left(\frac{k}{h}\right)^{\frac{2n+1}{2n}}\right]\cos\left(\frac{2n+1}{2n}\varphi\right) + \frac{Ak}{1-2n}\left[h^{\frac{1-2n}{2n}} - \left(\frac{k}{h}\right)^{\frac{1-2n}{2n}}\right]\cos\left(\frac{1-2n}{2n}\varphi\right) \tag{29}$$

Fig. 8 gives the case $n = 1/3$ as an example.

(c) For the General Case:

$$F = F(\tau) \text{ and } \omega = 0°$$

For $\omega = 0$, i.e., $2n = 1$, the following general integral of equations (19) exists

$$u = -\frac{A}{\tau}\sin\varphi$$
$$v = \frac{A}{F}\cos\varphi \tag{30}$$

Here it follows that

$$x = -\frac{AC}{2\tau F}\sin(2\varphi)$$
$$y = AC\left(\frac{1+\cos 2\varphi}{2\tau F} + \int_{\tau_0}^{\tau}\frac{d\eta}{F(\eta)\eta^2}\right) \tag{31}$$

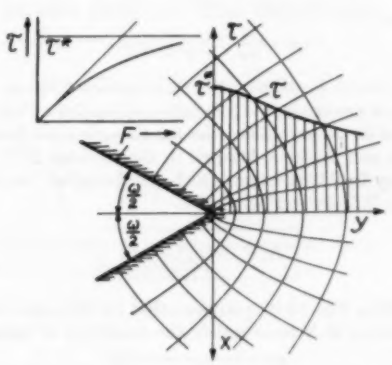

Fig. 8 Stress lines and stress distribution at a 60-deg notch for special deformation law (1b)

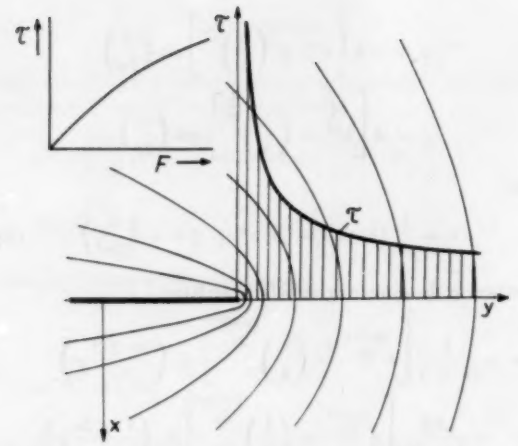

Fig. 9 Stress lines and stress distribution at a zero degree notch for deformation law $F = \tau + \lambda \cdot \tau^{\mu}$ with $\lambda = 4.4 \times 10^{-4}$ and $\mu = 10$

In Fig. 9 this case is represented for the stress-strain law

$$F = \tau + \lambda\tau^{\mu} \ (\lambda, \mu \text{ constants}).$$

Relation Between Maximum Stress for Any Deformation Law and That for Hooke's Law

As explained before, the theory for sharp notches gives the stress distribution and therefore also the maximum stress for Hooke's law and for any deformation law. Hence within the same boundary problem and at the same nominal stress τ_N the maximum stress for Hooke's law can be regarded as a function of the maximum stress for a certain deformation law.

Fig. 10 explains the functional connection between Hookian stress, real stress, and real strain. For technical materials with $F(\tau) > \tau$ the real strain is greater than the Hookian, but the real stress smaller than the Hookian. If the stress-concentration factor is introduced by the definition

$$\tau/\tau_N = \alpha_\sigma \tag{32}$$

and the strain-concentration factor by the definition

$$F(\tau)/F(\tau_N) = \alpha_\varepsilon \tag{33}$$

then it follows for $F > \tau$:

$$\boxed{\alpha_\varepsilon > \alpha_H > \alpha_\sigma} \tag{34}$$

respectively for $F < \tau$:

$$\alpha_\varepsilon < \alpha_H < \alpha_\sigma \tag{34a}$$

From this fact it is obvious that *there exists a function, which is neither stress nor strain, but a certain combination of both with the quality, that its concentration factor has the same value for all stress-strain laws* and therefore is equal to the Hookian SCF.

$N(\tau)$ may be this function, which may be called "leading function," then it is defined by

$$\boxed{N(\tau)/N(\tau_N) = \alpha_H} \tag{35}$$

Considering Fig. 10 it is obvious that for the same stress the possible values of N must satisfy the conditions of inequality:

$$\boxed{F(\tau) > N(\tau) > \tau} \tag{36}$$

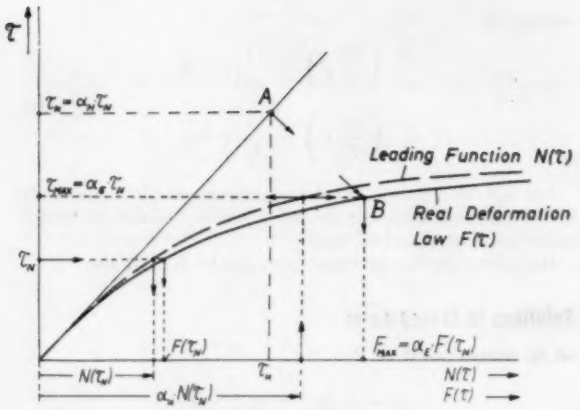

Fig. 10 Method of leading function

or for $F < \tau$

$$F < N < \tau \tag{36a}$$

According to (1*a*) for small stress values F goes to τ, therefore also

$$\lim_{\tau \to 0} \{N(\tau)\} = \tau \tag{37}$$

and in consequence

$$\lim_{\tau_N \to 0} \{N(\tau_N)\} = \tau_N \tag{38}$$

and it follows from (35)

$$\lim_{\tau_N \to 0} \{N(\tau)\} = \alpha_H \tau_N = \tau_H \tag{39}$$

This relation is very useful for the determination of $N(\tau)$. If τ_H remains finite, the value of α_H goes to infinity for very small values of the nominal stress τ_N. *Therefore $N(\tau)$ is identical with the Hookian stress for sharply curved notches.*

Equation (35) satisfies the following conditions:

1 In the region of small stresses the set (35) gives the relation for Hooke's law as must be guaranteed by (1*a*).

2 In correspondence with (39) it is exact for sharply curved notches.

3 In consistence with physical results it holds

$$F(\tau) > N(\tau) > \tau_H > \tau \quad \text{or} \quad F < N < \tau_H < \tau$$

4 For $\alpha_H = 1$ it follows that $N(\tau) = N(\tau_N)$; i.e., $\tau = \tau_N$. This means that if there is no stress concentration the stress value must be equal to the nominal stress for all deformation laws.

Fig. 10 shows an example. The deformation function $G\gamma = F(\tau)$ and the leading function $N(\tau)$ are plotted versus the stress τ. Starting from the nominal stress τ_N one gets the corresponding value of $N(\tau_N)$; this multiplied by α_H gives the value $\alpha_H \cdot N(\tau_N)$ and with the $N(\tau)$-curve the corresponding real maximum stress τ_{max}. The deformation γ_{max} related herewith can be found by means of the stress-deformation curve $F(\tau)$; cf. the arrows in Fig. 10.

Determination of the Leading Function

The curvature of the notch base is

$$\frac{1}{\rho} = \left| \frac{1}{h_u h_v} \frac{\partial h_u}{\partial v} \right|_{\substack{u=0 \\ v=v_0}} = \frac{1}{C} \left| \frac{\tau F'}{F} \frac{d\tau}{dv} \right|_{\substack{u=0 \\ v=v_0}} \tag{40}$$

This term must have the same value for Hooke's law; i.e., with

$$F = \tau = N(\tau) \quad \text{and} \quad v = \left(\frac{1}{\tau}\right)^{\frac{1}{2n}} = \left[\frac{1}{N(\tau)}\right]^{\frac{1}{2n}}$$

and for the general case with

$$v = f(\tau)$$

where f is a solution of (24) with the conditions

$$\lim_{\tau \to 0} f(\tau) = \lim_{\tau \to 0} g(\tau) = \left(\frac{1}{\tau}\right)^{\frac{1}{2n}} \text{ and (for simplification) } A = C = 1.$$

It follows that

$$\boxed{N(\tau) = \left|\frac{\tau F'}{2nFf'}\right|^{\frac{2n}{2n+1}}} \tag{41}$$

or with regard to (23)

$$\boxed{N(\tau) = \left|\frac{F}{g}\right|^{\frac{2n}{2n+1}}} \tag{41a}$$

Solutions for Leading Function $N(\tau)$ in Closed Form

(a) Hooke's Law:

$$F(\tau) = \tau \qquad f = \left(\frac{1}{\tau}\right)^{\frac{1}{2n}} = g$$

It follows from (41) or (41a) that

$$N(\tau) = \tau \tag{42}$$

as must be.

(b) Special Deformation Law:

$$F(\tau) = \tau/(1 - \tau^2/\tau^{*2})^{1/2}$$

We have

$$f = h^{\frac{1}{2n}}\left(\frac{k}{h}\right)^{\frac{1}{2n}}, \quad g = h^{\frac{1}{2n}} + \left(\frac{k}{h}\right)^{\frac{1}{2n}}$$

with

$$h = \frac{1}{2\tau}\left[1 + [1 - (\tau/\tau^*)^2]^{1/2}\right] \quad \text{and} \quad k = \left(\frac{1}{2\tau^*}\right)^2$$

The leading function is

$$N(\tau) = \frac{\tau}{\left[\left[1 - \left(\frac{\tau}{\tau^*}\right)^2\right]^{1/2}\left\{\left(\left(\frac{1}{2} + \frac{1}{2}\left[1 - \left(\frac{\tau}{\tau^*}\right)^2\right]^{1/2}\right)\right)^{\frac{\pi}{\pi-\omega}} + \left(\left(\frac{1}{2} - \frac{1}{2}\left[1 - \left(\frac{\tau}{\tau^*}\right)^2\right]^{1/2}\right)\right)^{\frac{\pi}{\pi-\omega}}\right\}\right]^{\frac{\pi-\omega}{2\pi-\omega}}} \tag{43}$$

As can be seen in Fig. 11 the notch-angle influence is so small that the curve for $\omega = 0°$ can be used for all values of ω.

(c) General Case:

It follows for $\omega = 0°$ (i.e., $2n = 1$) that

$$f = \frac{1}{F}, \quad g = \frac{1}{\tau}$$

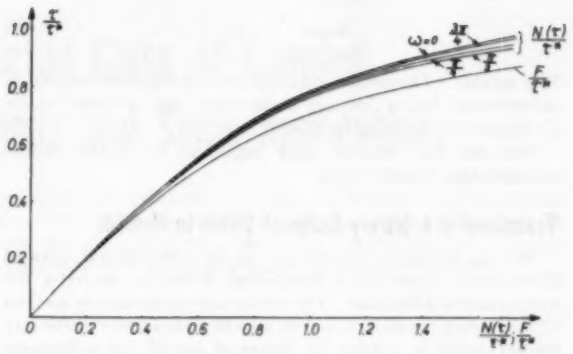

Fig. 11 Leading function for law $F(\tau) = \tau/(1 - \tau^2/\tau^{*2})^{1/}$ for various notch angles

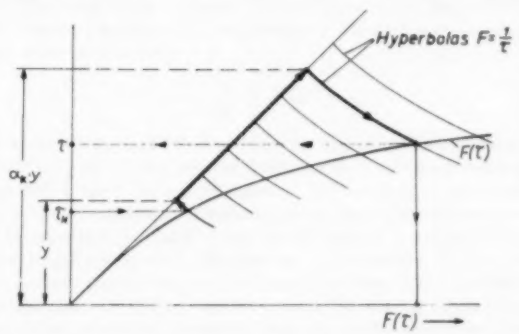

Fig. 12 Diagram for determination of real stress from nominal stress and Hookian SCF by means of hyperbolas [cf. equation (44)]

and therefore

$$\boxed{N(\tau) = [\tau \cdot F(\tau)]^{1/2}} \tag{44}$$

Hence the leading function is the geometrical mean value of stress and deformation, and there exists a simple method to determine the real maximum stress in zero-degree notches for any deformation law, Fig. 12. *Since the notch-angle influence can be neglected, this rule holds also for any notch angle* (the notch angle is considered already at the determination of α_H).

Relation Between Stress and Strain Concentration

From equations (33) and (44) it follows that

$$[\tau_{max} F(\tau_{max})]^{1/2} = \alpha_H [\tau_N F(\tau_N)]^{1/2} \tag{45}$$

Introducing stress and strain-concentration factors for any stress-strain law by the definitions

$$\alpha_\sigma = \tau_{max}/\tau_N \tag{46}$$

$$\alpha_\epsilon = F(\tau_{max})/F(\tau_N) \tag{47}$$

one obtains from (45) the simple rule

$$\boxed{(\alpha_\sigma \alpha_\epsilon)^{1/2} = \alpha_H} \tag{48}$$

This means: *"The geometrical mean value of the stress and strain-concentration factors (at any stress-strain law) is equal to the Hookian stress-concentration factor."*

This rule may become really important for further stress-concentration research work.

Transition to Arbitrary States of Stress in Notches

For the foregoing formulation the two-dimensional state of shear stress served as a mechanical model to encounter the mathematical difficulties. The results and especially the method of the leading function, however, may be generalized for arbitrary loading states in notches by means of one of the well-known theories of failure. We use the distortion-energy theory. Herewith the working or comparison stress σ_w, which leads to the same energy to distort the element as the three components σ_x, σ_y, and τ_{xy} of the plane state of stress generally possible in the notch base, is calculated by

$$\sigma_w = (\sigma_x^2 - \sigma_x\sigma_y + \sigma_y^2 + 3\tau_{xy}^2)^{1/2} \tag{49}$$

This relation is used for the evaluation of a comparison nominal stress σ_N from the separate nominal stresses as well as for the evaluation of the comparison stress σ_H from the separate notch stresses valid for Hooke's law. Hence one obtains for the Hookian SCF the value

$$\alpha_H = \sigma_H/\sigma_N \tag{50}$$

For the determination of the real stress equations (32), (33), (35), and (44) can be used if τ is replaced by $\sigma/\sqrt{3}$ and F by $\frac{E\epsilon}{\sqrt{3}} = F^*/\sqrt{3}$, respectively, τ_N by $\sigma_N/\sqrt{3}$, $F(\tau_N)$ by $\frac{E\epsilon(\sigma_N)}{\sqrt{3}} = \frac{F^*(\sigma_N)}{\sqrt{3}}$.

Further investigations of this question are intended.

C. S. HSU
Associate Professor
of Engineering Mechanics,
Department of Mechanical Engineering,
University of California,
Berkeley, Calif.

On a Restricted Class of Coupled Hill's Equations and Some Applications[1]

A class of systems of coupled Hill's equations is studied. It is shown that for systems of equations in this class, completely decoupled Hill's equations may be obtained and the stability of the solutions may be studied in a very much simpler manner. Several physically significant problems are treated to demonstrate the nature of the method.

In the course of a study on ship motions [1],[2] it was found that systems of coupled Mathieu's equations may arise through nonlinear coupling between various types of motion. Such systems of ordinary differential equations with periodic coefficients are also of considerable interest in other fields of engineering. It is, therefore, thought desirable to make a general investigation on the properties of the solutions of such systems. In what follows we present some of the results obtained in a study concerning the question of stability or boundedness of these solutions.

This paper is concerned mainly with differential equations of the type

$$\frac{d^2\mathbf{x}}{dt^2} + \mathbf{B}(t)\mathbf{x} = \mathbf{o} \tag{1}$$

where $\mathbf{x}$ is a column matrix of the dependent variables $x_1, x_2, \ldots, x_n$, $\mathbf{B}(t)$ is a real $n \times n$ square matrix whose elements $b_{ij}(t)$ are periodic in t with period L. The system of equations (1) may be looked upon as a set of n coupled Hill's equations which when the periodic elements are simple harmonic in t may be further referred to as a set of n coupled Mathieu's equations. These equations emerge quite naturally as the variational equations in the study of the stability of periodic solutions of some nonlinear systems [2]. On the other hand, for certain dynamic systems, equations of the type (1) are in fact the governing differential equations. Although the method of solution described here is applicable to both categories, specific examples used in this paper to demonstrate applications of the method of solution are selected from the latter.

In most cases of stability investigations, the primary interest is in determining whether the trivial solution $\mathbf{x} = \mathbf{o}$ is stable or unstable. This question is in turn resolved by knowing whether the nontrivial solutions of (1) remain bounded or unbounded as t increases. The final result is usually indicated by means of stable and unstable regions in a space of the system parameters.

The literature on the stability of solutions of linear ordinary differential equations with periodic coefficients is abundant; for an account of the subject, reference may be made to Cesari [3], where other references are cited. Most of the work on the stability deals with a system of equations, more general than (1); namely, a system of linear ordinary differential equations of first order as follows:

$$\frac{d\mathbf{y}}{dt} = \mathbf{A}(t)\mathbf{y} \tag{2}$$

to which the system (1) may easily be reduced. In comparison with (1), $\mathbf{y}$ in (2) is a column matrix of $2n$ dependent variables and $\mathbf{A}(t)$ a $2n \times 2n$ square matrix. When (2) is in its general form, the available stability analyses are very involved and, as is to be expected, the stability criteria can usually be obtained only after lengthy numerical calculations. It is for this reason that the present paper deals with a restricted class of (1) for which the question of stability may be answered in a fairly simple manner. First, a general discussion is given for this restricted class, and then, several examples of application are offered; all of them are problems of considerable physical interest and, in so far as the author is aware, have not been treated before.

A Restricted Class of Equations (1)

It is well known in the theory of matrices [4] that if $\mathbf{C}$ is a square matrix with constant elements and if, and only if, for each of the characteristic values of $\mathbf{C}$ the multiplicity and the nullity are equal, then a similarity (or collineatory) transformation exists such that

$$\mathbf{\Lambda} = \mathbf{M}^{-1}\mathbf{C}\mathbf{M} \tag{3}$$

where $\mathbf{\Lambda}$ is a diagonal matrix and $\mathbf{M}$ is a nonsingular matrix usually referred to as a fundamental (or modal) matrix for $\mathbf{C}$. In the following, we shall call $\mathbf{C}$ diagonable if (3) holds.

Now we are in a position to define precisely the restricted class of (1) to be treated in this paper. The system (1) is said to be in our restricted class if for a given $\mathbf{B}(t)$ a nonsingular matrix $\mathbf{T}$ with constant elements exists such that

$$\mathbf{T}^{-1}\mathbf{B}(t)\mathbf{T} = \Lambda(t) \tag{4}$$

where $\Lambda(t)$ is a diagonal matrix. Since the elements of $\mathbf{B}(t)$ are periodic in t with period L, the elements of $\Lambda(t)$ are necessarily so with the same period. The motivation in studying this restricted class is now apparent. With (4) being satisfied, we can introduce a column matrix $\mathbf{z}$ such that

$$\mathbf{z} = \mathbf{T}^{-1}\mathbf{x} \tag{5}$$

and (1) may then be reduced to

$$\frac{d^2\mathbf{z}}{dt^2} + \mathbf{\Lambda}(t)\mathbf{z} = \mathbf{o} \tag{6}$$

Since $\mathbf{\Lambda}(t)$ is a diagonal matrix, (6) consists of n completely de-

[1] The work reported in this paper was carried out at the University of California, Berkeley, Calif., under the Office of Naval Research Contract Nonr-222(75), administered by the David W. Taylor Model Basin.

[2] Numbers in brackets designate References at end of paper.

Contributed by the Applied Mechanics Division and presented at the Winter Annual Meeting, New York, N. Y., November 25–December 1, 1961, of THE AMERICAN SOCIETY OF MECHANICAL ENGINEERS.

Discussion of this paper should be addressed to the Editorial Department, ASME, United Engineering Center, 345 East 47th Street, New York 17, N. Y., and will be accepted until January 10, 1962. Discussion received after the closing date will be returned. Manuscript received by ASME Applied Mechanics Division, November 16, 1960. Paper No. 61—WA-7.

coupled Hill's equations, with the dependent variables $x_1, x_2, \ldots, x_n$, respectively, appearing alone in each. Once this is done we need only to construct the regions of stability and instability in the parameter space for each decoupled Hill's equation. The totality of n such separate stability investigations in the parameter space then yields the stability criteria for the entire system (1). The work of finding the stability regions for (6) is further reduced, if some or all of the equations (6) belong to a group of special Hill's equations for which the stability "charts" are already available. Some of these are the Mathieu equation [5], the Meissner equation [6], the Hill equation with two harmonic terms [7], and so on.

Next, we proceed to discuss various properties of this restricted class of (1) and, particularly, we wish to formulate conditions which will enable us to determine beforehand whether or not a given system (1) belongs to the restricted class. Let us express $\mathbf{B}(t)$ as a sum of matrices in the form:

$$\mathbf{B}(t) = \mathbf{B}_0 + \sum_{i=1}^{m} f_i(t)\mathbf{B}_i \tag{7}$$

where $\mathbf{B}_0$ and $\mathbf{B}_i (i = 1,2, \ldots, m)$ are square matrices of order n with constant elements and $f_i(t)$ are scalar periodic functions of t with period L. If m is infinite we shall require the series to be convergent for all values of t. With $\mathbf{B}(t)$ given by (7) the condition (4) will be satisfied if there exists a nonsingular matrix $\mathbf{T}$ such that

$$\mathbf{T}^{-1}\mathbf{B}_j\mathbf{T} = \mathbf{\Lambda}_j, \quad j = 0, 1, \ldots, m \tag{8}$$

where $\mathbf{\Lambda}_j$ are diagonal matrices with constant elements. Equation (8) means that all the $\mathbf{B}_j (j = 0, 1, \ldots, m)$ must be diagonable by one and the same fundamental matrix $\mathbf{T}$. In order to verify (8) one needs to know $\mathbf{T}$: To find such a fundamental matrix for a matrix of high order involves, however, very lengthy calculations. We shall therefore offer here the following conditions, with the aid of which we can determine beforehand and without actually calculating $\mathbf{T}$ whether (1) with $\mathbf{B}(t)$ given by (7) belongs to our restricted class. A necessary condition for (8) to be true is that all the $\mathbf{B}_j (j = 0, 1, \ldots, m)$ must be commutable with each other. This is obvious because for any two $\mathbf{B}_j$, say $\mathbf{B}_k$ and $\mathbf{B}_l$, (8) implies

$$\mathbf{B}_k = \mathbf{T}\mathbf{\Lambda}_k\mathbf{T}^{-1}, \quad \mathbf{B}_l = \mathbf{T}\mathbf{\Lambda}_l\mathbf{T}^{-1} \tag{9}$$

and two matrices of the form (9) always commute. The sufficiency conditions for (8) to be true are (i) that one of the $\mathbf{B}_j (j = 0, 1, \ldots, m)$, say $\mathbf{B}_k$, has distinct characteristic values,[1] and (ii) that it commutes with all the other $\mathbf{B}_j$. Let $\mathbf{B}_l$ be one of the members of the latter group. By condition (i) $\mathbf{B}_k$ is diagonable. Let $\mathbf{T}$ be a fundamental matrix for $\mathbf{B}_k$ so the first of (9) holds. What remains is for us to show that $\mathbf{B}_l$ is diagonable by the same $\mathbf{T}$ if $\mathbf{B}_k$ and $\mathbf{B}_l$ commute. Postmultiplying both sides of the first of (9) by $\mathbf{T}$ one obtains

$$\mathbf{B}_k\mathbf{T} = \mathbf{T}\mathbf{\Lambda}_k \tag{10}$$

Next, premultiplying both sides of (10) by $\mathbf{B}_l$ and using the commutativity of $\mathbf{B}_k$ and $\mathbf{B}_l$ we obtain the following sequence of equalities

$$\mathbf{B}_k\mathbf{B}_l\mathbf{T} = \mathbf{B}_l\mathbf{B}_k\mathbf{T} = \mathbf{B}_l\mathbf{T}\mathbf{\Lambda}_k \tag{11}$$

The equality of the first and the last terms in (11) implies that $\mathbf{B}_l\mathbf{T}$ is also a fundamental matrix for $\mathbf{B}_k$. Since all the fundamental matrices of one and the same matrix which has distinct characteristic values must have their corresponding columns proportional, we are led to

$$\mathbf{B}_l\mathbf{T} = \mathbf{T}\mathbf{\Lambda}_l \tag{12}$$

from which the second of (9) follows. Hence the proof of sufficiency is complete.

Thus far we have defined a restricted class of (1) by the requirement (4) and have also given specific necessary and sufficient conditions for differential systems (1) of the type (7) to belong to the restricted class. In what follows, several physical problems are studied within the framework of the foregoing theory. Only linearized systems are treated here. The results obtained should therefore be interpreted strictly within the scope of linear theory. The question concerning the effects of neglected nonlinear terms on the stability characteristics is not relevant to the main issue of this paper and hence is not discussed.

Coupled Pendulums With Oscillating Supports

As a first example of application, let us consider two identical compound pendulums attached to a common support, Fig. 1(*a*). Let us consider the case where the two are uncoupled and the support is subjected to an oscillating motion $f(t)$. Since the pendulums are identical, the differential equations of motion will be the same for both. Assuming small oscillation amplitudes, the equation of motion is given by

$$\frac{d^2x}{dt^2} + \frac{cg}{k_0^2}\left(1 - \frac{1}{g}\frac{d^2f}{dt^2}\right)x = 0 \tag{13}$$

where x may be either one of the angular displacements x_1 and x_2, k_0 is the radius of gyration of the pendulum about its point of suspension, and c the distance between the point of suspension and the centroid of the pendulum. It is well known [8] that, for certain motions of the support, the solutions x of (13) may grow and become unbounded. Under these conditions the vertically hanging down equilibrium position of each pendulum is an unstable one. If $f(t)$ is a simple harmonic motion such that

$$f(t) = a\cos\Omega t \tag{14}$$

(13) may be written as a Mathieu equation of the form

$$\frac{d^2x}{d\tau^2} + (\delta + \epsilon\cos\tau)x = 0 \tag{15}$$

where $\tau = \Omega t, \quad \delta = cg/k_0^2\Omega^2, \quad \epsilon = ca/k_0^2$ (16)

In this case the question of stability of the equilibrium position can be answered completely with the aid of the stability chart for Mathieu's equation; the criteria may be indicated by means of regions of stability and instability in the $\Omega - a$ plane. We note here that identical stability criteria apply to both pendulums.

Next, let us modify the system by introducing an elastic coupling between these two pendulums in the form of a spring with a spring constant k, Fig. 1(*b*). Now a question arises. What is

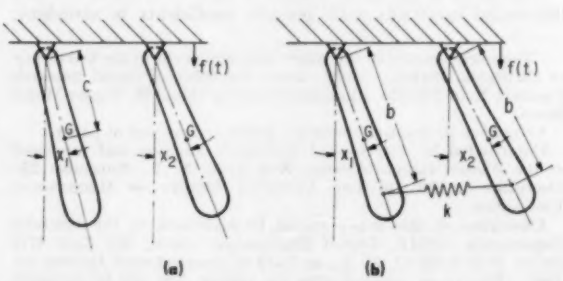

Fig. 1 Geometry of two identical pendulums, uncoupled or coupled by a linear spring, with oscillating supports

[1] The condition of distinctness of the characteristic values may be relaxed. However, to simplify the analysis we shall not treat the more general case in this paper.

the effect of the spring on the stability of the system? Would the presence of the spring tend to enhance or reduce the stability? By this we mean whether the stable regions in the $\Omega - a$ plane will be enlarged or reduced. The answer is not quite obvious, although once the analysis is carried out it becomes apparent.

Again considering only small amplitudes of oscillation we obtain the equations of motion as follows:

$$\frac{d^2\mathbf{x}}{dt^2} + \left(\mathbf{B}_0 - \frac{c}{k_0^2}\frac{d^2f}{dt^2}\mathbf{B}_1\right)\mathbf{x} = \mathbf{0} \tag{17}$$

where

$$\mathbf{x} = \begin{pmatrix} x_1 \\ x_2 \end{pmatrix}, \quad \mathbf{B}_1 = \begin{pmatrix} 1 & 0 \\ 0 & 1 \end{pmatrix},$$

$$\mathbf{B}_0 = \begin{pmatrix} \dfrac{cg}{k_0^2} + \dfrac{k}{m}\dfrac{b^2}{k_0^2} & -\dfrac{kb^2}{mk_0^2} \\ -\dfrac{kb^2}{mk_0^2} & \dfrac{cg}{k_0^2} + \dfrac{kb^2}{mk_0^2} \end{pmatrix}, \tag{18}$$

m is the mass of each pendulum and b is the distance from the point of suspension to the point where the coupling spring is attached. In view of the fact that $\mathbf{B}_1$ is a unit matrix, $\mathbf{B}_0$ and $\mathbf{B}_1$ certainly commute. Hence both may be diagonalized by a same fundamental matrix $\mathbf{T}$. One easily finds that in this case (17) may be reduced to

$$\frac{d^2\mathbf{z}}{dt^2} + \mathbf{A}(t)\mathbf{z} = 0 \tag{19}$$

where

$$\mathbf{z} = \begin{pmatrix} z_1 \\ z_2 \end{pmatrix} = \begin{pmatrix} x_1 + x_2 \\ x_1 - x_2 \end{pmatrix},$$

$$\mathbf{A}(t) = \begin{pmatrix} \dfrac{cg}{k_0^2} - \dfrac{c}{k_0^2}\dfrac{d^2f}{dt^2} & 0 \\ 0 & \dfrac{cg}{k_0^2} + \dfrac{2kb^2}{mk_0^2} - \dfrac{c}{k_0^2}\dfrac{d^2f}{dt^2} \end{pmatrix} \tag{20}$$

The matrix equation (19) consists of two decoupled Hill's equations. If $f(t)$ is such that the stability charts of these Hill's equations are known, then the stability problem of the original system (17) is essentially solved. For example, let us assume that $f(t)$ is given by (14). In this case (19) becomes two Mathieu's equations and may be put in a standard form

$$\frac{d^2z_i}{dt^2} + (\delta_i + \epsilon_i \cos\tau)z_i = 0, \quad i = 1, 2 \tag{21}$$

where

$$\tau = \Omega t,$$

$$\delta_1 = \frac{cg}{k_0^2\Omega^2}, \qquad \epsilon_1 = \frac{ca}{k_0^2},$$

$$\delta_2 = \frac{cg}{k_0^2\Omega^2}\left[1 + \frac{2kb^2}{mcg}\right], \qquad \epsilon_2 = \frac{ca}{k_0^2} \tag{22}$$

We can now construct for each equation of (21) the stable and unstable regions in a parameter space, say, for example, a three-dimensional space with $cg/k_0^2\Omega^2$, ca/k_0^2 and kb^2/mcg as its rectangular co-ordinates. The regions which are stable for both equations are then stable for the whole system. As an illustration, let us take $kb^2/mcg = 1$. In this case the stable regions in the parameter plane of $cg/k_0^2\Omega^2$ and ca/k_0^2 for the first equation of (21) are the areas shaded by 45-deg lines (in one direction only)

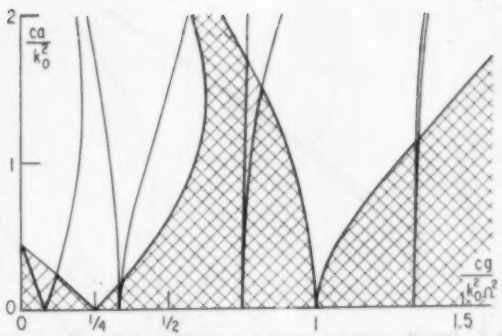

Fig. 2 Stability chart for "regular" equilibrium position of a system of two coupled pendulums with their supports subjected to identical simple harmonic motions. $kb^2/mcg = 1$

in Fig. 2. For the second equation only the demarcation lines between the stable and unstable regions are shown. This is done to enhance the clarity of the diagram. The regions which represent stability for the whole system are those which are cross-hatched. Remembering that the areas shaded with 45-deg lines (in one direction only) are also the regions of stability for the uncoupled system, it is evident that the presence of elastic coupling tends to reduce the stability of the system as a whole. For example, with small oscillation amplitudes of the support the uncoupled system is unstable only in the neighborhoods of frequencies

$$cg/k_0^2\Omega^2 = 1/4, 1, 9/4, \ldots,$$

while the coupled system is unstable in the neighborhoods of frequencies

$$cg/k_0^2\Omega^2 = 1/12, 1/3, 3/4, 4/3, \ldots$$

as well.

An analysis similar to that given in the foregoing may be carried out for the case where the coupled pendulums are in their inverted positions. Let the motion of the supports again be $f(t)$, positive in the downward direction as before, and let x_1 and x_2 be the angular displacements of the pendulum with respect to their *inverted* equilibrium positions. With other notations remaining the same as before, we find the equations of motion again given by (17) but with

$$\mathbf{B}_0 = \begin{pmatrix} -\dfrac{cg}{k_0^2} + \dfrac{kb^2}{mk_0^2} & -\dfrac{kb^2}{mk_0^2} \\ -\dfrac{kb^2}{mk_0^2} & -\dfrac{cg}{k_0^2} + \dfrac{kb^2}{mk_0^2} \end{pmatrix}, \quad \mathbf{B}_1 = -\begin{pmatrix} 1 & 0 \\ 0 & 1 \end{pmatrix} \tag{23}$$

Again let us assume $f(t)$ to have the form of (14). After carrying out the diagonalization and introducing a new time variable $\tau = \Omega t$, the equations of motion are reduced to a pair of Mathieu equations like (21) with

$$\delta_1 = -\frac{cg}{k_0^2\Omega^2}, \qquad \epsilon_1 = -\frac{ca}{k_0^2}$$

$$\delta_2 = -\frac{cg}{k_0^2\Omega^2}\left(1 - \frac{2kb^2}{mcg}\right), \qquad \epsilon_2 = -\frac{ca}{k_0^2} \tag{24}$$

We are now again in a position to construct the regions of stability and instability in the parameter space with the aid of the stability chart for the Mathieu equation. Taking $kb^2/mcg = 1$ as before, the stable regions are shown in Fig. 3. The areas

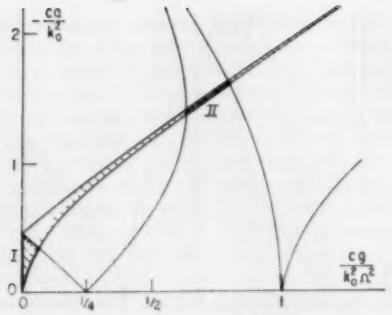

Fig. 3 Stability chart for inverted equilibrium position of a system of two coupled pendulums with their supports subjected to identical simple harmonic motions. $kb^2/mcg = 1$

shaded with 135-deg lines (only one area is shown, others being outside the diagram) are the stable regions for the first Mathieu equation and simultaneously also for the uncoupled system. However, the regions of stability common to both equations, hence for the coupled system as a whole, are only those areas which are crosshatched. Two of them, a nearly triangular region labeled I and a thin strip labeled II, can be seen in Fig. 3. Here we observe that the elastic coupling has caused a drastic reduction of the stable regions.

One sees that the analysis may easily be extended to a system of n identical coupled pendulums. The elastic couplings between the pendulums need not be the same. As a matter of fact, even the pendulums need not be identical, provided only that they have the same equivalent length k_0^2/c. If the last condition is satisfied, the equations of motion will be of the form

$$\frac{d^2\mathbf{x}}{dt^2} + \left(\mathbf{B}_0 \pm \frac{c}{k_0^2}\frac{d^2f}{dt^2}\mathbf{I}\right)\mathbf{x} = \mathbf{0} \tag{25}$$

where I is a unit matrix and the negative and the positive signs are used for the regular and the inverted positions, respectively. Again this equation can be reduced to a system of n decoupled Hill's equations and the stability property of the system may be studied accordingly. Since no essential new features will appear we shall not present here the detailed analysis. It suffices to say that because of the large number of degrees of freedom the regions of stability will be reduced very drastically indeed in comparison with those for the uncoupled system.

A Double Pendulum With Oscillating Support

In this section we shall discuss systems of equations (1) of another type which also belong to our restricted class. Let us investigate the stability of the four possible equilibrium positions of a double pendulum when its support is subjected to an oscillatory motion $f(t)$, Fig. 4. Fig. 4(a) gives the geometrical description of the pendulum while the four possible displacement configurations about the equilibrium positions are shown in Fig. 4(b). They will be referred to henceforth as configurations *DD*, *DU*, *UD*, and *UU*. Let us further denote the masses of the pendulums by m_1 and m_2 and the radii of gyration about their respective points of suspension by k_1 and k_2. Then, considering only small amplitudes the equations of motion for the configuration *DD* may be written as

$$\frac{d^2\mathbf{x}}{dt^2} + \left(g - \frac{d^2f}{dt^2}\right)\mathbf{B}_1\mathbf{x} = \mathbf{0}, \quad \mathbf{x} = \begin{pmatrix} x_1 \\ x_2 \end{pmatrix} \tag{26}$$

where

$$\mathbf{B}_1 = \begin{pmatrix} b_{11} & -b_{12} \\ -b_{21} & b_{22} \end{pmatrix} \quad \text{(for } DD\text{)} \tag{27}$$

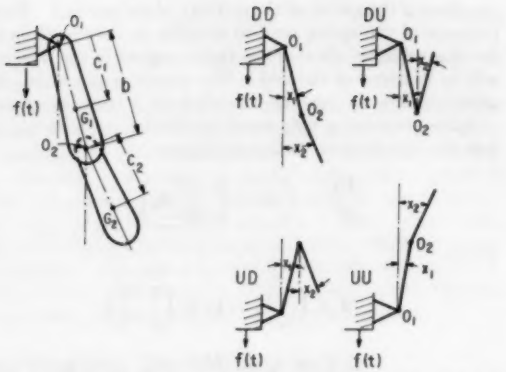

Fig. 4 Geometry and four possible equilibrium positions, *DD*, *DU*, *UD*, and *UU*, of a double pendulum

and

$$b_{11} = \frac{k_2^2(c_1m_1 + bm_2)}{m_1k_1^2k_2^2 + m_2b^2(k_2^2 - c_2^2)} \tag{28a}$$

$$b_{12} = \frac{m_2bc_2^2}{m_1k_1^2k_2^2 + m_2b^2(k_2^2 - c_2^2)} \tag{28b}$$

$$b_{21} = \frac{bc_2(m_1c_1 + bm_2)}{m_1k_1^2k_2^2 + m_2b^2(k_2^2 - c_2^2)} \tag{28c}$$

$$b_{22} = \frac{c_2(m_1k_1^2 + m_2b^2)}{m_1k_1^2k_2^2 + m_2b^2(k_2^2 - c_2^2)} \tag{28d}$$

The quantities b_{11}, b_{12}, b_{21}, and b_{22} are all positive and are of dimension 1/length. For the other three configurations $\mathbf{B}_1$ takes on the following forms, respectively:

$$\mathbf{B}_1 = \begin{pmatrix} b_{11} & b_{12} \\ -b_{21} & -b_{22} \end{pmatrix} \quad \text{(for } DU\text{)} \tag{29a}$$

$$\mathbf{B}_1 = \begin{pmatrix} -b_{11} & -b_{12} \\ b_{21} & b_{22} \end{pmatrix} \quad \text{(for } UD\text{)} \tag{29b}$$

$$\mathbf{B}_1 = \begin{pmatrix} -b_{11} & b_{12} \\ b_{21} & -b_{22} \end{pmatrix} \quad \text{(for } UU\text{)} \tag{29c}$$

Let us assume now that $\mathbf{B}_1$ may be diagonalized, which is the case for the present problem. Then (26) belongs to our restricted class and can therefore be reduced to a pair of Hill's equations, and the question of stability may be studied accordingly. To be specific, let us take $f(t)$ as given by (14) and also take, for the sake of simplicity of the analysis,

$$m_1 = m_2 \tag{30}$$

$$c_1 = c_2 = b = k_1 = k_2 \tag{31}$$

Conditions (30) and (31) imply a double pendulum consisting of two identical simple pendulums. Making the diagonalization and introducing $\tau = \Omega t$, (26) is reduced to

$$\frac{d^2z_i}{d\tau^2} + (\delta_i + \epsilon_i \cos \tau)z_i = 0, \quad i = 1, 2 \tag{32}$$

where

$$z_1 = x_1 + \frac{1}{\sqrt{2}}x_2, \qquad z_2 = x_1 - \frac{1}{\sqrt{2}}x_2,$$

$$\delta_1 = (2 - \sqrt{2})\frac{g}{c_1\Omega^2}, \qquad \delta_2 = (2 + \sqrt{2})\frac{g}{c_1\Omega^2},$$

$$\epsilon_1 = (2 - \sqrt{2})\frac{a}{c_1}, \qquad \epsilon_2 = (2 + \sqrt{2})\frac{a}{c_1}. \quad \text{(For } DD\text{)} \quad (33)$$

For the other three configurations z_i, δ_i, and ϵ_i are found to be as follows:

$$\text{(For } DU\text{)} \begin{cases} z_1 = x_1 + \left(1 + \dfrac{1}{\sqrt{2}}\right) x_2, \\ z_2 = x_1 + \left(1 - \dfrac{1}{\sqrt{2}}\right) x_2, \\ \delta_1 = -\sqrt{2}\,\dfrac{g}{c_1\Omega^2}, \quad \delta_2 = \sqrt{2}\,\dfrac{g}{c_1\Omega^2}, \\ \epsilon_1 = -\sqrt{2}\,\dfrac{a}{c_1}, \quad \epsilon_2 = \sqrt{2}\,\dfrac{a}{c_1}, \end{cases} \quad (34)$$

$$\text{(For } UD\text{)} \begin{cases} z_1 = x_1 + \left(1 + \dfrac{1}{\sqrt{2}}\right) x_2, \\ z_2 = x_1 + \left(1 - \dfrac{1}{\sqrt{2}}\right) x_2, \\ \delta_1 = \sqrt{2}\,\dfrac{g}{c_1\Omega^2}, \qquad \delta_2 = -\sqrt{2}\,\dfrac{g}{c_1\Omega^2}, \\ \epsilon_1 = \sqrt{2}\,\dfrac{a}{c_1}, \qquad \epsilon_2 = -\sqrt{2}\,\dfrac{a}{c_1}, \end{cases} \quad (35)$$

$$\text{(For } UU\text{)} \begin{cases} z_1 = x_1 + \dfrac{1}{\sqrt{2}} x_2, \quad z_2 = x_1 - \dfrac{1}{\sqrt{2}} x_2, \\ \delta_1 = -(2 - \sqrt{2})\,\dfrac{g}{c_1\Omega^2}, \\ \delta_2 = -(2 + \sqrt{2})\,\dfrac{g}{c_1\Omega^2}, \\ \epsilon_1 = -(2 - \sqrt{2})\,\dfrac{a}{c_1}, \quad \epsilon_2 = -(2 + \sqrt{2})\,\dfrac{a}{c_1}. \end{cases} \quad (36)$$

The stability regions in the parameter space of $g/c_1\Omega^2$ and a/c_1 for the configurations *DD*, *DU*, and *UU* are shown in Figs. 5, 6, and 7, respectively. In each case the demarcation curves which belong to the first equation are labeled 1 and those belonging to the second equation 2. Fig. 6 will also apply for the configuration *UD* if the equation labels are interchanged. Upon inspecting Fig. 7, one finds only a very small "triangular" region of stability near the origin. This means that, at least for this example, the *UU* equilibrium position is always unstable unless the motion of the support is of very high frequency ($c_1\Omega^2/g > 100$) and has just the correct amplitudes.

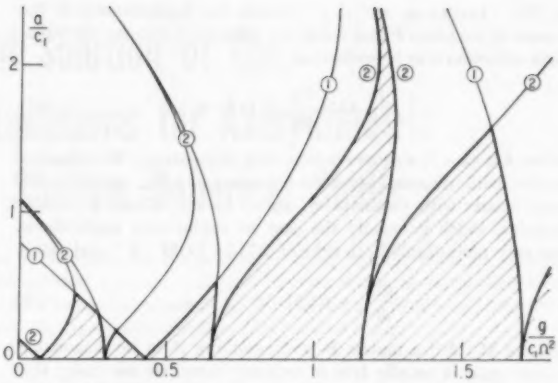

Fig. 5 Stability chart for *DD* equilibrium position of a double pendulum with its support subjected to a simple harmonic motion. $m_1 = m_2$, $c_1 = c_2 = b = k_1 = k_2$

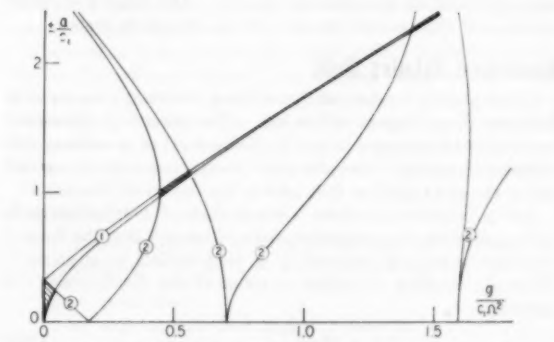

Fig. 6 Stability chart for *DU* equilibrium position of a double pendulum with its support subjected to a simple harmonic motion. $m_1 = m_2$, $c_1 = c_2 = b = k_1 = k_2$

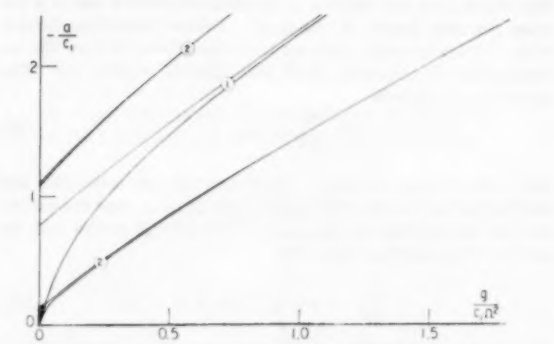

Fig. 7 Stability chart for *UU* equilibrium position of a double pendulum with its support subjected to a simple harmonic motion. $m_1 = m_2$, $c_1 = c_2 = b = k_1 = k_2$

Vibration of Masses on a Noncircular Rotating Shaft

Another group of problems for which the governing differential equations also belong to our restricted class is that of the stability of a system of several masses mounted on a noncircular rotating shaft. It is well known that with a single mass instability may occur under certain circumstances [9]. Therefore, an extension of the analysis to systems with a number of masses will be of considerable interest for engineering applications. Let us consider a shaft rotating in a vertical position and denote its length by l. Let n masses $m_1, m_2, \ldots, m_n$ be attached to the shaft at distances $\alpha_1 l, \alpha_2 l, \alpha_3 l, \ldots, \alpha_n l$ measured from one end of the shaft. For the sake of simplicity we shall assume that the masses are constrained so as to move in a fixed vertical axial plane P and that the shaft mass is negligibly small in comparison with the attached masses. Let us further assume that the cross section of the shaft, although noncircular, is uniform along the whole length and that the speed of the shaft is constant. Because of the lack of circular symmetry, the flexural rigidity EI of the shaft in the plane P will depend upon the angular position of the shaft with respect to P, and will, therefore, be a periodic function of t. It follows that the influence numbers[4] (referred to plane P) will also be periodic functions of t. Let us denote them by

[4] An influence number α_{ij} of an elastic system is defined as the deflection at station i caused by a unit force at station j.

$a_{ij}/f(t)$. Letting $x_1, x_2, \ldots, x_n$ denote the displacements of the masses in the plane P and using the influence numbers, the equations of motion may be written as

$$\frac{1}{f(t)} \mathbf{AM} \frac{d^2\mathbf{x}}{dt^2} + \mathbf{Ix} = \mathbf{o} \tag{37}$$

where $\mathbf{A}$ is an $n \times n$ square matrix with elements a_{ij}, $\mathbf{M}$ a diagonal matrix with diagonal elements $m_1, m_2, \ldots, m_n$, and $\mathbf{x}$ a column matrix with elements $x_1, x_2 \ldots, x_n$. When $\mathbf{A}$ is nonsingular, which is usually the case in engineering applications, one may premultiply both sides of (37) by $f(t)\mathbf{M}^{-1}\mathbf{A}^{-1}$ and obtain

$$\frac{d^2\mathbf{x}}{dt^2} + f(t)\mathbf{M}^{-1}\mathbf{A}^{-1}\mathbf{x} = \mathbf{o} \tag{38}$$

Calling $\mathbf{M}^{-1}\mathbf{A}^{-1}$ a matrix $\mathbf{B}_1$ and assuming it to be diagonable, which again is usually true in ordinary cases, we see easily that (38) belongs to our restricted class and may hence be decoupled into n ordinary Hill's equations. Once this is accomplished one can study separately the stability of the solutions of each equation and establish the stability criteria. The totality of these criteria will then govern the stability of the whole system.

Noncircular Rotating Shaft

In this section we shall study problems involving systems with infinitely many degrees of freedom. The governing differential equations can no longer be put in the form (1) of n ordinary differential equations. Nevertheless, the analyses may be carried out in the same spirit as that used in the preceding discussion.

Let us consider a uniform vertical shaft of noncircular cross section rotating at a constant speed and assume that the flexural vibration, if any, is restricted to a fixed vertical axial plane P. Then the equation of motion in terms of the displacement v is given by

$$[C_0 + C(t)] \frac{\partial^4 v}{\partial x^4} = -\mu \frac{\partial^2 v}{\partial t^2} \tag{39}$$

where C_0 is the average flexural rigidity of the shaft, $C(t)$ is the fluctuating part and hence a peridodic function of t, and μ is the mass per unit length of the shaft. Before proceeding further with (39) let us write down some pertinent results from the investigation of a circular shaft with flexural rigidity C_0. The governing equation is

$$C_0 \frac{\partial^4 v}{\partial x^4} = -\mu \frac{\partial^2 v}{\partial t^2} \tag{40}$$

For a set of given boundary conditions one can solve (40) and find the normal modes of vibration $v_1(x), v_2(x), \ldots$ and the natural circular frequencies $\omega_1, \omega_2, \ldots$. The normal modes and the natural frequencies are such that

$$C_0 \frac{d^4 v_i}{dx^4} = \mu\omega_i^2 v_i, \quad i = 1, 2, \ldots \tag{41}$$

Now let us go back to (39) and assume that the same set of boundary conditions prevails for the noncircular shaft. Let us express v in terms of the normal modes

$$v = \sum_{i=1}^{\infty} z_i(t) v_i(x) \tag{42}$$

Substituting (42) into (39), utilising (41) and recalling that the normal modes v_i form an orthogonal set, one is led immediately to a system of ordinary differential equations in the z_i as follows:

$$\frac{d^2 z_i}{dt^2} + \omega_i^2 \left(1 + \frac{C(t)}{C_0}\right) z_i = 0, \quad i = 1, 2, \ldots. \tag{43}$$

Each equation of (43) is a Hill equation. Here we recall that the ω_i can be determined if the boundary conditions are known. If, in addition, the periodic variation $C(t)$ is also known, the stability criteria for the equilibrium position of shaft (corresponding to $z_i = 0, i = 1, 2, \ldots$) can then be obtained from a study of (43). For example, if $C(t)$ is given by

$$C(t) = C_0\eta \cos m\Omega t \tag{44}$$

where Ω is the angular velocity of the shaft and m is an even integer,[5] one can reduce (43) to the following standard form of Mathieu's equation:

$$\frac{d^2 z_i}{d\tau^2} + (\delta_i + \epsilon_i \cos \tau) z_i = 0, \quad i = 1, 2, 3, \ldots \tag{45a}$$

where

$$\delta_i = \frac{\omega_i^2}{m^2\Omega^2}, \qquad \epsilon_i = \frac{\omega_i^2 \eta}{m^2\Omega^2} \tag{45b}$$

Here $\tau = m\Omega t$. Utilizing the stability chart for Mathieu's equation one can conclude immediately that there will be instability at frequencies near

$$\Omega = \frac{2}{mn}\omega_i, \quad i, n = 1, 2, 3, \ldots. \tag{46}$$

The instability is particularly serious near the frequencies

$$\Omega = \frac{2}{m}\omega_i, \quad i = 1, 2, 3, \ldots \tag{47}$$

because of the large instability region in the stability chart for Mathieu's equation near $\delta_i = 1/4$.

Before concluding this section it should be mentioned that there are many other problems similar in nature to those treated in this and the preceding sections of this paper. One may mention here, for example, the problem of the stability of a hanging chain with an oscillating support. This problem may be considered to be a natural extension of the double-pendulum problem treated earlier and can be analyzed following the same general lines of approach as those discussed in this section. One also recalls the problems of the stability of columns and strings under periodically varying forces which have been analyzed in detail by Lubkin and Stoker [10].

References

1 J. R. Paulling and R. M. Rosenberg, "On Unstable Ship Motions Resulting From Nonlinear Coupling," *Journal of Ship Research*, vol. 3, 1959, pp. 36–46.

2 S. Lefschetz, "Differential Equations: Geometric Theory," Interscience Publishers, Inc., New York, N. Y., 1957.

3 Lamberto Cesari, "Asymptotic Behavior and Stability Problems in Ordinary Differential Equations," Springer-Verlag, Berlin-Göttingen-Heidelberg, Germany, 1959.

4 R. A. Frazer, W. J. Duncan, and A. R. Collar, "Elementary Matrices," Cambridge University Press, New York, N. Y., 1947.

5 N. W. McLachlan, "Theory and Application of Mathieu Equations," Oxford University Press, London, England, 1947.

6 B. Van der Pol and M. J. O. Strutt, "On the Stability of the Solutions of Mathieu's Equation," *Philosophical Magazine*, vol. 5, 1928, p. 18.

7 Karl Kotter and Gertrud Kotowski, "Über die Stabilität der Lösungen Hillscher Differential gleichungen mit drei unabhängigen Parametern," *Zeitschrift für angewandte Mathematik und Mechanik*, vol. 23, 1943, pp. 149–155.

8 J. J. Stoker, "Nonlinear Vibrations," Interscience Publishers, Inc., New York, N. Y., 1950.

9 J. P. Den Hartog, "Mechanical Vibrations," McGraw-Hill Book Company, Inc., New York, N. Y., 1947.

10 S. Lubkin and J. J. Stoker, "Stability of Columns and Strings Under Periodically Varying Forces," *Quarterly of Applied Mathematics*, vol. 1, 1943, pp. 215–236.

[5] For example, for a splined shaft with $2p$ splines of proper shape, $m = 2p$.

G. A. THURSTON
Shell Structures Specialist,
Flight Propulsion Laboratory Department,
General Electric Company,
Cincinnati, Ohio

A Numerical Solution of the Nonlinear Equations for Axisymmetric Bending of Shallow Spherical Shells

A numerical solution is obtained for the nonlinear equations for clamped, shallow spherical shells under external pressure. Results are presented in the postbuckling range which have not been computed previously. The upper and lower buckling pressures are compared with the experimental data of Kaplan and Fung.

This paper is concerned with the solution of the nonlinear differential equations for shallow spherical shells under external pressure. Clamped-edge boundary conditions were assumed although the method of solution is applicable for any set of finite conditions.

The spherical-cap problem has been the subject of a great number of investigations. Some of the early results for buckling pressures showed disagreement with each other. Most of the confusion arose from the fact that the solution for the nonlinear problem must be formulated as a sequence of linear problems. This made it difficult to distinguish between instability in the sequence of numerical calculations and points of instability of the differential equations which correspond to the classical buckling pressures.

Recently, Budiansky [1][1] obtained results for the upper buckling pressure for various ratios of the shell rise to thickness. Weinitschke [2] also arrived at essentially the same values for these pressures by another method. Results for the lower buckling pressure have been published by Keller and Reiss [3] for a limited range of parameters. The results of the present study show good agreement with those in the foregoing references and include lower buckling pressures which have not been obtained previously.

In addition, pressure-deflection curves are presented in the postbuckling range. These show three solutions to the differential equations for the range of pressures between the lower and upper buckling pressures. These solutions correspond to the three possible equilibrium states postulated by von Karman and Tsien [4]. However, solutions were found *above* the upper buckling pressure which show that the pressure-deflection curve determined by the differential equations is not monotonic in this range although these equilibrium states are apparently unstable for the shell.

The buckling pressures are compared with the experimental results of Kaplan and Fung [5]. This comparison shows that the finite-deflection equations for a perfect spherical cap are inadequate to predict the experimental buckling pressures. The lower buckling pressure from this theory does represent a lower bound for postbuckling pressures which gives relatively good agreement with experiment.

The method of solution of the present paper is to assume a solution for the nonlinear differential equations. A correction for this solution is obtained by solving the linear nonhomogeneous "variational" equations for the nonlinear system of equations. This correction is used to compute a new assumed solution and the process is repeated until the correction approaches zero.

Nomenclature

The nomenclature in this paper follows that of E. Reissner [6] and his students [7–9] for most variables (see Fig. 1):

ξ = polar angle
β = angular deflection of shell middle surface
ψ = stress function
α = value of ξ at edge of shell
h = shell thickness
p = external pressure
ν = Poisson's ratio
m^4 = $12(1 - \nu^2)$
D = Eh^3/m^4 flexural rigidity
a = radius of sphere
H = shell rise above horizontal plane through edge
u, w = radial and axial deflections of middle surface

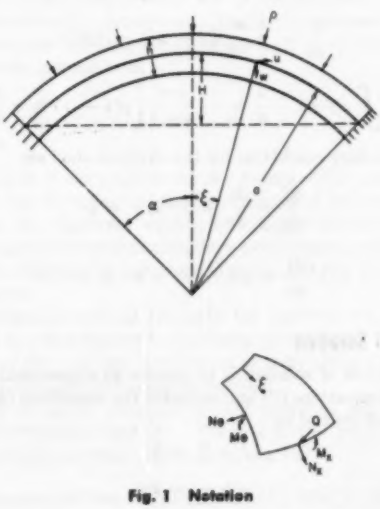

Fig. 1 Notation

[1] Numbers in brackets designate References at end of paper.

Presented by the Applied Mechanics Division of THE AMERICAN SOCIETY OF MECHANICAL ENGINEERS, at the Tenth International Congress of Applied Mechanics, Stresa, Italy, August 31–September 7, 1960.

Discussion of this paper should be addressed to the Editorial Department, ASME, United Engineering Center, 345 East 47th Street, New York 17, N. Y., and will be accepted until January 10, 1962. Discussion received after the closing date will be returned. Manuscript received by ASME Applied Mechanics Division, October 27, 1960.

The basic differential equations can be obtained by specializing E. Reissner's equations [6] for arbitrary shells of revolution in the form

$$\frac{D}{a}\left(\beta'' + \frac{1}{\xi}\beta' - \frac{\beta}{\xi^2}\right) = -\left(\psi + \frac{\rho a^2 \xi}{2} - \frac{\beta\psi}{\xi}\right)$$
$$\psi'' + \frac{1}{\xi}\psi' - \frac{\psi}{\xi^2} = aEh\left(\beta - \frac{\beta^2}{2\xi}\right) \tag{1}$$

Primes denote differentiation with respect to ξ. The first of equations (1) is the moment equation for a differential element of the shell. The second is the relevant compatibility equation. In both equations, cot ξ, has been replaced by $1/\xi$ which restricts their validity to shallow shells.

The equations are nondimensionalized by introducing a geometrical parameter, μ^2, and a load parameter, γ, defined by

$$\mu^2 = m^2 a\alpha^2/h = 2m^2 H/h, \qquad \gamma = m^6 a^4 \alpha^4 \rho / 4Eh^4$$

The new variables are

$$\xi = \alpha x, \quad f = -4Eh^3\beta/m^4\rho a^3\alpha^3 x, \qquad g = -4h\psi/m^2\rho a^3\alpha^3 x$$

The differential equations, equations (1), become

$$x\frac{d^3 f}{dx^3} + 3\frac{df}{dx} + \mu^2 xg + \gamma x f g = 2x$$
$$x\frac{d^3 g}{dx^3} + 3\frac{dg}{dx} - \mu^2 x f - \frac{\gamma x f^2}{2} = 0 \tag{2}$$

In this notation, g is positive for compressive meridional stresses at the middle surface and the "membrane solution" for positive external pressure, ρ, is

$$g = 2/\mu^2$$
$$f = 0 \tag{3}$$

The stress resultants, couples, and displacements are given by

$$\frac{aN_x}{Eh^2} = -\frac{\gamma}{m^2\mu^2}\, g, \quad \frac{aN_\theta}{Eh^2} = -\frac{\gamma}{m^2\mu^2}\left(g + x\frac{dg}{dx}\right)$$
$$\frac{6aM_x}{Eh^2} = -\frac{6\gamma}{m^4\mu^4}\left[x\frac{df}{dx} + (1+\nu)f\right],$$
$$\frac{6aM_\theta}{Eh^2} = -\frac{6\gamma}{m^4\mu^4}\left[\nu x\frac{df}{dx} + (1+\nu)f\right] \tag{4}$$
$$\frac{Q}{\rho a} = -\frac{\alpha}{4}\left[2 - \mu^2 g - \gamma f g\right]x$$
$$\frac{w}{h} = \frac{\gamma}{m^2}\int x f\, dx, \quad \frac{u}{h} = -\frac{\alpha\gamma}{m^2\mu^2}\left[g(1-\nu) + x\frac{dg}{dx}\right]$$

The boundary conditions for the clamped shell are

$$\frac{df}{dx} = \frac{dg}{dx} = 0 \quad \text{at } x = 0$$
$$f = \frac{dg}{dx} + g(1-\nu) = 0 \quad \text{at } x = 1 \tag{5}$$

Method of Solution

The method of solution is to assume an approximate solution (f_n, g_n) for equations (2) and solve for the correction $(\delta f_n, \delta g_n)$ to this solution defined by

$$f = f_n + \delta f_n$$
$$g = g_n + \delta g_n \tag{6}$$

Substituting equations (6) into the differential equations, equations (2), obtains

$$L(\delta f_n) + \mu^2 x\delta g_n + \gamma x(f_n\delta g_n + g_n\delta f_n + \delta f_n\delta g_n) = -E_{1n}(x)$$
$$L(\delta g_n) - \mu^2 x\delta f_n - \gamma x\left[f_n\delta f_n + \frac{(\delta f_n)^2}{2}\right] = -E_{2n}(x) \tag{7}$$

where

$$E_{1n}(x) = L(f_n) + x(\mu^2 g_n + \gamma f_n g_n - 2)$$
$$E_{2n}(x) = L(g_n) - x\left(\mu^2 f_n + \frac{\gamma f_n^2}{2}\right)$$

and

$$L(y) = x\frac{d^2 y}{dx^2} + 3\frac{dy}{dx}$$

It can be seen that minus the right sides of equations (7), $E_{1n}(x)$ and $E_{2n}(x)$, represent the errors in the assumed solution (f_n, g_n). The left sides of these equations contain nonlinear terms of the same form as the original equations, equations (2), but these nonlinear terms will be small compared to the linear terms, if the assumed solution (f_n, g_n) is near an exact solution of equations (2). This is in contrast to equations (2) where the nonlinear terms become large for solutions in the postbuckling region.

Neglecting the nonlinear terms in equations (7) gives

$$L(\delta f_n) + \gamma x g_n\delta f_n + x(\mu^2 + \gamma f_n)\delta g_n = -E_{1n}(x)$$
$$L(\delta g_n) - x(\mu^2 + \gamma f_n)\delta f_n = -E_{2n}(x) \tag{8}$$

The procedure is to solve equations (8) for δf_n and δg_n, compute a new approximate solution (f_{n+1}, g_{n+1}) from

$$f_{n+1} = f_n + \delta f_n$$
$$g_{n+1} = g_n + \delta g_n \tag{9}$$

and substitute this solution back into equations (8) which are then solved for a new correction $(\delta f_{n+1}, \delta g_{n+1})$. If the correction $(\delta f_m, \delta g_m)$ approaches zero as m increases, then the approximate solution (f_{m+1}, g_{m+1}) must approach an exact solution of the original nonlinear equations, equations (2).

The converse is not necessarily true, and the conditions when it is not true are of particular interest. If the approximate solution (f_n, g_n) is also the exact solution, equations (8) become

$$L(\delta f) + \gamma x g\,\delta f + x(\mu^2 + \gamma f)\delta g = 0$$
$$L(\delta g) - x(\mu^2 + \gamma f)\delta f = 0 \tag{10}$$

Equations (10) are the linear "variational" equations for the nonlinear system, equations (2). There are values of μ^2, γ, f, and g for which equations (10) can have a nonzero solution. In fact, these values of γ serve to define the classical buckling pressures since a nonzero solution implies another possible equilibrium position for the shell infinitesimally near the one defined by (f, g). In "linearized" classical theory, the f and g in equations (10) are obtained by solving equations (2) with $\gamma = 0$. The results of the present study indicate that the linearized theory gives good approximations to the critical values of γ. Budiansky also discusses this point in comparing eigenvalues of the linearized theory using the "membrane" solution of equations (2) defined by equations (3) with modified boundary conditions and critical values of γ obtained by an iterative solution of nonlinear equations equivalent to equations (2) and the clamped boundary conditions of equations (5).

In the neighborhood of critical values of $\gamma = \gamma_c$ defined as eigenvalues of equations (10), it can be expected that the con-

vergence of the sequence of approximate solutions of equations (8) and equations (9) will be poor. This is indeed the case and "exact" values of γ_e cannot be obtained in this manner. However, approximate values of γ_e can be obtained by extrapolation or by finding upper or lower bounds for it.

Numerical Solution

The set of linear differential equations, equations (8), does not have closed form solutions for most functions of f_n and g_n so that these equations must be solved approximately. The method used here has proved useful in other high-speed digital computer programs for shell analysis [10] and has certain advantages for this type of problem:

1 Bending stresses can be computed nearly as accurately as membrane stresses.

2 Location of stations is arbitrary so that stations can be clustered near the boundaries to better approximate "edge effects."

3 Problems with any linear set of boundary conditions can be solved directly without resorting to superposition.

The numerical solution is applicable to equations written in the general form

$$\sum_{j=1}^{n} [R_{ij}(x)y_j''(x) + P_{ij}(x)y_j'(x) + Q_{ij}(x)y_j(x)] = F_i(x) \qquad i = 1, 2, 3 \ldots n \quad (11)$$
$$a \leq x \leq b$$

Primes denote differentiation with respect to x. The R, P, Q, and F are known functions of x and the $y_j(x)$ are the dependent variables. After equations (11) are formally integrated by parts twice, they become

$$\sum_{j=1}^{n} R_{ij}(x)y_j(x) = \sum_{j=1}^{n} \left[R_{ij}(a)y_j(a) \left(\frac{b-x}{b-a}\right) + R_{ij}(b)y_j(b) \left(\frac{x-a}{b-a}\right)\right] - \int_a^b \frac{\partial K(x,t)}{\partial t} \left[\sum_{j=1}^{n} H_{ij}(t)y_j(t)\right] dt + \int_a^b K(x,t) \left\{\left[\sum_{j=1}^{n} G_{ij}(t)y_j(t)\right] - F_i(t)\right\} dt \quad (12)$$

where

$$H_{ij}(x) = P_{ij}(x) - 2R_{ij}'(x)$$
$$G_{ij}(x) = Q_{ij}(x) - P_{ij}'(x) + R_{ij}''(x) \quad (13)$$

$$K(x,t) = \begin{cases} \dfrac{(b-x)(t-a)}{(b-a)} & a \leq t \leq x \\ \dfrac{(b-t)(x-a)}{(b-a)} & x \leq t \leq b \end{cases} \quad (14)$$

$$\frac{\partial K(x,t)}{\partial t} = \begin{cases} \dfrac{(b-x)}{(b-a)} & a \leq t < x \\ -\dfrac{(x-a)}{(b-a)} & x < t \leq b \end{cases}$$

The numerical solution solves the set of integral equations by transforming them into a set of linear algebraic equations which are then solved by Gaussian elimination. The transformation makes use of quadrature formulas of the form

$$\int_a^b \frac{\partial K(x,t)}{\partial t} H(t)y(t)dt \cong -\sum_{r=1}^{m} A_r(x)H(t_r)y(t_r) \quad (15)$$

$$\int_a^b K(x,t)G(t)y(t)dt \cong \sum_{r=1}^{m} B_r(x)G(t_r)y(t_r) \quad (16)$$

The method of computing the sets of coefficients $A_r(x)$ and $B_r(x)$ is derived in reference [10]. It should be mentioned here that the kernels, $K(x,t)$ and

$$\frac{\partial K(x,t)}{\partial t}$$

are used as "weight functions" so that their discontinuities at $x = t$ do not affect the accuracy of the quadrature formulas, equations (15) and (16). Also, the locations of the m stations t_r are arbitrary.

The end points of the interval are convenient stations so that $t_1 = a$ and $t_m = b$. Substituting the quadrature formulas into the integral equations for the $(m-2)$ interior values of $x_r = t_r$ obtains

$$\sum_{j=1}^{n} |R_{ij}(x_k)y_j(x_k)| = \left[\sum_{j=1}^{n} R_{ij}(a)y_j(a)\right] \left|\frac{(b-x_k)}{(b-a)}\right| + \left[\sum_{j=1}^{n} R_{ij}(b)y_j(b)\right] \left|\frac{(x_k-a)}{(b-a)}\right| + \|A_r(x_k)\| \left|\sum_{j=1}^{n} H_{ij}(x_r)y_j(x_r)\right| + \|B_r(x_k)\| \left|\sum_{j=1}^{n} G_{ij}(x_r)y_j(x_r)\right| - \|B_r(x_k)\| \, |F_i(x_r)|$$
$$i = 1, 2 \ldots n$$
$$j = 1, 2 \ldots n$$
$$r = 1, 2 \ldots m$$
$$k = 2, 3 \ldots m-1 \quad (17)$$

where $|\ |$ denotes a column vector and $\|\ \|$ a matrix of $(m-2)$ rows and m columns.

Equations (17) are a set of $r(m-2)$ linear algebraic equations in rm unknown $y_j(x_r)$. The remaining relations necessary to make a linearly independent set of nm-equations are contained in the boundary conditions. The boundary conditions are assumed to be linear combinations of the $y_j(x)$ and their first derivatives in the general form

$$\sum_{j=1}^{n} [C_j y_j(x) + D_j y_j'(x)] = E \quad x = a, \quad x = b \quad (18)$$

The derivatives of the $y_j(x)$ at the end points of the interval appearing in the boundary conditions represent additional unknowns in the algebraic equations. These derivatives are eliminated by replacing them with the p-point Lagrange interpolation formula passing through the end point and the neighboring $(p-1)$ points.

The boundary conditions complete the algebraic set of equations which are then solved by Gaussian elimination. The first derivatives of the $y_j(x)$ are determined next by using the known $y_j(x_r)$ in a Lagrange interpolation formula.

The IBM computer program[3] for the spherical cap problem begins by solving equations (8). For this pair of equations, the numerical solution outlined in the foregoing has

[3] The numerical solution was programmed by Mrs. D. Stallone.

$n = 2, m = 19, y_1(x) = \delta f_n$ and $y_2(x) = \delta g_n$

$R_{11} = x$	$R_{12} = 0$	$F_1 = -E_{1n}(x)$
$H_{11} = 1$	$H_{12} = 0$	
$G_{11} = \gamma x g_n$	$G_{12} = x(\mu^2 + \gamma f_n)$	
$R_{21} = 0$	$R_{22} = x$	$F_2 = -E_{2n}(x)$
$H_{21} = 0$	$H_{22} = 1$	
$G_{21} = -x(\mu^2 + \gamma f_n)$	$G_{22} = 0$	

The 19 stations were located at $x = 0, 0.011, 0.036, 0.074, 0.124, 0.186, 0.256, 0.332, 0.415, 0.5, 0.585, 0.668, 0.744, 0.814, 0.876, 0.926, 0.964, 0.989$, and 1.0. This distribution of values makes almost all of the elements of the $\mathbf{B}_r(x_k)$ quadrature matrix positive with the largest elements near the trace $r = k$. The quadrature formulas of equations (16) are exact for polynomials of degree $(m - 1)$ in the integrand excluding the kernels. Most of the results given here were computed using quadrature matrices with elements accurate to approximately 5 significant figures. Recently this has been improved to 8 significant figures. Comparisons with "exact" solutions for this type of problem indicate that the peak answers for the dependent variables will be correct to 3 significant figures and 5 or 6 figures, respectively, for the 5 and 8-figure-accuracy matrices.

The input data to the program consist of the parameters ν, μ^2, and γ along with the values at the 19 stations of the initial guess on the solution f_0 and g_0 plus $L(f_0)$ and $L(g_0)$ for use in computing $E_{1n}(x)$ and $E_{2n}(x)$. It is assumed that f_0 and g_0 satisfy the boundary conditions for the clamped shell, equations (5), so that δf_n and δg_n satisfy the same homogeneous conditions.

The program solves equations (8) numerically starting with the initial guess (f_0, g_0) and computes new approximations from equations (9). This operation is performed a given number of times N, prescribed as input data. The values of δf_n and δg_n for each value of n up to N are printed as output for a check on convergence. The value of f_{N+1} is then substituted into the original nonlinear equations, equations (2), and these are solved numerically in the form

$$L(f) + \mu^2 x g + (\gamma x f_{N+1}) g = 2x$$
$$L(g) - x\left(\mu^2 + \frac{\gamma f_{N+1}}{2}\right) f = 0 \qquad (19)$$

along with the differential equation for the axial deflection w. The solution (f_{N+1}, g_{N+1}) can then be compared with the solution (f, g) from equations (19) as a further check on convergence.

The values of $L(f)$ and $L(g)$ are then computed from the values of f and g, using equations (19). These functions are useful as input data for an initial guess at the solution for neighboring values of μ^2 and γ. In fact, if additional pairs of μ^2 and γ are given as input, the current values of f, g, $L(f)$ and $L(g)$ are used by the program as initial guesses f_0, g_0, $L(f_0)$, and $L(g_0)$ for the next pair of μ^2 and γ. Finally, the stress resultants and couples of equations (4) are computed from f and g and their derivatives.

The original choices for f_0 and g_0 will be discussed in the next section along with the results.

Numerical Results

The pressure-deflection curves for given values of μ^2 and $\nu = 0.32$ are plotted in Figs. 2 and 3. The dimensionless deflections are the maximum value of w/h appearing in the tabulated output at the given stations. The results in Fig. 2 for values of μ^2 up to 25 are relatively easy to obtain and are not new. The pressure-deflection curves are monotonic up to $\mu^2 \approx 11$. Above this value of μ^2, the curves have two horizontal tangents, labeled U and L on the curve for $\mu^2 = 25$. These horizontal tangents split the curves into three branches for computing purposes and for the initial estimate on the solution, (f_0, g_0).

The guess $f_0 = g_0 = 0$ makes the solution converge to the initial portion of the curve OU. On this case (f_1, g_1) is the well-known solution from linear shell theory in terms of Kelvin functions.

Answers were obtained in the postbuckling region LN by starting with the monotonic curve for a flat plate ($\mu^2 = 0$). The nonlinear membrane solution for this problem was easily adapted for an initial guess on f_0 and g_0 at high values of γ. Then, holding γ constant and increasing μ^2, the solution converged to the postbuckled branch for the other curves.

The results on this branch are characterized by tensile stress resultants, N_x and N_θ, at the center and over most of the shell and by high bending moments and normal shear resultant near the edge necessary to satisfy the fixed-edge boundary conditions.

After the branches OU and LN were established for $\mu^2 = 16$, a rather crude interpolation between the two known solutions was sufficiently accurate to force convergence on the unstable branch UL at $\gamma = 120$. Having this solution, μ^2 and γ were varied simultaneously to get solutions for higher values of μ^2 on the unstable branch.

After a solution converged on a given branch, it was not difficult to move up and down that branch by varying γ with constant μ^2. Nearing the horizontal tangents, the convergence became poor, so that these points are extrapolated values.

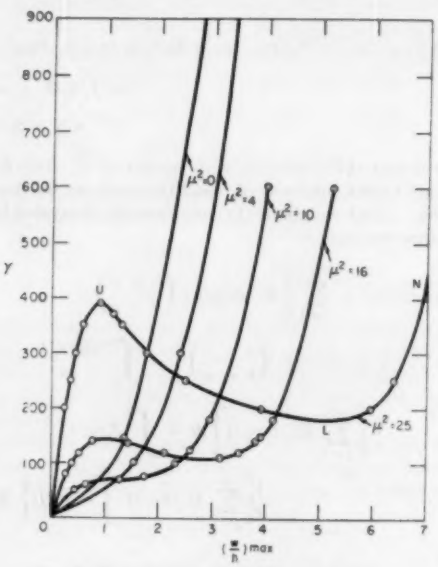

Fig. 2 Pressure-maximum deflection curves

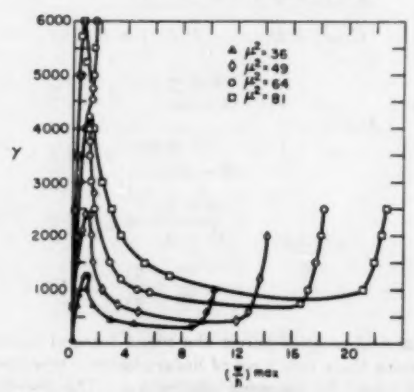

Fig. 3 Pressure-maximum deflection curves

The results for $\mu^2 \geq 36$ in Fig. 3 are complicated by the fact that there is apparently a *trifurcation* in the solution at the upper buckling pressure γ_U. There are three distinct branches to the curve in the vicinity of γ_U. These are also shown to a larger scale and plotted against the center deflection $w(0)/h$ in Fig. 4.

For example, on the curve for $\mu^2 = 64$, it was possible to proceed from the origin up the curve with increasing γ until the solution failed to converge at approximately $\gamma = 4550$. However, the initial guess $f_0 = g_0 = 0$ again led to a convergent solution of a higher mode shape at $\gamma = 6000$. Proceeding up this branch, the solutions again fail to converge at $\gamma = 7200$. This branch was also followed from 6000 down to $\gamma = 4500$ with good convergence all the way.

The unstable branch UL was also computed in this vicinity, but the lack of convergence in the solution near $\gamma = 4550$ prevented determining how the three branches behave in the neighborhood of this critical point.

The few results calculated above the upper buckling pressure γ_U indicate that there are solutions for higher mode shapes and higher buckling pressures other than those presented here. This possibility is of theoretical interest; however, these equilibrium states are obviously unstable for the shell.

Some of the results plotted as a function of x for various values of γ and $\mu^2 = 64$ are shown in Figs. 5, 6, and 7. They show the marked differences in the shape of the solutions on different branches for the same values of γ.

On proceeding down the postbuckled branch of the curve LN toward the lower buckling pressure γ_L, the convergence again fails. Near this critical point, the numerical solutions jumped back to the unbuckled branch as γ decreased. No similar jump was observed at the upper critical point. The numerical solution tended to oscillate about the initial assumed solution near γ_U.

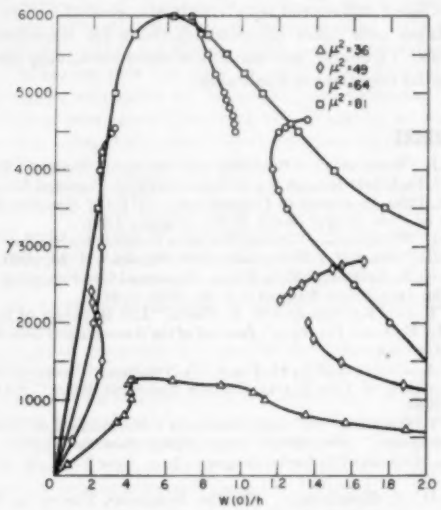

Fig. 4 Pressure-center deflection curves

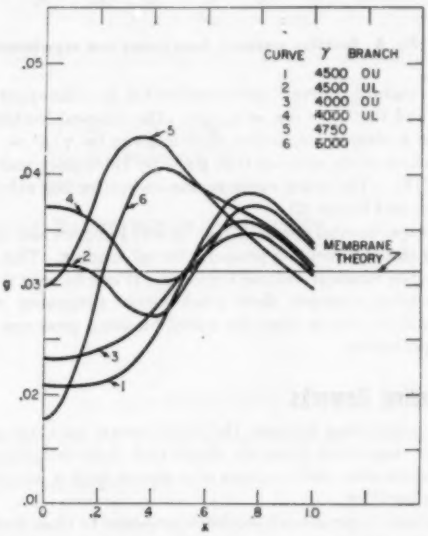

Fig. 6 Meridional stress for cap with $\mu^2 = 64$ for given values of γ

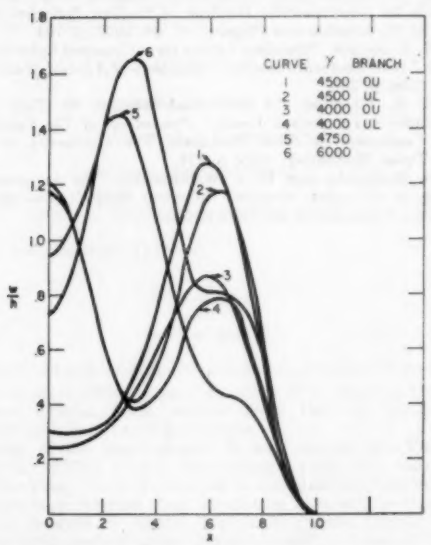

Fig. 5 Deflection of cap with $\mu^2 = 64$ for given values of γ

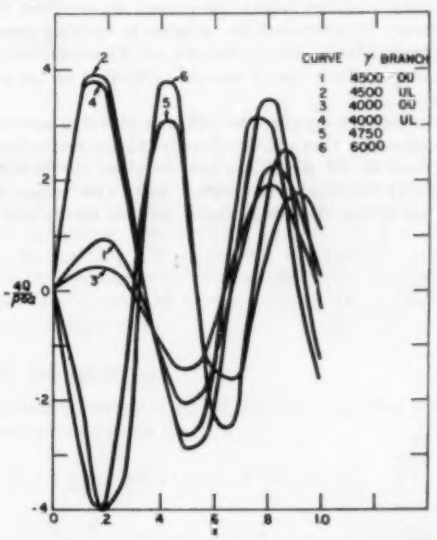

Fig. 7 Normal shear resultant for cap with $\mu^2 = 64$ for given values of γ

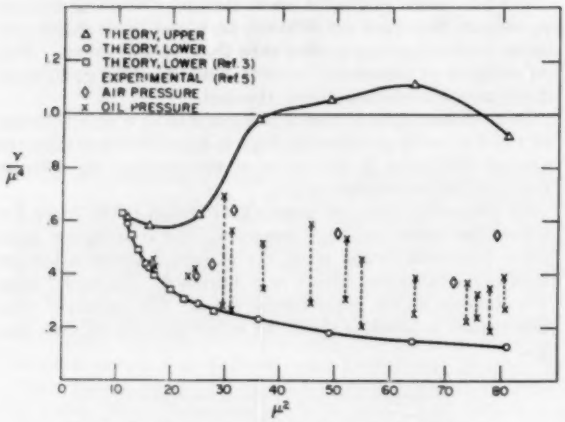

Fig. 8 Buckling pressures from theory and experiment

The "stability curves" are plotted in Fig. 8. The upper curve is γ_U/μ^4 and the lower one is γ_L/μ^4. The classical buckling pressure for a complete spherical shell is given by $\gamma/\mu^4 = 1$. The upper curve is the same as that given by Budiansky and Weinitschke [11]. The lower curve is new except for the values given by Reiss and Keller [3].

The experimental results of Kaplan and Fung are also shown including the postbuckling pressures for oil loading. This loading approaches constant-volume buckling. It can be seen that these postbuckling pressures show much better agreement with the lower stability curve than the initial buckling pressures do with the upper curve.

Concluding Remarks

The comparison between the experimental buckling pressures and the theoretical pressures shows that finite-deflection theory for axisymmetric deformations of a perfect shell is inadequate to predict buckling.

Alternate approaches have been proposed to close the gap between theory and experiment. These include considering the effect of initial axisymmetric imperfections or investigating unsymmetrical buckling modes for perfect or imperfect shells.

Budiansky [1] computed the variation in buckling pressure resulting from different amplitudes of a given axisymmetric imperfection shape. These results showed little effect on the buckling pressure.

In the author's opinion, the influence of initial axisymmetric imperfections deserves additional study using imperfection shapes of the form of the deflections calculated on the unstable and postbuckled branches of the perfect shell. One reason for this conclusion is that the disagreement between theory and experiment extends to the pressure-deflection curves. For higher values of μ^2, the experimental curves of Kaplan and Fung for pressure versus center deflection fall well below those of theory and have a much smaller slope at the origin. This indicates that there was appreciable bending deflection long before buckling in these shells. It seems probable that this can be explained by the "membrane rotation" in an imperfect shell using small finite-deflection theory. Preliminary results seem to bear this out.

The possibility of unsymmetrical buckling is by no means excluded for the clamped shell since the compressive circumferential stresses are high compared to the meridional stresses at some points. In the complete sphere, it seems unreasonable to assume unsymmetrical buckling without again introducing the effect of initial imperfections.

The formulation of the problem as a sequence of linear differential equations in terms of the "variational" equations for an assumed solution is general and can be extended to other nonlinear differential equations. The numerical solution used here for the linear differential equations is also general and has some advantages over other computer methods for boundary-value problems. Of course, any suitable method for solving the linear differential equations is applicable.

References

1 B. Budiansky, "Buckling of Clamped Shallow Spherical Shells," Technical Report No. 5, Nonr 1866(02) Harvard University, August, 1959, to appear in *Proceedings of IUTAM Symposium on the Theory of Thin Elastic Shells*, Delft, August, 1959.

2 H. Weinitschke, "On the Stability Problem for Shallow Spherical Shells," *Journal of Mathematics and Physics*, vol. 38, 1960, p. 209.

3 H. B. Keller and E. L. Reiss, "Spherical Cap Snapping," *Journal of the Aero/Space Sciences*, vol. 26, 1959, p. 643.

4 T. von Karman and H. S. Tsien, "The Buckling of Spherical Shells by External Pressure," *Journal of the Aeronautical Sciences*, vol. 7, 1939, p. 368.

5 A. Kaplan and Y. C. Fung, "A Nonlinear Theory of Bending and Buckling of Thin Elastic Shallow Spherical Shells," NACA TN 3212, 1954.

6 E. Reissner, "On Axisymmetrical Deformations of Thin Shells of Revolution," *Proceedings Third Symposium in Applied Mathematics*, McGraw-Hill Book Company, Inc., New York, N. Y., 1950, pp. 27–52.

7 H. J. Weinitschke, "On the Nonlinear Theory of Shallow Spherical Shells," *Journal of the Society of Industrial and Applied Mathematics*, vol. 6, 1958, p. 209.

8 R. M. Simons, "A Power Series Solution of the Nonlinear Equations for Axisymmetric Bending of Shallow Spherical Shells," *Journal of Mathematics and Physics*, vol. 35, 1956, p. 164.

9 R. R. Archer, "Stability Limits for a Clamped Spherical Shell Segment Under Uniform Pressure," *Quarterly of Applied Mathematics*, vol. 15, 1958, p. 355.

10 G. A. Thurston, "A Numerical Solution for Thin Conical Shells Under Asymmetrical Loads," *Proceedings of The Fourth Midwestern Conference on Solid Mechanics*, The University of Texas, Austin, Texas, September, 1959, p. 171.

11 B. Budiansky and H. J. Weinitschke, "On Axisymmetrical Buckling of Clamped, Shallow, Spherical Shells," *Journal of the Aero/Space Sciences*, vol. 27, 1960, p. 545.

T. K. CAUGHEY
Professor,
Division of Engineering,
California Institute of Technology,
Pasadena, Calif.

H. J. STUMPF
California Institute of Technology,
Pasadena, Calif.

Transient Response of a Dynamic System Under Random Excitation

This paper analyzes the transient response of a simple harmonic oscillator to a stationary random input having an arbitrary power spectrum. The application of the results of this analysis to the response of structures to strong-motion earthquakes is discussed.

A NUMBER of recent papers [1, 2, 3, 4][1] have considered the response of dynamic systems to random excitation. With the exception of Bogdanoff's paper [3], the analysis has been confined to the stationary aspects of the motion. The study of the transient motion of a system under random excitation has a history extending over the past 30 years. The first solution to the problem was given by Uhlenbeck and Ornstein [5] in 1930, and in a later paper Uhlenbeck and Wang [6] solved the same problem using the Fokker-Planck equation for the system. Housner [7] was the first to treat the earthquake problem as an example of random excitation; unfortunately, he did not publish his results. The most recent paper on the subject is that of Bogdanoff and Goldberg [3] who solved exactly the same problem as Uhlenbeck and Ornstein [5]. With the exception of Housner [7], all these authors assumed the input process to be white; this assumption radically simplifies the mathematical problems of analysis.

The purpose of this paper is to analyze the transient motion of a single-degree-of-freedom oscillator subjected to a stationary random input having an arbitrary power spectrum. An approximate solution is presented for the case of small damping and a smooth power spectrum having no sharp peaks. The application of the results of this analysis to determining the response of structures to strong motion earthquakes is discussed.

Analysis

Consider a simple harmonic oscillator acted upon by a random force. The equation of motion is

$$m\ddot{x} + \beta\dot{x} + kx = m\alpha(t) \tag{1}$$

where
m = mass of oscillator
β = constant of viscous damper
k = linear spring constant
$m\alpha(t)$ = external force acting on mass (2)

Divide both sides of (1) by m:
Let

$$\beta/m = 2\zeta\omega_0$$
$$k/m = \omega_0^2 \tag{3}$$

Equation (1) becomes

$$\ddot{x} + 2\omega_0\zeta\dot{x} + \omega_0^2 x = \alpha(t) \tag{4}$$

In the analysis which follows, it will be assumed that:

(a) $\alpha(t)$ is stationary
(b) $\alpha(t)$ is Gaussian
(c) $\alpha(t)$ has mean zero
(d) $\alpha(t)$ has power spectrum $\phi(\omega)$ (5)

Let $h(t)$ be the impulse response of the system:

$$h(t) = \frac{e^{-\zeta\omega t}}{\omega_1}\sin\omega_1 t, \quad t \geq 0$$
$$= 0 \qquad\qquad t < 0 \tag{6}$$

where

$$\omega_1 = \omega_0(1 - \zeta^2)^{1/2}$$

Only the case where $\zeta < 1$ will be considered, since it is the case of most interest.

If the initial conditions are

$$x(0) = a; \quad \dot{x}(0) = b \tag{7}$$

Then, if $\alpha(t)$ is assumed to be mean square continuous, a valid solution of (4) is

$$x(t) = ae^{-\zeta\omega t}\left[\cos\omega_1 t + \frac{\zeta\omega_0}{\omega_1}\sin\omega_1 t\right] + \frac{b}{\omega_1}e^{-\zeta\omega t}\sin\omega_1 t + \int_0^t h(t-\tau)\alpha(\tau)d\tau \tag{8}$$

Since it was assumed that $\alpha(t)$ was Gaussian, and since the system is linear, it may be shown that $x(t)$ is Gaussian also [6, 9]. For a Gaussian process, only the mean and the variance are required to characterize the complete process. It is therefore necessary to compute the stochastic, or ensemble average, $\langle x(t)\rangle$, and the variance $\sigma^2(t)$ to characterize the $x(t)$ process. Once these two functions of time are known, the probabilistic description of $x(t)$ is known.

Stochastic Average of $x(t)$

The stochastic average of $x(t)$ is obtained by taking the stochastic average of equation (8).

$$\therefore \mu(t) = \langle x(t)\rangle = ae^{-\omega\zeta t}\left[\cos\omega_1 t + \frac{\omega_0\zeta}{\omega_1}\sin\omega_1 t\right] + \frac{b}{\omega_1}e^{-\omega\zeta t}\sin\omega_1 t + \int_0^t h(t-\tau)\langle\alpha(\tau)\rangle d\tau \tag{9}$$

[1] Numbers in brackets designate References at the end of the paper.

Presented at the West Coast Conference of the Applied Mechanics Division, Seattle, Wash., August 28–30, 1961, of THE AMERICAN SOCIETY OF MECHANICAL ENGINEERS.

Discussion of this paper should be addressed to the Editorial Department, ASME, United Engineering Center, 345 East 47th Street, New York, 17, N. Y. and will be accepted until January 10, 1962. Discussion received after the closing date will be returned. Manuscript received by ASME Applied Mechanics Division, September 21, 1960; revised draft, March 2, 1961. Paper No. 61—APMW-20.

But by assumption (5c), $\langle \alpha(\tau) \rangle = 0$. Hence,

$$\mu(t) = \langle x(t) \rangle = ae^{-\omega_0 \zeta t} \left[\cos \omega_1 t + \frac{\omega_0 \zeta}{\omega_1} \sin \omega_1 t \right] + \frac{b}{\omega_1} e^{-\omega_0 \zeta t} \sin \omega_1 t \quad (10)$$

It is seen from the foregoing that the stochastic mean of the motion depends only on the initial conditions.

Variance of $x(t)$

The variance of $x(t)$ is defined to be

$$\sigma^2(t) = \langle [x(t) - \mu(t)]^2 \rangle \quad (11)$$

Using equations (8) and (10) and substituting in (11),

$$\sigma^2(t) = \int_0^t \int_0^t h(t-\tau)h(t-\tau') \langle \alpha(\tau)\alpha(\tau') \rangle d\tau \, d\tau' \quad (12)$$

The quantity $\langle \alpha(\tau)\ \alpha(\tau') \rangle$ is by definition, $R_\alpha(\tau,\tau')$, the autocorrelation function for $\alpha(\tau)$. Since it was assumed in (5a) that $\alpha(t)$ was stationary, then

$$\langle \alpha(\tau)\ \alpha(\tau') \rangle = R_\alpha(\tau,\tau') = R_\alpha(\tau - \tau') \quad (13)$$

The autocorrelation function for a stationary process depends only on the time difference $(\tau - \tau')$, and not on τ and τ' individually. The simplest problem to treat is that of a completely random function, for which $R(\tau - \tau')$ is given simply by $2D\ \delta(\tau - \tau')$. Such a process has a white power spectrum with a spectral density $4D$/cycle. Although such a process allows considerable mathematical simplification, it is a process which can never be realized physically since it would involve infinite mean-squared power. All physically realizable processes involve power spectra which go to zero for sufficiently high frequencies. If $\phi(\omega)$ is the power spectrum under consideration, the requirement of physical realizability is that

$$\int_0^\infty \phi(\omega) d\omega < \infty \quad (14)$$

For a stationary random process, the autocorrelation function may be obtained from the power spectrum or vice versa, since they form a Fourier cosine pair (6).

The autocorrelation function $R_\alpha(\tau - \tau')$ is given by

$$R_\alpha(\tau - \tau') = \int_0^\infty \phi(\omega) \cos \omega(\tau - \tau') d\omega \quad (15)$$

where $\phi(\omega)$ is the power spectrum of $\alpha(t)$. Substituting (15) into (12), the variance is given by

$$\sigma^2(t) = \int_0^t \int_0^t \int_0^\infty \phi(\omega) \cos \omega(\tau - \tau') h(t-\tau) h(t-\tau') d\omega d\tau d\tau' \quad (16)$$

Since the integrals involved in (16) are convergent, the order of integration may be reversed. Using the expression for $h(t)$ given in equation (6),

$$\sigma^2(t) = \int_0^\infty \frac{\phi(\omega)}{\omega_1^2} \int_0^t \int_0^t e^{-\zeta\omega(2t-\tau-\tau')} \sin \omega_1(t-\tau) \sin \omega_1(t-\tau') \cos \omega(\tau - \tau') d\omega d\tau \, d\tau' \quad (17)$$

The double integral on t occurring in (17) may be evaluated after some tedious algebra, giving

$$\sigma^2(t) = \int_0^\infty \frac{\phi(\omega)}{|z(\omega)|^2} \left[1 + e^{-2\omega_0\zeta t} \left\{ 1 + \frac{2\omega_0}{\omega_1} \zeta \sin \omega_1 t \cos \omega_1 t - e^{\omega_0 \zeta t} \left(2 \cos \omega_1 t + \frac{2\omega_0 \zeta}{\omega_1} \sin \omega_1 t \right) \cos \omega t - e^{\omega_0 \zeta t} \frac{2\omega}{\omega_1} \sin \omega_1 t \sin \omega t + \frac{(\omega_0\zeta)^2 - \omega_1^2 + \omega^2}{\omega_1^2} \sin^2 \omega_1 t \right\} \right] d\omega \quad (18)$$

where

$$|z(\omega)|^2 = (\omega_0^2 - \omega^2)^2 + (2\omega\omega_0\zeta)^2 \quad (19)$$

Equation (18) exhibits some interesting properties. They are:
(1) As $t \to 0$

$$\sigma^2(t) \to 0, \text{ as would be expected;}$$

(2) As $t \to \infty$

$$\sigma^2(t) \to \int_0^\infty \frac{\phi(\omega)d\omega}{|z(\omega)|^2},$$ the result which would be predicted from generalized harmonic analysis for the stationary problem;

(3) If $\phi(\omega)$ is set equal to $(2D/\pi)$ and the integral (18) evaluated by contour integration, then

$$\sigma_x^2(t) = \frac{D}{2\zeta\omega_0^3} \left[1 - \frac{e^{-2\omega_0\zeta t}}{\omega_1^2} \left\{ \omega_1^2 + \omega_0\omega_1\zeta \sin 2\omega_1 t + \frac{(2\omega_0\zeta)^2}{2} \sin^2 \omega_1 t \right\} \right] \quad (20)$$

As would be expected, this result is identical with the result obtained by Uhlenbeck [5] for a white process.

Approximate Evaluation of Equation (18)

For any analytic function $\phi(\omega)$, equation (18) can be evaluated by contour integration. If $\phi(\omega)$ is given numerically, then equation (18) can be evaluated numerically. However, if $\phi(\omega)$ is a smooth function of ω, having no sharp peaks, and ζ is small, then a very good approximation may be obtained in the following way: If ζ is small, the function $1/|z(\omega)|^2$ is sharply peaked at $\omega = \omega_0$; therefore, the main contribution to the integral comes from the region around $\omega = \omega_0$. By analogy with Laplace's method of evaluating integrals, equation (18) may be approximated by

$$\sigma_x^2(t) \simeq \phi(\omega_0) \left[\int_0^\infty \frac{1}{|z(\omega)|^2} \left[1 + e^{-2\omega_0\zeta t} \left\{ 1 + \frac{2\omega_0\zeta}{\omega_1} \sin \omega_1 t \cos \omega_1 t - e^{\omega_0\zeta t} \left(2 \cos \omega_1 t + \frac{2\omega_0\zeta}{\omega_1} \sin \omega_1 t \right) \cos \omega t - e^{\omega_0\zeta t} (\sin \omega_1 t \sin \omega t) \left(\frac{2\omega}{\omega_1} \right) + \frac{(\omega_0\zeta)^2 - \omega_1^2 + \omega^2}{\omega_1^2} \sin^2 \omega_1 t \right\} \right] d\omega \right] \quad (21)$$

Evaluating the integral in (21) by contour integration,

$$\sigma_x^2(t) \simeq \frac{\pi\phi(\omega_0)}{4\zeta\omega_0^3} \left[1 - \frac{e^{-2\omega_0\zeta t}}{\omega_1^2} \left\{ \omega_1^2 + \frac{(2\omega_0\zeta)^2}{2} \sin^2 \omega_1 t + \omega_0\omega_1\zeta \sin 2\omega_1 t \right\} \right] \quad (22)$$

Zero Damped Oscillator

Of special interest is the case when ζ is zero. The results for this case can be obtained from equation (22) by a limiting process:

$$\sigma_x^2(t)_{\zeta=0} = \lim_{\zeta\to 0} \frac{\pi}{4}\frac{\phi(\omega_0)}{\zeta\omega_0^3}\left[1 - \frac{e^{-2\omega_0\zeta t}}{\omega_1^2}\left\{\omega_1^2 + \frac{(2\omega_0\zeta)^2}{2}\sin^2\omega_1 t + \omega_0\omega_1\zeta \sin 2\omega_1 t\right\}\right]$$

$$= \frac{\pi}{4}\frac{\phi(\omega_0)}{\omega_0^3}\lim_{\zeta\to 0}\left[\{1 - (1 - 2\omega_0\zeta t)(1 + \zeta \sin 2\omega_0 t) + 0[(\zeta t)^2]\}\zeta^{-1}\right] \quad (23)$$

$$\therefore \sigma_x^2(t) \simeq \frac{\pi}{4}\frac{\phi(\omega_0)}{\omega_0^3}[2\omega_0 t - \sin 2\omega_0 t] \quad (24)$$

Results

For convenience, equation (22) may be written

$$\frac{2\sigma_x^2}{\pi}\frac{\omega_0^3}{\phi(\omega_0)} \simeq \frac{1}{2\zeta}\left[1 - e^{-2\zeta\theta}\left\{1 + \frac{2\zeta^2}{1-\zeta^2}\sin^2(1-\zeta^2)^{1/2}\theta + \frac{\zeta}{(1-\zeta^2)^{1/2}}\sin 2(1-\zeta^2)^{1/2}\theta\right\}\right] \quad (25)$$

where $\theta = \omega_0 t$.

Plots of equation (25) are shown in Fig. 1 for $\zeta = 0$, 0.025, 0.05, and 0.10. It will be observed that for $\zeta = 0.1$, the system approaches stationarity in roughly three cycles. Hence, even though the output process is nonstationary, only a slight error is made by treating it as a stationary process, provided the stationary input is applied for a sufficiently large number of cycles.

Distribution Functions for $x(t)$

As was pointed out previously, $x(t)$ is Gaussian if $\alpha(t)$ is Gaussian. Hence the probability that x lies in the interval x to $x + dx$ is given by

$$p(x)dx = \frac{1}{(2\pi)^{1/2}\sigma(t)}\exp\left\{-\frac{(x-\mu(t))^2}{2\sigma^2(t)}\right\}dx \quad (26)$$

where

$$\mu(t) = \langle x(t)\rangle$$
$$\sigma^2(t) = \langle[x(t) - \mu(t)]^2\rangle \quad (27)$$

The stochastic average $\mu(t)$ is given by equation (9), and depends only on the initial velocity and displacement. The variance $\sigma^2(t)$ is given by equation (18), and is independent of the initial conditions.

Probability of Exceeding a Given Value

The probability that $x(t)$ exceeds a given value, $k\sigma$, is obtained by integration of equation (26):

$$P(x > k\sigma) = \int_{k\sigma}^{\infty}\frac{1}{(2\pi)^{1/2}\sigma}\exp\left\{-\frac{(x-\mu)^2}{2\sigma^2}\right\}dx \quad (28)$$

$$= \tfrac{1}{2}\left[1 - \operatorname{erf}\left\{\frac{k\sigma - \mu}{2^{1/2}\sigma}\right\}\right] \quad (29)$$

where erf is the error function.

For some physical processes, for example brittle failure, the sign of $x(t)$ is unimportant. The probability that the modulus of $x(t)$, $|x|$, exceeds a given value, $k\sigma$, is obtained by integration of equation (26):

$$\therefore P(|x| > k\sigma) = \int_{k\sigma}^{\infty}\frac{1}{(2\pi)^{1/2}\sigma}\exp\left\{-\frac{(x-\mu)^2}{2\sigma^2}\right\}dx + \int_{-\infty}^{-k\sigma}\frac{1}{(2\pi)^{1/2}\sigma}\exp\left\{-\frac{(x-\mu)^2}{2\sigma^2}\right\}dx \quad (30)$$

$$\therefore P(|x| > k\sigma) = 1 - \tfrac{1}{2}\left\{\operatorname{erf}\frac{(k\sigma-\mu)}{2^{1/2}\sigma} + \operatorname{erf}\frac{(k\sigma+\mu)}{2^{1/2}\sigma}\right\} \quad (31)$$

In the special case of a system starting from rest, the probability that x exceeds $k\sigma$ is given by

$$P(|x| > k\sigma) = \left(1 - \operatorname{erf}\frac{k}{2^{1/2}}\right) \quad (32)$$

It is interesting to note that the right-hand side of equation (32) does not involve time, even though x and σ are both functions of time. This is in contrast to the situation in equations (29) and (31), where the right-hand side of the equations is also a function of time.

Application of Results to Strong Motion Earthquakes

An intensive study of strong motion earthquakes has been

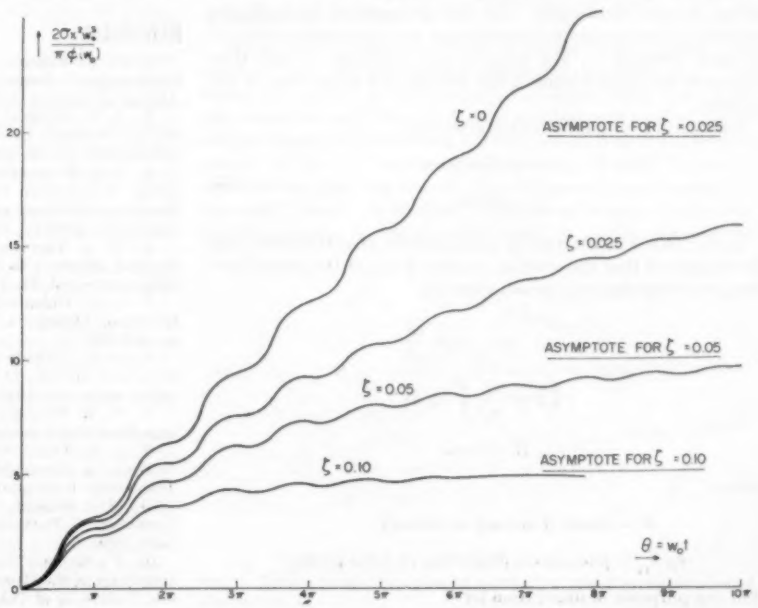

Fig. 1 Transient response of a dynamic system under random excitation

made at the California Institute of Technology [8] over the past 25 years. As a result of these studies, the following statements may be made:

1 The duration of strong motion earthquakes is in direct relation to their intensity. The stronger the earthquake, the longer it lasts.

2 The strong earthquakes tend to be quite random in nature. The weak ones tend to be more deterministic.

3 While no earthquake is completely stationary, since it must first build up, and must eventually die out, the very strong earthquakes exhibit long portions of quasi-stationary behavior.

4 No earthquake exhibits a white-power spectrum. All earthquakes so far analyzed show a peaked power spectrum falling off sharply at high frequencies.

5 Unfortunately, the amount of data on strong motion earthquakes is quite limited, so it has not been possible to obtain anything like a complete statistical description of earthquakes. However, the available data show that, at least out to the 3σ point, the stronger earthquakes exhibit Gaussian statistics with mean zero.

Applying these statements to the foregoing analysis we see that:

(*a*) The results of the analysis may be applied with some confidence to the very strong, long-duration earthquakes, since the analysis did not assume a white process.

(*b*) For the shorter earthquakes, some attempt should be made to account for the nonstationarity of the input process. This has been done for a particular class of inputs by Stumpf [9] in his Doctoral thesis.

(*c*) Some caution must be exercised in applying the distribution function for the displacement in the case of earthquakes. It is well known that the probability of exceeding a specified value is quite sensitive to the tail of the distribution function, and this is the very area where our ignorance is greatest in the earthquake problem.

Example

As an illustration of the application of the foregoing theory to earthquakes, consider the response of a single-story building to a strong motion earthquake. For the purposes of analysis, the building will be treated as a roof of mass m, supported by columns of shear stiffness k. The variable x in equation (1) will then represent the displacement of the roof relative to the base of the building.

Let ω_0 and ζ in equation (4) be given by

$$\left.\begin{aligned}\omega_0 &= 5 \text{ rad/sec}\\ \zeta &= 0.025\end{aligned}\right\} \tag{33}$$

Kanai [10] has analyzed a large number of earthquakes and has suggested that the spectral density, $\phi(\omega)$, of the ground motion of earthquakes may be expressed by

$$\phi(\omega) = \frac{1 + 4h_g^2 \dfrac{\omega^2}{\nu_g^2}}{\left(1 - \dfrac{\omega^2}{\nu_g^2}\right)^2 + 4h_g^2 \dfrac{\omega^2}{\nu_g^2}} B \tag{34}$$

$$B = \text{const}$$

where

B = spectral density at bedrock

ν_g, h_g = parameters depending on local geology

For the purposes of illustration let

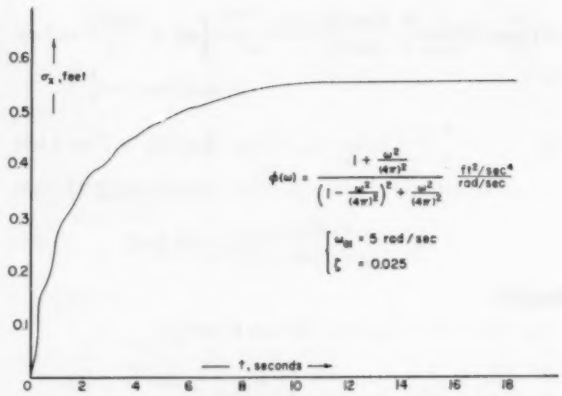

Fig. 2 Transient response of building to random earthquake

$$\left.\begin{aligned}h_g &= 0.5\\ \nu_g &= 4\pi\\ B &= 1 \text{ ft}^2/\text{sec}^4/\text{rad/sec}\end{aligned}\right\} \tag{35}$$

These values were so chosen that $\phi(\omega)$ approximates that for the El Centro, Calif., earthquake of May 1940 [8], which lasted for 25 sec. Using equation (22), the root-mean-squared displacement, $\sigma_x(t)$, is given by

$$\sigma_x(t) \simeq \left[\left[\frac{\pi\phi(\omega_0)}{4\zeta\omega_0^3}\left\{1 - \frac{e^{-2\omega_0\zeta t}}{\omega_1^2}\left[\omega_1^2 + \frac{(2\omega_0\zeta)^2}{2}\sin^2\omega_1 t + \omega_0\omega_1\zeta \sin 2\omega_1 t\right]\right\}\right]\right]^{1/2} \tag{36}$$

Fig. 2 shows the numerical results of substituting (33), (34), and (35) into (36).

It will be seen that the root-mean-squared displacement σ_x reaches a stationary value of 0.57 ft in roughly 9 sec. Since the earthquake is assumed to last for 25 sec, little error would result in treating the problem as a stationary one.

References

1 A. C. Eringen, "Response of a Tall Building to Random Earthquakes," *Proceedings of the Third U. S. National Congress of Applied Mechanics*, ASME, June, 1958, pp. 141–153.

2 A. C. Eringen, "Response of Beams and Plates to Random Loads," JOURNAL OF APPLIED MECHANICS, vol. 24, TRANS. ASME, vol. 80, 1957, pp. 46–52.

3 J. L. Bogdanoff and J. E. Goldberg, "On the Transient Behavior of a System Under a Random Disturbance," Fourth Mid-Western Conference on Solid Mechanics, The University of Texas, September, 1959, pp. 488–496.

4 W. S. Thomson and M. V. Barton, "The Response of Mechanical Systems to Random Excitation," JOURNAL OF APPLIED MECHANICS, vol. 24, TRANS. ASME, vol. 80, 1957, pp. 248–251.

5 G. E. Uhlenbeck and L. S. Ornstein, "On the Theory of the Brownian Motion, I," *Physical Review*, vol. 36, September, 1930, pp. 823–841.

6 G. E. Uhlenbeck and M. C. Wang, "On the Theory of the Brownian Motion, II," *Reviews of Modern Physics*, vol. 17, nos. 2 and 3, April–July 1945, pp. 323–342.

7 G. W. Housner, "Random Excitation of Vibrating Systems," unpublished manuscript, 1945.

8 J. L. Alford, G. W. Housner, and R. R. Martel, "Spectrum Analysis of Strong-Motion Earthquakes," California Institute of Technology Earthquake Research Laboratory Report, August, 1951.

9 H. J. Stumpf, "Response of Mechanical Systems to Random Excitation," PhD thesis, California Institute of Technology, June, 1960.

10 K. Kanai, "Semi-Empirical Formula for the Seismic Characteristics of the Ground," *Bulletin of the Earthquake Research Institute*, University of Tokyo, Tokyo, Japan, vol. 35, 1957.

On the Stability of Rotation of a Rotor With Rotationally Unsymmetric Inertia and Stiffness Properties

S. H. CRANDALL
Professor,
Department of Mechanical Engineering,
Massachusetts Institute of Technology,
Cambridge, Mass,
Mem. ASME

P. J. BROSENS
Assistant Professor,
Department of Mechanical Engineering,
Massachusetts Institute of Technology,
Cambridge, Mass.

The stability of uniform rotation of a rigid body about a principal axis of inertia is analyzed for the case where there is a diametral inertia inequality and there is an elastic restoring mechanism with a diametral stiffness inequality which rotates with the body. This model is an idealization for systems such as a two-bladed propeller rotating on a flexible shaft whose stiffness characteristics are not rotationally symmetric. It is found that many such systems possess unstable speed ranges. The instability may be due to either type of asymmetry alone or due to the interaction of the two. Quantitative analytical results are obtained which relate the unstable speed range to the gyroscopic coupling, the inertia inequality, the stiffness inequality, and the relative orientation of the principal axes of inertia with respect to the principal axes of stiffness. Three-dimensional stability surfaces are plotted to give a qualitative overview of the interplay of the various parameters.

THE dynamics of a rapidly rotating rotor subjected to transverse elastic restraint constitu s one of the classical problems of applied mechanics. In the simplest models the inertia and stiffness properties are taken to have rotational symmetry, and gyroscopic effects are neglected. More sophisticated models, including either gyroscopic effects or unsymmetrical flexibility of the nonrotating bearing supports or unsymmetrical flexibility of the rotating shaft, are well known.[1] In a remarkable paper presented in 1933, D. M. Smith[2] discussed qualitatively the simultaneous effect of these three items and also included unsymmetrical inertia properties. A quantitative analysis for the case of simultaneous asymmetries of the bearing and shaft flexibilities but without gyroscopic coupling was given by Foote, Poritsky, and Slade[3] in 1943.

Recently the present authors obtained a quantitative solution[4] for the stability problem of a rotor with unsymmetrical inertia properties and unsymmetrical bearing-support flexibilities. The present paper contains a quantitative analysis of the stability problem for a rotor which has unsymmetrical inertia properties and unsymmetrical flexibility of the rotating shaft. We find that many systems of this type possess an unstable speed range which depends on the gyroscopic coupling, the inertia inequality, the stiffness inequality, and the relative orientation of the principal axes of inertia with respect to the principal axes of stiffness. These results are in agreement with the qualitative predictions of Smith.[2] The interplay of the various parameters in determining the unstable speed range is exhibited analytically and graphically. An interesting result is that, for fixed inertia and stiffness inequalities, the unstable speed range is greatest for that orientation of the axes which gives the smallest difference between the zero-speed natural frequencies.

Equations of Motion

We consider a rigid rotor with principal axes of inertia $\xi\eta\zeta$ rotating with uniform angular velocity ω about the axis ζ and study the stability of this motion when linear elastic restraint of the orientation of ζ is provided by massless springs that oppose displacements about the axes a, b which revolve with the rotor as shown in Fig. 1. The diametral moments of inertia I_ξ and I_η need not be equal and the effective stiffnesses k_a and k_b need not be equal. This is an idealized model for systems such as a two-bladed propeller carried on a flat shaft. We study the effect on

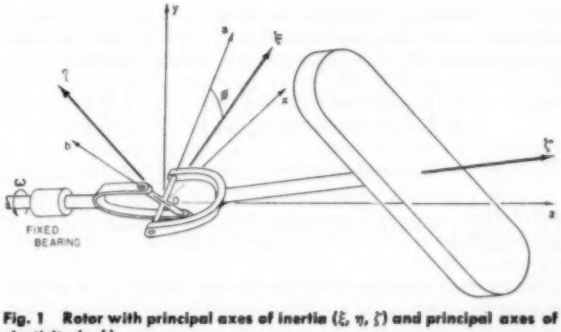

Fig. 1 Rotor with principal axes of inertia (ξ, η, ζ) and principal axes of elasticity (a, b)

[1] See, for example, C. B. Biezeno and R. Grammel, "Engineering Dynamics, Vol. III, Steam Turbines," Blackie and Sons, Limited, London, England, 1954.

[2] D. M. Smith, "The Motion of a Rotor Carried by a Flexible Shaft in Flexible Bearings," *Proceedings of The Royal Society*, London, England, series A, vol. 142, 1933, pp. 92–118.

[3] W. R. Foote, H. Poritsky and J. J. Slade, Jr., "Critical Speeds of a Rotor With Unequal Shaft Flexibilities, Mounted in Bearings of Unequal Flexibility—1," JOURNAL OF APPLIED MECHANICS, vol. 10, TRANS. ASME, vol. 65, 1943, p. A77.

[4] P. J. Brosens and S. H. Crandall, "Whirling of Unsymmetrical Rotors," ASME Paper No. 61—APM-10.

Presented by the Applied Mechanics Division of THE AMERICAN SOCIETY OF MECHANICAL ENGINEERS, at the Tenth International Congress of Applied Mechanics, Stresa, Italy, August 31–September 7, 1960.

Discussion of this paper should be addressed to the Editorial Department, ASME, United Engineering Center, 345 East 47th Street, New York 17, N. Y., and will be accepted until January 10, 1962. Discussion received after closing date will be returned. Manuscript received by ASME Applied Mechanics Division, November 22, 1960.

the stability of the inertia inequality, the stiffness inequality, and the angle ϕ between the principal axes of inertia and the principal axes of stiffness.

The stability of the steady rotation (ξ coinciding with z in Fig. 1) depends on the speed ω and on the following four parameters:

$$\epsilon_i = \frac{I_\xi - I_\eta}{I_\xi + I_\eta} \text{ (inertia inequality)}$$
$$\epsilon_i = \frac{k_a - k_b}{k_a + k_b} \text{ (stiffness inequality)} \quad (1)$$
$$\phi = \text{(angle between principal axes of inertia and stiffness)}$$
$$A = \frac{I_\zeta}{I_\zeta + I_\eta} \text{ (axial inertia term)}$$

The inertia inequality parameter has the range $-1 < \epsilon_i < 1$ and the axial term has the range $0 < A < 1$ but for any real rotor

$$\frac{\epsilon_i}{A} = \frac{\int(\eta^2 - \xi^2)dm}{\int(\eta^2 + \xi^2)dm} \quad (2)$$

and therefore $|\epsilon_i| < A$. Actually, without any loss of generality, we may suppose that $I_\xi \geqslant I_\eta$ and $k_a \geqslant k_b$ and, restrict our considerations to the following ranges:

$$0 \leqslant \epsilon_i < A < 1$$
$$0 \leqslant \epsilon_s < 1 \quad (3)$$
$$0 \leqslant \phi \leqslant \frac{\pi}{2}$$

A straightforward method of obtaining the stability equations is to linearize the general equations of motion for the Hooke's joint obtained by means of Lagrange's equations. Using the displacements θ_a and θ_b about the axes a and b as generalized co-ordinates, the potential and kinetic energies are

$$V = \tfrac{1}{2}k_a\theta_a^2 + \tfrac{1}{2}k_b\theta_b^2$$
$$T = \tfrac{1}{2}(I_\xi\omega_\xi^2 + I_\eta\omega_\eta^2 + I_\eta\omega_\zeta^2) \quad (4)$$

where

$$\omega_\xi = \dot\theta_a \cos\phi - \dot\theta_b \sin\phi \cos\theta_a - \omega(\sin\phi \sin\theta_a \cos\theta_b + \cos\phi \sin\theta_b)$$
$$\omega_\eta = \dot\theta_a \sin\phi + \dot\theta_b \cos\phi \cos\theta_a + \omega(\cos\phi \sin\theta_a \cos\theta_b - \sin\phi \sin\theta_b)$$
$$\omega_\zeta = -\dot\theta_b \sin\theta_a + \omega \cos\theta_a \cos\theta_b \quad (5)$$

Application of Lagrange's equations yields a pair of simultaneous nonlinear second-order differential equations for θ_a and θ_b. After linearization these equations are considerably simplified by introducing the displacements θ_ξ and θ_η shown in Fig. 2, which for small motions are related to θ_a and θ_b by the rotational transformation T_ϕ, here represented in matrix notation:

$$\begin{bmatrix}\theta_a\\ \theta_b\end{bmatrix} = \begin{bmatrix}\cos\phi & \sin\phi\\ -\sin\phi & \cos\phi\end{bmatrix}\begin{bmatrix}\theta_\xi\\ \theta_\eta\end{bmatrix} = T_\phi\begin{bmatrix}\theta_\xi\\ \theta_\eta\end{bmatrix} \quad (6)$$

The resulting linearized equations in θ_ξ and θ_η are

$$\begin{bmatrix}I_\xi & 0\\ 0 & I_\eta\end{bmatrix}\begin{bmatrix}\ddot\theta_\xi\\ \ddot\theta_\eta\end{bmatrix} + \omega(I_\zeta - I_\zeta - I_\eta)\begin{bmatrix}0 & 1\\ -1 & 0\end{bmatrix}\begin{bmatrix}\dot\theta_\xi\\ \dot\theta_\eta\end{bmatrix} + \omega^2\begin{bmatrix}I_\zeta - I_\eta & 0\\ 0 & I_\xi - I_\zeta\end{bmatrix}\begin{bmatrix}\theta_\xi\\ \theta_\eta\end{bmatrix} + T_\phi^{-1}\begin{bmatrix}k_a & 0\\ 0 & k_b\end{bmatrix}T_\phi\begin{bmatrix}\theta_\xi\\ \theta_\eta\end{bmatrix} = 0 \quad (7)$$

These same equations may be obtained directly in a simpler manner by adopting the small-motion relations from the start and writing the torque-angular momentum equations. Thus instead

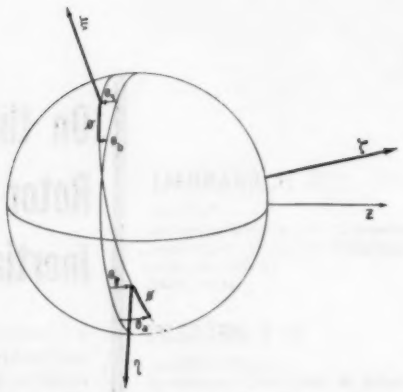

Fig. 2 The small angles θ_ξ, θ_η and θ_a, θ_b are produced when the diametral plane is tipped slightly

of (5) we use the linearized approximations

$$\omega_\xi = \dot\theta_\xi - \omega\theta_\eta$$
$$\omega_\eta = \dot\theta_\eta + \omega\theta_\xi$$
$$\omega_\zeta = \omega \quad (8)$$

in the angular momentum

$$\mathbf{h} = \mathbf{i}_\xi I_\xi\omega_\xi + \mathbf{i}_\eta I_\eta\omega_\eta + \mathbf{i}_\zeta I_\zeta\omega_\zeta \quad (9)$$

along with the differentiation laws

$$\frac{d\mathbf{i}}{dt} = \boldsymbol{\omega} \times \mathbf{i} \quad (10)$$

for the unit vectors to obtain (7) as the statement that the ξ, η components of torque equal the corresponding components of the time rate of change of $\mathbf{h}$.

Stability Analysis

For the stability analysis we assume solutions to (7) in the form

$$\theta_j = c_j e^{\lambda\omega t} \qquad j = \xi, \eta \quad (11)$$

and investigate the conditions under which at least one λ lies in the lower half plane (instability). When (11) is substituted in (7) we obtain an eigenvalue problem for λ. By introducing the parameters (1) and the following "average natural frequency" for diametral oscillations at zero speed

$$\omega_0^2 = \frac{k_a + k_b}{I_\xi + I_\eta} \quad (12)$$

the characteristic equation for the eigenvalue problem can be written as

$$\alpha\lambda^4 - 2\beta\lambda^2 + \gamma = 0 \quad (13)$$

where

$$\alpha = 1 - \epsilon_i^2$$
$$\beta = A^2 - \epsilon_i^2 + (1 - A)^2 + \left(\frac{\omega_0}{\omega}\right)^2(1 - \epsilon_i\epsilon_s\cos 2\phi) \quad (14)$$

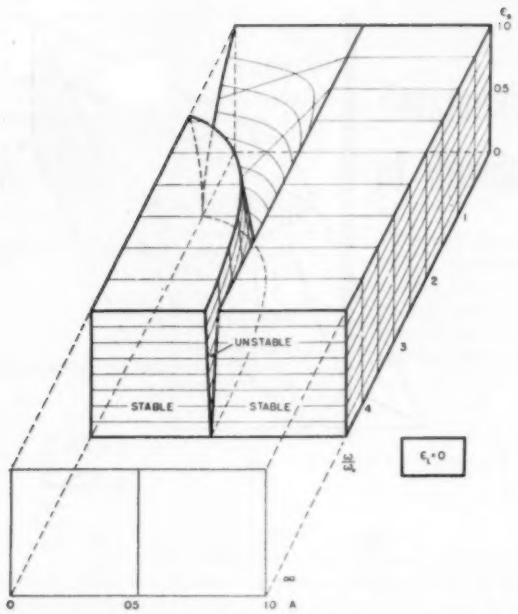

Fig. 3 Stability diagram for rotors with stiffness inequality and gyroscopic coupling but symmetrical inertia properties

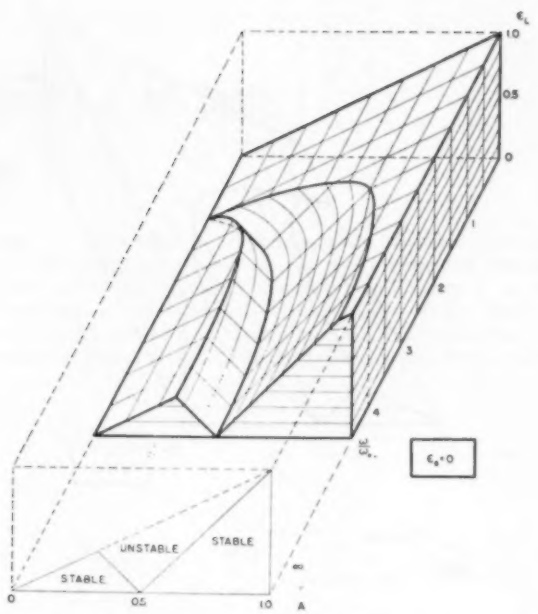

Fig. 4 Stability diagram for rotors with inertia inequality and gyroscopic coupling but symmetrical elastic properties

$$\gamma = \left(\frac{\omega_0}{\omega}\right)^4 (1 - \epsilon_e^2) - 2\left(\frac{\omega_0}{\omega}\right)^2 (1 - 2A + \epsilon_i\epsilon_e \cos 2\phi) + (1 - 2A)^2 - \epsilon_i^2$$

For every combination of parameters there are four roots of (13) for λ. Since $-\lambda$ is always a root if λ is, it follows that for a stable combination the roots of (13) for λ^2 must be real and positive. If α is positive (which according to (3) is in fact the case) the necessary and sufficient conditions for the quadratic (13) to have real and positive roots are

$$\beta > 0, \quad \beta^2 > \alpha\gamma, \quad \gamma > 0 \tag{15}$$

It turns out that the first two of these conditions are satisfied for all speeds when the parameters ϵ_i, ϵ_e, ϕ, and A lie in the ranges (3) and thus that the third condition of (15) is the governing stability criterion. The first condition is clearly true since according to (3) $A^2 - \epsilon_i^2$ is positive and thus β can be considered as the sum of three positive terms. The second condition is less clearly true. The expression $\beta^2 - \alpha\gamma$ is a quadratic in $(\omega_0/\omega)^2$ which is positive at the origin and at infinity. To show that $\beta^2 - \alpha\gamma$ is never negative in between we examine the expression for the zeros of $\beta^2 - \alpha\gamma$ in the $(\omega_0/\omega)^2$ plane and find that the roots can be real and negative or can be complex conjugates in the right half plane but that in the ranges (3) the zeros of $\beta^2 - \alpha\gamma$ are never real and positive and hence the second condition is satisfied for all speeds.

The condition $\gamma > 0$ is thus the governing stability criterion. According to (14) γ is a quadratic in $(\omega_0/\omega)^2$ with the four parameters of (1) entering into the coefficients. Depending on the system elastic and inertia properties which fix the inertia inequality ϵ_i, the stiffness inequality ϵ_e, the angle ϕ between the principal axes of inertia and stiffness and the axial-inertia term A, a rotor can have one of three different behaviors with regard to stability as the speed ω is increased from zero to infinity:

(*a*) The rotor is stable for all speeds.

(*b*) The rotor is stable for low speeds, but is unstable for all speeds above a certain critical speed ω_1.

(*c*) The rotor is stable for low speeds, unstable for a certain range $\omega_1 < \omega < \omega_2$ and then stable for all speeds greater then ω_2.

The critical speeds ω_1 and ω_2 are obtained from the roots of the equation $\gamma = 0$.

$$\left(\frac{\omega}{\omega_0}\right)^2_{1,2} = \frac{1 - \epsilon_e^2}{1 - 2A + \epsilon_i\epsilon_e \cos 2\phi \pm \{[(1 - 2A)\epsilon_e + \epsilon_i \cos 2\phi]^2 + \epsilon_i^2(1 - \epsilon_e^2) \sin^2 2\phi\}^{1/2}} \tag{16}$$

When the combination of parameters gives negative values for both roots of (16) we have case (*a*), when root 1 is positive but root 2 is negative we have case (*b*), and when both roots are positive we have case (*c*).

Discussion of Results

Three-dimensional diagrams portraying the surfaces defined by (16) are shown in Figs. 3, 4, 5, and 6. In Fig. 3 the interaction of axial inertia and elastic anisotropy is shown for the case of no inertia inequality. When $A > 1/2$ the rotor is stable for all speeds. When $A < 1/2$ we have case (*c*) with an unstable speed range which is wider for larger stiffness inequalities.

Fig. 4 shows the interaction of diametral inertia anisotropy with axial inertia for the case of no stiffness inequality. Here in contrast with the preceding figure the "unstable valley" remains wide open as the speed increases. This corresponds to the case (*b*) behavior. At high speeds there is an interesting tie-in here with classical results. As $\omega \to \infty$ the inertia effects become large in comparison with the elastic effects. We thus approach the case of a free rigid rotor rotating about a principal axis of inertia. It is well known that such motion is unstable when the

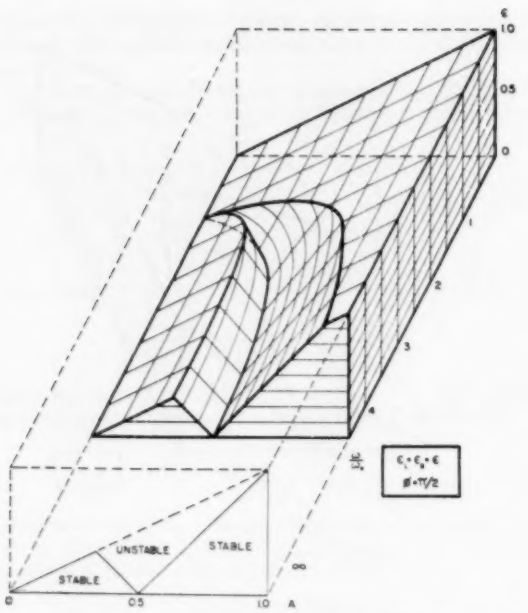

Fig. 5 Stability diagram for rotors with equal elastic and inertia inequalities; maximum inertia axis aligned with minimum stiffness axis

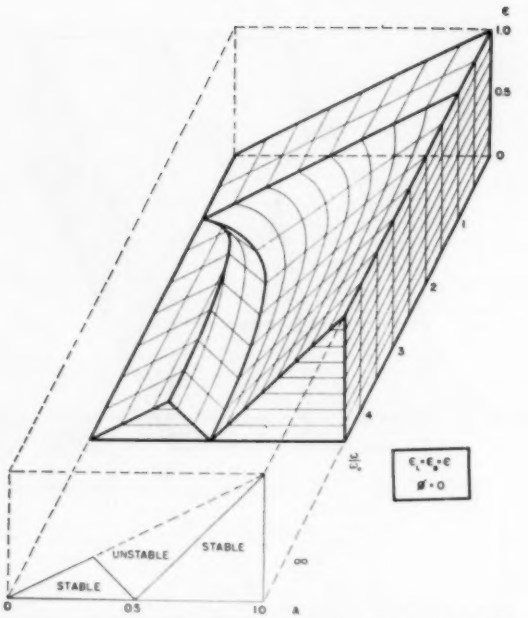

Fig. 6 Stability diagram for rotors with equal elastic and inertia inequalities; maximum inertia axis aligned with maximum stiffness axis

axis of rotation is the axis of the intermediate moment of inertia; i.e., we have instability for rotation about the ζ-axis when

$$I_\eta < I_\zeta < I_\xi \tag{17}$$

which in terms of the parameters (1) is when

$$\tfrac{1}{2}(1 - \epsilon_i) < A < \tfrac{1}{2}(1 + \epsilon_i)$$

This, however, is exactly the unstable triangle shown at $\omega = \infty$ in Fig. 4.

To illustrate the effect of the angle between the principal axes of inertia and the principal axes of stiffness we show in Figs. 5 and 6 the extreme orientations $\phi = \pi/2$ and $\phi = 0$ for the case $\epsilon_e = \epsilon_i$. At high speeds, the elastic effects become negligible and we have in both cases the same limiting behavior as in Fig. 4. At low speeds, however, the stiffness inequality and its relative orientation has a marked effect. Comparison of Figs. 5 and 6 shows that in passing from $\phi = \pi/2$ to $\phi = 0$ with the same magnitudes of inequalities the "unstable valley" has widened; i.e., the untable speed range has been increased.

This result can be shown to be a general one by studying (16). We examine the sign of $d(\omega/\omega_0)^2/d(\cos 2\phi)$ and find that in case (b) the sign is always negative for ω_1 and that in case (c) the signs are always negative for ω_1 and positive for ω_2. Thus the unstable speed range increases as $\cos 2\phi$ increases. A given inertia and stiffness combination has the smallest unstable range when $\phi = \pi/2$; i.e., when the maximum diametral inertia is aligned with the minimum stiffness. This is also the orientation which gives the largest spread between the two natural frequencies of free vibration when $\omega = 0$. This effect of orientation is in marked contrast with the effect of increasing ϵ_e when $\epsilon_i = 0$ (or vice versa) where we obtain simultaneously an increase in the unstable speed range and an increase in the spread between the two natural frequencies for $\omega = 0$.

H. GARNET
Research Engineer,
Grumman Aircraft Engineering Corporation,
Bethpage, L. I., N. Y.
Assoc. Mem. ASME

M. A. GOLDBERG
Research Engineer,
Grumman Aircraft Engineering Corporation,
Bethpage, L. I., N. Y.

V. L. SALERNO[1]
Consulting Engineer,
Grumman Aircraft Engineering Corporation,
Bethpage, L. I., N. Y.
Mem. ASME

Torsional Vibrations of Shells of Revolution

Torsional-vibration modes are uncoupled from the bending and extensional modes in thin shells of revolution. The solution for the uncoupled torsional modes then depends upon a linear second-order differential equation. The governing equation is subsequently solved for the frequencies of a conical shell. A tabulation of the first five frequencies for varying ratios of the terminal radii is presented. These frequencies are identical to those of an annular plate which has the same supports as the conical shell.

THE existence of uncoupled torsional and bending modes of vibration in thin circular cylindrical shells is well known. An analogous situation is present in the circular conical shell[2] and its limiting case, an annular disk. Uncoupling of the torsional and bending modes is demonstrated for arbitrary thin shells of revolution.

Statement of Problem

We consider an element cut from a shell of revolution, Figs. 1 and 2. The curvilinear co-ordinates, α and β, are lines of principal curvature of the middle surface of the undeformed shell. The z-axis is taken normal to this surface. Associated with these orthogonal axes α, β, and z, are the displacements u, v, and w, respectively.

Axisymmetric deformations usually are characterized by the displacements u and w as a function of one co-ordinate only and $v = 0$. Here, however, we stipulate that

$$u = u(\alpha)$$
$$v = v(\alpha) \qquad (1)$$
$$w = w(\alpha)$$

Substituting (1) into the stress-strain[3] and strain-displacement[4] relations yields the specialized stress-strain relations

$$T_\alpha = \frac{E\delta}{1-\mu^2}\left[\frac{1}{A_1}\frac{\partial u}{\partial \alpha} + \frac{\mu}{A_1A_2}\frac{\partial A_2}{\partial \alpha}u + \left(\frac{1}{R_1} + \frac{\mu}{R_2}\right)w\right] \qquad (2a)$$

$$T_\beta = \frac{E\delta}{1-\mu^2}\left[w\left(\frac{1}{R_2} + \frac{\mu}{R_1}\right) + \frac{\mu}{A_1}\frac{\partial u}{\partial \alpha} + \frac{1}{A_1A_2}\frac{\partial A_2}{\partial \alpha}u\right] \qquad (2b)$$

$$T_{\alpha\beta} = T_{\beta\alpha} = \frac{E\delta}{2(1+\mu)}\left[\frac{A_2}{A_1}\frac{\partial}{\partial \alpha}\left(\frac{v}{A_2}\right)\right] \qquad (2c)$$

$$M_\alpha = -\frac{E\delta^3}{12(1-\mu^2)}\left[\frac{1}{A_1}\frac{\partial}{\partial \alpha}\left\{\frac{1}{A_1}\frac{\partial w}{\partial \alpha} - \frac{u}{R_1}\right\} + \frac{\mu}{A_1A_2}\frac{\partial A_2}{\partial \alpha}\left\{\frac{1}{A_1}\frac{\partial w}{\partial \alpha} - \frac{u}{R_1}\right\}\right] \qquad (2d)$$

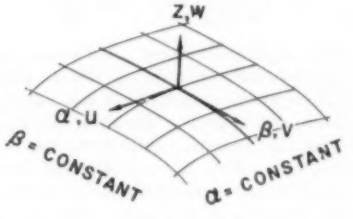

Fig. 1 Co-ordinate notation

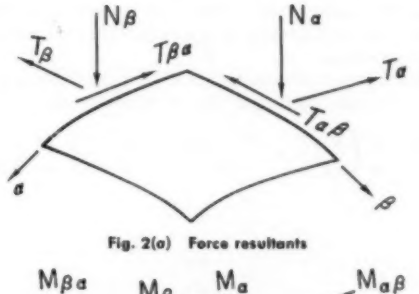

Fig. 2(a) Force resultants

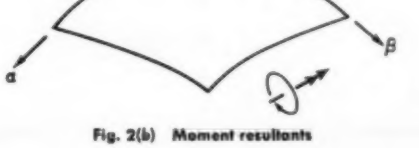

Fig. 2(b) Moment resultants

[1] Also, Dean, School of Engineering and Science, Fairleigh Dickinson University, Teaneck, N. J.

[2] The problem considered here arose during the course of a doctoral dissertation at the Polytechnic Institute of Brooklyn, conducted by H. Garnet, under the supervision of Prof. Joseph Kempner.

[3] V. V. Novozhilov, "The Theory of Thin Shells," P. Noordhoff Limited, Groningen, Netherlands, 1959, p. 52.

[4] Ibid., p. 24.

Contributed by the Applied Mechanics Division and presented at the Winter Annual Meeting, New York, N. Y., November 26–December 1, 1961, of THE AMERICAN SOCIETY OF MECHANICAL ENGINEERS.

Discussion of this paper should be addressed to the Editorial Department, ASME, United Engineering Center, 345 East 47th Street, New York 17, N. Y., and will be accepted until January 10, 1962. Discussion received after the closing date will be returned. Manuscript received by ASME Applied Mechanics Division, June 6, 1960. Paper No. 61—WA-6.

$$M_\beta = -\frac{E\delta^3}{12(1-\mu^2)}\left[\frac{1}{A_1A_2}\frac{\partial A_2}{\partial\alpha}\left\{\frac{1}{A_1}\frac{\partial w}{\partial\alpha} - \frac{u}{R_1}\right\} + \frac{\mu}{A_1}\frac{\partial}{\partial\alpha}\left\{\frac{1}{A_1}\frac{\partial w}{\partial\alpha} - \frac{u}{R_1}\right\}\right] \quad (2e)$$

$$M_{\alpha\beta} = \frac{E\delta^3}{12(1+\mu)}\frac{A_2}{A_1R_2}\frac{\partial}{\partial\alpha}\left(\frac{v}{A_2}\right) \quad (2f)$$

In the foregoing, δ is the thickness of the shell and μ is Poisson's ratio. The parameters A_1 and A_2 are metric coefficients, given in the usual form

$$ds^2 = A_1^2d\alpha^2 + A_2^2d\beta^2 \quad (3)$$

Also R_1 and R_2 are the principal radii of curvature.

Substituting equations (2) into the force and moment equations of equilibrium[3] we confirm that (1) describes a possible displacement field subject to the added restriction that the body-distributed forces must depend upon α only. Replacing the body forces by the inertia terms in the equations of equilibrium and neglecting the terms N_1/R_i and N_2/R_2, we have, letting ρ equal the mass density per unit thickness:

$$\frac{1}{A_1A_2}\left[(T_\alpha - T_\beta)\frac{\partial A_2}{\partial\alpha} + A_2\frac{\partial T_1}{\partial\alpha}\right] - \rho\delta\frac{\partial^2u}{\partial t^2} = 0 \quad (4a)$$

$$\frac{1}{A_1A_2^2}\frac{\partial(A_2^2T_{\alpha\beta})}{\partial\alpha} - \rho\delta\frac{\partial^2v}{\partial t^2} = 0 \quad (4b)$$

$$\frac{1}{A_1A_2}\frac{\partial(A_2N_\alpha)}{\partial\alpha} - \frac{T_\alpha}{R_1} - \frac{T_\beta}{R_2} - \rho\delta\frac{\partial^2w}{\partial t^2} = 0 \quad (4c)$$

$$\frac{1}{A_1A_2^2}\frac{\partial(A_2^2M_{\alpha\beta})}{\partial\alpha} = N_\beta \quad (4d)$$

$$\frac{1}{A_1A_2}\left[(M_\alpha - M_\beta)\frac{\partial A_2}{\partial\alpha} + A_2\frac{\partial M_\alpha}{\partial\alpha}\right] = N_\alpha \quad (4e)$$

where N_α is a function of u and w only and N_β depends on v alone. The first three equations in the foregoing are the conditions for force equilibrium in the α, β, and z-directions, respectively. The transverse shear N_α, appearing in (4c), may be eliminated by using the moment equilibrium equation (4e). Attention may then be confined to (4a), (4b), and (4c). Examining equations (4a, b, c) and recalling the stress-strain relations (2) we note that (4b) depends upon v only. The two remaining equations are functions of u and w only. Hence for shells of revolution the torsional mode of vibration is uncoupled from the bending and extensional modes.

We now restrict our attention to the torsional modes described by (4b). To this end we put (2c) in (4b) to obtain

$$\frac{\partial}{\partial\alpha}\left[\frac{A_2^3}{A_1}\frac{\partial}{\partial\alpha}\left(\frac{v}{A_2}\right)\right] = \frac{2(1+\mu)\rho}{E}A_1^2\left(\frac{A_2^3}{A_1}\right)\frac{\partial^2}{\partial t^2}\left(\frac{v}{A_2}\right) \quad (5a)$$

Letting

$$f(\alpha) = \frac{A_2^3}{A_1}$$

$$V = \frac{v}{A_2} \quad (5b)$$

$$\lambda^2 = \frac{2(1+\mu)\rho}{E}$$

we have

[3] Novoshilov,[2] p. 36, equations (7.4), and p. 38, equations (7.8).

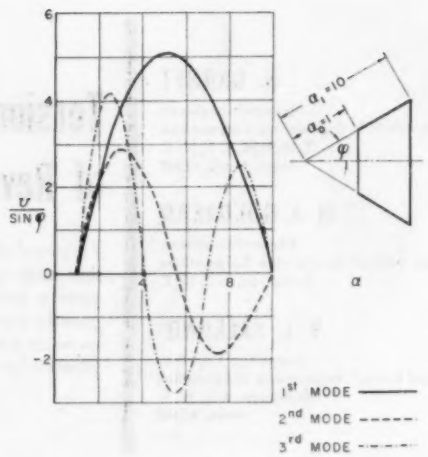

Fig. 3 Torsional mode shapes for a conical shell

Table 1

η	1st Root (η-1)ψ	2nd Root (η-1)ψ	3rd Root (η-1)ψ	4th Root (η-1)ψ	5th Root (η-1)ψ
1.0	3.1416	6.2832	9.4248	12.5664	15.7080
1.1	3.1427	6.2837	9.4251	12.5666	15.7082
1.2	3.1455	6.2852	9.4261	12.5674	15.7088
1.3	3.1498	6.2873	9.4275	12.5684	15.7096
1.4	3.1550	6.2900	9.4293	12.5698	15.7107
1.5	3.1609	6.2931	9.4314	12.5713	15.7119
1.6	3.1675	6.2965	9.4337	12.5731	15.7133
1.8	3.182	6.304	9.439	12.577	15.716
2.0	3.197	6.312	9.444	12.581	15.720
2.5	3.235	6.335	9.460	12.593	15.729
3.0	3.271	6.357	9.476	12.605	15.739
3.5	3.305	6.381	9.493	12.619	15.750
4.0	3.336	6.403	9.509	12.631	15.760
5	3.389	6.445	9.541	12.657	15.782
6	3.432	6.482	9.572	12.682	15.802
8	3.498	6.546	9.626	12.728	15.842
10	3.547	6.598	9.673	12.770	15.879
12	3.583	6.639	9.714	12.807	15.913
14	3.611	6.674	9.749	12.840	15.943
16	3.634	6.704	9.780	12.870	15.971
18	3.652	6.728	9.806	12.896	15.997
20	3.667	6.749	9.830	12.920	16.020
25	3.696	6.790	9.88	12.97	16.07
30	3.717	6.820	9.91	13.01	16.11
35	3.732	6.844	9.94	13.04	16.14
40	3.743	6.861	9.96	13.06	16.17
45	3.752	6.875	9.98	13.09	16.19
50	3.760	6.887	9.99	13.10	16.21

$$\frac{\partial}{\partial\alpha}\left[f(\alpha)\frac{\partial V}{\partial\alpha}\right] = A_1^2\lambda^2f(\alpha)\frac{\partial^2V}{\partial t^2} \quad (6)$$

The variable V appears to be an efficient parameter, since the boundary conditions on v also depend on v/A_2 or V. If we assume V in the form

$$V = X(\alpha)e^{ipt} \quad (7)$$

equation (6) reduces to the Sturm-Liouville equation

$$\frac{d}{d\alpha}\left[f(\alpha)\frac{dX}{d\alpha}\right] + A_1^2\lambda^2p^2f(\alpha)X = 0 \quad (8)$$

The boundary conditions are either

$$V = V_0; \text{ at } \alpha = \alpha_0; \text{ restrained edge} \tag{9a}$$

or from (2c)

$$\frac{E\delta}{2(1+\mu)}\left(\frac{A_2}{A_1}\right)\frac{\partial V}{\partial \alpha} = (T_{\alpha\beta})_0; \text{ at } \alpha = \alpha_0; \text{ loaded edge} \tag{9b}$$

Conical shell. Equation (8) will now be solved for the torsional vibrations of a conical shell fixed at both ends. Here

$$A_1 = 1$$

$$A_2 = \alpha \sin \varphi, \varphi = \text{const}; \text{ semivertex angle of cone} \tag{10a}$$

$$\alpha_0 \leq \alpha \leq \alpha_1; \ \alpha_0 > 0$$

Then from (5b)

$$f(\alpha) = \alpha^3 \sin^2 \varphi \tag{10b}$$

and (8) becomes

$$\alpha \frac{d^2X}{d\alpha^2} + 3\frac{dX}{d\alpha} + \lambda^2 p^2 \alpha X = 0 \tag{10c}$$

Equation (10c) is Bessel's equation and has the solution[6]

$$X = \frac{1}{\alpha}\left[C_1 J_1(\lambda p \alpha) + C_2 Y_1(\lambda p \alpha)\right] \tag{11}$$

where C_1 and C_2 are arbitrary constants. At a fixed end (9a),

$$X(\alpha) = 0 \tag{12}$$

It is to be noted that equation (10c) is independent of the semivertex angle φ of the cone. Consequently, equation (10c) is also the controlling equation for the torsional vibration of a flat annulus. Hence the solution obtained for the cone is valid for the annular disk.

From (11) and (12), the characteristic equation for the frequencies of the cone p is

$$J_1(\psi)Y_1(\psi\eta) - J_1(\psi\eta)Y_1(\psi) = 0 \tag{13}$$

where

$$\psi = \lambda p \alpha_0, \quad \text{and} \quad \eta = \alpha_1/\alpha_0$$

This equation has an infinite number of roots. The first five have been tabulated by Dwight[7] and are reproduced in Table 1 for values of η from 1 to 50. The mode shapes associated with the first three frequencies for the case $\eta = 10$ are shown in Fig. 3, where $v/\sin\varphi$ is plotted to show the variation of the displacement v along the meridional co-ordinate α.

Acknowledgments

The authors wish to acknowledge the assistance rendered by Mrs. Mildred Sudwischer in typing, Mr. George Clark in editorial matters, and Miss Catherine O'Reagen for preparation of the illustrations.

[6] E. Kamke, "Differentialgleichungen Lösungsmethoden und Lösungen," Chelsea Publishing Company, Bronx, N. Y., 1948, p. 440, equation 2.162 (Ia).

[7] H. B. Dwight, "Table of Roots for Natural Frequencies in Coaxial Type Cavities," *Journal of Mathematics and Physics*, vol. 27, 1948, pp. 84–89.

T. R. KANE[1]
Professor of Engineering Mechanics,
Stanford University,
Stanford, Calif.
Mem. ASME

Dynamics of Nonholonomic Systems

A general method for obtaining the differential equations governing motions of a class of nonholonomic systems is presented. Several supplementary theorems are stated, and the use of the method is illustrated by means of two examples.

Kinematics

Consider a dynamical system S whose configuration in a Newtonian reference frame R^* can be specified by n generalized co-ordinates q_r $(r = 1, \ldots, n)$ and which is subject to constraints such that m nonintegrable differential equations of the form

$$\sum_{r=1}^{n} A_{sr}\dot{q}_r + B_s = 0 \quad (s = 1, \ldots, m) \tag{1}$$

where A_{sr} and B_s $(r = 1, \ldots, n;\ s = 1, \ldots, m)$ are functions of $q_1, \ldots, q_n$, and the time t, must be satisfied throughout every motion. For the sake of brevity, such systems will be called *nonholonomic*, although this term is sometimes taken to have a broader meaning. (Note that the situation described includes, as a special case, holonomic systems; i.e., systems whose generalized co-ordinates are completely unrestricted within their range of definition.)

As equations (1) are linear in $\dot{q}_1, \ldots, \dot{q}_n$, they may be solved for m, say the last m, of these quantities:

$$\dot{q}_{\bar{n}+s} = \sum_{r=1}^{\bar{n}} \dot{q}_r C_{r\bar{n}+s} + D_s \quad (s = 1, \ldots, m) \tag{2}$$

where $C_{r\bar{n}+s}$ and $D_s (r = 1, \ldots, \bar{n};\ s = 1, \ldots, m)$ are again functions of $q_1, \ldots, q_n$, and t, and $\bar{n} = n - m$ is the number of degrees of freedom of the system.

Let P_i be a typical particle of S and $\mathbf{p}_i$ the position vector of P_i relative to a point fixed in R^*. Then $\mathbf{p}_i$ may be regarded as a vector function of the independent variables, $q_1, \ldots, q_n$, and t, and the velocity $\mathbf{v}^{P_i}$ of P_i can be expressed as

$$\mathbf{v}^{P_i} = \frac{d\mathbf{p}_i}{dt} = \sum_{r=1}^{n} \frac{\partial \mathbf{p}_i}{\partial q_r}\dot{q}_r + \frac{\partial \mathbf{p}_i}{\partial t} \tag{3}$$

or, splitting the sum in the right-hand member into two parts, as

$$\mathbf{v}^{P_i} = \sum_{r=1}^{\bar{n}} \frac{\partial \mathbf{p}_i}{\partial q_r}\dot{q}_r + \sum_{s=1}^{m} \frac{\partial \mathbf{p}_i}{\partial q_{\bar{n}+s}}\dot{q}_{\bar{n}+s} + \frac{\partial \mathbf{p}_i}{\partial t} \tag{4}$$

Substitution from equations (2) into equation (4) then gives

$$\mathbf{v}^{P_i} = \sum_{r=1}^{\bar{n}} \left(\frac{\partial \mathbf{p}_i}{\partial q_r} + \sum_{s=1}^{m} \frac{\partial \mathbf{p}_i}{\partial q_{\bar{n}+s}} C_{r\bar{n}+s} \right) \dot{q}_r + \sum_{s=1}^{m} \frac{\partial \mathbf{p}_i}{\partial q_{\bar{n}+s}} D_s + \frac{\partial \mathbf{p}_i}{\partial t} \tag{5}$$

and, if $\bar{n}$ vectors $\mathbf{v}_{,q_r}^{P_i}$ $(r = 1, \ldots, \bar{n})$ are defined as

$$\mathbf{v}_{,q_r}^{P_i} = \frac{\partial \mathbf{p}_i}{\partial q_r} + \sum_{s=1}^{m} \frac{\partial \mathbf{p}_i}{\partial q_{\bar{n}+s}} C_{r\bar{n}+s} \quad (r = 1, \ldots, \bar{n}) \tag{6}$$

equation (5) reduces to

$$\mathbf{v}^{P_i} = \sum_{r=1}^{\bar{n}} \mathbf{v}_{,q_r}^{P_i}\dot{q}_r + \sum_{s=1}^{m} \frac{\partial \mathbf{p}_i}{\partial q_{\bar{n}+s}} D_s + \frac{\partial \mathbf{p}_i}{\partial t} \tag{7}$$

The vectors $\mathbf{v}_{,q_r}^{P_i}$, introduced in equations (6), play a central role in the sequel. Note that they need not be evaluated by means of equations (6), which might be very laborious, but can, in fact, be found by inspection as soon as any expression for $\mathbf{v}^{P_i}$ in terms of $q_1, \ldots, q_n$ and $\dot{q}_1, \ldots, \dot{q}_{\bar{n}}$ has been obtained: Equation (7) shows that $\mathbf{v}_{,q_r}^{P_i}$ is simply the coefficient of $\dot{q}_r$ in such an expression.

The m equations obtained by setting $B_1, \ldots, B_m$ equal to zero, and t, wherever it appears explicitly, equal to any constant, say $\bar{t}$, in equations (1) are called *equations of instantaneous constraint:*

$$\sum_{r=1}^{n} A_{sr}\dot{q}_r = 0 \quad (s = 1, \ldots, m) \tag{8}$$

For motions of S compatible with these equations, D_s must be deleted in equations (2) and, as $\partial \mathbf{p}_i/\partial t$ is equal to zero when t is held constant, it then follows from equation (7) that the equation

$$\bar{\mathbf{v}}^{P_i} = \sum_{r=1}^{\bar{n}} \mathbf{v}_{,q_r}^{P_i}\dot{\bar{q}}_r \tag{9}$$

yields for every arbitrary assignment of values $\dot{q}_r$ to $\dot{q}_r$ $(r = 1, \ldots, \bar{n})$ a velocity $\bar{\mathbf{v}}^{P_i}$ of P_i compatible with equations (8). This is the underlying reason for the importance of the quantities $\mathbf{v}_{,q_r}^{P_i}$, and it suggests, in view of equations (6), that $\mathbf{v}_{,q_r}^{P_i}$ may be described verbally as *the partial rate of change with respect to q_r of the position of P_i in R^*, compatible with the instantaneous constraints.*

When some of the particles of S are rigidly connected to each other, forming a rigid body R, the angular velocity $\boldsymbol{\omega}^R$ of R can, in general, be expressed as [1][2]

$$\boldsymbol{\omega}^R = \sum_{r=1}^{n} \mathbf{w}_r^R \dot{q}_r + \mathbf{w}_t^R \tag{10}$$

where $\mathbf{w}_r^R$ and $\mathbf{w}_t^R$ are functions of $q_1, \ldots, q_n$, and t. Elimination of $\dot{q}_{\bar{n}+1}, \ldots, \dot{q}_n$ by means of equations (2) then leads to

$$\boldsymbol{\omega}^R = \sum_{r=1}^{\bar{n}} \left(\mathbf{w}_r^R + \sum_{s=1}^{m} \mathbf{w}_{\bar{n}+s}^R C_{r\bar{n}+s} \right) \dot{q}_r + \sum_{s=1}^{m} \mathbf{w}_{\bar{n}+s}^R D_s + \mathbf{w}_t^R \tag{11}$$

---

[1] Formerly, Associate Professor of Mechanical Engineering, University of Pennsylvania, Philadelphia, Pa.

Presented at the West Coast Conference of the Applied Mechanics Division, Seattle, Wash., August 28–30, 1961, of The American Society of Mechanical Engineers.

Discussion of this paper should be addressed to the Editorial Department, ASME, United Engineering Center, 345 East 47th Street, New York 17, N. Y., and will be accepted until January 10, 1962. Discussion received after the closing date will be returned. Manuscript received by ASME Applied Mechanics Division, January 31, 1961. Paper No. 61—APMW-9.

[2] Numbers in brackets designate References at end of paper.

so that, if $\bar{n}$ vectors $\boldsymbol{\omega}_{,q_r}{}^R$ $(r = 1, \ldots, \bar{n})$ are defined as

$$\boldsymbol{\omega}_{,q_r}{}^R = \mathbf{w}_r{}^R + \sum_{s=1}^{m} \mathbf{w}_{\bar{n}+s}{}^R C_{r\,\bar{n}+s} \quad (r = 1, \ldots, \bar{n}) \tag{12}$$

the angular velocity is seen to be given by

$$\boldsymbol{\omega}^R = \sum_{r=1}^{\bar{n}} \boldsymbol{\omega}_{,q_r}{}^R \dot{q}_r + \sum_{s=1}^{m} \mathbf{w}_{\bar{n}+s}{}^R D_s + \mathbf{w}_t{}^R \tag{13}$$

As $\mathbf{w}_t{}^R$ (like $\partial \mathbf{p}_i/\partial t$) vanishes when t is held constant, it follows from equation (13) that every angular velocity $\bar{\boldsymbol{\omega}}^R$ given by

$$\bar{\boldsymbol{\omega}}^R = \sum_{r=1}^{\bar{n}} \boldsymbol{\omega}_{,q_r}{}^R \bar{q}_r \tag{14}$$

where $\bar{q}_1, \ldots, \bar{q}_{\bar{n}}$ are values arbitrarily assigned to $\dot{q}_1, \ldots, \dot{q}_{\bar{n}}$, is an angular velocity of R compatible with equations (8). Accordingly, $\boldsymbol{\omega}_{,q_r}{}^R$ may be described as *the partial rate of change with respect to q_r of the orientation of R in R^*, compatible with the instantaneous constraints.* Note that once again it is not necessary to use the defining equations to determine the quantities of interest: $\boldsymbol{\omega}_{q_r}{}^R$ can be found by inspection as soon as any expression for $\boldsymbol{\omega}^R$ in terms of $q_1, \ldots, q_n$ and $\dot{q}_1, \ldots, \dot{q}_{\bar{n}}$ has been obtained, because equation (13) shows that $\boldsymbol{\omega}_{,q_r}{}^R$ is the coefficient of $\dot{q}_r$ in any such expression.

It may be verified that the following $\bar{n}$ relationships, which involve both partial rates of change of position and partial rates of change of orientation,

$$\mathbf{v}_{,q_r}{}^P = \mathbf{v}_{,q_r}{}^Q + \boldsymbol{\omega}_{,q_r}{}^R \times \mathbf{r} \quad (r = 1, \ldots, \bar{n}) \tag{15}$$

where P and Q are points fixed on R and $\mathbf{r}$ is the position vector of P relative to Q, are a consequence of equations (5), (7), (11), (13) and the well-known relationship

$$\mathbf{v}^P = \mathbf{v}^Q + \boldsymbol{\omega}^R \times \mathbf{r}$$

where $\mathbf{v}^P$ and $\mathbf{v}^Q$ are the velocities of P and Q.

Kinetics

Let N be the number of particles comprising S, and $\mathbf{F}_i$ the resultant of all gravitational and contact forces acting on particle P_i. Such forces will henceforth be called "active forces," and they may be forces exerted on the particles of S by each other or by bodies which are not a part of S.

K_{q_r}, defined as

$$K_{q_r} = \sum_{i=1}^{N} \mathbf{v}_{,q_r}{}^{P_i} \cdot \mathbf{F}_i \quad (r = 1, \ldots, \bar{n}) \tag{16}$$

[see equations (6) for $\mathbf{v}_{,q_r}{}^{P_i}$] will be called *the generalized active force corresponding to q_r;* and $K_{q_r}{}'$, defined as

$$K_{q_r}{}' = \sum_{i=1}^{N} \mathbf{v}_{,q_r}{}^{P_i} \cdot \mathbf{F}_i{}' \quad (r = 1, \ldots, \bar{n}) \tag{17}$$

where $\mathbf{F}_i{}'$ is the inertia force associated with P_i in reference frame R^*, will be called *the generalized inertia force corresponding to q_r.* (In terms of the mass m_i and acceleration $\mathbf{a}^{P_i}$ of P_i, $\mathbf{F}_i{}'$ is given by $\mathbf{F}_i{}' = -m_i \mathbf{a}^{P_i}$, and the line of action of $\mathbf{F}_i{}'$ passes through P_i.)

Equations of Motion

D'Alembert's principle, applied to P_i, asserts that

$$\mathbf{F}_i + \mathbf{F}_i{}' = 0 \quad (i = 1, \ldots, N) \tag{18}$$

Multiply equations (18) scalarly with $\mathbf{v}_{,q_r}{}^{P_i}$, add the resulting equations, and use equations (16) and (17). This gives the $\bar{n}$ equations

$$K_{q_r} + K_{q_r}{}' = 0 \quad (r = 1, \ldots, \bar{n}) \tag{19}$$

which, together with the m equations (2), furnish n equations governing all permissible motions of the system S.

The ease with which equations (19) were obtained is, perhaps, deceiving; that is, it may cause one to wonder whether anything useful can have been accomplished. Nevertheless, this is the case. For, among others, precisely those forces which render problems of the class under consideration difficult have been eliminated by the foregoing procedure. To be more specific: Suppose that the set of active forces $\mathbf{F}_1, \ldots, \mathbf{F}_N$ contains a subset of forces $\bar{\mathbf{F}}_1, \ldots, \bar{\mathbf{F}}_N$ (some of which may be equal to zero) such that

$$\sum_{i=1}^{N} \mathbf{v}^{P_i} \cdot \bar{\mathbf{F}}_i = 0 \tag{20}$$

for every set of velocities $\mathbf{v}^{P_1}, \ldots, \mathbf{v}^{P_N}$ compatible with equations (8). Then, using equation (9),

$$\sum_{i=1}^{N} \sum_{r=1}^{\bar{n}} \mathbf{v}_{,q_r}{}^{P_i} \cdot \bar{\mathbf{F}}_i \bar{q}_r = 0$$

or, interchanging the order in which the summations are performed,

$$\sum_{r=1}^{\bar{n}} \left(\sum_{i=1}^{N} \mathbf{v}_{,q_r}{}^{P_i} \cdot \bar{\mathbf{F}}_i \right) \bar{q}_r = 0$$

from which it follows, in view of the fact that any values whatsoever may be assigned to $\bar{q}_1, \ldots, \bar{q}_{\bar{n}}$, that

$$\sum_{i=1}^{N} \mathbf{v}_{,q_r}{}^{P_i} \cdot \bar{\mathbf{F}}_i = 0$$

which shows that the total contribution of $\bar{\mathbf{F}}_1, \ldots, \bar{\mathbf{F}}_N$ to K_{q_r} [see equations (16)] is equal to zero. Now, the so-called "nonholonomic constraint forces" turn out to be precisely such forces. Thus the present method eliminates them from further consideration.

The validity of the claim made in the preceding paragraph has not, of course, been proved. Hence, when dealing with particular problems, one must retain all forces acting on particles of S, unless one has first shown by means of equation (20) that they may be omitted. Those which could have been omitted will then disappear automatically.

The forces exerted on a rigid body by any surface on which the body rolls can easily be shown to belong to the class of forces which contribute nothing to K_{q_r}: During every motion of S compatible with equations (8), such a surface is at rest and, by definition of rolling, the velocity $\mathbf{v}^{P_i}$ of any particle P_i of the rolling body must thus be equal to zero when P_i is in contact with the surface. Consequently, equation (20) is satisfied.

It may be verified that other forces which do not contribute to K_{q_r} are those listed by Whittaker [2] as "forces which do no work."

Equations (19) will now be used for the solution of an illustrative problem.

Consider the following system: Two sharp-edged circular disks, D and D', each of radius r, are mounted at the extremities of a rod of length $2r$, the axis of the rod coinciding with the axes of the disks. Each disk is free to revolve about the rod as an axis, and equal particles, P and P', whose masses are large in comparison with those of the disks and of the rod, are placed at the centers of D and D'. Equations governing the motion of this

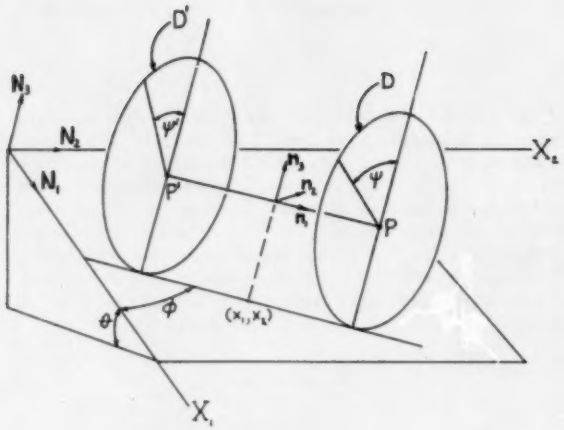

Fig. 1

system on a perfectly rough plane inclined at an angle θ to the horizon are to be obtained.[3]

In Fig. 1, X_1 and X_2 designate orthogonal axes fixed in the plane on which the motion takes place; x_1 and x_2 the X_1 and X_2 coordinates of the mid-point of the rod; $\mathbf{N}_1$, $\mathbf{N}_2$, $\mathbf{N}_3$ mutually perpendicular unit vectors; $\mathbf{n}_1$, $\mathbf{n}_2$, $\mathbf{n}_3$ mutually perpendicular unit vectors, with $\mathbf{n}_3 = \mathbf{N}_3$; ψ and ψ' angles between lines fixed in the disks and a line normal to the plane; and ϕ the angle between the rod and the X_1-axis.

If the plane is perfectly rough, every motion of the disks is a rolling motion and the velocities $\mathbf{v}^P$ and $\mathbf{v}^{P'}$ of P and P' can be expressed as

$$\mathbf{v}^P = -r\dot{\psi}\mathbf{n}_2, \quad \mathbf{v}^{P'} = -r\dot{\psi}'\mathbf{n}_2 \tag{21}$$

But, as both P and P' lie on the same rigid body, $\mathbf{v}^P$ and $\mathbf{v}^{P'}$ are not independent:

$$\mathbf{v}^{P'} = \mathbf{v}^P + \dot{\phi}\mathbf{n}_3 \times (-2r\mathbf{n}_1) \tag{22}$$

Consequently

$$r\dot{\psi}' = r\dot{\psi} + 2r\dot{\phi} \tag{23}$$

and, integrating,

$$r(\psi' - \psi_0') = r(\psi - \psi_0) + 2r(\phi - \phi_0) \tag{24}$$

where ψ_0, ψ_0', and ϕ_0 are the initial values of ψ, ψ', and ϕ.

The velocity of the mid-point of the rod is equal both to

$$\dot{x}_1\mathbf{N}_1 + \dot{x}_2\mathbf{N}_2$$

and to

$$\mathbf{v}^P + \dot{\phi}\mathbf{n}_3 \times (-r\mathbf{n}_1)$$

Equating these and using the first of equations (21), one finds that

$$\dot{x}_1 = r(\dot{\psi} + \dot{\phi})\sin\phi, \quad \dot{x}_2 = -r(\dot{\psi} + \dot{\phi})\cos\phi \tag{25}$$

The configuration of the system can be specified completely by the quantities ϕ, ψ, ψ', x_1, x_2. As equation (24) yields ψ' as soon as ϕ and ψ are known, ψ' need not be considered further. Equations (25) may be regarded as playing the part of equations (2) of the general theory, and differential equations governing ψ and ϕ will be obtained by using equations (19).

After noting that, from the second of equations (21) together with equation (23),

$$\mathbf{v}^{P'} = -r(\dot{\psi} + 2\dot{\phi})\mathbf{n}_2$$

the required partial rates of change of position are found by inspection:

$$\mathbf{v}_{,\phi}^{P} = 0, \quad \mathbf{v}_{,\phi}^{P'} = -2r\mathbf{n}_2 \tag{26}$$

$$\mathbf{v}_{,\dot{\psi}}^{P} = -r\mathbf{n}_2, \quad \mathbf{v}_{,\dot{\psi}}^{P'} = -r\mathbf{n}_2 \tag{27}$$

The only active forces which contribute to K_ϕ and K_ψ are two gravitational forces, one acting on P, the other on P', and both given by

$$\mathbf{G} = mg(\sin\theta\,\mathbf{N}_2 - \cos\theta\,\mathbf{N}_3) \tag{28}$$

where m is the mass of either particle. Thus from equations (16) and (26)–(28),

$$K_\phi = \mathbf{v}_{,\phi}^{P}\cdot\mathbf{G} + \mathbf{v}_{,\phi}^{P'}\cdot\mathbf{G} = 2grm\sin\theta\sin\phi \tag{29}$$

and

$$K_\psi = \mathbf{v}_{,\dot{\psi}}^{P}\cdot\mathbf{G} + \mathbf{v}_{,\dot{\psi}}^{P'}\cdot\mathbf{G} = 2grm\sin\theta\sin\phi \tag{30}$$

The accelerations $\mathbf{a}^P$ and $\mathbf{a}^{P'}$ of P and P' are given by

$$\mathbf{a}^P = \frac{d\mathbf{v}^P}{dt} = r(\dot{\phi}\dot{\psi}\mathbf{n}_1 - \ddot{\psi}\mathbf{n}_2) \tag{31}$$

$$\mathbf{a}^{P'} = \frac{d\mathbf{v}^{P'}}{dt} = r[\dot{\phi}(\dot{\psi} + 2\dot{\phi})\mathbf{n}_1 - (\ddot{\psi} + 2\ddot{\phi})\mathbf{n}_2] \tag{32}$$

Hence equations (17), (26), (27), (31), and (32) lead to the following generalized inertia forces:

$$K_{\phi'} = \mathbf{v}_{,\phi}^{P}\cdot(-m\mathbf{a}^P) + \mathbf{v}_{,\phi}^{P'}\cdot(-m\mathbf{a}^{P'}) = -2mr^2(\ddot{\psi} + 2\ddot{\phi}) \tag{33}$$

$$K_{\psi'} = \mathbf{v}_{,\dot{\psi}}^{P}\cdot(-m\mathbf{a}^P) + \mathbf{v}_{,\dot{\psi}}^{P'}(-m\mathbf{a}^{P'}) = -2mr^2(\ddot{\psi} + \ddot{\phi}) \tag{34}$$

Substitution from equations (29) and (33) into equation (19) gives

$$\ddot{\psi} + 2\ddot{\phi} = \frac{g}{r}\sin\theta\sin\phi \tag{35}$$

and equations (30), (34), and (19) yield

$$\ddot{\psi} + \ddot{\phi} = \frac{g}{r}\sin\theta\sin\phi \tag{36}$$

System Containing Rigid Bodies

As the definitions of the generalized forces K_{q_r} and K_{q_r}' [see equations (16) and (17)] involve the individual particles of the system S, the application of equations (19) to systems containing one or more rigid bodies would be burdensome, were it not for the fact that the contributions to K_{q_r} and K_{q_r}' of forces associated with the particles of such bodies can be expressed in various forms which make it unnecessary to consider the particles individually; that is, a gross separation of kinematic ingredients from kinetic or inertial ingredients of these contributions can be effected. Two theorems, illustrating this fact, will be discussed.

1 Suppose that the first N' particles of S are rigidly connected to each other, forming a rigid body R. Let $\mathbf{F}$ be a force, applied at a point P of R, and $\mathbf{T}$ the torque of a couple,[4] such that this force and couple are together equivalent[5] to the system of all active forces exerted on R by other bodies. (Note that the system of active forces exerted on R by other bodies is not identical with the system of all active forces $\mathbf{F}_1, \ldots, \mathbf{F}_{N'}$ associated with the

[3] The author first encountered a modified form of this problem in a course given by Prof. S. L. Quimby at Columbia University.

[4] Reference [3], p. 97.

[5] Ibid., p. 104.

body R; the latter contains forces exerted by the particles of R on each other, the former does not.)

It will be shown that the contribution to K_{θ_r} of the forces $\mathbf{F}_1, \ldots, \mathbf{F}_{N'}$ is given by

$$\sum_{i=1}^{N'} \mathbf{v}_{,\theta_r}^{P_i} \cdot \mathbf{F}_i = \mathbf{v}_{,\theta_r}^{P} \cdot \mathbf{F} + \boldsymbol{\omega}_{,\theta_r}^{R} \cdot \mathbf{T} \quad (r = 1, \ldots, \bar{n}) \tag{37}$$

where $\mathbf{v}_{,\theta_r}^{P}$ and $\boldsymbol{\omega}_{,\theta_r}^{R}$ $(r = 1, \ldots, \bar{n})$ are partial rates of change of position and orientation, of the kind defined by equations (6) and (12).

Let $\mathbf{r}_i$ be the position vector of a typical particle P_i of R, relative to point P. Then, in accordance with equations (15),

$$\mathbf{v}_{,\theta_r}^{P_i} = \mathbf{v}_{,\theta_r}^{P} + \boldsymbol{\omega}_{,\theta_r}^{R} \times \mathbf{r}_i \quad (r = 1, \ldots, \bar{n}) \tag{38}$$

Hence

$$\sum_{i=1}^{N'} \mathbf{v}_{,\theta_r}^{P_i} \cdot \mathbf{F}_i = \sum_{i=1}^{N'} \mathbf{v}_{,\theta_r}^{P} \cdot \mathbf{F}_i + \sum_{i=1}^{N'} \boldsymbol{\omega}_{,\theta_r}^{R} \times \mathbf{r}_i \cdot \mathbf{F}_i$$

$$= \mathbf{v}_{,\theta_r}^{P} \cdot \sum_{i=1}^{N'} \mathbf{F}_i + \boldsymbol{\omega}_{,\theta_r}^{R} \cdot \sum_{i=1}^{N'} \mathbf{r}_i \times \mathbf{F}_i \quad (r = 1, \ldots, \bar{n}) \tag{39}$$

Now, the law of action and reaction asserts that those of the forces $\mathbf{F}_1, \ldots, \mathbf{F}_{N'}$ exerted by the particles of R an each other constitute a self-equilibrating set. Consequently

$$\sum_{i=1}^{N'} \mathbf{F}_i$$

is equal to the resultant of all active forces exerted on R by other bodies, and

$$\sum_{i=1}^{N'} \mathbf{r}_i \times \mathbf{F}_i$$

is equal to the sum of the moments of these forces about the point P. It thus follows from the definition of equivalence of two systems of vectors that

$$\sum_{i=1}^{N'} \mathbf{F}_i = \mathbf{F}, \quad \sum_{i=1}^{N'} \mathbf{r}_i \times \mathbf{F}_i = \mathbf{T}$$

and substitution of these results into equations (39) gives equations (37).

2 In a manner similar to that employed in the foregoing, it may be verified that the contribution to K_{θ_r}' of the inertia forces $\mathbf{F}_1', \ldots, \mathbf{F}_{N'}'$ associated with the rigid body R is given by

$$\sum_{i=1}^{N'} \mathbf{v}_{,\theta_r}^{P_i} \cdot \mathbf{F}_i' = \mathbf{v}_{,\theta_r}^{P^*} \cdot \mathbf{F}^R + \boldsymbol{\omega}_{,\theta_r}^{R} \cdot \mathbf{T}^R \tag{40}$$

where P^* is the mass center of R, and $\mathbf{F}^R$ and $\mathbf{T}^R$ are the inertia force and the torque of the inertia couple[4] acting on R. To render the present discussion self-contained, it is noted that

$$\mathbf{F}^R = -m\mathbf{a}^{P^*} \tag{41}$$

where m is the mass of R and $\mathbf{a}^{P^*}$ the acceleration of the mass center P^*, and that one form in which $\mathbf{T}^R$ may be expressed is

$$\mathbf{T}^R = [(\phi_{22} - \phi_{33})\omega_2^R \omega_3^R - \phi_{11}\alpha_1^R]\mathbf{n}_1 + [(\phi_{33} - \phi_{11})\omega_3^R \omega_1^R - \phi_{22}\alpha_2^R]\mathbf{n}_2 + [(\phi_{11} - \phi_{22})\omega_1^R \omega_2^R - \phi_{33}\alpha_3^R]\mathbf{n}_3 \tag{42}$$

where $\mathbf{n}_1, \mathbf{n}_2, \mathbf{n}_3$ is a right-handed set of mutually perpendicular principal directions of R for P^* (and $\mathbf{n}_1, \mathbf{n}_2, \mathbf{n}_3$ need not be fixed in R); ω_i^R and α_i^R $(i = 1, 2, 3)$ are the $\mathbf{n}_i$ measure numbers of, respectively, the angular velocity $\boldsymbol{\omega}^R$ and angular acceleration $\boldsymbol{\alpha}^R$ of R in the Newtonian reference frame R_*^*; and ϕ_{ii} is the moment of inertia of R with respect to a line passing through P^* and parallel to $\mathbf{n}_i$.

As an illustration in the use of these results, consider a system geometrically identical with that discussed in the earlier illustrative problem, but having the following inertial properties (Fig. 1): Each of the disks D and D' has a mass m which is large in comparison with that of the rod and of the particles P and P'. $\mathbf{n}_1, \mathbf{n}_2, \mathbf{n}_3$ are principal directions of the disks for the mass centers of the disks (for all values of ψ and ψ'), these mass centers coinciding with P and P', respectively; and the associated moments of inertia have the values

$$\phi_{11} = mk^2, \quad \phi_{22} = \phi_{33} = \frac{mk^2}{2} \tag{43}$$

As the total contribution to K_ϕ and K_ψ of forces exerted on D and D' by the supporting surface and by the rod is equal to zero, and the system of gravitational forces acting on the disks is equivalent to the system of gravitational forces previously associated with the particles P and P', it follows from equations (16) and (37) that K_ϕ and K_ψ are again given by [see equations (29) and (30)]

$$K_\phi = K_\psi = 2qrm \sin\theta \sin\phi \tag{44}$$

In accordance with equations (17), (40), and (41), the generalized inertia forces become

$$K_\phi' = \mathbf{v}_{,\phi}^{P} \cdot (-m\mathbf{a}^{P}) + \mathbf{v}_{,\phi}^{P'} \cdot (-m\mathbf{a}^{P'}) + \boldsymbol{\omega}_{,\phi}^{D} \cdot \mathbf{T}^{D} + \boldsymbol{\omega}_{,\phi}^{D'} \cdot \mathbf{T}^{D'} \tag{45}$$

and

$$K_\psi' = \mathbf{v}_{,\psi}^{P} \cdot (-m\mathbf{a}^{P}) + \mathbf{v}_{,\psi}^{P'} \cdot (-m\mathbf{a}^{P'}) + \boldsymbol{\omega}_{,\psi}^{D} \cdot \mathbf{T}^{D} + \boldsymbol{\omega}_{,\psi}^{D'} \cdot \mathbf{T}^{D'} \tag{46}$$

where, from equations (42) and (43),

$$\mathbf{T}^D = -\frac{mk^2}{2}[2\alpha_1^D \mathbf{n}_1 + (\omega_3^D \omega_1^D + \alpha_3^D)\mathbf{n}_2 - (\omega_1^D \omega_2^D - \alpha_3^D)\mathbf{n}_3]$$

and

$$\mathbf{T}^{D'} = -\frac{mk^2}{2}[2\alpha_1^{D'} \mathbf{n}_1 + (\omega_3^{D'} \omega_1^{D'} + \alpha_2^{D'})\mathbf{n}_2 - (\omega_1^{D'} \omega_2^{D'} - \alpha_3^{D'})\mathbf{n}_3]$$

Now

$$\boldsymbol{\omega}^D = \dot{\psi}\mathbf{n}_1 + \dot{\phi}\mathbf{n}_3$$

and

$$\boldsymbol{\omega}^{D'} = \dot{\psi}'\mathbf{n}_1 + \dot{\phi}\mathbf{n}_3 = (\dot{\psi} + 2\dot{\phi})\mathbf{n}_1 + \dot{\phi}\mathbf{n}_3$$

Hence

$$\boldsymbol{\omega}_{,\phi}^{D} = \mathbf{n}_3, \quad \boldsymbol{\omega}_{,\phi}^{D'} = 2\mathbf{n}_1 + \mathbf{n}_3$$

$$\boldsymbol{\omega}_{,\psi}^{D} = \mathbf{n}_1, \quad \boldsymbol{\omega}_{,\psi}^{D'} = \mathbf{n}_1$$

Furthermore

$$\boldsymbol{\alpha}^D = \frac{d\boldsymbol{\omega}^D}{dt} = \ddot{\psi}\mathbf{n}_1 + \dot{\psi}\dot{\phi}\mathbf{n}_2 + \ddot{\phi}\mathbf{n}_3$$

$$\boldsymbol{\alpha}^{D'} = \frac{d\boldsymbol{\omega}^{D'}}{dt} = (\ddot{\psi} + 2\ddot{\phi})\mathbf{n}_1 + \dot{\phi}(\dot{\psi} + 2\dot{\phi})\mathbf{n}_2 + \ddot{\phi}\mathbf{n}_3$$

Carrying out the operations indicated in equations (45) and (46) [which is facilitated by using equations (33) and (34)], one finds

[4] Reference [4], chap. 4.

$$K_\phi' = -2m(r^2 + k^2)(\ddot{\psi} + 2\ddot{\phi}) - mk^2\ddot{\phi} \quad (47)$$

and

$$K_\psi' = -2m(r^2 + k^2)(\ddot{\psi} + \ddot{\phi}) \quad (48)$$

Equations (19), (44), (47), and (48) then lead to the following differential equations of motion:

$$\ddot{\psi} + \frac{4r^2 + 5k^2}{2(r^2 + k^2)}\ddot{\phi} = \frac{gr}{r^2 + k^2}\sin\theta\sin\phi$$

$$\ddot{\psi} + \ddot{\phi} = \frac{gr}{r^2 + k^2}\sin\theta\sin\phi$$

For $k = 0$ these equations reduce, as they must, to equations (35) and (36), respectively.

Conclusion

A general method for obtaining the differential equations governing motions of both holonomic and nonholonomic systems has been presented. When applied to holonomic systems, it differs from the method of Lagrange[7] in this respect: The requisite kinematical analysis must be carried further than when one uses Lagrange's equations. That is, accelerations and, if the system contains rigid bodies, angular accelerations must be studied, whereas Lagrange's equations, involving kinetic energies, can be formed as soon as sufficient information about velocities and angular velocities is available. This is a disadvantage of the present method. However, it is less serious than it might appear to be, because the partial differentiations (of kinetic energy) required by Lagrange's method can at times become very laborious, even in situations in which the study of accelerations would not be so. Thus, for holonomic systems, the relative advantages of these two methods depend on the character of the problem under consideration.

As regards nonholonomic systems, the new method enjoys a clear-cut advantage over the Lagrangian one applicable to such systems; i.e., over the use of undetermined multipliers.[8]

The foregoing methods can also be compared with one suggested by Appell,[9] which is applicable to both holonomic and nonholonomic systems and shares certain features, albeit the worst, with each of the other two: Appell's equations require partial differentiations of a scalar function which depends on accelerations, and accelerations enter this function in such a way that no readily available results [compare with equations (40)–(42)] can be used to suppress the appearance of individual particles.

[7] Reference [2], p. 34.

[8] Reference [2], p. 214.

[9] Ibid., p. 258.

References

1 T. R. Kane, "Partial Rates of Change of Position and of Orientation," Manchester College of Science and Technology, *Bulletin of Mechanical Engineering Education*, No. 17, 1960, pp. 17–24.

2 E. T. Whittaker, "A Treatise on the Analytical Dynamics of Particles and Rigid Bodies," Dover Publications, Inc., New York, N. Y., 1937, p. 31.

3 T. R. Kane, "Analytical Elements of Mechanics," vol. 1, Academic Press, New York and London, 1959.

4 T. R. Kane, "Analytical Elements of Mechanics," vol. 2, Academic Press, New York and London, 1961.

The Effect of Rotatory Inertia and of Shear Deformation on the Frequency and Normal Mode Equations of Uniform Beams With Simple End Conditions

T. C. HUANG

Associate Professor of Engineering Mechanics, University of Florida, Gainesville, Fla.

New frequency and normal mode equations for flexural vibrations of six common types of simple, finite beams are presented. The derivation includes the effect of rotatory inertia and transverse-shear deformation. A specific example is given.

THE classical one-dimensional Bernoulli-Euler theory of flexural motions of elastic beams has been known to be inadequate for the vibration of higher modes. It is also inadequate for those beams when the effect of the cross-sectional dimensions on frequencies cannot be neglected. Rayleigh [1][1] introduced the effect of rotatory inertia and Timoshenko [2, 3] extended it to include the effect of transverse-shear deformation. On the other hand, the exact equations, due to Pochhammer [4] and to Chree [5], have been derived from the general equations of the theory of elasticity, and the resulting frequency equation for flexural vibrations is discussed by Bancroft [6] and the necessary computations are carried out by Hudson [7]. Davis [8] shows that the results from Timoshenko's equation are in remarkably good agreement with those obtained by Hudson from the exact elasticity equations.

Since then there has been considerable research interest in applying the Timoshenko theory to the transient responses of beams as well as the free and forced vibrations. The present paper deals with the frequency equations and normal modes of free flexural vibrations of finite beams including the effect of shear and rotatory inertia for various cases of simple beams. Anderson [9] and Dolph [10], in dealing with this problem, give general solutions and complete analysis of uniform hinged-hinged beam. Using methods of Ritz and Galerkin, Huang [11] also presents the results for a hinged-hinged beam. Dolph, in addition, includes the analog-computer solution for the free-free beam due to Howe, et al. [12]. Earlier, Kruszewski [13] obtained frequency equations for cantilever and free-free beams by solving a complete differential equation in deflection with prescribed nonhomogeneous boundary conditions. Some of these conditions are lengthy and complicated and make the problem not easy to deal with. It is these nonhomogeneous boundary conditions which limit his solutions only to the two types of beams mentioned. In the present paper a somewhat different approach is used. The novel features are (*a*) the solutions are obtained for two complete differential equations in total deflection and bending slope, respectively, (*b*) the constants in these solutions are related by any one of the two original coupled equations from which the foregoing two complete differential equations are derived, and (*c*) the boundary conditions prescribed are homogeneous. The frequency and normal mode equations for all six common types of simple, finite beams are obtained. A numerical example is given.

[1] Numbers in brackets designate References at end of paper.

Presented at the Summer Conference of the Applied Mechanics Division, Chicago, Ill., June 14–16, 1961, of THE AMERICAN SOCIETY OF MECHANICAL ENGINEERS.

Discussion of this paper should be addressed to the Editorial Department, ASME, United Engineering Center, 345 East 47th Street, New York 17, N. Y., and will be accepted until January 10, 1962. Discussion received after the closing date will be returned. Manuscript received by ASME Applied Mechanics Division, November 16 1960. Paper No. 61—APM-25.

Differential Equations and Boundary Conditions

The coupled equations for the total deflection y and the bending slope ψ are given by Timoshenko [14] as

$$EI\frac{\partial^2\psi}{\partial x^2} + k\left(\frac{\partial y}{\partial x} - \psi\right)AG - \frac{I\gamma}{g}\frac{\partial^2\psi}{\partial t^2} = 0 \tag{1}$$

$$\frac{\gamma A}{g}\frac{\partial^2 y}{\partial t^2} - k\left(\frac{\partial^2 y}{\partial x^2} - \frac{\partial\psi}{\partial x}\right)AG = 0 \tag{2}$$

in which

E = modulus of elasticity
G = modulus of rigidity
I = area moment of inertia of cross section
A = cross-sectional area
γ = weight per unit volume
k = numerical shape factor for cross section

Eliminating ψ or y from equations (1) and (2), the following two complete differential equations in y and ψ are obtained:

$$EI\frac{\partial^4 y}{\partial x^4} + \frac{\gamma A}{g}\frac{\partial^2 y}{\partial t^2} - \left(\frac{\gamma I}{g} + \frac{EI}{gk}\frac{\gamma}{G}\right)\frac{\partial^4 y}{\partial x^2\partial t^2} + \frac{\gamma I}{g}\frac{\gamma}{gkG}\frac{\partial^4 y}{\partial t^4} = 0 \tag{3}$$

$$EI\frac{\partial^4\psi}{\partial x^4} + \frac{\gamma A}{g}\frac{\partial^2\psi}{\partial t^2} - \left(\frac{\gamma I}{g} + \frac{EI}{gk}\frac{\gamma}{G}\right)\frac{\partial^4\psi}{\partial x^2\partial t^2} + \frac{\gamma I}{g}\frac{\gamma}{gkG}\frac{\partial^4\psi}{\partial t^4} = 0 \tag{4}$$

Let

$$y = Ye^{ipt} \tag{5}$$

$$\psi = \Psi e^{ipt} \tag{6}$$

$$\xi = x/L \tag{7}$$

where

Y = normal function of y
Ψ = normal function of ψ
ξ = nondimensional length of beam
j = $\sqrt{-1}$
p = angular frequency
L = length of beam

Omitting the factor e^{jpt}, equations (1) to (4) are reduced to

$$s^2\Psi'' - (1 - b^2r^2s^2)\Psi + Y'/L = 0 \quad (8)$$

$$Y'' + b^2s^2Y - L\Psi' = 0 \quad (9)$$

$$Y^{iv} + b^2(r^2 + s^2)Y'' - b^2(1 - b^2r^2s^2)Y = 0 \quad (10)$$

$$\Psi^{iv} + b^2(r^2 + s^2)\Psi'' - b^2(1 - b^2r^2s^2)\Psi = 0 \quad (11)$$

where

$$b^2 = \frac{1}{EI}\frac{\gamma A}{g}L^4p^2 \quad (12)$$

$$r^2 = \frac{I}{AL^2} \quad (13)$$

$$s^2 = \frac{EI}{kAGL^2} \quad (14)$$

and the primes for Y and Ψ represent differentiation with respect to ξ.

The necessary and sufficient boundary conditions for the beams are found as follows:

Hinged end

$$Y = 0 \quad (15)$$

$$\Psi' = 0 \quad (16)$$

Clamped end

$$Y = 0 \quad (17)$$

$$\Psi = 0 \quad (18)$$

Free end

$$\Psi' = 0 \quad (19)$$

$$\frac{1}{L}Y' - \Psi = 0 \quad (20)$$

Solutions

The solutions of (10) and (11) can be found as

$$Y = C_1 \cosh b\alpha\xi + C_2 \sinh b\alpha\xi + C_3 \cos b\beta\xi + C_4 \sin b\beta\xi \quad (21)$$

$$\Psi = C_1' \sinh b\alpha\xi + C_2' \cosh b\alpha\xi + C_3' \sin b\beta\xi + C_4' \cos b\beta\xi \quad (22)$$

where

$$\begin{matrix}\alpha \\ \beta\end{matrix} = \frac{1}{\sqrt{2}}\left\{\mp(r^2 + s^2) + [(r^2 - s^2)^2 + 4/b^2]^{1/2}\right\}^{1/2} \quad (23)$$

and

$$[(r^2 - s^2)^2 + 4/b^2]^{1/2} > (r^2 + s^2)$$

is assumed.

In case

$$[(r^2 - s^2)^2 + 4/b^2]^{1/2} < (r^2 + s^2),$$

we write

$$\alpha = \frac{1}{\sqrt{2}}\left\{(r^2 + s^2) - [(r^2 - s^2)^2 + 4/b^2]^{1/2}\right\}^{1/2} j = j\alpha' \quad (24)$$

then (21) and (22) are replaced by

$$Y = C_1 \cos b\alpha'\xi + jC_2 \sin b\alpha'\xi + C_3 \cos b\beta\xi + C_4 \sin b\beta\xi \quad (25)$$

$$\Psi = jC_1' \sin b\alpha'\xi + C_2' \cos b\alpha'\xi + C_3' \sin b\beta\xi + C_4' \cos b\beta\xi \quad (26)$$

Solutions of (21–22), or (25–26) are naturally the solutions of the original coupled equations (8) and (9).

Only one half of the constants in equations (21) and (22) are independent. They are related by the equations (8) or (9) as follows:

$$C_1 = \frac{L}{b\alpha}[1 - b^2s^2(\alpha^2 + r^2)]C_1' \quad (27)$$

$$C_2 = \frac{L}{b\alpha}[1 - b^2s^2(\alpha^2 + r^2)]C_2' \quad (28)$$

$$C_3 = -\frac{L}{b\beta}[1 + b^2s^2(\beta^2 - r^2)]C_3' \quad (29)$$

$$C_4 = \frac{L}{b\beta}[1 + b^2s^2(\beta^2 - r^2)]C_4' \quad (30)$$

or

$$C_1' = \frac{b}{L}\frac{\alpha^2 + s^2}{\alpha}C_1 \quad (31)$$

$$C_2' = \frac{b}{L}\frac{\alpha^2 + s^2}{\alpha}C_2 \quad (32)$$

$$C_3' = -\frac{b}{L}\frac{\beta^2 - s^2}{\beta}C_3 \quad (33)$$

$$C_4' = \frac{b}{L}\frac{\beta^2 - s^2}{\beta}C_4 \quad (34)$$

Frequency Equations

The application of appropriate boundary conditions (15–20) and relations of integration constants (27–34) to equations (21) and (22) yields for each type of beam a set of four homogeneous linear algebraic equations in four constants C_1 to C_4 with or without primes. In order that the solutions other than zero may exist the determinant of the coefficients of C_i must be equal to zero. This leads to the frequency equation in each case from which the natural frequencies can be determined.

In the following, six common types of beams will be identified by a compound adjective which describes the end conditions at $\xi = 0$ and $\xi = 1$ or $x = 0$ and $x = L$. They are (*a*) supported-supported or hinged-hinged, (*b*) free-free, (*c*) clamped-clamped, (*d*) clamped-free, (*e*) clamped-supported, and (*f*) supported-free.

The frequency equations thus obtained are as follows:

(*a*) Supported-supported beam

$$\sin b\beta = 0 \quad (35)$$

(*b*) Free-free beam

$$2 - 2\cosh b\alpha \cos b\beta + \frac{b}{(1 - b^2r^2s^2)^{1/2}}$$

$$[b^2r^2(r^2 - s^2)^2 + (3r^2 - s^2)] \sinh b\alpha \sin b\beta = 0 \quad (36)$$

(*c*) Clamped-clamped beam

$$2 - 2\cosh b\alpha \cos b\beta + \frac{b}{(1 - b^2r^2s^2)^{1/2}}$$

$$[b^2s^2(r^2 - s^2)^2 + (3s^2 - r^2)] \sinh b\alpha \sin b\beta = 0 \quad (37)$$

(*d*) Clamped-free beam

$$2 + [b^2(r^2 - s^2)^2 + 2] \cosh b\alpha \cos b\beta - \frac{b(r^2 + s^2)}{(1 - b^2r^2s^2)^{1/2}} \sinh b\alpha \sin b\beta = 0 \quad (38)$$

(*e*) Clamped-supported beam

$$\lambda\zeta \tanh b\alpha - \tan b\beta = 0 \quad (39)$$

(*f*) Supported-free beam

$$\lambda \tanh b\alpha - \zeta \tan b\beta = 0 \quad (40)$$

in which

$$\lambda = \alpha/\beta \quad (41)$$

$$\zeta = (\alpha^2 + r^2)/(\alpha^2 + s^2) = (\beta^2 - s^2)/(\beta^2 - r^2) = (\alpha^2 + r^2)/(\beta^2 - r^2) = (\beta^2 - s^2)/(\alpha^2 + s^2) \quad (42)$$

When

$$[(r^2 - s^2)^2 + 4/b^2]^{1/2} < (r^2 + s^2), \qquad b^2r^2s^2 > 1$$

correspondingly. It is convenient to use $\alpha = j\alpha'$ and

$$(1 - b^2r^2s^2)^{1/2} = j(b^2r^2s^2 - 1)^{1/2} \quad (43)$$

$$\lambda = j\lambda' \quad (44)$$

where $\lambda' = \alpha'/\beta$ and transform the frequency equations (31–36) for the case

$$[(r^2 - s^2)^2 + 4/b^2]^{1/2} > (r^2 + s^2)$$

to those for the case

$$[(r^2 - s^2)^2 + 4/b^2]^{1/2} < (r^2 + s^2)$$

Thus we obtain the frequency equations as follows:

(*a*) Supported-supported beam

$$\sin b\beta = 0 \quad (45)$$

(*b*) Free-free beam

$$2 - 2\cos b\alpha' \cos b\beta + \frac{b}{(b^2r^2s^2 - 1)^{1/2}}$$

$$[b^2r^2(r^2 - s^2)^2 + (3r^2 - s^2)] \sin b\alpha' \sin b\beta = 0 \quad (46)$$

(*c*) Clamped-clamped beam

$$2 - 2\cos b\alpha' \cos b\beta + \frac{b}{(b^2r^2s^2 - 1)^{1/2}}$$

$$[b^2s^2(r^2 - s^2)^2 + (3s^2 - r^2)] \sin b\alpha' \sin b\beta = 0 \quad (47)$$

(*d*) Clamped-free beam

$$2 + [b^2(r^2 - s^2)^2 + 2] \cos b\alpha' \cos b\beta - \frac{b(r^2 + s^2)}{(b^2r^2s^2 - 1)^{1/2}} \sin b\alpha' \sin b\beta = 0 \quad (48)$$

(*e*) Clamped-supported beam

$$\lambda'\zeta \tan b\alpha' + \tan b\beta = 0 \quad (49)$$

(*f*) Supported-free beam

$$\lambda' \tan b\alpha' + \zeta \tan b\beta = 0 \quad (50)$$

Normal Modes

For each type of beam the roots of the frequency equations, b_i, $i = 1, 2, 3, \ldots$, give the eigenvalues of the problem. The corresponding eigenfunctions, normal modes Y_i and Ψ_i, can be obtained accordingly. In the following list of normal modes the subscript i is omitted for Y, Ψ, b, α, β, and the constants D and H. Since the coefficients in Y and Ψ are related, the constants D and H are connected through any one of the equations of (27–30) or (31–34).

The normal modes Y and Ψ for various simple beams are as follows: In case there are two pairs of Y and Ψ the first pair is for the case when

$$[(r^2 - s^2)^2 + 4/b^2]^{1/2} > (r^2 + s^2)$$

and the second pair,

$$[(r^2 - s^2)^2 + 4/b^2]^{1/2} < (r^2 + s^2).$$

(*a*) Supported-supported beam

$$Y = D \sin b\beta\xi \quad (51)$$

$$\Psi = H \sin b\beta\xi \quad (52)$$

(*b*) Free-free beam

$$Y = D\left[\cosh b\alpha\xi + \lambda\delta \sinh b\alpha\xi + \frac{1}{\zeta}\cos b\beta\xi + \delta \sin b\beta\xi\right] \quad (53)$$

$$\Psi = H\left[\cosh b\alpha\xi - \frac{\delta}{\lambda}\sinh b\alpha\xi + \zeta \cos b\beta\xi + \frac{1}{\delta}\sin b\beta\xi\right] \quad (54)$$

where

$$\delta = \frac{\cosh b\alpha - \cos b\beta}{\lambda \sinh b\alpha - \zeta \sin b\beta} \quad (55)$$

and

$$Y = D\left[\cos b\alpha'\xi - \lambda'\eta \sin b\alpha'\xi + \frac{1}{\zeta}\cos b\beta\xi + \eta \sin b\beta\xi\right] \quad (56)$$

$$\Psi = H\left[\cos b\alpha'\xi - \frac{\eta}{\lambda'}\sin b\alpha'\xi + \zeta \cos b\beta\xi + \frac{1}{\eta}\sin b\beta\xi\right] \quad (57)$$

where

$$\eta = -\frac{\cos b\alpha' - \cos b\beta}{\lambda' \sin b\alpha' + \zeta \sin b\beta} \quad (58)$$

(c) Clamped-clamped beam

$$Y = D[\cosh b\alpha\xi + \lambda\zeta\delta \sinh b\alpha\xi - \cos b\beta\xi + \delta \sin b\beta\xi] \quad (59)$$

$$\Psi = H\left[\cosh b\alpha\xi + \frac{\theta}{\lambda\zeta}\sinh b\alpha\xi - \cos b\beta\xi + \theta \sin b\beta\xi\right] \quad (60)$$

where

$$\delta = \frac{-\cosh b\alpha + \cos b\beta}{\lambda\zeta \sinh b\alpha + \sin b\beta} \quad (61)$$

$$\theta = \frac{-\cosh b\alpha + \cos b\beta}{\frac{1}{\lambda\zeta}\sinh b\alpha + \sin b\beta} \quad (62)$$

and

$$Y = D[\cos b\alpha'\xi - \lambda'\zeta\eta \sin b\alpha'\xi - \cos b\beta\xi + \eta \sin b\beta\xi] \quad (63)$$

$$\Psi = H\left[\cos b\alpha'\xi + \frac{\mu}{\lambda'\zeta}\sin b\alpha'\xi - \cos b\beta\xi + \mu \sin b\beta\xi\right] \quad (64)$$

where

$$\eta = \frac{\cos b\alpha' - \cos b\beta}{\lambda'\zeta \sin b\alpha' - \sin b\beta} \quad (65)$$

$$\mu = \frac{-\cos b\alpha' + \cos b\beta}{\frac{1}{\lambda'\zeta}\sin b\alpha' + \sin b\beta} \quad (66)$$

(d) Clamped-free beam

$$Y = D[\cosh b\alpha\xi - \lambda\zeta\delta \sinh b\alpha\xi - \cos b\beta\xi + \delta \sin b\beta\xi] \quad (67)$$

$$\Psi = H\left[\cosh b\alpha\xi + \frac{\theta}{\lambda\zeta}\sinh b\alpha\xi - \cos b\beta\xi + \theta \sin b\beta\xi\right] \quad (68)$$

where

$$\delta = \frac{\frac{1}{\lambda}\sinh b\alpha - \sin b\beta}{\zeta \cosh b\alpha + \cos b\beta} \quad (69)$$

$$\theta = -\frac{\lambda \sinh b\alpha + \sin b\beta}{\frac{1}{\zeta}\cosh b\alpha + \cos b\beta} \quad (70)$$

and

$$Y = D[\cos b\alpha'\xi + \lambda'\zeta\eta \sin b\alpha'\xi - \cos b\beta\xi + \eta \sin b\beta\xi] \quad (71)$$

$$\Psi = H\left[\cos b\alpha'\xi - \frac{1}{\lambda'\zeta}\mu \sin b\alpha'\xi - \cos b\beta\xi + \mu \sin b\beta\xi\right] \quad (72)$$

where

$$\eta = \frac{\frac{1}{\lambda'}\sin b\alpha' - \sin b\beta}{\zeta \cos b\alpha' + \cos b\beta} \quad (73)$$

$$\mu = \frac{\lambda' \sin b\alpha' - \sin b\beta}{\frac{1}{\zeta}\cos b\alpha' + \cos b\beta} \quad (74)$$

(e) Clamped-supported beam

$$Y = D[\cosh b\alpha\xi - \coth b\alpha \sinh b\alpha\xi - \cos b\beta\xi + \cot b\beta \sin b\beta\xi] \quad (75)$$

$$\Psi = H\left[\cosh b\alpha\xi + \frac{\theta}{\lambda\zeta}\sinh b\alpha\xi - \cos b\beta\xi + \theta \sin b\beta\xi\right] \quad (76)$$

where

$$\theta = -\frac{\lambda \sinh b\alpha + \sin b\beta}{\frac{1}{\zeta}\cosh\ b\alpha + \cos b\beta} \quad (77)$$

and

$$Y = D[\cos b\alpha'\xi - \cot b\alpha' \sin b\alpha'\xi - \cos b\beta\xi + \cot b\beta \sin b\beta\xi] \quad (78)$$

$$\Psi = H\left[\cos b\alpha'\xi - \frac{1}{\lambda'\zeta}\mu \sin b\alpha'\xi - \cos b\beta\xi + \mu \sin b\beta\xi\right] \quad (79)$$

where

$$\mu = \frac{\lambda' \sin b\alpha' - \sin b\beta}{\frac{1}{\zeta}\cos b\alpha' + \cos b\beta} \quad (80)$$

(f) Supported-free beam

$$Y = \lambda \frac{\cos b\beta}{\cosh b\alpha} \sinh b\alpha\xi + \sin b\beta\xi \quad (81)$$

$$\Psi = \frac{1}{\lambda}\frac{\sin b\beta}{\sinh b\alpha}\cosh b\alpha\xi + \cos b\beta\xi \quad (82)$$

and

$$Y = -\lambda' \frac{\cos b\beta}{\cos b\alpha'} \sin b\alpha'\xi + \sin b\beta\xi \quad (83)$$

$$\Psi = -\frac{1}{\lambda'}\frac{\sin b\beta}{\sin b\alpha'}\cos b\alpha'\xi + \cos b\beta\xi \quad (84)$$

The condition of orthogonality of normal modes can be found [11] as

$$\int_0^1 (Y_m Y_n + r_g^2 \Psi_m \Psi_n) d\xi = 0 \quad m \neq n \quad (85)$$

for mth and nth modes, and r_g is the radius of gyration of the cross section around the principal axis normal to the plane of motion and is given as

$$r_g^2 = I/A \tag{86}$$

The normal modes would also be useful for studying the forced vibration of beams, and beam and plate vibrations by variational methods as they are used for conventional beams and plates.

Deflection, Slope, Moment, and Shear

With Y and Ψ known, the total deflection, slopes, moment, and shear can be written as follows:

Total deflection

$$y = \Sigma a_i Y_i e^{jp_i t + \epsilon_i} \tag{87}$$

Bending slope

$$\psi = \Sigma \bar{a}_i \Psi_i e^{jp_i t + \bar{\epsilon}_i} \tag{88}$$

Total slope

$$\frac{\partial y}{\partial x} = \Sigma\, a_i \frac{dY_i}{dx} e^{jp_i t + \epsilon_i} \tag{89}$$

Shear slope

$$\varphi = \frac{\partial y}{\partial x} - \psi \tag{90}$$

Moment

$$M = -EI \frac{\partial \psi}{\partial x} \tag{91}$$

Shear

$$Q = k\varphi AG = k\left(\frac{\partial y}{\partial x} - \psi\right) AG \tag{92}$$

The constants a_i, ϵ_i, $\bar{a}_i$, and $\bar{\epsilon}_i$ have to be evaluated from the given initial conditions; i.e., the initial values of y and ψ and their time derivatives.

Numerical Example

For a given beam with r and s known, the b_i ($i = 1, 2, 3, \ldots$) can be found from the appropriate frequency equations and the corresponding p_i are then calculated by the equation (12). However, these frequency equations are highly transcendental and not to be solved simply. This difficulty is overcome by the use of frequency charts which are obtained from the solution of these transcendental frequency equations for various types of beams and various combinations of r and s.

In this paper the frequency chart is given only for a special case of clamped-free beam as an illustration. Assume $k = {}^2/_3$, $E/G = {}^8/_3$, then $E/kG = 4$ and $s = 2r$ for this special case. Let p_0 be the corresponding frequencies from classical theory; the graphical representation of p/p_0 versus r for the first five modes of a finite cantilever beam is presented in Fig. 1 with the range of r from 0 to 0.10. It is seen that the reduction of the ratio of natural frequencies is increased by increasing the values of r and s and for the higher modes. In the curves shown as high as 70 per cent reduction is possible.

The application of these curves of the frequency chart will now be illustrated for a steel cantilever beam 14.4 in. in length, 1 sq in. in square cross section, $E = 30 \times 10^6$ psi, and $\gamma = 0.28$ lb/in.^{3} Assuming $k = {}^2/_3$, $E/G = {}^8/_3$, we have $r = 0.02$, $s = 0.04$. Since $s = 2r$ we have from Fig. 1

$$p/p_0 = 0.985, 0.975, 0.930, 0.883, 0.835 \tag{93}$$

for the first five modes. Since

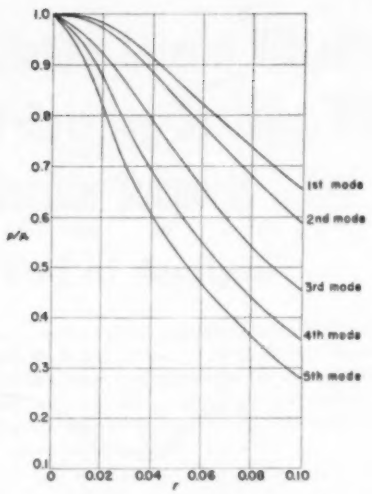

Fig. 1 Corrections in natural frequencies of a clamped-free beam owing to rotatory inertia and shear deformation

$$b/b_0 = p/p_0 \tag{94}$$

and the corresponding b_0 are

$$b_0 = 3.51, 22.0, 61.9, 121.2, 199.9 \tag{95}$$

we have

$$b = 3.46, 21.4, 57.5, 107.0, 167.0 \tag{96}$$

The p_i are then obtained from (12) as

$$p = 977, 6040, 16200, 30200, 47200 \tag{97}$$

Equations (23) give values of α_i and β_i for each b_i. The corresponding values of λ_i, ζ_i, δ_i, and θ_i are then calculated from (41–42) and (69–70.) The normal modes Y and Ψ are then given by (67–68). For the instance of foregoing example the superimposed modes of the first five normal modes of Y and Ψ are shown by the solid curves in (a) and (b) of Fig. 2, respectively. The relative magnitudes of each of these five component normal modes are so chosen that they reduce to the magnitudes according to the classical theory given by reference [15]. The corresponding superimposed modes of Y and Ψ from these reduced magnitudes are shown by the dotted curves in the same figure for comparison.

Frequency charts[2] for the first five modes of six common types of beams with various combinations of r and s are available.

References

1 Lord Rayleigh, "Theory of Sound," second edition, The Macmillan Company, New York, N. Y., pp. 293–294.

2 S. P. Timoshenko, "On the Correction for Shear of the Differential Equation for Transverse Vibrations of Prismatic Bars," *Philosophical Magazine*, series 6, vol. 41, 1921, pp. 744–746.

3 S. P. Timoshenko, "On the Transverse Vibrations of Bars of Uniform Cross Sections," *Philosophical Magazine*, series 6, vol. 43, 1922, pp. 125–131.

4 L. Pochhammer, "Ueber die Fortpflanzungsgeschwindigkeiten Schwingungen in einem isotropen Kreiscylinder," *Journal für Mathematik*, vol. 81, 1876, pp. 324–336.

5 C. Chree, "The Equations of an Isotropic Elastic Solid in Polar and Cylindrical Coordinates, Their Solution and Application," *Transactions of the Cambridge Philosophical Society*, vol. 14, 1889, p. 250.

[2] Bulletin of the Florida Engineering and Industrial Experiment Station, University of Florida.

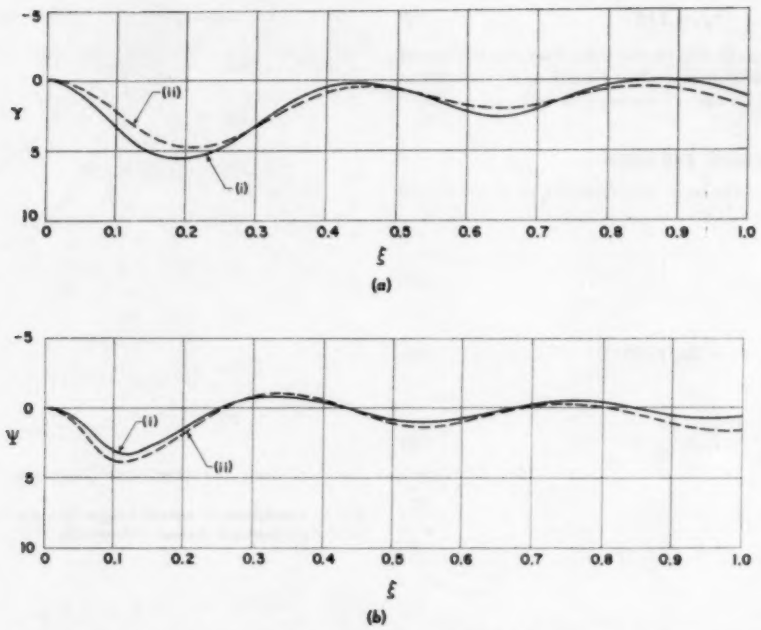

Fig. 2 Comparison of superimposed modes of five component modes each according to classical theory and according to derived relations (a) deflection, (b) bending slope (i for derived relations, ii for classical theory)

6 D. Bancroft, "The Velocity of Longitudinal Waves in Cylindrical Bars," *Physical Review*, vol. 59, 1941, pp. 588–593.

7 G. E. Hudson, "Dispersion of Elastic Waves in Solid Circular Cylinder," *Physical Review*, vol. 63, 1943, pp. 46–51.

8 R. M. Davis, "A Critical Study of the Hopkinson Pressure Bar," *Philosophical Transactions of the Royal Society*, series A, vol. 240, 1948, pp. 375–457.

9 R. A. Anderson, "Flexural Vibrations in Uniform Beams According to the Timoshenko Theory," JOURNAL OF APPLIED MECHANICS, vol. 20, TRANS. ASME, vol. 75, 1953, pp. 504–510.

10 C. L. Dolph, "On the Timoshenko Beam Vibrations," *Quarterly of Applied Mathematics*, vol. 12, 1954, pp. 175–187.

11 T. C. Huang, "Effect of Rotatory Inertia and Shear on the Vibration of Beams Treated by the Approximate Methods of Ritz and Galerkin," *Proceedings of The Third U. S. National Congress of Applied Mechanics*, ASME, 1958, pp. 189–194.

12 C. Howe, R. Howe, and L. Rauch, "Application of the Electric Differential Analyzer to the Oscillation of Beams, Including Shear and Rotatory Inertia," Ext. Memo. UMM-79, University of Michigan Research.

13 E. T. Kruszewski, "Effect of Transverse Shear and Rotatory Inertia on the Natural Frequency of a Uniform Beam," NACA TN 1909, 1949.

14 S. P. Timoshenko, "Vibration Problems in Engineering," third edition, D. Van Nostrand Company, Inc., New York, N. Y., 1955, pp. 329–331.

15 Dana Young and R. P. Felgar, "Tables of Characteristic Functions Representing Normal Modes of Vibration of a Beam," The University of Texas Publication No. 4913.

Analysis for Calculating Lateral Vibration Characteristics of Rotating Systems With Any Number of Flexible Supports

Part 1—The Method of Analysis

E. C. KOENIG
Engineering Analysis Section,
Allis-Chalmers Manufacturing Company,
Milwaukee, Wis.

A method is presented for calculating the lateral vibration characteristics of rotating systems and establishes improved criteria for design. The method is also applicable to the vibration analysis of interconnected beam systems which are nonrotating and lying in a single plane. This first part restricts itself to the development of the method of analysis. A companion paper describes the experiences related to the computer program and to some of the applications of the method since 1957.

For many years, methods have been established for calculating the critical speeds of rotors of varying flexural rigidity with any number of rigid supports [1–4].[1] In recent years some improvements in the methods have been published, but they apply mainly to two support systems [5–7]. Two-bearing rotors with equal support stiffness characteristics have been analyzed [8]. All these methods analyze the rotor systems as free-vibration problems and the results give only the values of the resonant frequencies of the rotor and the corresponding nodes.

The method presented in this paper gives results which vastly improve the criteria for designing rotor systems and applies to multiple-support systems, with dissimilar elasticity and damping in the bearings and dissimilar elasticity and masses of the bearing supports. It not only gives the values of the resonant frequency of a rotor but also provides the following information:

1 Lateral deflections of the rotor, useful for:

(*a*) Calculating rotor stresses.

(*b*) Determining clearances between rotor and stationary structures.

(*c*) Determining relative severity of vibrations at the different resonant frequencies.

2 Vibration amplitudes of the bearing supports, valuable for:

(*a*) Determining support resonant frequencies, where these resonant frequencies may be different than the resonant frequencies of the rotor.

(*b*) Determining system performance since these are the vibrations physically observed and measured.

(*c*) Obtaining a best design of a system through modifications of the bearings and their supports as well as through modifications of the rotor. The sensitivity and response of the bearing supports to rotor unbalance may be one of the factors which influence the design.

[1] Numbers in brackets designate References at end of paper.

Presented at the West Coast Conference of the Applied Mechanics Division, Seattle, Wash., August 28–30, 1961, of THE AMERICAN SOCIETY OF MECHANICAL ENGINEERS.

Discussion of this paper should be addressed to the Editorial Department, ASME, United Engineering Center, 345 East 47th Street, New York 17, N. Y., and will be accepted until January 10, 1962. Discussion received after the closing date will be returned. Manuscript received by ASME Applied Mechanics Division, January 26, 1961. Paper No. 61—APMW-16A.

Nomenclature

a_{uv} = matrix of a disk for section u in span v
b_{uv} = matrix of a massless shaft section u in span v
B_{uv} = $(EI)_{uv}$ = flexural rigidity of section u in span v, in.
c_{uv} = matrix of a combined weightless section and disk when rotor supported on rigid supports
c_{uv}' = matrix of a combined weightless section and disk when rotor supported on flexible supports
C_{uv0q} = dynamic influence of a unit force of unbalance applied at section 0 of span q on section u of span v, in/lb
C_{0v}' = oil-film damping at section 0 of span v
d_i = inside diameter of hollow cylindrical disk, in.
d_o = outside diameter of hollow cylindrical disk, in.
G_{uv0q} = $C_{uv0q} - C_{u-1,v0q}$ = difference in dynamic influence coefficients on ends of section u of span v when unit force is acting at section 0 of span q, in/lb
h_d = thickness of hollow cylindrical disk, in.
I_{uv}' = mass moment of inertia of disk of section u in span v, lb-in. sec²
K_{0v}' = oil-film stiffness at section 0 of span v, lb/in.
K_{0v}'' = support stiffness at section 0 of span v, lb/in.
l_{uv} = length of section u in span v, in.
m_d = mass of hollow cylindrical disk, lb sec²/in.
m_{uv} = balanced mass of section u in span v, lb sec²/in.
m_{uv}' = mass of unbalance attached to section mass, lb sec²/in.
m_{0v}'' = mass of support at section 0 of span v, lb sec²/in.
M_{uv} = moment at right end of section u in span v, lb-in.
n = number of sections in a span
r_{uv} = distance of mass of unbalance, m_{uv}', from center of gravity of section mass, in.
R_{0q} = support reaction at section 0 of span q, lb
U_{uv} = $m_{uv}'r_{uv}$, lb sec²
V_{uv} = shear at right end of section u in span v, lb
y_{uv} = deflection at right end of section u in span v, in.
z = number of spans in a rotor system
Z_{0v} = support impedance at section 0 of span v, lb/in.
θ_{uv} = slope at the right end of section u in span v, radians
ω_{uv} = frequency, radians/sec

To obtain this information the following conditions are included in the analysis if they exist:

1 Forces of unbalance with complete freedom of selection of numbers, size, and location.
2 Elasticity and damping of the bearings.
3 Elasticity and mass of the bearing supports.
4 Damping on the rotor body.
5 Mass moments of inertia of disks.
6 Special conditions, such as flexible couplings.

All frequencies are assumed single frequencies. This assumption requires that:

1 Effects of gravity can be neglected.
2 The elasticity and damping of the bearings and supports can be considered constant with shaft rotation.

Present-day digital computers of high speed and large memory capacities make it possible and economical to perform the large volume of calculations required for an accurate analysis of large systems. The basic analysis to include the effects of flexible supports in large systems was accomplished in 1953 by the author as part of research for a thesis [9]. Since that time various improvements have been incorporated in the method and numerous solutions obtained on digital computers. Systems with two flexible supports were first analyzed in 1957 using an IBM 650 computer. Since 1958 more complex systems have been analyzed using an IBM 704 computer. The present IBM 704 program contains all the features of the method and is capable of handling systems of 15 flexible supports. Magnetic tapes and 8000 words of core memory are required. Part 2 of the paper describes the program and its application in detail.

As is customary, the method assumes a rotor of uniform or nonuniform flexural rigidity to be made up of a large number of massless sections and an equal number of concentrated balanced masses between the massless sections. In addition, the method provides the option of adding masses of unbalance to each of the principal masses.

There is no theoretical limit to the number of flexible bearing supports that can be analyzed by the method, and all support stiffness characteristics may be dissimilar. Elasticity and damping of the bearings and elasticity and mass of the bearing supports may be represented for the analysis as equivalent lumped-parameter systems or by finite-difference systems established from partial differential equation descriptions. There are no restrictions on the types of equivalent support systems that may be selected except it is required that the support characteristics be considered constant with shaft rotation.

The effect of damping on the rotor between the bearing supports may be significant in systems where the rotor revolves in a liquid as in pump applications. To include this damping effect, a special type of support is considered to exist at the location of the rotor body damping. This fictitious support is included in the analysis in the same manner as a regular bearing support.

Since the method includes damping, the mechanical impedance, Z_m, is a complex quantity. At a critical frequency the magnitude is a minimum but greater than zero. If damping is neglected, Z_m is a real number and at a critical frequency is equal to zero. True deflections at all values of frequency can be calculated if forces, F, due to masses of unbalance are included as well as the damping. The deflections are defined by the general expression [10]

$$y = F/Z_m$$

In a free-vibration analysis, F is omitted and critical frequencies are calculated from Z_m. For the analysis presented in this paper, masses of unbalance may be considered to be attached to any of the section masses. Therefore the method can be applied as a simulator to study the vibration characteristics of a system under various conditions of unbalance. Sprung or bent rotors and crankshaft systems can also be handled as special cases of unbalance.

The method employs matrix algebra. Matrix algebra has been employed in the past in the analysis of vibration problems [11–14]. It is an elegant systematic way of handling otherwise cumbersome mathematical operations [15] and is especially suitable for digital-computer programming, reducing the programming time and the amount of memory storage, and providing generality in the application of the program. Matrix algebra in this application also eliminates the need of performing a number of part calculations frequently used by other methods in calculating critical speeds [1, 4]. The number of part calculations required by these other methods increases with the number of unknown boundary conditions, and for large systems the total calculations can become very lengthy and costly. Round-off error may also become a problem.

For the analysis presented in this paper, the basic matrix of a shaft section is expanded to include masses of unbalance, mass moments of inertia of the disks, and the effects of elasticity and damping in the bearings and elasticity and masses of the bearing supports. The size of the basic section matrix is linearly related to the number of flexible bearing supports and the number of locations of rotor damping. Multiplication of the section matrices must be performed for each rotational speed under study to obtain the span matrices. The simultaneous solution of the resulting equations provides the necessary boundary values for obtaining shear, moment, slope, and deflection at all adjacent rotor sections through the repeated matrix multiplication along the system.

By mathematical reasoning, the method should be stable, and experience in its use has shown this reasoning to be correct. Scaling of the equations is done automatically by the computer to keep coefficients of the matrices of comparable size. The scaling method is similar to that used in the application of electronic analog computers when it is required to keep voltages within amplifier range [16]. The scaling assumes accurate results with the normal eight decimal digits of computer accuracy in handling large complex systems. Scaling is discussed in detail in the companion paper.

Basic Matrix of an Unbalanced Section of a Rotor on Rigid Supports

A disk of infinite flexural rigidity is shown in Fig. 1. A mass of unbalance, m'_{uv}, is attached to the principal balanced mass, m_{uv}, at a distance r_{uv} from the center of gravity of the principal mass. When the disk is rotating at a constant circular frequency, ω, with its center of gravity displaced from the axis of rotation by a constant distance, $y_{u-1,v}$, the forces acting are

$$m_{uv}\omega^2 y_{u-1,v}$$

and

$$m_{uv}'\omega^2(r_{uv} + y_{u-1,v})$$

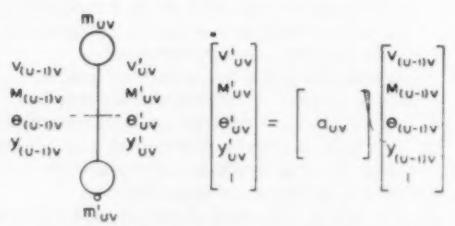

Fig. 1 Unbalanced disk of infinite flexural rigidity and its associated matrix

For assumed small deflections, the component

$$m_{uv}\omega^2 y_{u-1,v}$$

of the latter force may be neglected and

$$m_{uv}'\omega^2(r_{uv} + y_{u-1,v}) \cong U_{uv}\omega^2 \tag{1}$$

where

$$U_{uv} = m_{uv}'r_{uv}$$

For the case of a sprung or bent shaft, m_{uv}' is equal to the principal mass of the section, m_{uv}, and r_{uv} is equal to the eccentricity at zero speed. For crankshaft systems m_{uv}' is also equal to m_{uv}, and r_{uv} is the length of the crank.

The shear, moment, slope, and deflection on the right side of the disk are related to these quantities on the left side by the matrix eqdation:

$$\begin{bmatrix} V' \\ M' \\ \theta' \\ y' \\ 1 \end{bmatrix}_{uv} = \begin{bmatrix} 1 & 0 & 0 & m\omega^2 & U\omega^2 \\ 0 & 1 & I'\omega^2 & 0 & 0 \\ 0 & 0 & 1 & 0 & 0 \\ 0 & 0 & 0 & 1 & 0 \\ 0 & 0 & 0 & 0 & 1 \end{bmatrix}_{uv} \begin{bmatrix} V \\ M \\ \theta \\ y \\ 1 \end{bmatrix}_{u-1,v} \tag{2}$$

$$= [a]_{uv} \begin{bmatrix} V \\ M \\ \theta \\ y \\ 1 \end{bmatrix}_{u-1,v}$$

where I_{uv}' is the mass moment of inertia of the disk. Its effect is to change the moment across the disk and, for small values of θ, this change of moment as given by matrix equation (2) is equal to $I_{uv}'\omega^2\theta_{u-1,v}$ [1, 4, 17]. The value of I' for a hollow cylindrical disk to include gyroscopic effect in rotating systems is given by the equation

$$I_{uv}' = \left[\frac{m_d}{16}(d_o^2 + d_i^2) - \frac{m_d}{12}h_d^2\right]_{uv} \tag{3}$$

For the nonrotating case

$$I_{uv}' = -\left[\frac{m_d}{16}(d_o^2 + d_i^2) + \frac{m_d}{12}h_d^2\right]_{uv} \tag{4}$$

A weightless shaft section is shown in Fig. 2. If the shear and inertia are assumed constant along the length of the section, the shear, moment, slope, and deflection on the right end are defined in terms of these quantities on the left by the matrix equation:

$$\begin{bmatrix} V \\ M \\ \theta \\ y \end{bmatrix}_{uv} = \begin{bmatrix} 1 & 0 & 0 & 0 \\ l & 1 & 0 & 0 \\ \frac{l^2}{2B} & \frac{l}{B} & 1 & 0 \\ \frac{l^3}{6B} & \frac{l^2}{2B} & l & 1 \end{bmatrix}_{uv} \begin{bmatrix} V' \\ M' \\ \theta' \\ y' \end{bmatrix}_{uv} = [b]_{uv} \begin{bmatrix} V' \\ M' \\ \theta' \\ y' \end{bmatrix}_{uv} \tag{5}$$

If the disk and shaft are connected as shown in Fig. 3, the shear, moment, slope, and deflection on the right end of the disk are equal to those on the left of the weightless shaft. A matrix c_{uv} of the combined disk and shaft is obtained as a product of matrices b_{uv} and a_{uv}:

$$\begin{bmatrix} V \\ M \\ \theta \\ y \\ 1 \end{bmatrix}_{uv} = [b]_{uv}[a]_{uv} \begin{bmatrix} V \\ M \\ \theta \\ y \\ 1 \end{bmatrix}_{u-1,v} = [c]_{uv} \begin{bmatrix} V \\ M \\ \theta \\ y \\ 1 \end{bmatrix}_{u-1,v}.$$

$$= \begin{bmatrix} 1 & 0 & 0 & m\omega^2 & U\omega^2 \\ l & 1 & I'\omega^2 & lm\omega^2 & lU\omega^2 \\ \frac{l^2}{2B} & \frac{l}{B} & \frac{l}{B}I'\omega^2 + 1 & \frac{l^2}{2B}m\omega^2 & \frac{l^2}{2B}U\omega^2 \\ \frac{l^3}{6B} & \frac{l^2}{2B} & \frac{l^2}{2B}I'\omega^2 + l & \frac{l^3}{6B}m\omega^2 + 1 & \frac{l^2}{6B}U\omega^2 \\ 0 & 0 & 0 & 0 & 1 \end{bmatrix}_{uv} \begin{bmatrix} V \\ M \\ \theta \\ y \\ 1 \end{bmatrix}_{u-1,v} \tag{6}$$

This matrix c_{uv} describes any section u of span v consisting of a weightless shaft and a disk when the rotor is supported on rigid supports and with the conditions of unbalance and mass moment of inertia included.

The deflection, y_{uv}, of matrix equation (6) is the sum of the deflection, $y_{u-1,v}$, at the opposite end of the section and the deflection terms due to bending along the length of the section. The value of y_{uv} is properly defined if the bearing supports are rigid.

Basic Matrix of an Unbalanced Section of a Rotor on Flexible Supports

Curve y in Fig. 4 shows the center line of the rotor of a three-span rotating system under the conditions of elastic supports and oil film. The vectors y_{01}, y_{02}, y_{03}, and y_{04} are the displacements of the center line of the rotor at the bearing supports from the axis of rotation, shown as curve c. Curve f would be the center line of the rotor if the masses of the rotor were set equal to zero and the bearing reaction forces were equal to those reaction forces which exist when the masses equal their true values and rotating at the given speed. The deflection, y_{uv}, for secton u shown in the figure is defined by matrix equation (6) with the addition of the term $(f_{uv} - f_{u-1,v})$ which is the difference in the distances at the ends of the section between curve f and the axis of rotation, curve c. The value of y_{uv} is then defined by the equation:

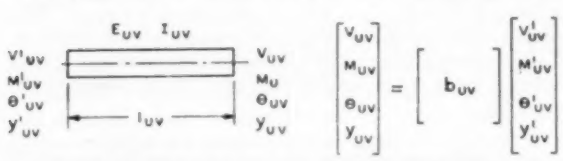

Fig. 2 Weightless shaft section and its associated matrix

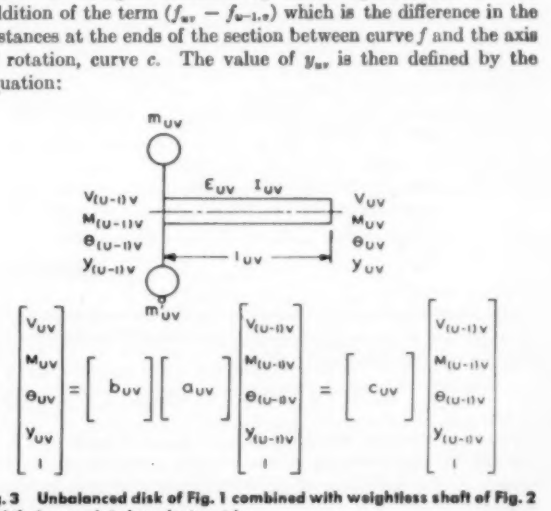

Fig. 3 Unbalanced disk of Fig. 1 combined with weightless shaft of Fig. 2 and their associated product matrix

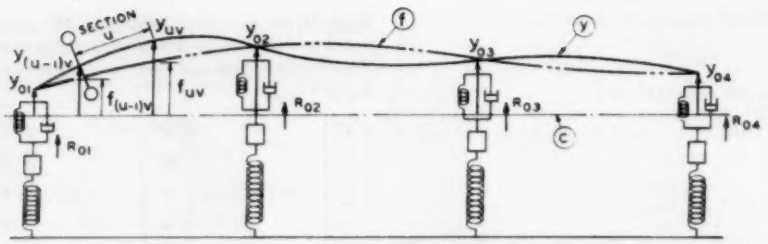

Fig. 4 Three-span system on flexible bearing supports for purpose of establishing method of analysis

$$y_{uv} = \left[\frac{l^3}{6B}\right]_{uv} V_{u-1,v} + \left[\frac{l^2}{2B}\right]_{uv} M_{u-1,v} + \left[\frac{l^3}{2B} I'\omega^2 + l\right]_{uv} \theta_{u-1,v} + \left[\frac{l^3}{6B} m\omega^2 + 1\right]_{uv} y_{u-1,v} + \left[\frac{l^3}{6B} U\omega^2\right]_{uv} + [f_{uv} - f_{u-1,v}] \quad (7)$$

The quantities f_{uv} and $f_{u-1,v}$ can be related to the support reactions, R_{0q}, through the use of dynamic influence coefficients. For any system of z-spans f_{uv} is defined as:

$$f_{uv} = \sum_{q=1}^{z+1} C_{uv0q} R_{0q} \quad (8)$$

$$\begin{bmatrix} V_{uv} \\ M_{uv} \\ \theta_{uv} \\ y_{uv} \\ 1 \\ V_{01} - V_{u0} \\ \cdots \\ V_{0,z+1} - V_{uz} \end{bmatrix} = [c_{uv}'] \begin{bmatrix} V_{u-1,v} \\ M_{u-1,v} \\ \theta_{u-1,v} \\ y_{u-1,v} \\ 1 \\ V_{01} - V_{u0} \\ \cdots \\ V_{0,z+1} - V_{uz} \end{bmatrix} \quad (11)$$

where

$$[c_{uv}'] = \begin{bmatrix} 1 & 0 & 0 & m_{uv}\omega^2 & U_{uv}\omega^2 & 0 & \cdots & 0 \\ l_{uv} & 1 & I_{uv}'\omega^2 & [lm]_{uv}\omega^2 & [lU]_{uv}\omega^2 & 0 & \cdots & 0 \\ \left[\frac{l^2}{2B}\right]_{uv} & \left[\frac{l}{B}\right]_{uv} & \left[\frac{l}{B} I'\right]_{uv}\omega^2 + 1 & \left[\frac{l^2}{2B} m\right]_{uv}\omega^2 & \left[\frac{l^2}{2B} U\right]_{uv}\omega^2 & 0 & \cdots & 0 \\ \left[\frac{l^2}{6B}\right]_{uv} & \left[\frac{l^2}{2B}\right]_{uv} & \left[\frac{l^2}{2B} I'\right]_{uv}\omega^2 + l_{uv} & \left[\frac{l^3}{6B} m\right]_{uv}\omega^2 + 1 & \left[\frac{l^3}{6B} U\right]_{uv}\omega^2 & G_{uv01} & \cdots & G_{uv0,z+1} \\ 0 & 0 & 0 & 0 & 1 & 0 & \cdots & 0 \\ 0 & 0 & \cdots & 0 & 0 & 1 & \cdots & 0 \\ \cdots & \cdots & 0 & \cdots & \cdots & \cdots & \cdots & \cdots \\ 0 & 0 & 0 & 0 & 0 & 0 & \cdots & 1 \end{bmatrix}$$

where the quantities C_{uv0q} are the dynamic influence coefficients obtained by applying a unit force of unbalance, $U_{0q}\omega^2 = 1$, at section 0 of span q containing a support. The coefficients are obtained with the system rotating at the speed under consideration and with all masses set equal to zero, except the unit force of unbalance at the support $0q$.

From equation (8) the quantity $(f_{uv} - f_{u-1,v})$ appearing in equation (7) may be written as

$$[f_{uv} - f_{u-1,v}] = \sum_{q=1}^{z+1} [C_{uv0q} - C_{u-1,v0q}] R_{0q}$$
$$= [C_{uv01} - C_{u-1,v01}] R_{01} + [C_{uv02} - C_{u-1,v02}] R_{02} + \ldots + [C_{uv0,z+1} - C_{u-1,v0,z+1}] R_{0,z+1} \quad (9)$$

The reactions, R_{0q}, may be defined as the differences in shears on either side of the supports or as the product of the support impedance and the deflections; namely,

$$R_{0q} = V_{0q} - V_{u,q-1} = -Z_{0q} y_{0q} \quad (10)$$

After substituting the value of $f_{uv} - f_{u-1,v}$ of equation (9) in equation (7) and rewriting matrix equation (6) incorporating the change in the definition of y_{uv}, the following matrix equation results:

where

$$G_{uv0q} = C_{uv0q} - C_{u-1,v0q}$$

and

$$V_{0q} - V_{u,q-1} = R_{0q}$$

from equation (10).

The matrix c_{uv}' describes any section u of span v consisting of a uniform weightless shaft and disk when the rotor system is supported on flexible supports and with the conditions of unbalance and mass moment of inertia included.

General Application of Basic Matrices

Fig. 5 shows a rotor system of z-spans with the spans connected end to end and the spans and the sections of each span numbered from left to right. The first support on the left is shown to consist of only a damper which represents rotor-body damping and is included in the analysis in the same manner as a support. The lumped-parameter representation of the supports is not restricted. If the supports are represented by the lumped-parameter system shown in Fig. 5, the mechanical impedance, Z_{0v}, is defined by the equation:

$$Z_{0v} = \frac{(j\omega C_{0v}' + K_{0v}')(-\omega^2 m_{0v}'' + K_{0v}'')}{-\omega^2 m_{0v}'' + K_{0v}'' + K_{0v}' + j\omega C_{0v}'} \quad (12)$$

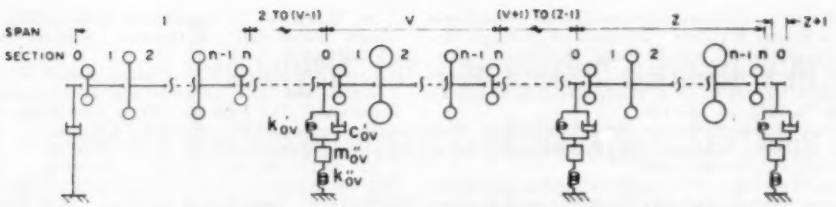

Fig. 5 General system of z-spans with damper on left end representing rotor body damping at that location

The basic matrix for a rotor section c_{uv}' of equation (11) is used in construction of the following matrix equation for any span v of the rotor system in Fig. 5:

$$\begin{bmatrix} V_{uv} \\ M_{uv} \\ \theta_{uv} \\ y_{uv} \\ 1 \\ V_{01} - V_{u0} \\ \cdots \\ V_{0,z+1} - V_{uz} \end{bmatrix} = [c_{uz}'] \cdots [c_{2v}'][c_{1v}'] \begin{bmatrix} V_{0v} \\ M_{0v} \\ \theta_{0v} \\ y_{0v} \\ 1 \\ V_{01} - V_{u0} \\ \cdots \\ V_{0,z+1} - V_{uz} \end{bmatrix} \tag{13}$$

The total number of equations for a rotor system obtained from matrix equation (13) is $4z$ and the number of unknowns is $8z$. Additional equations are obtained by equating certain quantities at the ends of adjacent spans. These equations are

$$\begin{aligned} M_{u,v-1} &= M_{0v} \\ \theta_{u,v-1} &= \theta_{0v} \\ y_{u,v-1} &= y_{0v} \end{aligned} \tag{14}$$

Also, at the ends of the rotor system

$$\begin{aligned} M_{01} &= 0 \\ M_{uz} &= 0 \end{aligned} \tag{15}$$

Additional equations are obtained from equation (10). These are

$$y_{0v} = \frac{V_{u,v-1} - V_{0v}}{Z_{0v}} \tag{16}$$

The number of equations to be solved simultaneously can be reduced to $4z$ by the simple substitution of the quantities of equations (14), (15), and (16) in the equations resulting from matrix equation (13).

Matrix equation (13) and equations (14), (15), and (16) are used to perform the complete analysis. The influence coefficients C_{uv0q} are first calculated by setting these same quantities equal to zero in the matrices c_{uv}. The principal mass quantities, m_{uvv}, are also set equal to zero. All forces of unbalance, $U_{uv}\omega^2$, are set equal to zero except one of the $U_{1v}\omega^2$ or $U_{uv}\omega^2$ forces which is given a value of magnitude equal to unity and angle equal to zero. A simultaneous solution of the equations of matrix equation (13) and equations (14), (15), and (16) yield the boundary values of each span. With the boundary values known, repeated matrix multiplications are performed through each span to obtain the deflections or the influence coefficients for that unit force acting on the system. An identical calculating procedure is used for the condition of unity assigned to each of the $U_{1v}\omega^2$ or $U_{uv}\omega^2$ forces. A total of $z + 1$ sets of calculations is required in obtaining a complete set of influence coefficients for a given value of speed.

After the dynamic influence coefficients are calculated, the values are substituted in the matrices c_{uv}' and the mass quantities, m_{uvv}, given their actual values. The quantities U_{uv} are independent variables and are assigned the desired values. A calculating procedure identical to that used in calculating the influence coefficients is used to obtain the desired values of shear, moment, slope, and deflection at adjacent sections throughout the rotor system.

To reduce calculating time in obtaining the influence coefficients, matrices a_{uv} and b_{uv} of matrix equations (2) and (5), respectively, may be used instead of matrix c_{uv}' in constructing matrix equation (13). Trivial multiplications which result from setting m_{uv} and U_{uv} equal to zero are avoided.

The rotor system shown in Fig. 5 is a general system, and the analysis procedure for this system can be applied directly to variations in the system. Rotors with overhanging end spans are analyzed by letting the end-support impedances Z_{01} and $Z_{0,z+1}$ approach zero. Rotors with assumed rigid supports are analyzed by letting the support impedances approach infinity. Couplings in rotor systems are considered as junctions of spans. The impedances of the assumed supports at the couplings are set equal to zero and equations (14), relating the end conditions of the spans adjacent to the couplings, modified depending on the types of couplings.

An identical procedure of analysis applies to nonrotating-beam systems which may be interconnected and lying in a plane. Equations (14) may require modifications to agree with the end conditions of the spans. The forces of unbalance become sinusoidal forces applied to the beam system.

Conclusion

The method for analyzing complex systems with dissimilar support characteristics is quite general in application. It includes conditions previously neglected by other methods and provides information which vastly improves the design criteria. The method has been found to be numerically stable and does not require part calculations used by other methods. Its full potential will not be realized until theoretical and experimental investigations are made to obtain more accurate input information than is presently available. Part 2 of the paper describes a single computer program incorporating all the features of the method and capable of analyzing any system up to 15 supports. The results of a few of the past applicatics are also discussed.

References

1 M. A. Prohl, "A General Method for Calculating Critical Speeds of Flexible Rotors," JOURNAL OF APPLIED MECHANICS, vol. 12, TRANS. ASME, vol. 67, 1945, p. A-142.

2 N. O. Myklestad, "A New Method for Calculating Natural Modes of Uncoupled Bending Vibrations of Airplane Wings and Other Types of Beams," *Journal of the Aeronautical Sciences*, vol. 11, 1944, pp. 153–162.

3 A. Stodala, "Steam and Gas Turbines," McGraw-Hill Book Company, Inc., New York, N. Y., 1927.

4 R. L. Urban, "Extension of Holzer-Myklestad-Prohl Calculation of Turbo-Rotor Critical Speeds," ASME Paper No. 58-A-246 (unpublished).

5 R. A. Di Taranto, "Natural Frequencies of Nonuniform Beams on Multiple Elastic Supports," JOURNAL OF APPLIED MECHANICS, vol. 25, TRANS. ASME, vol. 80, 1958, pp. 57–63.

6 D. F. Miller, "Forced Lateral Vibration of Beams on Damped Flexible End Supports," JOURNAL OF APPLIED MECHANICS, vol. 20, TRANS. ASME, vol. 75, 1953, pp. 167–172.

7 E. Downham, "The Influence of Plain Bearings on Shaft Whirling," Royal Aircraft Establishment, Farnborough, Hants, Report No: Structures 192, October, 1955.

8 W. J. Caruso, "Prediction of Critical Speeds of Steam Turbines by Dynamic Stiffness Method," ASME Colloquium on Mechanical Impedance Methods for Mechanical Vibrations, 1959, p. 137.

9 E. C. Koenig, "A Rotating Systems Analyzer for Balancing and Simulating Rotating Systems," PhD thesis, University of Wisconsin, 1956.

10 H. F. Olson, "Dynamical Analogies," D. Van Nostrand Company, Inc., New York, N. Y., 1943.

11 W. T. Thomson, "Matrix Solution for the Vibration of Nonuniform Beams," JOURNAL OF APPLIED MECHANICS, vol. 17, TRANS. ASME, vol. 72, 1950, pp. 337–339.

12 H. Fuhrke, "Determination of Frams Vibrations With Matrix Calculations" (in German), *Ingenieur-Archiv*, vol. 24, 1956, pp. 27–42.

13 R. Zurmuhl, "Calculation of Bending Vibrations of Stepped Shafts With Intermediate Restrictions by Means of Transporting Matrix" (in German), *Ingenieur-Archiv*, vol. 26, 1958, pp. 398–407.

14 H. Fuhrke, "Determination of Beam Vibrations With Help of Matrix Calculations" (in German), *Ingenieur-Archiv*, vol. 23, 1955, pp. 329–348.

15 R. A. Frazer, W. J. Duncan, and A. R. Collar, "Elementary Matrices and Some Applications to Dynamics and Differential Equations," The University Press, Cambridge, England, 1938.

16 A. S. Jackson, "Analog Computation," McGraw-Hill Book Company, Inc., New York, N. Y., 1960.

17 S. Timoshenko, "Vibration Problems in Engineering," D. Van Nostrand Company, Inc., New York, N. Y., 1937.

18 F. C. Linn and M. A. Prohl, "The Effect of Flexibility of Support Upon the Critical Speeds of High-Speed Rotors," *Trans. SNAME*, vol. 59, 1951, pp. 536–553.

19 A. C. Hagg, "The Influence of Oil-Film Journal Bearings on the Stability of Rotating Machines," JOURNAL OF APPLIED MECHANICS, vol. 13, TRANS. ASME, vol. 68, 1946, p. A-211.

20 Kurt Schmidt, "Zur Spannungsberechnung unrunder Rohre unter Aussbendruck," Part 1, *VDI Zeitschrift*, Bd. 101, 1959, pp. 47–54.

21 Karl Schaff and K. H. Krieb, "Schwingungserscheinungen an Turbogeneratoren mit Stahlfundamenten," Part 3, *VDI Zeitschrift*, Bd. 101, 1959, pp. 117–124.

22 N. H. Jasper, "A Design Approach to the Problem of Critical Whirling Speeds of Shaft-Disk Systems," U. S. Navy Department, Washington, D. C., Report 890, December, 1954.

Analysis for Calculating Lateral Vibration Characteristics of Rotating Systems With Any Number of Flexible Supports

Part 2—Application of the Method of Analysis

T. G. GUENTHER
D. C. LOVEJOY
Assoc. Mem. ASME
Engineering Analysis Section,
Allis-Chalmers Manufacturing Company,
Milwaukee, Wis.

A description is given of computer programs based on Part 1[1] of this paper, and some of the results of using those programs are presented.

MANY methods have been developed in the past for calculating critical speeds, but it has often been found that the calculated natural frequencies, particularly the higher ones, were not the same as the observed natural frequencies. Part 1 of this paper presents a method of calculating vibration characteristics of large rotor systems more accurately than by previous methods. It includes the effect of damping and flexibility of the oil films and mass and flexibility of the supports. The method includes the concept of support stiffness being a function of speed.

Part 2 describes a computer program based on that method, and shows the results of applying the program to various rotor systems. It will also be shown that a proper description of support parameters is just as essential as the description of rotor geometry when predicting critical speeds of systems with flexible supports.

Matrix algebra, which is used in the analysis, is particularly suited to high-speed computers. A rotor with several supports takes from one to several hours for a thorough analysis of vibration characteristics, depending on the size of the system and the need to include damping. The program to be described has been used on an IBM 704 at the authors' company for several hundred hours over the past 2 years.

A third part of this paper is being planned which will include methods of calculating support parameters and comparisons of test results with results computed by the program.

Description of Program

The initial computer program based upon reference [1][2] was written for the IBM 650. Since the computer had only 2000 words of storage, this program was very limited in scope. It was capable of finding the natural frequency and the mode of vibration of a system of two supports and three spans only. The only support parameter which was taken into account was flexibility. The mass and damping in the support were ignored. Even though this program had limited application, it made possible the finding of critical speeds to greater accuracy than methods which assumed rigid supports, and verified the correctness of the theory upon which it was based.

After this preliminary success, a much more ambitious program was planned and written for the IBM 704. It takes into account all of the variables mentioned in Part 1. Small systems (less than 6 spans and less than 65 sections) can be solved readily with 8000 words of storage and no tape or drums. With four tape units, systems having as many as fourteen spans and any number of sections can be handled conveniently. This limitation is imposed only because it was desired to have the sets of simultaneous equations small enough to fit entirely in core. The entire 704 program consists of about 6000 instructions, and took about $1^1/_2$ man-years of analysis and programming time.

The primary input to the program is a description of each section of the system and a description of each support. In addition, it is possible to specify the values of shear, moment, slope, and deflection at any support as either unknown, unknown but equal to some other unknown variable, or known and equal to a given value.

As shown in Part 1, the basic matrix equation relating shear, moment, slope, and deflection at the two ends of a section is as follows:

$$\begin{bmatrix} V_{us} \\ M_{us} \\ \theta_{us} \\ Y_{us} \\ 1 \\ V_{01} - V_{n0} \\ \cdots \\ V_{0(s+1)} - V_{us} \end{bmatrix} = [c_{us}'] \begin{bmatrix} V_{(u-1)s} \\ M_{(u-1)s} \\ \theta_{(u-1)s} \\ Y_{(u-1)s} \\ 1 \\ V_{01} - V_{n0} \\ \cdots \\ V_{0(s+1)} - V_{us} \end{bmatrix} \quad (1)$$

[1] Part 1 of this paper is entitled "The Method of Analysis," by E. C. Koenig; see this issue, pp. 585–590.

[2] Numbers in brackets designate References at end of paper.

Presented at the West Coast Conference of the Applied Mechanics Division, Seattle, Wash., August 28–30, 1961, of THE AMERICAN SOCIETY OF MECHANICAL ENGINEERS.

Discussion of this paper should be addressed to the Editorial Department, ASME, United Engineering Center, 345 East 47th Street, New York 17, N. Y., and will be accepted until January 10, 1962. Discussion received after the closing date will be returned. Manuscript received by ASME Applied Mechanics Division, January 26, 1961. Paper No. 61—APMW-16B.

where

$$[c_{uv}'] = \begin{bmatrix} 1 & 0 & 0 & m_{uv}\omega^2 & U_{uv}\omega^2 & 0 & \dots & 0 \\ l_{uv} & 1 & I_{uv}'\omega^2 & [lm]_{uv}\omega^2 & [lU]_{uv}\omega^2 & 0 & \dots & 0 \\ \left[\frac{l^2}{2B}\right]_{uv} & \left[\frac{l}{B}\right]_{uv} & \left[\frac{l}{B}I'\right]_{uv}\omega^2+1 & \left[\frac{l^2}{2B}m\right]_{uv}\omega^2 & \left[\frac{l^2}{2B}U\right]_{uv}\omega^2 & 0 & \dots & 0 \\ \left[\frac{l^3}{6B}\right]_{uv} & \left[\frac{l^2}{2B}\right]_{uv} & \left[\frac{l^2}{2B}I'\right]_{uv}\omega^2+l_{uv} & \left[\frac{l^3}{6B}m\right]_{uv}\omega^2+1 & \left[\frac{l^3}{6B}U\right]_{uv}\omega^2 & G_{uv01} & \dots & G_{uv0(z+1)} \\ 0 & 0 & 0 & 0 & 1 & 0 & \dots & 0 \\ 0 & 0 & 0 & 0 & 0 & 1 & \dots & 0 \\ \dots & \dots & \dots & \dots & \dots & \dots & \dots & \dots \\ 0 & 0 & 0 & 0 & 0 & 0 & \dots & 1 \end{bmatrix}$$

(The meaning of each symbol used is given in Part 1 of this paper.) In order to minimize the danger of developing numbers which are too large or too small for the computer, a scale factor, S, is introduced, changing the equations represented by the foregoing matrices to:

$$\frac{V_{uv}}{S} = \frac{V_{(u-1)v}}{S} + \frac{m_{uv}}{S}\omega^2 + \frac{U_{uv}}{S}\omega^2$$

$$\frac{M_{uv}}{S} = l_{uv}\frac{V_{(u-1)v}}{S} + \frac{M_{(u-1)v}}{S} + \frac{I_{uv}'}{S}\omega^2\theta_{(u-1)v} + \left[l\frac{m}{S}\right]_{uv}\omega^2 Y_{(u-1)v} + \left[l\frac{U}{S}\right]_{uv}\omega^2$$

$$\theta_{uv} = \left[\frac{l^2}{2B}\right]_{uv}\frac{V_{(u-1)v}}{S} + \left[\frac{l}{B}\right]_{uv}\frac{M_{(u-1)v}}{S} + \left[\frac{l}{B}\frac{I'}{S}\right]_{uv}\omega^2\theta_{(u-1)v} + \theta_{(u-1)v} + \left[\frac{l^2}{2B}\frac{m}{S}\right]_{uv}\omega^2 Y_{(u-1)v} + \left[\frac{l^2}{2B}\frac{U}{S}\right]_{uv}$$

$$Y_{uv} = \left[\frac{l^3}{6B}\right]_{uv}\frac{V_{(u-1)v}}{S} + \left[\frac{l^2}{2B}\right]_{uv}\frac{M_{(u-1)v}}{S} + \left[\frac{l^2}{2B}\frac{I'}{S}\right]_{uv}\omega^2\theta_{(u-1)v} + l_{uv}\theta_{(u-1)v} + \left[\frac{l^3}{6B}\frac{m}{S}\right]_{uv}\omega^2 Y_{(u-1)v} + Y_{(u-1)v} + \left[\frac{l^3}{6B}\frac{U}{S}\right]_{uv}\omega^2 + G_{uv01}S\left(\frac{V_{01}}{S} - \frac{V_{u0}}{S}\right) + \dots + G_{uv0(z+1)}S\left(\frac{V_{0(z+1)}}{S} - \frac{V_{uz}}{S}\right)$$

The matrices for a complete span are set up as follows:

$$\begin{bmatrix} V_{uv} \\ M_{uv} \\ \theta_{uv} \\ Y_{uv} \\ 1 \\ V_{01} - V_{u0} \\ \dots \\ V_{0(z+1)} - V_{uz} \end{bmatrix} = [c_{uv}'][c_{(u-1)v}'] \dots [c_{2v}'][c_{1v}'] \begin{bmatrix} V_{0v} \\ M_{0v} \\ \theta_{0v} \\ Y_{0v} \\ 1 \\ V_{01} - V_{u0} \\ \dots \\ V_{0(z+1)} - V_{uz} \end{bmatrix}$$

Normally the quantities contained in the column matrices are not all known, but the matrices c_{uv}' contain known information so that they may be multiplied together giving

$$\begin{bmatrix} V_{uv} \\ M_{uv} \\ \theta_{uv} \\ Y_{uv} \\ 1 \\ V_{01} - V_{u0} \\ \dots \\ V_{0(z+1)} - V_{uz} \end{bmatrix} = \begin{bmatrix} v_{11} & v_{12} & v_{13} & v_{14} & v_{15} & v_{16} & \dots & v_{1(4+z)} \\ v_{21} & v_{22} & v_{23} & v_{24} & v_{25} & v_{26} & \dots & v_{2(4+z)} \\ v_{31} & v_{32} & v_{33} & v_{34} & v_{35} & v_{36} & \dots & v_{3(4+z)} \\ v_{41} & v_{42} & v_{43} & v_{44} & v_{45} & v_{46} & \dots & v_{4(4+z)} \\ 0 & 0 & 0 & 0 & 1 & 0 & \dots & 0 \\ 0 & 0 & 0 & 0 & 0 & 1 & \dots & 0 \\ \dots & \dots & \dots & \dots & \dots & \dots & \dots & \dots \\ 0 & 0 & 0 & 0 & 0 & 0 & \dots & 1 \end{bmatrix} \begin{bmatrix} V_{0v} \\ M_{0v} \\ \theta_{0v} \\ Y_{0v} \\ 1 \\ V_{01} - V_{u0} \\ \dots \\ V_{0(z+1)} - V_{uz} \end{bmatrix} \quad (2)$$

The equations represented by matrices (2) have as unknowns $V_{uv}, M_{uv}, \theta_{uv}, Y_{uv}, V_{0v}, M_{0v}, \theta_{0v}, Y_{0v}, (V_{01} - V_{u0}), \dots, (V_{0(z+1)} - V_{uz})$. The first four of the equations should be kept, and the rest discarded. By a procedure similar to the one described, the element matrices of the other spans in the system are multiplied together, each span yielding four more equations. At this time there will be $4z$ equations and $8z$ unknowns, where z is the number of spans in the system. However, the number of unknowns can be reduced to $4z$ by observing which of the following equalities are true, and making the proper substitutions:

$$A = \text{known values}$$

$$M_{0v} = M_{u(v-1)}$$

$$\theta_{0v} = \theta_{n(v-1)}$$

$$Y_{0v} = Y_{n(v-1)} = \frac{(V_{0v} - V_{n(v-1)})}{-Z_{0v}}$$

where Z_{0v} is support stiffness, and A represents the boundary values at any span end.

In theory, this set of $4x$ simultaneous equations could be solved, giving the values of all the unknowns in the foregoing column matrices. With these matrices known, the multiplication shown in equation (1) can be performed, and the value of deflection calculated at every element in the system. Other values of frequency could be chosen, and this same procedure repeated, setting up simultaneous equations, solving them, and calculating deflections. Then a plot could be made for all elements in the system, showing at each element the relation between frequency and deflection. The frequency which causes any part of the system to vibrate at a maximum deflection would be the natural frequency.

Actually, much of this computing is avoided by recognizing that any deflection which appeared as an unknown in the set of simultaneous equations can be found by finding the ratio of two determinants, $Y = D_1/D$, where D_1 turns out to be a function of unbalance, and D a function of impedance. When we are working with frequencies near the natural frequency, the denominator of this fraction changes much more rapidly than the numerator, so when the denominator is at its minimum value, the fraction will be very near to its maximum. Therefore the natural frequency is actually found by having the program consider a plot of frequency versus the determinant D. Only when the critical speed is found does the program solve the simultaneous equations and perform the multiplications of equation (1) to find the deflections of the system if damping and unbalance are given, or to find the mode if damping and unbalance are not given. A numerical example is given in the Appendix.

Verification of Program

As an indication of the accuracy of the program in finding the natural frequency of a system with rigid supports, consider a shaft 100 in. long, 5 in. diam, with a support at each end. Take its weight to be 557.631 lb, moment of inertia equal to 30.679615 in.^{4}, and the modulus of elasticity equal to 2.9×10^7 psi. One formula [2] for natural frequency gives

$$\omega_1 = \frac{\pi^2}{l^2}\left(\frac{EI}{\rho}\right)^{1/2} \text{ with } \omega_2 = 4\omega_1 \text{ and } \omega_3 = 9\omega_1,$$

where ρ = mass/unit length (g = 386.4 in./sec^2). These formulas give ω_1 = 2340.1310, ω_2 = 9360.5240, ω_3 = 21061.179 rpm.

Using the computer program with elements of various lengths gives results as shown in Table 1. These results seem to indicate

Table 1 Effect of number of elements on critical speeds

Number of elements	ω_1	ω_2	ω_3
5	2339.8547	9337.3818	20670.316
10	2340.1163	9359.4167	21047.090
20	2340.1316	9360.4658	21060.521
50	2340.1324	9360.5254	21061.312
100	2340.1324	9360.5289	21061.322
200	2340.1323	9360.5228	21061.437

that the accuracy is almost independent of the number of elements. Even with a small number of elements, there is a high degree of accuracy. An extremely large number of elements introduces some round-off error. Between these extremes it appears that the program is approaching a value slightly higher than the theoretical frequency.

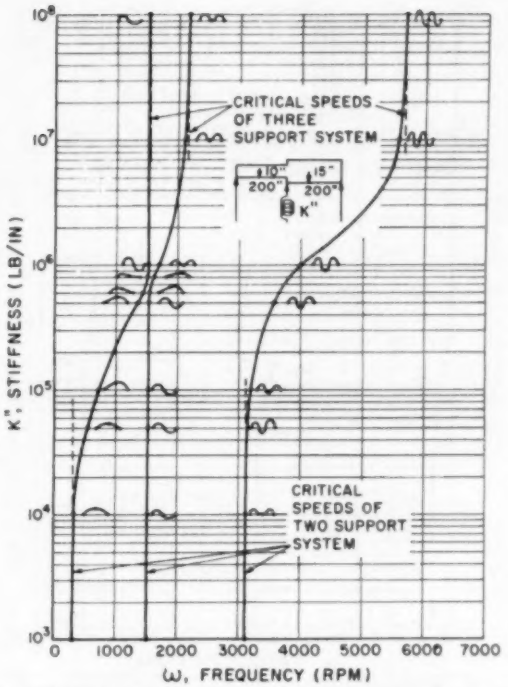

Fig. 1 Change in critical speed due to change in support stiffness

To gain some idea of the accuracy of the program in handling systems with flexible supports, consider a shaft with three supports, Fig. 1. When all three supports are rigid, the natural frequency can be found easily. If the middle support is allowed to become extremely flexible, the system should have a natural frequency close to that of the same system without any middle support. Fig. 1 shows that these expected results actually are achieved, and also shows the gradual change in critical speeds as the stiffness of the center support is changed. (The small figure next to each point indicates the mode shape at that speed.)

Somewhat the same type of approach can be taken to see the effect of damping on critical speed. A system having a rigid support at each end and a very small amount of damping at the center should have approximately the same natural frequencies as a system with the same two supports, but no damping. At the other extreme, it seems reasonable that an infinite amount of damping at the center of the system should have the same effect as putting a third rigid support at that position. Fig. 2 shows that the program actually gives these results, and also shows the effect on critical speeds as the amount of damping is varied between the two extremes. As the amount of damping increases, the first critical occurs at lower values and would presumably disappear altogether with an infinite amount of damping. With that condition, the natural frequency that occurs at 1527 rpm would be the first natural frequency, the same value as the first critical of a system with three rigid supports. The critical which occurs at 1527 rpm is changed by only a few rpm with a change in damping at the center of the system, undoubtedly because the mode form at this particular speed has a nodal point so near to the center that it is only slightly affected by any type of restraint at that point.

Something similar happens to the fourth critical speed, which is around 5900 rpm; but this critical shows a little more change with varied damping. The third critical speed shows the most

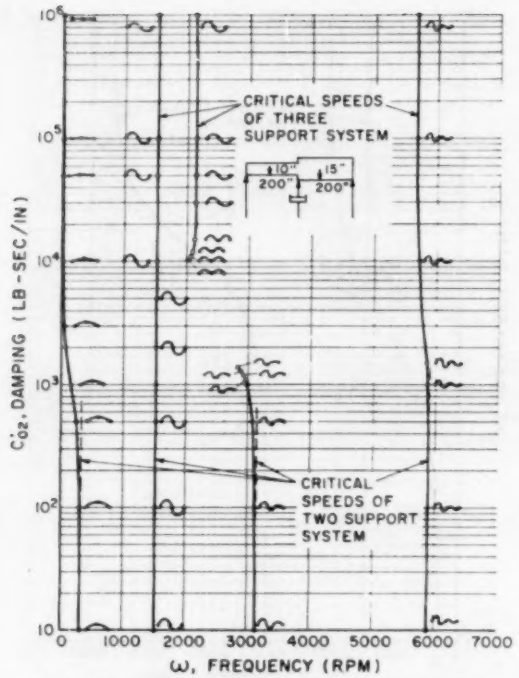

Fig. 2 Change in critical speed due to change in damping

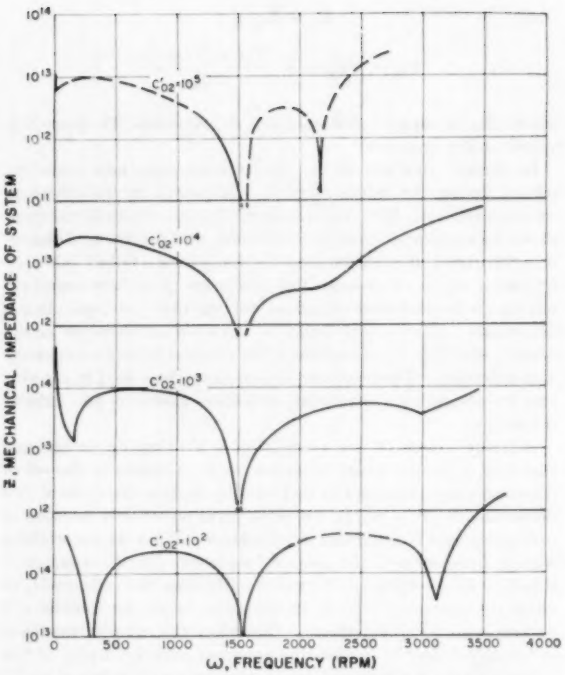

Fig. 3 Comparison of shift in natural frequencies with change in damping

unusual effect with changed damping. As damping varies between zero and 1150 lb-sec/in., the system is a two-support one and the critical speed varies moderately. When the damping is about 10000 lb-sec/in., the system seems to be roughly equivalent to a three-support system; but when the damping is between 1500 and 10000 lb-sec/in., the system seems not to be equivalent to a two-support nor a three-support system, and no critical speed can be found with the mode form of a third natural frequency.

Fig. 3 attempts to give more information on this matter. Each graph is a plot of frequency versus the determinant of the simultaneous equations. (The determinant is inversely proportional to deflection.) Each plot points out the location of a critical speed by a minimum point on the curve. It can be seen that as the damping increases, the minimum points in the vicinity of 3000 rpm become less pronounced, and finally disappear, indicating that this critical speed no longer exists. Also, as damping increases, a minimum point gradually comes into existence around 2100 rpm, indicating that a critical speed exists with the higher damping values.

R. L. Urban [3] refers to a rotor described by M. A. Prohl [4], and shows the changes in critical speeds when taking into account the gyroscopic effect of disks. That same rotor was analyzed with the program described here, and a comparison of critical speeds is given in Table 2. (A slight modification was made in the representation of the rotor by making each disk a separate element.)

Table 2 Comparison of critical speeds by various calculation methods

Method	1st critical	2nd	3rd
Prohl (without gyroscopic effect)	2230	4220	11790
Koenig (without)	2222	4409	12532
Koenig (with)	2231	4442	12903
Urban (without)	2200	4420	12680
Urban (with)	2200	4450	13100

Support Representation

W. J Caruso has shown that, when calculating the critical speeds of a shaft, the support stiffness changes with speed [5]. He has shown that a reliable way to predict critical speeds of a two-support system, where the support characteristics are identical, is to determine the intersections of the rotor dynamic-stiffness curves and the support dynamic-stiffness curves, where the support curves are obtained from test data. This paper will support the work of Caruso and also show how the dynamic-stiffness concept can be extended analytically to systems of more than two dissimilar supports. The method of this paper allows supports to be represented as a certain combination of springs, masses, and dampers such that the dynamic stiffness of each support, hereafter called support mechanical impedance, is defined at each speed. The inclusion of the support mechanical impedance in the matrix calculation is shown in Part 1.

A support was chosen to be represented as shown in Fig. 4, where the mechanical impedance z is a function of oil-film stiffness and damping, the mass and stiffness of the support, and speed. Curves of support mechanical impedance z versus excitation frequency with and without damping for constant values of K'', M'', K', and C' are shown in Fig. 4. The support at point A, Fig. 4, is theoretically defined as the support mass stiffness and the static stiffness of the oil film in series. When $K'' = M''\omega^2$, and therefore $Z = 0$, the support is vibrating at a natural frequency. When a support is represented in this manner, damping stiffens the support considerably beyond point B, but only slightly stiffens the support at speeds less than the support fundamental frequency.

Application of Method on Two-Support Rotor Systems

The method of this paper necessitates a knowledge of support parameters as well as rotor geometry in order to accurately predict critical speeds of flexible support systems. A procedure to

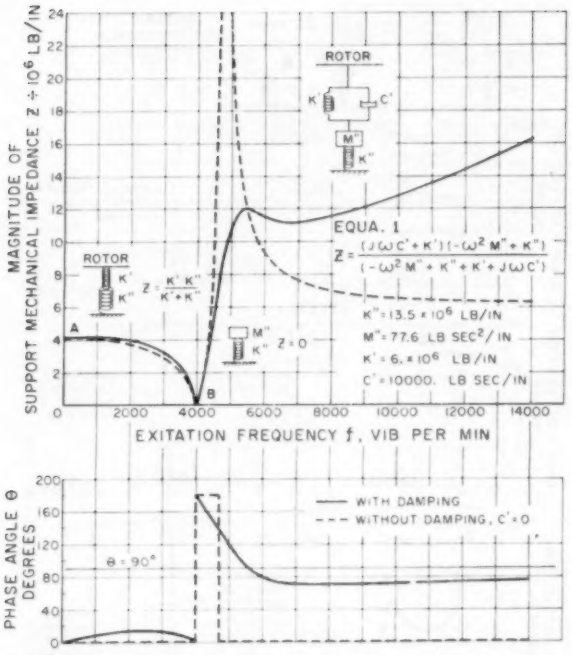
MAGNITUDE OF SUPPORT MECHANICAL IMPEDANCE Z ÷ 10⁶ LB/IN
ROTOR
EQUA. 1
K" = 13.5 × 10⁶ LB/IN
M" = 77.6 LB SEC²/IN
K' = 6. × 10⁶ LB/IN
C' = 10000. LB SEC/IN
EXITATION FREQUENCY f, VIB PER MIN
PHASE ANGLE Θ DEGREES
WITH DAMPING
WITHOUT DAMPING, C' = 0
Θ = 90°

Fig. 4 Lump parameter support representation, with and without damping

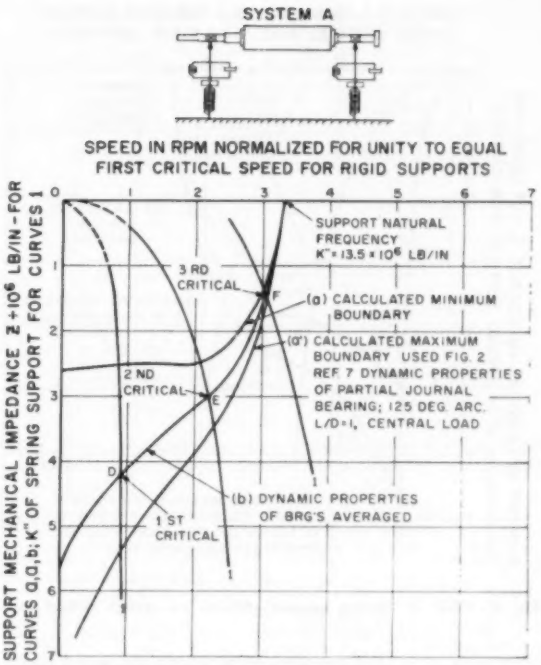
SYSTEM A
SPEED IN RPM NORMALIZED FOR UNITY TO EQUAL FIRST CRITICAL SPEED FOR RIGID SUPPORTS
SUPPORT MECHANICAL IMPEDANCE Z ÷ 10⁶ LB/IN - FOR CURVES a, a', b; K" OF SPRING SUPPORT FOR CURVES 1
SUPPORT NATURAL FREQUENCY K" = 13.5 × 10⁶ LB/IN
3 RD CRITICAL
(a) CALCULATED MINIMUM BOUNDARY
(a') CALCULATED MAXIMUM BOUNDARY USED FIG. 2 REF. 7 DYNAMIC PROPERTIES OF PARTIAL JOURNAL BEARING; 125 DEG. ARC. L/D = 1, CENTRAL LOAD
2 ND CRITICAL
(b) DYNAMIC PROPERTIES OF BRG'S AVERAGED
1 ST CRITICAL

Fig. 5 Calculated critical speeds of rotor-support system A

predict the critical speeds of rotor systems on two flexible supports has been demonstrated [5]. It has been shown that the bearing support mechanical impedance is a function of rotor speed [5]. One method of predicting system natural frequencies is to consider the rotor system and support systems independently. System *A*, Fig. 5, represents a rotor on two identical supports. Curves numbered 1, Fig. 5, are determined by calculating a number of natural frequencies of the rotor supported by identical single springs of varying stiffness. These curves show how the rotor-system critical speeds change with changing support stiffness. Curves *a* and *a'*, Fig. 5, are plotted from the solution of equation (1), Fig. 4, using minimum and maximum values of K' and C' at each speed, as determined from information given in reference [7]. Curves *a* and *a'* represent the dynamic behavior of the support systems. Curve *b* is obtained when the minimum and maximum values of K' and C' are averaged. The intersections of curve *b* with curves numbered 1 define the first three rotor support system critical speeds. This method clearly indicates the interaction of the rotor and support systems, allowing the effects of design changes on either system to be assessed. This method, although useful in defining the behavior of each system, has severe limitations in that multiple support systems can be analyzed only where the characteristics of each support are identical.

A more direct method is to incorporate the support data and the rotor data in a single system critical-speed calculation. The method of Part 1 is such a method. This method has the advantage of being able to consider the parameters of each support independently and of being able to calculate the system critical speeds without establishing the rotor-system curves numbered 1 as shown in Fig. 5. In order to use this method, it is necessary to know the support parameters; i.e., oil-film stiffness and damping, and support stiffness and mass, for each support. It is anticipated that a third part to this paper will include a discussion of the methods used to determine support parameters as well as comparisons with test results. For the purpose of this paper support parameters will be selected in order to demonstrate the capabilities of the method.

Using the same support parameters as were used to determine curve *b*, Fig. 5, and the rotor data used to calculate curves 1, Fig. 5, the critical speeds and values of support mechanical impedance, given in Table 3, are calculated by the method of Part 1.

Table 3 Normalized critical speeds

Normalized speed.	0.920	2.19	3.03
Support mechanical impedance...	4.21×10^6	3.04×10^6	1.45×10^6

The first three critical speeds given in Table 3 are plotted as points *D*, *E*, and *F*, Fig. 5. Points *D*, *E*, and *F* coincide with the points of intersection of curves 1 and curve *b* in Fig. 5.

The change in critical speeds due to increasing the natural frequency of both supports of system *A* from 3.3 to 4.55 rpm is shown in Fig. 6. The first critical speed increased only slightly, since the oil-film stiffness has the predominant effect at lower speeds. The second critical speed was increased approximately 7 per cent and the third by 14 per cent. The ability to predict changes in critical speeds as a result of modifications on support systems is of practical use in rotor design.

Theoretical Study of Systems With Three Flexible Supports

The critical speeds of a generator rotor and exciter mounted on three flexible supports, shown in Fig. 7 as system *B*, are calculated for three conditions of support stiffness. Only the third support stiffness was modified. A constant force of unbalance was applied on the rotor midway between supports 1 and 2. Shaft deflections at the first three supports and mode forms approximated in one plane at each critical speed are shown in Fig. 7. The need for accuracy in support representation will be exemplified. The

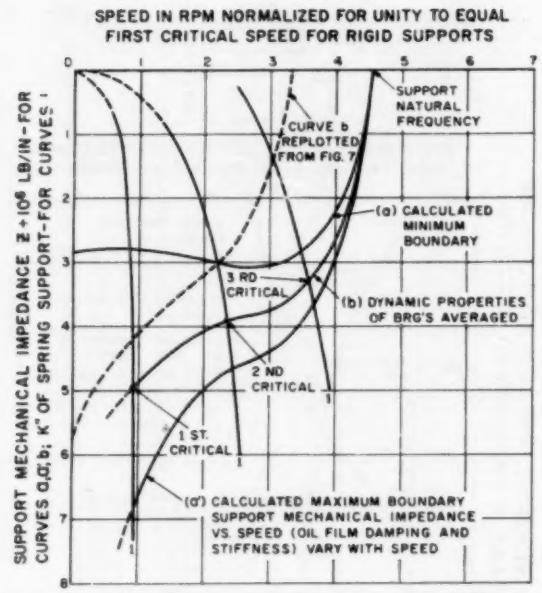
SPEED IN RPM NORMALIZED FOR UNITY TO EQUAL FIRST CRITICAL SPEED FOR RIGID SUPPORTS
SUPPORT MECHANICAL IMPEDANCE Z÷10⁶ LB/IN-FOR CURVES a,c; b; K° OF SPRING SUPPORT-FOR CURVES
SUPPORT NATURAL FREQUENCY
CURVE b REPLOTTED FROM FIG. 7
(a) CALCULATED MINIMUM BOUNDARY
3 RD CRITICAL
(b) DYNAMIC PROPERTIES OF BRG'S AVERAGED
2 ND CRITICAL
1 ST. CRITICAL
(c) CALCULATED MAXIMUM BOUNDARY SUPPORT MECHANICAL IMPEDANCE VS. SPEED (OIL FILM DAMPING AND STIFFNESS) VARY WITH SPEED

Fig. 6 Effect of varying support stiffness on system critical speeds

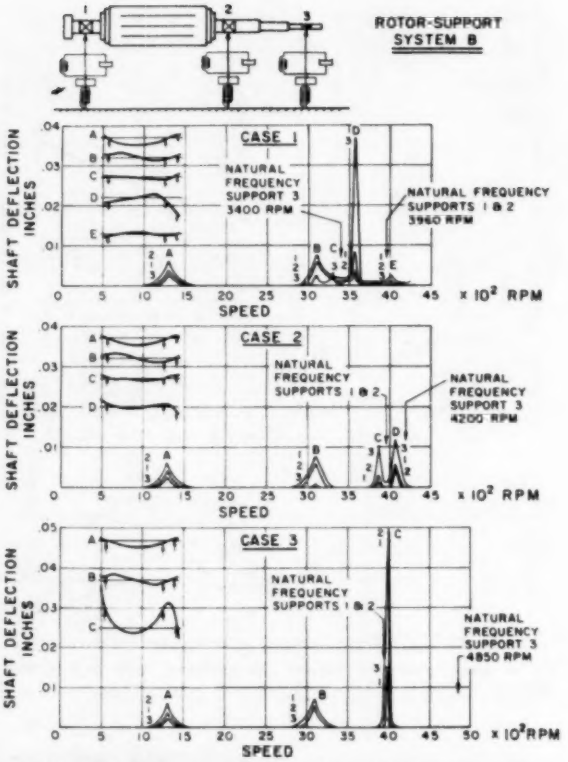
ROTOR-SUPPORT SYSTEM B
CASE 1
NATURAL FREQUENCY SUPPORT 3 3400 RPM
NATURAL FREQUENCY SUPPORTS 1 & 2 3960 RPM
CASE 2
NATURAL FREQUENCY SUPPORTS 1 & 2
NATURAL FREQUENCY SUPPORT 3 4200 RPM
CASE 3
NATURAL FREQUENCY SUPPORTS 1 & 2
NATURAL FREQUENCY SUPPORT 3 4850 RPM
SHAFT DEFLECTION INCHES
SPEED
x 10² RPM

Fig. 7 Shaft resonance as a function of support natural frequencies

occurrence of critical speeds existing within the speed range of support natural frequencies will also be shown. For the three cases which follow, the first and second support natural frequencies will remain constant at 3960 vpm.

For Case 1, the natural frequency of the third support will be assumed equal to 3400 vpm. Five critical speeds, peaks *A*, *B*, *C*, *D*, and *E*, are calculated and shown in Fig. 7. Peaks *A*, *B*, and *E* would normally be considered the first, second, and third critical speeds according to the mode forms. Peak *C* occurs at a speed slightly less than the speed at which the mechanical impedance of the third support is zero; i.e., at the natural frequency of the third support. Mode *C* is of the form *B* with less vibration at supports 1 and 2 and greater vibration at support 3. The greatest deflection, peak *D*, is also caused primarily by the lack of stiffness of support 3 and occurs at a speed slightly higher than the natural frequency of support 3. Peak *E* occurs at a speed in excess of the natural frequency of supports 1 and 2.

For Case 2, the stiffness of support 3 was increased, causing a change in the support natural frequency from 3400 to 4200 vpm. The first and second natural frequencies are almost unaffected by this change in support stiffness, as the oil-film stiffness has a large effect on the mechanical impedance at these speeds. Peaks *C* and *D* occur in the speed range of low support stiffnesses.

For Case 3, the stiffness of the third support was increased again, causing a change in the support natural frequency from 4200 to 4850 vpm. Only three critical speeds exist in the speed range previously considered. The large shaft amplitudes at the third critical speed, mode *C*, reflect the lack of stiffness of the first two supports at 4000 rpm.

It is of further interest to compare the results given in Fig. 7 with the critical speeds of the same rotor system when support 3 is removed. The first three critical speeds of the two-support system are 1278, 2452, and 3132 rpm. At 3132 rpm the rotor-mode form is quite similar to the second critical mode forms *B* in Fig. 7 with greater deflection occurring at the overhang. The third critical speed of 3132 rpm for the rotor system on two supports is nearly equal to the second critical speed of 3119 rpm for the rotor system on three supports. Cases 1, 2, and 3, Fig. 7, indicate that as the third-support natural frequency increases, the third condition of system resonance occurs at increasingly higher speeds. The highest speed at which the third condition of resonance occurs for this rotor-support system is slightly in excess of the natural frequency of supports 1 and 2. The lowest speed at which the third condition of resonance could occur is slightly in excess of the third natural frequency of the system on two supports.

To predict critical speeds of multiple span systems on flexible supports, it is necessary to be able to include in a system calculation, the characteristics of each support as well as the rotor characteristics. The need for defining accurately the stiffness and mass of each support has been demonstrated. The ability to determine the resonant behavior of the rotor-support system when changing the characteristics of any part of the system is of practical use in design. If the supports had been considered rigid, the first three critical speeds would have been 1602, 4653, and 8468 rpm, respectively.

Consideration of Forces of Unbalance

A generator rotor with a shaft extension supported by a steady bearing somewhat similar to system *B* was used for the support mass deflection plots in Fig. 8. Support mass deflection means approximately pedestal deflection as contrasted to shaft deflection. The magnitude of support mass deflections is plotted as the rotor speed is increased through the range of the first four critical speeds. Oil-film stiffness and damping were calculated at each speed using data from reference [7]. Each support mass was calculated from physical dimensions, while each support stiffness was calculated knowing an approximate support fundamental frequency. The solid-line curves, Case A, Fig. 8, indicate the deflections of each of the three support masses when an unbalance of

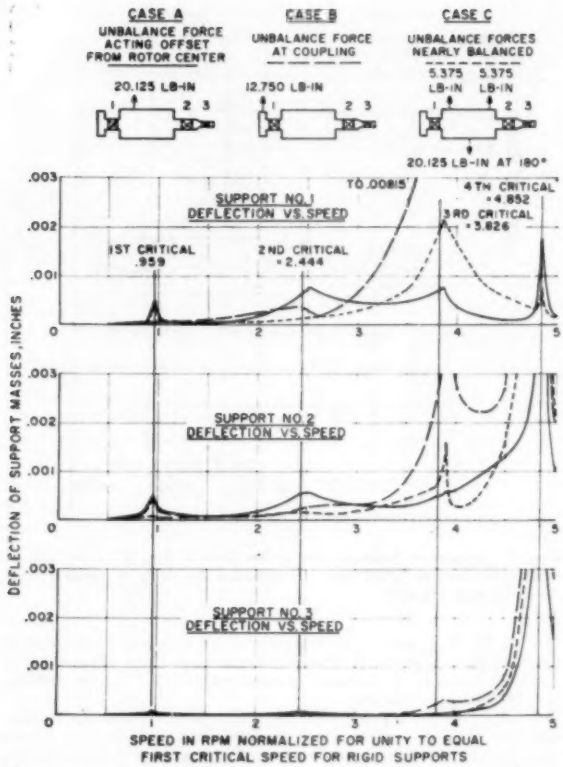

Fig. 8 Support mass deflection as a function of position of unbalance forces

20.125 lb-in. acts offset from the rotor center. The long dash curves, Case B, indicate support mass deflections when an unbalance of 12.75 lb-in. acts at the coupling. The short dash curves, Case C, indicate support mass deflections when an unbalance of 5.375 lb-in. acts in a positive direction at each end of the rotor and an unbalance of 20.125 lb-in. acts in a negative direction at the center of the rotor.

Although the critical speeds do not change with change in position of unbalance forces, the support mass deflections do differ considerably. The force of unbalance on the coupling causes excessive vibration above the value of 3.5 normalized for unity to equal the first critical speed for rigid supports. The support mass deflection at the second critical speed is reduced by balancing the rotor as per Case C.

It appears that the greatest support mass vibration can occur at speeds somewhat greater than the critical speeds of the rotor-support system. For example, Fig. 8, Case A, shows the first and second support masses vibrating at a maximum at a speed greater than the calculated second critical speed. This should perhaps be considered when comparing calculated critical speeds with test results.

The excessive vibration of supports 2 and 3 at the fourth critical speed can be attributed to the third support natural frequency being equal to the normalized value of 5.28.

When the force of unbalance acts offset from the mid-point between supports 1 and 2, Case A, Fig. 8, the support mass and shaft vibrate at maximum amplitudes at a speed of 2.525 rpm on the normalized speed scale. Fig. 9 is a plot of the shaft amplitudes along the length of the rotor for this case. Points 1 through 17 and support locations shown in Fig. 9 correspond to the points

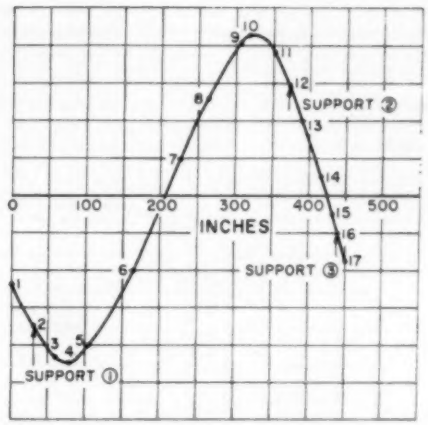

Fig. 9 Shaft amplitudes along length of rotor for Case A, Fig. 8, at 2.525 rpm normalized for unity to equal first critical speed for rigid supports

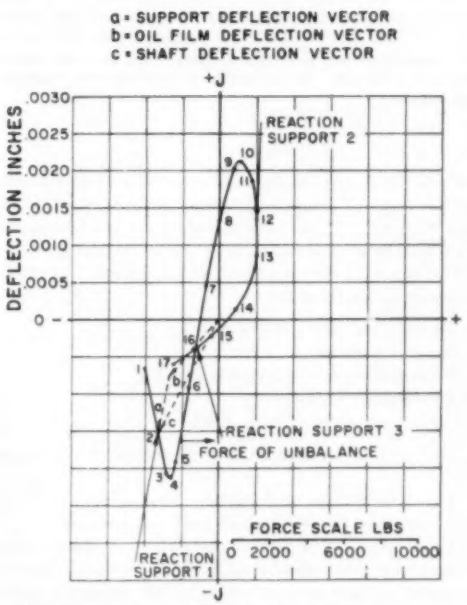

Fig. 10 Unbalance force as shown for Case A, Fig. 8. Same as for rectilinear plot in Fig. 9. Polar plot of rotor deflections at 2.525 rpm. Normalized for unity to equal first critical speed for rigid supports.

on polar plots 10, 11, and 12 corresponding to Cases A, B, and C, respectively, in Fig. 8.

Polar plots 10, 11, and 12 show the magnitude and direction of shaft deflections, support reaction vectors, and force of unbalance vectors. The force of unbalance, Fig. 10, acts at an angle of zero degrees. The dotted vectors at support 1, Fig. 10, indicate the shaft-deflection vector c as the vectoral sum of the support mass deflection vector a, and the oil-film deflection vector b. A rotor-deflection curve is shown for each of the three conditions of unbalance, Fig. 8. Unbalance forces placed as shown in Fig. 12 effectively limit rotor deflection at the second critical speed.

Summary

1 The method of analysis described in the companion paper, Part 1, has been programmed for an IBM 704 computer and

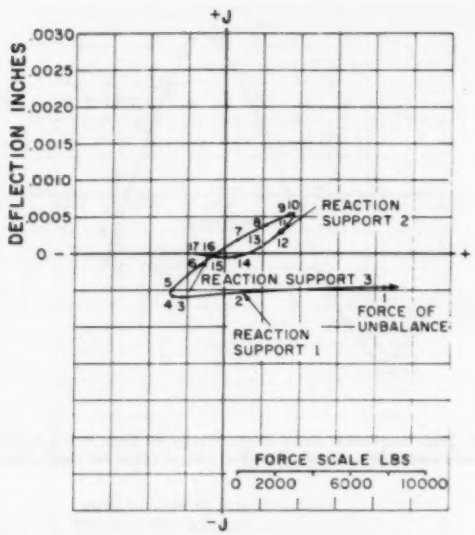

Fig. 11 Unbalance force as shown for Case B, Fig. 8. Polar plot of rotor deflections at 2.525 rpm. Normalized for unity to equal first critical speed for rigid supports.

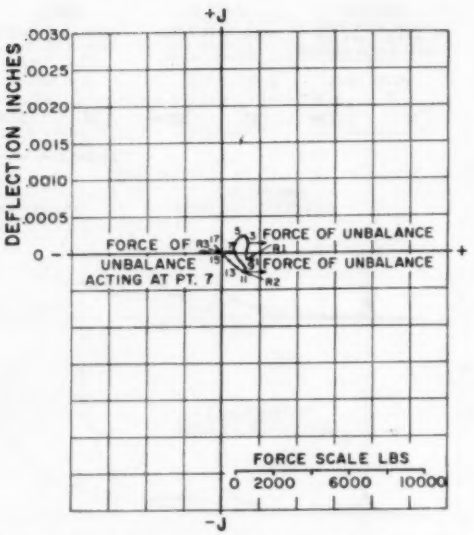

Fig. 12 Unbalance forces as shown for Case C, Fig. 8. Polar plot of rotor deflections at 2.525 rpm. Normalized for unity to equal critical speed for rigid supports.

used to calculate vibration characteristics of a variety of systems.

2 The customary assumptions were made on example systems and the resonant frequencies obtained by the method were found to check with those obtained by other known methods.

3 The ability of the method to include the effect of the following has been demonstrated:

(*a*) Uniform and nonuniform rotors.
(*b*) Support stiffness and mass.
(*c*) Oil-film stiffness and viscous damping.
(*d*) Unbalanced forces.
(*e*) Gyroscopic effect of large disks.

4 The need for accurate support description has been emphasized.

5 The occurrence of resonant conditions at speeds close to the natural frequency of each support has been discussed.

6 The method can be used to calculate the natural frequencies of systems having any number of flexible supports. The values of support stiffness and mass as well as oil-film flexibility and damping may be different at each support.

7 It is recognized that this paper leaves many questions unanswered. A third paper is being planned which will attempt to answer some of them and in particular will explain how support parameters would be determined and how the results of this program compare with test results.

References

1 E. C. Koenig, "A Rotating Systems Analyzer for Balancing and Simulating Rotating Systems," PhD thesis, University of Wisconsin, 1956.

2 von Karman and Biot, "Mathematical Methods in Engineering," McGraw-Hill Book Company, Inc., New York, N. Y., 1940.

3 R. L. Urban, "Extension of Holzer-Myklestad-Prohl Calculation of Turbo-Rotor Critical Speeds," ASME Paper No. 58—A-246 (unpublished).

4 M. A. Prohl, "A General Method for Calculating Critical Speeds of Flexible Rotors," JOURNAL OF APPLIED MECHANICS, vol. 12, TRANS. ASME, vol. 67, 1945, p. A-142.

5 W. J. Caruso, "Prediction of Critical Speeds of Steam Turbines by Dynamic Stiffness Method," ASME Colloquium on Mechanical Impedance Methods for Mechanical Vibrations, 1959, p. 137.

6 A. C. Hagg and G. O. Sankey, "Some Dynamic Properties of Oil-Film Journal Bearings With Reference to Unbalance Vibration of Rotors," JOURNAL OF APPLIED MECHANICS, vol. 23, TRANS. ASME, vol. 78, 1956, pp. 302–306.

7 A. C. Hagg and G. O. Sankey, "Elastic and Damping Properties of Oil-Film Journal Bearings for Application to Unbalance Vibration Calculations," JOURNAL OF APPLIED MECHANICS, vol. 25, TRANS. ASME, vol. 80, 1958, pp. 141–142.

APPENDIX

Numerical Example

Consider a shaft having the properties shown in Table 4, and having a support at each end with parameters $K' = 10^{15}$, $K' = 10^5$, and $m' = C' = 0$. Let the shaft rotate at 1909.86 rpm = 200 radians/sec, and let the scale factor = 1.

Table 4

ELEM	W	I	l	E
1	386.4	10	10	3×10^7
2	386.4	10	10	3×10^7
3	386.4	10	10	3×10^7
4	386.4	10	10	3×10^7
5	386.4	10	10	3×10^7
6	386.4	10	10	3×10^7
7	386.4	10	10	3×10^7
8	386.4	10	10	3×10^7
9	386.4	10	10	3×10^7
10	386.4	10	10	3×10^7

The first step that must be taken is to find the dynamic influence coefficients. The influence coefficients for support 1 are found by applying a dynamic force of unbalance of 1 lb on the support and setting the mass of the rotor to zero. The program does this by putting a fictitious element into the system at this point with a weight of 1 lb and a length of zero. The matrix for this element then is

$$c_{01}' = \begin{bmatrix} 1 & 0 & 0 & 0 & -1 \\ 0 & 1 & 0 & 0 & 0 \\ 0 & 0 & 1 & 0 & 0 \\ 0 & 0 & 0 & 1 & 0 \\ 0 & 0 & 0 & 0 & 1 \end{bmatrix}$$

The matrix of each of the ten main elements is

$$c_{n1}' = \begin{bmatrix} 1 & 0 & 0 & 0 & 0 \\ 10 & 1 & 0 & 0 & 0 \\ 1.67 \times 10^{-7} & 3.33 \times 10^{-6} & 1 & 0 & 0 \\ 5.56 \times 10^{-7} & 1.67 \times 10^{-7} & 10 & 1 & 0 \\ 0 & 0 & 0 & 0 & 1 \end{bmatrix}$$

and the product of these 11 matrices gives

$$\begin{bmatrix} V_{n1} \\ M_{n1} \\ \theta_{n1} \\ Y_{n1} \\ 1 \end{bmatrix} = \begin{bmatrix} 1 & 0 & 0 & 0 & -1 \\ 100 & 1 & 0 & 0 & -100 \\ 1.67 \times 10^{-6} & 3.33 \times 10^{-7} & 1 & 0 & -1.67 \times 10^{-6} \\ 5.56 \times 10^{-4} & 1.67 \times 10^{-6} & 100 & 1 & -5.56 \times 10^{-4} \\ 0 & 0 & 0 & 0 & 1 \end{bmatrix} \begin{bmatrix} V_{01} \\ M_{01} \\ \theta_{01} \\ Y_{01} \\ 1 \end{bmatrix}$$

The known boundary conditions are

$$M_{01} = 0$$

$$M_{n1} = 0$$

$$Y_{01} = \frac{V_{01}/S}{-Z_{01}/S} = \frac{V_{01}}{-10^6}$$

$$Y_{n1} = \frac{-V_{n1}/S}{-Z_{01}/S} = \frac{V_{n1}}{10^6}$$

Taking the first four equations from the span matrix, making the foregoing substitutions, and combining like terms, we get the equations

$$V_{01} - V_{n1} = 1$$

$$100\ V_{01} = 100$$

$$1.67 \times 10^{-6}\ V_{01} + \theta_{01} - \theta_{n1} = 1.67 \times 10^{-6}$$

$$5.456 \times 10^{-4}\ V_{01} - 10^{-6}\ V_{n1} + 100\ \theta_{01} = 5.56 \times 10^{-4}$$

The solution to these equations is

$$V_{01} = 1$$

$$V_{n1} = 0$$

$$\theta_{01} = 10^{-7}$$

$$\theta_{n1} = 10^{-7}$$

We can now perform the multiplication indicated in equations (1) for each element. This will give us deflections as shown in the middle column of Table 5. These are the influence coefficients associated with support 1.

By putting the unbalance on the second support and going through the same procedure as just described, the influence coefficients shown in the last column of Table 5 will be found.

Now we are ready to set up the matrices which include the rotor weight and the influence coefficients. The program considers the weight of the element to be concentrated at the ends of the elements. Therefore the weight concentrated at the beginning of element 1 is half of 386.4 lb. The weight at the end of that element is half the sum of the weights of elements 1 and 2.

Keeping in mind this method of dividing weights, the matrix for the first element becomes

$$c_{01}' = \begin{bmatrix} 1 & 0 & 0 & 20{,}000 & 0 & 0 & 0 \\ 10 & 1 & 0 & 200{,}000 & 0 & 0 & 0 \\ 1.67 \times 10^{-7} & 3.33 \times 10^{-6} & 1 & 3.33 \times 10^{-3} & 0 & 0 & 0 \\ 5.56 \times 10^{-7} & 1.66 \times 10^{-7} & 10 & 1.0111 & 0 & 10^{-6} & -10^{-6} \\ 0 & 0 & 0 & 0 & 1 & 0 & 0 \\ 0 & 0 & 0 & 0 & 0 & 1 & 0 \\ 0 & 0 & 0 & 0 & 0 & 0 & 1 \end{bmatrix}$$

Each of the next nine element matrices is

$$c_{0v}' = \begin{bmatrix} 1 & 0 & 0 & 40{,}000 & 0 & 0 & 0 \\ 10 & 1 & 0 & 400{,}000 & 0 & 0 & 0 \\ 1.67 \times 10^{-7} & 3.33 \times 10^{-6} & 1 & 6.67 \times 10^{-3} & 0 & 0 & 0 \\ 5.56 \times 10^{-7} & 1.67 \times 10^{-7} & 10 & 1.0222 & 0 & 10^{-6} & -10^{-6} \\ 0 & 0 & 0 & 0 & 1 & 0 & 0 \\ 0 & 0 & 0 & 0 & 0 & 0 & 0 \\ 0 & 0 & 0 & 0 & 0 & 1 & 1 \end{bmatrix}$$

Table 5

Influence coeff. at end of support No.	Associated with support No. 1	Associated with support No. 2
0	-10×10^{-6}	0
1	-9×10^{-6}	-1×10^{-6}
2	-8×10^{-6}	-2×10^{-6}
3	-7×10^{-6}	-3×10^{-6}
4	-6×10^{-6}	-4×10^{-6}
5	-5×10^{-6}	-5×10^{-6}
6	-4×10^{-6}	-6×10^{-6}
7	-3×10^{-6}	-7×10^{-6}
8	-2×10^{-6}	-8×10^{-6}
9	-1×10^{-6}	-9×10^{-6}
10	0	-10×10^{-6}

The last matrix of the span is for an element of length zero, but whose weight is one half the weight of the last element, this weight being concentrated at the end of the last element.

The matrix is

$$c_{0.11'} = \begin{bmatrix} 1 & 0 & 0 & 20{,}000 & 0 & 0 & 0 \\ 0 & 1 & 0 & 0 & 0 & 0 & 0 \\ 0 & 0 & 1 & 0 & 0 & 0 & 0 \\ 0 & 0 & 0 & 1 & 0 & 0 & 0 \\ 0 & 0 & 0 & 0 & 1 & 0 & 0 \\ 0 & 0 & 0 & 0 & 0 & 1 & 0 \\ 0 & 0 & 0 & 0 & 0 & 0 & 1 \end{bmatrix}$$

The product of these 11 matrices is

$$\begin{bmatrix} V_{n1} \\ M_{n1} \\ \theta_{n1} \\ Y_{n1} \\ 1 \\ V_{01} - 0 \\ 0 - V_{n1} \end{bmatrix} = \begin{bmatrix} 109 & 6.56 & 1.15 \times 10^{8} & 7.39 \times 10^{6} & 0 & 11.5 & -11.5 \\ 1690 & 103 & 1.80 \times 10^{9} & 1.15 \times 10^{8} & 0 & 180 & -180 \\ 9.56 \times 10^{-6} & 5.80 \times 10^{-6} & 103 & 6.56 & 0 & 1.02 \times 10^{-5} & -1.05 \times 10^{-5} \\ 1.59 \times 10^{-3} & 9.56 \times 10^{-6} & 1690 & 109 & 0 & 1.69 \times 10^{-4} & -1.69 \times 10^{-4} \\ 0 & 0 & 0 & 0 & 1 & 0 & 0 \\ 0 & 0 & 0 & 0 & 0 & 1 & 0 \\ 0 & 0 & 0 & 0 & 0 & 0 & 1 \end{bmatrix} \begin{bmatrix} V_{01} \\ M_{01} \\ \theta_{01} \\ Y_{01} \\ 1 \\ V_{01} \\ -V_{n1} \end{bmatrix}$$

The known boundary conditions are again

$$M_{01} = 0$$

$$M_{n1} = 0$$

$$Y_{01} = V_{01}/-10^{6}$$

$$Y_{n1} = V_{n1}/10^{6}$$

and the simultaneous equations this time are

$$\begin{aligned} 46.52\, V_{01} &+ 1.148 \times 10^{8}\, \theta_{01} + 10.48\, V_{n1} &= 0 \\ 720.8\, V_{01} &+ 1.799 \times 10^{9}\, \theta_{01} + 179.9\, V_{n1} &= 0 \\ 4.020 \times 10^{-6}\, V_{01} &+ 102.6\, \theta_{01} + 1.016 \times 10^{-5}\, V_{n1} - \theta_{n1} &= 0 \\ 6.719 \times 10^{-4}\, V_{01} &+ 1689\, \theta_{01} + 1.589 \times 10^{-4}\, V_{n1} &= 0 \end{aligned}$$

The determinant of this set of equations is the system impedance and its value is recorded together with the value of frequency which was used. After several of these points have been found, the minimum point on the curve represented by them will be the natural frequency. The first natural frequency of this system is 487 rpm. After having found the natural frequency, we can perform the calculations indicated by equations (1) to find the true deflections of each element if damping and unbalance have been given, or we can at least find the mode form if damping and unbalance have not been given.

P. S. THEOCARIS
Professor and Director, Laboratory for Testing Materials, Athens National Technical University, Athens, Greece. Mem. ASME.

C. MYLONAS
Professor, Division of Engineering, Brown University, Providence, R. I. Mem. ASME

Viscoelastic Effects in Birefringent Coatings[1]

The method of birefringent coatings for the determination of elastic and plastic surface strains of opaque bodies like metals assumes perfect elasticity of the coating material. In reality the coating, assumed much softer than the metal, presents the problem of a general viscoelastic layer under prescribed boundary displacements (at the metal-plastic interface). As already shown, this problem is greatly simplified for isotropic linear viscoelastic coatings, for small strains, for a linear law of strain birefringence, and for interface displacements expressed as a product of a function of space co-ordinates by a time function. The obviously advantageous stress-strain-optical linearity was experimentally verified in pure and in plasticized epoxy resins which make the best coatings. Tests were carried out in uniaxial loading and in shear, in creep, as well as in relaxation. The main conclusion is that the pure epoxy resins show negligible inelasticity, and the plasticized have a linear photo-viscoelastic behavior. Explicit laws were fitted to the creep and relaxation curves. Tests were also carried out with deeply notched coated steel bars deformed in the plastic range. The variation of fringe pattern with time was found to be negligible for the pure epoxy resins and to diminish slightly and proportionally with time throughout the model for the plasticized resins.

IN GENERAL, the method of birefringent coatings [1][2] is used with the assumption that the photoelastic layer cemented on the surface of the opaque body exhibits perfect mechanical and optical elasticity. However, several photoelastic materials show creep or inelasticity even in the pure state, and particularly when plasticized. The question arises whether the distribution of birefringence changes in the coatings and how well it represents the interface strains. Usually the birefringent coatings are much softer and weaker than the body to which they are cemented so that the interface strains can be assumed to be unaffected by the stress relaxation in the coating.[3] The coating consists of an isotropic layer subjected to small prescribed boundary strains (those of the interface). The problem is not difficult if the coating is infinitely thin. Its strains will be identical with those of the interface and the stresses will relax under constant strain. The birefringence will also relax with time, unless the coating exhibits pure strain birefringence. If the appearing fringe pattern, though diminishing with time, is to remain proportional to the strain distribution on the interface, the optical relaxation law must be linear in the strains. The law of stress relaxation is then of no interest.

The problem is somewhat more complicated when the thickness of the coating and the gradient of the interface strains are such as to produce a three-dimensional variation of stress and strain through the coating thickness [2]. The relation between observed fringe pattern and interface strains is more complicated and depends on Poisson's ratio. Simple proportionality does not exist even with an elastic coating. The problem with a viscoelastic coating reduces to whether the changing fringe pattern remains proportional to the pattern of the "elastic" case. If the influence of Poisson's ratio is neglected, a reasoning similar

[1] The results presented in this paper were obtained in the course of research sponsored by the National Academy of Sciences—National Research Council under the Scientific Research Project TA-01-101-4006, and by the Ballistic Research Laboratories of Aberdeen Proving Ground under Contract DA-19-020-ORD-4674, at the Division of Engineering, Brown University, Providence, R. I.

[2] Numbers in brackets designate References at end of paper.

[3] In some instances the coating contributes significantly to the strength of the coated structure, and then of course an interaction occurs between the stress relaxation in the coating and the interface strains, and the results of the present paper do not apply without modification.

Presented at the Summer Conference of the Applied Mechanics Division, Chicago, Ill., June 14–16, 1961, of THE AMERICAN SOCIETY OF MECHANICAL ENGINEERS

Discussion on this paper should be addressed to the Editorial Department, ASME, United Engineering Center, 345 East 47th Street, New York 17, N. Y., and will be accepted until January 10, 1962. Discussion received after the closing date will be returned. Manuscript received by ASME Applied Mechanics Division, September 20, 1960. Paper No. 61—APM-23.

Nomenclature

A, B = constants in creep or relaxation law
C_σ = stress-optical coefficient, a material fringe value with units of stress per fringe for a 1-in. thickness
C_ϵ = strain-optical coefficient, a material fringe value with units of strain per fringe for a 1-in. thickness
E_t = relaxation modulus at a time t after straining
E_ϵ = material constant in relaxation law with units of relaxation modulus
J_t = creep compliance at time t after loading
J_σ = material constant in the creep law with units of creep compliance
K_t = inverse of stress-optical coefficient C_σ at time t
K_σ = material constant in the optical creep law with units of K_t
N_t = relative retardation in fringes (λ = 5461 Å) at time t
R_t = inverse of the strain-optical coefficient C_ϵ at time t
R_ϵ = material constant in the law of optical relaxation with units of R_t
a, b, c, d = material constants in the laws of mechanical and optical creep
f_t = symbol for relative retardation or for strain in a general type of creep law
f_σ = constant in a general creep law
$g(t)$ = a function of time
t = time
u_i = rectangular component of displacement (i = 1, 2, 3)
Φ_t = symbol for relative retardation or for stress in a general type of creep law
Φ_ϵ = constant in a general creep law
α, β = material constants in laws of mechanical and optical relaxation
ϵ_t = strain at time t
λ = wave length of light

to the previous one indicates that linearity in stress-strain as well as strain-optical relations is required to insure proportional changes in the fringe pattern. The advantageous linearity of stress-strain-optical behavior is exhibited by the better epoxy coatings and will be solely considered in the present paper.

Photoelastic Analysis With Linear Loading

The problem of viscoelastic stress distribution without consideration of optical effects has been the object of extensive study in linear materials [4–6].

The problem of viscoelastic effects in birefringent coatings must be considered as a special case of general photoviscoelasticity which was studied by Mindlin [3]. He assumed small strains of a rather specialized linear viscoelastic material in which the birefringence is due solely to the elastic elements. It may be thought that the omission of other causes of birefringence would greatly limit Mindlin's results. However, the assumptions about the basic mechanism responsible for the photo-viscoelastic effect are only used to derive the (linear) stress-strain-optical relations. Beyond that point Mindlin's conclusions on the fringe pattern associated with the stress and strain distribution for various boundary conditions are valid for all materials found to obey linear photoviscoelastic laws, independently of the atomic or molecular cause of birefringence.

The problem of the linear photoviscoelastic birefringent coatings becomes particularly interesting when the interface strains change with time, as, e.g., during a variation of the loading. Then the relation between birefringence and strain is in general very complicated. However, a particularly simple relation exists under the following conditions [3]:

1 Isotropy of coating material, generally fulfilled.

2 Incompressibility of coating material, usually only approximately fulfilled, as Poisson's ratio though relatively high (0.35 or more) is not equal to $^1/_2$.

3 Smallness of strains.

4 Proportionality of variation of interface displacements, i.e., when the displacements can be written as products of a function $\bar{u}_i$ of space co-ordinates by a function $g(t)$ of time, which is the same for the whole body

$$u_i = \bar{u}_i g(t) \qquad (i = 1, 2, 3)$$

5 Absence of residual stresses, or a distribution of residual stress-deviation which could have resulted from a similar previous loading.

Then the principal axes of stress, strain, and birefringence coincide, and the appearing fringe pattern is always proportional to the one which would have existed in a perfectly elastic coating under the same boundary displacements. The effective strain-optical coefficient C_ϵ will be a function of time depending on the initial stresses, the time variation of the loading, and the photoviscoelastic relations. Again the coating may be used directly for the determination of relative magnitudes of strains, as e.g., for factors of strain concentration, without an exact knowledge of the function $C_\epsilon(t)$ or of the functions which determine it. These functions must be known exactly only when absolute values of strains are required.

Nonproportional Loading

However, the greatest usefulness of the method of birefringent coatings is not in the solution of purely elastic, but of elastic-plastic problems. Then the interface displacements do not vary proportionally, i.e., they are not product functions of a space by a unique time function, even if the variation of the loading forces is proportional. The same happens in problems of instability, or of contact strains, or when the actual loading is not proportional or the loads move. Under these conditions it is clear that the observed fringe pattern will not change proportionally with the interface strains and cannot be used even for the determination of relative strain magnitudes. Nevertheless, there is a practical way of treating such problems, if, as happens with epoxy resins, the viscoelastic behavior consists of instantaneous and delayed elasticity without any permanent set. The stress-strain-optical relations under constant stress or strain tend asymptotically to time-independent simple proportionalities as in purely elastic materials. It can be seen that if the interface displacements are held constant for a sufficiently long period the states of stress and birefringence due to all the loading history will come close enough to their asymptotic limits due to the final boundary conditions. The problem of stress analysis may be treated as purely elastic with the asymptotic values of the elastic and photoelastic constants. However, the restrictions of small strains and absence of structural instability or of stress dependent contact areas must in general be maintained. Thus, e.g., the magnitude of the strains during the spreading of the plastic zones in an elastic-plastic problem may be determined in successive steps separated by sufficiently long rest periods. The "sufficient" length of rest can be determined so as to insure a difference between the actual birefringence and its asymptotic value, due to all loading steps, smaller than a specified value or proportion. For this purpose it is advantageous to have a rapid delayed elastic behavior.

Uniqueness has been shown [3] to exist for variable boundary conditions which are "product functions" as previously defined. For nonproportional loading of materials of linear delayed elastic behavior without flow any transition from a state of stress or strain to another is permissible given sufficient time, hence uniqueness can be inferred from elastic materials.

Stress-Strain-Optical Relations

The previous discussion shows the great advantage of linear photo-viscoelastic behavior of coating materials. This linearity was checked in some of the epoxy resins which make the best coatings. As shown [4, 5], the linearity of the viscoelastic behavior for isotropic materials reduces to two pairs of linear differential operators between components of stress and corresponding components of strain, in complete analogy with the two independent elastic constants of isotropic elasticity. Similarly, two corresponding pairs of linear operator relations exist between stress or strain and double refraction. It is true that with incompressible materials the mean normal stress is independent of the vanishing dilatation, hence a single operator relation need be considered, e.g., between stress and strain deviators and between any of these deviators and birefringence. However, the condition of incompressibility is rarely fulfilled exactly, and therefore an unambiguous test of linearity of photo-viscoelastic behavior requires two sets of experiments, one for each operator relation. The simplest practical independent tests are uniaxial loading and pure shear.

Experimental Procedure

Eight formulations of two types of epoxy resins similar to those found most suitable for birefringent coatings were tested. A hot-setting resin was made of a liquid epoxy[4] with 40 per cent weight of phthalic anhydride hardener, and will be represented as H-100-40. A cold-setting resin was made of liquid epoxy[5] and 8 per cent tri-ethylene-tetramine (TET) hardener and is represented as C-100-0-8. Tests were made with these two resins in the pure state and with the cold-setting resin after having plasticized it in six different ways by one of two kinds of

[4] Under the trade name of "Hysol 6053."

[5] Under the trade name of "CIBA Araldite 6005."

plasticizers, namely, polysulphide liquid[6] or a 3:2 mixture of ethylene glycol monophenyl ether (EGRE) and di-butyl-phthalate (DBP) as previously used [9]. The polysulphide additions were in amounts of 10, 20, or 40 parts weight to 100 of epoxy and 8 of TET hardener, and are shown as C-100-10-8, C-100-20-8, C-100-40-8, where the letter indicates the type of epoxy resins and the three numbers show the parts by weight of resin, polysulphide plasticizer, and TET hardener in the same order. Similarly, the cold-setting epoxy plasticized with EGPE and DBP are indicated as C-80-12/8-8; C-85-9/6-8, C-90-6/4-8, where the two numbers separated by a stroke show the proportion by weight of the two plasticizers.

The hot-setting H-100-40 was prepared by the method described in [8]. The casting was made between metal plates covered with Dow Corning R-671 mold release agent, which worked very well at all temperatures. Casting was done at a temperature well above 90 C when the resin was very fluid and did not entrap air bubbles. The temperature was maintained constant until gelation. It was then raised to 150 C in 4 to 6 hr, and finally lowered to room temperature at a rate of 4–5 deg C per hr, in a regulated thermostatic oven. After removal from the molds the epoxy plates were slowly heated to 100 C and kept there for 36 hr, and finally were stored at room temperature for at least one month. This procedure had been found to produce optimum and stabilized properties.

The cold-setting resins were freed of air bubbles in a vacuum and were cast between glass plates covered with R-671 mold release grease. After gelation the molds were removed and the cast plates were subjected to the curing cycle previously described.

Tension specimens about $^1/_8$ in. and compression specimens about $^1/_4$ in. thick were machined from the cast sheets. The compression specimens were simple rectangular bars without any head, but their ends were centrally rounded on a router with a special rotating device so as to minimize the eccentricity of loading.

The tests in pure shear were executed with the system shown in Fig. 1. Two plastic blocks $^1/_2 \times {}^1/_2 \times 2$ in. were cemented by the long faces on opposite sides of a steel bar, and by their opposite faces to the interior of a rigid steel frame whose width could be adjusted to match the combined thickness of the bar with the two cemented plastics. The load was applied centrally along the length of the steel bar and resulted in a pure shear deformation of the central region of the plastics, since their length was greater than three times their width [7].

In both tension and compression creep tests the loading was applied almost instantaneously through a lever and dead loads.

[6] Under the trade name of "Thiokol Polysulphide LP-3."

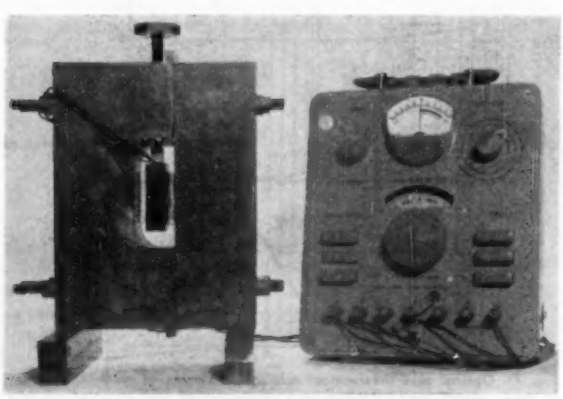

Fig. 1 Rigid frame used in double-shear tests

The strains were measured to $\pm 10^{-5}$ over a range of 2.4×10^{-3} with a special "Hortense" extensometer in conjunction with a Tuckerman optical gage. The fractions of a wave length (λ = 5461Å) in relative retardation were measured to ± 0.02, with a Soleil-Babinet compensator. Stresses were measured to ± 0.1 per cent.

In the tension and compression relaxation tests a displacement was suddenly applied and the strain was measured with the extensometer and was occasionally corrected by small amounts to the initial value. The load was measured on the spring balance of the straining frame.

Measurements of birefringence and either strain (creep tests) or stress (relaxation tests) were taken at regularly spaced time intervals from $^1/_4$ to 16 min. Only relaxation tests were made in pure shear. Preliminary tests of all resins up to creep strains of 3 per cent showed a complete recovery after sufficient time at room temperature, indicating an instantaneous and delayed elastic behavior without flow. This permitted the repeated loading of each specimen in consecutive steps of higher stress or strain, after complete recovery from the previous loadings.

The Laws of Creep and Relaxation

Creep and relaxation tests were carried out at room temperature with all the tension and compression specimens, and relaxation tests with the pure shear specimens. The loads or deformations applied to each specimen in consecutive steps were in the ratios 1:2:4. All tension and compression results were corrected for lateral strain, with Poisson's ratio equal to 0.35. The effective value of Poisson's ratio changes during viscoelastic deformation and may be calculated, but the change in the corrections of stress and birefringence will be negligible. Figs. 2–9 show typical results of the time variation of strain and relative retardation per unit thickness under constant stress, and of stress and relative retardation under constant strain for the four resins H-100-40, C-100-0-8, C-100-40-8, C-80-12/8-8. The results are also plotted as relations of strain or birefringence to stress (creep), or of stress or birefringence to strain at $^1/_2$, 2, and 8 min after loading. The results plot on straight lines, indicating immediately the linearity of the stress-strain-optical behavior. Each of the laws of creep, relaxation, optical creep, and optical relaxation were identical in tension and compression or shear. The values of the stress-optical and strain-optical coefficients[7] C_σ and C_ϵ as functions of time are given in Figs. 10 and 11. As can be seen these coefficients vary little within the periods of duration of the tests at room temperature. As has been frequently observed the strain-optical coefficient varied less than the stress-optical coefficient in all types of tests. The influence of the amount of plasticizer on the value of C_σ and C_ϵ at $^1/_2$ min after loading is shown in Fig. 12.

The variation of relative retardation and of strain under constant load and room temperature (25 ± 1 deg C) fitted well to laws of the type:

$$f_t = f_\sigma + At + B \log t, \tag{1}$$

where f_t stands in turn for the relative retardation in wave lengths N_t or for the strain ϵ_t at time t after loading, f_σ for a parameter of corresponding dimensions, and A, B for suitable constants in each case. Equation (1) is invalid for values of t smaller than about $^1/_4$ min and should not be extrapolated to $t = 0$. This shows that the initial stage of variation is different, though continuous with the law of equation (1). As the second term At is very small for $t = 1$, the parameters f_σ (i.e., N_σ or ϵ_σ) may be interpreted as the approximate values of birefringence or strain at unit time after loading, when the "initial stage" of the deformation is completed.

[7] Defined in the Nomenclature.

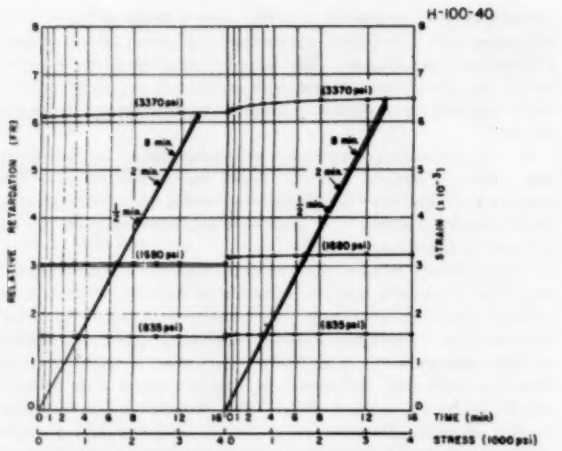

Fig. 2 Optical and mechanical creep curves of resin H-100-40 at three stresses, and instantaneous stress-optical and stress-strain relations at ½, 2, and 8 min after loading

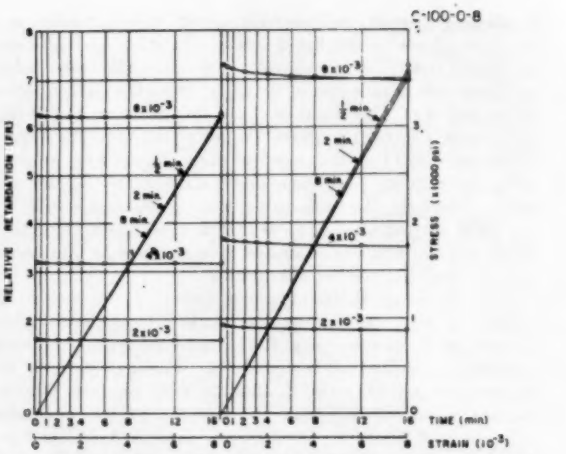

Fig. 5 Optical and mechanical relaxation curves of resin C-100-0-8 at three strains, and instantaneous strain-optical and stress-strain relations at ½, 2, and 8 min after straining

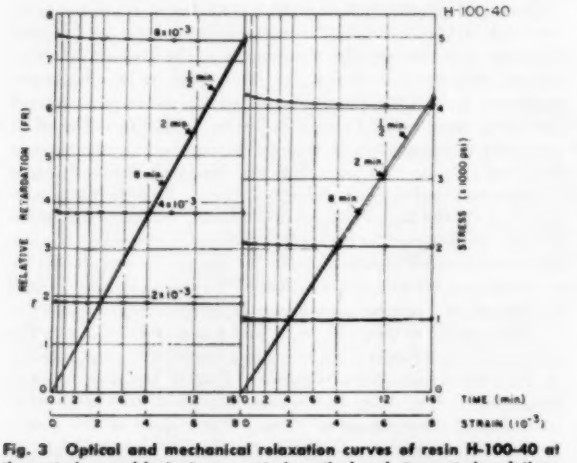

Fig. 3 Optical and mechanical relaxation curves of resin H-100-40 at three strains, and instantaneous strain-optical and stress-strain relations at ½, 2, and 8 min after straining

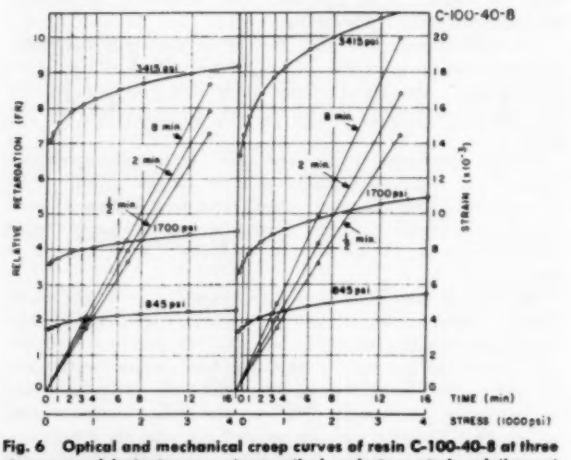

Fig. 6 Optical and mechanical creep curves of resin C-100-40-8 at three stresses, and instantaneous stress-optical and stress-strain relations at ½, 2, and 8 min after loading

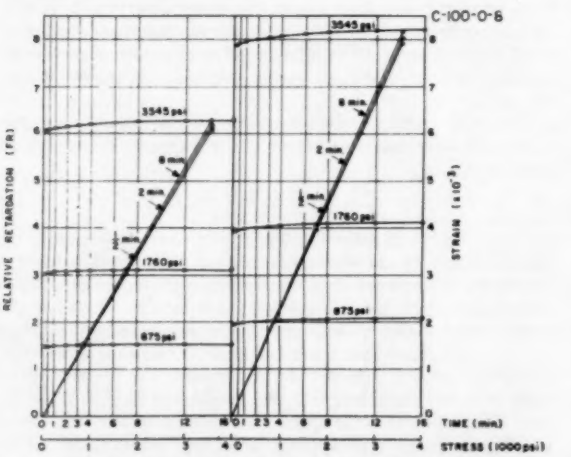

Fig. 4 Optical and mechanical creep curves of resin C-100-0-8 at three stresses, and instantaneous stress-optical and stress-strain relations at ½, 2, and 8 min after loading

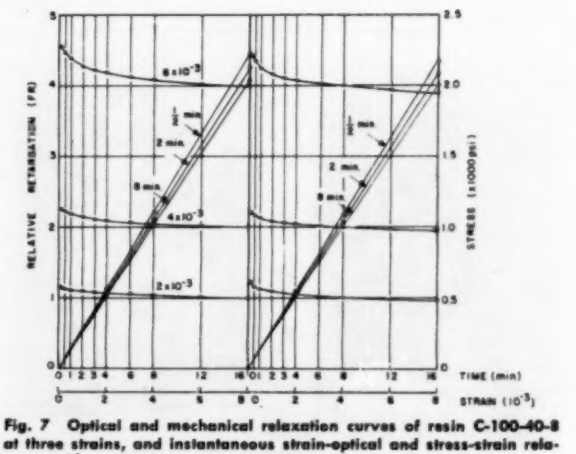

Fig. 7 Optical and mechanical relaxation curves of resin C-100-40-8 at three strains, and instantaneous strain-optical and stress-strain relations at ½, 2, and 8 min after straining

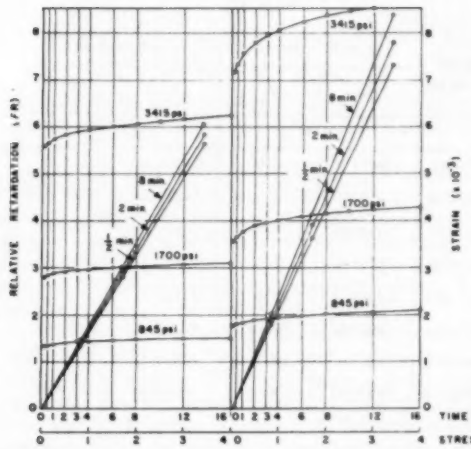

Fig. 8 Optical and mechanical creep curves of resin C-80-12/8-8 at three stresses, and instantaneous stress-optical and stress-strain relations at ½, 2, and 8 min after loading

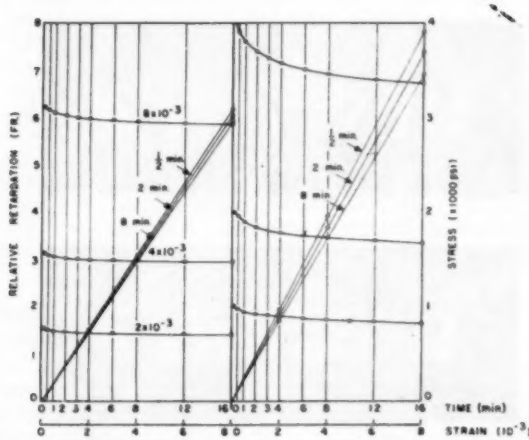

Fig. 9 Optical and mechanical relaxation curves of resin C-80-12/8-8 at three strains, and instantaneous strain-optical and stress-strain relations at ½, 2, and 8 min after straining

In general, the viscoelastic properties under constant stress are better described by the laws of variation of the *creep compliance* J_t and the inverse K_t of the stress optical coefficient C_σ, where

$$J_t = \epsilon_t/\sigma \tag{2}$$

$$K_t = 1/C_\sigma \tag{3}$$

Relations (1) then transform to

$$K_t = K_\sigma + at + b \log t \tag{4}$$

$$J_t = J_\sigma + ct + d \log t \tag{5}$$

with the corresponding parameters and constants dependent only on the material and the temperature. The values of these parameters for all resins tested are given in Table 1.

The variation of relative retardation and of stress at constant deformation and room temperature (25 ± 1 deg C) can be fitted well to laws of the type:

$$\Phi_t = \Phi_s - A \log t \tag{6}$$

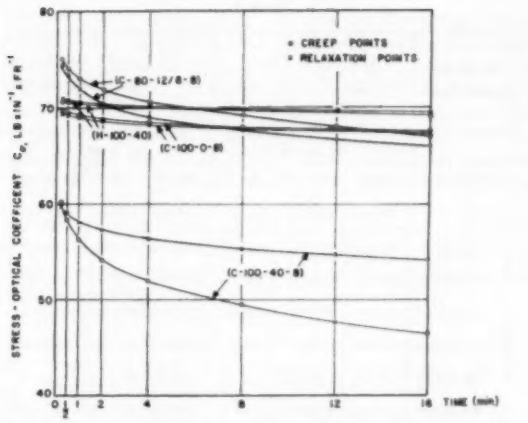

Fig. 10 Variation of stress-optical coefficient C_σ with time under creep or relaxation, for various resins

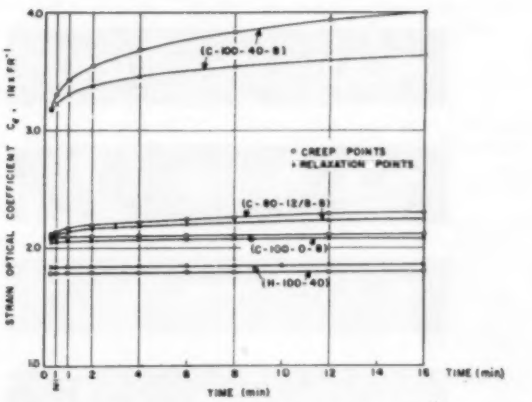

Fig. 11 Variation of strain-optical coefficient C_ϵ with time under creep or relaxation, for various resins

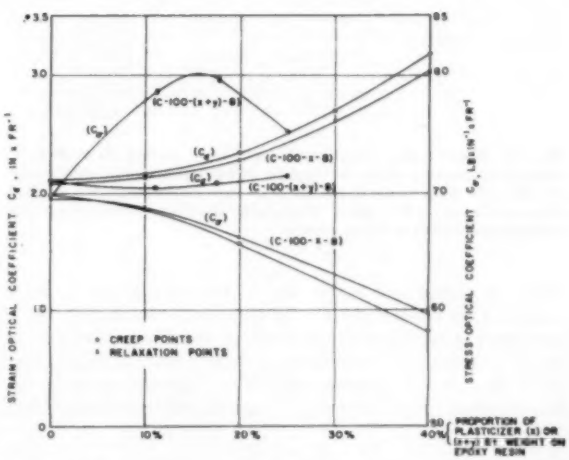

Fig. 12 Influence of amount of plasticizer on the stress and strain-optical coefficients at ½ min after loading

Table 1

TYPE OF EPOXY RESIN	$k_t = k_\sigma + at + b \log t$			$J_t = J_\sigma + ct + d \log t$		
	k_σ	a	b	J_σ	c	d
	$FR \times LB^{-1} \times IN^{-1}$	$FR \times LB \times Min^{-1} \times IN^{-1}$	$FR \times LB^{-1} \times IN^{-1}$	psi^{-1}	$psi^{-1} \times MIN^{-1}$	psi^{-1}
H-100-40	1.42×10^{-2}	5.62×10^{-6}	1.24×10^{-4}	1.88×10^{-5}	1.20×10^{-6}	2.40×10^{-5}
C-100-0-8	1.44×10^{-2}	9.59×10^{-6}	1.96×10^{-4}	2.24×10^{-5}	2.28×10^{-6}	4.22×10^{-5}
C-100-10-8	1.47×10^{-2}	1.83×10^{-5}	4.32×10^{-4}	2.34×10^{-5}	4.00×10^{-6}	7.68×10^{-5}
C-100-20-8	1.57×10^{-2}	5.61×10^{-5}	1.08×10^{-3}	2.74×10^{-5}	9.82×10^{-6}	2.11×10^{-4}
C-100-40-8	1.78×10^{-2}	9.55×10^{-5}	1.90×10^{-3}	4.50×10^{-5}	4.85×10^{-5}	9.70×10^{-4}
C-90-6/4-8	1.29×10^{-2}	1.57×10^{-5}	2.93×10^{-4}	1.94×10^{-5}	2.75×10^{-6}	5.83×10^{-5}
C-85-9/6-8	1.27×10^{-2}	2.55×10^{-5}	5.19×10^{-4}	1.99×10^{-5}	4.39×10^{-6}	9.12×10^{-5}
C-80-12/8-8	1.37×10^{-2}	3.30×10^{-5}	6.11×10^{-4}	2.19×10^{-5}	8.28×10^{-6}	1.73×10^{-4}

Table 2

TYPE OF EPOXY RESIN	$R_t = R_\epsilon - \alpha \log t$		$E_t = E_\epsilon - \beta \log t$	
	R_ϵ	α	E_ϵ	β
	$FR \times IN^{-1}$		psi	
H-100-40	0.543×10^{2}	0.385	516.5×10^{3}	0.91×10^{4}
C-100-0-8	0.486×10^{2}	0.259	451.2×10^{3}	1.08×10^{4}
C-100-10-8	0.458×10^{2}	0.473	429.9×10^{3}	1.87×10^{4}
C-100-20-8	0.440×10^{2}	0.820	391.0×10^{3}	1.62×10^{4}
C-100-40-8	0.302×10^{2}	2.158	236.0×10^{3}	2.93×10^{4}
C-90-6/4-8	0.496×10^{2}	0.440	511.5×10^{3}	2.49×10^{4}
C-85-9/6-8	0.482×10^{2}	0.825	507.5×10^{3}	3.10×10^{4}
C-80-12/8-8	0.464×10^{2}	1.464	442.5×10^{3}	4.27×10^{4}

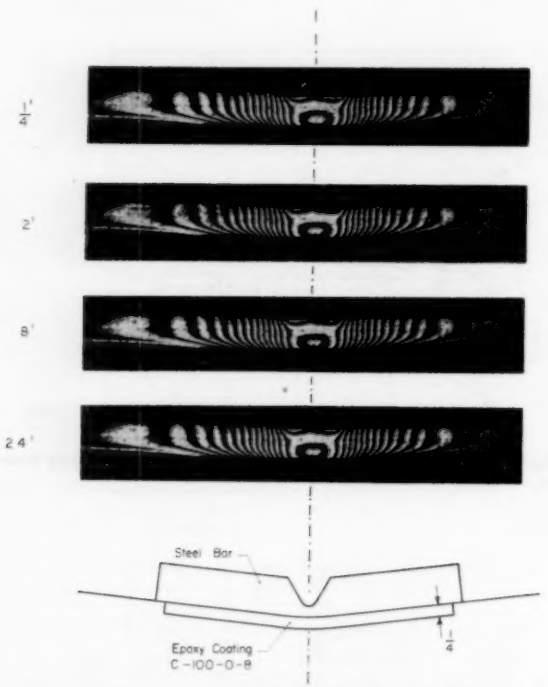

Fig. 13 Transmission fringe pattern of epoxy coating C-100-0-8 on notched bar bent as shown in diagram at bottom, between $^1/_4$ min and 24 min after straining. Upper edge of each photograph is cemented edge, and lower the free edge. Viscoelastic effect is too small to produce a detectable change of fringe pattern.

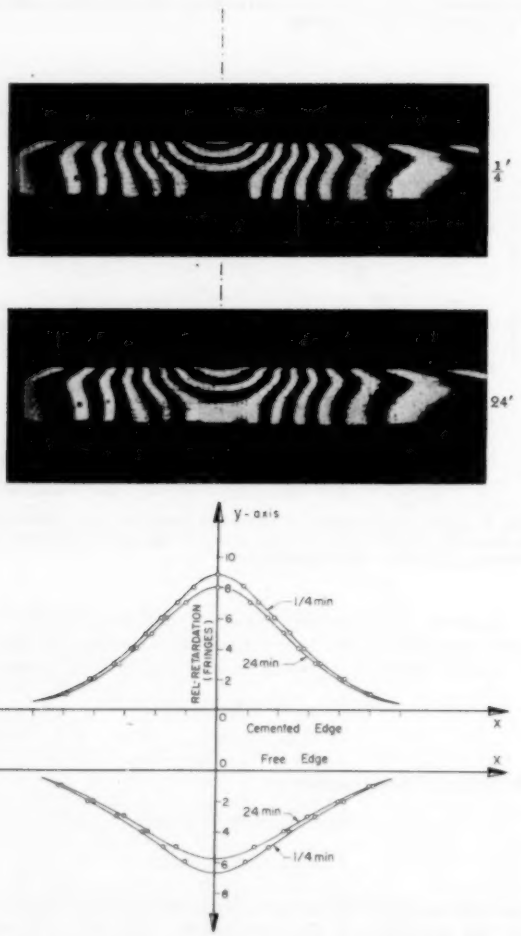

Fig. 14 Variation of fringe pattern of coating C-80-12/8-8 on bent notched bar, similar to that shown in Fig. 13, $^1/_4$ min (upper photograph) and 24 min (lower photograph). In both photographs upper edge is cemented edge and lower the free edge. Two upper curves show fringe variation along cemented edge, lower ones along free edge. Some decrease in fringe order is visible, but $^1/_4$ and 24-min curves are proportional.

where Φ_t stands in turn for the relative retardation in wave lengths N_t or for the stress σ_t at time t after loading, Φ_ϵ for a parameter of corresponding dimensions, and A is a suitable constant. The law (6) has the same limitations as (1) for small times t and Φ_ϵ a similar interpretation as f_σ. Introducing again the inverse strain optical coefficient R_t and the relaxation modulus E_t

$$R_t = 1/C_t \tag{7}$$

$$E_t = \sigma_t/\epsilon \tag{8}$$

one obtains

$$R_t = R - \alpha \log t \quad (9)$$

$$E_t = E - \beta \log t \quad (10)$$

The values of the parameters R, E, α, β are constant for any material and temperature and are given in Table 2 for all the resins tested.

It was also found that mechanical and optical creep fitted reasonably well to laws of the form $A + Bt^n$ with $n = 0.19$. Such expressions have been used to describe the photoelastic creep of a phenolic resin [9], and are convenient for purposes of extrapolation to small times. However, the laws (4), (5) and (9), (10) gave a better fit and appear to agree better with the accepted physical processes of viscoelastic behavior [10].

So far only uniform stress systems were considered. An additional check of photoviscoelastic linearity was carried out in strongly variable stress fields. As explained in the introduction a nonlinear behavior should result in a redistribution of stress, strain, and birefringence in nonuniform fields and should be discernible as a nonproportional variation of the fringe pattern. Rectangular bars notched on one side (semicircular, 30 and 45-deg V-notches were used) and coated on the other were bent permanently so as to produce extension on the coated side, with localized high strains over the root of the notch. The coating was viewed in transmitted light tangentially through its width, and not in reflected light across its thickness. Photographs were taken at regular intervals after the deformation. Fig. 13 shows the virtual absence of visible relaxation up to 24 min after straining of the pure cold-setting Araldite epoxy C-100-0-8. Fig. 14 shows the variation of the fringe pattern and of the fringe order at the edges of a similar bar coated with the plasticized Araldite C-80-12/8-8, between $^1/_4$ and 24 min after straining. The 24-min curves are directly proportional reductions of the $^1/_4$-min curves. This result obtained for the special instance of the coated permanently bent notched bar confirms the conclusions obtained by Mindlin with a rather specialized material.

Conclusions

Two types of pure epoxy resins (H-100-40 and C-100-0-8) and two groups of plasticized epoxy resins (C-100-x-8 and C-100-x/y-8, respectively) were examined in creep and relaxation at room temperature. It was found that within the range of the experiments:

(*a*) Pure epoxy resins presented insignificant creep and relaxation.

(*b*) The creep and relaxation of the polymers was intensified with increasing amounts of plasticizer.

(*c*) Hot-setting epoxy resins H-100-40 presented the best values for both stress and strain-optical coefficients after a certain time-interval.

(*d*) Increase of plasticizer, in the case of Thiokol polysulfide LP3, resulted in a deterioration of the stress and strain-optical coefficients. Amounts of plasticizer up to 15 per cent did not influence considerably the characteristic properties of the polymers. Increase of plasticizer, in the case of EGPE and DBP, improved the stress and strain-optical coefficients and their optimum value was obtained for a total amount of plasticizer of the order of 12 per cent weight of epoxy (EGPE:DBP = $^3/_4$).

(*e*) The stress-strain-optical relations of all resins were linear, without permanent set and were identical in tension, compression, and pure shear. Linearity was also checked in nonuniform stress fields.

(*f*) In the creep tests the birefringence and the strain at time t after loading could be expressed in the form: $f_t = f_o + at + b \log t$ where f_o, a, and b are parameters depending on the material properties and ambient experimental conditions.

(*g*) The relaxation law could be expressed as a logarithmic function of the time t.

(*h*) The general conclusion is that all these materials are suitable for use as birefringent coatings when the interface strains are given by a "product function." When the strains are not "product functions," the photoelastic measurements must be made after a relatively long time following each strain variation.

References

1 J. D'Agostino, D. C. Drucker, C. K. Liu, and C. Mylonas, "An Analysis of Plastic Behavior of Metals With Bonded Birefringent Plastic," *Proc. SESA*, vol. 7, 1955, pp. 115–122.

2 J. W. Duffy, "Thickness Effects in Birefringent Coatings," *Experimental Mechanics*, vol. 1, 1961, pp. 74–82.

3 R. D. Mindlin, "A Mathematical Theory of Photo-Viscoelasticity," *Journal of Applied Physics*, vol. 20, 1949, pp. 206–216.

4 T. Alfrey, "Mechanical Behavior of High Polymers," Interscience Publishers, New York, N. Y., 1957.

5 E. H. Lee, "Viscoelastic Stress Analysis," Report C11-42 of the Division of Applied Mathematics, Brown University, January, 1958, to be published in the *Proceedings of the First Symposium on Naval Structural Mechanics*.

6 W. T. Read, Jr., "Stress Analysis for Inelastic Materials," *Journal of Applied Physics*, vol. 21, 1958, pp. 671–674.

7 C. Mylonas, "Experiments With Composite Models," *Proc. SESA*, vol. 12, 1955, pp. 129–142.

8 J. D'Agostino, D. C. Drucker, D. K. Liu, and C. Mylonas, "Epoxy Adhesives and Casting Resins as Photoelastic Plastics," *Proc. SESA*, vol. 12, 1955, pp. 123–128.

9 C. Mylonas, "The Mechanical and Optical Properties of Catalin 800 and Its Suitability as Photoelastic Material," *Proceedings of the 8th International Congress of Applied Mechanics*, London, England, 1948, vol. 4, Paper 14, pp. 165–177.

10 W. T. Lyons, "The General Relations for Flow in Solids and Their Application to the Plastic Behavior of Tire Cords," *Journal of Applied Physics*, vol. 17, 1946, pp. 472–482.

G. R. ABRAHAMSON
Research Engineer,
Stanford Research Institute,
Menlo Park, Calif.
Formerly, Research Assistant,
Stanford University

J. N. GOODIER
Professor of
Engineering Mechanics,
Stanford University,
Stanford, Calif.

The Hump Deformation Preceding a Moving Load on a Layer of Soft Material[1]

When a load, for instance a heavy roller, moves slowly along the surface of a solid mass of soft material, a "hump" deformation is often observed to precede it. The process of formation from an initially level surface, and the final form of hump established, are investigated analytically for a purely viscous material, in two-dimensional motion. It becomes evident that a material showing nonlinear creep, or a viscoelastic material, would show qualitatively similar behavior, the simple viscous model being adequate to exhibit the essential qualitative features.

In the familiar process of rolling out a slab of dough with a rolling pin, a hump deformation is driven in front of the roller. Many technical operations involving the rolling out or drawing out of materials are of the same nature, and so also are certain phenomena of a more obscure character. One of these is the peculiar corrugation of an originally smooth metal surface sometimes caused by explosive loading [1][2] or by oblique impact when these are equivalent to a high-speed jet traversing the surface. It is convenient to think of a stationary localized load q, Fig. 1, on a layer of material which travels under it slowly with velocity U. If the material were elastic the deformation would be symmetrical, with equal humps upstream and downstream. Since, in fact, a pronounced hump is formed upstream only, inelastic behavior is involved. In view of the very common occurrence of such humping, it does not appear to be associated with any very specific law of flow or creep. The problem is solved here for a purely viscous material. It will be apparent that it could also be solved readily for viscoelastic materials, and that qualitatively similar behavior under a moving load may be expected wherever creep of any kind occurs in the penetration of a load stationary with respect to the material.

Viscous Material—Shape of Surface

At time t the profile of the originally level surface is described by a function $F_1(x, t)$ representing the small elevation above the original level, Fig. 1, so that $F_1(x, 0) = 0$. If the material were stationary ($U = 0$) this profile would be changing on account of penetration of the load into the material. If the penetration ceases for a moment, and the material is given the horizontal velocity U, this convective velocity brings the hump under the load. The actual profile is determined by the combination of penetration and convection.

In the penetration process ($U = 0$) the fixed and unchanging load causes both horizontal and vertical surface motion, with velocity components $u_0(x)$, $v_0(x)$, independent of t for sufficiently small deformation.

The origin of x is stationary with the load, in Fig. 1, and the layer of material moves as a whole to the right with velocity U. At time t the surface particle at abscissa x has the velocity components $u_0(x)$ and $v_0(x)$ due to the load, in addition to the convective velocity U. Its ordinate, $F_1(x, t)$ in Fig. 1, is changed after time dt to

$$F_1[x + (U + u_0)dt, t + dt]$$

and its vertical velocity component is therefore given by the Eulerian expression

$$(U + u_0)\frac{\partial F_1}{\partial x} + \frac{\partial F_1}{\partial t}$$

This vertical velocity is also represented by v_0. Neglecting u_0 in comparison with U we have the equation

$$\frac{\partial F_1}{\partial t} + U\frac{\partial F_1}{\partial x} = v_0(x) \tag{1}$$

A particular solution is obtained by taking F_1 to be a function of x only. The general solution is

$$F_1 = F(x - Ut) + \frac{1}{U}I(x) \tag{2}$$

where F denotes an arbitrary function, and

$$I(x) = \int_0^x v_0(\eta)d\eta \tag{3}$$

The starting condition $F_1(x, 0) = 0$ determines F, and (2) becomes

$$F_1 = \frac{1}{U}[I(x) - I(x - Ut)] \tag{4}$$

To interpret this it is convenient to consider first a symmetrical loading. Then $v_0(x)$ will be an even function, appreciable only

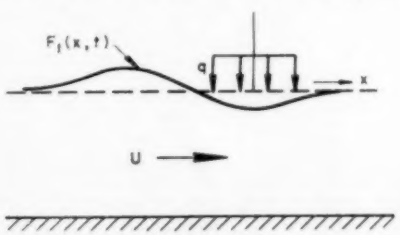

Fig. 1 Profile of layer traveling under fixed load

[1] From research sponsored by the Structural Mechanics Branch of the Office of Naval Research through Contract Nonr 225(29) with Stanford University.

[2] Numbers in brackets designate References at end of paper.

Presented at the West Coast Conference of the Applied Mechanics Division, Seattle, Wash., August 28–30, 1961, of THE AMERICAN SOCIETY OF MECHANICAL ENGINEERS.

Discussion of this paper should be addressed to the Editorial Department, ASME, United Engineering Center, 345 East 47th Street, New York 17, N. Y., and will be accepted until January 10, 1962. Discussion received after the closing date will be returned. Manuscript received by ASME Applied Mechanics Division, September 26, 1960. Paper No. 61—APMW-5.

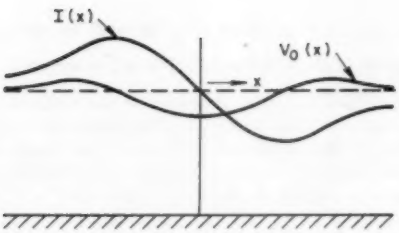

Fig. 2 Penetration velocity distribution $v_0(x)$ for fixed layer and load, and its integral $I(x)$

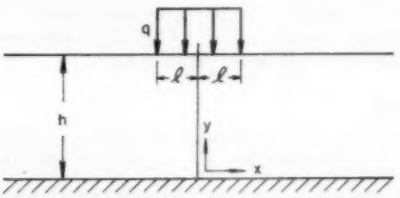

Fig. 3 Elastic and viscous penetration problems for $v_0(x)$ due to uniform loading on a segment

in the neighborhood of the load. If the material is incompressible $I(x)$ will be an odd function, appreciable only near $x = 0$; that is, near the load, Fig. 2. After a sufficient time, the term $I(x - Ut)$ in (4), which represents a "wave" traveling downstream with the material, will no longer affect the profile in the neighborhood of the load. In that neighborhood the profile is determined by the term $I(x)$, yielding an upstream hump, fixed relative to the load.

Curves showing the development of the permanent upstream stationary hump from the initial level surface are shown in Fig. 5, the loading being uniform on a segment as in Fig. 3 (and with $h/l = 10$). Details of the solution are given in the next section.

Loading Uniform on a Segment—Elastic and Viscous Penetration

The function $v_0(x)$ in (1), on which the solution depends, represents the vertical velocity of the surface in the slow motion of the viscous layer (with $U = 0$) under the load q, now taken as uniform on a segment of length $2l$. For small departures from the originally level surface the change of the profile need not be taken into account—the boundary condition is applied as though the surface were still level. The problem is solvable by the Fourier method, and the boundary conditions are accordingly taken in the form

On $y = h$,

$$\sigma_y = -\frac{2q}{\pi}\int_0^\infty \frac{1}{\alpha}\sin \alpha l \cos \alpha x \, d\alpha, \quad \tau_{xy} = 0 \qquad (5)$$

On $y = 0$,

$$u = v = 0 \qquad (6)$$

where σ_y is normal stress, τ_{xy} shear stress, and u and v are the components of velocity.

The material being incompressible, the problem is analogous to that of an elastic (incompressible) layer under the same boundary conditions, the elastic displacements becoming the viscous velocities when the shear modulus G is replaced[3] by the viscosity μ.

[3] See, for instance, reference [2]. The analogy is mentioned by Rayleigh, "Theory of Sound," vol. 2, p. 313. For the more general analogy to viscoelastic material, for which the problem of this paper can also be solved, see reference [3].

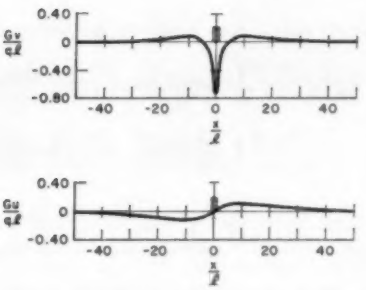

Fig. 4 Vertical and horizontal displacements, v and u, due to a uniform load on a surface segment of an elastic, incompressible, layer

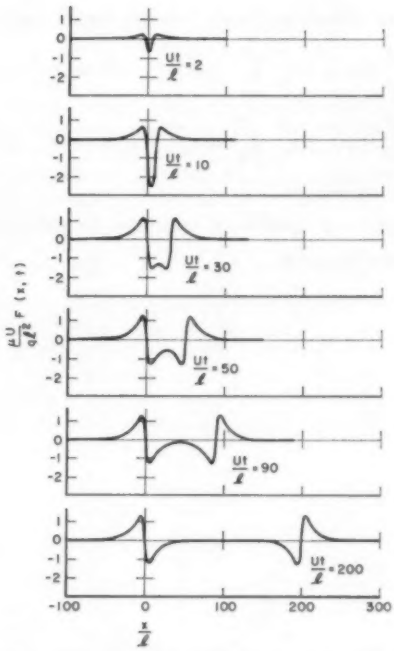

Fig. 5 Profile $F_1(x, t)$ at various times after application of fixed uniform segment loading on viscous layer traveling under it. A fixed hump forms to left of $x/l = 0$, load center, and a reversed hump is carried to right with layer.

For a loading $(\sigma_y)_{y=h}$ proportional to $\cos \alpha x$ we may use the Kolossoff complex potentials[4]

$$\psi(z) = -iA \cos \alpha z - B \sin \alpha z \qquad (7)$$

$$\chi(z) = (C + iAz)\cos \alpha z + (iD + Bz)\sin \alpha z \qquad (8)$$

with A, B, C, D, functions of α. The plane-strain displacement components u, v in the elastic solid vanish at $y = 0$ provided

$$\alpha C = 4(1 - \nu)B \qquad \alpha D = 2(1 - 2\nu)A \qquad (9)$$

where ν is Poisson's ratio and is $1/2$ for the incompressible material.

The complex potentials

$$\psi_1(z) = l\int_0^\infty \psi(z)d\alpha$$

$$\chi_1(z) = l\int_0^\infty \chi(z)d\alpha \qquad (10)$$

[4] See, for instance, reference [4], p. 187.

derived from (7) and (8) then satisfy the surface conditions (5) if

$$A = \frac{q}{\pi\alpha\Delta}\frac{\sin\alpha l}{\alpha l}\left(\alpha h\cosh\alpha h - \frac{1-\nu}{1+\nu}\sinh\alpha h\right) \quad (11)$$

$$B = \frac{q}{\pi\alpha\Delta}\frac{\sin\alpha l}{\alpha l}\left(\frac{2}{1+\nu}\cosh\alpha h + \alpha h\sinh\alpha h\right) \quad (12)$$

where

$$\Delta = \alpha^2h^2 - \left(\frac{1-\nu}{1+\nu}\right)^2\sinh^2\alpha h + \left(\frac{2}{1+\nu}\right)^2\cosh^2\alpha h \quad (13)$$

The plane-strain displacements u, v, are found from the formula[5]

$$2G(u+iv) = (3-4\nu)\psi_1(z) - z\bar{\psi}_1'(\bar{z}) - \bar{\chi}_1'(\bar{z}) \quad (14)$$

and yield the following expressions for the surface displacements:

$$\frac{G}{ql}(u)_{y=h} = \frac{1}{\pi}\int_0^\infty g_1(\lambda)\lambda^{-2}\sin\lambda\sin\lambda\frac{x}{l}\cdot d\lambda \quad (15)$$

$$\frac{G}{ql}(v)_{y=h} = \frac{1}{\pi}\int_0^\infty g_2(\lambda)\lambda^{-2}\sin\lambda\cos\lambda\frac{x}{l}\cdot d\lambda \quad (16)$$

where $\lambda = \alpha l$ and

$$g_1(\lambda) = g^{-1}[\alpha^2h^2 - (3-4\nu)(1-2\nu)\sinh^2\alpha h] \quad (17)$$

[5] Reference [4], p. 188.

$$g_2(\lambda) = 2g^{-1}(1-\nu)[\alpha h - (3-4\nu)\cosh\alpha h\sinh\alpha h] \quad (18)$$

$$g = \alpha^2h^2 - (1-2\nu)^2\sinh^2\alpha h + 4(1-\nu)^2\cosh^2\alpha h \quad (19)$$

It may be seen that the quantities on the right of (15), (16) are functions of x/l and of h/l. In the conversion of the elastic problem to the viscous-flow problem we have simply to change G to μ, the coefficient of viscosity, in the expressions on the left, and interpret u and v as the velocity components.

Curves of $G(u)_{y=h}/ql$ and $G(v)_{y=h}/ql$ as functions of x/l for the case $h/l = 1/10$ are shown in Fig. 4. The dimensionless surface-displacement component $G(v)_{y=h}/ql$ here becomes the dimensionless surface velocity component $\mu v_0(x)/ql$, where $v_0(x)$ is the velocity distribution on the right of equation (1). The solution of this equation then leads, as explained previously, to the profile curves at various times shown in Fig. 5.

References

1 G. R. Abrahamson, "Permanent Periodic Surface Deformations Due to a Traveling Jet," see this issue of the JOURNAL, pp. 519–528.

2 J. N. Goodier, "Slow Viscous Flow and Elastic Deformation," *Philosophical Magazine*, vol. 22, 1936, p. 678.

3 E. H. Lee, "Viscoelastic Stress Analysis," Structural Mechanics, Proceedings, First Symposium on Naval Structural Mechanics, edited by J. N. Goodier and N. J. Hoff, Pergamon Press, New York, N. Y., 1960.

4 S. Timoshenko and J. N. Goodier, "Theory of Elasticity," McGraw-Hill Book Company, Inc., New York, N. Y., 1951.

The Rolling Contact of a Rigid Cylinder With a Viscoelastic Half Space

S. C. HUNTER[1]
Brown University, Providence, R. I., and Division of Engineering Mechanics, Stanford University, Stanford, Calif.

The problem of a rigid cylinder rolling on the surface of a viscoelastic solid is solved in an approximation in which inertial forces are neglected. With the introduction of viscoelastic effects, the symmetry associated with the corresponding elastic problem is destroyed, and in particular the cylinder motion is impeded by a resistive force. For a standard linear solid, the resulting coefficient of friction, a function of the rolling velocity V, tends to zero for small and large values of V, and attains a single maximum at an intermediate value.

THERE is some evidence that the frictional resistance encountered in the rolling of steel balls and cylinders on the surface of elastomer and high-polymer specimens arises primarily from the viscoelastic nature of those materials (Tabor [1],[2] From [2]). Fig. 1, a schematic diagram of the contact geometry for a cylinder rolling on the surface of a viscoelastic solid, shows the origin of the friction more clearly. Relative to the symmetric position $x = 0$ (occupied by the center of the contact region for an elastic solid), the contact region is displaced in the direction of rolling, while at the same time the detailed stress distribution across the contact region depends on rolling velocity. Thus, even in the absence of surface shear tractions, the net force on the cylinder possesses a nonvanishing component opposing the forward motion.

This paper is concerned with a theoretical analysis of the rolling contact of a rigid cylinder over the surface of a viscoelastic half space.[3] Inertial forces in the viscoelastic medium are neglected and the mechanical properties of the solid idealized in two respects: (*a*) The solid is assumed characterized by a fixed value of Poisson's ratio; (*b*) the behavior in shear is taken to be that of a standard linear solid, for which the creep-strain response to a unit step function stress pulse is given by

$$\gamma(t) = \mu_D^{-1}(1 + f(1 - e^{-t/\tau}))$$

Here μ_D is the dynamic shear modulus, τ the retardation time, and f the strength of the single-line retardation spectrum. The analysis is carried out within the usual framework of a linear theory, in which the strains are assumed infinitesimal and the surface boundary conditions applied to the undeformed medium. Within these approximations and with the assumption of dy-

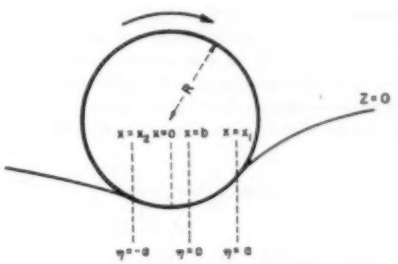

Fig. 1 Schematic diagram of rolling cylinder

[1] Now at A. R. D. E. Fort Halstead, Sevenoaks, Kent, England.
[2] Numbers in brackets designate References at end of paper.
[3] A heuristic treatment of this problem has been given recently by May, Morris, and Atack [3].

Contributed by the Applied Mechanics Division and presented at the Winter Annual Meeting, New York, N. Y., November 25–December 1, 1961, of THE AMERICAN SOCIETY OF MECHANICAL ENGINEERS.

Discussion of this paper should be addressed to the Editorial Department, ASME, United Engineering Center, 345 East 47th Street, New York 17, N. Y., and will be accepted until January 10, 1962. Discussion received after the closing date will be returned. Manuscript received by ASME Applied Mechanics Division, August 30, 1960; revised draft, Feb. 24, 1961. Paper No. 61—WA-8.

Nomenclature

x, y, z = position variables
u_i = displacement vector
σ_{ij} = stress tensor
ϵ_{ij} = strain tensor
u_s = normal surface displacement
$\sigma_s \equiv -P$ = normal surface stress
t = time
$\phi, \phi_1, \psi, \psi_1$ = potential functions
$A(\mathbf{q})$ = Fourier spectrum of potential function ϕ
μ_D = dynamic shear modulus
$\mu(p)$ = transform modulus
p = parameter entering Laplace transform
ν = Poisson's ratio
$\gamma(t)$ = creep function in shear
f_n, τ_n = parameters entering creep function
R = radius of cylinder
V = velocity of cylinder
x_1, x_2 = limits of contact region
$a = (x_1 - x_2)/2$ = semicontact width
a_0 = semicontact width for zero velocity
$b = (x_1 + x_2)/2$ = off-center displacement of cylinder
$\eta = x - b$
$h = \dfrac{a(1+f)}{V\tau}$
$k = \dfrac{a}{V\tau}$
W = weight per unit length of cylinder
Γ_1, Γ_2 = parameters (functions of velocity) entering pressure distribution
I_0, I_1 = Bessel functions of imaginary argument
K_0, K_1 = modified Bessel functions of imaginary argument
F_x, F_s = components of force on rolling cylinder
$\chi = F_x/F_s$ = coefficient of friction

namic similarity,[4] we have been able to effect an analytic solution for the two-dimensional rolling problem.

There appears to be some difficulty in generalizing the analysis to include the case of a more general viscoelastic solid, whose creep response, characterized by a number of relaxation times, is given by

$$\gamma(t) = \mu_D^{-1}\left[1 + \sum_n f_n(1 - e^{-t/\tau_n})\right] \tag{1}$$

The present theory predicts a coefficient of friction which approaches zero for small and large rolling speeds, and attains a single maximum value for a velocity of order a_0/τ, where a_0 is the semicontact width for the stationary cylinder; this is in qualitative agreement with the experimental evidence.

The paper is divided into two principal sections. As a necessary preliminary, the second section is concerned with deriving the viscoelastic analog of the Boussinesq formula

$$u_z = \frac{(1-\nu)}{2\pi\mu_D}\iint \frac{P(x', y')dx'dy'}{[(x-x')^2 + (y-y')^2]^{1/2}}$$

which expresses the normal surface displacement u_z as an integral over the distribution of surface pressure $P(x, y)$. The two-dimensional rolling contact problem is solved in the third section.

Quasi-State Response of a Viscoelastic Half Space to Moving Loads

In this section we derive the normal surface displacement of a viscoelastic half space subject to a pressure distribution moving at uniform velocity V across the free surface. In the analysis, the acceleration terms in the equations of motion are neglected, and the resulting solution is valid for velocities V small compared to sound propagation velocities for the viscoelastic medium; for most high polymers and elastomers this places a conservative upper limit of about 10^2 cm/sec on the maximum value of V.

For a half space $z \geq 0$, subject to zero shear tractions on the surface $z = 0$, the elasticity equations admit a general solution in terms of a single harmonic function ϕ, Green and Zerna [4]. In particular the normal surface displacement and stress may be written

$$\mu u_z = -(1-\nu)(\phi)_{z=0} \tag{2}$$

$$\sigma_z = -(\partial\phi/\partial z)_{z=0} \tag{3}$$

where ϕ satisfies the Laplace equation

$$\nabla^2\phi = 0 \tag{4}$$

and where μ and ν denote, respectively, the elastic shear modulus and Poisson's ratio.

The viscoelastic analogs of equations (2) and (3) follow from the correspondence of the elasticity equations with the transformed viscoelastic equations,

$$\frac{\partial\bar{\sigma}_{ij}}{\partial x_j} = 0, \quad \bar{\sigma}_{ij} = \lambda(p)\bar{\epsilon}_{kk}\delta_{ij} + 2\mu(p)\bar{\epsilon}_{ij}$$
$$\bar{\epsilon}_{ij} = \frac{1}{2}\left(\frac{\partial\bar{u}_i}{\partial x_j} + \frac{\partial\bar{u}_j}{\partial x_i}\right) \tag{5}$$

In equations (5) the bars denote Laplace transforms with respect to time, e.g.,

$$\bar{\sigma}_{ij}(x, y, z, p) = \int_0^\infty \sigma_{ij}(x, y, z, t)e^{-pt}dt$$

[4] That is, the assumption that with respect to a co-ordinate system centered on the cylinder, the deformation pattern is stationary in time.

while $\lambda(p)$, $\mu(p)$ are transform moduli, Hunter [5], defined by either the creep or relaxation behavior in both shear and dilation. For example, for a solid deformed in shear, whose shear-strain response to a step-function stress pulse is given by $\gamma(t)$, the transform shear modulus is

$$\mu(p) = [p\bar{\gamma}(p)]^{-1} \tag{6}$$

The transform bulk modulus $[\lambda(p) + 2\mu(p)/3]$ may be obtained similarly from the creep curve in dilation.

The exact correspondence of equations (5) with the equations of classical elasticity implies that for a viscoelastic half space, free from surface shear tractions, the transformed normal surface displacement and stress may be derived from a potential function $\bar{\phi}_1$,

$$\bar{u}_z = -\frac{1-\nu}{\mu(p)}(\bar{\phi}_1)_{z=0}, \quad \bar{\sigma}_z = -(\partial\bar{\phi}_1/\partial z)_{z=0} \tag{7}$$

Here $\bar{\phi}_1(x, y, z, p)$ is a harmonic function of the co-ordinates x, y, z while ν now denotes the ratio

$$\nu = \lambda(p)/2[\lambda(p) + \mu(p)] \tag{8}$$

In what follows we make the simplifying assumption that the material behaves similarly in both shear and dilation; then, equation (8) defines an unequivocal value of Poisson's ratio, independent of p. This approximation is not unduly restrictive since a more refined treatment in this respect merely substitutes a more complicated function of time for the quantity $\gamma(t)$ appearing in the ensuing analysis.

With the assumption that ν is constant and with the help of the Faltung theorem for Laplace transforms, we may formally invert equations (7) in the form

$$u_z = -(1-\nu)\psi_1(x, y, 0, t), \quad \sigma_z = -(\partial\phi_1(x, y, z, t)/\partial z)_{z=0} \tag{9}$$

where ϕ_1 is the Laplace inversion of $\bar{\phi}_1$ and where ϕ_1 and ψ_1 are related by a Volterra equation

$$\psi_1(x, y, z, t) = \int_{-\infty}^{t} \gamma(t-t')\frac{\partial}{\partial t'}\phi_1(x, y, z, t')dt' \tag{10}$$

We now restrict the analysis to steady-state problems for which the stress and deformation fields appear stationary to an observer traveling with constant velocity V in the positive x-direction. For such problems the stress, strain, and displacement fields depend on x and t through the composite independent variable $x - Vt$ rather than on x and t separately. If in addition x is measured in a co-ordinate system traveling with the velocity V, the variable t is eliminated from the analysis and equations (9) and (10) take the form

$$u_z = -(1-\nu)\psi(x, y, 0), \quad \sigma_z = -(\partial\phi(x, y, z)/\partial z)_{z=0}$$
$$\psi = -\int_0^\infty \gamma(s/V)\frac{\partial}{\partial s}\phi(x+s, y, z)ds \tag{11}$$

where ϕ and ψ are harmonic functions of x, y, z.

We expand ϕ as a double Fourier integral

$$\phi = \int_{-\infty}^{\infty}\int_{-\infty}^{\infty} A(\mathbf{q})e^{-i\mathbf{q}\cdot\mathbf{r}-|\mathbf{q}|z}dq_1dq_2 \tag{12}$$

in which the vector $\mathbf{q} = (q_1, q_2, 0)$ is restrained to lie in the (xy)-plane. The Fourier representation of ϕ automatically satisfies the Laplace equation and insures $\phi \to 0$ as $z \to \infty$; from the complete elastic solution given by Green and Zerna this latter restriction is required if all components of the displacement, stress, and strain fields are to vanish as $z \to \infty$.

Substituting for $\gamma(t)$ and ϕ, respectively, from (1) and (12) into equations (11), and assuming $\phi \to 0$ as $x \to \infty$, lead to the

following Fourier representations for the normal surface displacement and stress:

$$u_z = -(1-\nu)\int_{-\infty}^{\infty}\int_{-\infty}^{\infty}\mu^{-1}(iq_1V)A(\mathbf{q})e^{-i\mathbf{q}\cdot\mathbf{r}}dq_1dq_2 \quad (13)$$

$$\sigma_z = \int_{-\infty}^{\infty}\int_{-\infty}^{\infty}|\mathbf{q}|A(\mathbf{q})e^{-i\mathbf{q}\cdot\mathbf{r}}dq_1dq_2 \quad (14)$$

Here $\mu(iq_1V)$ is the complex shear modulus for circular frequency q_1V, e.g., see Hunter (1960) [5],

$$\mu^{-1}(iq_1V) = \mu_D^{-1}\left[1+\sum_n \frac{f_n}{1+iq_1V\tau_n}\right] \equiv (\mu^{-1}(p))_{p=iq_1V} \quad (15)$$

where $\mu(p)$ is given by (6) while the f_n and τ_n are parameters entering the creep function, equation (1).

Choosing

$$A(\mathbf{q}) = -P_0/4\pi^2|\mathbf{q}|$$

yields the fundamental case of a point force P_0 acting at the moving origin, i.e.,

$$\sigma_z = -P_0\delta(x)\delta(y)$$

where δ is the Dirac delta function. The associated displacement is given by

$$u_z = \frac{(1-\nu)P_0}{4\pi^2\mu_D}\int_{-\infty}^{\infty}\int_{-\infty}^{\infty}|\mathbf{q}|^{-1}\left[1+\sum_n\frac{f_n}{1+iq_1V\tau_n}\right]e^{-i\mathbf{q}\cdot\mathbf{r}}dq_1\,dq_2 \quad (16)$$

which, after some algebra (Appendix), may be expressed in the simpler form

$$u_z = \frac{(1-\nu)P_0}{2\pi\mu_D}\left[(x^2+y^2)^{-1/2}+\sum_n f_n\int_0^{\infty}d\xi e^{-\xi}\{(x+V\tau_n\xi)^2+y^2\}^{-1/2}\right] \quad (17)$$

Superimposing point-force solutions of the type (17) gives the displacement for a distributed pressure $P(x, y)$:

$$u_z = \frac{(1-\nu)}{2\pi\mu_D}\left[\iint\frac{P(x',y')dx'dy'}{\{(x-x')^2+(y-y')^2\}^{1/2}} + \sum_n f_n\int_0^{\infty}e^{-\xi}d\xi\iint\frac{P(x',y')dx'dy'}{\{(x-x'+V\tau_n\xi)^2+(y-y')^2\}^{1/2}}\right] \quad (18)$$

The first term on the right-hand side of (18) is the familiar result for an elastic solid with shear modulus μ_D. In the limit $V \to \infty$, the remaining terms vanish so that for sufficiently large velocities V, the viscoelastic medium behaves as an elastic solid with shear modulus μ_D. On the other hand, as $V \to 0$, the right-hand side again reduces to the elastic result but with μ_D replaced by the static modulus

$$\mu_D\Big/\left(1+\sum_n f_n\right)$$

For a given moving pressure distribution $P(x, y)$, equation (18) directly determines the surfacedisplacement. However, for the rolling-contact problems considered here, the displacement is prescribed within the contact region, and equation (18) may then be regarded as an integral equation for $P(x, y)$.

A serious complication, arising in the example of the rolling ball, is that the shape of the contact area is unknown *a priori*. To date, the difficulty of determining the shape of the contact region, concomitantly with the pressure distribution, has proved insuperable, and we have been unable to effect a solution of the rolling-ball problem. For the two-dimensional problem of a rolling cylinder, the shape of the contact region is specified solely by two parameters delineating the limits of contact. This results in a considerable simplification in the analysis and it proves possible to find an analytic solution for the case of a rigid cylinder rolling on the surface of a standard linear solid; the analysis follows immediately.

Two-Dimensional Rolling Contact Problem

The two-dimensional analog of equation (18) follows from writing $P(x, y) \equiv P(x)$ and effecting the y integration explicitly. By suitably redefining the origin of displacement to dispose of an (infinite) constant, we obtain

$$u_z(x) = -\frac{(1-\nu)}{\pi\mu_D}\left\{\int P(x')\log|x-x'|dx' + \sum_n f_n\int_0^{\infty}d\xi e^{-\xi}\int P(x')\log|x+V\tau_n\xi-x'|\,dx'\right\} \quad (19)$$

The present method of solution devolves on casting equation (19) into a form in which the integral kernels

$$\log|x+V\tau_n\xi-x'|$$

are replaced by the elastic kernel $\log|x-x'|$, and the ξ-integrations eliminated. This is most easily accomplished for the standard linear solid which is specified by a single pair of parameters (f, τ). For this case (19) reduces to

$$u_z(x) = -\frac{(1-\nu)}{\pi\mu_D}\left\{\int P(x')\log|x-x'|\,dx' + f\int_0^{\infty}d\xi e^{-\xi}\int P(x')\log|x+V\tau\xi-x'|\,dx'\right\} \quad (20)$$

We have

$$\frac{du_z}{dx} = -\frac{(1-\nu)}{\pi\mu_D}\left\{-\int P(x')\frac{d}{dx'}\log|x-x'|\,dx' + (f/V\tau)\int_0^{\infty}d\xi e^{-\xi}\frac{d}{d\xi}\int P(x')\log|x+V\tau\xi-x'|\,dx'\right\}$$

or on integrating by parts and assuming $P(x)$ to vanish as $|x| \to \infty$,

$$\frac{du_z}{dx} = -\frac{(1-\nu)}{\pi\mu_D}\left\{\int(dP/dx')\log|x-x'|\,dx' - (f/V\tau)\int P(x')\log|x-x'|\,dx' + (f/V\tau)\int_0^{\infty}d\xi e^{-\xi}\int P(x')\log|x+V\tau\xi-x'|\,dx'\right\} \quad (21)$$

From (20) and (21) we derive

$$u_z - V\tau\frac{du_z}{dx} = -\frac{(1-\nu)}{\pi\mu_D}\int[(1+f)P(x') - V\tau dP/dx']\log|x-x'|\,dx' \quad (22)$$

If we recall that the operator $-Vd/dx$ is effectively equivalent to d/dt, it is seen that equation (22) resembles closely the differential form of the constitutive equation for the standard linear solid, i.e.,

$$\dot{\epsilon} + \tau^{-1}\epsilon = \mu_D\{\dot{\sigma} + (1 + f)\tau^{-1}\sigma\}$$

This suggests that for a more complicated solid with a number of relaxation mechanisms and the constitutive equation

$$\Sigma a_n(d^n\epsilon/dt^n) = \Sigma b_n(d^n\sigma/dt^n),$$

there exists a corresponding form of equation (3.4); viz.,

$$\Sigma(-)^n a_n V^n(d^n u_x/dx^n) = -\frac{(1-\nu)}{\pi\mu_D}\Sigma\int(-)^n b_n V^n(d^n P/dx^n)\log|x - x'|\,dx'$$

Indeed it is possible to derive such an equation formally by the method used before for the standard linear solid. However, the derivation is invalid since the intermediate steps entail consideration of divergent integrals of the type

$$\int P(x')\frac{d^n}{dx'^n}\log|x - x'|\,dx', \quad n > 1$$

For the standard linear solid, $n = 1$, and all the integrals involved converge as Cauchy principal values.

In the rolling-contact problem the pressure is restricted to be nonzero in a finite region $x_2 < x < x_1$, where, *a priori*, x_1, and x_2 are unknown. It is convenient to define the semicontact width

$$a = (x_1 - x_2)/2$$

and a new independent variable

$$\eta = x - b$$

where

$$b = (x_1 + x_2)/2$$

is the distance between the center of the contact strip and the lowest point of the cylinder, Fig. 1. In terms of η, a, and b, equation (22) becomes

$$u_x - V\tau\frac{du_x}{d\eta} = -\frac{(1-\nu)}{\pi\mu_D}\int_{-a}^{a}[(1 + f)P(\eta') - V\tau\,dP/d\eta']\log|\eta - \eta'|\,d\eta' \quad (23)$$

Within the contact strip the displacement is defined by the geometry of the indenter, i.e.,

$$u_x = \alpha - x^2/2R = \alpha - (\eta + b)^2/2R, \quad |\eta| < a, \quad (24)$$

in which R is the cylinder radius and where the constant α is initialiy unknown. Substituting from (24) for u_x, equation (23) becomes for $|\eta| < a$

$$\alpha' - \Gamma_1\eta/R - \eta^2/2R = -\frac{(1-\nu)}{\pi\mu_D}\int_{-a}^{a}[(1 + f)P(\eta') - V\tau dP/d\eta']\log|\eta - \eta'|\,d\eta' \quad (25)$$

with

$$\alpha' = \alpha + (bV\tau - b^2/2)/R$$

and

$$\Gamma_1 = b - V\tau \quad (26)$$

Formally, equation (25) is an integral equation for the pressure distribution

$$\pi(\eta) = (1 + f)P(\eta) - V\tau dP/d\eta \quad |\eta| < a$$
$$= 0 \quad |\eta| > a \quad (27)$$

of an elastic indentation problem; the associated displacement in the contact region is given by

$$\alpha' - \Gamma_1\eta/R - \eta^2/2R \quad (28)$$

The three terms in (28) correspond to indentation by a flat punch, a flat tilted punch, and a cylindrical punch. The solutions of these three elastic problems are known and are most simply obtained using the method of Green and Zerna [4]. Superimposing the three solutions yields

$$\pi(\eta) = \frac{\mu_D}{\pi(1-\nu)R}\{(a^2 - \eta^2)^{1/2} + (\Gamma_2 - \Gamma_1\eta)/(a^2 - \eta^2)^{1/2}\}, \quad |\eta| < a \quad (29)$$
$$= 0, \quad |\eta| > a$$

in which the additional parameter Γ_2 is a function of α determined in the following text.

Inserting (29) into (23) yields

$$u_x - V\tau\frac{du_x}{d\eta} = -R^{-1}\{(\Gamma_2 + a^2/2)\log(a/2) - a^2/4 + \Gamma_1\eta + \eta^2/2\} \quad \text{for} \quad |\eta| < a. \quad (30)$$

$$= -R^{-1}\{\eta^2/2 \mp \eta(\eta^2 - a^2)^{1/2} - a^2/4 + (\Gamma_2 + a^2/2)[\cosh^{-1}(|\eta|/a) + \log(a/2)] + \Gamma_1[(\eta \mp (\eta^2 - a^2)^{1/2}]\} \quad \text{for} \quad |\eta| > a \quad (31)$$

where the upper and lower sign are to be chosen, respectively, for $\eta > a$, $\eta < -a$.

For $|\eta| > a$, equation (31) constitutes a differential equation for u_x; for $|\eta| < a$, we already have in equation (24)

$$u_x = \alpha - (\eta + b)^2/2R$$

which, on comparing with (30), yields

$$\alpha = -[bV\tau - b^2/2 + (\Gamma_2 + a^2/2)\log(a/2) - a^2/4]/R$$

determining α in terms of Γ_2. In particular, this gives the displacement at $\eta = a$ in terms of Γ_2,

$$u_x(a) = \alpha - (a + b)^2/2R = -R^{-1}\{(\Gamma_2 + a^2/2)\log(a/2) + a^2/4 + ab + bV\tau\} \quad (32)$$

a result we shall need subsequently.

From equations (27) and (29) the pressure $P(\eta)$ satisfies the differential equation

$$(1 + f)P - V\tau dP/d\eta = \frac{\mu_D}{(1-\nu)R}\{(a^2 - \eta^2)^{1/2} + (\Gamma_2 - \Gamma_1\eta)/(a^2 - \eta^2)^{1/2}\} \quad (33)$$

with solution

$$P = \frac{\mu_D a^2}{(1-\nu)RV\tau}e^{h\eta/a}\int_{\eta/a}^{1}e^{-hy}\{(1 - y^2)^{1/2} + (\Gamma_2/a^2 - \Gamma_1 y/a)/(1 - y^2)^{1/2}\}\,dy \quad (34)$$

where

$$h = a(1 + f)/V\tau \quad (35)$$

and where we have absorbed the constant of integration by means of the boundary condition

$$P = 0 \quad \eta/a = 1$$

Imposing $P = 0$ for $\eta/a = -1$ provides a relation connecting Γ_1 and Γ_2,

$$\int_{-1}^{1} e^{-hy}\{(1-y^2)^{1/2} + (\Gamma_2/a^2 - \Gamma_1 y/a)/(1-y^2)^{1/2}\}\,dy = 0 \tag{36}$$

The definite integrals involved in (36) are all expressible in terms of Bessel functions of imaginary argument; we find

$$(h^{-1} + \Gamma_1/a)I_1(h) + (\Gamma_2/a^2)I_0(h) = 0 \tag{37}$$

A second relation is provided by the quation

$$W = \int_{-a}^{a} P(\eta)d\eta$$

where W is the load per unit length of the cylinder. The pressure integral is most simply obtained by integrating both sides of equation (33); the term

$$\int_{-a}^{a} (dP/d\eta)d\eta$$

vanishes by the previously imposed boundary conditions, leaving

$$W = \frac{\pi\mu_D a^2}{2(1-\nu)(1+f)R}(1 + 2\Gamma_2/a^2)$$

or

$$\Gamma_2/a^2 = \tfrac{1}{2}[(a_0/a)^2 - 1] \tag{38}$$

where a_0 is the semicontact width for a stationary cylinder,

$$a_0^2 = \frac{2(1-\nu)(1+f)R}{\pi\mu_D} W \tag{39}$$

From (37) and (38)

$$\Gamma_1/a = -h^{-1} - \tfrac{1}{2}[(a_0/a)^2 - 1]I_0(h)/I_1(h) \tag{40}$$

A third relation, provided by the continuity of u_z at $\eta = a$, determines (a/a_0) as a function of $(V\tau/a_0)$. From the integral formula (20) it is readily verified that the asymptotic form of the normal surface displacement is given by

$$u_z(x) \sim -\frac{a_0^2}{2R}\log|x| + 0(x^{-1}), \quad |x| \gg a$$

or in terms of $\eta = x - b$,

$$u_z \sim -\frac{a_0^2}{2R}\log|\eta| + 0(\eta^{-1}) \tag{41}$$

An equivalent form of (41), more suitable for present purposes, is

$$u_z \sim -\frac{a_0^2}{2R}[\cosh^{-1}(|\eta|/a) + \log(a/2)] + 0(\eta^{-1})$$

$$= -\frac{(\Gamma_2 + \frac{1}{2}a^2)}{2R}[\cosh^{-1}(|\eta|/a) + \log(a/2)] + 0(\eta^{-1}) \tag{42}$$

We write, for $\eta \gg a$

$$u_z(\eta) = -\frac{(\Gamma_2 + \frac{1}{2}a^2)}{2R}[\cosh^{-1}(\eta/a) + \log(a/2)] + g(\eta) \tag{43}$$

where

$$g(\eta) \to 0, \quad \eta \to \infty \tag{44}$$

Substituting (43) into (31) gives

$$g - V\tau\frac{dg}{d\eta} = -R^{-1}Q_1(\eta) \tag{45}$$

where

$$Q_1(\eta) = \eta^2/2 - \eta(\eta^2 - a^2)^{1/2}/2 - a^2/4 + \Gamma_1[\eta - (\eta^2 - a^2)^{1/2}] + V\tau(\Gamma_2 + a^2/2)/(\eta^2 - a^2)^{1/2} \tag{46}$$

and where

$$Q_1(\eta) \sim \eta^{-1} \quad \text{for} \quad \eta \to \infty$$

The solution of (45) satisfying (44) is

$$g = -(RV\tau)^{-1}e^{\eta/V\tau}\int_{\eta}^{\infty} e^{-y/V\tau}Q_1(y)dy$$

Continuity of u_z at $\eta = a$ requires, from (32), (43),

$$a^2/4 + b(a + V\tau) = (RV\tau)^{-1}\int_a^{\infty} e^{(a-y)/V\tau}Q_1(y)dy \tag{47}$$

The definite integrals, obtained by substituting for Q_1 from (46) into (47), are either elementary or expressible in terms of modified Hankel functions of order zero and unity. Ultimately (47) reduces to

$$\frac{\Gamma_2}{a^2} = \frac{K_1(k)}{K_0(k)}\left[\frac{\Gamma_1}{a} + k^{-1}\right] \tag{48}$$

where K_0 and K_1 are defined as in Watson [6] and k is the parameter

$$k = (a/V\tau) \tag{49}$$

Substituting for Γ_1/a and Γ_2/a^2 from (38) and (40) leads to the transcendental equation

$$\left(\frac{a_0}{a}\right)^2 = 1 + \frac{2f/h}{K_0(k)/K_1(k) + I_0(h)/I_1(h)} \tag{50}$$

where

$$k = a/V\tau, \quad h = a(1+f)/V\tau = (1+f)k$$

For a specified value of the parameter f,[5] equation (50) determines a/a_0 as a function of $V\tau/a$ and hence a/a_0 in terms of $V\tau/a_0$. From (38) and (40), Γ_1/a and Γ_2/a^2 are then determined in terms of $V\tau/a_0$ and the solution is complete.

It is readily verifiable that the solution obtained degenerates into the appropriate elastic solution for the three limiting cases: (*a*) $f = 0$ (no viscoelasticity); (*b*) $V \to 0$ (material behaves as elastic solid with shear modulus $\mu_D/(1+f)$; (*c*) $V \to \infty$ (material behaves as elastic solid with shear modulus μ_D).

Curiously, in order to determine sufficient relations between the various parameters in the solution, there has been no necessity to invoke continuity of u_z at $\eta = -a$. However, imposing continuity at $\eta = -a$ leads to an expression for the surface displacement with the correct asymptotic form, equation (41); for $\eta < -a$ the surface displacement is given by

$$u_z(\eta) = -R^{-1}[(\Gamma_2 + a^2/2)\cosh^{-1}(|\eta|/a) + \log(a/2)] - R^{-1}[a^2/4 + b(V\tau - a)]e^{-|\eta|/V\tau} + (RV\tau)^{-1}\int_a^{|\eta|} Q_2(y)e^{y-|\eta|}dy$$

where

$$Q_2(y) = [y^2/2 - y(y^2 - a^2)^{1/2} - a^2/4 - \Gamma_1[y - (y^2 - a^2)^{1/2}] + V\tau(\Gamma_2 + a^2/2)/(y^2 - a^2)^{1/2}]$$

Since from (30), (31), we have continuity of

$$u_z - V\tau du_z/d\eta \quad \text{at} \quad \eta = \pm a,$$

[5] That is, for specified values of the ratio of dynamic to static modulus $(1+f)$; it is of interest to note that the absolute values of these moduli do not enter significantly into the analysis.

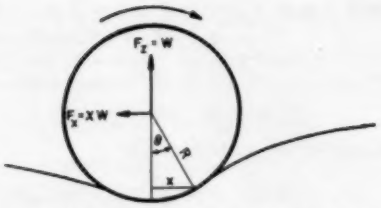

Fig. 2 Reaction of medium on cylinder

imposition of continuity of u_z implies continuity of the derivative $du_z/d\eta$.

It remains to verify that within the contact region the pressure distribution (34) is non-negative. In fact equations (38), (40), and (50) yield the inequalities

$$\Gamma_1 < 0, \quad \Gamma_2 > 0, \quad |\Gamma_1|a > \Gamma_2$$

which suffice to prove that

$$P(\eta)e^{-h_0/a}$$

given by equation (34), is positive for $|\eta| < a$.

The force impeding the cylinder motion is an integral property of the solution. From Fig. 2 the total reaction of the viscoelastic solid on the cylinder is directed through the center of gravity with components

$$F_z = \int_{x_2}^{x_1} P \cos\theta dx, \quad F_x = \int_{x_2}^{x_1} P \sin\theta dx$$

where $\sin\theta = x/R$.

To first order in x/R

$$F_z = \int_{x_2}^{x_1} P dx = W$$

and

$$F_x = R^{-1}\int_{x_2}^{x_1} xP dx = R^{-1}\int_{-a}^{a} (\eta + b)P(\eta)d\eta$$

$$= bW/R + R^{-1}\int_{-a}^{a} \eta P(\eta)d\eta \quad (51)$$

This integral may be evaluated directly using the differential equation (33); multiplying through by η, integrating, and noting the result

$$\int_{-a}^{a} \eta(dP/d\eta)d\eta = -\int_{-a}^{a} Pd\eta = -W$$

we find

$$R^{-1}\int_{-a}^{a} \eta P(\eta)d\eta = -\frac{V\tau W}{(1+f)R} - \frac{\mu_D \Gamma_1 a^2 \pi}{2(1-\nu)(1+f)R}$$

$$= -\frac{W}{R}\left[\frac{V\tau}{1+f} + \Gamma_1 \frac{a^2}{a_0^2}\right] \quad (52)$$

on using (39). From (51) and (52) the coefficient of friction χ is given by

$$\chi = F_x/F_z = R^{-1}\left[b - \frac{V\tau}{1+f} - \Gamma_1 \frac{a^2}{a_0^2}\right]$$

or since $b = V\tau + \Gamma_1$

$$R\chi/a_0 = \frac{f}{1+f}\frac{V\tau}{a_0} + \frac{\Gamma_1}{a}\left[\frac{a}{a_0} - \left(\frac{a}{a_0}\right)^3\right] \quad (53)$$

which, by previous results, determines $R\chi/a_0$ as a function of $V\tau/a_0$.

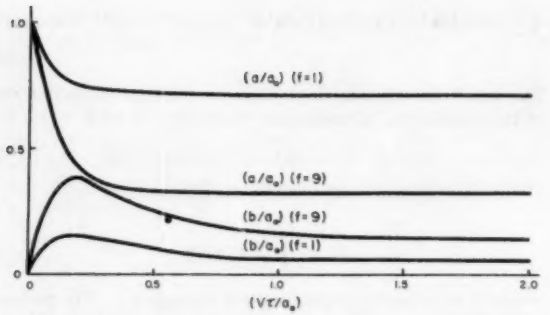

Fig. 3 Variation of semicontact width, a, and off-center displacement, b, with rolling velocity

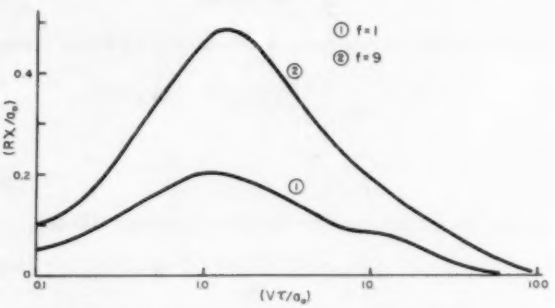

Fig. 4 Variation of coefficient of friction χ with velocity

There is some difficulty in the derivation of (53) in that the analysis, undertaken in a linear approximation, presupposes the pressure $P(x)$ to be directed perpendicularly to the initially undeformed surface $z = 0$. Thus, strictly, the linear approximation yields $F_x = 0$; on the other hand, the vertical component F_z is no longer directed through the center of gravity of the cylinder so that the cylinder encounters a resisting couple

$$M = \int_{x_2}^{x_1} xP(x)dx$$

To maintain the cylinder motion requires a frictional force with moment

$$F_x R = \int_{x_2}^{x_1} xP(x)dx$$

so that

$$F_x = R^{-1}\int_{x_2}^{x_1} xP(x)dx$$

as previously indicated. This latter viewpoint is adopted (among others) by May, Morris, and Atack [3]. However, it is clear that from a more refined treatment, in which the stress boundary conditions are applied to the deformed surface, we would obtain a resistive force rather than couple; to first order in (a_0/R) the associated coefficient of friction is given by (53).

Detailed numerical work has been undertaken for two values of the parameter f. Fig. 3 shows a/a_0 and b/a_0 as functions of $V\tau/a_0$ for $f = 1, f = 9$. The corresponding plots for $R\chi/a_0$ are displayed in Fig. 4, using a logarithmic scale for the abscissa; in each case the maximum value of χ is encountered for a value of $V\tau/a_0$ of order unity. Fig. 5 shows the detailed pressure distribution at maximum χ for the case $f = 1$. Here

$$V\tau/a_0 = 1.005$$

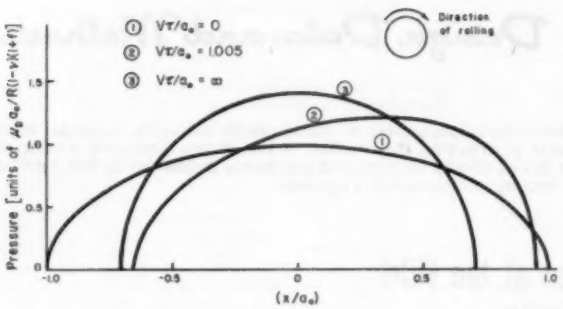

Fig. 5 Pressure distribution under rolling cylinder ($f = 1$)

On the same plot are displayed the Hertzian pressure distributions obtaining for $V = 0$ and $V = \infty$.

Fig. 4 appears to account qualitatively for the principal feature of rolling experiments, namely, that χ displays a maximum value for velocities of order a_0/τ, where τ is some measure of the mean relaxation time; also $\chi \to 0$ for sufficiently small and large values of the rolling velocity, e.g., From [2]. However, a detailed comparison between theory and experiment is hardly justified in view of the fact that the standard linear solid provides a rather inadequate description for the mechanical behavior of most high polymers and elastomers.

Acknowedgments

The author is indebted to the Commonwealth Fund of New York for the award of a Harkness Fellowship, during the tenure of which the present work was undertaken. It is a pleasure to acknowledge the interest and helpful discussions of Prof. E. Sternberg.

References

1 D. Tabor, "The Mechanism of Rolling Friction," *Philosophical Magazine*, series 7, vol. 43, 1952, pp. 1055–1059.
2 D. G. From, "Rolling Friction of Polymeric Materials," *Journal of Applied Physics*, vol. 31, 1960, pp. 306–314.
3 W. D. May, E. L. Morris, and D. Atack, "Rolling Friction of a Hard Cylinder Over a Viscoelastic Material," *Journal of Applied Physics*, vol. 30, 1959, pp. 1713–1724.
4 A. E. Green and W. Zerna, "Theory of Elasticity," Clarendon Press, Oxford, England, 1954, p. 171.
5 S. C. Hunter, "Viscoelastic Waves," Progress in Solid Mechanics, vol. 1, North Holland Publishing Company, Amsterdam, Holland, 1960, p. 48.
6 G. N. Watson, "Bessel Functions," Cambridge University Press, Cambridge, England, second edition, 1952, p. 78.

APPENDIX

Reduction of Equation (16) to (17). The result

$$(2\pi)^{-1}\int_{-\infty}^{\infty}\int_{-\infty}^{\infty}|q|^{-1}e^{-iq\cdot r}dq_1dq_2 = |r|^{-1} \tag{54}$$

is well known and also follows as a special case of

$$I = (2\pi)^{-1}\int_{-\infty}^{\infty}\int_{-\infty}^{\infty}\frac{e^{-iq\cdot r}}{|q|(1+iq_1V\tau)}\,dq_1dq_2$$

$$= \int_0^{\infty}\frac{e^{-\xi}d\xi}{\{(x+V\tau\xi)^2+y^2\}^{1/2}} \tag{55}$$

the proof of which is outlined as follows:

Expressing q and r in polar co-ordinates

$$q_1 = m\cos\phi, \quad q_2 = m\sin\phi, \quad x = r\cos\theta, \quad y = r\sin\theta,$$

and rationalizing the integrand, we have

$$I = (2\pi)^{-1}\int_0^{2\pi}d\phi\int_0^{\infty}dm\,\frac{\cos[mr\cos(\phi-\theta)] - mV\tau\cos\phi\sin[mr\cos(\phi-\theta)]}{1+m^2V^2\tau^2\cos^2\phi} \tag{56}$$

the imaginary part of the integral vanishing from angular symmetry.

The integrand in (56) gives identical contributions for ϕ and $\phi+\pi$ so that by inserting a factor of 2 we may rewrite the limits of ϕ as δ, $\delta+\pi$ where δ may be chosen at convenience. The analysis is simplified by the choice of $\delta = \theta - \pi/2$; then with an additional change of variable from ϕ to $\psi = \phi - \theta$ we easily derive

$$I = \pi^{-1}\int_{-\pi/2}^{\pi/2}d\psi\int_0^{\infty}dm\,\frac{\cos[mr\cos\psi] - mV\tau\cos(\psi+\theta)\sin(mr\cos\psi)}{1+m^2V^2\tau^2\cos^2(\theta+\psi)}$$

or on effecting the integration with respect to m

$$I = (2V\tau)^{-1}\int_{-\pi/2}^{\pi/2}\exp\left\{-\frac{r\cos\psi}{V\tau\,|\cos(\theta+\psi)|}\right\}\{|\cos(\theta+\psi)|^{-1} - \cos(\theta+\psi)\}\,d\psi \tag{57}$$

The analysis proceeds slightly differently according to whether $0 < \theta < \pi$ or $\pi < \theta < 2\pi$. We consider the former case in detail; the analysis for $\pi < \theta < 2\pi$ leads to the same final result.

For $0 < \theta < \pi$ the nonvanishing contributions to (57) arise for $\pi/2 - \theta < \psi < \pi/2$, thus

$$I = -(V\tau)^{-1}\int_{(\pi/2)-\theta}^{\pi}\frac{\exp\left\{\dfrac{r\cos\psi}{V\tau\cos(\theta+\psi)}\right\}}{\cos(\theta+\psi)}\,d\psi$$

$$= (V\tau)^{-1}\exp\left(\frac{r\cos\theta}{V\tau}\right)\int_{\pi/2}^{(\pi/2)+\theta}\frac{\exp\left\{\dfrac{r}{V\tau}\sin\theta\tan\psi\right\}}{\cos\psi}\,d\psi \tag{58}$$

Changing the variable in (58) from ψ to $z = -\tan\psi$ results in

$$I = (V\tau)^{-1}\int_{\cot\theta}^{\infty}\frac{\exp\dfrac{r}{V\tau}\{(\cos\theta - z\sin\theta)\}\,dz}{(1+z^2)^{1/2}}$$

Finally, substituting

$$z = \cot\theta + \frac{V\tau}{r}\,\xi$$

and remembering $x = r\cos\theta$, $y = r\sin\theta$ we derive the required result (55)

$$I = \int_0^{\infty}\frac{e^{-\xi}d\xi}{\{(x+V\tau\xi)^2+y^2\}^{1/2}}$$

which reduces to (54) in the limit $V\tau \to 0$.

Journal of APPLIED MECHANICS

Design Data and Methods

It is important that the data contained in technical papers be made readily available to design engineers. In order to satisfy these needs of industry, this section of the Journal includes a concise presentation of data and information drawn chiefly from papers previously published by the Applied Mechanics Division of The American Society of Mechanical Engineers.

Stress Distribution at the Fillet of an Internal Flange

K. E. HOFER Jr.,[1] and A. J. DURELLI[2]

This paper deals with the determination of the stress distribution at the fillet of a flange attached internally to a hollow cylinder. A load parallel to the axis of the cylinder and of variable eccentricity acts on a bearing plate which rests on the flange. The strains are measured by means of electrical resistance wire strain gages. The ratios of the mean cylinder diameter to the cylinder wall thickness and of the mean cylinder diameter to the flange thickness are varied. The principal stresses at the fillet are given as functions of these parameters. The experimental results are compared with the stresses calculated on the basis of an approximate theoretical solution for both an axial and an eccentric load.

Introduction

TUBING and pipes are connected by means of flanged joints. Cover plates and other machine parts are attached also to the ends of hollow cylinders through the use of flanges. The obvious need for external disassembly of these component parts generally demands that the flanged joints be external. However, there often exist conditions (in particular in airshafts, tunnels, storage cylinders, and so on) where the attachment of the components is achieved by means of flanged joints internal to the structural system.

When a machine element contains an internal flange, the resultant loading on the cylinder often is parallel to the axis, but eccentric. The eccentric loading makes a theoretical analysis difficult. Moreover, in the machine element, one is often confronted with the problem of lack of working room and hence must be satisfied with relatively narrow flanges. For this reason the radius of the fillet connecting the flange to the shell may be quite small, giving rise to a severe stress concentration at the fillet. This stress concentration will then produce stresses which are quite high in the flange fillet.

E. G. Coker and L. N. G. Filon [1][3] conducted a photoelastic investigation of a vertical cylindrical shaft in the earth where cast-iron cylinders with internal flanges are bolted together to form the internal lining of the shaft. The large D_m/t ratio of the cylinder and the symmetry of loading warranted Coker's assumption that the strain in any axial plane may be obtained from a plane model without much loss of accuracy.

It is desired to find the stress distribution at the fillet of an internal flange located at the end of a hollow cylinder, as shown in Fig. 1, for loads directed parallel to the axis of the cylinder and transmitted to the flange by means of a plate. It is desired to find the stress distribution at the fillet for various positions of the load P along the radial line CO. The effect of changes in the cylinder wall thickness t and flange thickness T will be taken into consideration. The parameters to be held constant are the internal diameter D, fillet radius ρ, flange width W, and the geometry of the bearing plate.

This investigation deals with flanges attached internally to hollow cylinders with D_m/t ratios of from 13 to 30, where D_m is the mean diameter of the cylinder. For the first part of the study the ratio D_m/T was 25. Further investigations were carried out holding the ratio $D_m/t = 30$ constant and varying the ratio D_m/T from 25 to 50. These values were selected because they seem to bracket the range of current designs and may be increasingly used in the future.

The loading conditions are realized by applying to the bearing plate a force parallel to the axis of the cylinder at different eccentricities. The load is transmitted from the bearing plate to a circular annular area in the center of the flange.

The stresses on the cylinder depend critically on the distance between the cylinder wall and the line of action of the force acting on the flange. It is therefore important to define this distance accurately. In this investigation this distance is $W/2$. The corners of the bearing plate and the flange were machined away as shown in the detail of Fig. 2, so that the resulting forces on the flange are contained in the narrow annular region shown. During

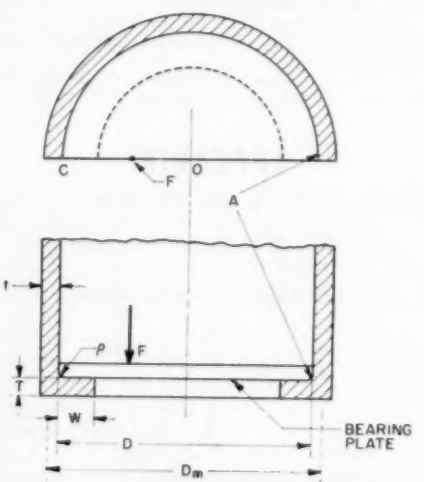

Fig. 1 Internal flange at the end of a hollow cylinder. The axial and eccentric load is transmitted to the flange by means of a plate.

[1] Armour Research Foundation, Illinois Institute of Technology, Chicago, Ill.

[2] Professor of Civil Engineering, Catholic University of America, Washington, D. C. Assoc. Mem. ASME.

Manuscript received by ASME Applied Mechanics Division, July 20, 1960; revised draft, December 19, 1960.

[3] Numbers in brackets indicate References at end of paper.

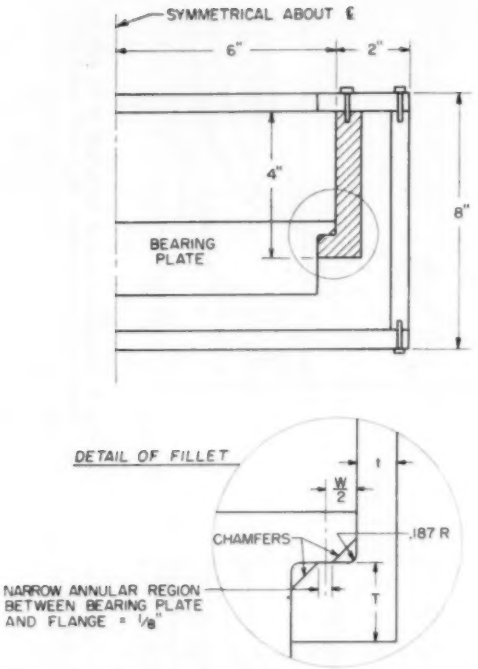

Fig. 2 Geometry of the cylinder and bearing plate used in the experimental analysis

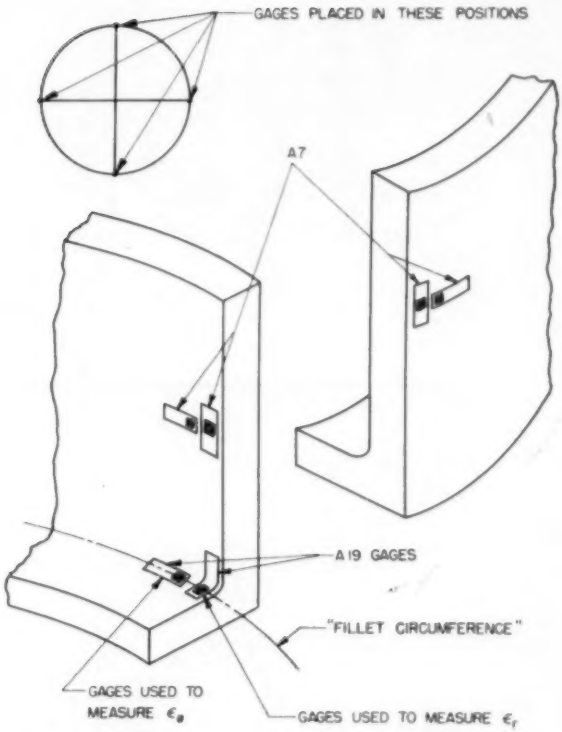

Fig. 3 Location of electrical strain gages on the cylinder and fillet between cylinder and flange

deformation as this region rotates slightly, it is assumed that the resultant forces do not appreciably change their distance from the cylinder wall. In the results shown later, the linearity of the response of the strain gages shows that this assumption is justified.

An approximate theoretical approach to the solution of this problem is presented in an appendix, and a comparison of the results obtained using this approach and those obtained from the experiments is presented in the discussion.

Experimental Approach to the Problem

A cylinder with an internal flange was machined from cast aluminum tooling plate to the shape shown in Fig. 2. Electrical resistance wire strain gages (gage length = 1/16 in.) were placed in the fillet of the internal flange as shown in Fig. 3 at four symmetric positions along the fillet circumference. Two gages were placed on both the inside and outside of the cylinder as shown in Fig. 3.

A bearing plate was used to transmit the load to the internal flange. Forty-five degree chamfers on the bearing plate and the flange constrained the forces to a narrow annular region on the flange (see the detail of Fig. 2), and also provided the necessary working room in the flange fillet for placing the gages.

Readings were recorded for the central position of the load and four positions along two radial lines 45 deg apart. This procedure permitted a larger number of points along the fillet circumference to be studied with a minimum number of strain gages.

The directions of the principal stresses at every point along the fillet for eccentric loading were found by applying brittle coating[4] techniques. Only two positions of the load were examined: (*a*) the most extreme eccentrically loaded position $\left(\frac{m}{r} = 4/6\right)$, and (*b*) the median eccentrically loaded position $\left(\frac{m}{r} = 2/6\right)$. The

[4] Stresscoat 1207, a product manufactured by the Magnaflux Corporation, Chicago, Ill.

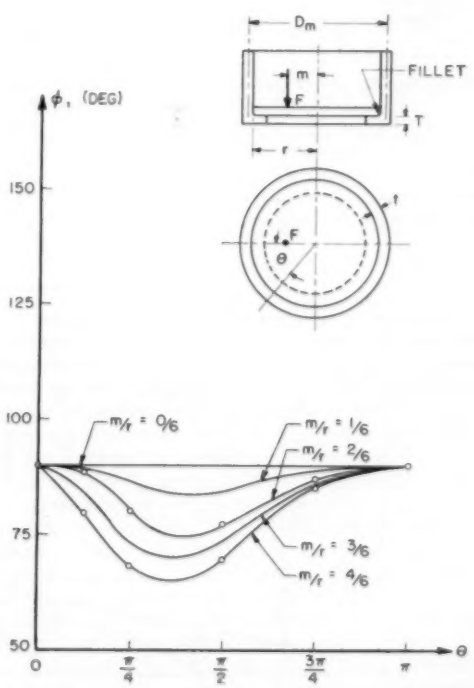

Fig. 4 Principal directions at the fillet for the internal flange loaded in bearing. The parameter m/r is the measure of eccentricity of loading

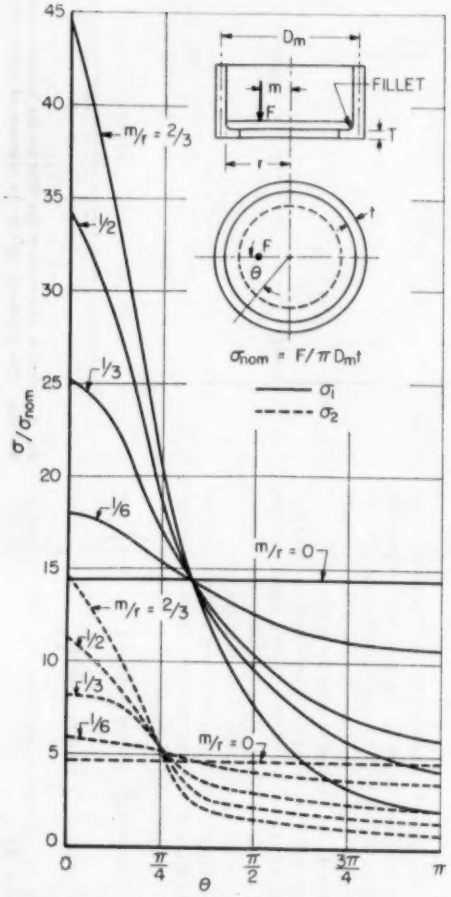

Fig. 5 Principal stresses at the bottom of the fillet for different eccentricities of load. $D_m/t = 13$, and $D_m/T = 25$.

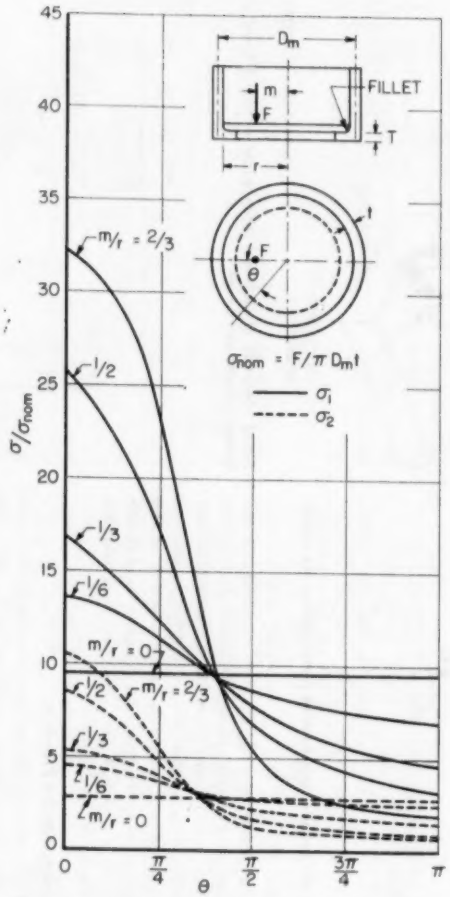

Fig. 6 Principal stresses at the bottom of the fillet for different eccentricities of load. $D_m/t = 21$, and $D_m/T = 25$.

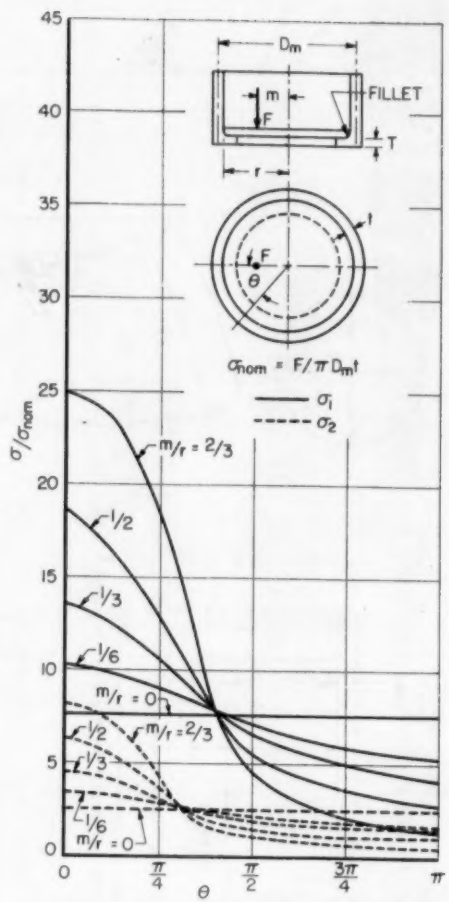

Fig. 7 Principal stresses at the bottom of the fillet for different eccentricities of load. $D_m/t = 30$, and $D_m/T = 25$.

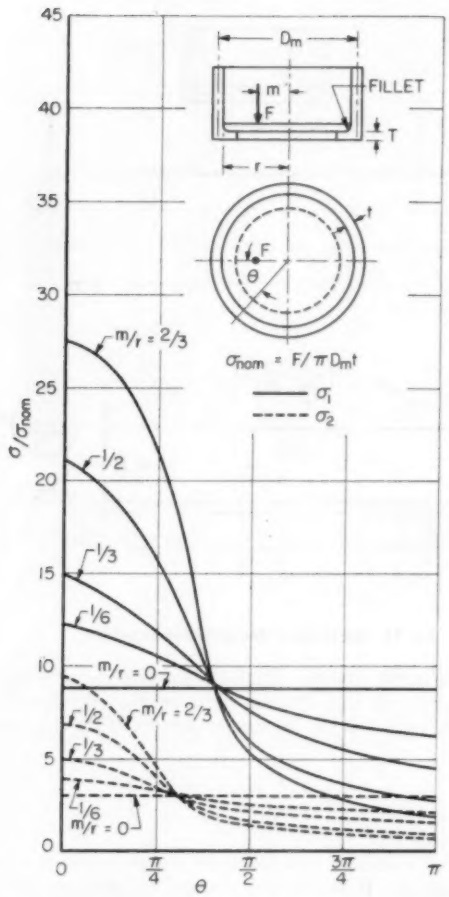

Fig. 8 Principal stresses at the bottom of the fillet for different eccentricities of load. $D_m/t = 30$, and $D_m/T = 35$.

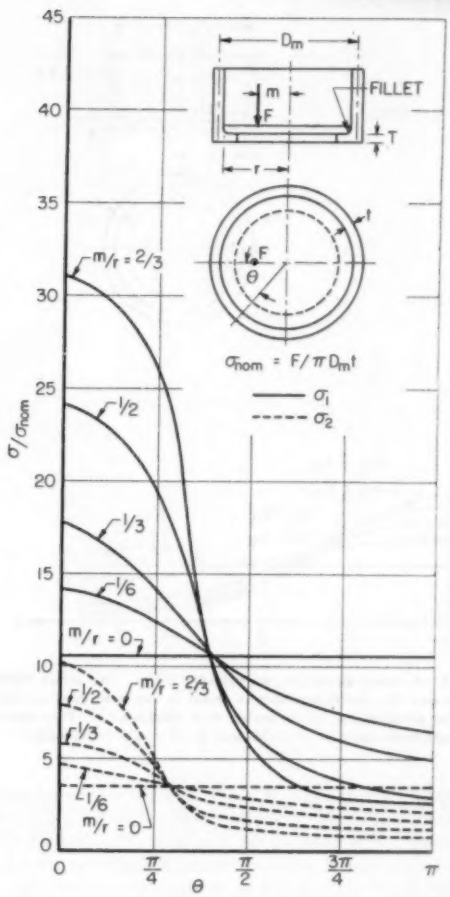

Fig. 9 Principal stresses at the bottom of the fillet for different eccentricities of load. $D_m/t = 30$, and $D_m/T = 50$.

values for the other two eccentrically loaded positions were obtained by interpolation. For the centrally located position of the load every axial plane is a principal plane, due to symmetry, and hence no test was made for this case. See Fig. 4 for the results of these tests. It was assumed that the directions at the fillet would not change appreciably for the various thicknesses of the cylinder wall and flange, and hence the directions were determined for only one given wall thickness and flange thickness.

After the data had been obtained for the first wall thickness, material was machined from the outside of the cylinder, new A-7 gages were cemented to the outside of the cylinder, and the tests were conducted for the new wall thickness. This process was repeated until four different wall thicknesses had been studied. Then material was machined from the bottom of the flange and the tests were again repeated.

The analysis of the resulting data was accomplished by using Hooke's law and Mohr's circle.

Results

Figs. 5–7 illustrate the distribution of the principal stresses around the fillet circumference, with D_m/t and m/r as parameters. The ratio of the mean diameter to the flange thickness is held constant at $D_m/T = 25$. The results for three values of D_m/T at a constant $D_m/t = 30$ are shown in Figs. 7–9.

In Figs. 5–9 it can be noted that the curves which were obtained for various eccentricities of loading intersect at a common point. The angular position of this common point is different for the σ_1/σ_{nom} and the σ_2/σ_{nom} curves. The position of the common point in both the σ_1/σ_{nom} and σ_2/σ_{nom} curves seems to depend somewhat on the D_m/t ratio but is independent of the D_m/T ratio for the range of parameters tested.

Discussion and Conclusions

A load equilibrium check on the accuracy of the entire procedure was available from the results of the readings of gages placed on the cylinder wall. In Fig. 10 the average cylinder axial stresses are plotted for typical D_m/t and D_m/T ratios. The area beneath these curves has to be equal to the respective applied loads. In most cases it was observed that this is accomplished to within a few per cent of the applied load.

The approximate theoretical solution derived in the Appendix may be compared with the experimental results if a stress concentration factor is assumed for this case. For zero eccentricity the maximum stress resulting from the theoretical equations is 11,800 psi for a load of $F = 100{,}000$ lb; for an eccentricity ($m/r = 1/3$) the values of the maximum stresses (at $\theta = 0$) are 23,200 psi and 18,900 psi for the linear and cosine distributions, respectively. An approximate stress concentration factor ($k = 3.76$) can be obtained from the case of a flat plate angle section under a bending load [3]. For zero eccentricity the value of the maximum stress resulting from the use of this stress multiplier is

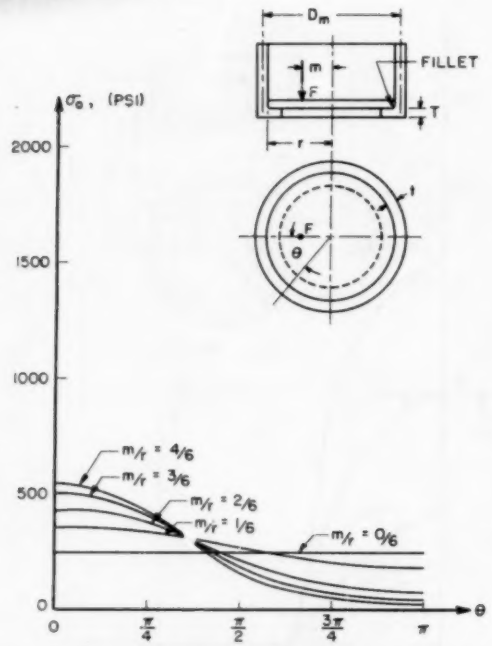

Fig. 10 Average stress (σ_θ) on cylinder walls. The areas between the curves and the horizontal axis is equal to the total load carried by the cylinder divided by the cylinder wall thickness t. This loading corresponds to the case $D_m/t = 13$, and $D_m/T = 25$. The load $F = 10{,}000$ lb.

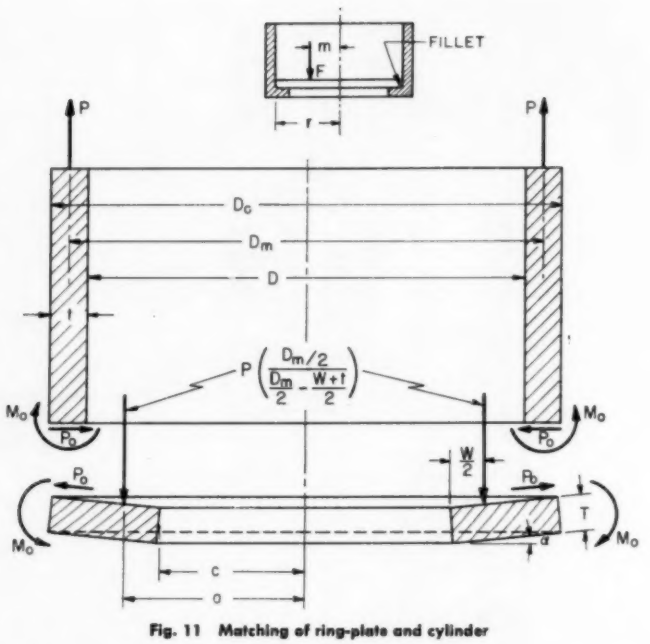

Fig. 11 Matching of ring-plate and cylinder

45,500 psi. For the case of $m/r = 1/3$, the maximum stresses are 89,100 psi and 72,500 psi for the linear and cosine distributions, respectively. The value of the experimentally derived maximum stress for the case of zero eccentricity is 35,000 psi. When $m/r = 1/3$ the maximum stress from experiment is 61,500 psi. Therefore the calculated values of σ_{max} are higher than the experimental values. This difference is probably explained by the fact that a two-dimensional stress concentration factor is used when actually a three-dimensional multiplier is needed. The experimentally determined factor for zero eccentricity is $k = 35{,}000/11{,}800 = 2.97$, and for an eccentricity of $m/r = 1/3$ (and a cosine distribution) it is $k = 61{,}500/18{,}900 = 3.25$.

References

1 E. G. Coker and L. N. G. Filon, "A Treatise on Photoelasticity," second edition, Cambridge University Press, 1957, pp. 677–680.

2 S. Timoshenko, "Strength of Materials, Part I—Advanced Theory and Problems," third edition, D. Van Nostrand and Company, 1956, pp. 138–143.

3 Lipson, Noll, and Clock, "Stress and Strength of Manufactured Parts," McGraw-Hill Book Company, Inc., New York, N. Y., 1950, p. 100.

APPENDIX

Approximate Theoretical Approach to the Problem

Timoshenko [2] presents the solution for the symmetric problem of an external flange with a strength of materials approach. By modifying this approach the solution for the problem of an eccentric load on the plate resting on the internal flange is obtained.

If a circular ring plate is attached to the end of a hollow cylinder as shown in Fig. 11, the nominal stresses at the fillet may be calculated from the bending moments and shearing forces at the joint. Let P be the force per unit length of the mean circumference in the cylinder. The force per unit length acting on the flange (if such a distribution occurs midway between the inner cylinder wall and the inner circumference of the ring) will be

$$P\left(\frac{D_m/2}{\frac{D_m}{2} - \frac{W+t}{2}}\right)$$

Under the action of these forces the ring plate will rotate through an angle α. If the bending moment and shearing force at the joint between ring plate and cylinder are given, respectively, by M_0 and P_0 (see Fig. 11), the magnitude of these quantities can be determined from the condition that at the joint distortions of the cylinder and the ring plate must be continuous across the joint.

The torque per unit length about the center point of the flange cross section is given by

$$M_t = \frac{D_m}{2a}\left[\left(\frac{W+t}{2}\right)P - M_0(1 + T\beta/2/2)\right] \qquad (1)$$

where

$$\beta = \sqrt[4]{\frac{3(1-\nu^2)}{(D/2)^2t^2}}$$

is the "foundation" modulus obtained by a consideration of the restraining forces of neighboring axial elements in the cylinder. Thus M_0 is given by

$$M_0 = \frac{\left(\frac{W+t}{2}\right)P}{\left(\frac{2aT^3(1-\nu^2)\ln(D_0/2c)}{\beta t^3 D_m^2}\right) + 1 + T\beta/2} \qquad (2)$$

The maximum bending stress in the cylindrical shell from simple strength of materials is given by $\sigma_{max} = 6M_0/t^2$. Thus,

$$\sigma_{max} = \frac{3(W+t)P}{\left(\frac{2aT^3(1-\nu^2)\ln(D_0/2c)}{\beta t D_m^2}\right) + t^2 + Tt\beta/2} \qquad (3)$$

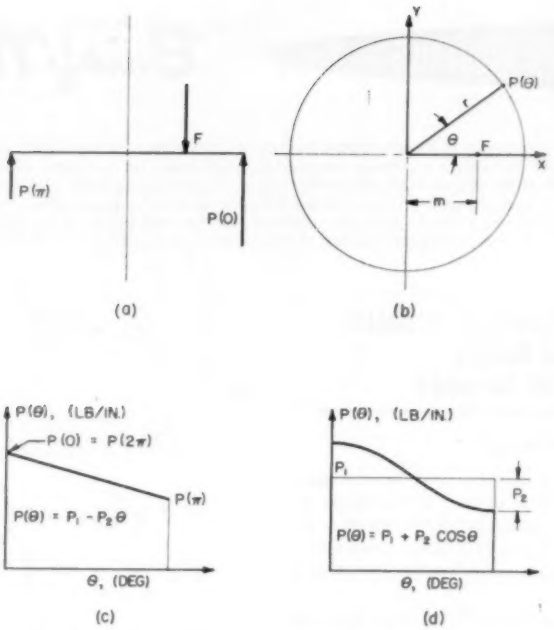

Fig. 12 Possible transmission of load F to flange through the bearing plate

If we add this to the tensile stress in the cylinder, $\sigma = P/t$, we obtain

$$\sigma_{total} = \frac{P}{t}\left\{1 + \frac{3(W+t)}{\left(\frac{2aT^2(1-\nu^2)\ln(D_0/2c)}{\beta t^3 D_m^2} + t + Tt\beta/2\right)}\right\} \tag{4}$$

Equation (4) gives the nominal stress at the junction between the flange and the cylinder. This nominal stress is for the case of zero eccentricity and does not include the effect of stress concentration.

It is possible to estimate the maximum stresses in the fillet for the eccentric case if we assume that the load is transmitted to the flange by distributions such as are shown in Figs. 12(c) and 12(d). From the summation of forces in the z-direction we obtain

$$\int_0^\pi P(\theta) r d\theta = \frac{F}{2} \tag{5}$$

and from the summation of moments about the y-axis (normal to the radial line along which the position of the load varies) we obtain

$$\int_0^\pi r P(\theta) \cos\theta r d\theta = \frac{Fm}{2} \tag{6}$$

Performing the integration and solving the resulting pair of equations simultaneously, one obtains

$$P(\theta) = \frac{F}{2r}\left(\frac{m\pi}{4r} + \frac{1}{\pi} - \frac{\theta_m}{2r}\right) \tag{7}$$

for the linear distribution shown in Fig. 12(c) and

$$P(\theta) = \frac{F}{2\pi r}\left(1 + \frac{2m}{r}\cos\theta\right) \tag{8}$$

for the cosine distribution shown in Fig. 12(d).

By replacing P in Equation (4) by $P(\theta)$ from either Equation (7) or Equation (8), an approximate value of the nominal stress at the junction between the flange and the cylinder will be obtained for any value of θ.

It should be noted that the load distributions assumed in Figs. 12(c) and 12(d) are valid only if $m/r \leq 4/\pi^2$ for the linear distribution and $m/r \leq 1/2$ for the cosine distribution. For greater eccentricities, $P(\theta)$ becomes tensile, which is not possible physically.

Journal of APPLIED MECHANICS

Brief Notes

On the recommendation of the Executive Committee of the ASME Applied Mechanics Division, it was decided to initiate a section devoted to brief notes on technical matters in mechanics. These notes must not be longer than 750 words (about 2½ double-spaced typewritten pages, including figures) and will be subject to the usual review procedure prior to publication. After approval such notes will be published as soon as possible, normally in the next issue of the Journal. The notes should be submitted to the Technical Editors of the Journal of Applied Mechanics.

Lowest Natural Frequency of Elastic Arc for Vibrations Outside the Plane of Initial Curvature

E. VOLTERRA[1] **and J. D. MORELL**[2]

THIS brief note supplements a previous one by the same authors.[3] The Rayleigh-Ritz method is used to determine the lowest natural frequency of elastic arcs with clamped ends. The arcs have the center lines in the forms of a circle, a cycloid, a catenary, and a parabola. Vibrations occur outside the plane of initial curvature of the arc.

With reference to Figs. 1 and 2, the following expressions are used for the potential energy U and the kinetic energy T of the arc:

$$U = \frac{EI}{2}\int_0^L \left[\frac{\beta}{R} - \frac{\partial^2 v}{\partial s^2}\right]^2 ds + \frac{GIp}{2}\int_0^L \left[\frac{\partial \beta}{\partial s} + \frac{1}{R}\frac{\partial v}{\partial s}\right]^2 ds \quad (1)$$

$$T = \frac{\rho\Omega}{2}\int_0^L \left[\left(\frac{\partial v}{\partial t}\right)^2 + \frac{Ip}{\Omega}\left(\frac{\partial \beta}{\partial t}\right)^2\right] ds \quad (2)$$

ρ being the density of the material of the arc, ν its Poisson ratio, Ω the cross-section area, and EI and GIp its flexural and torsional rigidities. In all the results presented the cross section of the arc is considered circular.

For the following boundary conditions:

$$v = \frac{\partial v}{\partial s} = \beta = 0 \qquad \text{for} \qquad s = \begin{cases} = 0 \\ = L \end{cases} \quad (3)$$

suitable analytical expressions for the displacements satisfying equations (3) are:

$$\left.\begin{aligned} v &= A\left[1 - \cos\frac{2\pi s}{L}\right]\sin \omega t \\ \beta &= B \sin\frac{\pi s}{L}\sin \omega t \end{aligned}\right\} \quad (4)$$

By inserting equations (4) into equations (1) and (2), one obtains:

$$U_{max} = \frac{E\Omega L}{4}\,\delta^2\left[\left(\frac{A}{L}\right)^2 k + B^2 m + 2\left(\frac{A}{L}\right)Bn\right] \quad (5)$$

$$T_{max} = \frac{3\rho\Omega L^3}{4}\,\omega^2\left[\left(\frac{A}{L}\right)^2 + \delta^2 B^2\right] \quad (6)$$

with:

$$k = \left(2\pi\right)^4 + \frac{(2\pi)^2}{(1+\nu)}\frac{2}{L}\int_0^L \left(\frac{L}{R}\right)^2 \sin^2\left(\frac{2\pi s}{L}\right) ds$$

$$m = \frac{\pi^2}{(1+\nu)} + \frac{2}{L}\int_0^L \left(\frac{L}{R}\right)^2 \sin^2\left(\frac{\pi s}{L}\right) ds \quad (7)$$

$$n = \frac{2\pi^2}{(1+\nu)}\frac{2}{L}\left[\int_0^L \left(\frac{L}{R}\right)\sin\left(\frac{2\pi s}{L}\right)\cos\frac{\pi s}{L}\, ds - (1-\nu)\int_0^L \left(\frac{L}{R}\right)\sin\left(\frac{\pi s}{L}\right)\cos\left(\frac{2\pi s}{L}\right) ds\right]$$

From the condition that $U_{max} = T_{max}$ it follows that

$$\Phi^2\left[3\left(\frac{A}{L}\right)^2 + 2\delta^2 B^2\right] = \delta^2\left[\left(\frac{A}{L}\right)^2 k + B^2 m + 2\left(\frac{A}{L}\right)Bn\right] \quad (8)$$

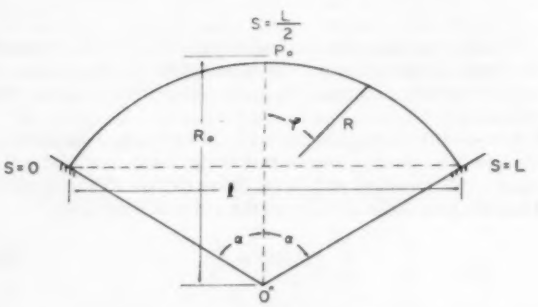

Fig. 1

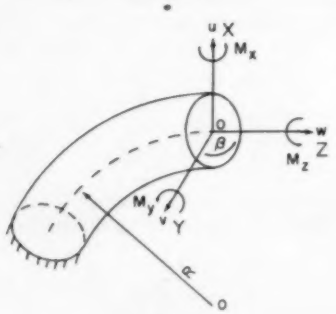

Fig. 2

[1] Professor of Engineering Mechanics, The University of Texas, Austin, Texas. Mem. ASME.

[2] Graduate Student, Department of Mechanical Engineering, The University of Texas, Austin, Texas.

[3] E. Volterra and J. D. Morell, "A Note on the Lowest Natural Frequency of Elastic Arcs," JOURNAL OF APPLIED MECHANICS, vol. 27, TRANS. ASME, vol. 83, Series E, December, 1960, pp. 744–746.

Manuscript received by ASME Applied Mechanics Division, March 16, 1961.

Table 1 Values of the constant Φ. (Upper left should read R_0/r.)

R_0/R \ α	5°	10°	15°	20°	25°	30°	35°	40°	
20	6.832	13.667	19.967	21.904	22.008	21.939	21.827	21.700	Circle
	6.823	13.601	17.560	21.861	22.006	21.963	21.884	21.803	Cycloid
	6.849	13.753	20.148	21.891	21.923	21.748	21.478	21.119	Catenary
	6.853	13.877	20.148	22.249	21.974	21.810	21.548	21.211	Parabola
30	10.246	20.214	29.391	32.359	22.249	22.113	21.965	21.815	Circle
	10.233	20.125	22.184	32.362	22.268	22.153	22.041	21.934	Cycloid
	10.065	16.690	22.383	23.323	22.161	21.921	21.617	21.233	Catenary
	10.276	16.936	22.220	22.330	22.169	21.946	21.650	21.287	Parabola
40	13.657	22.512	22.537	22.440	22.309	22.163	22.008	21.852	Circle
	13.640	22.506	22.568	22.444	22.330	22.205	22.084	21.968	Cycloid
	13.678	24.011	22.528	22.404	22.233	21.968	21.661	21.27	Catenary
	13.694	22.520	22.567	22.402	22.222	21.987	21.683	21.313	Parabola
50	17.052	21.339	22.578	22.468	22.334	22.184	22.027	21.821	Circle
	17.036	22.639	22.579	22.605	22.356	22.228	22.109	21.993	Cycloid
	17.082	22.644	22.570	22.433	22.299	21.995	21.681	21.290	Catenary
	17.095	22.639	22.450	22.430	22.244	22.005	21.704	21.324	Parabola
75	20.763	22.694	22.609	22.494	22.356	22.204	22.043	21.885	Circle
	20.762	22.694	22.611	22.501	22.379	22.249	22.123	22.010	Cycloid
	22.688	22.532	22.602	22.460	22.272	22.017	21.700	21.305	Catenary
	22.617	22.691	22.492	22.455	22.265	22.023	21.712	21.366	Parabola
100	22.753	22.706	22.619	22.502	22.364	22.211	22.051	21.890	Circle
	22.753	22.673	22.620	22.510	22.387	22.256	22.130	22.016	Cycloid
	22.760	22.710	22.612	22.469	22.282	22.022	21.706	21.311	Catenary
	22.728	22.703	22.505	22.462	22.272	21.648	21.717	21.340	Parabola

where $\delta = \frac{r}{L}$ ($r = \sqrt{\frac{I}{\Omega}}$ being the radius of gyration of the cross section of the curved bar) and:

$$\Phi^2 = \frac{\rho\omega^2 L^2}{E}$$

By expressing that

$$\frac{\partial[\Phi]^2}{\partial A} = \frac{\partial[\Phi]^2}{\partial B} = 0$$

the following frequency equation

$$6\Phi^4 - \Phi^2\left[2k - \frac{3m}{\delta^2}\right] + \left[\frac{km - n^2}{\delta^2}\right] = 0 \qquad (9)$$

is obtained.

In Table 1 the values of the lowest root Φ of equation (9) are given for the arcs of the circle, cycloid, catenary, and parabola for values of the ratio R_0/r varying from 20 to 100 and of the angle α varying from 5 deg to 40 deg.

In the case of small angles α, it is more convenient to express the results under the form:

$$\omega = \frac{C}{l^2}\sqrt{\frac{EI}{\rho\Omega}} \qquad (10)$$

where l is the length of the chord subtending the arc (see Fig. 1).

The numerical values of the constant C for cycloid, catenary, and parabola are given, respectively, in Figs. 3, 4, and 5. These values are compared in each figure with the corresponding values for the circle. The following relationships are verified:

For the circle:

$$\left.\begin{aligned} k &= \left(2\pi\right)^4 + \frac{16\alpha^2\pi^2}{(1+\nu)} \\ m &= \frac{\pi^2}{1+\nu} + (2\alpha)^2 \\ n &= \frac{32\pi\alpha}{3}\,\frac{(2+\nu)}{(1+\nu)} \end{aligned}\right\} \qquad (11)$$

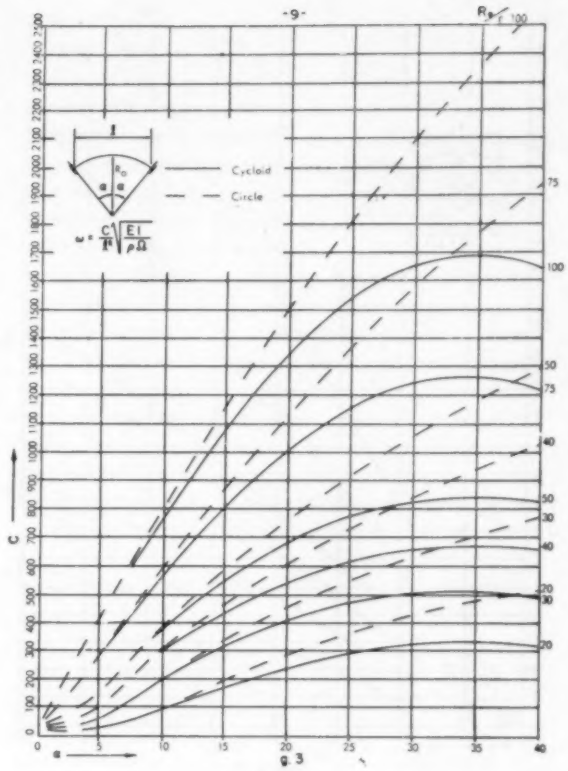

Fig. 3

For the cycloid:

$$R = R_0 \cos\varphi$$

$$s = R_0(\sin\varphi + \sin\alpha)$$

$$L = 2R_0 \sin\alpha$$

For the catenary:

$$R = \frac{R_0}{\cos^2\varphi}$$

$$s = R_0(\tan\varphi + \tan\alpha)$$

$$L = 2R_0 \tan\alpha$$

For the parabola:

$$R = \frac{R_0}{\cos^2\varphi}$$

$$s = \frac{1}{2}R_0\left[\frac{\sin\varphi}{\cos^2\varphi} + \frac{1}{2}\ln\left(\frac{1+\sin\varphi}{1-\sin\varphi}\right) + \frac{\sin\alpha}{\cos^2\alpha} + \frac{1}{2}\ln\left(\frac{1+\sin\alpha}{1-\sin\alpha}\right)\right]$$

$$L = R_0\left[\frac{\sin\alpha}{\cos^2\alpha} + \frac{1}{2}\ln\left(\frac{1+\sin\alpha}{1-\sin\alpha}\right)\right]$$

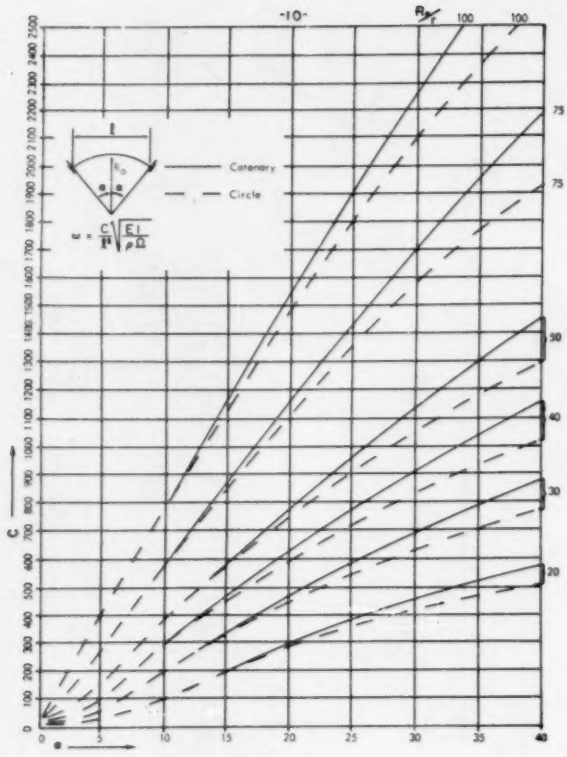

Fig. 4

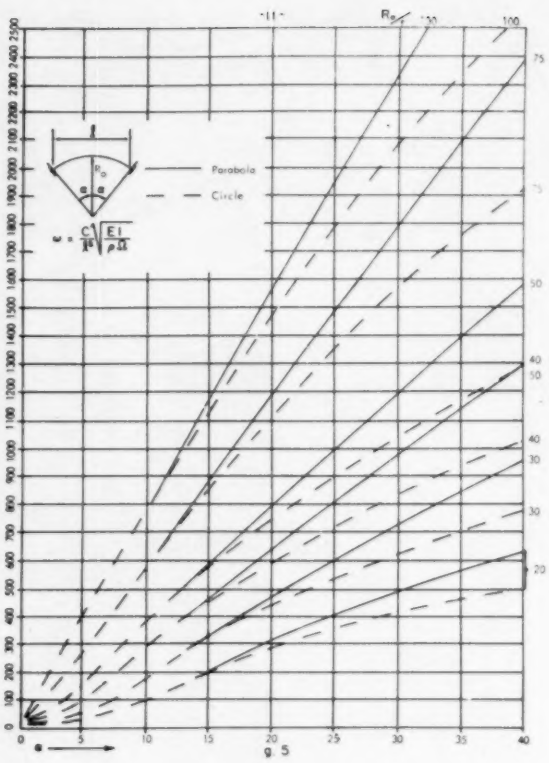

Fig. 5

If the following boundary conditions are assumed in place of equations (3):

$$v = \frac{\partial v}{\partial s} = \beta = \frac{\partial \beta}{\partial s} = 0 \quad \text{for} \quad s = \begin{cases} = 0 \\ = L \end{cases} \tag{12}$$

Table 2 Values of the constant Φ. (Upper left should read R_0/r.)

R_0/R \ α	5°	10°	15°	20°	25°	30°	35°	40°	
20	7.920	15.675	21.309	21.874	21.779	21.575	21.368	21.243	Circle
	7.876	15.666	21.656	22.230	22.207	22.100	21.962	21.799	Cycloid
	7.906	15.907	21.907	22.317	22.299	22.215	22.138	22.063	Catenary
	7.916	15.990	21.967	22.332	22.309	22.243	22.168	22.127	Parabola
30	11.818	21.884	22.339	22.203	21.995	21.744	21.507	21.166	Circle
	11.812	22.125	22.531	22.466	22.361	22.226	22.073	21.901	Cycloid
	11.857	22.236	22.555	22.496	22.410	22.297	22.200	22.110	Catenary
	11.872	22.248	22.553	22.496	22.408	22.313	22.218	22.162	Parabola
40	15.744	22.533	22.450	22.276	22.054	21.796	21.552	21.206	Circle
	15.741	22.641	22.604	22.515	22.401	22.263	22.108	21.932	Cycloid
	15.801	22.654	22.619	22.537	22.441	22.322	22.220	22.126	Catenary
	15.821	22.649	22.614	22.534	22.437	22.334	22.235	22.174	Parabola
50	19.620	22.610	22.487	22.306	22.080	21.819	21.572	21.225	Circle
	19.639	22.690	22.628	22.534	22.419	22.279	22.123	21.949	Cycloid
	19.713	22.709	22.640	22.553	22.454	22.333	22.229	22.133	Catenary
	19.737	22.693	22.635	22.549	22.449	22.344	22.242	22.180	Parabola
75	22.713	22.654	22.518	22.332	22.104	21.840	21.591	21.243	Circle
	22.746	22.718	22.648	22.551	22.435	22.294	22.138	21.963	Cycloid
	22.754	22.726	22.658	22.568	22.467	22.344	22.238	22.140	Catenary
	22.747	22.719	22.652	22.563	22.460	22.353	22.249	22.185	Parabola
100	22.746	22.664	22.528	22.341	22.112	21.848	21.598	21.249	Circle
	22.767	22.725	22.654	22.557	22.440	22.299	22.143	21.968	Cycloid
	22.774	22.733	22.664	22.573	22.471	22.347	22.241	22.142	Catenary
	22.767	22.726	22.657	22.567	22.464	22.356	22.252	22.187	Parabola

suitable analytical expressions for the displacements satisfying equations (12) are:

$$\left.\begin{aligned} v &= A\left[1 - \cos\left(\frac{2\pi s}{L}\right)\right]\sin \omega t \\ \beta &= B\left[1 - \cos\left(\frac{2\pi s}{L}\right)\right]\sin \omega t \end{aligned}\right\} \tag{13}$$

For this case, the frequency equation is:

$$18\Phi^4 - \Phi^2\left[6k + \frac{3m}{\delta^2}\right] + \left[\frac{km - n^2}{\delta^2}\right] = 0 \tag{14}$$

with:

$$\left.\begin{aligned} k &= \left(2\pi\right)^4 + \frac{(2\pi)^2}{(1+\nu)}\,\frac{2}{L}\int_0^L \left(\frac{L}{R}\right)^2 \sin^2\left(\frac{2\pi s}{L}\right) ds \\ m &= \frac{(2\pi)^2}{(1+\nu)} + \frac{2}{L}\int_0^L \left(\frac{L}{R}\right)^2 \left[1 - \cos\left(\frac{2\pi s}{L}\right)\right]^2 ds \end{aligned}\right\} \tag{15}$$

$$n = \left(2\pi\right)^2 \left\{\frac{2}{L}\int_0^L \left(\frac{L}{R}\right)\cos^2\left(\frac{2\pi s}{L}\right) ds + \frac{1}{(1+\nu)}\,\frac{2}{L}\int_0^L \left(\frac{L}{R}\right)\sin^2\left(\frac{2\pi s}{L}\right) ds\right\}$$

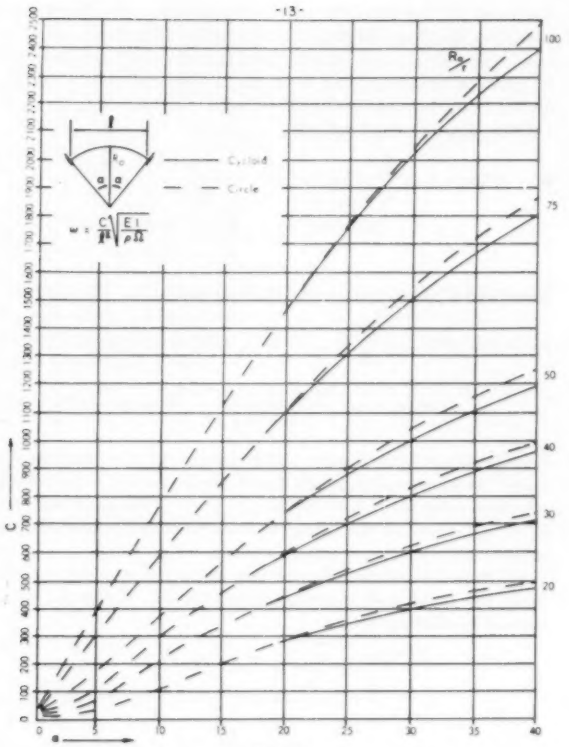

Fig. 6

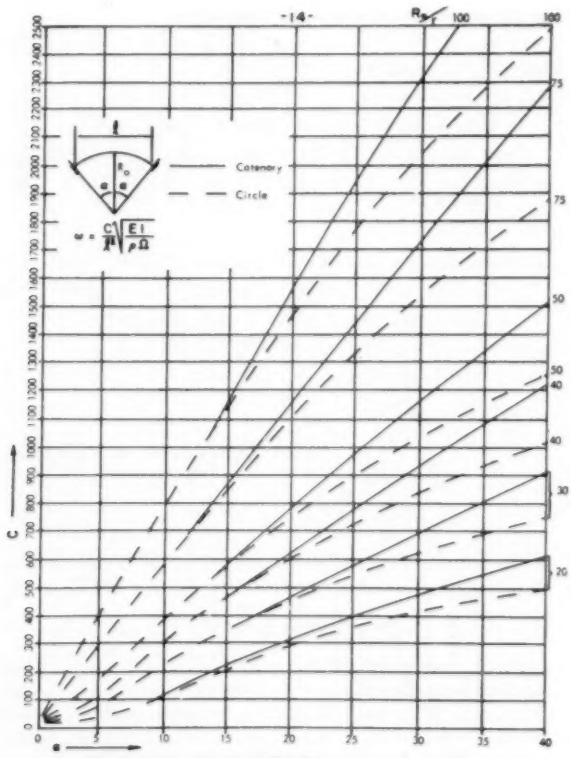

Fig. 7

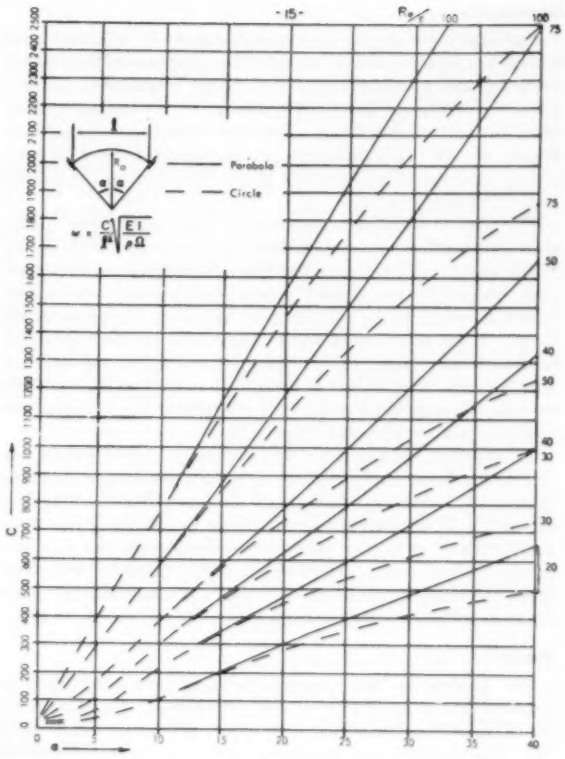

Fig. 8

In the case of the circle, equations (15) reduce to:

$$k = \left(2\pi\right)^4 + \frac{(2\pi)^2}{(1+\nu)}\ 4\alpha^2$$

$$m = 4\alpha^2\left[\left(\frac{\pi}{\alpha}\right)^2 \frac{1}{(1+\nu)} + 3\right] \qquad (16)$$

$$n = \left(2\pi\right)^2\ 2\alpha\ \frac{(2+\nu)}{(1+\nu)}$$

In Table 2 and in Figs. 6, 7, and 8 the values of the lowest root Φ of equation (14) and of the constants C are given for the arcs of the circle, cycloid, catenary, and parabola.

In all the numerical calculations it was assumed for Poisson's ratio the value $\nu = 0.29$.

Acknowledgment

This brief note is written in connection with research sponsored at The University of Texas by the National Science Foundation under Grant No. 4544.

The Bending of an Incomplete Torus of Rectangular Cross Section

H. D. CONWAY[1] and J. R. MOYNIHAN[2]

Introduction

THE elastic bending of an incomplete torus of arbitrary cross section is a problem of very considerable analytical difficulty and, excepting the well-known and elementary solutions of Golovin given in Timoshenko and Goodier's book [1],[3] for the plane strain cases, the only exact solution appears to be that of Sadowsky and Sternberg [2] for the bending by couples of a circular cross-section torus. An exhaustive summary of the literature on the subject is included in the latter.

The present discussion concerns the incomplete torus of constant rectangular cross section bent either by pure couples or by radial forces. Solutions to the three-dimensional problems are first obtained by the Clebsch procedure of seeking solutions for which $\sigma_z = \tau_{zz} = \tau_{\theta z} = 0$, z being normal to the plane of the torus. If the tractions on the terminal faces are distributed according to the results of this theory, the solutions will be exact. If not, appeal must be had to Saint Venant's principle; naturally enough, the rings envisaged have a sufficiently large angle of embrace and are not like split tubes.

An approximate method of solution using a perturbation procedure has been applied to the circular cross-section torus by Göhner [3]. Since the method can also be applied to other cross sections, it is interesting to compare its results with those from the foregoing solutions. This has been done for the case of a square cross section. The results are also compared with those from the engineering theory of Winkler [4], and also the plane strain solutions of Golovin [1].

Analysis

(a) **Loading by Pure Couples:** Consider the axisymmetrical problem of the incomplete ring sector shown in Fig. 1, the terminal faces being subjected to tractions producing pure couples M. The well-known plane strain solution is due to Golovin [1], the stress function being

$$\phi_0 = A \log r + Br^2 \log r + Cr^2 \tag{1}$$

where

$$A = -\frac{4M}{N} r_0^2 r_i^2 \log r_0/r_i, \qquad B = -\frac{2M}{N}(r_0^2 - r_i^2),$$

$$C = \frac{M}{N}[r_0^2 - r_i^2 + 2(r_0^2 \log r_0 - r_i^2 \log r_i)]$$

$$N = [4r_0^2 r_i^2 (\log r_0/r_i)^2 - (r_0^2 - r_i^2)^2]2h$$

However, a plane strain solution requires a stress component σ_z, whereas the side faces of the ring are free from stress. The plane strain solution is therefore modified [5] to free these faces from stress, the new stress function for plane stress being obtained from

$$\phi = \phi_0 + \frac{\nu}{6(1+\nu)}(h^2 - 3z^2)\nabla^2\phi_0 \tag{2}$$

where $2h$ is the thickness. The second term gives stresses additional to those of plane strain which, however, produce no change in the mean values of the stresses across the thickness of the plate. If the tractions on the terminal faces are distributed according to those derived from Equation (2), the solution is exact. If they are not but still produce only a pure couple, the foregoing solution will still hold for sections sufficiently far removed from the ends for Saint Venant's principle to apply.

From Equations (1) and (2)

$$\phi = A \log r + B\left[r^2 \log r + \frac{2\nu(h^2 - 3z^2)(1 + \log r)}{3(1+\nu)}\right] + C\left[r^2 + \frac{2\nu(h^2 - 3z^2)}{3(1+\nu)}\right] \tag{3}$$

The stress of prime importance is the circumferential one, given by

$$\sigma_\theta = \partial^2\phi/\partial r^2 = -\frac{4M}{N}\left(-\frac{r_0^2 r_i^2}{r^2}\log r_0/r_i + r_0^2 \log r/r_0 + r_i^2 \log r_i/r - \nu\frac{[r_0^2 - r_i^2][h^2 - 3z^2]}{3(1+\nu)r^2} + r_0^2 - r_i^2\right) \tag{4}$$

As pointed out by Sadowsky and Sternberg [2], it is important to note that axisymmetrical solutions such as the above have little practical value for $R/a = (r_0 + r_i)/(r_0 - r_i)$ values of less than about 3, because of the appeal to Saint Venant's principle which must be assumed in a practical problem.

We now investigate the problem by the Göhner procedure. Since the problem is axisymmetrical, the two nontrivial equations of equilibrium are

$$\frac{\partial\sigma_r}{\partial r} + \frac{\partial\tau_{rz}}{\partial z} + \frac{\sigma_r - \sigma_\theta}{r} = 0$$

$$\frac{\partial\tau_{rz}}{\partial r} + \frac{\partial\sigma_z}{\partial z} + \frac{\tau_{rz}}{r} = 0 \tag{5}$$

together with the four compatibility equations

$$\nabla^2\sigma_r - \frac{2}{r^2}(\sigma_r - \sigma_\theta) + \frac{1}{1+\nu}\frac{\partial^2\Theta}{\partial r^2} = 0;$$

$$\nabla^2\sigma_z + \frac{1}{1+\nu}\frac{\partial^2\Theta}{\partial z^2} = 0; \quad \nabla^2\sigma_\theta + \frac{2}{r^2}(\sigma_r - \sigma_\theta) + \frac{1}{1+\nu}\frac{1}{r}\frac{\partial\Theta}{\partial r} = 0; \quad \nabla^2\tau_{rz} - \frac{1}{r^2}\tau_{rz} + \frac{1}{1+\nu}\frac{\partial^2\Theta}{\partial r\partial z} = 0 \tag{6}$$

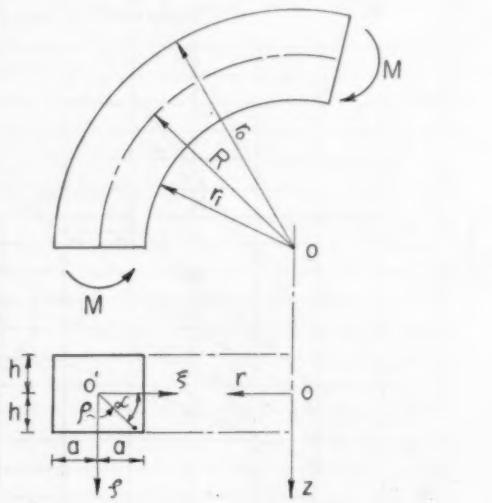

Fig. 1 Incomplete torus subjected to pure bending

[1] Professor of Mechanics, Cornell University, Ithaca, N. Y.
[2] Professor of Materials, Cornell University.
[3] Numbers in brackets indicate References at end of paper.

Manuscript received by ASME Applied Mechanics Division, January 31, 1961.

where $\nabla^2 = \partial^2/\partial r^2 + \partial^2/\partial z^2$ and $\Theta = \sigma_r + \sigma_\theta + \sigma_z$.

Göhner's method [3] of attack on the problem is to first transfer the above equations to the new co-ordinates ξ, ζ by means of

$$\xi = R - r, \quad \zeta = z \tag{7}$$

As a first approximation to the solution of the problem, the stresses may be taken as

$$\begin{aligned} \sigma_\xi = \sigma_\zeta = \tau_{\xi\zeta} = 0 \\ \sigma_\theta = -cE\xi, \quad c = 3M/4a^4E \end{aligned} \tag{8}$$

these being the solution for the case when $R \gg a$.

As a second approximation, ξ/R is considered sufficiently small for products of ξ/R to be neglected and small corrections in the stresses to be treated as small quantities of higher order. Equations (5) then approximate to

$$\begin{aligned} \frac{\partial \sigma_\xi}{\partial \xi} + \frac{\partial \tau_{\xi\zeta}}{\partial \zeta} - \frac{cE\xi}{R} = 0 \\ \frac{\partial \tau_{\xi\zeta}}{\partial \xi} + \frac{\partial \sigma_\zeta}{\partial \zeta} = 0 \end{aligned} \tag{9}$$

together with the compatibility equations

$$(1+\nu)\Delta\sigma_\xi + \frac{\partial^2\Theta}{\partial\xi^2} = 0; \quad R(1+\nu)\Delta\sigma_\theta + (2+\nu)cE = 0$$

$$(1+\nu)\Delta\sigma_\zeta + \frac{\partial^2\Theta}{\partial\zeta^2} = 0; \quad (1+\nu)\Delta\tau_{\xi\zeta} + \frac{\partial^2\Theta}{\partial\xi\partial\zeta} = 0 \tag{10}$$

where $\Delta^2 = \partial^2/\partial\xi^2 + \partial^2/\partial\zeta^2$ and $\Theta = \sigma_\xi + \sigma_\zeta + \sigma_\theta$.

A stress function ϕ is now introduced so that the stress components satisfy the equilibrium equations (9) and, for the rectangular cross section,

$$\sigma_\xi = \frac{cE}{2R}(\xi^2 - a^2) + \frac{cE}{R}\frac{\partial^2\phi}{\partial\zeta^2},$$

$$\sigma_\zeta = \frac{cE}{R}\frac{\partial^2\phi}{\partial\xi^2}, \quad \tau_{\xi\zeta} = -\frac{cE}{R}\frac{\partial^2\phi}{\partial\xi\partial\zeta} \tag{11}$$

Substituting in Equations (10), it is found for this case that

$$\Delta\Delta\phi = -\frac{\nu}{1+\nu} \tag{12}$$

This differs from the circular cross-section solution, where the stresses are

$$\begin{aligned} \sigma_\xi = \frac{cE}{2R}(\xi^2 + \zeta^2 - a^2) + \frac{cE}{R}\frac{\partial^2\phi}{\partial\zeta^2}, \\ \sigma_\zeta = \frac{cE}{R}\frac{\partial^2\phi}{\partial\xi^2}, \quad \sigma_{\xi\zeta} = -\frac{cE}{R}\frac{\partial^2\phi}{\partial\xi\partial\zeta} \end{aligned} \tag{13}$$

and where, from the compatibility equations

$$\Delta\Delta\phi = -\frac{1+2\nu}{1+\nu} \tag{14}$$

The boundary conditions in the present square section case are the same as those for the circle, namely

$$\phi = d\phi/dn = 0 \tag{15}$$

where n denotes a direction normal to the boundary. Thus the problem of finding ϕ is identical with that of finding the deflected form of a uniformly loaded and clamped plate. In the circular case treated by Göhner [3], the exact solution of the auxiliary plate problem is elementary, but in the case of the square it is unknown. However, an excellent approximate solution has recently been given by the author [6] by the method of point-matching, and it will be shown that this is very satisfactory to use here.

The afore-mentioned solution satisfies the differential equation exactly and the boundary conditions very closely. It is

$$\phi = \frac{-\nu}{64(1+\nu)}\left[\rho^4 + Aa^4 + Ba^2\rho^2 + \left(C\rho^4 + \frac{D\rho^8}{a^4}\right)\cos 4\alpha + \left(E\frac{\rho^8}{a^4} + F\frac{\rho^{10}}{a^6}\right)\cos 8\alpha\right] \tag{16}$$

where A, B, C, D, E, and F are constants, not all of which will be required for the present solution. Those required will be given later. Equation (16) is easily transformed into a function of ξ and ζ by means of

$$\rho^2 = \xi^2 + \zeta^2, \quad \cos\alpha = \xi/\rho \tag{17}$$

From (11) and the compatibility equations (10), it may be shown that

$$\begin{aligned} \frac{R}{cE}\frac{\partial^2\sigma_\theta}{\partial\xi^2} = -\nu\frac{\partial^2}{\partial\zeta^2}(\Delta\phi) - \frac{2+2\nu+\nu^2}{1+\nu} \\ \frac{R}{cE}\frac{\partial^2\sigma_\theta}{\partial\zeta^2} = -\nu\frac{\partial^2}{\partial\xi^2}(\Delta\phi) + \frac{\nu}{1+\nu} \\ \frac{R}{cE}\frac{\partial^2\sigma_\theta}{\partial\xi\partial\zeta} = \nu\frac{\partial^2}{\partial\xi\partial\zeta}(\Delta\phi) \end{aligned} \tag{18}$$

From the last of these equations, we write

$$\frac{R}{\nu cE}\sigma_\theta = \Delta\phi + C_0 + C_1\xi + C_2\xi^2 + C_3\xi^3 + \ldots + C_2{}^1\zeta^2 + C_4{}^1\zeta^4 + \ldots \tag{19}$$

only even powers of ζ being retained because of symmetry and, by substitution in the other two compatibility equations, it follows that

$$\begin{aligned} C_2 = -\frac{1}{\nu}, \quad C_3 = C_4 = \ldots 0, \\ C_2{}^1 = \frac{1}{2}, \quad C_4{}^1 = C_6{}^1 = \ldots = 0 \end{aligned} \tag{20}$$

and hence

$$\frac{R}{\nu cE}\sigma_\theta = \Delta\phi + C_0 + C_1\xi - \frac{\xi^2}{\nu} + \frac{\zeta^2}{2} \tag{21}$$

From the stress function given in Equation (16), it is seen that the terms involving A, C, and E are harmonic and, hence, from Equation (21), σ_θ is independent of these.

It follows from Equation (21) that

$$\frac{R}{\nu cE}\sigma_\theta = \frac{-\nu}{64(1+\nu)}\left[16(\xi^2+\zeta^2) + 4Ba^2 + 20\frac{D}{a^2}(\xi^4 - 6\xi^2\zeta^2 + \zeta^4) + 36\frac{F}{a^6}(\xi^8 - 28\xi^6\zeta^2 + 70\xi^4\zeta^4 - 28\xi^2\zeta^6 + \zeta^8)\right] + C_0 + C_1\xi - \xi^2/\nu + \zeta^2/2 \tag{22}$$

The values of C_0 and C_1 are found from the equations

$$\int_{-a}^{a}\int_{-a}^{a}\sigma_\theta d\xi d\zeta = 0; \quad \int_{-a}^{a}\int_{-a}^{a}\sigma_\theta \xi d\xi d\zeta = -M \tag{23}$$

and finally

$$\sigma_\theta = \frac{M}{8a^4R}(2a^2 + \nu a^2 - 6R\xi - 6\xi^2 + 3\nu\zeta^2)$$
$$- \frac{\nu^2 M}{1280(1+\nu)a^4R}\left[240(\xi^2 + \zeta^2) + 300\frac{D}{a^2}(\xi^4 - 6\xi^2\zeta^2 + \zeta^4)\right.$$
$$+ 540\frac{F}{a^4}(\xi^6 - 28\xi^4\zeta^2 + 70\xi^2\zeta^4 - 28\xi^2\zeta^6 + \zeta^8)$$
$$\left. - 160a^2 + 80Da^2 - 192Fa^2\right] \quad (24)$$

where, from the solution for a uniformly loaded and clamped square plate (6), $D = 0.307846$, $F = 0.002069$.

Finally, we record the approximate curved beam formula due to Winkler [4] which gives, for the square cross section

$$\sigma_\theta = \frac{M(r - r_n)}{4a^2r(5a - r_n)} \quad (25)$$

where $r_n = 2a/\log_e 1.5 = 4.9326a$ is the radius of the neutral surface. The stresses may now be obtained according to the plane stress theory and from the plane strain, Göhner, and Winkler theories. They are compared in Table 1 for the case of a square cross section of side $2a$ and for $R/a = 5$.

Table 1 Pure bending, square cross section $R/a = 5$

Coefficients K in the circumferential stress equation $\sigma_\theta = KM/a^2$

Point	Plane stress[a]	Plane strain	Göhner[a]	Winkler
$\xi = a, \zeta = 0$	−0.876	−0.867	−0.861	−0.865
$\xi = a, \zeta = a$	−0.848	−0.867	−0.836	−0.865
$\xi = -a, \zeta = 0$	0.658	0.662	0.639	0.660
$\xi = -a, \zeta = a$	0.670	0.662	0.664	0.660

[a] Poisson's ratio = 0.3.

From Table 1 it is seen that the plane strain and Winkler theories agree very well with one another, and although they do not indicate a variation of stress through the thickness as the Göhner theory does, they give the best over-all approximations to the circumferential stresses. Sadowsky and Sternberg [2] also found that the Winkler theory gave excellent results from the case of a circular cross-section torus; the plane strain solution does not, of course, apply to this case. The Winkler theory is very simple to apply, and is applicable to rings of arbitrary cross section. Thus it appears to be superior to the Göhner perturbation procedure as regards accuracy, simplicity, and generality.

(b) Loading by Radial Forces. Considering the case of an incomplete torus bent by radial forces P as shown in Fig. 2, the well-known plane strain solution is also due to Golovin [1], the stress function being

$$\phi_0 = (Ar^3 + B/r + Dr\log r)\sin\theta$$

Where $A = P/2N$, $B = -Pr_0^2r_i^2/2N$, $D = -P(r_0^2 + r_i^2)/N$, and $N = [(r_0^2 + r_i^2)\log r_0/r_i + r_i^2 - r_0^2]2h$. The corresponding plane stress solution obtained from Equation (2) is then

$$\phi = \left\{A\left[r^3 + \frac{4\nu r(h^2 - 3z^2)}{3(1+\nu)}\right] + \frac{B}{r}\right.$$
$$\left. + D\left[r\log r + \frac{\nu(h^2 - 3z^2)}{3r(1+\nu)}\right]\right\}\sin\theta \quad (26)$$

and the circumferential stress follows

$$\sigma_\theta = \frac{P}{N}\left[3r - \frac{r_0^2r_i^2}{r^3} - \frac{r_0^2 + r_i^2}{r}\right.$$
$$\left. - \frac{2\nu(h^2 - 3z^2)(r_0^2 + r_i^2)}{3r^3(1+\nu)}\right]\sin\theta \quad (27)$$

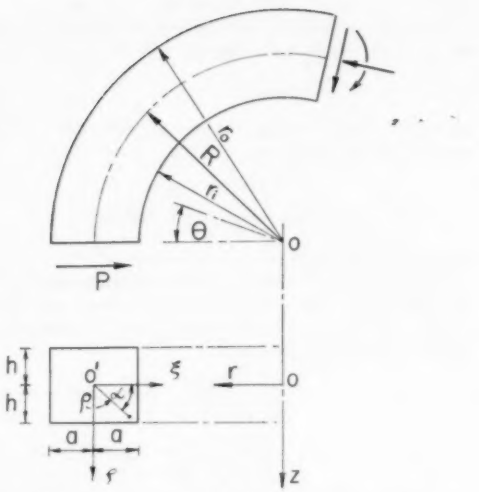

Fig. 2 Incomplete torus subjected to radical concentrated force

The Göhner perturbation procedure may be adapted to the present case of bending by radial forces as follows. The approximate equilibrium equations for this case are

$$\frac{\partial\sigma_\xi}{\partial\xi} + \frac{\partial\tau_{\xi\zeta}}{\partial\zeta} - \frac{cE\xi}{R} = 0$$
$$\frac{\partial\tau_{\xi\zeta}}{\partial\xi} + \frac{\partial\sigma_\zeta}{\partial\zeta} = 0$$
$$\frac{\partial\tau_{\theta\xi}}{\partial\xi} + \frac{\partial\tau_{\theta\zeta}}{\partial\zeta} - \frac{cE\xi}{R} = 0 \quad (28)$$

whereas the corresponding compatibility equations are

$$(1+\nu)\Delta\sigma_\xi + \frac{\partial^2\Theta}{\partial\xi^2} = 0;\ (1+\nu)\Delta\sigma_\zeta + \frac{\partial^2\Theta}{\partial\zeta^2} = 0$$
$$R(1+\nu)\Delta\sigma_\theta + (2+\nu)cE = 0;\ (1+\nu)\tau_{\xi\zeta} + \frac{\partial^2\Theta}{\partial\xi\partial\zeta} = 0$$
$$R(1+\nu)\Delta\tau_{\theta\xi} = cE;\ \Delta\tau_{\theta\zeta} = 0 \quad (29)$$

It will be noticed that the first two of Equations (28) are the same as Equations (9) for the bending by couples, and the first four of Equations (29) are the same as Equations (10). The stress σ_θ is not involved in the remainder of Equations (28) and (29). It follows that the expression for σ_θ given in Equation (22) will also hold for the present case of loading by radial forces P, with the exception that C_0 and C_1 must now be found from the equations

$$\int_{-a}^{a}\int_{-a}^{a}\sigma_\theta d\xi d\zeta = -P\sin\theta,$$
$$\int_{-a}^{a}\int_{-a}^{a}\sigma_\theta\xi d\xi d\zeta = -PR\sin\theta \quad (30)$$

In Equation (22), it will be noted that it is only the term $C_1\xi$ which produces a moment. The expression for σ_θ in the present case can then be found immediately from Equation (24) by adding a constant direct stress of magnitude $-P\sin\theta/4a^2$ and writing $M = PR\sin\theta$.

This then gives

$$\sigma_\theta = \frac{P\sin\theta}{8a^4}(3\nu\zeta^2 - \nu a^2 - 6R\xi - 6\xi^2) - \nu^2\frac{P\sin\theta}{1280(1+\nu)a^4}\times$$

$$\left[240(\xi^2+\zeta^2)+300\frac{D}{a^2}(\xi^4-6\xi^2\zeta^2+\zeta^4)\right.$$
$$+540\frac{F}{a^4}(\xi^6-28\xi^4\zeta^2+70\xi^4\zeta^4$$
$$\left.-28\xi^2\zeta^6+\zeta^8)-160a^2+80Da^2-192Fa^2\right] \quad (31)$$

where again $D = 0.307846$ and $F = 0.002069$.

Numerical results for this case obtained by the various theories may now be computed. They are compared in Table 2 for the square cross-section case and for $R/a = 5$.

Table 2 Bending by radial forces, square cross-section, $R/a = 5$

Coefficients K in the circumferential stress equation $\sigma_\theta = KP/a^2$

Point	Plane stress[a]	Plane strain	Göhner[3]	Winkler
$\xi = a, \zeta = 0$	−4.669	−4.612	−4.557	−4.577
$\xi = a, \zeta = a$	−4.497	−4.612	−4.429	−4.577
$\xi = -a, \zeta = 0$	3.057	3.075	2.943	3.051
$\xi = -a, \zeta = a$	3.109	3.075	3.071	3.051

[a] Poission's ratio = 0.3.

It is seen that the plane strain solution gives the best approximation to the greatest stress although it does not, of course, indicate the variation of stress through the thickness. However, the Winkler solution is excellent and, because of its simplicity and scope, is recommended over all others.

Experiment

In order to check the foregoing analysis, a split steel ring was subjected to vertical radial loading in a lever testing machine. The ring was of 3.50 in. internal diameter, 5.25 in. external diameter, and 0.875 in. thick. Thus $R/a = (r_0 + r_i)/(r_0 - r_i) = 5$ and the cross section is square as in the previous numerical calculations.

In order to minimize eccentricity of loading, the loads were applied through 0.75-in-diam steel balls, and the ring was slightly recessed at the loading points to accommodate the balls. The circumferential strains at the inner and outer curved surfaces were measured using $^1/_8$-in. gage-length electrical strain gages attached at one end of a horizontal diameter and remote from the gap. Three gages were attached circumferentially at each surface, one on the center line in each case and the two others as near the edges as possible. Since the stresses are uniaxial, these were obtained directly from the strains by multiplying by the modulus of elasticity. A tension test on a specimen of the steel showed this to be 30,000,000 psi.

As a result of the tests, the average circumferential stress through the thickness at the inner surface was found to be given by $4.70\ P/a^2$, and at the outer by $3.10\ P/a^2$. These compare with the factors given in Table 2. The slight eccentricity of loading and the inability to locate gages exactly at the edges because of their finite width, all tended to mask the variations of circumferential stress through the thickness. However, the features of the exact solution were noted but to a smaller extent.

References

1 S. Timoshenko and J. N. Goodier, "Theory of Elasticity," McGraw-Hill Book Company, Inc., New York, N. Y., 1951, pp. 61 and 73.

2 M. A. Sadowsky and E. Sternberg, "Pure Bending of an Incomplete Torus," JOURNAL OF APPLIED MECHANICS, vol. 20, TRANS. ASME, vol. 75, 1953, p. 215.

3 O. Göhner, "Spannungsverteilung in Einem an den Endquerschnitten belasteten Ringstabsektor," *Ingenieur-Archiv*, vol. 2, 1931, p. 381.

4 E. Winkler, *Zivilingenieur*, vol. 4, 1858, p. 232. See also S. Timoshenko, "Strength of Materials," second edition, part 2, D. van Nostrand Company, Inc., 1941, p. 74.

5 R. V. Southwell, "Theory of Elasticity," second edition, Oxford University Press, 1941, p. 380.

6 H. D. Conway, "The Approximate Analysis of Certain Boundary-Value Problems," JOURNAL OF APPLIED MECHANICS, vol. 27, TRANS. ASME, vol. 83, Series E, 1960, p. 275.

Disk Heated by Internal Source

T. D. RINEY[1]

Introduction

A STUDY of the temperature and stresses produced in semiconductor devices during operation has led to the consideration of the following idealized situation: A thin, thermally insulated disk initially at a uniform temperature is suddenly heated by a source of uniform volume density in a circular area at the center. Expressions for the temperature and the stresses can be determined by standard methods, but they are apparently not in the literature. The results are presented since the series solutions have been evaluated for a range of the parameters and since they may be of interest in other applications. For example, the disk may be the anode of an electron tube being bombarded by a beam of electrons.

Solution of Problem

The temperature distribution $T(r, t)$ at radial distance r and time t is given by the solution to the following boundary-value problem:

$$\frac{1}{r}\frac{\partial}{\partial r}\left(r\frac{\partial T}{\partial r}\right)+\frac{q}{k}=\frac{1}{\kappa}\frac{\partial T}{\partial t}$$
$$T(r,0)=0 \qquad \frac{\partial T(b,t)}{\partial t}=0, \quad (1)$$

where $q = q_0$ for $0 \leq r < a$ and $q = 0$ for $a < r \leq b$. Here k is the thermal conductivity and κ the thermal diffusivity.

This problem is most easily solved by utilizing the finite Hankel transform defined by [1][2]

$$\bar{f}(p)=\int_0^b rJ_0(pr)f(r)dr, \quad (2)$$

where p is a non-negative root of $J_1(pb) = 0$. The inverse transform of (2) is

$$f(r)=\sum_p A_p J_0(pr), \quad (3)$$

where

$$A_p=\frac{2}{b^2}\int_0^b rf(r)dr \qquad A_p=\frac{2}{b^2}\frac{\bar{f}(p)}{[J_0(pb)]^2}$$
$$(p=0) \qquad (p>0) \quad (4)$$

Application of (2) reduces (1) to

$$\frac{d\bar{T}}{dt}+\kappa p^2\bar{T}=\frac{\kappa}{k}\bar{q} \qquad \bar{T}]_{t=0}=0,$$

[1] General Electric Company, Space Sciences Laboratory, Philadelphia, Pa.

[2] Numbers in brackets indicate References at end of Note.

Manuscript received by ASME Applied Mechanics Division, May 3, 1931.

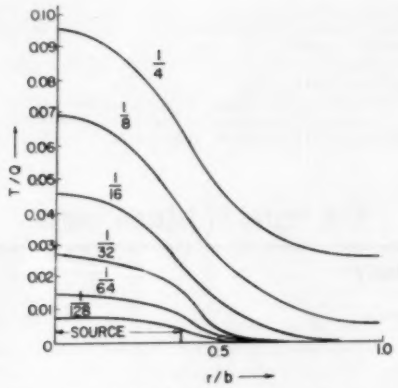

Fig. 1 Temperature distributions for the indicated values of the time parameter $\tau = t/b^2$. The source is of radius $r/b = 0.4$.

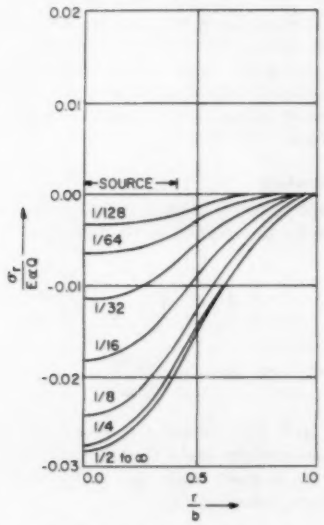

Fig. 2 Radial stress distributions for the indicated values of time parameter $\tau = t/b^2$

whence

$$\bar{T} = \frac{aq_0}{kp^2} J_1(ap)[1 - \exp(-\kappa p^2 t)].$$

The inversion may now be carried out by (3) and (4) to yield the temperature solution

$$\frac{T}{Q} = (a/b)^2\tau + 2(a/b) \sum_{\lambda} J_0(\lambda r/b) F_\lambda(\tau), \tag{5}$$

where the summation extends over all the positive roots of $J_1(\lambda) = 0$ and

$$Q = q_0 b^2/k \qquad \tau = \kappa t/b^2$$
$$F_\lambda(\tau) = \frac{J_1(\lambda a/b)}{\lambda^2 [J_0(\lambda)]^2} [1 - \exp(-\tau\lambda^2)]. \tag{6}$$

If (5) is substituted into the well-known expressions for the axial

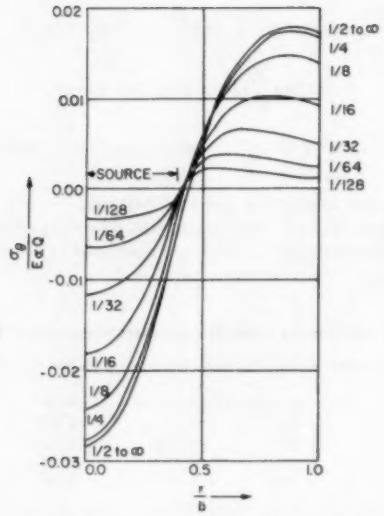

Fig. 3 Circumferential stress distribution for the indicated values of the time parameter $\tau = t/b^2$

symmetric stresses in a thin plate [2] and the required integrations carried out, the results are

$$\sigma_r = -2(a/b) \sum_{\lambda} \frac{J_1(\lambda r/b)}{\lambda r/b} F_\lambda(\tau),$$
$$\sigma_\theta = 2(a/b) \sum_{\lambda} \left[\frac{J_1(\lambda r/b)}{\lambda r/b} - J_0(\lambda r/b)\right] F(\tau). \tag{7}$$

Discussion

The formulas for the temperature and the thermal stress have been evaluated for the special case that $a/b = 0.4$. The temperature radial distribution for various values of the time parameter τ are shown in Fig. 1. The corresponding values of the radial and hoop thermal stresses are shown in Fig. 2 and Fig. 3, respectively. The radial stress is always compressive and at any instant decreases from a maximum value at the center to zero at the edge of the disk. The circumferential stress also has its maximum compressive value at the center but changes to tension in the vicinity of the hot spot perimeter. The location of the crossover point moves slightly outward with increasing time as does the location of the maximum tensile stress.

It is of interest to note that each of the stresses tends to an asymptotic distribution as time tends to infinity. In fact, the limiting distribution in each case is already closely approximated when $\tau = 1/4$. On the other hand, we see from Fig. 1 that at $\tau \leq 1/16$ the temperature at the edge of the disk has barely started to change and is still relatively low even for $\tau = 1/4$. Although the solution always breaks down eventually, as there is no method for the heat to escape, these considerations show that the maximum stresses may be attained for small values of τ.

References

1 C. J. Tranter, "Integral Transforms in Mathematical Physics," second edition, John Wiley & Sons, Inc., New York, 1956, p. 88.

2 S. Timoshenko and J. N. Goodier, "Theory of Elasticity," second edition, McGraw-Hill Book Company, Inc., New York, 1951, p. 418.

The Integration of Some Expressions Arising in Beam Theory

A. ORMEROD[1]

Introduction

EXPRESSIONS containing "Macaulay terms" to represent discontinuities are widely used in engineer's beam theory [1].[2] The Macaulay term is enclosed in distinctive brackets which have the significance of a Heaviside unit function [2].

Re-actions and deflections in beams and more complex structures can often be found by integrating the product of two expressions, each of which may contain one or more discontinuities [3]. The use of Macaulay's device in this situation, coupled with an appropriate method of integration, leads to economy of labor.

Method of Integration

The integration of a product is performed by parts in a particular way. For example,

where

$$\int_0^l \{x-a\}\{x-c\}\,dx \text{ is required and } a > c,$$

if the integration is performed so that each part of the integral contains terms in $(x-a)$, then the original limits are retained throughout.

Thus

$$\int_0^l \{x-a\}\{x-c\}\,dx = \left[\frac{1}{2}\{x-c\}\{x-a\}^2 - 1/6\{x-a\}^3\right]_0^l$$

and

$$\int_0^l x\{x-a\}\,dx = \left[\frac{1}{2}x\{x-a\}^2 - 1/6\{x-a\}^3\right]_0^l$$

The method is applied to two simple examples chosen purely for the purpose of brief illustration; each of the examples would of course normally be worked by other methods.

[1] Royal Military College of Sciences, Shrivenham, Swindon, Wilts., England.

[2] Numbers in brackets indicate References at end of Note.

Manuscript received by ASME Applied Mechanics Division, May 5, 1961.

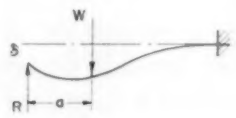

Fig. 1

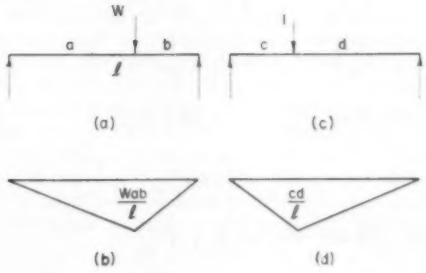

Fig. 2

First Example

The re-action R induced at the end of the propped cantilever of uniform section shown in Fig. 1 may be obtained from the relation,

$$EI\delta = \int_0^l M\,\frac{\partial M}{\partial R}\,dx$$

As $M = -Rx + \{W(x-a)\}$ and $\dfrac{\partial M}{\partial R} = -x$,

$$EI\delta = \int_0^l x[Rx - \{W(x-a)\}]dx$$

$$= \int_0^l [Rx^2 - Wx\{(x-a)\}]dx$$

$$= \left[\frac{1}{3}Rx^3 - \frac{1}{2}Wx\{(x-a)^2\} + 1/6W\{(x-a)^3\}\right]_0^l$$

$$= \frac{1}{3}Rl^3 - \frac{1}{2}Wl(l-a)^2 + 1/6W(l-a)^3$$

and from this equation R is evaluated.

Second Example

The deflection y at a distance c from the left-hand end of the uniform beam shown in Fig. 2 is given by the expression:

$$EIy = \int_0^l M \cdot M_c\,dx,$$

where

$$M = -Wxb/l + W\{x-a\},$$

and

$$M_c = -xd/l + \{x-c\},$$

Thus

$$EIy = W\int_0^l [xb/l - \{x-a\}][xd/l - \{x-c\}]dx,$$

$$= W\int_0^l [x^2bd/l^2 - xb/l\{x-c\} - xd/l\{x-a\} + \{x-a\}\{x-c\}]dx$$

$$= W\left[\frac{1}{3}x^3bd/l^2 - xb/2l\{(x-c)^2\} + b/6l\{(x-c)^3\} - dx/2l\{(x-a)^2\} + d/6l\{(x-a)^3\} + \frac{1}{2}\{x-c\}\{(x-a)^2\} - 1/6\{(x-a)^3\}\right]_0^l$$

$$= 1/6W[2bdl - 3b(l-c)^2 + (l-c)^3b/l - 3d(l-a)^2 + (l-a)^3d/l + 3(l-c)(l-a)^2 - (l-a)]^3,$$

which reduces to

$$EIy = 1/6W\,bc/l(l^2 - b^2 - c^2).$$

References

1 R. Macaulay, *Messenger of Mathematics*, vol. 48, 1919.
2 C. L. Brown, *Quarterly of Applied Mathematics*, vol. 1, 1944, p. 349.
3 Matheson, J. A. L., *Hyperstatic Structures*, vol. 1, 1959, p. 170.

Stresses and Deflections in an Elastically Restrained Circular Plate Under Hydrostatic Normal Pressure Over a Segment[1]

MAHER NASSIF.[2] The authors, "after a considerable amount of algebraic manipulation and reduction," tried to put the results in the simplest possible form. However, a simplification can be effected if we note that the terms involving the negative powers of t in $\phi(z, \gamma)$ and $\psi(z, \gamma)$ [equations (27) and (30) of the paper] are the singular parts of the terms involving

$$\log \lambda \frac{1 - te^{-i\gamma}}{1 - te^{i\gamma}}$$

Thus the combination of these terms yields the regular parts of the terms involving

$$\log \frac{1 - te^{-i\gamma}}{1 - te^{i\gamma}}$$

With this consideration $\phi_1(z, \gamma)$ of equation (27a), for example, can be written

$$\phi_1(z, \gamma) = -kc^4\Bigg[tU(t, \gamma) + \gamma\left(\frac{t^4}{48} - \frac{\cos^2\gamma}{2}t^2 + \frac{2\cos^3\gamma}{3}t - \frac{\cos^4\gamma}{2}\right) + \frac{\sin\gamma}{48}t^3 + \frac{1}{12}\left(\gamma + \frac{1}{8}\sin 2\gamma\right)t^2 - \frac{1}{24}\left(\sin\gamma - \frac{5}{2}\sin 3\gamma\right)t - \frac{1}{16}\left(\gamma + 2\sin 2\gamma + \frac{1}{2}\sin 4\gamma\right) + \text{Reg}\left\{-\frac{i}{96}(t - 2\cos\gamma + t^{-1})^3 (t + 6\cos\gamma + t^{-1})\log\frac{1 - te^{-i\gamma}}{1 - te^{i\gamma}}\right\}\Bigg],$$

where Reg means the regular part of. This notation can be adopted whenever it is of any use.

An interesting point suggests itself in connection with the paper. This is the problem of a plane vertical base of a cylindrical tank of horizontal axis and which is partially filled with two immiscible liquids. Referring to Fig. 2 of the paper, the plate in this case is divided into three regions, where region I bounded by the chord AA' is free, region 2 bounded by the chords AA', EE', and region 3 bounded by the chord EE' are laterally loaded with respective load intensity px and $p'x$, $P < P'$.

Let the complex potential functions be

$$\Phi_i(z) \text{ and } \Psi_i(z)[i = 1, 2, 3],$$

and put

$$K = \frac{p}{16\pi D}, \quad K' = \frac{p'}{16\pi D}, \quad \gamma = X\hat{O}A, \quad \gamma' = X\hat{O}E,$$
$$f = OB = c\cos\gamma, \quad f' = c\cos\gamma'$$

The particular integrals may be taken as

$$W_1 = 0, \quad W_2 = \frac{\pi}{24}Kz^2\bar{z}^2(z + \bar{z}),$$
$$W_3 = \frac{\pi}{24}K'z^2\bar{z}^2(z + \bar{z}) \tag{1}$$

The continuity conditions across AA' are given by

$$[\Phi(z)]_2^3 = \pi K\left(\frac{1}{48}z^4 - \frac{1}{2}f^2z^2 + \frac{2}{3}f^3z - \frac{1}{2}f^4\right)$$
$$[\Psi(z)]_2^3 = \pi K\left(\frac{1}{240}z^5 - \frac{1}{6}f^2z^3 + \frac{2}{3}f^3z^2 - \frac{1}{2}f^4z + \frac{4}{15}f^5\right) \tag{2}$$

as given in equations (23). The same conditions across EE' will be

$$[\Phi(z)]_2^3 = \pi(K' - K)\left(\frac{1}{48}z^4 - \frac{1}{2}f'^2z^2 + \frac{2}{3}f'^3z - \frac{1}{2}f'^4\right)$$
$$[\Psi(z)]_2^3 = \pi(K' - K)\left(\frac{1}{240}z^5 - \frac{1}{6}f'^2z^3 + \frac{2}{3}f'^3z^2 - \frac{1}{2}f'^4z + \frac{4}{15}f'^5\right) \tag{3}$$

The functions $\Phi_1(z)$, $\Psi_1(z)$ will be obtained by the principle of superposition. Thus if $\phi_1(z, p, \gamma)$, $\psi_1(z, p, \gamma)$ be the complex potential functions corresponding to hydrostatic pressure of intensity px over the segment of angle 2γ and $\phi_1(z, p' - p, \gamma')$, $\psi_1(z, p' - p, \gamma')$ be those corresponding to hydrostatic pressure of intensity $(p' - p)x$ over the segment of angle $2\gamma'$, then

$$\Phi_1(z) = \phi_1(z, p, \gamma) + \phi_1(z, p' - p, \gamma')$$

and

$$\Psi_1(z) = \psi_1(z, p, \gamma) + \psi_1(z, p' - p, \gamma')$$

Applying equations (27) of the paper we obtain

$$\Phi_1(z) = -Kc^4\Bigg[tU(t, \gamma) + \gamma\left(\frac{1}{48}t^4 - \frac{\cos^2\gamma}{2}t^2 + \frac{2\cos^3\gamma}{3}t - \cos^4\gamma\right) + \frac{\sin\gamma}{48}t^3 + \frac{1}{12}\left(\gamma + \frac{\sin 2\gamma}{8}\right)t^2 - \frac{1}{24}\left(\sin\gamma - \frac{5}{2}\sin 3\gamma\right)t - \frac{1}{16}\left(\gamma + 2\sin 2\lambda + \frac{1}{2}\sin 4\gamma\right) + \text{Reg}\left\{\frac{-i}{96}(t - 2\cos\gamma + t^{-1})^3 (t + 6\cos\gamma + t^{-1})\log\frac{1 - te^{-i\gamma}}{1 - te^{i\gamma}}\right\}\Bigg] - (K' - K)c^4\Bigg[tU(t, \gamma') + \gamma'\left(\frac{t^4}{48} - \frac{\cos^2\gamma'}{2}t^2 + \frac{2\cos^3\gamma'}{2}t - \cos^4\gamma'\right) + \frac{\sin\gamma'}{48}t^3 + \frac{1}{12}\left(\gamma' + \frac{1}{8}\sin 2\gamma'\right)t^2$$

---

[1] By W. A. Bassali and N. O. M. Hanna, published in the March, 1961, issue of the JOURNAL OF APPLIED MECHANICS, vol. 28, TRANS. ASME, vol. 83, Series E, pp. 91–102.

[2] Head of Mathematics Department, Assiut University, Assiut, Egypt, UAR.

$$- \frac{1}{24}\left(\sin\gamma' - \frac{5}{2}\sin 3\gamma'\right)t - \frac{1}{16}\left(\gamma' + 2\sin 2\gamma' + \frac{1}{2}\sin 4\gamma'\right) + \mathrm{Reg}\left\{\frac{-i}{96}(t - 2\cos\gamma' + t^{-1})^2 (t + 6\cos\gamma' + t^{-1})\log\frac{1 - te^{-i\gamma'}}{1 - te^{i\gamma'}}\right\}\Bigg],$$

and

$$\Psi_1(z) = Kc^3\Bigg[U(t,\gamma) - \gamma\left(\frac{t^6}{240} - \frac{\cos^2\gamma}{6}t^3 + \frac{2\cos^3\gamma}{3}t^3 - \frac{\cos^4\gamma}{2}t + \frac{4}{15}\cos^5\gamma\right) - \frac{\sin\gamma}{240}t^4 - \frac{\sin 2\gamma}{480}t^3 + \frac{1}{24}\left(\sin\gamma + \frac{29}{30}\sin 3\gamma\right)t^2 - \frac{1}{48}\left(\gamma - \frac{7}{10}\sin 4\gamma\right)t - \frac{\sin\gamma}{24} + \frac{5\sin 3\gamma}{48} + \mathrm{Reg}\left\{\frac{i}{480}(t - 2\cos\gamma + t^{-1})^2 [(t - 4t^{-1})(t + 6\cos\gamma + t^{-1}) - 16\cos^2\gamma]\log\frac{1 - te^{-i\gamma}}{1 - te^{i\gamma}}\right\}\Bigg]$$

$$+ (K' - K)c^3\Bigg[U(t,\gamma') - \gamma'\left(\frac{t^6}{240} - \frac{\cos^2\gamma'}{6}t^3 + \frac{2\cos^3\gamma'}{3}t^2 - \frac{\cos^4\gamma'}{2}t + \frac{4}{15}\cos^5\gamma'\right) - \frac{\sin\gamma'}{240}t^4 - \frac{\sin 2\gamma'}{480}t^3 + \frac{1}{24}\left(\sin\gamma' + \frac{29}{30}\sin 3\gamma'\right)t^2 - \frac{1}{48}\left(\gamma' - \frac{7}{10}\sin 4\gamma'\right)t - \frac{\sin\gamma'}{24} + \frac{5\sin 3\gamma'}{48} + \mathrm{Reg}\left\{\frac{i}{480}(t - 2\cos\gamma' + t^{-1})^2 [(t - 4t^{-1})(t + 6\cos\gamma + t^{-1}) - 16\cos^2\gamma']\log\frac{1 - te^{-i\gamma'}}{1 - te^{i\gamma'}}\right\}\Bigg]$$

Applying equations (2) we get $\Phi_2(z)$ and $\Psi_2(z)$ to which, if equations (3) are applied, we obtain $\Phi_3(z)$, $\Psi_3(z)$. The problem can thus be solved completely.

On the Stability of the Linearly Related Modes of Certain Nonlinear Two-Degree-of-Freedom Systems[1]

B. AULD.[2] In one of the references given in the paper, R. M. Rosenberg shows that the equations of motion of this system are analogous to the equations of motion of a mass particle sliding around in a potential well. This picture appears to be quite useful in visualizing some of the phenomena discussed in this paper. In the case of the linear problem it may be shown that the contour lines of the potential surface are ellipses in the x_1 - x_3 plane. It is quite apparent then that, if the particle is placed at a certain point in the potential well and released, the projection of the particle path on the x_1 - x_3 plane will be a straight line only if the particle has been placed initially on the major or minor axes of the elliptical contours, Fig. 1 of this discussion. In the case of the nonlinear problem it may be shown that for small displacements from the potential minimum the contour lines are again elliptical. However, the higher potential contour lines will exhibit kinks resulting from the spring nonlinearities. Because of these kinks the walls of the potential will exhibit topographical features in the form of ridges and canyons.

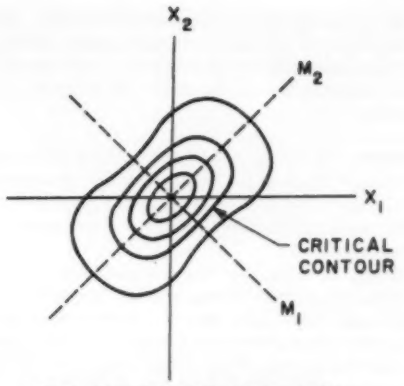

Fig. 1 Potential well for a linear problem

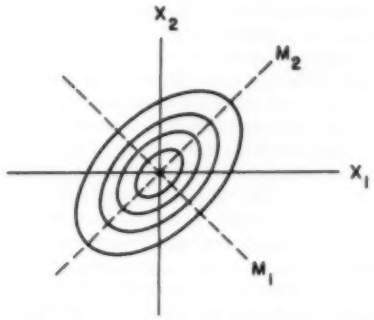

Fig. 2 Typical potential well for a nonlinear problem

In connection with this paper we are chiefly concerned with what might be called "linear" ridges and canyons; that is, cases where the x_1 - x_3 projection of the top of a ridge or the bottom of a canyon is a straight line, Fig 2. In the figure there is a linear canyon along line M_2 and it is clear that a particle placed on the base of the canyon will oscillate back and forth along the canyon. This will be a stable oscillation regardless of the initial potential level of the particle, because the walls of the canyon exert restoring forces on the particle. In the case of line M_1, however, it is seen that the contours change from concave inward at low potentials to concave outward at high potentials. Thus topographical feature is a canyon at low elevations but turns into a ridge at high elevations. If a particle is initially placed on M_1, it will tend to oscillate back and forth along this line. If the initial elevation is below the critical contour at which the curvature of the contours changes sign, the oscillation will be stable because it lies in a canyon. However, if the initial elevation is above the critical contour line, the particle spends part of its period on a ridge and the motion will be unstable.

Depending on the degree of nonlinearity of the problem, there may be more than two linear topographical features in the potential walls. However, it is apparent from Fig. 2 that a necessary condition for the existence of more than two linearly related modes is that the contour lines in the vicinity of the minimum must be circles. This is because a particle can move linearly only

[1] By C. P. Atkinson, published in the March, 1961, issue of the JOURNAL OF APPLIED MECHANICS, vol. 28, TRANS. ASME, vol. 83, Series E, pp. 71–77.

[2] Stanford University, Stanford, Calif.

along the major and minor axes of an ellipsoidal well. The condition for the existence of these circular contours is just that the coupling spring should have no linear term ($A_1 = O$) which was given in the paper as the condition for the occurrence of four modal constants.

T. K. CAUGHEY.[3] The author is to be congratulated on an interesting extension of the work on "natural modes" in nonlinear systems begun by Professor Rosenberg and the author [1].[4]

The writer would like to raise two points in connection with the stability analysis.

(*a*) It should be made clear that the author is discussing the stability of the assumed solutions, and not the system. If the system is a conservative one, then the system must be stable, since there are no external forces and hence no energy input to the system. This means that if the exact solution to the problem were known, it would be stable. On the other hand, if solutions are assumed, these solutions may fail to describe the behavior of the system, even approximately, for certain ranges of initial conditions. When the assumed solutions fail to describe the behavior of the system, analysis of the stability of the system will show the system to be unstable. However, it is the assumed solution which is "unstable" and not the system.

(*b*) If the perturbations (21) of the paper, are inserted into equations (5) there results a pair of coupled equations with periodic coefficients. Equations (22) and (26) are therefore in error, since they are uncoupled. If the coupling terms are neglected, equations (22) and (26) result. It should be noted, that since the perturbation equations are coupled, if the assumed solution proves to be unstable, then both x_1 and x_2 are unstable. In Fig. 5, the author shows x_1 to be unstable for amplitudes in excess of 0.354, but shows x_2 to be stable for all values of amplitude. If x_1 is unstable, however, x_2 must also be unstable. Similar remarks apply to Fig. 6.

On Duffing's Equation[1]

C. H. PAK.[2] The following comments are offered to this interesting Note. Correcting the obvious typographical error (reading *cn* for C_n) and interpreting the quantity θ (which appears nowhere else in the note) as the time t, it may be verified that the author's equation (4) is correct only for the *hardening* spring. For the softening spring, the correct relationship is

$$y(t) = A\, cd\{[(1 - k)(1 - C_2A^2/2)]^{\frac{1}{2}}t\}$$

This may be checked with a solution already in the literature by observing that $cd\ x = sn(x + K)$ and comparing with the case $C_2 = \frac{1}{2}$ given by Sadowsky.[3] This correction will undoubtedly account for the unexpected shape of the dotted curve in the authors' Fig. 4.

Both Harvey's method and Hsu's method, cited by the authors, are of importance in adding to our knowledge of nonlinear forced oscillations. Harvey's method has the virtue of being rather widely applicable, while Hsu's seems to be confined to the Duffing case. However, in this case, Hsu's method may possess a considerable advantage if one is considering essentially *sinusoidal* excitation. Hsu's excitation is of the form $y(t)$, while Harvey's is of the form $y(t) + C_4y^4(t)$. It may easily be verified that distortion (as compared to sinusoidal excitation) is much greater for the latter than for the former.

Authors' Closure

The authors would like to thank Lieutenant Pak for his comments. It is unfortunate that a misunderstanding arose. Perhaps the following remarks will clarify matters.

The quantity θ should replace t in equations (1)–(5) as well as in the derivative which appears in (1). θ is defined as $\omega_n t$ in which ω_n is the circular frequency of free vibrations, when $C_2 = 0$, and t is time. Indeed, equation (4) "is correct only for the hardening spring." This is obvious because a softening spring (i.e., $C_2 < 0$) would yield an imaginary modulus in equation (5). The correct expression used to obtain equation (7), Fig. 2, as well as the "soft system" curve of Fig. 4 is:

$$\left[(1 - k)\left(1 + \frac{C_2A^2}{2}\right)\right]^{1/2}\theta = -K\left(\left[-\frac{C_2A^2}{2 + C_2A^2}\right]^{1/2}\right) + F\left(\left[-\frac{C_2A^2}{2 + C_2A^2}\right]^{1/2}, \psi\right), \quad -1 < C_2A^2 \leq 0$$

This last relationship follows after $y = \sin\psi$ is substituted into equation (3).

The solution to the softening case with the above substitution is:

$$y(\theta) = A\, cd\left\{\left[(1 - k)\left(1 + \frac{C_2A^2}{2}\right)\right]^{1/2}\theta\right\}$$

The difference in the negative sign may be explained if the discusser used the absolute value of C_2A^2, and his equation is correct if θ replaces t.

We should also like to call attention to the fact that, contrary to Lieutenant Pak's comment, Hsu considers excitations both of the form $y(\theta)$ and $y(\theta) + By^3(\theta)$, in which B is an open parameter used to approximate better an actual forcing function.

On the Response of Linear Systems to Time-Dependent, Multidimensional Loadings[1]

D. M. PARKE.[2] The author is to be commended for a clear and incisive discussion of multidimensional power spectral methods. The extensions indicated for these methods are welcome and should provide direction for attempts to measure multidimensional transfer functions. By exploring the possibilities offered, the author has shown the way to extend the methods used in communication engineering to linear mechanical systems subjected to multidimensional loading, thrown light on the role of the gaging system, and indicated some of the limitations on the analysis. For instance, the writer has felt that the application of multidimensional power spectral methods using the influence function has been unnecessarily awkward. By making use of the technique of cross correlating imput and output, the analysis of the response should be more direct. In a real sense, then, this paper provides both the perspective and the heuristic exploration that is needed to stimulate further investigation and application.

---

[3] California Institute of Technology, Pasadena, Calif.

[4] Reference in original paper.

[1] By I. U. Ojalvo and G. L. Bleckman, published in the March, 1961, issue of the JOURNAL OF APPLIED MECHANICS, vol. 28, TRANS. ASME, vol. 83, Series E, pp. 139–140.

[2] Lieut. (jg), Republic of Korea Navy. Student, U. S. Naval Postgraduate School, Monterey, Calif.

[3] M. A. Sadowsky, "Nonlinear Springs," *J. Franklin Institute*, vol. 240, December, 1945, p. 469.

[1] By F. P. Beer, published in the March, 1961, issue of the JOURNAL OF APPLIED MECHANICS, vol. 28, TRANS. ASME, vol. 83, Series E, pp. 50–56.

[2] Mechanical Research Laboratory, E. I. du Pont de Nemours & Company, Inc., Wilmington, Del.

Since the various power spectra and the transfer functions will be statistical estimates, it would be useful (and probably crucial) to know more about the confidence limits on these estimates. There is reason to believe that this information would be difficult to obtain in the multidimensional case. Also, one wonders how completely the extraneous disturbances will be eliminated by cross correlation; and, therefore, how reliable the estimates will actually be in the presence of substantial extraneous loading or pseudo loading. A more tractable question is the effect on the estimates of both the maximum practical length of the records of input and output and the minimum practical spacing of the input-measuring instruments. These are questions which have troubled the writer and, unfortunately, the pressure of other interests has indefinitely postponed his attempting to find their solution for multidimensional loading.

Journal of APPLIED MECHANICS

Book Reviews

Unsteady Gas Dynamics

Unsteady Motion of Continuous Media. By K. P. Stanyukovich. Pergamon Press, New York, N. Y., 1960. Cloth, 6 × 10 in., xiii and 745 pp. $15.

REVIEWED BY F. S. SHERMAN[1]

PROFESSOR Stanyukovich's book, after a few chapters of classical introductory material, reviews the development of unsteady gas dynamics in the Soviet Union, primarily during the 1940's. Stanyukovich's personal contribution to this development has been a massive one, and nearly a third of this 745-page volume gives an account of problems solved by him either individually or in co-operation with other well-known Russian scientists such as Landau and Zel'dovich.

The contents of the book are well indicated by the chapter headings.

I *Mathematical and Thermodynamic Methods of Gas Dynamics.* (An extremely thorough survey of classical equations and theorems, including much on the Lagrangian viewpoint, and an unusual amount on flows in gravity fields.)

II *Investigation of the Fundamental Equations of Nonstationary Gas Dynamics by the Method of Characteristics.* (A discussion of the notion of characteristic surfaces and the various forms into which the differential equations may be cast. Nothing yet on boundary conditions, domain of dependence, etc.)

III *Self-Similar Motion of a Medium.* (Equations are derived under the assumption that two independent variables effectively collapse into one. The treatment in this chapter is quite formal, no attention being paid to the required similarity of boundary conditions, to singular points of the similarity equations, etc.)

IV *Solutions of Equations for One-Dimensional Isentropic Motions of a Medium.* (This chapter introduces the proposal to use $p = A_0(\rho^3 - \rho_0^3)$ as an approximate isentrope for gases. This device, which makes characteristic lines straight even in nonsimple wave regions, is mentioned in almost all gas-dynamics texts, but rarely exploited as thoroughly as in this book.)

V *One-Dimensional Isentropic Motions of a Medium.* (After a review of steady channel flow equations, some wave-interaction problems are solved.)

VI *Elementary Theory of Shock Waves.* (Another comprehensive review chapter. Shocks are treated as discontinuities; results are given for general equations of state and for polytropic gases.)

VII *Theory of Detonation Waves.* (Mostly a review chapter based on the works of Zel'dovich, Mikhel'son, and Grib plus an interesting discussion of the equation of state of condensed detonation products due to Landau and the author.)

VIII *Plane Detonation Waves and Escape of Detonation Products.* (A collection of problems originally solved by author and by A. A. Grib.)

IX *Theory of Propagation of Nonstationary Shock Waves.* (Reflection and transmission of shocks and detonation waves at a boundary between different media. Laws of decay of shock waves driven impulsively by detonation of a finite charge. Solution of the constant-area shock-tube problem.)

X *Three-Dimensional Motion of a Gas.* (Self-similar motions with planar, cylindrical, and spherical symmetry.)

XI *Unsteady Motion in Condensed Media.* (Phenomena accompanying explosions in liquids. Surface waves in open-channel flow. Stress waves in solids.)

XII *Propulsion of Bodies by a Gas Stream.* (Lagrange's ballistic problem.)

XIII *Motion of Gas in a Gravitational Field.* (One-dimensional transient motions in a uniform gravity field. Steady constant-area flows with gravity variable with distance. Some effects of radiant heat transfer. Stellar eruptions are treated without reference to any magnetic effects.)

XIV *Limiting Motion of Rarefied and Very Dense Media.* (A very unusual approach to the theory of rarefied gas motions is given. Motion of a gas in its own gravitational field is discussed. The adequacy of the simple equations employed is not convincingly demonstrated.)

XV *Certain Problems in the Relativistic Mechanics of Continuous Media.* (The energy-momentum tensor is written, with viscous forces, heat conduction, electromagnetic effects neglected. Continuum equations and shock-wave jump relations are derived. The application of these concepts to a discussion of the scattering of nonelementary particles at relativistic speeds was lost on this reviewer.)

A final word should be said about the translating, editing, and printing of the book. I cannot judge the accuracy of the translation, but its style and smoothness are excellent. Both Professor Holt and Mr. Adashko are to be congratulated for a job well done. The reproduction of the book by photolithography is only barely adequate. The very small scale on which the equations appear has occasionally caused vital bits of symbols to disappear altogether, and produces considerable eyestrain even at its best.

[1] Associate Professor, Division of Aeronautical Sciences, University of California, Berkeley, Calif.

Automatic Control

Feedback Control Systems. By J. C. Gille, M. J. Pélegrin, and P. Decaulne. McGraw-Hill Book Company, Inc., New York, N. Y., 1960. Cloth, 6 × 9 in., x and 793 pp. $16.50.

REVIEWED BY L. A. MacCOLL[2]

THIS book is intended to serve as a textbook for seniors and first-year graduate students, and also to serve as a reference book for the engineer working in the automatic control field. It contains a great amount of material, touching on almost every concept or problem that arises in connection with the design and operation of control systems. A collection of problems for the student, an extensive five-language glossary with complementary notes, and an excellent critical bibliography enhance the value of the work. The authors have had considerable experience in teaching the subject at the École Nationale Supérieure de l'Aéronautique in Paris and at Laval University; and in consequence the exposition is almost always clear and effective. As might be expected, the authors manifest some predilection for problems relating to the control of aircraft.

If one criticism of the book is to be made, it is that the treatment of the fundamental theory is left at a rather too elementary level. Thus, for instance, although complex numbers and complex exponentials are used freely, no knowledge of the theory of functions of a complex variable is required of the reader, and no use is made of that theory beyond a few fragments which are developed *ad hoc*. A fuller and freer use of the available mathematical tools could have resulted in a more concise and coherent book. However, the volume as it stands will undoubtedly be of great interest and value to many persons.

Experimentation

Theories of Engineering Experimentation. By Hilbert Schenck, Jr. McGraw-Hill Book Company, Inc., New York, N. Y., 1961. Cloth, 6 × 9 in., x and 239 pp. $7.00.

REVIEWED BY P. D. RICHARDSON[3]

THE design, performance, and interpretation of experiments are treated as something of a poor relation in many undergraduate curricula. This is undeservedly so, both from the pedagogical viewpoint that students should be thoroughly aware of the capabilities of experiments as means of gaining knowledge, and from the practical standpoint that questions are frequently resolved by experiment—indeed, it is quite probable that more money is spent resolving questions by experiment than by analysis. Past and present neglect of the subject has given rise to much poor experimental work, which persists sometimes as far as research literature. It is not to be denied that good experimentation is something of an art, even as is good design; but logic and analysis have an essential role in both. Under these circumstances, some good texts on the subject are particularly needed.

Professor Schenck expresses his belief that exactly what type of equipment is used in teaching laboratories is not as important as a vigorous exposition of the general principles of experimental work. The book reviews (sometimes with considerable clarity) the nature of errors, error propagation, dimensional analysis, Graeco-Latin square planning schemes, the chi-squared and student's t tests, Poisson distribution, least squares, data analysis and checks, including Chauvenet's criterion.

The book neglects to discuss the problem that in many experiments it is impossible to attain the specific state about which the experimenter wishes to inquire, the apparatus or the method altering the phenomena in some way. In such experiments it is common practice deliberately to study the systematic, biasing effect which experimental conditions produce in order to estimate behavior in the absence of the biasing effect. Simple examples which come to mind are the perfect-gas thermometer with which the effects of real-gas density produce a systematic bias, the Cooke and Larke compression test, and the cooled-disk technique of measuring adiabatic laminar flame speeds. This bias study method is of so extensive use in engineering experiments that a thorough description of it should not be omitted from such a book.

The book also contains some imprecise and incorrect statements. For example, it is difficult to understand why the pi-theorem has been misrepresented, when at least two of the references cited give a clear exposition of the essential point which has been confused. In discussing the question of extrapolation, the book argues that "quite obviously, the Lagrange (interpolation) formula will work with equal ease for values that lie outside the test region," a statement that neglects the implications of the Weierstrass theorem (under the protection of which the interpolation formulas are developed), and also ignores the experience that, when such an extrapolation is attempted, any (experimental) errors in the numerical values used are amplified in the result by prohibitively large factors, making such attempts futile. In the discussion of convective heat transfer, the momentum and energy equations are written down in the forms corresponding to the assumptions of steady laminar boundary-layer flow and constant properties. While these assumptions give great simplification in analysis, an experimenter with his wits about him would consider such equations in their general form so that he would not obscure real effects: in this instance, for example, the temperature dependence of viscosity in liquids can be particularly significant.

The reviewer cannot recommend this book for use as a text or as a reference.

Astronautics

Space Flight Technology. Edited by K. W. Gatland. Academic Press, Inc., London, 1960. Cloth, 6½ × 9½ in., xv and 355 pp. $11.

REVIEWED BY S. B. BATDORF[4]

IN AUGUST, 1959, the British Interplanetary Society held a three-day symposium at which representatives from industry, universities, and the government were invited to give their detailed views on the type of work which Britain and her Commonwealth partners might undertake in the field of astronautics. This volume contains the principal papers presented at that meeting.

The contributions may be divided into three main categories. The first category consists of those papers directly related to British astronautical endeavor. These include discussions of reasons for engaging in space flight and of the objectives and costs associated with various types of space programs; a review of applicable facilities (such as the Woomera range and the Jodrell Bank radio telescope); and a listing of organizations that might be expected to participate. Also included is a discussion of the space payload capabilities of a British booster vehicle based on the Black Knight and the Blue Streak. The second category deals with the general propulsion problem in space. Solid-propellant rocket design parameters are reviewed. An account is given of nuclear rocket performance considering uranium

[2] Bell Telephone Laboratories, Inc., New York, N. Y.

[3] Assistant Professor of Engineering, Brown University, Providence, R. I. Assoc. Mem. ASME.

[4] Aeronutronics Division of Ford Motor Company, Newport Beach, Calif.

and plutonium as fuel and hydrogen and ammonia as propellent (in all cases, graphite is the moderator and the propellant temperature is 2000 C). The problem of soft landing instruments on the moon is also treated. The third category deals with other space-flight problems—re-entry heating, recovery of earth satellites, cabin conditioning equipment for manned space flight, and instrumentation available for conducting scientific experiments using unmanned earth satellites.

A large number of topics related to space-flight technology are treated very lightly or omitted entirely—for example, trajectories for orbital insertion or for interplanetary probes, automatic control and guidance, space orientation subsystems, electrical propulsion, testing and reliability, data processing, and so on. This is doubtless because the book was not intended to be an engineering text but rather to provide a general background on the basis of which the proper level for British astronautical effort might be discussed, a purpose to which it is very well suited.

Most American readers will be more interested in the papers of the second and third categories than those of the first. In general, the engineering subjects treated in the volume are handled in a competent and readable fashion. Accordingly, the book can be recommended either as an introduction to or as a review of these subjects.

Impact

Impact: The Theory and Physical Behavior of Colliding Solids. By Werner Goldsmith. Edward Arnold, London, 1960. Cloth, 6 × 9½ in., xv and 379 pp. $15.

REVIEWED BY J. T. FRASIER[5]

To the reviewer's knowledge, this book provides the first attempt at a comprehensive coverage of the subject of the behavior of colliding solids. Its purpose, as stated in the preface, is "to serve as a source of reference for workers in the fields of applied mechanics and certain areas of applied mathematics and physics, or as a text for an advanced course in these disciplines." To accomplish this purpose, the author has chosen to present his material with a sharp demarkation between theory and experiment with major emphasis on the former. The first five chapters of the book's total of seven are devoted almost entirely to an exposition of general theory and theoretical results. These initial chapters consist of a brief introduction and coverage of the topics of Stereo-Mechanical Impact, Vibrational Aspects of Impact, Contact Phenomena Produced by the Impact of Elastic Bodies, and Dynamic Processes Involving Plastic Strains. In these chapters little effort is given to description of the physical processes involved during impact phenomena, nor are the physical implications of the numerous theoretical results given with any detail. The final two chapters of the book, Results of Impact Experiments, and Dynamic Properties of Materials, are reviews of experimental techniques and results related to the theoretical topics covered in the initial chapters.

The amount of material the author has managed to incorporate in the book is extensive and the text is appended by an excellent bibliography. As a result, he has accomplished his purpose of providing a reference source. However, in the reviewer's opinion, the book would have been of greater value both as a text and as a reference for research workers if the sharp separation between the presentation of theory and experiment had not been made. The consequence of this is that the book is more a compendium of results than a unified treatment providing physical insight into the impact process as such.

[5] Professor, Division of Engineering, Brown University, Providence, R. I.

Four-Bar Linkages

Kinematics and Linkage Design. By A. S. Hall, Jr. Prentice-Hall, Englewood Cliffs, N. J., 1961. Cloth 7 × 10 in., xi and 162 pp. $8.50.

REVIEWED BY T. P. GOODMAN[6]

In industrial and military applications, the design of a mechanical linkage almost never occurs as an isolated problem. Usually the combined design of a linkage and the associated equipment can best be carried out by an engineer or designer with a broad background in mechanical design, rather than by a specialist who deals exclusively in kinematics. For this reason there has been a need for a book on kinematics at an intermediate level to provide information beyond that contained in the elementary textbooks (of which there are at least twenty) in a form that can be readily assimilated by a graduate or advanced undergraduate engineer as part of a curriculum in mechanical engineering design. Professor Hall's book admirably fills this need.

The book is limited primarily to four-bar linkages, although the principles developed can be applied to more complex link mechanisms as well. The first chapter is a survey of engineering applications of four-bar linkages with many intriguing examples. Graphical vector solutions for velocities and accelerations in linkages are then reviewed. The morphology of four-bar linkages is discussed in a chapter on "gross motions." There follow chapters on the theory and applications of coupler curves, path curvature, polode curvature, analytical design equations, and graphical design procedures for finite displacements. The unusual typography, clear illustrations, and interesting examples make the book a pleasure to read.

The book is concerned solely with kinematics in the classical sense, i.e., the study of motions without regard to the forces required to produce them. There is no discussion of dynamic effects in mechanisms, nor of the reciprocal relationship between force ratios and velocity ratios which can be exploited in designing a linkage for a desired nonuniform mechanical advantage.

This book, appropriately supplemented by material on forces and dynamic effects, can be heartily recommended as a textbook for graduate and advanced undergraduate mechanical-design curriculums, as well as for engineers and designers in industry.

Disks and Shells

Die Berechnung von rotierenden Scheiben und Schalen. By Kurt Löffler. Springer Verlag, Berlin, 1961. Cloth, viii and 241 pp. DM 42.

REVIEWED BY A. M. WAHL[7]

In this book the author has brought together a large amount of information, widely scattered throughout the literature, on methods for the elastic calculation of rotating disks and shells. The treatment is given from the viewpoint of the machine designer, and includes not only methods for disks having profiles such as are used in practical gas turbine and compressor disks, but also methods for calculating the effects of flanges, hubs, rims, ribs, etc., which are important design components. An unusual feature is the extensive treatment of rotating shells of various profiles such as are used in practice, and the wide use of matrix methods requiring digital computers. Another feature is the discussion of inverse methods of design whereby the disk profile is found for an assumed stress distribution. Stresses due to temperature, axial loading, and torque, as well as those due to centrifugal force are also treated.

[6] General Engineering Laboratory, General Electric Company, Schenectady, N. Y. Mem. ASME.

[7] Advisory Engineer, Westinghouse Research Laboratories, Pittsburgh, Pa.

Besides the well-known earlier methods of rotating-disk calculations such as those developed by Grammel and others, an extensive treatment is given of more recently developed procedures including difference methods and those which involve the division of the disk profile into a number of conical-shaped segments, which are then fitted together.

Since the author limits himself mainly to elastic conditions, very little information is given on such important practical subjects as the effects of plastic flow, creep, and fracture. In spite of this limitation, the book nevertheless should be of considerable interest and value to research men and designers.

Statistical Techniques

Statistical Theory and Methodology in Science and Engineering. By K. A. Brownlee. John Wiley & Sons, Inc., New York, N. Y., 1960. Cloth, 6 × 9 in., xi and 570 pp. $16.75.

REVIEWED BY WALTER FREIBERGER[8]

SCIENTISTS and engineers wishing to use modern statistical techniques but not content, on the one hand, with a book of recipes for the standard methods nor willing, on the other hand, to study the difficult and abstract recent developments in estimation and testing theory, will find the book under review an admirable guide. The mathematical prerequisites are slight and the level of exposition is reasonably high. About half the book is devoted to analysis of variance and regression analysis, and these topics are given a thoroughly useful treatment. The deductions of the various results are complete since the background is developed in the earlier chapters. There are enough numerical examples to illustrate the procedures without cluttering the book with numbers.

Fluid Dynamics

Handbook of Fluid Dynamics. By V. L. Streeter. McGraw-Hill Book Company, Inc., New York, N. Y. 1961. Cloth, 6½ × 9½ in., x and 1230 pp. $24.

REVIEWED BY J. KESTIN[9]

IT IS practically impossible to write a conscientious review of the Handbook, indeed of any handbook. The value of a handbook, as the name implies, lies in its ready availability for reference which can only be judged by extended use. This review, by necessity, is based on short acquaintance and on the application of quick tests, as it is impracticable to read, and even less, to study and absorb, the wealth of information contained in its more than a thousand pages.

The formula applied in the compilation of the Handbook was to select a panel of authorities, preferably authors of well-known books on individual branches of the subject, and to ask them to select, and then to compress into small space what they consider to be the essence of their particular specialty. The editor provided a thoughtful and well-conceived classification of the subject of fluid dynamics into branches under twenty-seven headings, but, unfortunately, did not go much further than that. The result is a collection of unevenly written articles, but not a homogeneous, well-rounded handbook.

The aim was to describe "new methods of attacking fluid dynamics problems .... the present status, latest theory, and the most promising methods of analysis in fields of application covering most of the engineering profession... The handbook is directed to the engineer or scientist with some background in fluid mechanics and mathematics." This is a formidable task, requiring the utmost of co-operation on the part of the editor and the contributors, a lack of which is evident, even on cursory examination, by the presence of many trivial repetitions. For example, the viscosity of a fluid is defined six times (Sections 1,2,5,6,9,22), sometimes in nearly identical terms, but not all of these definitions are listed in the Index; the Blasius solution is discussed twice (Secs. 9,15), stability of laminar motion is discussed twice (Secs. 5,8), and so on.

The Handbook can, therefore, be treated only as a collection of survey articles, and each of them must be judged alone on its merits. As might be expected, the standards are uneven. Some contributions are outstanding, a pleasure to read, and a source of easy and quick revision for specialists, or of excellent introduction for others. However, some contributions are quite weak and unsatisfactory and occasionally misleading. Moreover, very often the scope of the articles is far too narrow for the attainment of the previously stated purpose of the publication.

The Index, as already noted, leaves something to be desired, but the quality of the paper, printing, and binding is outstanding.

Boundary-Layer Theory

Boundary Layer Theory, fourth edition. By Hermann Schlichting, translated by J. Kestin. McGraw-Hill Book Company, Inc., New York N. Y., 1960. Cloth, 6½ × 8 in., xx and 647 pp. $16.50.

REVIEWED BY A. H. SHAPIRO[10]

THIS is the second English edition of a book which during the past ten years has become a standard textbook and reference work. In its present form it has been expanded by some 130 pages through numerous additions and modifications which bring the book up to date. The stated purpose remains unchanged, however, to provide for practicing and research engineers a theoretical foundation for the understanding and calculation of boundary-layer flows. As in earlier editions, however, the book goes further than this in that it rightly contains numerous experimental results which are useful in their own right and which also delineate the extent to which the current theories are valid.

In scope and organization there are no major changes. For instance, the statistical theory of turbulence is omitted on the grounds that it is not yet important for engineers.

The principal additions are on the following topics: exact solutions of the Navier-Stokes equations; boundary-layer control by suction; compressible boundary layers; boundary-layer transition; boundary-layer stability; calculation of turbulent boundary layers.

Congratulations again to Dr. Schlichting, and to the translator, Dr. Kestin, for conserving this most useful reference work against the flood of published literature.

[8] Associate Professor, Division of Applied Mathematics, Brown University, Providence, R. I.

[9] Professor, Division of Engineering, Brown University, Providence, R. I. Mem. ASME.

[10] Professor of Mechanical Engineering, Massachusetts Institute of Technology, Cambridge, Mass.

TRANSACTIONS OF THE ASME
Series E

Journal of
APPLIED MECHANICS
VOLUME 28 . SERIES E . NUMBER 4
December 1961

CONTENTS
CONTINUED

TECHNICAL PAPERS (Cont.)

601 Viscoelastic Effects in Birefringent Coatings (61—APM-23)
P. S. Theocaris and C. Mylonas

608 The Hump Deformation Preceding a Moving Load on a Layer of Soft Material (61—APMW-5)
G. R. Abrahamson and J. N. Goodier

611 The Rolling Contact of a Rigid Cylinder With a Viscoelastic Half Space (61—WA-8)
S. C. Hunter

DESIGN DATA AND METHODS

618 Stress Distribution at the Fillet of an Internal Flange, *K. E. Hofer, Jr., and A. J. Durelli*

BRIEF NOTES

Lowest Natural Frequency of Elastic Arc for Vibrations **624**
E. Volterra and J. D. Morell

The Bending of an Incomplete Torus of Rectangular Cross Section **628**
H. D. Conway and J. R. Moynihan

631 Disk Heated by Internal Source
T. D. Riney

633 The Integration of Some Expressions Arising in Beam Theory
A. Ormerod

DISCUSSION

634 Discussion of previously published papers by *W. A. Bassali and N. O. M. Hanna; C. P. Atkinson; I. U. Ojalvo and G. L. Bleckman; F. P. Beer*

BOOK REVIEWS

Unsteady Motion of Continuous Media **637**

Feedback Control Systems **638**

Theories of Engineering Experimentation **638**

Space Flight Technology **638**

Impact: Theory and Physical Behavior of Colliding Solids **639**

639 Kinematics and Linkage Design

639 Die Berechnung von rotierenden Scheiben und Schalen

640 Statistical Theory and Methodology

640 Handbook of Fluid Dynamics

640 Boundary Layer Theory

FOURTH U. S. NATIONAL CONGRESS OF APPLIED MECHANICS

University of California, Berkeley, Calif.

June 18—21, 1962

The U. S. National Congresses of Applied Mechanics are held every fourth year and are planned to supplement the International Congresses of Applied Mechanics.

Research workers are cordially invited to submit papers constituting original experimental or theoretical contributions to Applied Mechanics, including mechanics of rigid bodies and deformable solids, mechanics of fluids and gases, thermodynamics, and heat transfer.

It is expected that papers accepted will be published in the Proceedings of the Congress. **Complete papers and manuscripts must be submitted to the Chairman of the Editorial Committee before January 1, 1962. The final manuscript must be accepted before May 1, 1962.**

Inquiries regarding the Congress should be addressed to Professor W. Goldsmith, Secretary of Applied Mechanics Congress, University of California, Berkeley 4, Calif.